An Experimental Study in the Variation of the Near-Circular Polarisation Properties in Scarabaeoidae Beetles

Photonics Group
Department of Physics
Imperial College London

Ian Edward Carter

July 2017

Supervisors: Doctor K. Weir and Professor M. W. McCall.

This thesis is submitted in partial fulfilment of the requirements for the degree of Doctor of Philosophy (Ph.D) Imperial College London

The contents within this thesis are the author's own work, unless stated otherwise.

The copyright of this thesis rests with the author and is made available under a Creative Commons Attribution Non-Commercial No Derivative licence. Researchers are free to copy, distribute or transmit the thesis on the condition that they attribute it, that they do not use it for commercial purpose and that they do not alter, transform or build upon it. For any reuse or redistribution, researchers must clear to others the licence terms of this work.

Abstract

The scientific study of structural colour in nature dates back over 300 years. The structural colours being observed are a result of millions of years of evolution. It occurs in many different forms in nature from diffraction gratings to interference from multi layered structures and from plants to cephalopods.

This thesis focuses on the near circularly polarised (CP) reflection from the helicoidally arranged chitin within the shells of selected beetles from the Scarabaeoidae superfamily. An experimental setup was refined in order to measure broadband CP light in reflection from the beetles. A large variation in the left CP reflection was seen both within and between species, genera, subfamilies and families. This included broadband reflection from silver coloured beetles to narrower reflection of dominant green colour (other colours were observed). A wide variety of spectral shapes were observed including single wavelength peaks, multiple oscillations and peaks far apart. In the *Chrysina* genus several new species were observed to reflect both right and left CP light.

Several perturbations of the CP reflection were modelled based upon Berreman calculus. Further to the CP measurements electron, atomic force and scanning near-field optical microscope images were taken of both the helicoidal structure and surface of the beetles.

A fuller description of the polarisation of the reflected near CP light from the beetles' shells was obtained using a broadband Mueller Matrix (MM) ellipsometer, which was built and designed using liquid crystal variable retarders. From the MMs, the ellipticity, the degree of polarisation and azimuth angle were calculated. As with the CP measurements large variations were observed from highly polarised metallic to less polarised matt specimens.

This study of the beetle optical properties will help to inspire the design of various optical devices as well as the further biological investigation into beetles' polarised vision.

Acknowledgements

It has been quite a journey. I am thankful and feel lucky to have met and been supported by the many people around me. There are so many people to thank, and I apologise in advance if I leave somebody off the list.

It has been five amazing years since I first arrived at Imperial College and experienced these wonderfully colourful beetles as part of my MRes course in 2012. I was lucky enough to be able to continue to research such magnificent creatures for another four years as part of the PhD. Even after the PhD, entomology will most certainly be close to my heart.

This thesis would have not been possible if it were not for both of my supervisors (Doctor Kenny Weir and Professor Martin McCall).

I am very grateful firstly to Kenny, who always had the time to discuss, guide and inspire me in my many experimental investigations.

I also owe a large gratitude to Martin, whose advice and thorough mathematical explanations spurred me on to acquire a deeper understanding of the subject.

I want to thank the Natural History Museum London for the opportunity to investigate numerous specimens of beetle and general advice upon beetles. I wish to particularly thank Professor Andrew Parker for his insightful views upon the subject.

Other people I wish to thank are various members of the Experimental Solid State group at Imperial College, particularly Professor Chris Phillips and William Hart for their help and assistance with the understanding and collaborating on imaging beetles structures.

I also wish to thank various Post Docs for their help, including Sunil who was always there with help and advice.

I need to thank the EPSRC for their funding of my PhD, without them, this would not be possible.

A big thank you to all my fellow students at Imperial College, from Noemi, David, Jack, Ilya, Cheryll, Yuchen, Chengze and anyone else I have overlooked. For all the laughs, frustrations and general good times.

I would also like to thank the administrative team in the office of Marcia, Judith and Sanja for always being friendly faces and helping me with paperwork which I was rather confused with.

I would also like to thank my family for the constant support. From my grandparents, parents, sister and nephew, I thank you all from the bottom of my heart.

To my wonderful and supportive girlfriend Peggy, thank you for your continued support and the simply putting up with me whilst writing my thesis. It has been wonderful, now a whole new world awaits!

Abbreviations

AFM	Atomic Force Microscope
CLC	Cholesteric Liquid Crystal
(L/R)CP	(Left/Right) Circularly Polarised
(S/T)EM	(Scanning/Transmission) Electron Microscope
HCP	Hexagonally Close Packed
LCVR(s)	Liquid Crystal Variable Retarder(s)
LP	Linear Polariser
Ma	Million Years Ago
MM(s)	Mueller Matrix/Matrices
MMSE	Mueller Matrix Spectra Ellipsometry
NIR	Near Infra-Red
QP	Quarter Waveplate
(s-)SNOM	(Scattering-) Scanning Near-Field Optical Microscope
UV	Ultraviolet

Table of Figures

1.1	Photographs of an *Ischiopsopha bifasciata* beetle through a LCP filter (left) and RCP filter (right). This specimen was collected in Indonesia in 2014. All the specimens in this study were measured from the top of the head to the bottom of the abdomen (or elytra if longer), this specimen measured 29mm.
1.2	Photographs of Pollia condensate fruits of A) a single fruit specimen and B) a cluster of fruits. Used with permission, from [1].
2.1	Polarisation ellipse with polarimetric angles, displaying left handed elliptical polarisation, with the beam propagating out of the page. θ is the azimuth angle and ε is the angle of ellipticity.
3.1	Reflection grating, showing the 1st (m=1) and 2nd (m=2) diffracted orders.
3.2	a) Scanning Electron Microscope (SEM) image of the diffraction grating in a *Sphaeridiinae gen. sp.* Beetle and b) a photograph showing the 1st, 2nd and 3rd order diffraction reflections. Used with permission, from [2].
3.3	Light incident from the medium of refractive index ni, onto a single layer of film (of thickness d) with refractive index nf, which is placed on a substrate medium of refractive index ns. The variables are incident angle of light (βi) and in the inside the film (βf) The positions along the beam paths are labelled a, b, c and e.
3.4	Light reflection from a multi-layered structure embedded upon a substrate, with the light ray paths shown in red.
3.5	a) Photograph of a *Chrysochroa fulgidissima* beetle with a 5mm scale bar, with Transmission Electron Microscope (TEM) image cross sections in the b) green and c) purple sections of the *Chrysochroa fulgidissima* shell with a 1µm scale bar. Used with permission, from [3].
3.6	Circularly polarising signal in the stomatopod crustacean *Odontodactylus cultrifer* (male). (A) Photograph where the scale equates to 1 cm. (Photograph by Chrissy Huffard.) (B) More detail of the telson keel (as framed in [A]) photographed through a left-handed circular polariser. (C) The same as (B) except through a right circular polariser. Used with permission, from [4].
3.7	Polarised reflection from the *Pollia condensata* fruit. (A) Left handed and (B) Right handed optical micrographs of the same area of the fruit under epi-illumination. The insets show a zoom of the central areas, with white lines marking the edges of the cells. Both images were obtained using a × 10 objective. Used with permission, from [1].
3.8	a) Photograph of a juvenile (blue) and adult (green) leaf of *Danaea nodosa*. b) TEM transverse section image of the outer cell wall of a juvenile leaf with a scale bar of 300nm. Used with permission, from [5].
3.9	TEM image through a micro mirror on a *Papilio palinurus* green scale, with an inset SEM image of the surface of the scale. Where the scale bar is of 1µm for the main image and 7µm for the inset image. Used with permission, from [6].
3.10	(a) Confocal pseudo-2D micrographs of *Papilio palinurus* in fluorescence reflection mode, showing a single wing scale in xy, yz, and xz orientations. The yz and xz images correspond to the area along the red dotted lines in xy image. An optical micrographs of *Papilio palinurus* with incident white light with (b) a single linear polariser and (c) under crossed polarisers. The reflection from the centre/bottom of the bowls is extinguished under crossed polarisers. (d) White light diagram of the reflection from the bottom and sides of the concavity. Used with permission, from [7].
3.11	a) Photograph of *L. augustus*. b) Optical micrograph under white-light illumination of individual scales of *L. augustus*. c) SEM image cross section of a single scale. d) Cross-sectional SEM image of a scale. Used with permission, from [8].
3.12	Bright White reflection from beetle scales. (a,c), Photographs of *Cyphochilus* and *Lepidiota stigma* beetles, respectively. (b,d), SEM images of the cross-section of the scales of the respective species. Used from [9] under CC 4.0 License.
3.13	a) Blue rump/faced mandrill, adpated from [10] by Brian Michelsen (under CC 2.0) b) Vervet monkey blue scrotum, from [11] by Bjørn Christian Tørrissen (under CC 3.0).
3.14	TEM images of collagen arrays from structurally coloured mammal skin. a) Male mandrill facial skin at 40000×. Scale bar, 250nm. b) Vervet monkey (*Cercopithecus aethiops*) scrotum at 25·000×. Scale bar, 500nm. Used with permission, from [12].

3.15	*Enallagma civile* dragonfly, with a strong structural blue colour. Adapted from [13] (Andrew C) (under CC 2.0).
3.16	TEMs of the structure of the familiar bluet, *Enallagma civile*, showing (A) The cuticle and epidermal pigment cells with a scale bar of 5μm and (D) Light- scattering nanospheres, with a scale bar of 500nm. Where abbreviations are used: c, cuticle; cm, cell membranes of neighbouring pigment cells; s, light-scattering spheres. Used with permission, from [14].
3.17	SEM of scattering structure in (a) *Heikertingerella sp*. (Chrysomelidae: Alticinae), and (b) *Mychocerus sp*. (Cerylonidae). (c) Photo of *Mychocerus sp*. (Cerylonidae) with diffuse reflectance. Used with permission, from [2].
3.18	Diagram of cephalopod skin with brown, red and yellow chromatophores, iridophores and leucophores in two different states of chromophore expansion (a) and (b), with three distinct ray paths (1), (2) and (3). (c) Photographs of (i) cuttlefish skin showing leucophores (white), chromatophores (yellow, red and dark brown) and irridophores (blue-green) and (ii) squid skin, showing chromatophores (yellow, red and brown) and iridophores (yellow and red). Used with permission, from [15].
3.19	a) Diagram of the porous photonic structure of a male *Hoplia coerulea* beetle. Where the water droplets are on the permeable envelope (1) and transfer through the permeable envelope (2) to the photonic structure. b) Photograph of a beetle's scale in wet and dry states with water, with scale of 20μm. Adapted from [16] (under CC 4.0).
3.20	Photographs of the Panamanian Tortoise beetle (*Charidotella egregia*) transforming from its a) normal gold state to b) an in between state and the c) an alarmed red state. Used with permission, from [17].
3.21	Photographs and reflection spectra of the chameleon grasshopper (*Kosciuscola tristis*) at a) over 25℃ and b) under 10℃. Used with permission, from [18].
3.22	Diagram of the carapace of the chameleon grasshopper (*Kosciuscola tristis*) at a) over 10℃ and b) under 25℃. Reproduced from Key and Day (1954), with permission from CSIRO Publishing [19].
3.23	Schematic of the gradual change in orientation of the thread-like molecules between consecutive layers of chitin material. The half pitch distance relates to a 180° rotation of the chitin molecules. Published by the author in [20].
3.24	TEM microscope image of fibrous chitin in helicoidal layers from a green *Chrysina boucardi* beetle. The half pitch distance is shown with red arrows. Adapted from [21] (under CC 3.0).
3.25	Schematic of structural perturbations to a single pitch values in beetles of a) multiple distinct pitches (cross sectional view), b) a chirped structure or varying pitches (cross sectional view), c) sudden jump in the molecule orientation (if all the chitin layers orientations (represented by the lines) could be seen at once, between two pitches) (top view) and d) an absorbing layer within the material (cross sectional view). Published by the author in [20].
3.26	EM image of a unixial half waveplate-like layer (b) of a *Chrysina resplendens* beetle between helicoidal stacks (a). Used with permission, from [22].
3.27	Contour plot of incident angle (θ, this figure only), against wavelength (λ), for a *Cetonia aurata* beetle, showing a) the Fully Normalised MM element m_{41} (which is the same as $\mathbf{M}_{30}$ in this study) b) the degree of polarisation (P), c) the ellipticity (e) and d) the modulus of azimuth angle ($\lvert\alpha\rvert$ (this figure only)). Used with permission, from [23].
3.28	Contour plot of incident angle (ϕ), against wavelength (λ), for a *Chrysina macropus* beetle, showing a) the Fully Normalised MM element m_{41} (which is the same as $\boldsymbol{M}_{30}$ in this study), b) the degree of polarisation (*P*), c) the ellipticity (*e*) and d) the modulus of azimuth angle ($\lvert\theta\rvert$). Note these plots have been rescaled due to their low values. Used with permission, from [24].
3.29	Contour plot of incident angle (ϕ), against wavelength (λ), for a *Chrysina chrysargyrea* beetle, showing a) the Fully Normalised MM element m_{41} (which is the same as $\boldsymbol{M}_{30}$ in this study), b) the degree of polarisation (*P*), c) the ellipticity (*e*) and d) the modulus of azimuth angle ($\lvert\theta\rvert$). Note these plots have been rescaled due to their low values. Used with permission, from [24].
3.30	Contour plot of incident angle (ϕ), against wavelength (λ), for a *Chrysina resplendens* beetle, showing a) the Fully Normalised MM element m_{41} (which is the same as $\boldsymbol{M}_{30}$ in this study), b) the degree of polarisation (*P*), c) the ellipticity (*e*) and d) the modulus of azimuth angle ($\lvert\theta\rvert$). Note these plots have been rescaled due to their low values. Used with permission, from [24].
3.31	A *Chalcothea resplendens* beetle viewed directly on the right of each image and in a mirror on the left with the imaged viewed through a) a LCP and b) a RCP filter.

3.32	A) an optical micrograph of a green area in a *Chrysina gloriosa*'s shell, with B) corresponding vornoi analysis of blue pentagons, white hexagons and red heptagons. Used with permission, from [25].
3.33	SEM cross section of: a) green area and below, the optical axis intersects the surface polygon in its centre. b) silver stripe. The distance between two consecutive lines of equal contrast is related to the helicoidal pitch, while the helicoidal axis is perpendicular to the lines. Used with permission, from [26].
3.34	100x100µm images of the surfaces of (a) a metallic *Chrysina aurigans* and (b) a matt green *Chrysina aurora* [27]. Reprinted from Opt. Mater. Express vol. 4, no. 12, pp. 2632-2645, 2014 under a CC BY license, with permission from OSA, original copyright 2014.
3.35	Blaze grating reflection setup, with the Littrow configuration shown by the green line.
3.36	SEM of a blazed grating structure *Mycterophallus sp*. with a) a view of the surface and b) a cross sectional view, revealing an 8.5° blazed grating. Used with permission, from [28].
3.37	Efficiency of s (dashed line) and p (solid line) polarised light on a blazed grating with an angle of 9°. (It should be noted the grating in this figure was labelled as d, whereas in this thesis it is labelled a) [29]. Reprinted from Appl. Opt. vol. 16, no. 10, pp. 2711-2721, 1977 under a CC BY license, with permission from OSA, original copyright 1977.
3.38	Chromatogenesis of *Cetonia aurata* from 0 hours top left to 60 hours in the bottom right photograph. Used with permission, from [30].
3.39	A schematic of a beetle's cuticle structure. Used with permission, from [31].
3.40	Pitch variation with depth (z) in (a) red and gold *Chrysina aurigans* and (b) silver and gold *Chrysina chrysargyrea*. Reproduced from [32] under CC 4.0.
3.41	a) Diagram of a twisted column formation of a chiral sculpted thin film by serial bideposition. Used with permission, from [33]. b) SEM of magnesium fluoride twist column structure on glass substrate, with a pitch of 360nm. Used with permission, from [34].
3.42	Titania chiral sculpted thin films through a) a left handed (LH), b) no filter and c) a right handed (RH) filter. Used with permission from [33].
3.43	Diagram of eight rhabdoms from an ommatidium in the midband from the eye of the stomatopod *Odontodactylus*. On the left the R8 rhabdomere acts as a quarter wave retarder and converts circularly polarised light (spirals) into linear polarised light which can then be detected by the rhabdomeres R1–7 beneath. The distinction between left circularly polarised (LC-pol) and right circularly polarised (RC-pol) is made by the microvillar orientations of the rhabdoms (R1-7). The processing from LCP and RCP light to +45° and -45° respectively can be seen in the diagram on the right. Used with permission, from [4].
3.44	Keyrings and pendants of beetles; 1-Chalcothea resplendens, 2-Mimela splendens, 3-Popillia mutans, 4-Popillia mongolica, 5-Popillia flavosellata, 6- Mimela splendens, 7-Protaetia brevaitis, under normal illumination.
3.45	A few examples of stamps with beetle with helicoidal structures from various countries a) Euchirinae:*Cheirotonus battareli* from Vietnam b) Rutelinae:*Chrysina (plusiotis) argenteola* from Cuba, c) Scaraeinae:*Garretta nitens* from South West Africa (presently Namibia), d) Trichiinae:*Gnorimus nobilis* from the United Kingdom, e) Melolonthinae:*Melolontha melolontha* from Guernsey and f) Cetoniinae:*Jumnos ruckeri tonkinensis* from Vietnam.
3.46	Taxonomic map of subfamilies that contain optically active Coleoptera. The classifications hierarchical form going from the highest on the left to the lowest on the right. It should be noted that below subfamily comes genus then species followed by subspecies. It should also be noted that some classifications use tribe between subfamily and genus. Published by the author in [35].
3.47	Photograph of a male *Phanaeus mexicanus* beetle from Mexico.
3.48	Photograph of a female *Agestrata luzonica* beetle from the Philippines.
3.49	Photograph of a Gnorimus nobilis beetle from Poland.
3.50	Photograph of a *Chrysina adelaida* beetle.
3.51	a) Gold and b) silver colour morphs of *Chrysina chrysargyrea* from Costa Rica.
3.52	a) Low reflecting green and b) high reflecting gold colour morphs of *Chrysina boucardi*.
3.53	Photograph of a *Phaenomeris besckei* beetle from Tanzania.
3.54	Photograph of an *Agaocephala urus* beetle from Brazil.
3.55	Photograph of a *Pyronota festiva* beetle from New Zealand, image from [36].
3.56	Photograph of a Male of *Cheirotonus battareli* beetle from Vietnam.
3.57	*Ceratocanthus vicarious*, in a) dorsal and b) lateral views. From [37] under CC BY-NC-ND 4.0.

4.1	The RealD 3D glasses in side profile, with the orientation of light propagation through them shown by the red arrow.
4.2	Transmission of a) LCP light and b) RCP light through LCP and RCP lenses (filters), over the wavelength range 450nm to 1000nm.
4.3	Side view of the setup for photographing beetles through CP filters.
4.4	Typical main body parts of a beetle (*Plaesiorrhinella plana cincta*). This photograph is taken without any filter.
4.5	Four typical beetles whose CP reflection were measured from a) the fused scutellum (Cetoniinae:*Lomaptera geelvinkiana*), b) top of the left elytra (Scarabaeinae:*Garreta azureus*), c) top of the left elytra (Rutelinae:*Anplognathus aereus*) and d) pronotum (Rutelinae:*Strigidia sanctijacobi*). These photographs were taken without any filters.
4.6	The broadband experimental CP reflection setup using a beetle sample, with the full angle between the two arms being 22.5° (3sf), it should be noted that this diagram is not to scale and is a simplified schematic.
4.7	Path of unpolarised light entering a polarising beamsplitting cube and being split into two perpendicular rays, the s-polarised and p-polarised rays.
4.8	a) The progression of light through the Fresnel rhomb. At position 1 linearly polarised light must be present with ±45° polarisation. It will then become elliptically polarised upon the first total internal reflection at position 2. Finally it will become CP at position 3 after the second total internal reflection. b) The input linear polarisations with the corresponding CP outputs are being shown on the left.
4.9	Plot of the Sellmeier equation for wavelength between 400nm and 1000nm for BK7 glass.
4.10	Plot of the variation in the phase difference from 45° upon each reflection within the Fresnel Rhomb against wavelength, setting the internal angle of the Fresnel Rhomb as 55.33° (with an error of ±0.833°) as given by the manufacturer.
4.11	LCP light input and response on a system configured using two different spot sizes, with a small spot of $1mm^2$ (using a focusing lens of f=25mm focal length) and a larger spot of $2mm^2$ (using a collecting lens of f=40mm) upon a *Lomaptera pseudodichropus* beetle.
4.12	Intensity plot from the system with a mirror in LR configuration, demonstrating the scaling of the graphs with increasing time base. Starting from an initial time base of 20ms increasing to 80ms at 20ms intervals and setting a boxcar of five and averaging of the spectra of one.
4.13	Plot comparing the ratio of the signal for 1 and 50 averages compared to one of 100 averages (ie the signals divided by the 100 average signal), with a time base of 90ms and boxcar of zero.
4.14	Intensity plot of the background demonstrating the difference to the signal between not using the boxcar method (i.e. zero) and a boxcar of five adjacent points.
4.15	Ratio of the LR signals varying with time from a reference system using a mirror. All are given as ratio to a signal reading which was taken at half an hour.
4.16	The ratio of the LR signals varying with number of samples taken from a reference system using a mirror, all are ratios to the initial reading.
4.17	Two sets of CP reflection spectra, a) and b) from the elytron of a red Popillia sp. beetle, collected from Mikumi National Park, Tanzania in 2013.
4.18	Two sets of CP reflection spectra, a) and b) from the elytron of a *Chrysina resplendens* beetle, from Cerro Bellavista, Rio Guacimo, Costa Rica in 2015.
4.19	CP reflection spectra from the elytron of a *Repsimus aeneus* beetle. This specimen was collected from Polly Creek, Garradunga, North Queensland, Australia in 2014. The specimen measures 24mm.
4.20	CP reflection spectra from the pronotum of a *Melolontha melolontha* beetle. This specimen was collected from Bourg-le-Comte, Saone et Loire, France in 2013. The CP spectra were taken with an integration time of 500ms. The specimen measures 31mm.
4.21	The difference in colour of the pronotum of another *Melonontha melolontha* beetle through a LCP filter on the left and RCP filter on the right.
4.22	CP reflection spectra from the pronotum of an *Augoderia nitidula* beetle. This specimen was collected from Nova Fiburgo, Rio de Janiero, Brasil in 2012. The specimen measures 19mm.
4.23	CP reflection spectra from the pronotum of a female *Cheirotonus battareli* beetle. This specimen was collected from Sapa Mountain, Lao Cai, Vietnam in 2015. The specimen measures 54mm.
4.24	CP reflection spectra from the elytron of a *Gnorimus nobilis* beetle. This specimen was collected from Poland in 2015. The specimen measures 19mm.

4.25	Colour morphs of the species *Gnorimus nobilis*. Used with permission from [38].
4.26	CP reflection spectra from the elytron of a *Phaenomeris besckei* beetle. This specimen was collected from Mikumi-Udzungwa, Tanzania in 2009. The measured wavelength scale was 440-1000nm for this beetle. The CP spectra were taken with an integration time of 500ms. The specimen measures 21mm.
4.27	CP reflection spectra from the gold part of the pronotum of a *Diabroctis mimas* beetle. This specimen was collected from Campo Zanja Moroti, Concepción, Paraguay in 2007. The specimen measures 31mm.
4.28	CP reflection spectra from the elytron of a Protaetia angustata pyrodea beetle. This specimen was collected from Padau, Italy in 2012. The specimen measures 23mm.
4.29	CP reflection spectra from the elytron of a *Ceratocanthopsis fulgida* beetle. This specimen was collected from Belizon, French Guiana in 2015. The specimen measures 3mm.
4.30	CP reflection spectra from the elytron of a *Chrysina cupreomarginata* beetle. This specimen was collected from Cerro Chompipe, Costa Rica in 2015. The specimen measures 21mm.
4.31	CP reflection spectra from the elytron of a) a brown and b) a green *Chrysina tricolour* beetle. These specimens were collected from Cerro de la Muerta, Costa Rica in 2014 and 2013 respectively. The CP spectra were taken with an integration time of 500ms. The specimens measure a) 25mm and b) 25mm.
4.32	CP reflection spectra from the elytron of a *Chrysina clypealis* beetle. This specimen was collected from Costa Rica in 2015. The specimen measures 24mm.
4.33	CP reflection spectra from the elytron of a) a silver, b) a gold and c) a red *Chrysina optima* beetle. The silver specimen was collected from Cerro Chompipe, the gold specimen from Cartago, Orosi, and the red from Cerro las 3 Marias, all in Costa Rica in 2015. The specimens measure a) 24mm, b) 24mm and c) 26mm.
4.34	CP reflection spectra from the elytron of a) a green and b) a brown *Chrysina modesta* beetle. The specimens were collected in Ville de Bravo, Mexico in 2016. The CP spectra were taken with an integration time of 500ms. The specimens measure a) 33mm and b) 34mm.
4.35	CP reflection spectra from a) the golden elytron and b) red pronotum of a metallic and c) the elytron of a matt green *Chrysina boucardi* beetle. The gold specimen was collected from Caño Sucio, Chiriqui Grande, Bocas del Toro, Panama in 2012, whilst the green was collected from Limon, Costa Rica in 2015. The specimens measure a) 32mm and b) 29mm.
4.36	CP reflection spectra from a) the red pronotum b) the predominantly red area of the elytron and c) the predominantly green area of the elytron of a *Chrysina vitoriana* beetle. This specimen was collected from Sierra de Juarez, Oaxaca, Mexico in 2013. The CP spectra were taken with an integration time of 500ms. The specimen measures 31mm.
4.37	CP reflection spectra from the elytron of a *Chrysina chalcothea* beetle. This specimen was collected from Cerro de la Muerta, Costa Rica in 2015. The specimen measures 25mm.
4.38	CP reflection spectra from the elytron of a silver *Chrysina limbata* beetle. This specimen was collected from Costa Rica in 2015. The specimen measures 25mm.
4.39	CP reflection spectra from the elytron of a *Chrysina turckheimi* beetle. This specimen was collected from Camino La Fraternidad a El Bojonal, San Marcos, Guatemala in 2012. The CP spectra were taken with an integration time of 500ms. The specimen measures 24mm.
4.40	CP reflection spectra from the elytron of a *Chrysina macropus* beetle. This specimen was collected from Venta Grande, Puebla, Mexico in 2004. The CP spectra were taken with an integration time of 500ms. The specimen measures 33mm.
4.41	Photograph of a) a *Chrysina cunninghami*, b) a *Chrysina moroni* and c) a *Chrysina purulhensis* specimen. Used with permission from K. Robacker and also [39].
4.42	CP spectra of *Lomaptera* species, where the LL spectrum is defined as a) Single peak (S) (*L. soror*), b) Double Close (DC) (*L. humeralis*), c) Oscillations After (OA) (*L. helleriana*), d) Oscillations Before (OB) (*L. soror*), e) Double Apart (DA) (*L. geelvinkiana*), f) Not Classified (NC) (*L. soror*).
4.43	Ratios of LL spectral shape variation within and between different species of the *Lomaptera* genus. The number in brackets denotes the number of specimens investigated.
4.44	Calculated mean pitch variations (from the reflection spectra peaks) with standard deviation error bars of the beetles of different spectral shapes in the *Lomaptera* genus, where 1 and 2 after double close and apart labels relate to the lower and higher peaks respectively.
4.45	Calculated mean pitch variations (from the reflection spectra peaks) with standard deviation error bars of different species from the *Lomaptera* genus.

4.46	CP reflection spectra from the elytron of a *Mycterophallus duboulayi* beetle.
4.47	LL CP spectra of *Mycterophallus duboulayi*, the spectral shapes are defined as a) Single (S), b) Double Close (DC), c) Oscillations After (OA), d) Oscillations Before (OB) and e) Not Classified (NC).
4.48	Distribution of the LL spectral type of *Mycterophallus duboulayi* beetles.
4.49	Distribution of mean peak wavelength values with standard deviation errors of the main peak in the LL spectrum by spectral type for *Mycterophallus duboulayi* beetles.
4.50	CP reflection spectra from the elytron of a *Thaumastopeus pugnator* beetle. This specimen was collected from Mount Talang, West Sumatra, Indonesia in 2015. The species measures ~34mm.
4.51	LL CP spectra of *Thaumastopeus pugnator* specimens, where the spectra have a) two, b) three and c) four peaks.
4.52	LL spectral distribution of numbers of peaks of *Thaumastopeus pugnator* beetles.
4.53	Distribution of mean peak wavelength values with standard deviation errors of the highest and lowest peaks in the LL spectrum of each number of peaks for the *Thaumastopeus pugnator* beetles. The number 1 corresponds to the lowest peak and the higher number corresponds to the highest peak value of each spectral shape. Dashed lines were added to highlight the trends of the lower and upper peaks.
4.54	CP reflection spectra from a green part of the elytron of a *Protaetia brevitarsis* beetle. This specimen was collected in Hubei, China in 2013. The species measures ~24mm.
4.55	LL CP spectra of *Protaetia brevitarsis* specimens, where the spectra have a) three, b) four, c) five, d) six, e) seven, f) eight and g) nine peaks.
4.56	LL spectral distribution of numbers of peaks of Protaetia brevitarsis beetles.
4.57	Distribution of mean peak wavelength values with standard deviation errors of the highest and lowest peaks in the LL spectrum of each number of peaks for the *Protaetia brevitarsis* beetles. The number 1 corresponds to the lowest peak and the higher number corresponds to the highest peak value of each spectral shape. Dashed lines were added to highlight the trends of the lower and upper peaks.
4.58	LL CP spectra of *Cetonia auruata aurata* specimens, where the LL spectra are defined as a) Single peak (S), b) Double Close (DC), c) Triple (T), d) Oscillations After (OA), e) Oscillations between peaks (X), f) Unclassified (UC). The specimens in this study were measured as ~20mm.
4.59	Distribution of the LL spectral types of *Cetonia aurata* beetles. Published by the author in [35].
4.60	Mean peak wavelength variations with standard deviation error bars of the beetles of different spectral shapes in the species *Cetonia aurata aurata*. The 1, 2 and 3 after DC and T correspond to the first, second and third peaks respectively. The Xi and Xf represent the initial and final peaks in the X shaped spectra. Dashed lines were added to highlight the trends of the lower and upper peaks.
4.61	CP reflection spectra from the right elytron of an *Ischiopsopha aruensis* beetle. This specimen was collected from Kai Besar Island, Indonesia in 2014. The species measures ~24mm.
4.62	LL CP spectra of *Ischiopsopha aruensis* specimens, where the spectra have a) two, b) three and c) four peaks.
4.63	LL spectral distribution of numbers of peaks of *Ischiopsopha aruensis* beetles.
4.64	Distribution of mean peak wavelength values with standard deviation errors of the highest and lowest peaks in the LL spectrum of each number of peaks for the *Ischiopsopha aruensis* beetles. The number 1 corresponds to the lowest peak and the higher number corresponds to the highest peak value of each spectral shape. Dashed lines were added to highlight the trends of the lower and upper peaks.
4.65	CP reflection spectra from the right elytron of an *Agestrata luzonica* beetle. This specimen was collected from the Philippines in 2014. The species measures ~37mm.
4.66	LL CP spectra of *Agestrata luzonica* specimens, where the spectra have a) two, b) three, c) four, d) five, e) six and f) seven peaks.
4.67	LL spectral distribution of numbers of peaks of *Agestrata luzonica* beetles.
4.68	*Agestrata luzonica* LL spectra (Black) and the line of the maximum peak intensity/exp(1) (red), with the intersections between the two shown with a dashed blue line.

4.69	Distribution of mean wavelength intersect values with standard deviation errors of the highest and lowest peaks in the LL spectrum of each number of peaks for the *Agestrata luzonica* beetles. The number 1 corresponds to the lower boundary and the higher number corresponds to the higher boundary of each spectral shape. Dashed lines were added to highlight the trends of the lower and upper peaks.
4.70	CP reflection spectra from the scutellum of a *Protaetia himalayana* beetle. This was a captive bred specimen from 2015, which originated from Thailand. The species measures ~21mm.
4.71	CP reflection spectra from the scutellum of an under developed *Protaetia himalayana* beetle. This was a captive bred specimen from 2015, which originated from Thailand.
4.72	LL CP spectra of *Protaetia himalayana* specimens, where the spectra have a) two, b) three and c) four peaks.
4.73	LL spectral distribution of numbers of peaks of *Protaetia himalayana* beetles.
4.74	Distribution of mean peak wavelength values with standard deviation errors of the highest and lowest peaks in the LL spectrum of each number of peaks for the *Protaetia himalayana* beetles. The number 1 corresponds to the lowest peak and the higher number corresponds to the highest peak value of each spectral shape. Dashed lines were added to highlight the trends of the lower and upper peaks.
4.75	CP reflection spectra from the elytron of an a) red, b) green, c) blue and d) light green *Popillia sp.* beetles. These specimens were collected from Mikumi National Park, Tanzania in 2013. The sizes of the different coloured popillia were a) ~12mm, b) ~13mm, c) ~11mm and d) ~11mm.
4.76	Distribution of different colours of *Popillia sp* from Mikumi National Park, Tanzania.
4.77	Distribution of the main peaks in the LL spectra of the blue, green and red *Popillia sp*, whilst the lowest peak (P1) and highest peak (P2) of the light green *Popillia sp* are analysed. The mean values are calculated and standard deviation used in the error bars.
4.78	CP reflection spectra from the elytra of a) a blue, b) a green-red, c) yellow-purple and d) black *Cetonia aurata pisina* beetles. These specimens were collected from Venaco, Haute-Corse, France in 2015. The specimens measure a) 21mm, b) 17mm, c) 20mm, and d) 20mm.
4.79	CP reflection spectra from the elytra of black, blue, green and red *Cetonia carthami* beetles. These specimens were collected from Iglesias, Sardinia, Italy in 2013. a) and b) were taken with an integration time of 500ms and c) and d) with an integration time of 100ms. The specimens measure a) 16mm, b) 16mm, c) 16mm and d) 16mm.
4.80	CP reflection spectra from the a) elytron and b) pronotum of a male and c) the elytron of a female *Viridimicus cyanochlorus* beetles. These specimens were collected from San Sebastian, Oaxaca, Mexico in 2013. The specimens measure a) 27mm and c) 23mm.
4.81	CP reflection spectra from the elytron of a Protaetia mirifica beetle. This specimen was collected from Bois de Païolive, Ardèche France in 2013. The specimen measures 26mm.
4.82	CP reflection spectra from a green part of the elytron of a *Plectrone tristis* beetle. This specimen was collected in Sancary, Java, Indonesia in 2008. The specimen measures 27mm.
4.83	CP reflection spectra from a) the red pronotum and b) the blue-green elytron of a *Protaetia speciosa jousselini* beetle. The specimen was collected from Turkey in 2014. The specimen measures 28mm.
4.84	Photograph of a variation of a *Protaetia speciosa jousselini* beetle which has blueshifted colours. The specimen measures 27mm.
4.85	CP reflection spectra from the right elytron in the orange part a) and the blue part b) of an *Ischiopsopha jamesi coerulea* beetle. This specimen was collected from Papau New Guinea in 2014. The CP spectra were taken with an integration time of 500ms. The specimen measures 27mm.
4.86	Photographs of *Heterorrhina sexmaculata*, through a range of CP filters. The last photograph demonstrates the large angular variation in colour of this beetle. The specimen measures 26mm.
4.87	CP reflection spectra from the elytron of an *Anoplognathus aureus* beetle. This specimen was collected from Polly Creek, Garradunga, North Queensland, Australia in 2015. The specimen measures 17mm.
4.88	CP reflection spectra from the pronotum of an *Anoplognathus porosus* beetle. This specimen was collected from Polly Creek, Garradunga, North Queensland, Australia in 2015. The specimen measures 18mm.

4.89	CP reflection spectra from the elytron of a *Chrysophora chrysochlora* beetle. This specimen was collected in Peru in 2015. The CP spectra were taken with an integration time of 500ms. The specimen measures 29mm.
4.90	CP reflection spectra from the elytron of a *Rutela laeta* beetle. This specimen was collected from San Fernando de Apure, Venezuela in 2016. The CP spectra were taken with an integration time of 500ms. The specimen measures 21mm.
4.91	CP reflection spectra from a) the green part and b) the red part of the elytron of a *Mimela ohausi* beetle. This specimen was collected from Phou Pane Mountain, Houaphanh, Laos in 2012. The CP spectra were taken with an integration time of 500ms. The specimen measures 17mm.
4.92	CP reflection spectra from the pronotum of a male *Phanaeus mexicanus* beetle. This specimen was collected from Catemaco, Veracruz, Mexico in 2004. The specimen measures 23mm.
4.93	CP reflection spectra from the scutellum of a green *Phaenomeris besckei* beetle. This specimen was collected from Tanzania. The CP spectra were taken with an integration time of 500ms. The specimen measures 20mm.
4.94	Photographs of a Cetoniinae:*Rhomborhina gigantea* beetle through a) a left circularly polarised filter, b) a right circularly polarised filter. The specimen measures 37mm.
4.95	Photograph of the reflected spot from the scutellum of a *Rhomborhina gigantea* beetle.
4.96	CP relectance spectra from the scutellum of a *Rhomborhina gigantea* beetle from a) the centre reflection spot and b) the green halo. The black spectra is LL, red is LR, blue is RL and pink is RR. The CP spectra were taken with an integration time of 500ms.
4.97	Photographs with CP filters of the upper side and underside of a *Plectron endroedii* beetle.
4.98	Photographs with CP filters of the upper side and underside of a *Protaetia cuprea cuprea* beetle.
4.99	Photographs with CP filters of the upper side and underside of a *Chrysina chrysargyrea* beetle.
4.100	Photographs with and without CP filters of the upper side and underside of a *Chrysina cupreomarginata* beetle.
4.101	Photographs without a filter of a *Protaetia speciosa jousselini* specimen at different angles.
4.102	Photographs without a filter of a *Chrysina curoei* specimen at different angles.
4.103	Photographs without a filter of a *Garreta azureus* specimen at different angles.
5.1	Co-ordinate system used in this derivation.
5.2	Showing two planes distance d apart, with the field coefficients $\vec{a}$ between them being transformed by the phase matrix $\hat{A}_d$. Based upon Figure 4.4 from [40], with permission.
5.3	Showing the tranformation of the total field across the layer, by the characteristic matrix of that layer. Based upon Figure 4.5 from [40], with permission.
5.4	Stack of N Biaxial layers. Based upon Figure 4.6 from [40], with permission.
5.5	Showing the tranformation of the total field across the layer, by the characteristic matrix of that layer. Based upon Figure 4.7 from [40], with permission.
5.6	Labelling scheme used for the amplitudes of the four basis vectors that propagate in the cover and the amplitudes of the four basis vectors in the substrate. Based upon Figure 5.1 from [40], with permission.
5.7	Experimental and modelled CP spectra from a *Popillia sp.* beetle. It should be noted the LR/RL in the model overlay each other as well at the RR model being absolutely zero. The structure was modelled as eight pitches thick and birefringent refractive indices of 1.434 and 1.45, having the cover medium as a refractive index as n=1.2 in order to take into account the waxy cuticle.
5.8	Single peak LL reflection graph with a clear single peak from a *L. pygmaea* specimen (black curve). The inset photographs show the appearance of the specimen through (a) left and (b) right circular polarisers. The red-dashed plot shows a theoretical plot of the Left-through-Left reflectivity of ten pitches thick with each individual chitin layer of 20nm and birefringent refractive indices of 1.475+0.008i and 1.50+0.008i. From the authors paper [20].
5.9	Double peak LCP reflection graph with a small trough from a beetle of the species *L. pygmeae* (black curve). The insets show the appearance of the specimen through (a) left and (b) right circular polarisers. The red-dashed theoretical curve is modelled upon a discontinuity in the pitch of 8/15 π, using complex birefringent refractive indices, of 1.46+0.025i and 1.52+0.025i to simulate absorption, and a layer of 11 pitches thickness in total. From the authors paper [20].

5.10	Double peak LL reflection graph with two clearly distinct peaks from a *L. geelvinkiana* specimen (black curve). The inset photographs show the appearance of the specimen through (a) left and (b) right circular polariser. The red-dashed theoretical curve is modelled upon two distinct pitch values, using complex birefringent refractive indices of 1.485+0.01i and 1.52+0.01i and having a thickness of 12.5 pitches in total. From the authors paper [20].
5.11	LL reflectance spectrum with gradually reducing oscillations at higher wavelengths of a beetle of *L. pseudodichropus* (black curve). The insets show the appearance of the specimen through (a) left and (b) right circular polarisers. The red-dashed theoretical curve is based upon a model of a structure of 19.5 pitches thick and discontinuities in the pitch of (1/6)π and (1/2)π, using complex birefringent refractive index of 1.498+0.002i and 1.52+0.002i. From the authors paper [20].
5.12	Experimental LCP reflectance spectrum with gradually increasing oscillations before the main peak of a beetle of *L. soror* (black curve). The red-dashed curve is based upon a theoretical model with two different twist defects. The model is based on a structure of 16.5 pitches thick structure with discontinuities in the pitch of (5/6)π and (3/2)π, using complex birefringent refractive indices of 1.498+0.006i and 1.52+0.006i. From the authors paper [20].
5.13	A plot of a LCP spectrum, this being one from a *L. soror* beetle, showing a response which could not be placed into the five chosen classifications (black curve). The red-dashed theoretical curve is from a model based upon a structure 13.5 pitches thick with discontinuities in the pitch of (1/15)π and (17/24)π, using complex birefringent refractive indices of 1.49+0.001i and 1.52+0.001i. From the authors paper [20].
5.14	LL spectral responses of *Cetonia aurata aurata* specimens with, described as (a) single peak (S), (b) double close (DC), (c) triple (T), (d) oscillations after (OA), (e) double apart (X) and (f) unclassified (U). The red lines are experimental data and the black are modelled. The inset photographs are of beetles through a LCP filter. Published by the author in [35].
5.15	CP reflection spectra with inset LCP (left) and RCP (right) filtered photographs of (a) Ceratocanthinae:*Ceratocanthopsis fulgida* (b) Scarabaeinae:*Diabroctis mimas* (pronotum) (c) Cetoniinae:*Protaetia angustata pyrodera*. (d) Trichiinae:*Gnorimus nobilis*. (e) Rutelinae:*Viridimicus aurescens*. (f) Phaenomeridinae:*Phaenomeris besckei*. (g) Dynastinae:*Augoderia nitidula* (pronotum). (h) Melolonthinae:*Melolontha melolontha* (pronotum). (i) Euchirinae:*Cheirotonus battareli* (pronotum). Experimental LL spectra are black, LR are red, RL are blue, RR are pink and modelled LL spectra are green. Published by the author in [35].
5.16	*Chrysina optima* (a) experimental CP spectral responses (b) modelled spectra responses and photographs through a LCP filter of (c) the silver form, (d) the gold form and (e) the red form. Published by the author in [35].
6.1	Transmission ellipsometer setup, in position a) 1 and b) 2, with linear polarisers (LP1, 2), quarter waveplate (QP) liquid crystals (LCVR1, 2).
6.2	LCVR calibration setup.
6.3	The transmission of the analogue (LCVR-A) and digital (LCVR-D) LCVRs.
6.4	The relative retardance of a LCVR at different driving voltages over the wavelength range available.
6.5	The relative retardance of a LCVR at different wavelengths across the driving voltage range.
6.6	Relative retardance of the two different LCVRs at different driving voltages at 750nm.
6.7	The difference in the MM element M02 for four and six polarisation inputs (which should ideally be close zero for a LP at 86°).
6.8	a) Intensity spectra of parallel and perpendicular LP configurations, with boxcar of 5, average of 1 and integration time of 40ms, with b) the experimental arrangement depicted below of two LPs (LP 1 and LP 2).
6.9	A diagram of the experimental arrangement for measuring the transmission of optical components.
6.10	Transmission (between 0 and 1) of linear polarisers (LP), non-rotating (NR) and rotating (R) and quarter waveplate (CP), with boxcar of 5, average of 1 and integration time of 40ms.
6.11	Plot of the MM elements from a LP at 86°, which should ideally be negligible.
6.12	Experimental setup to measure the chromatic variation of a circular polariser.
6.13	Intensity spectra of light generated from a QP sheet with a LP at 45° to the fast axis, with rotating analysing linear polariser (LP 2) at different angles, with boxcar of 5, average of 1 and integration time of 40ms.

6.14	The ratio of transimission compared to the light source for the QP sheet set to RCP output, over 180° on the LP2 for 450nm, 550nm, 650nm and 750nm. The major axis, minor axis and azimuth angles are labelled for 450nm in green.
6.15	Elliptical fix (EL) applied to the data compared to non-corrected (N) the data for the MM elements M_{03} and M_{13} using an 86° LP.
6.16	MM values of a LP at 86° using four driving voltages of LCVR-D and LCVR-A combinations (2.277V, 6.6V), (6.494V, 6.6V), (6.494V, 25.0V) and (3.777V, 6.6V).
6.17	M00 element values of a LP sample at 86°. One of the two driving voltages upon the LCVR-D is varied. The driving voltages combinations of the LCVR-D and LCVR-A were (VariableV, 6.6V), (VariableV, 25.0V), (6.494V, 6.6V) and (6.494V, 25.0V). The variable voltage (VariableV) values are stated in the inset key.
6.18	MM values of a LP at 86° using six driving voltages combinations of on the LCVR-D and LCVR-A respectively as (2.277V, 6.6V), (2.277V, 25.0V), (6.494V, 6.6V), (6.494V, 25.0V), (3.777V, 6.6V) and (3.777V, 25.0V).
6.19	Reflection ellipsometer setup, in a) position 1 and b) position 2, with linear polarisers (LP 1, 2), quarter waveplate (QP) and liquid crystals (LCVR 1, 2).
6.20	Normalised MM of reflection from the elytron of a *Repsimus aeneus* beetle.
6.21	Wavelength variation from the reflection on the elytron of a *Repsimus aeneus* beetle of a) the ellipticity, b) the polarised reflection, c) the azimuth angle and d) the degree of polarisation.
6.22	CP reflectance from a) the experimental setup in Chapter 4 (From Figure 4.19) and b) calculated from the measured MM from the beetle.
6.23	Normalised MM of reflection from the pronotum of a *Melolontha melolontha* beetle.
6.24	Wavelength variation from the reflection on the pronotum of a *Melolontha melolontha* beetle of a) the ellipticity, b) the polarised reflection, c) the azimuth angle and d) the degree of polarisation.
6.25	Normalised MM of reflection from the scutellum of a *Protaetia himalayana* beetle.
6.26	Wavelength variation from the reflection on the scutellum of a *Protaetia himalayana* beetle of a) the ellipticity, b) the polarised reflection, c) the azimuth angle and d) the degree of polarisation.
6.27	Normalised MM of reflection from the elytron of a silver *Chrysina optima* beetle.
6.28	Wavelength variation from the reflection on the elytron of a silver *Chrysina optima* beetle of a) the ellipticity, b) the polarised reflection, c) the azimuth angle and d) the degree of polarisation.
6.29	Normalised MM of reflection from the elytron of a gold *Chrysina optima* beetle.
6.30	Wavelength variation from the reflection on the elytron of a gold *Chrysina optima* beetle of a) the ellipticity, b) the polarised reflection, c) the azimuth angle and d) the degree of polarisation.
6.31	Normalised MM of reflection from the elytron of a red *Chrysina optima* beetle.
6.32	Wavelength variation from the reflection on the elytron of a red *Chrysina optima* beetle of a) the ellipticity, b) the polarised reflection, c) the azimuth angle and d) the degree of polarisation.
6.33	Normalised MM of reflection from the elytron of a matt green *Chrysina boucardi* beetle.
6.34	Wavelength variation from the reflection on the elytron of a matt green *Chrysina boucardi* beetle of a) the ellipticity, b) the polarised reflection, c) the azimuth angle and d) the degree of polarisation.
6.35	Normalised MM of reflection from the elytron of a metallic gold *Chrysina boucardi* beetle.
6.36	Wavelength variation from the reflection on the elytron of a metallic gold *Chrysina boucardi* beetle of a) the ellipticity, b) the polarised reflection, c) the azimuth angle and d) the degree of polarisation.
6.37	Normalised MM of reflection from the elytron of a *Chrysina cupreomarginata* beetle.
6.38	Wavelength variation from the reflection on the elytron of a *Chrysina cupreomarginata* beetle of a) the ellipticity, b) the polarised reflection, c) the azimuth angle and d) the degree of polarisation.
6.39	Normalised MM of reflection from the elytron of a *Chrysina clypealis* beetle.
6.40	Wavelength variation from the reflection on the elytron of a *Chrysina clypealis* beetle of a) the ellipticity, b) the polarised reflection, c) the azimuth angle and d) the degree of polarisation.

7.1	SEM images obtain with the Pt strip deposited on the left and then the trench milled on the right, where the sample can be seen to have fractured. Where HV is the high voltage applied to the ions and curr the current, WD the working distance, HFW the horizontal field width, while the det noted the detection method, which in this case was an Everhart-Thornley Detector ETD.
7.2	(a) SEM image cross section of the *Mycterophallus validipes* beetle's scutellum. (b) A greyscale profile taken along the line on the image in (a), (c) the associated LL optical spectrum with insect image of beetle through (i) LCP filter and (ii) RCP filter. Taken from the author's publication [20].
7.3	Surface SEM of *Mycterophallus validipes* beetle, with a yellow perpendicular cross section line.
7.4	A grayscale profile taken along the line on the surface SEM of the *Mycterophallus* beetle's shell.
7.5	SEM Cross section of the blaze-grating like structure of the *Mycterophallus validipes* beetle.
7.6	Schematic of the mode of operation of a "scattering-type Scanning Near-field Optical Microscope" (s-SNOM). An AFM tip hovers close to the sample surface and vibrates, vertically, at a frequency ω. IR laser light is focused onto the tip region, and concentrated, into a spatial area roughly corresponding to the tip diameter (inset), by the "lightning rod" effect. By detecting the portion of the backscattered light fluctuating at 3ω (i.e. a harmonic of the tip vibration), the light backscattered from this small region can be isolated. An interferometer (with a reference mirror oscillating at $\Omega << \omega$) is used to measure both the amplitude and phase of the backscattered light, from which the optical properties of the very small sample area that is interacting with the AFM tip can be inferred. An image is assembled by rastering the AFM tip across the sample in the usual way. Figure and caption from publication by the author [41].
7.7	AFM image of the surface of a *Mycterophallus validipes* beetle with imaging areas of a) 20x20um, b) 10x10um, and c) 5x5um.
7.8	a) AFM topography and b) operating wavelength λ=10.21um s-SNOM scattered amplitude image of a *Mycterphallus validipes* beetle. The voltage corresponds to the signal measured upon the detector. The s-SNOM image has given the chemical contrast of the components that make up the multilayers in the insect shell. In order to generate the shell's interference features in the visible part of the spectrum, the concentrations of these components vary on a sub-micron length scale, and only the s- SNOM can deliver chemical images at this resolution. The surface of the beetle being upon the left hand side. Taken from a publication by the author [41].
7.9	a) A s-SNOM amplitude image of 5x5µm of the Mycterophallus validipes beetle with the profile examined across the yellow line. b) The corresponding peak amplitude separation and wavelength.
8.1	Mueller matrix of a *Cetonia aurata* over an area 350µm x 220µm at 535nm. Used with permission, from [42].
8.2	Linear and circular polarisation patterns of the flower chafer, *Protaetia jousselini*, measured by imaging polarimetry at red (650 nm), green (550 nm) and blue (450 nm) wavelengths. The upper row shows the appearance through an LC polariser (a), an RC polariser (c) and without a polariser (b). The circular arrows here show the handedness of CP light transmitted by the polarisers. Below a–c, the panels are sorted by wavelength (650, 550, 450 nm). Rows d–f, g–i, j–l, m–o display the intensity I, degree of linear polarisation d_L, angle of polarisation α (measured clockwise from the vertical) and degree of circular polarisation d_c. Used with permission, from [43].

Table of Tables

4.1	Sellmeier coefficients for BK7 glass [44].
4.2	Convention for CP light in system. It should be noted that due to the 180° symmetry of the polarising cubes, 135° orientation is equivalent to -45°.
5.1	Minimum and maximum input parameters used in the models in Figure 5.14.
5.2	Minimum and maximum input parameters used in the models in Figure 5.15.
5.3	Minimum and maximum input parameters used in the models in Figure 5.16.
6.1	Advantages and disadvantages of different retarders, which were considered for use in a MM ellipsometer.
7.1	The reflection wavelength data arranged in alternating separations from the SEM in Figure 7.2, the lower the separation numbering the nearer to the surface of the cuticle the layer is.

References

[1] S. Vignolini, P. J. Rudall, A. V. Rowland, A. Reed, E. Moyroud, R. B. Faden, J. J. Baumberg, B. J. Glover, and U. Steiner, "Pointillist structural color in Pollia fruit," *Proc. Natl. Acad. Sci.*, vol. 109, no. 39, pp. 15712–15715, 2012.

[2] A. E. Seago, P. Brady, J.-P. Vigneron, and T. D. Schultz, "Gold bugs and beyond: a review of iridescence and structural colour mechanisms in beetles (Coleoptera)," *J. R. Soc. Interface*, vol. 6 Suppl 2, pp. S165-84, Apr. 2009.

[3] D. G. Stavenga, B. D. Wilts, H. L. Leertouwer, and T. Hariyama, "Polarized iridescence of the multilayered elytra of the Japanese jewel beetle, Chrysochroa fulgidissima," *Philos. Trans. R. Soc. Lond. B. Biol. Sci.*, vol. 366, no. 1565, pp. 709–23, Mar. 2011.

[4] T. H. Chiou, S. Kleinlogel, T. Cronin, R. Caldwell, B. Loeffler, A. Siddiqi, A. Goldizen, and J. Marshall, "Circular Polarization Vision in a Stomatopod Crustacean," *Curr. Biol.*, vol. 18, pp. 429–434, 2008.

[5] D. W. Lee, *Nature's Palette - The Science of Plant Color - ISBN:C*. Chicago: The University of Chicago Press, 2007.

[6] P. Vukusic, J. R. Sambles, and C. R. Lawrence, "Colour mixing in wing scales of a butterfly," *Nature*, vol. 404, no. 6777, p. 457, 2000.

[7] M. Crne, V. Sharma, J. Blair, J. O. Park, and C. J. Summers, "Biomimicry of optical microstructures of Papilio palinurus," *Europhys. Lett.*, vol. 93, no. 14001, 2011.

[8] M. H. Bartl, J. W. Galusha, L. R. Richey, J. S. Gardner, and J. N. Cha, "Discovery of a diamond-based photonic crystal structure in beetle scales," *Phys. Rev. E - Stat. Nonlinear, Soft Matter Phys.*, vol. 77, no. 5, pp. 2–5, 2008.

[9] M. Burresi, L. Cortese, L. Pattelli, M. Kolle, P. Vukusic, D. S. Wiersma, U. Steiner, and S. Vignolini, "Bright-White Beetle Scales Optimise Multiple Scattering of Light," *Sci. Rep.*, vol. 4, pp. 1–7, Aug. 2014.

[10] B. Michelsen, "Mandrill Photo," 2016. [Online]. Available: https://commons.wikimedia.org/wiki/File:Mandrill_at_san_francisco_zoo.jpg. [Accessed: 12-Dec-2016].

[11] B. C. Tørrissen, "Chlorocebus Blue Scrotum," 2016. [Online]. Available: https://commons.wikimedia.org/wiki/File:Chlorocebus-pygerythrus-private-parts.JPG. [Accessed: 12-Dec-2016].

[12] R. O. Prum and R. H. Torres, "Structural colouration of mammalian skin: convergent evolution of coherently scattering dermal collagen arrays," *J. Exp. Biol.*, vol. 207, no. 12, pp. 2157–2172, May 2004.

[13] A. C, "Enallagma civile." [Online]. Available: https://commons.wikimedia.org/wiki/File:Familiar_Bluet_(Enallagma_civile)_(15083515581).jpg. [Accessed: 12-Dec-2016].

[14] R. O. Prum, J. A. Cole, and R. H. Torres, "Blue integumentary structural colours in dragonflies (Odonata) are not produced by incoherent Tyndall scattering," *J. Exp. Biol.*, vol. 207, pp. 3999–4009, 2004.

[15] E. Kreit, L. M. Mäthger, R. T. Hanlon, P. B. Dennis, R. R. Naik, E. Forsythe, and J. Heikenfeld, "Biological versus electronic adaptive coloration: how can one inform the other?," *J. R. Soc. Interface*, vol. 10, no. 20120601, pp. 1–13, 2012.

[16] S. R. Mouchet, E. Van Hooijdonk, V. L. Welch, P. Louette, J.-F. Colomer, B.-L. Su, and O. Deparis, "Liquid-induced colour change in a beetle: the concept of a photonic cell," *Sci. Rep.*, vol. 6, no. 19322, pp. 1–10, 2016.

[17] J. P. Vigneron, J. M. Pasteels, D. M. Windsor, Z. Vértesy, M. Rassart, T. Seldrum, J. Dumont, O. Deparis, V. Lousse, L. P. Biró, D. Ertz, and V. Welch, "Switchable reflector in the Panamanian tortoise beetle Charidotella egregia (Chrysomelidae: Cassidinae)," *Phys. Rev. E - Stat. Nonlinear, Soft Matter Phys.*, vol. 76, no. 3, pp. 1–10, 2007.

[18] K. D. L. Umbers, "Turn the temperature to turquoise: Cues for colour change in the male chameleon grasshopper (Kosciuscola tristis) (Orthoptera: Acrididae)," *J. Insect Physiol.*, vol. 57, no. 9, pp. 1198–1204, 2011.

[19] K. Key and M. Day, "A temperature-controlled physiological colour response in the grasshopper Kosciuscola Tristis Sjost. (Orthoptera: Acrididae)," *Aust. J. Zool.*, vol. 2, no. 3, pp. 309–39, 1954.

[20] I. E. Carter, K. Weir, M. W. McCall, and A. R. Parker, "Variation in the circularly polarized light reflection of Lomaptera (Scarabaeidae) beetles," *J. R. Soc. Interface*, vol. 13, no. 120, pp. 1–9, Jul. 2016.

[21] S. A. Jewell, P. Vukusic, and N. W. Roberts, "Circularly polarized colour reflection from helicoidal structures in the beetle Plusiotis boucardi," *New J. Phys.*, vol. 9, no. 99, pp. 1–10, Apr. 2007.

[22] S. Caveney, "Cuticle Reflectivity and Optical Activity in Scarab Beetles: The Role of Uric Acid," *Proc. R. Soc. B Biol. Sci.*, vol. 178, no. 1051, pp. 205–225, Jun. 1971.

[23] L. Fernández del Río, "An Investigation of the Polarizing Properties and Structural Characteristics in the Cuticles of the Scarab Beetles Chrysina gloriosa and Cetonia aurata - MSc Thesis," Linköpings University, 2012.

[24] L. Fernández del Río, "An Investigation of the Polarization States of Light Reflected from Scarab Beetles of the Chrysina Genus - BSc Thesis," Linköpings University, 2011.

[25] V. Sharma, M. Crne, J. O. Park, and M. Srinivasarao, "Structural origin of circularly polarized iridescence in jeweled beetles," *Science*, vol. 325, no. 5939, pp. 449–51, Jul. 2009.

[26] G. Agez, C. Bayon, and M. Mitov, "Multiwavelength micromirrors in the cuticle of scarab beetle Chrysina gloriosa," *Acta Biomater.*, vol. 48, pp. 357–367, Jan. 2017.

[27] M. Hernández-Jiménez, D. E. Azofeifa, E. Libby, C. Barboza-Aguilar, Á. Solís, L. Arce-Marenco, I. García-Aguilar, A. Hernández, and W. E. Vargas, "Qualitative correlation between structural chirality through the cuticle of Chrysina aurigans scarabs and left-handed circular polarization of the reflected light," *Opt. Mater. Express*, vol. 4, no. 12, pp. 2632–45, Nov. 2014.

[28] M. Xu, A. E. Seago, T. D. Sutherland, and S. Weisman, "Dual structural color mechanisms in a scarab beetle," *J. Morphol.*, vol. 271, no. 11, pp. 1300–5, Nov. 2010.

[29] E. Loewen, M. Neviere, and D. Maystre, "Grating efficiency theory as it applies to blazed and holographic gratings," *Appl. Opt.*, vol. 16, no. 10, pp. 2711–2721, 1977.

[30] A. Lequet, "La Cétoine Dorée (Cetonia aurata)!" [Online]. Available: https://www.insectes-net.fr/cetoine/cetoi3.htm. [Accessed: 17-Dec-2016].

[31] T. Lenau and M. Barfoed, “Colours and Metallic Sheen in Beetle Shells — A Biomimetic Search for Material Structuring Principles Causing Light Interference,” *Adv. Eng. Mater.*, vol. 10, no. 4, pp. 299–314, Apr. 2008.

[32] W. E. Vargas, M. Hernández-Jiménez, E. Libby, D. E. Azofeifa, C. Barboza, and Á. Solis, “Light Reflection by Cuticles of Chrysina Jewel Scarabs: Optical Measurements, Morphology Characterization, and Theoretical Modeling,” *Opt. Photonics J.*, vol. 6, no. 7, pp. 146–163, 2016.

[33] L. De Silva, I. Hodgkinson, P. Murray, Q. H. Wu, M. Arnold, J. Leader, and A. Mcnaughton, “Natural and Nanoengineered Chiral Reflectors: Structural Color of Manuka Beetles and Titania Coatings,” *Electromagnetics*, vol. 25, no. 5, pp. 391–408, Jul. 2005.

[34] K. Robbie, M. J. Brett, and A. Lakhtakia, “Chiral sculptured thin films,” *Nature*, vol. 384, no. 6610. pp. 616–616, 1996.

[35] I. E. Carter, K. Weir, and M. W. McCall, “Investigation of the Variation of Near-Circular Polarization in Scarabaeoidea Beetles,” *Mater. Today Proc.*, vol. 4, no. 4, pp. 4942–4951, 2017.

[36] MAF Plant Health & Environmental Laboratory, “Manuka Beetle (Pyronota festiva),” 2011. [Online]. Available: http://www.padil.gov.au/maf-border/pest/main/140414/30082.

[37] Royal Belgian Institute of natural Sciences (RBINS), “Acanthocerus vicarius Bates, 1887.” [Online]. Available: http://virtualcollections.naturalsciences.be/virtual-collections/entomology/coleoptera/ceratocanthidae/ceratocanthus-vicarius. [Accessed: 11-Nov-2017].

[38] S. Peslier, “Note de chasse à Kalesmeno (Grèce), localité… très colorée,” *R.A.R.E*, vol. XVII, no. 1, pp. 38–39, 2008.

[39] K. Robacker, “Chrysina Gallery,” *University of Nebraska State Museum - Division of Entomology*. [Online]. Available: http://museum.unl.edu/research/entomology/Guide/Scarabs Gallery/Chrysina Gallery/index.html. [Accessed: 18-Dec-2016].

[40] M. W. McCall, I. J. Hodgkinson, and Q. H. Wu, *Birefringent Thin Films and Polarizing Elements: 2nd Edition - ISBN:9781783265350*. London: Imperial College Press, 2015.

[41] H. Amrania, L. Drummond, R. C. Coombes, S. Shousha, L. Woodley-Barker, K. Weir, W. Hart, I. Carter, and C. C. Phillips, “New IR imaging modalities for cancer detection and for intra-cell chemical mapping with a sub-diffraction mid-IR s-SNOM,” *Faraday Discuss.*, vol. 187, pp. 539–553, 2016.

[42] O. Arteaga, “Natural optical activity vs circular Bragg reflection studied by Mueller matrix ellipsometry,” *Thin Solid Films*, vol. 617, pp. 14–19, 2016.

[43] R. Hegedüs, G. Szél, and G. Horváth, “Imaging polarimetry of the circularly polarizing cuticle of scarab beetles (Coleoptera: Rutelidae, Cetoniidae),” *Vision Res.*, vol. 46, pp. 2786–2797, 2006.

[44] M. Polyanskiy, “Refractive Index of N-BK7.” [Online]. Available: http://refractiveindex.info/?group=SCHOTT&material=N-BK7. [Accessed: 08-Aug-2013].

Table of Contents

1. Introduction 1
2. Polarisation Formalisation 5
   - 2.1. Specific Cases of Polarisation 6
     - *2.1.1. Linearly Polarised Light 6*
     - *2.1.2. Circularly Polarised Light 7*
     - *2.1.3. Elliptically Polarised Light 7*
   - 2.2. Stokes Vectors 7
   - 2.3. Mueller Matrices 9
   - 2.4. References 11
3. Background into Structural Colour & Biology 12
   - 3.1. Structural Colour 12
     - *3.1.1. Diffraction Gratings 12*
     - *3.1.2. Photonic Crystals 13*
       - 3.1.2.1. Thin Film Interference 13
       - 3.1.2.2. Multi Layered Interference 14
       - 3.1.2.3. Heliocoidal Layered Interference 16
       - 3.1.2.4. Surface Mirrors 18
       - 3.1.2.5. 3D Photonic Crystals 19
     - *3.1.3. Scattered Colours 20*
     - *3.1.4. Summary 23*
   - 3.2. Pigmentary Colour 23
   - 3.3. Variable Colours 23
   - 3.4. Beetles with Heliocoidal Structures 27
     - *3.4.1. Structural Description 28*
     - *3.4.2. Structural Elliptical Studies 30*
     - *3.4.3. Mirror Image of a Beetle 34*
     - *3.4.4. Modelling 34*
     - *3.4.5. Surface Micromirrors 35*
     - *3.4.6. Surface Blazed Grating 37*
     - *3.4.7. Wavelength Formation/Variation 38*
     - *3.4.8. Artificial Structure 41*
     - *3.4.9. Purpose of the Heliocoidal Structure 42*
     - *3.4.10. Circularly Polarised Vision 42*

3.4.11. Homochirality from Astronomical Sources *44*
3.4.12. The Beetles in Modern Culture *44*
3.4.13. Summary *45*
3.5. Entomology of Beetles **46**
3.5.1. Scarabaeinae *47*
3.5.2. Cetoniinae *48*
3.5.3. Trichiinae *48*
3.5.4. Rutelinae *49*
3.5.5. Phaenomeridinae *50*
3.5.6. Dynastinae *50*
3.5.7. Melolonthinae *51*
3.5.8. Euchirinae *51*
3.5.9. Ceratocanthinae *52*
3.5.10. Summary *52*
3.6. References **52**
4. Circularly Polarised Measurements **63**
4.1. Introduction **63**
4.2. Preliminary Work **63**
4.2.1. Circularly Polarised Cinema Glasses *63*
4.2.2. Photographing Beetles *65*
4.2.3. Reflection Position upon the Beetle *66*
4.3. Experimental Setup **67**
4.3.1. Polarising Cubes *68*
4.3.2. Fresnel Rhomb *68*
4.3.3. Calibration *72*
4.3.4. Software Calibration *73*
4.3.5. Errors in Process *75*
4.3.6. Repeatability of Measurements *77*
4.4. Circularly Polarised Reflection Spectra from Beetles **78**
4.4.1. Typical Examples of Each Subfamily *79*
4.4.2. Rutelidae:Chrysina Genus *84*
4.4.2.1. Species with RR and LL responses 85
4.4.2.2. Measured Colour Variation 88
4.4.2.3. Variation in Intensity 90
4.4.2.4. Variation in the Elytra and Pronotum 91

4.4.2.5. Other Notable Species 93
4.4.2.6. Conclusion 94
4.4.3. Cetoniinae In-Depth Variation Studies 95
4.4.3.1. Lomaptera 95
4.4.3.2. Mycterophallus duboulayi 98
4.4.3.3. Thaumastopeus pugnator 100
4.4.3.4. Protaetia brevitarsis 102
4.4.3.5. Cetonia aurata aurata 104
4.4.3.6. Ischiopsopha aruensis 106
4.4.3.7. Agestrata luzonica 108
4.4.3.8. Protaetia himalayana 111
4.4.3.9. Conclusion 113
4.4.4. Variation in other Species 113
4.4.4.1. Popillia 113
4.4.4.2. Cetonia aurata pisina 115
4.4.4.3. Cetonia carthami 117
4.4.4.4. Other Species 118
4.4.5. Notable Single Species Studied 119
4.4.5.1. Cetoniinae 119
4.4.5.2. Rutelinae 122
4.4.5.3. Scarabaeinae 124
4.4.5.4. Phaenomeridinae 124
4.5. Lack of Circularly Polarised Response in Rhomborhina gigantea 125
4.6. Other Observed Variations 127
4.6.1. Variation on the Underside 127
4.6.2. Angle Variation 129
4.7. Conclusion 130
4.8. References 132
5. Modelling of Circularly Polarised Reflection 135
5.1. Introduction 135
5.2. Background 135
5.2.1. Maxwell's Equations – Electromagnetics 136
5.2.2. Propagating Waves 136
5.2.3. Field Matrix 138
5.2.4. Field Coefficients 139

5.2.5. Total Field 139
5.2.6. Phase Matrix 140
5.2.7. Characteristic Matrix 140
5.2.8. Rotation Matrix 142
5.2.9. Helix Definitions 143
5.2.10. Reflection and Transmission 143
5.2.10.1. All Biaxial Structures 143
5.2.10.2. Isotropic Cover and Substrate 145
5.2.10.3. Amplitude Reflection and Transmission Coefficients 146
5.2.10.4. Irradiance Reflectance and Transmittance Coefficients .. 146
5.3. Modelling Method 147
5.4. Different Basic Lomaptera Modelling Types 148
5.4.1. Single Pitch 148
5.4.2. Double Peak Close 149
5.4.3. Double Pitches Further Apart 150
5.4.4. Multiple Discontinuity 150
5.5. Modelled Cetonia aurata aurata 152
5.6. Modelled Examples from Each of the Nine Subfamilies 153
5.7. Broadband Model 154
5.8. Conclusion 155
5.9. References 156
6. Ellipsometry 158
6.1. Introduction 158
6.2. Retarder Types 158
6.3. Mueller Matrix Method 159
6.4. Calibration 161
6.4.1. Liquid Crystal Variable Retarder Calibration 161
6.4.2. Linear Polarisers 164
6.4.3. Testing the System 165
6.4.4. Quarter Waveplate Variation 165
6.4.5. Delta-like Function – Retardance Degeneracy 168
6.5. Reflection Mode 169
6.6. Beetle Reflection Mueller Matrices 170
6.6.1. Single Peak 170
6.6.2. Non Dominant LL Peak 173

6.6.3. Multiple Peaks 174
6.6.4. Colour Variation 176
6.6.5. Intensity Reflection 180
6.6.6. RR Reflection 183
6.6.7. Minor RR 187
6.7. Conclusion 188
6.8. References 187
7. Imaging the Optical Structures 188
7.1. Electron Micrographs 188
7.2. Scanning Nearfield Optical Microscopy/Atomic Force Microscopy 192
7.3. Conclusion 195
7.4. References 195
8. Future Research and Applications 196
8.1. References 199
9. Conclusion, Publications and Conferences 201
9.1. Conclusion 201
9.2. Publications 204
9.3. Talks 204
9.4. Posters 205
9.5. Notable Outreach 205

Chapter 1 - Introduction

It was Michelson who over 100 years ago first discovered the selective reflection of what was near Circularly Polarised (CP) (abbreviations at the start of the thesis) light from a *Chrysina (Plusiotis) resplendens* beetle, with the structure responsible being described as a "screw structure" of ultramicroscopic dimensions [1]. Since then the subject has been investigated across a wide range of fields, from biology, optics and even engineering [2]. The description and knowledge of such structures have consistently improved, this expanse of knowledge started when Gaubert in 1924 reported that the handedness reflected from the beetles he investigated appeared to Left Circularly Polarised (LCP) [3]. Later it was shown that a few beetles also reflected Right Circularly Polarised (RCP) light to some degree [4].

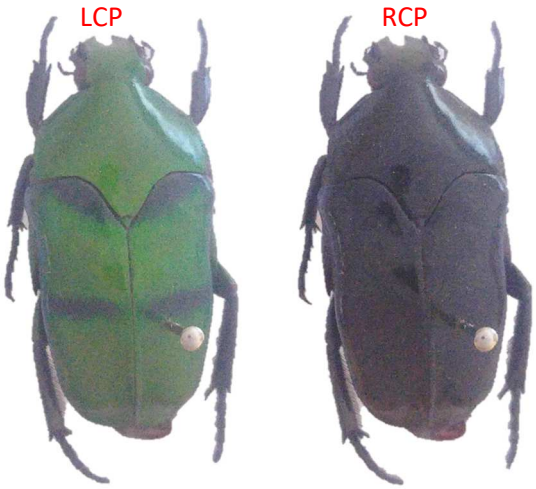


Figure 1.1 – Photographs of an *Ischiopsopha bifasciata* beetle through a LCP filter (left) and RCP filter (right). This specimen was collected in Indonesia in 2014. All the specimens in this study were measured from the top of the head to the bottom of the abdomen (or elytra if longer), this specimen measured 29mm.

There are very few examples of CP light interaction in nature with one of the more common examples coming from the Scarabaeoidae beetle superfamily. A typical example can be seen in Figure 1.1, where the beetle is colourful under a LCP filter (due to the structure which reflects CP light) and a dull black colour under the RCP filter (due to the melanin behind the circularly polarising structure). As well as beetles a wide range of species in nature are seen to interact with CP light. In the plant world circularly polarising structures have been observed in fruit such as the *Pollia condensate* (Figure 1.2) [5] and it has also been observed that LCP light leads to faster growth in pea and lentil plants, compared to RCP [6]. From the animal kingdom the stomatopod genus *Odontodactylus* (a type of mantis shrimp) is known to both be able to detect and reflect CP light as a means of communication [7],[8]. Another example is the Sapphirinidae Copepod which circularly polarises light when it is transmitted through them, interestingly this genus has a range which overlaps that of mantis shrimp [9]. Several species of firefly larvae

(*Photuris lucicrescens* and *Photuris versicolor*) are known to be bioluminescence CP light, with the left and right lanterns emitting opposite handedness of light. Natural arrangements such as a water-air interface can produce CP light from total internal reflection inducing a phase shift [10]. Starlight also has been observed to contain some CP radiation [11].

The reflection of CP light by scarab beetles was found to be enhanced by the presence of uric acid by Caveney in some genera (*Chrysina* and *Anoplognathus*) [12]. It was Pye who discovered that nine subfamilies of beetles contain some species which interacted with CP light [13]. The structures behind the CP reflection from beetles' cuticles consist of two dimensional layers of thread like molecules in the same orientation within a chitin-protein matrix. These 2D layers are then stacked on top of each other. There is a gradual rotation in the orientation of molecules occurring between layers, with a full 360° rotation known as the pitch. Multiple pitches stacked on top of each other form the helicoidal structures responsible for the selected reflection of CP light. The pitch is related to the reflected wavelength by multiplying with the average refractive index of the material. The species *Chrysina resplendens* was also found to reflect both LCP and RCP light [12], due to a uniaxial layer between two helicoidal stacks.

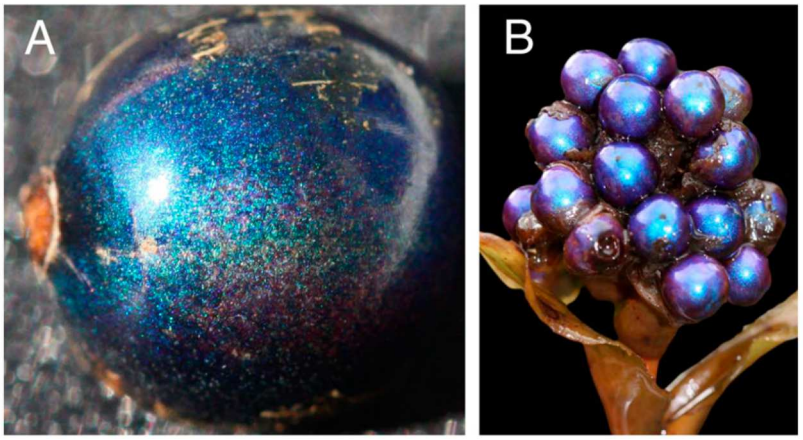


Figure 1.2 – Photographs of *Pollia condensate* fruits of A) a single fruit specimen and B) a cluster of fruits. Used with permission, from [14].

In this report the variation and perturbation of helicoidal structures within the beetles' shells and their CP reflection responses are studied.

Chapter 2 begins by demonstrating the mathematical formulae behind helicoidal polarising structures in beetles and mathematical methods of describing polarisation. In Chapter 3 a background upon the origin of structural colours that occur in nature is given, with particular focus given to previous research into Scarabaeidae which reflect CP light.

A broadband experimental setup which measures only the pure CP reflection is presented in Chapter 4. Different CP reflection spectra from a wide variety of beetles' shells are presented and discussed. The discussion of the variation which occurs is done in several different ways,

between subfamilies, genera and species and also within species. This reported variation in the measured CP spectra includes broadband and narrowband reflection, different handedness of CP reflection as well as intensity and colour morphs between specimens of the same species. The appendix contained a compendium of typical examples of CP reflection responses from the shells of a much wider range of beetles.

Chapter 5 demonstrates the modelling of basic spectral shapes of CP light from the helicoidal structure. Modelling was made upon both single peak narrowband and multiple peak broadband reflection spectra and the perturbations in between.

One of the more successful outcomes of the study was the design and production of a broadband Mueller Matrix (MM) ellipsometer (to measure beetles' reflection MMs), using Liquid Crystal Variable Retarders (LCVRs).

Using the known CP spectral variations in Chapter 4, a selection of beetles was chosen to take reflection ellipsometric MM measurements from (as described in Chapter 6). The MMs are a fuller description of the beetles' polarising properties than from the simple CP setup used in Chapter 4. There were several MMs which appear close to ideal circular polarisers, whilst some were dominated by features reminiscent of mirrors, and others were mixed, reflecting both right and left CP light.

Further to measuring and modelling the polarised reflection response, subwavelength imaging was done in order to observe the structures responsible for such a reflection. Both Electron Microscope (EM) and Scanning Near-field Optical Microscopy (SNOM) techniques were used to investigate a *Mycterophallus* beetle which reflected light at two distinct wavelengths. Helicoidal structures within the shell as well as a blazed-grating like structure was observed on the surface.

Later on in the report various applications and future research of the beetles' helicoidal structures are discussed (Chapters 8). One of the main future research fields being the manufacture of artificial structures for use in many applications due to their high reflection, but low heat and electrical conducting properties.

This study builds upon previous work into the CP reflection from beetles with many of the investigated species of beetles being considered for the first time. One of the most notable observations was within the *Chrysina* genus, where six new species were seen to reflect both LCP and RCP light.

Many previous studies focused upon single or very few specimens, in this study much larger sample sizes (of over 100 specimens) in several single species were used. This revealed large

variation in LCP spectral shape amongst the *Cetonia aurata aurata* subspecies, whilst slightly less spectral shape variation occurred in the *Ischiosopha aurensis* species. The *Cetonia aurata pisina* subspecies specimens revealed a variation in reflected wavelength from blue to the Near Infra-Red (NIR).

References

[1] A. Michelson, "On metallic colouring in birds and insects," *Philos. Mag.*, vol. 21, pp. 618–623, 1911.

[2] P. Vukusic, "Materials science. Evolutionary photonics with a twist," *Science*, vol. 325, no. 5939, pp. 398–9, Jul. 2009.

[3] P. Gaubert, "Sur la polarisation circulaire de la lumiere reflechie pas les insectes," *Comptes Rendus*, vol. 179, pp. 1148–1150, 1924.

[4] A. C. Neville and S. Caveney, "Scarabaeid beetle exocuticle as an optical analogue of cholesteric liquid crystals," *Biol. Rev. Camb. Philos. Soc.*, vol. 44, pp. 531–562, 1969.

[5] S. Vignolini, E. Moyroud, B. J. Glover, and U. Steiner, "Analysing photonic structures in plants Analysing photonic structures in plants," *Jorunal R. Soc. Interface*, vol. 10, no. 87, 2013.

[6] P. P. Shibayew and R. G. Pergolizzi, "The Effect of Circularly Polarized Light on the Growth of Plants," *Int. J. Bot.*, vol. 7, no. 1, pp. 113–117, 2011.

[7] T. H. Chiou, S. Kleinlogel, T. Cronin, R. Caldwell, B. Loeffler, A. Siddiqi, A. Goldizen, and J. Marshall, "Circular Polarization Vision in a Stomatopod Crustacean," *Curr. Biol.*, vol. 18, pp. 429–434, 2008.

[8] J. Marshall, T. W. Cronin, N. Shashar, and M. Land, "Behavioural evidence for polarisation vision in stomatopods reveals a potential channel for communication," *Curr. Biol.*, vol. 9, no. 14, pp. 755–8, Jul. 1999.

[9] Y. Baar, J. Rosen, and N. Shashar, "Circular polarization of transmitted light by sapphirinidae copepods," *PLoS One*, vol. 9, no. e86131, pp. 1–6, Jan. 2014.

[10] T. W. Cronin and J. Marshall, "Patterns and properties of polarized light in air and water," *Philos. Trans. R. Soc. Lond. B. Biol. Sci.*, vol. 366, no. 1565, pp. 619–626, 2011.

[11] J. Bailey, "Astronomical sources of circularly polarized light and the origin of homochirality," in *Origins of Life and Evolution of the Biosphere*, 2001, vol. 31, no. 1–2, pp. 167–183.

[12] S. Caveney, "Cuticle Reflectivity and Optical Activity in Scarab Beetles: The Role of Uric Acid," *Proc. R. Soc. B Biol. Sci.*, vol. 178, no. 1051, pp. 205–225, Jun. 1971.

[13] J. D. Pye, "The distribution of circularly polarized light reflection in the Scarabaeoidea (Coleoptera)," *Biol. J. Linn. Soc.*, vol. 100, no. 3, pp. 585–596, Jun. 2010.

[14] S. Vignolini, P. J. Rudall, A. V. Rowland, A. Reed, E. Moyroud, R. B. Faden, J. J. Baumberg, B. J. Glover, and U. Steiner, "Pointillist structural color in Pollia fruit," *Proc. Natl. Acad. Sci.*, vol. 109, no. 39, pp. 15712–15715, 2012.

Chapter 2 - Polarisation Formalisation

In order to be able to describe the polarising structures within the beetles presented in this study, a mathematical description must be employed. Light is classically described as having electric field ($\boldsymbol{E}$) and magnetic field ($\boldsymbol{B}$) components which are orthogonal to each other as well as to the direction of propagation of the electromagnetic wave [1].

If the electromagnetic wave is defined as propagating in the z-direction then it can be written in the form,

$$\boldsymbol{E}(z,t) = E_x\hat{\boldsymbol{x}} + E_y\hat{\boldsymbol{y}}, \tag{2.1}$$

where $\hat{\boldsymbol{x}}$ and $\hat{\boldsymbol{y}}$ are the direction vectors, E_x and E_y are the magnitudes of the x and y components of the electric field and $\boldsymbol{E}\,(z,\ t\,)$ is the electric field vector. If time (t) and propagation (z) dependence are taken into account then the x and y magnitudes become:

$$E_x = E_{ox}\cos(kz - \omega t), \tag{2.2a}$$

$$E_y = E_{oy}\cos(kz - \omega t + \delta). \tag{2.2b}$$

k is the wavenumber, ω is the angular frequency, δ is the phase difference between the x and y components, E_{ox} and E_{oy} are the amplitudes of the electric field components. The wavenumber and angular frequency are defined as

$$k = \frac{2\pi}{\lambda}, \tag{2.3}$$

$$\omega = 2\pi f, \tag{2.4}$$

where λ is the wavelength and f is the frequency. Using equations (2.1)-(2.3) and rearranging, the electric field gives

$$\boldsymbol{E}(z,t) = \left(E_{ox}\hat{\boldsymbol{x}} + E_{oy}\cos\delta\hat{\boldsymbol{y}}\right)\cos(kz - \omega t) - E_{oy}\sin(kz - \omega t)\sin\delta\hat{\boldsymbol{y}}. \tag{2.5}$$

By rearranging equations 2.2 and 2.3 gives

$$\frac{E_x}{E_{ox}} = \cos(kz - \omega t), \tag{2.6a}$$

$$\frac{E_y}{E_{oy}} = \cos(kz - \omega t + \delta). \tag{2.6b}$$

Using the double angle formula, equation 2.6b becomes

$$\frac{E_y}{E_{oy}} = \cos(kz - \omega t)\cos\delta - \sin(kz - \omega t)\sin\delta. \tag{2.7}$$

Then using the trigonometric identity ($\sin^2 A$+$\cos^2 A$=1) and combining with equation 2.6a, equation 2.7 becomes,

$$\frac{E_y}{E_{oy}} = \frac{E_x}{E_{ox}}\cos\delta - \sqrt{1-\left(\frac{E_x}{E_{ox}}\right)^2}\sin\delta. \tag{2.8}$$

Rearranging both sides of equation 2.8 and squaring gives

$$\left(1-\left(\frac{E_x}{E_{ox}}\right)^2\right)\sin^2\delta = \left(\frac{E_x}{E_{ox}}\right)^2\cos^2\delta + \left(\frac{E_y}{E_{oy}}\right)^2 - 2\left(\frac{E_x}{E_{ox}}\right)\left(\frac{E_y}{E_{oy}}\right)\cos\delta. \tag{2.9}$$

Using the trigonometric identity ($\sin^2 A+\cos^2 A=1$) again and rearranging equation 2.9 becomes

$$\left(\frac{E_y}{E_{oy}}\right)^2 + \left(\frac{E_x}{E_{ox}}\right)^2 - 2\left(\frac{E_x}{E_{ox}}\right)\left(\frac{E_y}{E_{oy}}\right)\cos\delta = \sin^2\delta. \tag{2.10}$$

Which can be graphically represented in the form of an ellipse as can be seen in Figure 2.1.

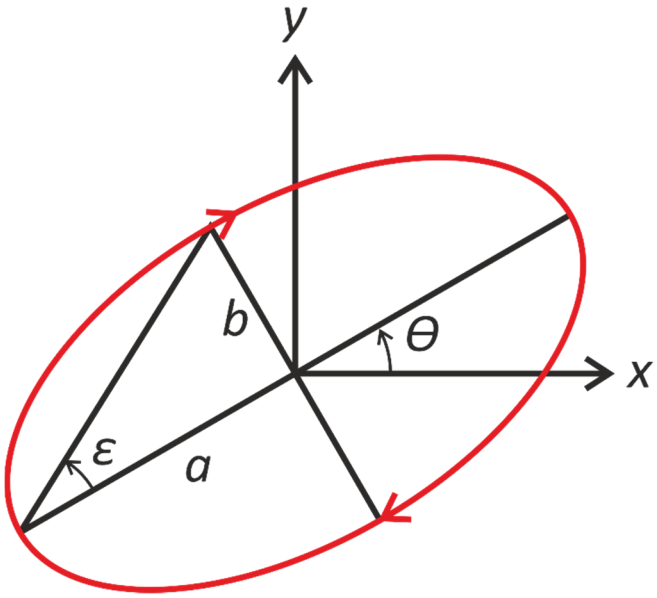


Figure 2.1 – Polarisation ellipse with polarimetric angles, displaying left handed elliptical polarisation, with the beam propagating out of the page. θ is the azimuth angle and ε is the angle of ellipticity.

The ratio of the two axis are known as the ellipticity, ξ.

$$\xi = \frac{b}{a}. \tag{2.11}$$

The angle of ellipticity ε can be obtained from the ratio of the major axis a to the minor axis b as

$$\varepsilon = \pm\arctan\left(\frac{b}{a}\right) = \pm\arctan(\xi). \tag{2.12}$$

2.1. Specific Cases of Polarisation

2.1.1. Linearly Polarised Light

There are specific types of linear polarisation when the following conditions are applied to equation 2.10. It should be noted that for all linear polarisation states the angle of ellipticity is equal to zero.

$$E_{oy} = 0, \qquad \text{Linear Horizontal} \tag{2.13}$$

$$E_{ox} = 0, \qquad \text{Linear Vertical} \tag{2.14}$$

$$\delta = m\pi, \quad \text{Linear } \pm 45° \tag{2.15}$$

$$E_{ox} = E_{oy}, \quad \text{Linear } +45° \tag{2.16}$$

$$E_{ox} = -E_{oy}. \quad \text{Linear } -45° \tag{2.17}$$

Where m is an integer value.

2.1.2. Circularly Polarised Light

The reflections measured from the majority of beetles in this study were close to being CP. There are specific variable constraints in order to define CP light. Most notably the electric field strengths in the x and y directions must be equal. As can be seen in equations 2.19-2.22, there are different phase and ellipticity angle conditions for LCP and RCP light, where m is an integer value.

$$E_{ox} = E_{oy}, \quad \text{Circularly Polarised} \tag{2.18}$$

$$\delta = \frac{\pi}{2}(1 + 2m), \quad \text{Right Circularly Polarised} \tag{2.19}$$

$$\varepsilon = \frac{\pi}{4} \quad \text{Right Circularly Polarised} \tag{2.20}$$

$$\delta = \frac{3\pi}{2}\ (1 + 2m), \quad \text{Left Circularly Polarised} \tag{2.21}$$

$$\varepsilon = -\frac{\pi}{4} \quad \text{Left Circularly Polarised} \tag{2.22}$$

2.1.3. Elliptically Polarised Light

Whilst most of the beetles reflected near CP light (ie equations 2.18-22 are only approximately satisfied), the light reflected was not perfectly CP and was in fact elliptically polarised. In Chapter 6 the handedness of left and right CP light is defined by the angle of ellipticity. The handedness of ellipitically polarised light is defined such that if it is positive then the light is right handed and if it is negative it is left handed, as in equations 2.23-2.24. The majority of beetles investigated in this study are left handed.

$$0 < \varepsilon \leq \frac{\pi}{4}, \quad \text{Right Handed Elliptically Polarised} \tag{2.23}$$

$$-\frac{\pi}{4} \leq \varepsilon < 0. \quad \text{Left Handed Elliptically Polarised} \tag{2.24}$$

2.2. Stokes Vectors

Stokes vectors and MMs were used in this study to characterise the reflection polarisation properties of the beetles which were studied (particularly Chapter 6). Stokes vectors rather than Jones vectors were used in this study since Jones vectors cannot represent unpolarised light. Jones vectors do not describe the overall intensity of light only the polarised response. The four components of a column vector that is a Stokes vector is shown in equation 2.25. Various examples of linear and circular polarisation are shown in equations 2.25a-d.

$$\boldsymbol{S} = \begin{bmatrix} S_0 \\ S_1 \\ S_2 \\ S_3 \end{bmatrix} \quad \text{General form of the Stokes vector} \tag{2.25}$$

$$\boldsymbol{S_U} = \begin{bmatrix} 1 \\ 0 \\ 0 \\ 0 \end{bmatrix} \quad \text{Unpolarised} \tag{2.25a}$$

$$\boldsymbol{S_{0°/90°}} = \begin{bmatrix} 1 \\ \pm 1 \\ 0 \\ 0 \end{bmatrix} \quad \text{Horizontal/Vertically Linearly Polarised} \tag{2.25b}$$

$$\boldsymbol{S_{\pm 45°}} = \begin{bmatrix} 1 \\ 0 \\ \pm 1 \\ 0 \end{bmatrix} \quad \pm 45° \text{ Linearly Polarised} \tag{2.25c}$$

$$\boldsymbol{S_{LCP/RCP}} = \begin{bmatrix} 1 \\ 0 \\ 0 \\ \pm 1 \end{bmatrix} \quad \text{Left/Right Circularly Polarised} \tag{2.25d}$$

The majority of the beetles presented in this study reflect light with Stokes vectors close to that of LCP light (equation 2.25d).

The individual components of the Stokes vector are related to irradiances of light signals which are polarised. The relation between the components and the polarised irradiances can be seen in equations 2.26-2.29.

$$S_0 = I_x + I_y, \tag{2.26}$$

$$S_1 = I_x - I_y, \tag{2.27}$$

$$S_2 = I_{+45°} - I_{-45°}, \tag{2.28}$$

$$S_3 = I_{RCP} - I_{LCP}, \tag{2.29}$$

The irradiances I_x, I_y, $I_{+45°}$ and $I_{-45°}$ correspond to linear polarisation component in the x(0°), y(90°), +45° and -45° directions respectively. The irradiances I_{RCP} and I_{LCP} are related to the right and left CP light respectively. The total intensity of light is represented by the Stokes component S_0, as in equation 2.30.

$$I_{total} = S_0 \tag{2.30}$$

The intensity of the polarised light can be found by taking the square root of the sum of the square of the other three Stokes vectors to give

$$I_{pol} = \sqrt{S_1^2 + S_2^2 + S_3^2}. \tag{2.31}$$

The unpolarised light can also be found by subtraction of the polarised intensity (equation 2.31) from the totally intensity (equation 2.30), to give

$$I_{unpol} = I_{total} - I_{pol}. \tag{2.32}$$

From the Stokes vectors various parameters can be calculated including the degree of polarisation (P) (equation 2.33), the ellipticy (ξ) (equation 2.34), the ellipticy angle (ε) (equation 2.35) and the azimuth angle (θ) (equation 2.36).

$$P = \frac{\sqrt{S_1^2 + S_2^2 + S_3^2}}{S_0} \tag{2.33}$$

$$\xi = \tan\left(\frac{1}{2}\arcsin\left(\frac{S_3}{\sqrt{S_1^2 + S_2^2 + S_3^2}}\right)\right) \tag{2.34}$$

$$\varepsilon = \frac{1}{2}\arcsin\left(\frac{S_3}{\sqrt{S_1^2 + S_2^2 + S_3^2}}\right) \tag{2.35}$$

$$\theta = \frac{1}{2}\arctan\left(\frac{S_2}{S_1}\right) \tag{2.36}$$

2.3. Mueller Matrices

MMs are 4x4 matrices used to characterise the polarisation response of a medium or optical component. In this study they are used to characterise the polarisation response in reflection from Scarabaeoidae beetles (Chapter 6). They are employed in a situation such that light of a known polarisation (defined by Stokes vector $\boldsymbol{S_b}$) is incident upon a medium with MM $\boldsymbol{M}$, the polarisation of light from the interaction with the medium ($\boldsymbol{S_a}$). The relation is given as

$$\boldsymbol{S_a} = \boldsymbol{M}\boldsymbol{S_b}. \tag{2.37}$$

The MM ($\boldsymbol{M}$) and Stokes vector ($\boldsymbol{S_b}$) are normalised by the components such that both M_{00} and S_{b0} are equal to 1. A MM is a 4x4 matrix, where each term is defined by the interaction with a medium as

$$\begin{bmatrix} S_{a0} \\ S_{a1} \\ S_{a2} \\ S_{a3} \end{bmatrix} = c \begin{bmatrix} M_{00} & M_{01} & M_{02} & M_{03} \\ M_{10} & M_{11} & M_{12} & M_{13} \\ M_{20} & M_{21} & M_{22} & M_{23} \\ M_{30} & M_{31} & M_{32} & M_{33} \end{bmatrix} \begin{bmatrix} S_{b0} \\ S_{b1} \\ S_{b2} \\ S_{b3} \end{bmatrix}, \tag{2.38}$$

where c is the absorption coefficient of the MM. Examples of typical MMs are shown (equations 2.39-2.43), including a perfect depolariser, perfect mirror, +/-45° linear polariser, quarter waveplate and left and right circular polarisers. The reflection MM of most beetles in this study are similar to the MM of the left circular polariser (equation 2.43).

$$\begin{bmatrix} 1 & 0 & 0 & 0 \\ 0 & 0 & 0 & 0 \\ 0 & 0 & 0 & 0 \\ 0 & 0 & 0 & 0 \end{bmatrix} \quad \text{Depolariser} \tag{2.39}$$

$$\begin{bmatrix} 1 & 0 & 0 & 0 \\ 0 & 1 & 0 & 0 \\ 0 & 0 & -1 & 0 \\ 0 & 0 & 0 & -1 \end{bmatrix} \quad \text{Perfect Mirror} \tag{2.40}$$

$$\frac{1}{2}\begin{bmatrix} 1 & 0 & \pm 1 & 0 \\ 0 & 0 & 0 & 0 \\ \pm 1 & 0 & 1 & 0 \\ 0 & 0 & 0 & 0 \end{bmatrix} \quad \text{+/-45° Linear Polariser} \tag{2.41}$$

$$\begin{bmatrix} 1 & 0 & 0 & 0 \\ 0 & 1 & 0 & 0 \\ 0 & 0 & 0 & 1 \\ 0 & 0 & -1 & 0 \end{bmatrix} \quad \text{Quarter waveplate (fast axis vertical)} \tag{2.42}$$

$$\frac{1}{2}\begin{bmatrix} 1 & 0 & 0 & \pm 1 \\ 0 & 0 & 0 & 0 \\ 0 & 0 & 0 & 0 \\ \pm 1 & 0 & 0 & 1 \end{bmatrix} \quad \text{Right (+)/Left (-) Circular Polariser} \tag{2.43}$$

A general linear polariser can be defined as:

$$\frac{1}{2}\begin{bmatrix} 1 & \cos(2\omega) & \sin(2\omega) & 0 \\ \cos(2\omega) & \cos^2(2\omega) & \sin(2\omega)\cos(2\omega) & 0 \\ \sin(2\omega) & \sin(2\omega)\cos(2\omega) & \sin^2(2\omega) & 0 \\ 0 & 0 & 0 & 0 \end{bmatrix}, \quad \text{General Linear Polariser} \tag{2.44}$$

where ω is the angle of fast axis of the polariser. The general MM for a linear retarder is defined as:

$$\begin{vmatrix} 1 & 0 & 0 & 0 \\ 0 & \cos^2(2\Omega) + \cos(\gamma)\sin^2(2\Omega) & \cos(2\Omega)\sin(2\Omega) - \cos(2\Omega)\cos(\gamma)\sin(2\Omega) & \sin(2\Omega)\sin(\gamma) \\ 0 & \cos(2\Omega)\sin(2\Omega) - \cos(2\Omega)\cos(\gamma)\sin(2\Omega) & \cos(\gamma)\cos^2(2\Omega) + \sin^2(2\Omega) & -\cos(2\Omega)\sin(\gamma) \\ 0 & -\sin(2\Omega)\sin(\gamma) & \cos(2\Omega)\sin(\gamma) & \cos(\gamma) \end{vmatrix} \tag{2.45}$$

where γ is the retardance and Ω is the angle of the fast axis of the retarder. A method which has been employed to analyse the reflection MM from a beetle has been discussed in Chapter 6 of this thesis. The following parameters in this section are used to describe such a reflection. These parameters are analogous to the Stokes vector analysis parameters in equation 2.30 to 2.36. The total reflection of light from a medium is given as:

$$R_{tot} = M_{00} \tag{2.46}$$

When the light is polarised the reflection of polarised light (R_{pol}) and unpolarised light (R_{unpol}) are:

$$R_{pol} = \sqrt{M_{10}^2 + M_{20}^2 + M_{30}^2} \tag{2.47}$$

$$R_{unpol} = R_{tot} - R_{pol} = M_{00} - \sqrt{M_{10}^2 + M_{20}^2 + M_{30}^2} \tag{2.48}$$

The ratio of polarised to unpolarised light is known at the degree of polarisation (P), which is then defined by:

$$P = \frac{\sqrt{M_{10}^2 + M_{20}^2 + M_{30}^2}}{M_{00}} \tag{2.49}$$

The ellipticty (ξ), ellipticity angle (ε) and azimuth angle (θ) can be defined from the MM as in equations (2.50-52).

$$\xi = \tan\left(\frac{1}{2}\arcsin\left(\frac{M_{30}}{\sqrt{M_{10}^2 + M_{20}^2 + M_{30}^2}}\right)\right) \tag{2.50}$$

$$\varepsilon = \frac{1}{2}\arcsin\left(\frac{M_{30}}{\sqrt{M_{10}^2 + M_{20}^2 + M_{30}^2}}\right), \tag{2.51}$$

$$\theta = \frac{1}{2}\arctan\left(\frac{M_{20}}{M_{10}}\right), \tag{2.52}$$

The four parameters that can be calculated in equations 2.49-2.52 give an in depth description of the beetles' polarising properties. By employing the MM formalisation it will allow us to describe the variation in polarisation of a known input upon reflection upon the beetles.

For a MM to be physically realizable it must satisfy the following basic constraints (equations 2.53 and 2.54) [1],[2]. The MM is unable to add to the Stokes vector $\mathbf{S_a}$ in equation 2.37 in that the Stokes vector cannot have any components greater than 1. This is stated in equation 2.53).

This is to say that the degree of polarisation cannot be greater than 1 (equation 2.54).

$$\sum_{g,h=0}^{3} M_{gh}^2 \leq 4M_{00}^2 \tag{2.53}$$

$$P \leq 1 \tag{2.54}$$

2.4. References

[1] D. H. Goldstein, *Polarized Light - ISBN:9781439830413*. Boca Raton: CRC Press, 2010.

[2] J. Gil, "Characteristic properties of Mueller matrices," *J. Opt. Soc. Am. A*, vol. 17, pp. 328–334, 2000.

Chapter 3 - Background into Structural Colour & Biology

Two general categories of colour production are made, the first is pigmentary colour, which is where colours are created chemically. The second type is structural colour of which some is iridescent (goniochromism) and can vary reflected wavelength (colour) and intensity at different viewing angles.

3.1. Structural Colour

The first fossil record of an animal with a structural reflector dates from 515Ma (million years ago) [1], whilst the first eyes with lenses evolved 521Ma [2]. It has been suggested that the development of eyes was the cause of the Cambrian Explosion, in which colours developed and continued to do so as part of an evolutionary arms race [1],[2]. The colours that developed have been used in camouflage, signalling and as a warning to other animals. This variation makes it suitable for visual communication within and between species [3]. The oldest recorded structurally coloured beetle dates from 47Ma [4].

There are many different structural mechanisms present in nature which can produce colour including diffraction gratings, photonic crystals, selective mirrors, crystal fibres, deformed matrices, heliocoidal stacks, surface blazed gratings and dynamic changes. A brief description of different types of structural colour are made in this section of the thesis and their presence in beetles is discussed. Structural colour has long been a research area of science with both Newton and Hooke initiating the field (describing the colours in peacock tail feathers) [5],[6].

3.1.1. Diffraction Gratings

Diffraction gratings consist of a series of parallel slits or ridges which reflect different wavelengths. The reflection separates white light into the constituent wavelengths over multiple orders, such that a rainbow feature can be observed. The peak reflected wavelength relates to the period of the structure. In nature diffraction gratings take many different forms for example scute modification, longitudinal ridges, flutes or cross ribs which exist in different types of butterflies, both inside and on the surface of their wings [7]. Diffraction gratings were first observed in beetles in the 1940's [8] and were shown to be widely distributed in beetle families [9]–[12].

A simple diffraction grating is shown in Figure 3.1. The angular dependence is given in terms of incident angle (θ), diffracted angle (β), wavelength (λ), diffraction order (m) and grating period (a) and in equation 3.1.

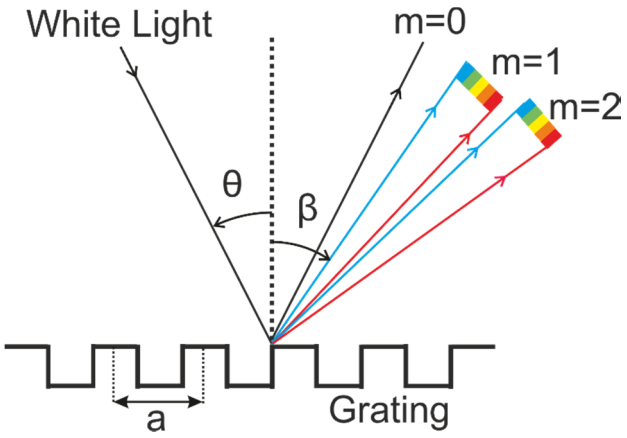


Figure 3.1 – Reflection grating, showing the 1st (m=1) and 2nd (m=2) diffracted orders.

$$a(\sin\theta - \sin\beta) = m\lambda \tag{3.1}$$

One such example of the simplest diffraction grating in beetles can be seen in Figure 3.2. More complex structures are known to occur and are discussed in a review paper by Seago [12].

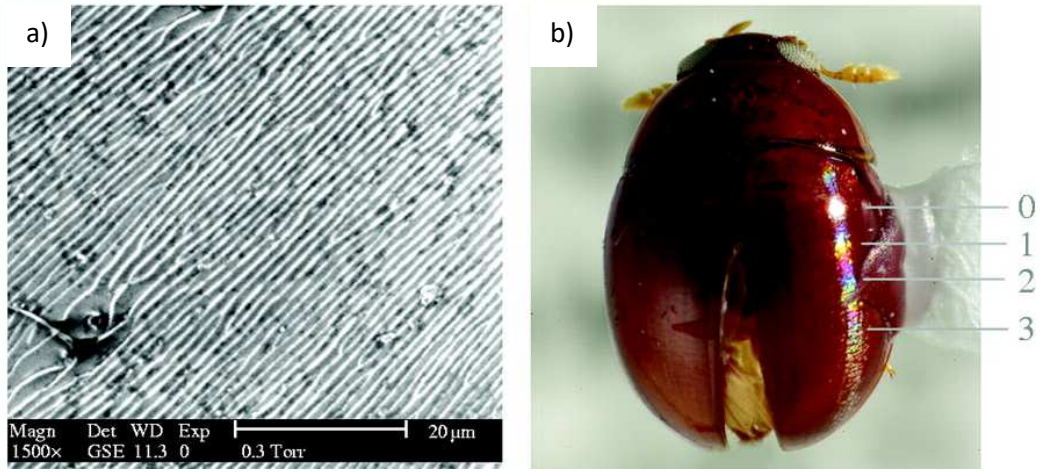


Figure 3.2 – a) Scanning Electron Microscope (SEM) image of the diffraction grating in a *Sphaeridiinae gen. sp.* Beetle and b) a photograph showing the 1st, 2nd and 3rd order diffraction reflections. Used with permission, from [12].

3.1.2. Photonic Crystals

3.1.2.1. Thin Film Interference

Colours from thin films which are observed in reflection, occur due to constructive interference [13]. The colour or colours of light reflected when a continuous white light ray is incident upon the layer relate to the thicknesses of the layer or layers. As well as the colour being related to the thickness of the layer it is also related to the refractive index of the materials and the angle at which the light travels through the material. As the incident angle increases from normal to the thin film surface the reflected wavelength will be is blue shifted.

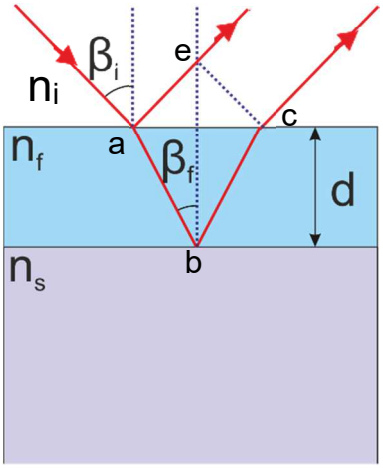


Figure 3.3 – Light incident from the medium of refractive index n_i, onto a single layer of film (of thickness d) with refractive index n_f, which is placed on a substrate medium of refractive index n_s. The variables are incident angle of light (β_i) and in the inside the film (β_f) The positions along the beam paths are labelled a, b, c and e.

The arrangement which will occur in most natural systems which are investigated in this study is $n_i < n_s < n_f$, this is shown in Figure 3.3. The optical path difference (Γ) of the two reflected paths is show is given as:

$$\Gamma = n_f(ab + bc) - ae. \tag{3.2a}$$

Through geometry of the different path lengths this becomes

$$\Gamma = 2n_f d\left[\frac{1}{\cos(\beta_f)} - \tan(\beta_f)\sin(\beta_f)\right] = 2n_f d\cos(\beta_f) \tag{3.2b}$$

For constructive constructive interference of such a system is given as

$$2\, n_f d\cos(\beta_f) = m\lambda, \tag{3.3a}$$

where m is the order of interference. Destructive interference occurs when

$$2\, n_f d\cos(\beta_f) = (m - \tfrac{1}{2})\lambda. \tag{3.3b}$$

3.1.2.2. Multi Layered Interference

Instead of a single layer of thin film, consider stacked multiple layers of thin films formed by two types of material of thickness d_1 and d_2 respectively. These layers differ from each other in refractive index (n_1 and n_2) and the angles of refraction are β_1 and β_2 in these materials respectively. The wavelength at which constructive interference occurs from such a structure can be found from equation 3.4.

$$m\lambda = 2(n_1 d_1 \cos\beta_1 + n_2 d_2 \cos\beta_2). \tag{3.4}$$

In the ideal quarter wavelength thin film situation, each of the layers will be of equal optical thickness as

$$n_1 d_1 = n_2 d_2. \tag{3.5}$$

When equation 3.5 is applied to equation 3.4 the resulting equation at a non-normal incident angle (β) becomes

$$m\lambda = 4n_2 d_2 \cos\beta. \tag{3.6}$$

If we consider this at normal incidence it becomes

$$4n_2d_2 = m\lambda. \quad (3.6)$$

Figure 3.4 shows a schematic of a multi-layered structure on a substrate of refractive index n_s, with the top surface exposed to a medium of refractive index n_a.

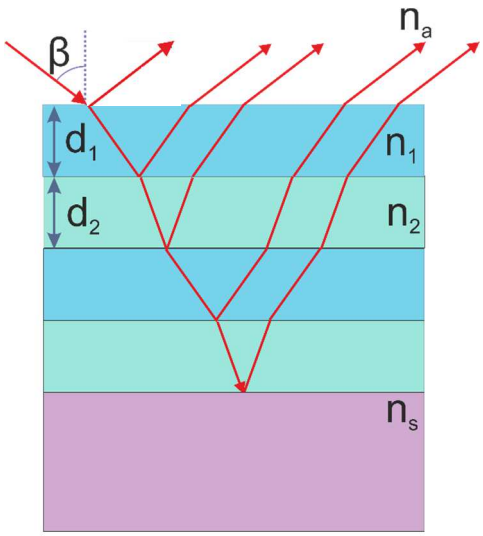


Figure 3.4 – Light reflection from a multi-layered structure embedded upon a substrate, with the light ray paths shown in red.

If equation 3.6 is obeyed and the refractive index of the material the stack (of multiple high-low layers) is placed on (n_s) is higher than that of the stack then the equation from reflected intensity (R) can be given as [14]:

$$R = \left[\frac{n_a(n_2)^{2N} - n_s(n_1)^{2N}}{n_a(n_2)^{2N} + n_s(n_1)^{2N}}\right]^2. \quad (3.8)$$

Where N is the number of pairs of n_1 and n_2 layers.

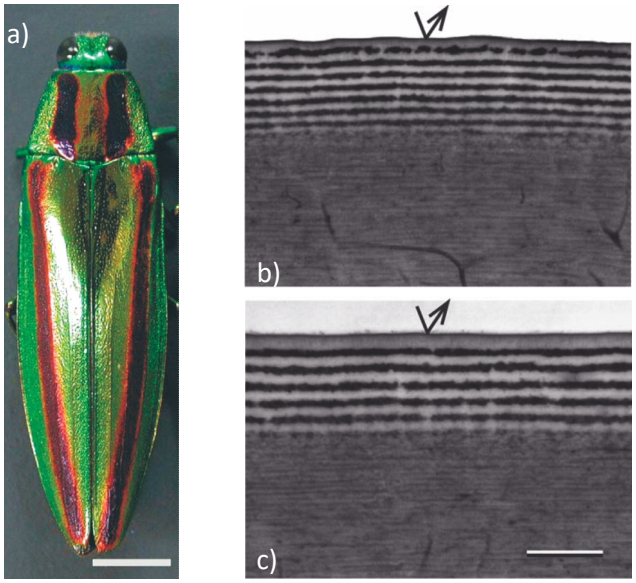


Figure 3.5 – a) Photograph of a *Chrysochroa fulgidissima* beetle with a 5mm scale bar, with Transmission Electron Microscope (TEM) image cross sections in the b) green and c) purple sections of the *Chrysochroa fulgidissima* shell with a 1µm scale bar. Used with permission, from [15].

One of the best known examples of multi-layered structure in nature is from the blue *morpho* butterfly, where the spectacular blue colour comes from a 'Christmas-tree' like structure [16]. In the beetle family, there are several examples of multi-layered structures such as in the *Chrysochroa* genus, which have multi-layered structures as seen in Figure 3.5 [15].

3.1.2.3. Heliocoidal Layered Interference

Helicoidally layered structures work in a similar way to the multi-layered structures, except instead of two different materials a single birefringent material is used. The material is arranged in a helicoidal manner such that the birefringent refractive indices rotate gradually (in plane) with depth from the surface. The dimensions of the structure relate to the colour of light which is reflected. The helix nature of the structure means that circularly polarised (CP) light is reflected. A full discussion of such a structure and its occurrence in beetles is discussed in Section 3.4.1.

CP interactions in nature are rare, primarily found amongst insects as well as a few plants. CP interaction has been observed in parts of various crustaceans (Figure 3.6), however it is greatly reduced by calcified layers in many shellfish and can be observed much more clearly after decalcification [17]. One special example is the mantis shrimp which can both reflect and detect CP light [18].

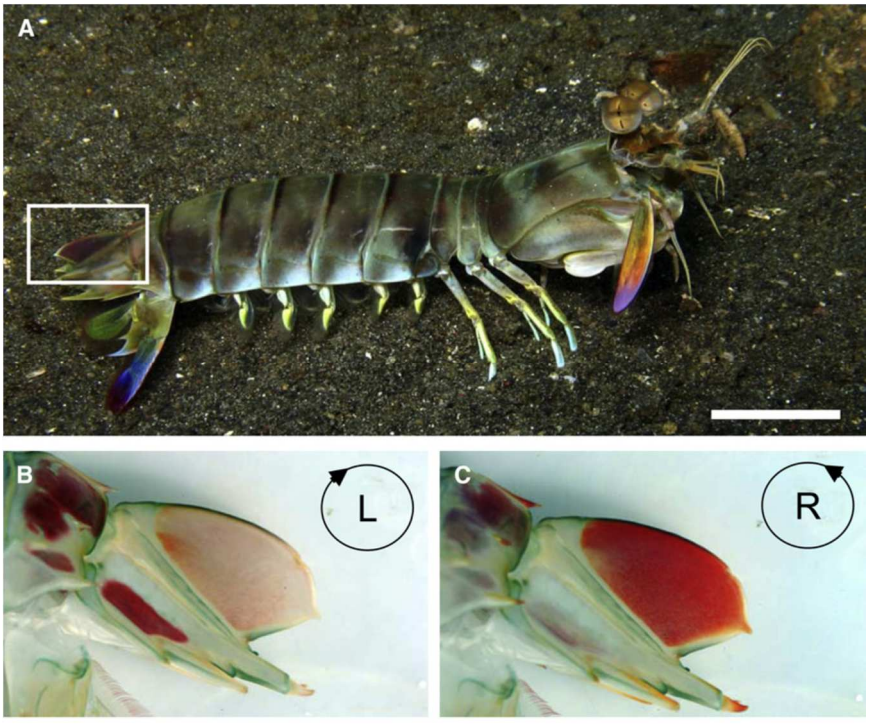


Figure 3.6 – Circularly polarising signal in the stomatopod crustacean *Odontodactylus cultrifer* (male). (A) Photograph where the scale equates to 1 cm. (Photograph by Chrissy Huffard.) (B) More detail of the telson keel (as framed in [A]) photographed through a left-handed circular polariser. (C) The same as (B) except through a right circular polariser. Used with permission, from [18].

Other sea creatures also interact with CP light including a prey of mantis shrimp, with a partially overlapping range, Sapphirinidae Copepods [19]. It has also been observed that dinoflagelates can circularly polarise light [20].

From the plant kingdom, both fruit and leaves have been seen to reflect CP light. The bright blue colour of Pollia berries is caused by helicoidal structures in cell walls within the epicarp [21]. The structures can both reflect left circularly polarised (LCP) and right circularly polarised (RCP) light within a single berry as seen in Figure 3.7. Also a strong CP response was seen from the fruit of *Margaritaria nobilis* (also known as the bastard hogberry) [22]. Some juvenile ferns have helicoidal structures which reflect CP light at blue wavelengths, for example in Figure 3.8 the species *Danaea nodosa* [23],[24].

Whilst not related to structural colour the effect of CP light upon growth has been seen in several plant species. In pea and lentil shoots exposure to LCP light was seen to accelerate growth [25]. In some species of marine algae (notably *Dunaliella euchlora*) exposure to RCP light was shown to increase photosynthesis, whilst exposure to LCP light decreased it [26].

The helicoidal structure is quite common in several subfamilies of beetle. The optical response from numerous examples is the focus of this thesis and further discussed in Section 3.4.

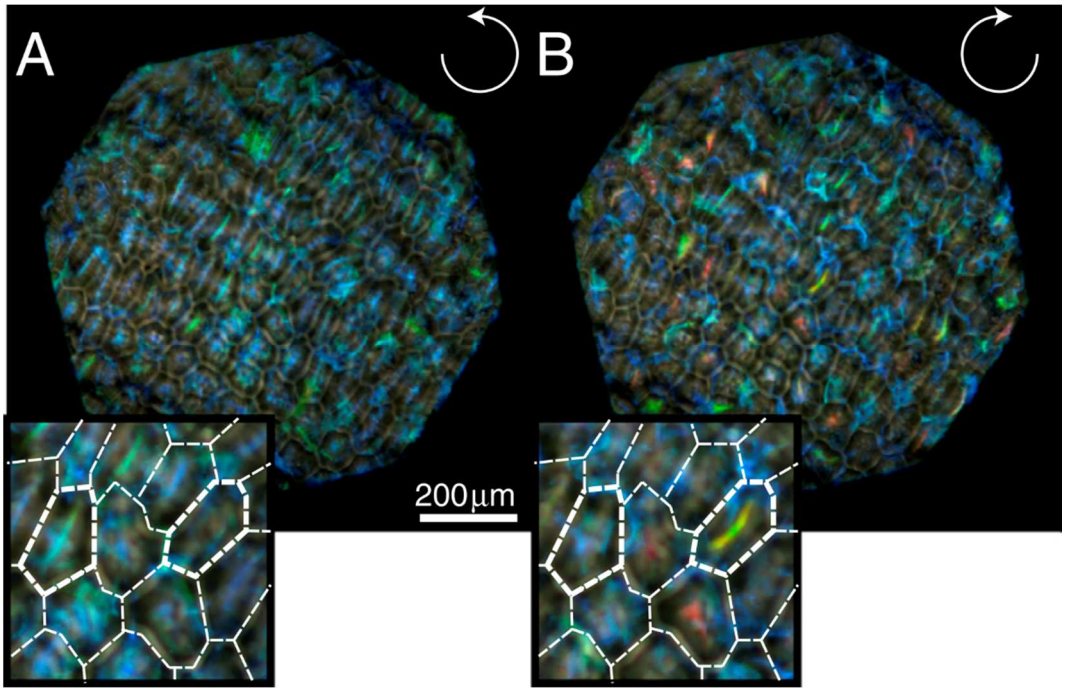


Figure 3.7 – Polarised reflection from the *Pollia condensata* fruit. (A) Left handed and (B) Right handed optical micrographs of the same area of the fruit under epi-illumination. The insets show a zoom of the central areas, with white lines marking the edges of the cells. Both images were obtained using a × 10 objective. Used with permission, from [21].

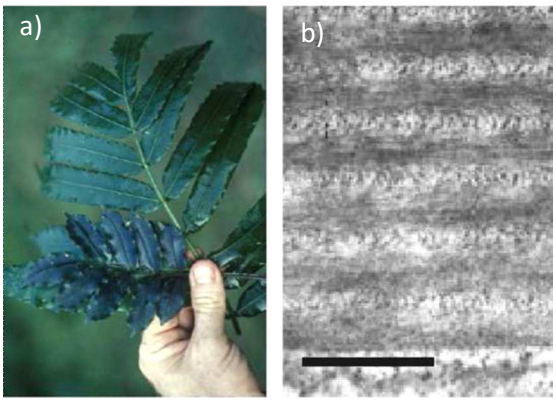


Figure 3.8 – a) Photograph of a juvenile (blue) and adult (green) leaf of *Danaea nodosa*. b) TEM transverse section image of the outer cell wall of a juvenile leaf with a scale bar of 300nm. Used with permission, from [23].

3.1.2.4. Surface Mirrors

Micro-mirrors (or bowl shaped concavities) are surface structure, which has been observed on the wing scales of the butterfly species *Papilio blumei* [27] and *Papilio palinurus* [28],[29]. The butterflies' scales are formed of a multi-layered stack of cuticle and air layers, the micro-mirrors perturb an otherwise straight surface as can be seen in Figure 3.9.

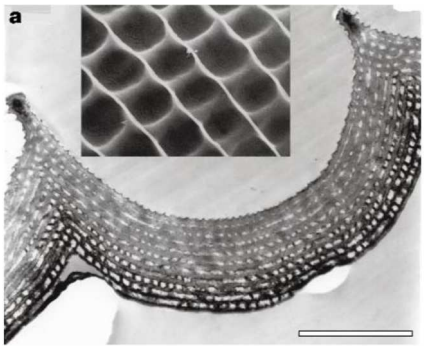


Figure 3.9 – TEM image through a micro mirror on a *Papilio palinurus* green scale, with an inset SEM image of the surface of the scale. Where the scale bar is of 1µm for the main image and 7µm for the inset image. Used with permission, from [28].

These butterflies create green colours by colour mixing of blue and yellow. If incident white light is normal to the micro-mirror, at the bottom of the concavity yellow light will be reflected, while at the side the reflection will be blue shifted, due to the angular dependence of multi-layered structures (Figures 3.10b and 3.10d). One other property of this structure results in the micro mirror acting as a retroreflector as seen in Figure 3.10d. If linearly polarised light is incident upon the structure the reflected blue light will have undergone two 90° phase shifts (180° total), whilst the yellow will have only undergone one, this was demonstrated with crossed polarisers in Figure 3.10c.

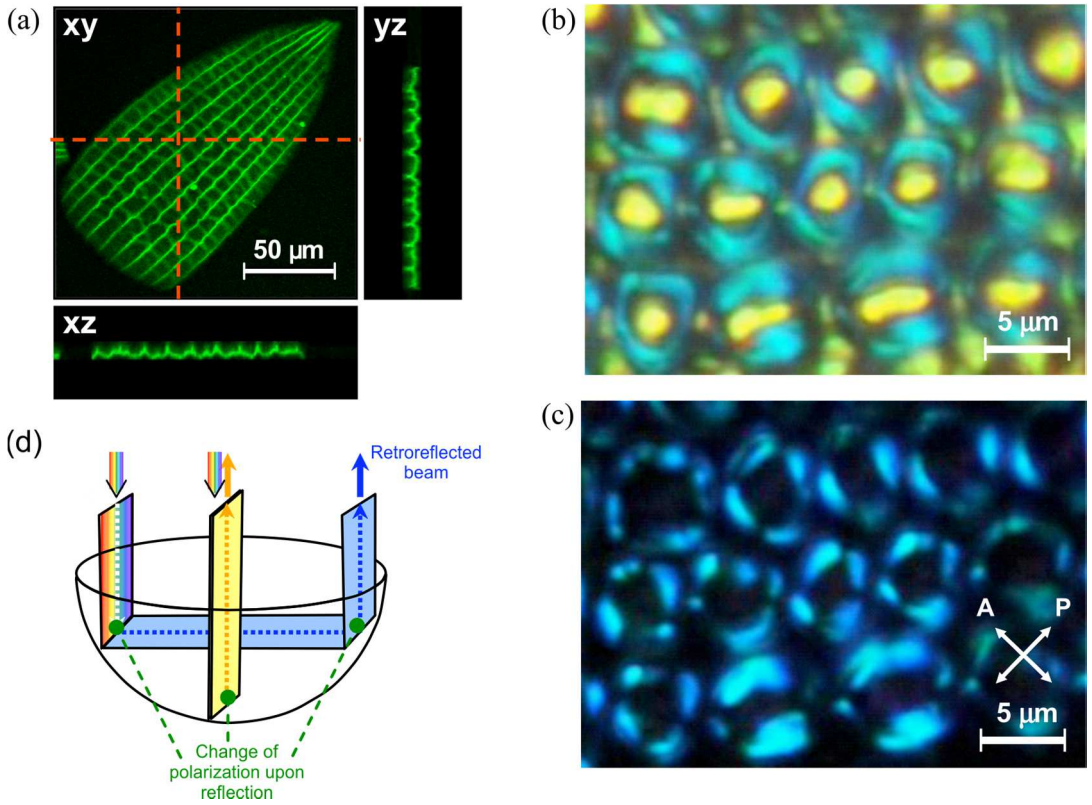


Figure 3.10 – (a) Confocal pseudo-2D micrographs of *Papilio palinurus* in fluorescence reflection mode, showing a single wing scale in xy, yz, and xz orientations. The yz and xz images correspond to the area along the red dotted lines in xy image. An optical micrographs of *Papilio palinurus* with incident white light with (b) a single linear polariser and (c) under crossed polarisers. The reflection from the centre/bottom of the bowls is extinguished under crossed polarisers. (d) White light diagram of the reflection from the bottom and sides of the concavity. Used with permission, from [29].

3.1.2.5. 3D Photonic Crystals

3D Photonic structures occur in nature, one of the more complex types is an opal like structure discovered in an Australian weevil [30]. Opals have ordered close packed spheres of silica, which vary in both diameter in different areas and also with different viewing angles. There have been several photonic arrangements observed within weevils, both ordered and disordered non-closepacked structures [31].

Circular spheres as well as bicontinuous diamond based architectures have been observed. A wide variation in the colours reflected from these beetles has been seen across the visible spectrum, caused by a wide range of lattice parameters. More complex structures occur including inverse structures consisting of holes. Bartl *et al*. discovered a diamond-based photonic crystal structure in the beetle *Lamprocyphus augustus* [32] as can be seen in Figure 3.11. This beetle is particularly interesting in the fact that it shows a high degree of angular independence in colour (due to each single scale being made of an array of differently oriented crystalline domains), unlike the structure of an opal.

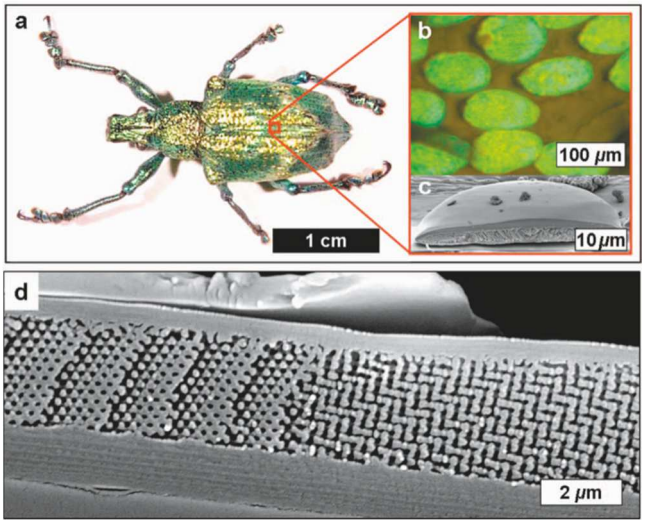


Figure 3.11 – a) Photograph of *L. augustus*. b) Optical micrograph under white-light illumination of individual scales of *L. augustus*. c) SEM image cross section of a single scale. d) Cross-sectional SEM image of a scale. Used with permission, from [32].

3.1.3. Scattered Colours

There are several different forms of scattering. The following describes three forms of scattering, Rayleigh, Tyndall and Mie. The definition of type of scattering varies, in this report the Scattering cross section ψ (equation 3.9) is used to define the type of scattering, this description is taken from [33] as

$$\psi = \lambda/\mathrm{D}, \tag{3.9}$$

where D is diameter of the scattering microsphere. Rayleigh scattering occurs when the particles involved in the scattering are approximately at least a magnitude smaller than the wavelengths as:

$$\psi \geq 10. \tag{3.10}$$

Mie scattering occurs when the wavelength of light is roughly the same size as the scattering particles as:

$$10^{-2} \leq \psi \leq 10. \tag{3.11}$$

Finally scattering which occurs when the particles are much larger than the wavelength of the molecules is termed Tyndall scattering. It is independent of wavelength, in this case:

$$\psi \leq 10^{-2}. \tag{3.12}$$

It should be noted that in this definition is not a definitive one and in many publications Tyndall scattering is often omitted and the point between Mie and Rayleigh scattering is not well defined.

Mie scattering is reported to occur from unordered filaments in the bright white beetles of the genera *Cyphochilus* and *Lepidiota* [34]–[36], as can be seen in Figure 3.12.

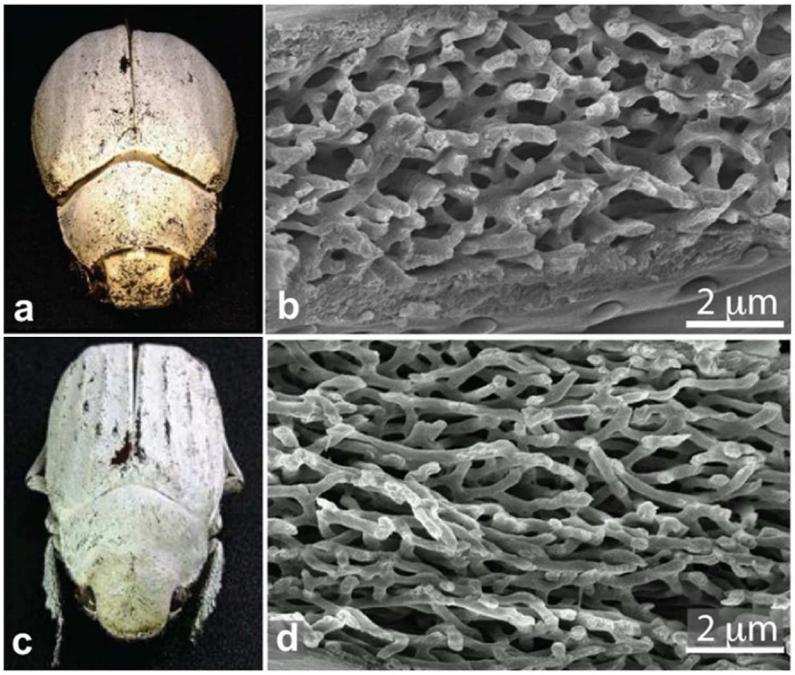


Figure 3.12 – Bright White reflection from beetle scales. (a,c), Photographs of *Cyphochilus* and *Lepidiota stigma* beetles, respectively. (b,d), SEM images of the cross-section of the scales of the respective species. Used from [34] under CC 4.0 License.

It was long thought that incoherent scattering from randomly oriented particles was responsible for many mainly blue skin colours in birds, mammals and in some dragonflies. However, recent studies have shown this not to be the case. Coherent scattering from quasi ordered arrays of collagen fibres is now thought to be responsible for the colour in of many avian species' skin [37] as well as in mammals (Figures 3.13 and 3.14) [38]. This was also seen to be the case in the blue *Odonata* dragonflies where a quasi-ordered structure was responsible for the colour (Figure 3.15 and 3.16) [39].

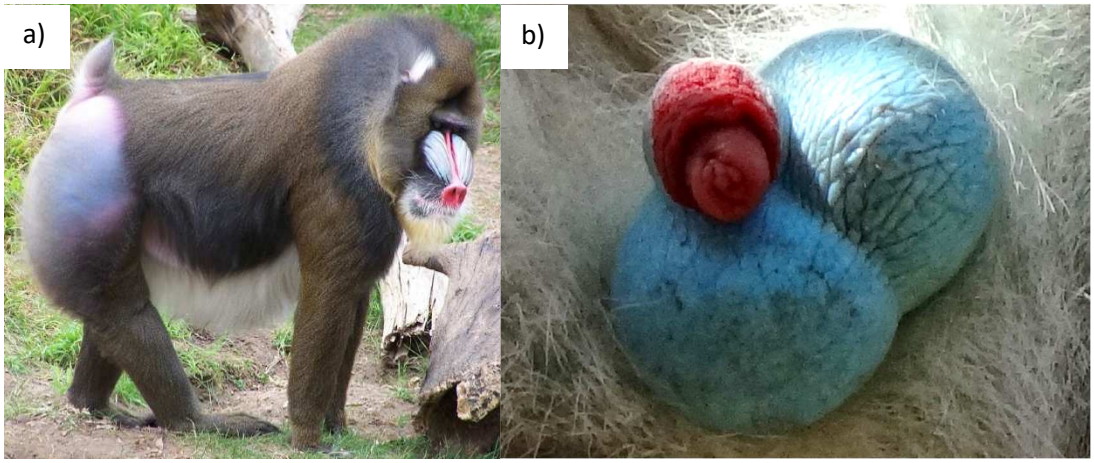


Figure 3.13 – a) Blue rump/faced mandrill, adpated from [40] by Brian Michelsen (under CC 2.0) b) Vervet monkey blue scrotum, from [41] by Bjørn Christian Tørrissen (under CC 3.0).

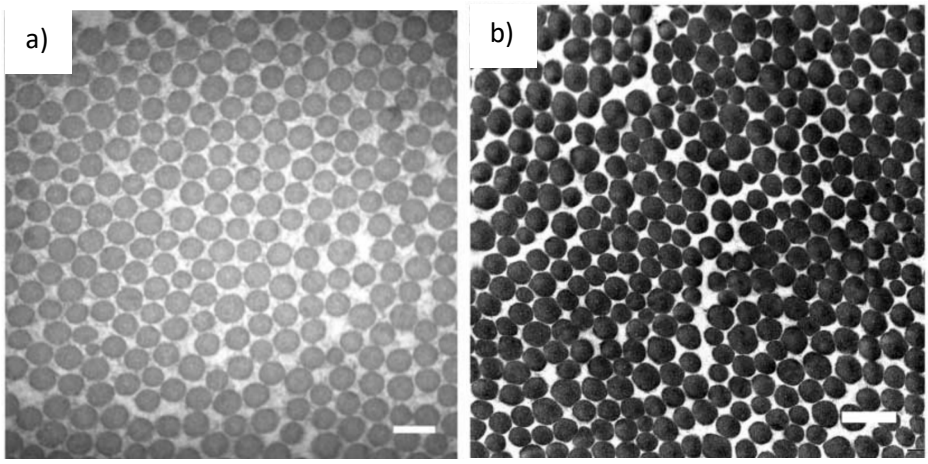


Figure 3.14 – TEM images of collagen arrays from structurally coloured mammal skin. a) Male mandrill facial skin at 40000×. Scale bar, 250nm. b) Vervet monkey (*Cercopithecus aethiops*) scrotum at 25·000×. Scale bar, 500nm. Used with permission, from [38].



Figure 3.15 – *Enallagma civile* dragonfly, with a strong structural blue colour. Adapted from [42] (Andrew C) (under CC 2.0).

A quasi-ordered colour structure has been observed in a *Eupholus* beetle [43]. It has also been beetles observed as the non-dominant colour structure in other beetles, where a faint blue or purple sheen can be seen in Figure 3.17 [12].

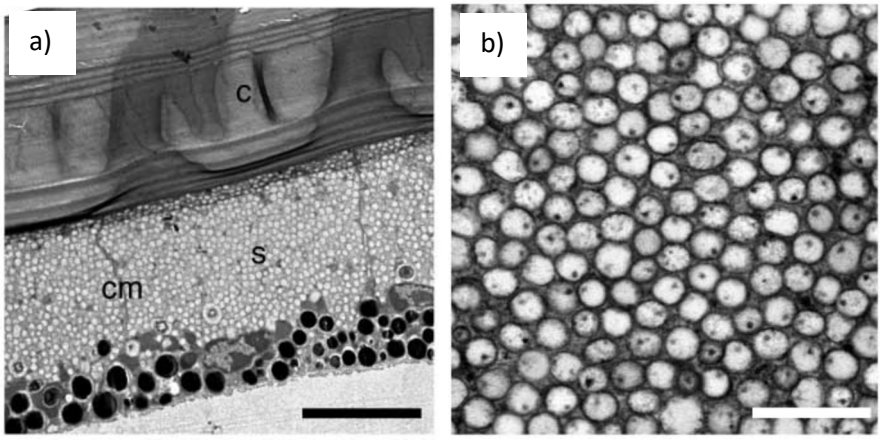


Figure 3.16 – TEMs of the structure of the familiar bluet, *Enallagma civile*, showing (A) The cuticle and epidermal pigment cells with a scale bar of 5µm and (D) Light- scattering nanospheres, with a scale bar of 500nm. Where abbreviations are used: c, cuticle; cm, cell membranes of neighbouring pigment cells; s, light-scattering spheres. Used with permission, from [39].

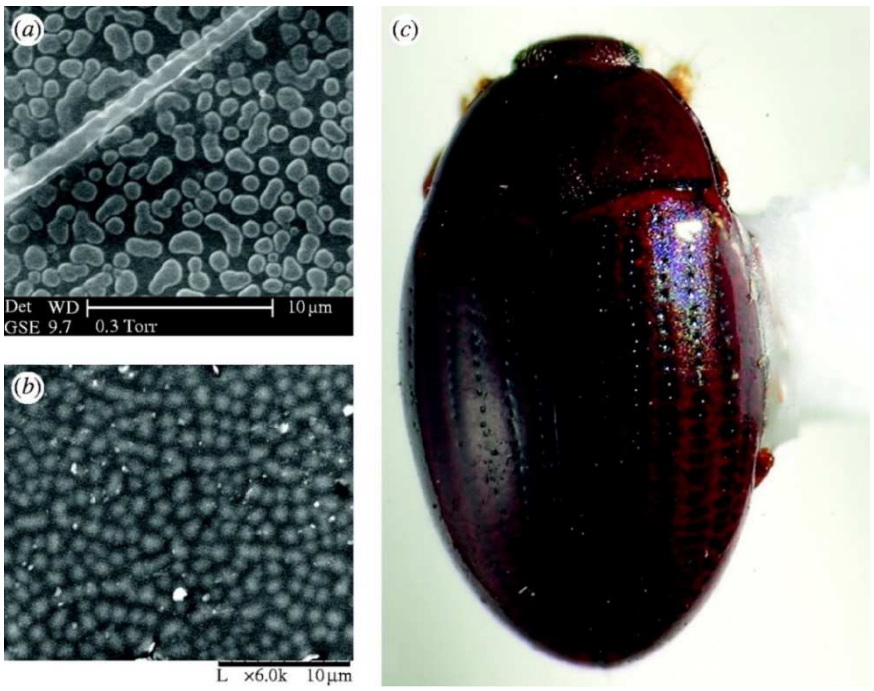


Figure 3.17 – SEM of scattering structure in (a) *Heikertingerella sp*. (Chrysomelidae: Alticinae), and (b) *Mychocerus sp*. (Cerylonidae). (c) Photo of *Mychocerus sp*. (Cerylonidae) with diffuse reflectance. Used with permission, from [12].

3.1.4. Summary

In this section structural colour which exists in many different forms in nature has been discussed. Such structures include diffraction gratings, multilayers, helicoidal structures, surface mirrors and scattered colours. The occurrence of such structures in beetles is also discussed in greater detail in Section 3.4.

3.2. Pigmentary Colour

Pigmentary colour differs from structural colour by the fact that it is caused by absorption and re-radiation through electron transitions. The wavelengths of light which the pigments cannot absorb are reflected, which gives rise to the coloured appearance of such structures. Unlike most structural colours, pigmentary colour is constant for all viewing angles. One of the more well-known examples is chlorophyll, which is responsible for the green colour of most plants. In many insects (including beetles) melanin is present, which usually produces either a brown or black colour.

3.3. Variable Colours

There are many ways in which colour in animals can reversibly alter. The first type of dynamic colour that will be discussed is observed in many species including cephalopods [44]–[47].

This type of reversible colour is caused by special cells within animals' skins which are called chromatophores. The chromatophores occur in four different colours through pigments; yellow (xanthophores), red (erythrophores), blue (cyanophores) and black-brown (melanophores).

There are two types of chromatophore which produce structural colour, the first are called iridophores which consist of platelets in a multilayer arrangement [48]. The second type of chromatophore are leucophorem, which cause a white appearance through scattering of light by physical particles [48].

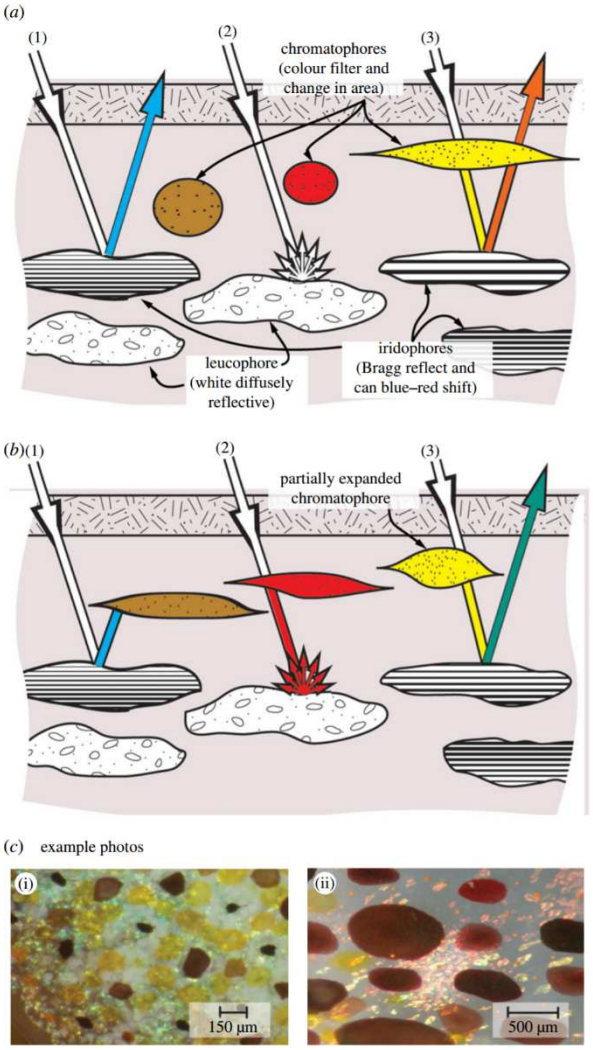


Figure 3.18 – Diagram of cephalopod skin with brown, red and yellow chromatophores, iridophores and leucophores in two different states of chromophore expansion (a) and (b), with three distinct ray paths (1), (2) and (3). (c) Photographs of (i) cuttlefish skin showing leucophores (white), chromatophores (yellow, red and dark brown) and irridophores (blue-green) and (ii) squid skin, showing chromatophores (yellow, red and brown) and iridophores (yellow and red). Used with permission, from [49].

Chromatophores can be expanded and contracted by muscles which alters their appearance as can be seen in Figure 3.18. The pigmentary chromatophore expansion means the pigments get spread over a wider area [49]. Iridophores' colours can be altered changing their lattice spacing, which was observed to happen in chameleons [50]. Switchable leucophores have also been observed in a squid species [51].

There are several more different structural colours which can alter dynamically. One mechanism of colour change is with porous layers and is known as hygrochromic colour change [52],[53]. An example is the male beetle of the species *Hoplia coerulea*, which lives in South

France/Northern Spain and is blue in normal conditions, but once in contact with water (or ethanol), it changes to green [54]–[56]. The colour change occurs due to the beetle's shell having micropores, which allow the water to enter the photonic structure. The presence of water changes the refractive index and hence the reflected wavelength. A diagram of the structure can be seen in Figure 3.19. The colour change happens over a few minutes and is reversible albeit more slowly.

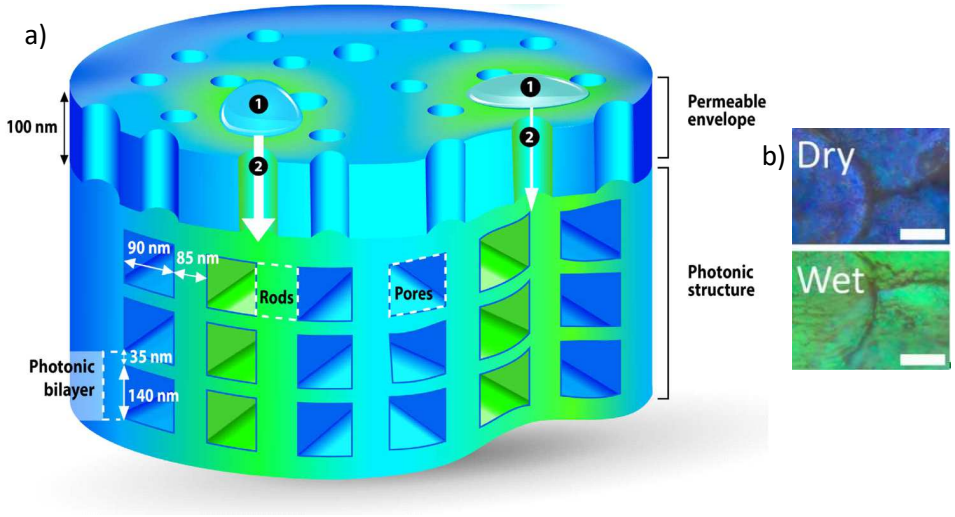


Figure 3.19 – a) Diagram of the porous photonic structure of a male *Hoplia coerulea* beetle. Where the water droplets are on the permeable envelope (1) and transfer through the permeable envelope (2) to the photonic structure. b) Photograph of a beetle's scale in wet and dry states with water, with scale of 20µm. Adapted from [54] (under CC 4.0).

The Panamanian Tortoise beetle, *Charidotella egregia* is usually observed in a golden state, due to a multi-layered structure. Once the beetle is alarmed or copulating the beetle undergoes a reversible colour change to red. Liquid from porous patches is forced into gaps in the multi-layered structure making its refractive index homogeneous and translucent such that only red pigmented colour behind can be observed (Figure 3.20) [57].

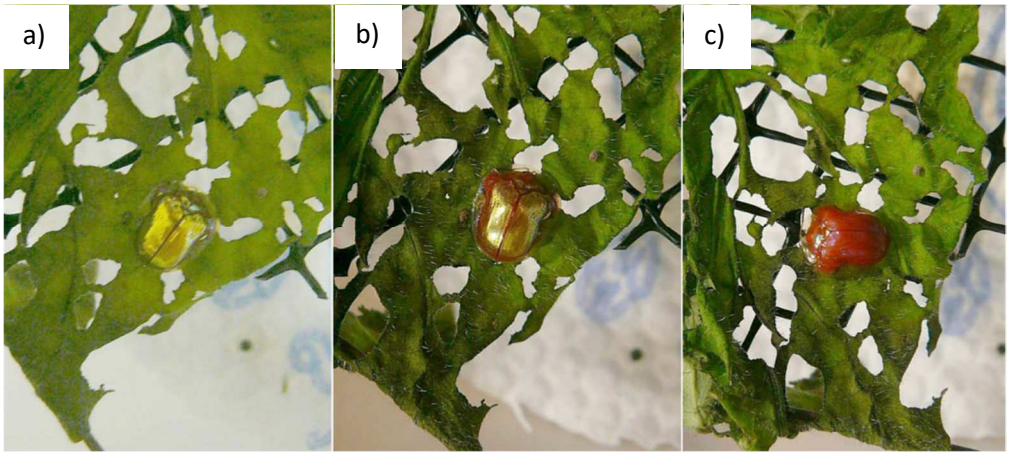


Figure 3.20 – Photographs of the Panamanian Tortoise beetle (*Charidotella egregia*) transforming from its a) normal gold state to b) an in between state and the c) an alarmed red state. Used with permission, from [57].

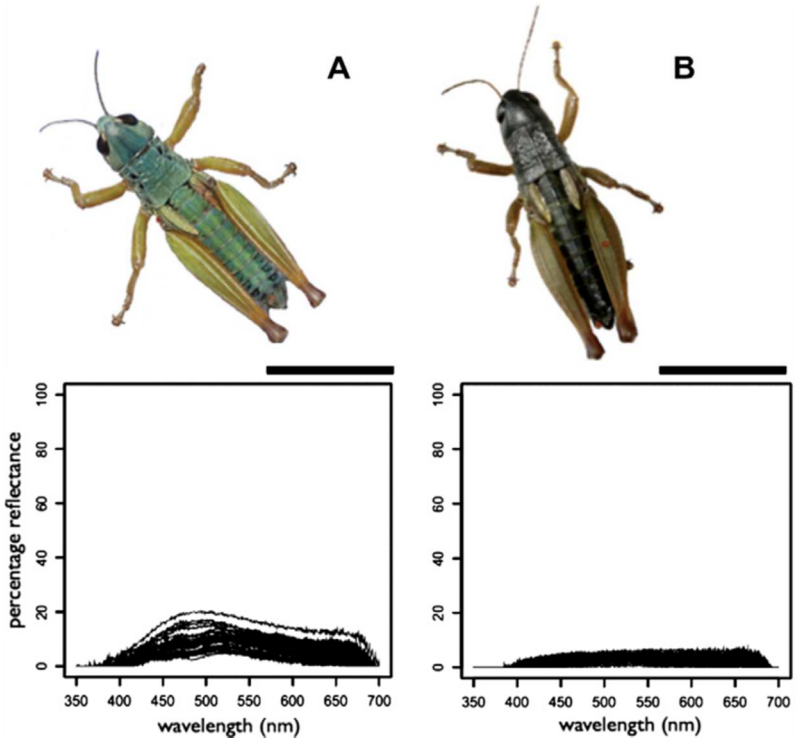


Figure 3.21 – Photographs and reflection spectra of the chameleon grasshopper (*Kosciuscola tristis*) at a) over 25°C and b) under 10°C. Used with permission, from [58].

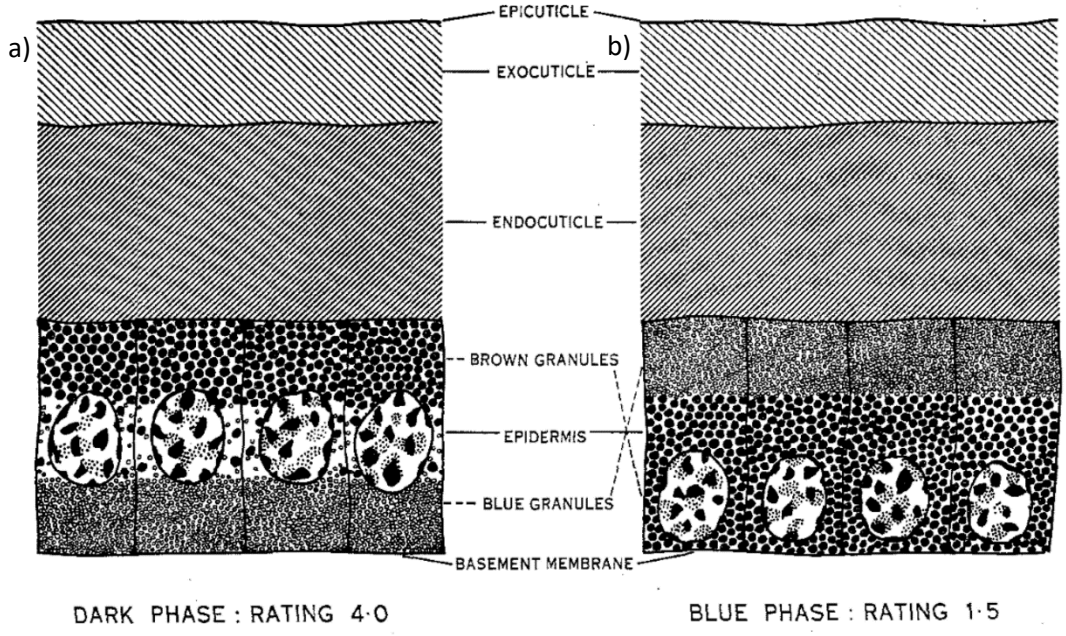


Figure 3.22 – Diagram of the carapace of the chameleon grasshopper (*Kosciuscola tristis*) at a) over 10°C and b) under 25°C. Reproduced from Key and Day (1954), with permission from CSIRO Publishing [59].

A colour change which is induced by temperature change can be seen in males of the chameleon grasshopper (*Kosciuscola tristis*) [60]. In ambient temperatures below 10°C the grasshopper is black in appearance and above 25°C is bright sky blue as can be observed in Figure 3.21 [58]. In the warm phase the blue colour is suggested to be caused by Tyndall scattering from closely packed small granules (average diameter of 0.17µm) which are near the surface. In the cold phase the black colour is caused by larger granules (1.0µm) moving towards the surface between the smaller granules, which reduces the Tyndall scattering (Figure 3.22). Whilst the colour

change is reversible with temperature, the black to blue transition is ten times faster than the reverse.

A large number of variable structural colour examples exist, only a few of which have been highlighted in this section.

3.4. Beetles with Heliocoidal Structures

This thesis focuses upon beetles with helicoidal structures within their shells, and as such the background upon beetles with this structure is described in more depth in this section. The study of beetles which selectively reflect near CP light was first undertaken by Michelson in 1911, who described the effect (in *Chrysina (Plusiotis) resplendens*) as being "due to a 'screw structure' of ultramicroscopic, probably molecular dimensions" [61]. The structure responsible for these reflections was described as an analogue of Cholesteric Liquid Crystals (CLCs) first by Gaubert (1923) who was first to describe the reflection being mainly LCP (except at the red extreme) for *Chrysina amena* [62]. Onslow found colour produced by layers in *Cetonia aurata* changed further into the beetle by removing layers at the surface from green to red (which implies a structure with a longer period) [63]. A *Chrysina (plusiotis) gloriosa* beetle was investigated by Mason in 1926, who described the colour as a layered structure, which was backed by pigment [53]. In 1937 a study by Mathieu and Farragi found eight species of beetle from the Cetoniinae and Rutelinae subfamilies which reflected CP light [64].

In 1966 Robinson reported that six subfamilies of Scarabaeidae contain beetles which reflected CP light [65]. A twisted lamellate structure was described as the cause of the CP reflection by Bouligand [66]. Further details about the structure were described by Neville and Caveney, who investigated more species and described the reflection of both RCP and LCP light by *Chrysina resplendens* [67]. It was found that the exceptionally high reflecting broadband metallic colours which can be seen in some species of the *Chrysina* genus was due to birefringent enhancement of the helicoidal structure by the presence of uric acid [68].

The number of studies has accelerated since the 1970's with interest coming from many scientific disciplines including engineering, biology and optics. There have been investigations into the heliciodal structure within the cuticle using various imaging techniques [68]–[75] and the surface structures [69],[76]–[81]. Beetles' optical and polarisation properties have also been widely investigated [67],[68],[71],[73],[75],[76],[80],[82]–[90]. A list of species which have been studied previously can be found in the Appendix A1.

A study of over 19,000 species of scarab beetle was undertaken by Pye who found CP reflection in over one hundred species in eight subfamilies from the Scarabaeidae family and one subfamily

from the Hybrosoridea family [91]. Pye measured the polarising properties of the beetles in terms of the ratio of LCP to RCP light.

Several review articles on the subject of metallic colours in beetles and insects also exist [12],[92],[93].

3.4.1. Structural Description

The structure responsible for this colouring is often analogised with the properties of CLCs [94]–[96]. The beetle shell structure is composed of thread-like chitin molecules (fibrils) in a protein matrix [97]. The orientation of these molecules is the same within an individual layer. The angle of the molecules' orientation systematically changes by a few degrees between consecutive layers, until eventually a full 360° rotation occurs, the thickness taken to achieve this is known at the pitch (Figure 3.23) and can be seen in a TEM, Figure 3.24.

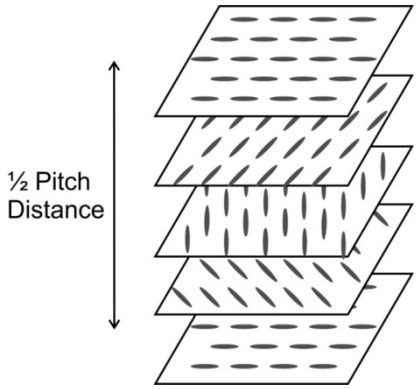


Figure 3.23 – Schematic of the gradual change in orientation of the thread-like molecules between consecutive layers of chitin material. The half pitch distance relates to a 180° rotation of the chitin molecules. Published by the author in [98].

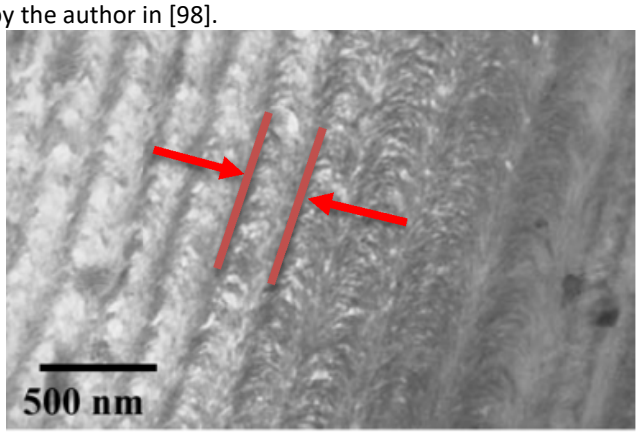


Figure 3.24 – TEM microscope image of fibrous chitin in helicoidal layers from a green *Chrysina boucardi* beetle. The half pitch distance is shown with red arrows. Adapted from [78] (under CC 3.0).

When an Electromagnetic wave is incident on such a surface it is reflected and polarised in the shape of the chitin orientation. The reflected wavelength (Bragg wavelength) (λ) of the structure is related to the pitch (p), average refractive index ($\bar{n}(\lambda)$) and incident angle (θ) as

$$\lambda = \bar{n}(\lambda) p \cos(\theta). \tag{3.13}$$

The reflected wavelength has an angular dependence, when viewed at a larger viewing angle the wavelength will blueshift. However in most of this study the measurements are taken at near normal incidence so the cos term tends to one, giving equation 3.14a. The peak width (full width at half maximum) $\Delta\lambda$ is related to the birefringence $\Delta n(\lambda)$, in equation 3.14b.

$$\lambda = \bar{n}(\lambda)p. \tag{3.14a}$$

$$\Delta\lambda = (\Delta n)p. \tag{3.14b}$$

The molecules' thread-like nature means they are optically birefringent and the addition of uric acid enhances this beyond that of the individual components [68]. The refractive indices have been reported to be between 1.4 and 1.8 [99],[100], with variation with wavelength (in nm) in chitin (from a shrimp) stated by a Sellmeier relation (equation 3.15) [99].

$$n^2(\lambda) = 1.0 + \frac{1.5133\lambda^2}{\lambda^2 - (134.7)^2}. \tag{3.15}$$

The birefringence in beetles was reported to be between 0.018 [73] and 0.2 [75]. Whilst the thickness of the constituent chitin fibrils has been reported as ~20nm (from crustaceans) [101]. The extinction coefficient was reported in helicoidal beetles as k=0.025, but can vary with chemical composition [99]. The number of pitches contained within each beetle changes within and between species of beetle, with tens of pitches being typical, with Brink reporting 41 and 74 pitches in scarabus beetles [86].

There are many perturbations to the single pitch structure that reflects a single peak of LCP light. Often perturbations to such a structure result in multiple peaks at different wavelengths. These variations include chirped or other gradual variations in pitch, which can result in broadband reflection occurring [65],[80],[98]. Another possible structure, which can result in a sudden trough in the reflected wavelengths is the sudden jump in the orientation of molecules between consecutive helicoidal layers. The sudden jump has previous been modelled as a possible structure within such beetles by Brink et al [89]. The possibility of an absorbing layer within the shell, which prohibits the reflection of certain wavelengths has been discussed (such as a blue wavelength absorbing pigment in insects [102]), although this is yet to be observed in beetles. Basic schematics of these four structures can be seen in Figure 3.25. Examples of such spectra are demonstrated in Section 4.3.

One of the most striking complex perturbations has been reported in the *Chrysina resplendens* beetle, which is seen to reflect both LCP and RCP light whilst preserving the handedness of incoming light. This was explained as a half waveplate like layer being between helicoidal stacks of chitin (Figure 3.26), this layer introduces a π phase shift and hence changes the handedness of LCP to RCP passing through it and vice versa [67]. This layer also acts as a twist like defect as the orientation of molecules between the helicoidal layers is interrupted [103].

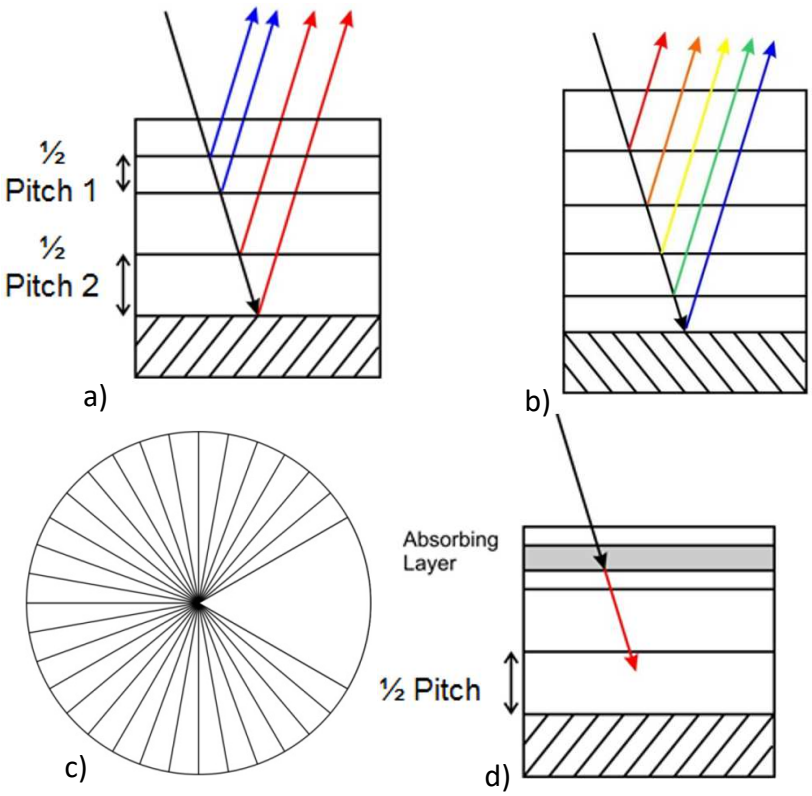


Figure 3.25 – Schematic of structural perturbations to a single pitch values in beetles of a) multiple distinct pitches (cross sectional view), b) a chirped structure or varying pitches (cross sectional view), c) sudden jump in the molecule orientation (if all the chitin layers orientations (represented by the lines) could be seen at once, between two pitches) (top view) and d) an absorbing layer within the material (cross sectional view). Published by the author in [98].

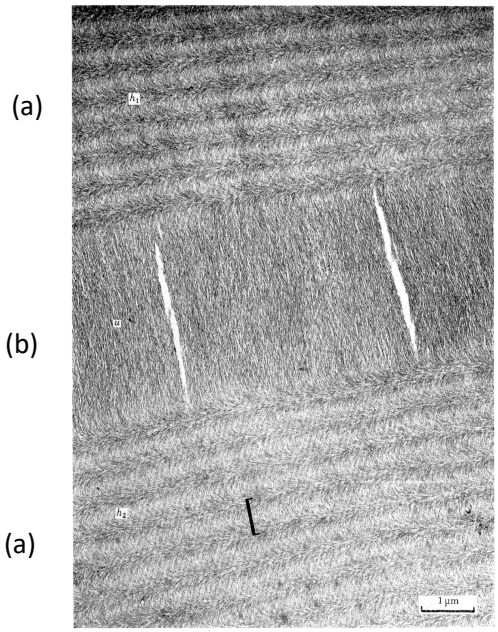


Figure 3.26 – EM image of a unixial half waveplate-like layer (b) of a *Chrysina resplendens* beetle between helicoidal stacks (a). Used with permission, from [68].

3.4.2. Structural Elliptical Studies

Studies which describe the beetle as simply reflecting LCP or RCP light are too simplistic and overlook very important details of the polarisation structure. This includes the fact the structure is not simply helicoidal, with non-uniform surface structures occurring in some species. All

species have a waxy cuticle of a different refractive index being above the helicoidal structure, whilst the majority of species have a layer of melanin behind the helicoidal layers. Ellipsometery has been used in order to measure the polarisation and to obtain important parameters such as degree of polarisation, the ellipticity and azimuth angle (as described in Section 2.3). A detailed discussion on ellipsometry upon beetles was made by Jarrendahl and Arwin [104].

A study by Lowrey *et al* used (non-MM) spectral ellipsometry to investigate the polarisation properties of several scarabs [105]. Due to the polarisation properties of these beetles, non-MM ellipsometry is not fully descriptive. The group to which Lowrey belonged progressed to Mueller Matrix Spectral Ellipsometer (MMSE) with a low cost setup over the wavelengths (400-900nm) [83],[106]. In the MMSE the beetle *Anoploganthus parvulus* had a broadband response with a high degree of left handed polarisation. The *Calloodes grayanus* showed a similar response, but was more narrowband. The *Chrysina resplendens* however showed a much weaker degree of polarisation and ellipticity.

One of the first sets of ellipsometeric measurements to obtain a fixed angle MM reflection (400-700nm) from scarabs was done by Goldstein upon four *Chrysina* species [107]. Three *Chrysina* species (*C. adelaida*, *C. clypealis* and *C. gloriosa*) showed a negative M_{30} MM element, which indicates left handed reflection. As with the previous studies the M_{30} MM element of *Chrysina resplendens* did not approach the negative extreme and was also positive at some wavelengths, which corresponds to right handed reflection.

MM ellipsometry of other species were also undertaken with variation with angle as well as MM imaging [108]. Non MM Imaging polarimetry of circularly polarised beetles has also been done, which enables measurement of the whole of a beetle at once [109].

The group at Linköping University in Sweden worked (and collaborated on) MMSE on beetles over a broadband range (200nm-1000nm) [110]–[113], with continuous variation over a range of incident angles (20°-75°**)** [114]–[116].

One MMSE study of particular note was a study of eight species from the genus *Chrysina* by Fernandez del Rio *et al* [117]. The MMs measured were used to calculate the degree of polarisation, ellipticity and modulus azimuth angle (as described in Section 2.3). These can be seen in Figures 3.27-3.30.

There are four quite different analyses of MM of beetles which reflect CP light, the first (Figure 3.27) being *Cetonia aurata*, which has no right handed reflection (since M_{30} is always positive), at near normal incidence this example shows a reflection narrowband peak which is close to fully LCP (as indicated by $M_{30}\approx-1$ and $e\approx-1$, with $P\approx1$) and is at a green wavelength with an

azimuth angle smaller than 90°. As the incidence angle gets larger reflected light would become more polarised, but also far from CP (as indicated by M_{30}≈0, e≈0). The *Chrysina macropus* beetle MM analysis can be seen (Figure 3.28) to be similar to the *Cetonia aurata*, however the polarised reflection is far less intense.

A MM analysis of a typical metallic *Chrysina*, *Chrysina chrysargyrea* (Figure 3.29) is a more broadband response than *Cetonia aurata*. The response differs in that at certain wavelengths at large incident angles the MM element M_{30}=1, which implies right handed reflection.

The last variation is *Chrysina resplendens*, which is known to reflect both RCP and LCP light is vastly different. The MM analysis of this beetle (Figure 3.30) at near normal incident suggests reflection of right handed light at NIR wavelengths and left handed light is dominant otherwise. Again it can be seen that the near circular polarisation is gradually lost as the incident angle increases.

MMSE is becoming an ever more popular tool to investigate such structures with ever more ellipsometric studies being undertaken [118],[119]. MM analysis such as Cloude decomposition and regression analysis have also been undertaken in order to calculate refractive indices, layer thickness, pitch, additional parameters as well as finding the different contributions of mirror like and circularly polarising components of the cuticle [100],[120],[121]. A larger description of ellipsometry and polarising nanostructures in nature can be found in reference [104].

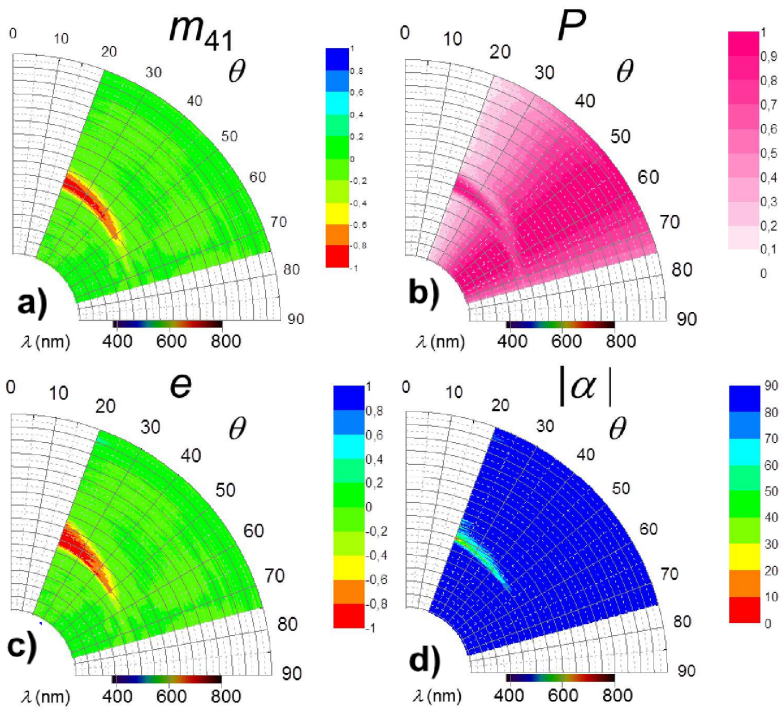


Figure 3.27 – Contour plot of incident angle (θ, this figure only), against wavelength (λ), for a *Cetonia aurata* beetle, showing a) the Fully Normalised MM element m_{41} (which is the same as $\mathbf{M}_{30}$ in this study) b) the degree of polarisation (P), c) the ellipticity (e) and d) the modulus of azimuth angle (|α| (this figure only)). Used with permission, from [122].

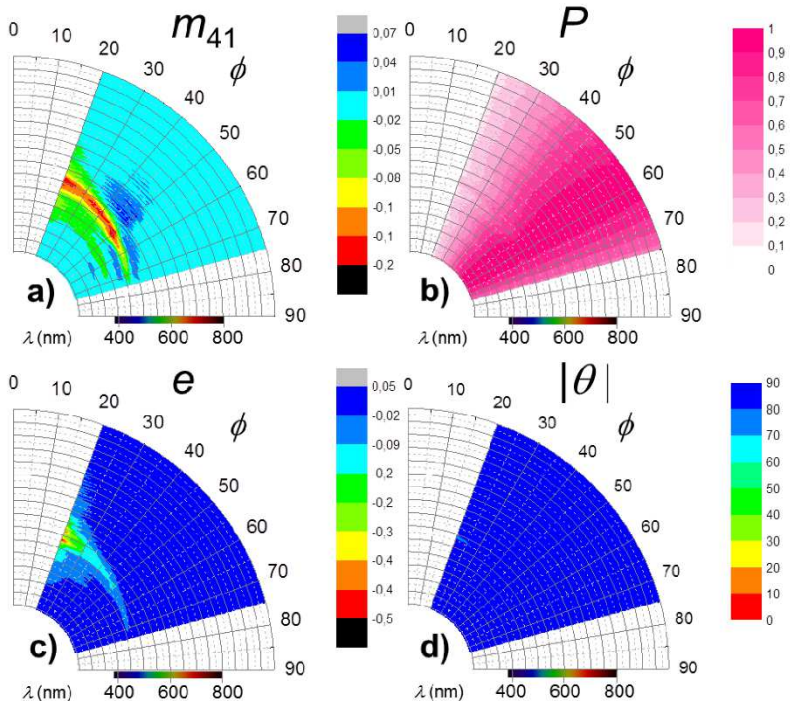


Figure 3.28 – Contour plot of incident angle (ϕ), against wavelength (λ), for a *Chrysina macropus* beetle, showing a) the Fully Normalised MM element m_{41} (which is the same as $\boldsymbol{M}_{30}$ in this study), b) the degree of polarisation (*P*), c) the ellipticity (*e*) and d) the modulus of azimuth angle (|θ|). Note these plots have been rescaled due to their low values. Used with permission, from [123].

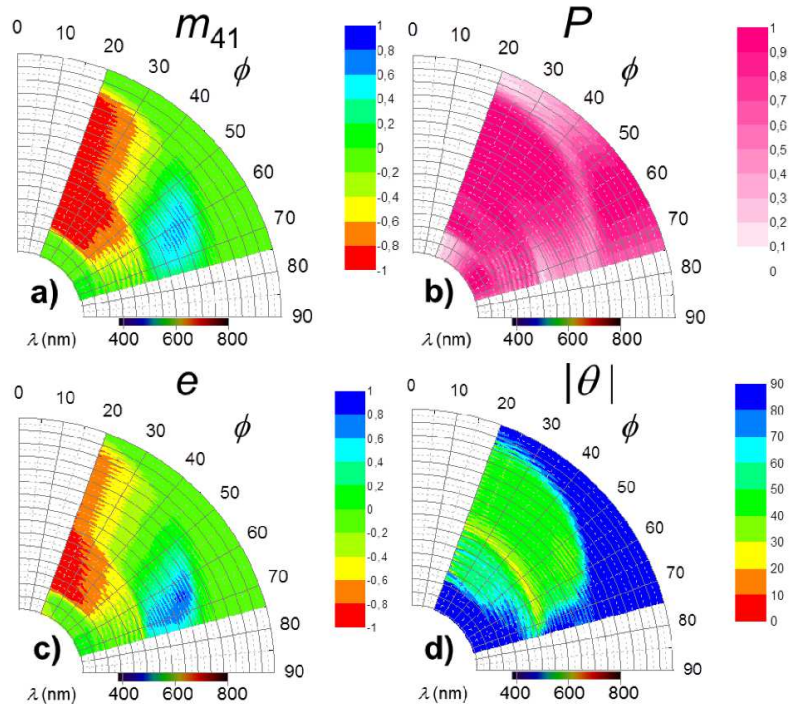


Figure 3.29 – Contour plot of incident angle (ϕ), against wavelength (λ), for a *Chrysina chrysargyrea* beetle, showing a) the Fully Normalised MM element m_{41} (which is the same as $\boldsymbol{M}_{30}$ in this study), b) the degree of polarisation (*P*), c) the ellipticity (*e*) and d) the modulus of azimuth angle (|θ|). Note these plots have been rescaled due to their low values. Used with permission, from [123].

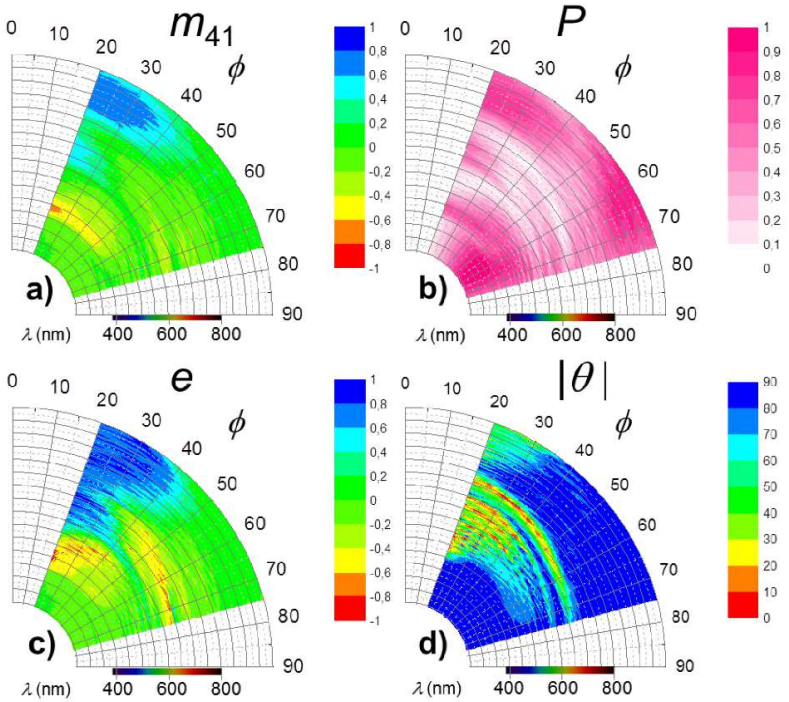


Figure 3.30 – Contour plot of incident angle (ϕ), against wavelength (λ), for a *Chrysina resplendens* beetle, showing a) the Fully Normalised MM element m_{41} (which is the same as $\boldsymbol{M}_{30}$ in this study), b) the degree of polarisation (*P*), c) the ellipticity (*e*) and d) the modulus of azimuth angle (|θ|). Note these plots have been rescaled due to their low values. Used with permission, from [123].

3.4.3 Mirror Image of a Beetle

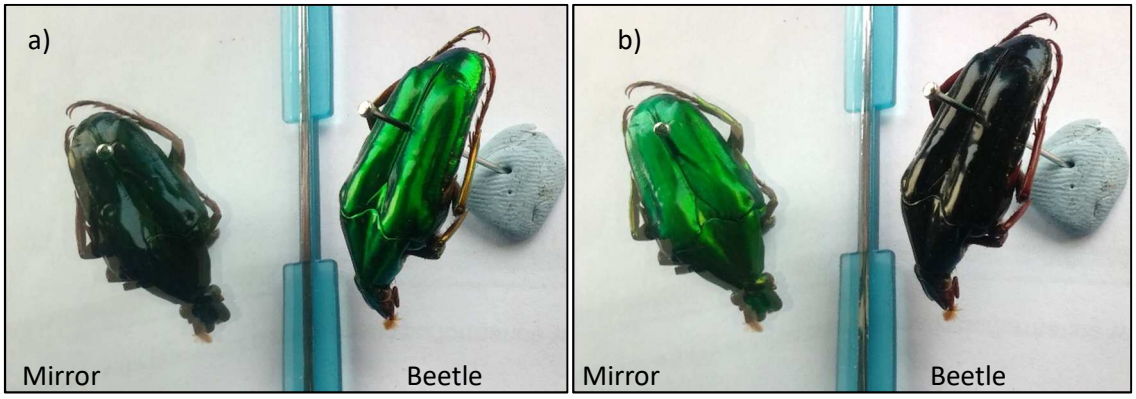


Figure 3.31 – A *Chalcothea resplendens* beetle viewed directly on the right of each image and in a mirror on the left with the imaged viewed through a) a LCP and b) a RCP filter.

One demonstration that is often used to show the beetle's CP reflection is by placing a beetle next to a mirror and using CP filters [124]. As can be seen the beetle appears as the opposite handedness in the mirror (Figure 3.31), this is due to the reflection of the mirror introducing a phase shift of π. This demonstrates the importance of considering the effects of mirrors within the experimental setup.

3.4.4. Modelling

Further to experimentally measuring the optical response of the reflection from the beetles, models of the optical structure have been created. Many different structural perturbations have been modelled with several of them described in this section. This includes variation in pitch

values with depth in beetles being modelled, which was suggested as leading to potential engineering of functional optical and thermoregulatory materials [125].

Simple multi-layered modelling of *Gymnopleurus* and *Proagoderus brucei* beetles was done by Brink *et al* [86],[126]. A model for the system structure was created (using optical theory to predict the optical properties of the system) for other species; *Ischiosopha bifasciata*, *Chrysina woodi* and *Chrysophora chrysochlora* [105]. Different responses and models for beetles were also discussed by Hawkins [127].

A more complex structure of the *Chrysina boucardi* beetle was also simulated [78]. A broadband reflection model of the *Chrysina aurigans* beetle has been made, with the variation of pitch measured with depth and also more complex interaction with the outer cuticle layers considered by several researchers based in Costa Rica [73],[88],[128],[129].

Further to this chiral micromirror concavities of Manuka and *Chrysina gloriosa* beetles have also been modelled, taking into account their wide angles of reflection [81],[83],[130]. Modelling of scattered light from beetles has been done by Valyukh *et al*, which takes into account the roughness of their exoskeletons [131].

MM modelling has been done by Hodgkinson *et al* for *Chrysina resplendens*, *Calloodes grayanus* and *Anoplognathus parvulus* [106]. Other MM modelling was done on the *Cetonia aurata*, *Liocola marmorata*, *Potosia cuprea* [112], *Chrysina gloriosa* [122]. MM models for colour variation in *Cetonia aurata* were created by Arwin *et al* [100],[111],[113],[115].

3.4.5. Surface Micromirrors

Surface micromirrors are a surface structure which are often present in several species of coleoptera. They differ from the structures described in Section 3.1.2.4, in that instead of multi-layered structure, a helicoidal structure is present. When viewed from above the surface structure in beetles appears to have a polygon basis, this was first observed in a *Chrysina gloriosa* beetle [132]. Vornoi analysis by Sharma *et al* was completed upon an optical micrograph of the image of the surface of the *Chrysina gloriosa* beetle, where polygons were fitted to the morphology as seen in Figure 3.32 [77]. The surface mirrors in beetles were found to have similar symmetry to manufactured CLC's near a free surface [133],[134].

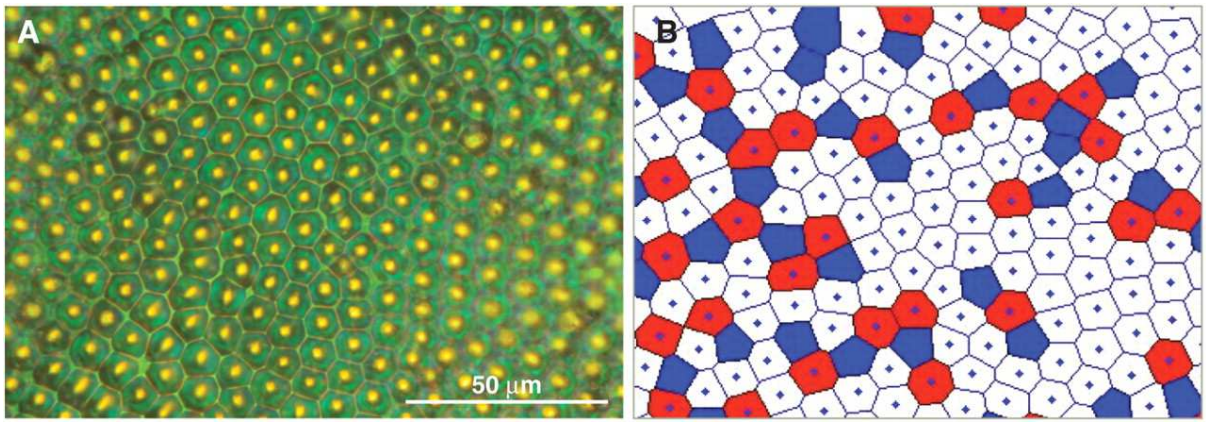


Figure 3.32 – A) an optical micrograph of a green area in a *Chrysina gloriosa*'s shell, with B) corresponding vornoi analysis of blue pentagons, white hexagons and red heptagons. Used with permission, from [77].

A further study on a *Chrysina gloriosa* beetle by Agez found the variation in pitch thickness and an SEM cross section showed the micro-mirror structures in cross-section (Figure 3.33) [81]. It can clearly be seen that the silver part of the beetle is lacking the concave micro mirrors.

Other species of beetle have also been found to have such micromirrors including several green types of *Chrysina* (*C. boucardi* [78], *C. aurora* [84]) from Central America, Manuka beetles (*Pyronata festiva*) [83] from New Zealand and *Anomala dimidata* [84] from the Indian subcontinent. However in the *Chrysina* genus only the matt green species which have been reported with such structures, metallic specimens are lacking surface micromirrors as seen in the optical micrographs (Figure 3.34).

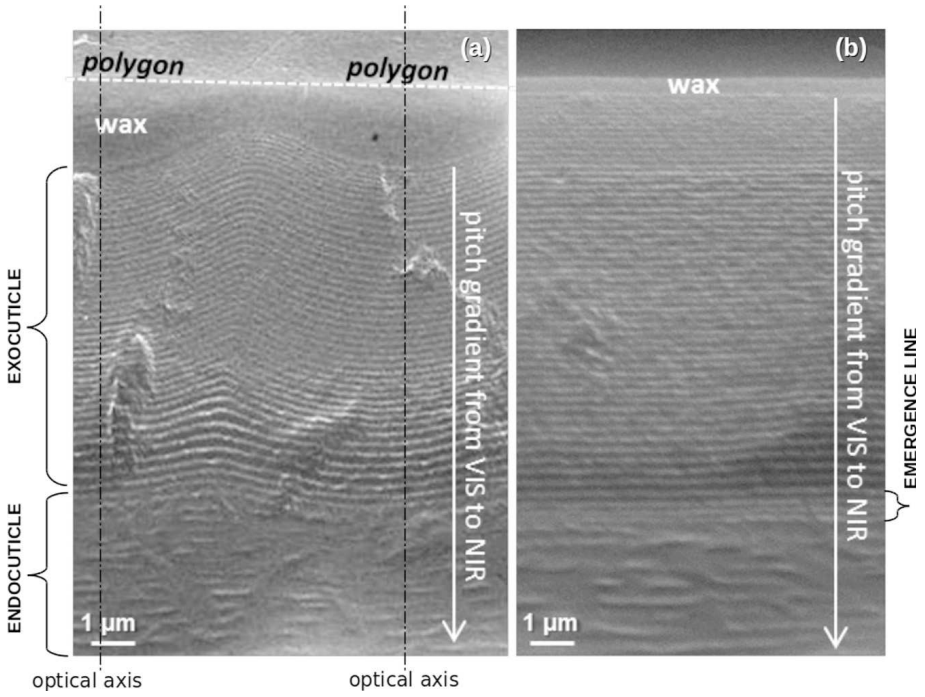
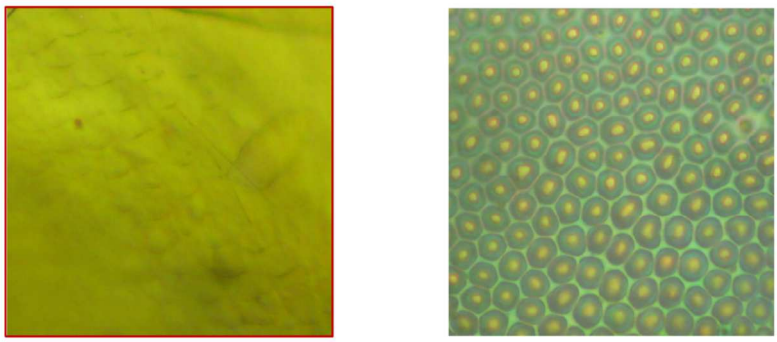


Figure 3.33 – SEM cross section from a Chrysina gloriosa of: a) the green area and below (the optical axis intersects the surface polygon in its centre) and b) the silver stripe. The distance between two consecutive lines of equal contrast is related to the helicoidal pitch, while the helicoidal axis is perpendicular to the lines. Used with permission, from [81].



(a) (b)

Figure 3.34 – 100x100µm images of the surfaces of (a) a metallic *Chrysina aurigans* and (b) a matt green *Chrysina aurora* [84]. Reprinted from Opt. Mater. Express vol. 4, no. 12, pp. 2632-2645, 2014 under a CC BY license, with permission from OSA, original copyright 2014.

3.4.6. Surface Blazed Grating

In nature a common configuration of producing colour on the surface of various animals is blazed gratings, the configuration of which can be seen in Figure 3.35, where the incoming light is at angle θ to the slope of the blazed grating. The angle of the blazed grating is α and β is the angle of the reflected light to the normal of the surface. The period of the blazed grating is labelled a.

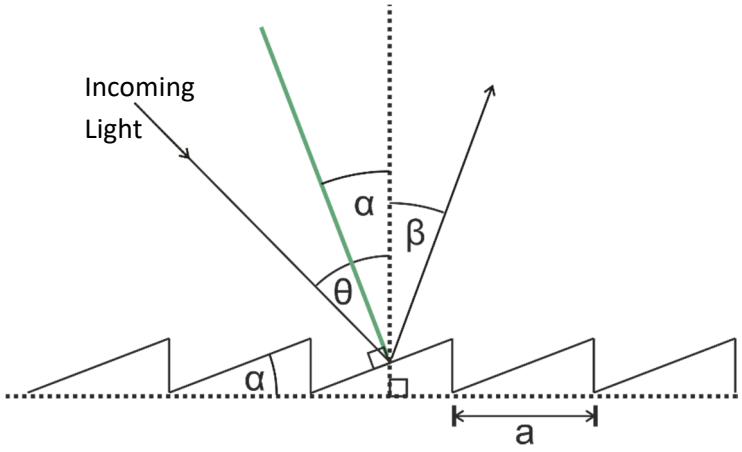


Figure 3.35 – Blaze grating reflection setup, with the Littrow configuration shown by the green line.

The green line in Figure 3.35 demonstrates the Littrow configuration, which is a selected geometry that ensures the diffraction angle, incident angle and grating angle are identical, as in:

$$\beta = \alpha = \theta. \tag{3.16}$$

The maximum reflectance wavelength related to the angle of the blaze grating is given as

$$\alpha = \arcsin\left(\frac{m\lambda}{2a}\right). \tag{3.17}$$

One example of a blazed grating occurring in nature is in a *Mycterophallus* beetle [69] as seen in Figure 3.36.

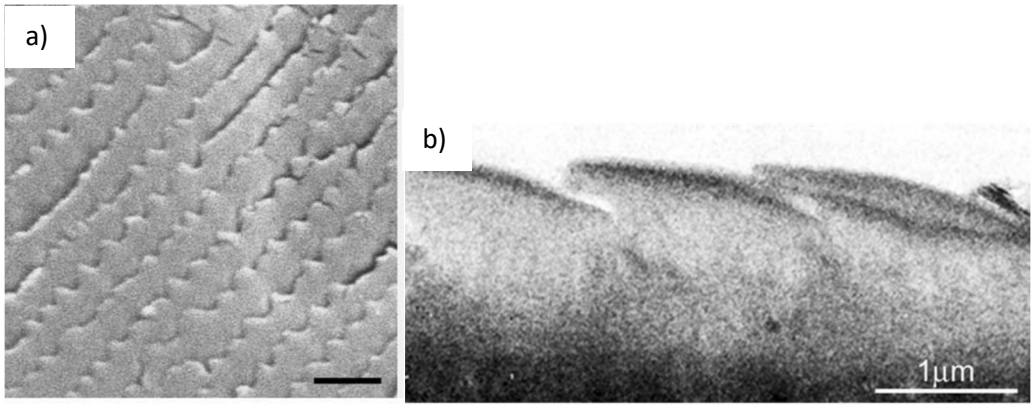


Figure 3.36 – SEM of a blazed grating structure *Mycterophallus sp*. with a) a view of the surface and b) a cross sectional view, revealing an 8.5° blazed grating. Used with permission, from [69].

The reflection from a blazed grating can create linearly polarised light at certain wavelengths. The efficiency of s and p-polarised light reflecting in the Littrow configuration from a blazed grating of similar angle can be seen in Figure 3.37. It can be seen that light is linearly polarised from such a structure.

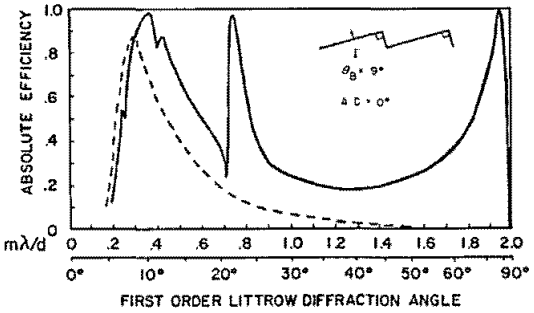


Figure 3.37 - Efficiency of s (dashed line) and p (solid line) polarised light on a blazed grating with an angle of 9°. (It should be noted the grating in this figure was labelled as d, whereas in this thesis it is labelled a) [135]. Reprinted from Appl. Opt. vol. 16, no. 10, pp. 2711-2721, 1977 under a CC BY license, with permission from OSA, original copyright 1977.

3.4.7. Wavelength Formation/Variation

Cuticle formation in multi-layered beetles (but not helicoidal) has been described in detail [136]. Still the question remains, "What causes colour variation?". The structural colour forms relatively quickly when the beetle leaves the pupae stage in a process called Chromatogenesis as seen in Figure 3.38, for a beetle known to have helicoidal structures (*Cetonia aurata*).

The helicoidal structures responsible for colour in beetles studied in this thesis are located in the exocuticle and also partly the endocuticle, the location of these layers are shown in Figure 3.39.

Variation with growth, day and night helicoidal cuticle formation was observed in locusts by Neville and Luke [97]. It was also discussed how exposure to constant light or darkness can affect the circadian rhythm [138].



Figure 3.38 – Chromatogenesis of *Cetonia aurata* from 0 hours top left to 60 hours in the bottom right photograph. Used with permission, from [137].

The layer formation in beetles (albeit with non helicoidal structures which were described as a pseudo-orthogonal 'plywood' as it does only a partial turn of the helix between unidirectional layers) appeared to be non-circadian (44 hours). Formation was shown to lead to colour variation in different body parts [139]. The number of layers in the endocuticle increases steadily over ~40 days then became constant, the rate at which the layers were deposited varied. The *Oryctes rhinoceros* beetle was shown to have varied in growth with temperature, at higher temperature the growth of the layers was faster, however these individual layers were thinner (although the total thickness of layers in the endocuticle was greater at higher temperatures). It was also suggested that the epidermal cells themselves may contain a non-circadian clock.

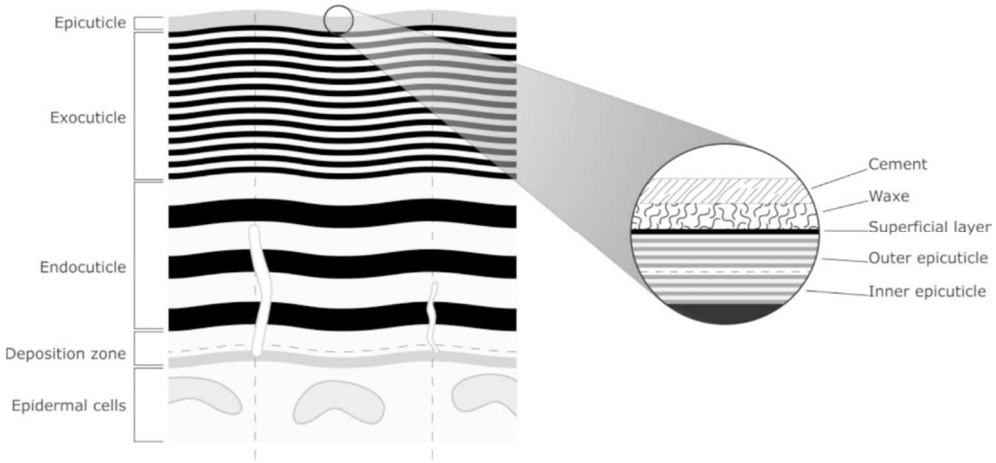


Figure 3.39 – A schematic of a beetle's cuticle structure. Used with permission, from [92].

Another variation in the development in *Aspicidomorpha tecta* a multi-layered, but non helicoidal metallic beetle, is that layers can be reabsorbed in the endocuticle if the beetle is suffering starvation [70]. This also leads to the possibility that lack of food is likely to alter the structure of a heliocoid of a coloured beetle during development. An underdeveloped example of *Protaetia himalayana* is shown in Figure 4.71.

The colour structure in a non-helicoidal multi-layered beetle species *Plateumaris sericea* which showed colour morphism from blackish-blue to red and was found to have varying layer thicknesses in just the epicuticle and not the exocuticle [140].

The variation of helicoidal pitches between a weak narrowband reflecting beetle and a more broadband gold beetle were discussed by Parker *et al* [71]. A more in depth measurement of the broadband reflection from the *Chrysina aurigans* beetle was taken, along with the variation of pitch with depth by the group at the University of Costa Rica [73],[88]. The pitches of the red and gold forms of the *Chrysina aurigans* beetles appear to both increase sharply from the surface, then they both gradually decrease until around 9µm from the beetles' shell surfaces (Figure 3.40a). The gold specimen has lower value pitches in the shell than the red specimen. The group also used EM images to measure the pitches in *Chrysina chrysargyrea* beetles, which were different variants (Figure 3.40b). The golden *Chrysina chrysargyrea* beetle has long pitch values upon the surface and decreases further in the structure; whilst the silver specimen starts with shorter pitches on the surface and increases until eventually after 10µm (from the surface) where the two specimens have comparable pitch values.

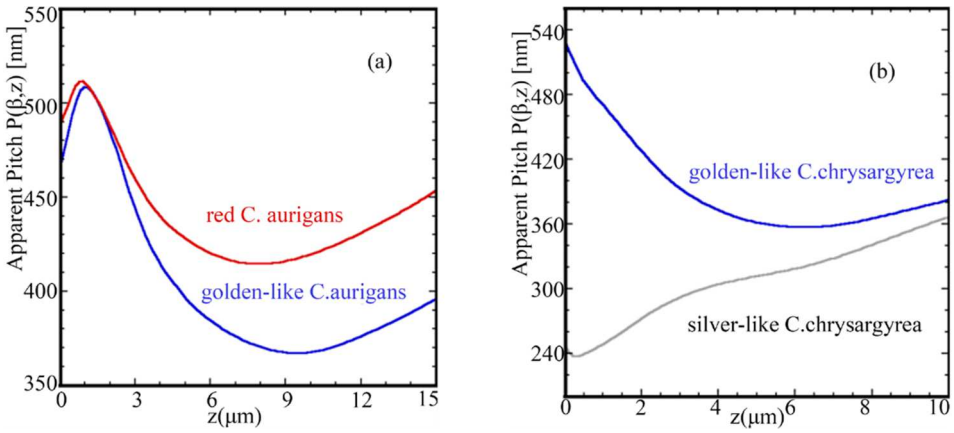


Figure 3.40 – Pitch variation with depth (z) in (a) red and gold *Chrysina aurigans* and (b) silver and gold *Chrysina chrysargyrea*. Reproduced from [73] under CC 4.0.

There has been a study which suggested the colour variations in scarabs:*Gymnopleurus humanus* (a genus known to be have specimens which selective reflect CP light) was linked to temperature of the environment, with different regions having different dominant colours of beetle [141]. One suggestion is that it may not directly correlate with an areas average yearly temperature as in some areas breeding may occur at different times of the year as a survival strategy. Hence development of different colours is due to different temperatures at different times of the year. The colour variation occurred from blue in the coolest regions to red in the warmest with a spectrum of colours in between. There was not a link with average rainfall, but there was a weak connection with altitude (however altitude and temperature are also clearly linked). There are some areas with wider variation of colours and it was proposed those areas had different microclimates within them.

Favila *et al* found that a duller red colour variation in the scarab *Canthon cyanellus cyanellus* subspecies (a genus known to be helicoidal [67],[102]), which is usually 'metallic' green was due to genetic mutation in particular a recessive allele [142].

In the entomology community it has been discussed that underdeveloped dwarfed beetles tended to have a blue shifted optical response and often had fragile shell structures, with anecdotal evidence of temperature and humidity variations in colour mentioned [143].

There is some evidence that both genetic variations and temperature dependences are causes of colour variation. It is possible some of the beetles have evolved to have different colours in different temperature areas. A case has been made for variation in some individuals being due to the change in temperature affecting the formation of the cuticle, in a liquid crystal temperature dependent analogy [144].

Many colour variations of beetles were measured as part of this thesis.

3.4.8. Artificial Structure

It was first discovered by Young and Kowal that optical activity arose from thin films being deposited on a rotating substrate [145]. Glancing angle deposition was seen to introduce form birefringence to an otherwise isotropic medium and it was also observed that rotation enhances the growth of helical columns as in Figure 3.41 [146].

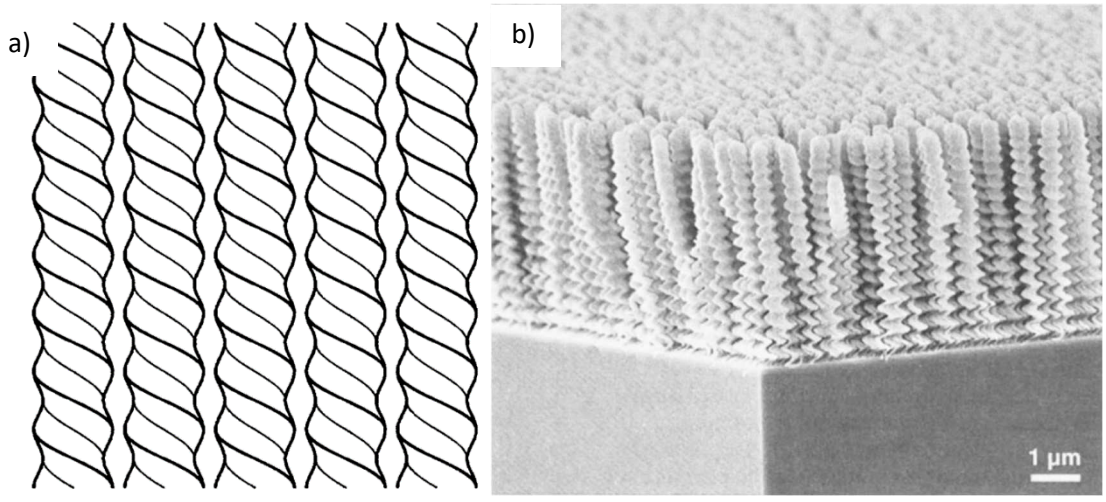


Figure 3.41 – a) Diagram of a twisted column formation of a chiral sculpted thin film by serial bideposition. Used with permission, from [83]. b) SEM of magnesium fluoride twist column structure on glass substrate, with a pitch of 360nm. Used with permission, from [146].

Chiral coatings have been made of titanium oxide is deposited upon textured silicon substrates [83]. They were not deposited in a series of angular positions, but by rotating the substrate with respect to the depositing e-beam. The speed of rotation determines the pitch distance and hence colour of the films (Figure 3.42), whilst the direction of rotation determines the handedness of the structure.

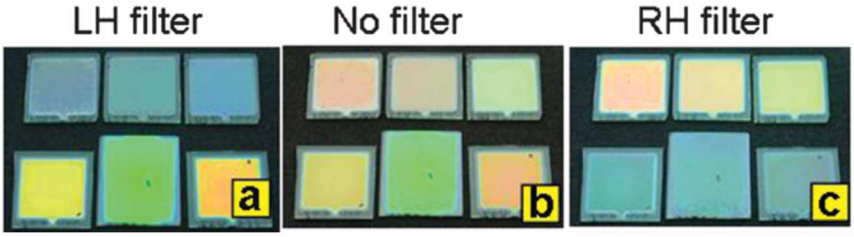


Figure 3.42 – Titania chiral sculpted thin films through a) a left handed (LH), b) no filter and c) a right handed (RH) filter. Used with permission from [83].

There have been several suggested uses for such films, one such use would be in optical sensing [147]. Other uses which have been suggested include commercial fibre-based devices [148] and quantum information processing [149]. A number of applications are described in Chapter 8.

3.4.9. Purpose of the Heliocoidal Structure

The purpose of the heliocoidal layers and selective reflection of CP light in beetles is a question with as yet no definitive answer. There are several ideas for why the structure has evolved. The two main ones being that it adds mechanical strength to the shell structure [150] and the second being for visual communication between the beetles [151]. Another less discussed possible cause being thermoregulation [152].

3.4.10. Circularly Polarised Vision

It is widely known that linearly polarised light sensitivity occurs in several species of beetle [153]–[155]. Circularly polarised light sensitivity is however less common in nature, it has been discovered that several species of stomatopod shrimp can actively detect CP light signals [18],[156]. The mechanism for the stomatopod CP vision can be seen in Figure 3.43.

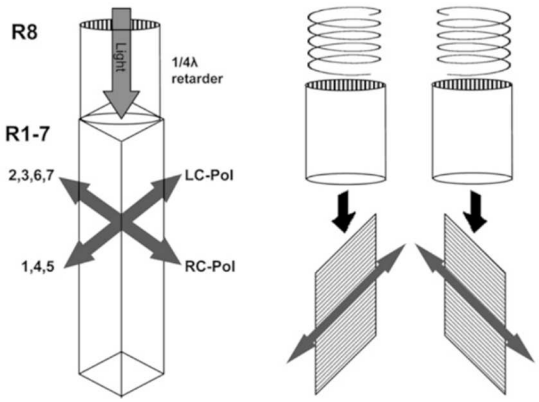


Figure 3.43 – Diagram of eight rhabdoms from an ommatidium in the midband from the eye of the stomatopod *Odontodactylus*. On the left the R8 rhabdomere acts as a quarter wave retarder and converts circularly polarised light (spirals) into linear polarised light which can then be detected by the rhabdomeres R1–7 beneath. The distinction between left circularly polarised (LC-pol) and right circularly polarised (RC-pol) is made by the microvillar orientations of the rhabdoms (R1-7). The processing from LCP and RCP light to +45° and -45° respectively can be seen in the diagram on the right. Used with permission, from [18].

There have been several studies into the behavioural response of beetles which reflect CP light to different handnesses of CP light, with conflicting outcomes.

A study by Brady and Cummings reported that *Chrysina glorioisa* had linear and CP sensitivity, whilst *Chrysina woodi* could not detect CP light [157]. This study led to excitement for potential signalling use by beetles [151]. There were however some criticisms made of the study [158]. The first of which was the LCP and RCP lights used as sources in the study were ~5% different in intensity. The unpolarised light was also 15-19% less intense than the polarised signals. The second criticism was that the boxes which contained the beetles during the study were black lined, which increases the chance of erroneous polarised signals than matt white lining due to the Umov effect [159]. The last criticism was that the numbers of beetles involved were too few to draw statistical conclusions.

Another study by Blahó *et al*. of four species known to reflect CP light (two cetoniinae: *Cetonia aurata* and *Protaetia cuprea* and two rutelinae: *Anomala dubia* and *Anomala vitas*) showed no apparent response to CP light [160]. It was seen that the beetles were attracted to floral scent and pheromones rather than optical responses. Blaho suggested that the helicoidal structures could be present due to adding a mechanical advantage or a chemical protection from changes in PH level, however this is still an untested hypothesis.

A study was also made by Miao *et al* on *Anomala corpulenta* beetles, where no evidence for CP vision was found [161]. There was found to be no clear sexual difference in the species' CP reflection and again attraction by pheromones seems to be more important factor in species interaction.

Several behavioural tests to CP light have been done, however they have not been conclusive. As the helicoidal structure is widespread in scarab beetles (both geographically and taxonomically) more behavioural studies would help to determine the role of CP light. Electroretinograms, and anatomy study of beetles could be used to determine their CP sensitivity to similar methods to investigating stomatopods [18]. It is quite possible that the beetles do not have CP vision. There are other examples in nature where optical effects which appear spectacular to humans are not seen by the animal. Notably the golden mole which has an amazingly iridescent colour structure, but is almost blind and lives underground [162] so the colour cannot be used to attract a mate, instead genital size is often used to find a choice of mate [163]. The helicoidal structures are quite widespread in nature, however most do not reflect at optical wavelengths (either due to different dimensions {for example locusts' helicoids correspond to reflection in the infra-red [97]} or blocked from reflection by a layer above the structure [164]).

3.4.11. Homochirality from Astronomical Sources

It is not known why LCP light reflection rather than RCP occurs in beetles. It could even be some kind of accident, with homochirality found on earth being suggested as a result of UV light from astronomical sources causing amino acids to become of a dominant handedness [165],[166]. As a result this handedness of molecules could cause the beetles to only have left handed structures on a larger scale, however it still appears unknown how this amplification to larger dimensions fully occurs [167].

3.4.12. The Beetles in Modern Culture

Beetles with CP polarising effects are commonly available both online and in shops, in jewellery [168], paperweights and keyrings as can be seen in Figure 3.44 (the CP filtered photographs of these items can be seen in Appendix A1). Such beetles have also been thrust into the spotlight upon postage stamps, examples of which can be seen Figure 3.45.



Figure 3.44 – Keyrings and pendants of beetles; 1-Chalcothea resplendens, 2-Mimela splendens, 3-Popillia mutans, 4-Popillia mongolica, 5-Popillia flavosellata, 6- Mimela splendens, 7-Protaetia brevaitis, under normal illumination.

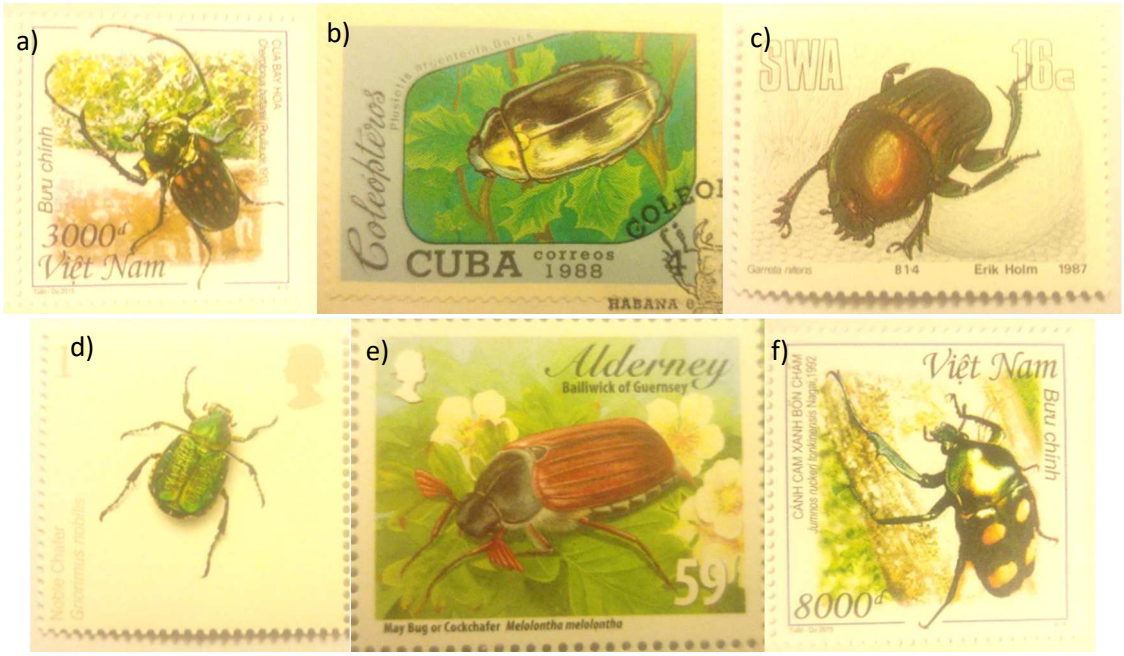


Figure 3.45 – A few examples of stamps with beetle with helicoidal structures from various countries a) Euchirinae:*Cheirotonus battareli* from Vietnam b) Rutelinae:*Chrysina (plusiotis) argenteola* from Cuba, c) Scaraeinae:*Garretta nitens* from South West Africa (presently Namibia), d) Trichiinae:*Gnorimus nobilis* from the United Kingdom, e) Melolonthinae:*Melolontha melolontha* from Guernsey and f) Cetoniinae:*Jumnos ruckeri tonkinensis* from Vietnam.

3.4.13. Summary

In this section the state of research into the helicoidal structure within beetles' shells was discussed. This included describing the structure and how the pitch relates to the reflected light in terms of wavelength and polarisation. The potential defects and other perturbations to the helicoidal structures are described including multiple pitches, twist defects and uniaxial layers.

An in-depth description of the ellipsometric measurements was made, including MMSE and the variation with angle. The different types of modelling are described from simple multi-layered models to more in-depth models based upon EM images.

A brief description was made of the micromirror type structure which was observed in several *Chrysina* specimens. Another surface structure with a blazed grating-like form was also described which has been observed in some Cetoniinae species.

Previous research into the multilayers' structure formation was described in terms of both genetic and environmental factors, as well as the growth development of colours. Artificial manufacturing of such structures by deposition upon a rotating structures was discussed.

The helicoidal structures' purpose is not fully known with the suggestion of mechanical strength, thermoregulation and CP vision being made. The previous studies in CP vision are discussed with no decisive studies being yet made. Briefly the astronomical source of dominant handedness of molecules on Earth was made. The suggestion is the CP radiation was caused by amino acid, to

be of a dominant handedness upon earth, which is then amplified to the chiral handedness within beetles' shells.

In the last part of Section 3.4, the occurrence and exposure of the beetles in jewellery and stamps to the general public is shown.

Over the next chapters this research will be built upon and advanced. Variation in spectral response is found and described across a wide range of subfamilies, genera and species.

3.5. Entomology of Beetles

Beetles are some of the most varied and widespread lifeforms on Earth, accounting for roughly 25% (350,000-400,000 species) of all described species (~1.5 million) [169]. Many species of beetle are yet to be discovered with an estimate of 1.5 million species in total. The role and appearance of beetles varies greatly with the species widespread both geographically and also in nearly every natural habitat from marine to fresh water, from flowers to tree bark and even in root systems [170].

To quote Max Barclay, the London Natural History Museum beetle collection manager [171]:

"Beetles are the most dominant, species-rich group of organisms in terrestrial eco-systems. They have divided the world up into very small pieces to specialise in their different jobs, managing to co-exist without competing with each other."

The wide range of variations in the insects has allowed scientific studies to reveal several potentially useful discoveries, specifically to this report, their shell's optical reflection [35],[172]. The colour from within beetles' shells can be caused by two mechanisms; pigmentary colour and structural colour. Pigmentary colour occurs when the material absorbs and reflect certain wavelengths. The structural based colour is far more complex and various structures appear in beetles, including diffraction gratings, 3D photonic crystals, quasi ordered scattering, reversible refractive index changing and simple multi-layered reflectors and helicoidal multi-layered structures as discussed in Section 3.1 [12].

In this study the selective reflection of near CP light from multi-layered helicoidal structures within beetles' shells of the superfamily Scarabaeoidae is investigated. A previous study by Pye found that nine different subfamilies from two different families had species within them that had examples which selectively reflected CP light, the taxonomic map of these is shown in Figure 3.46 (although not all species within a subfamily reflect CP light). Amongst this group of nine optically active subfamilies, there is a large variation in the beetles' lifestyles and appearances. Further to this type of structural colour being spread across two families, there has also been

fossil records of several examples of structural colour occurring in beetles 15 to 47 million years ago [4]. This suggests that this could be an ancient evolutionary feature.

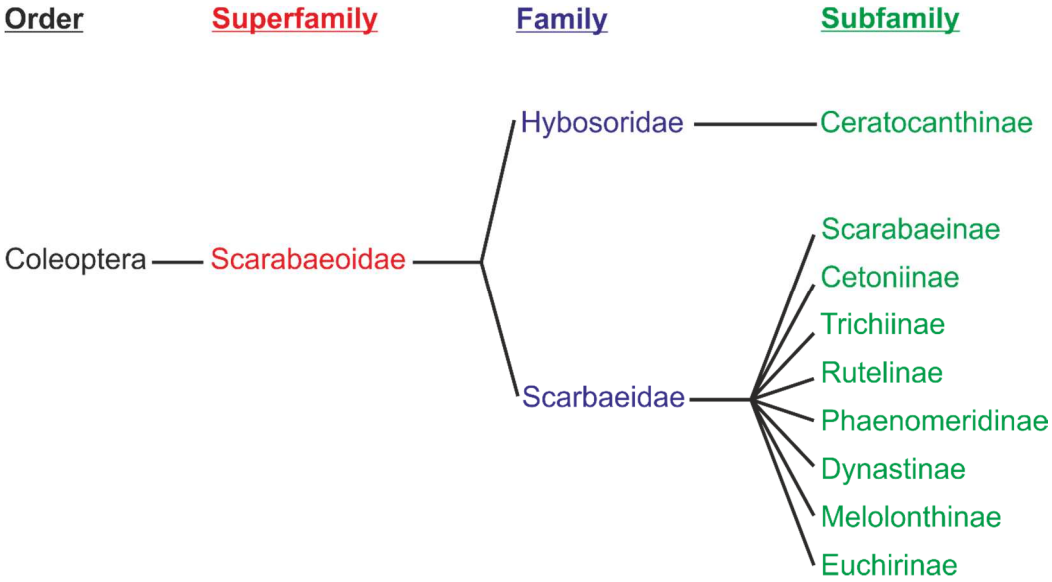


Figure 3.46 – Taxonomic map of subfamilies that contain optically active Coleoptera. The classifications hierarchical form going from the highest on the left to the lowest on the right. It should be noted that below subfamily comes genus then species followed by subspecies. It should also be noted that some classifications use tribe between subfamily and genus. Published by the author in [173].

It should be noted that in some entomological classifications Euchirinae and Trichiinae are considered as tribes in the subfamilies Melolonthinae and Cetoniinae respectively. As research continuing with genetic analysis of Scarabaeidae family structure the situation will likely be clarified soon [174],[175].

It should be noted that in this study the newest taxonomic names of the beetles are used whenever possible and as such may vary from previous published studies. A brief description of the lifestyle and variations in each subfamilies will be made.

3.5.1. Scarabaeinae

There are over 5,000 species of Scarabaeinae in 234 genera, or as they are more commonly known dung beetles, with many of the subfamily feeding exclusively upon dung, while there are several which feed upon mushrooms, rotting fruit and decomposing plant material [176]. Their size varies greatly from 2-25mm, with some males having horns on their heads such as the one in Figure 3.47, which are used in fending off competitors. They can be found on every continent except Antarctica. One species of dung beetle is known to navigate using the polarisation of light from the stars and moon [155].



Figure 3.47 – Photograph of a male *Phanaeus mexicanus* beetle from Mexico.

3.5.2. Cetoniinae

Cetoniinae are often referred to as fruit and flower chafers, flower beetles or flower scarabs. As these names suggest many species feed upon flower nectar and fruit, however some are predaceous feeding on various insect larvae. There are over 3,600 species in 510 genera of Cetoniinae described around the world, with no species present in New Zealand or polar regions [177]. Their size can vary greatly from a few mm to 100mm, with the shape of the body usually being flat, and none of them having horns [178]. An example of a Cetoniinae beetle which reflects CP light can be seen in Figure 3.48.



Figure 3.48 – Photograph of a female *Agestrata luzonica* beetle from the Philippines.

3.5.3. Trichiinae

The Trichiinae is sometimes considered part of the subfamily Cetoniinae and can be found widely distributed. Their size can vary from 6mm to 65mm in length [179]. Adults feed upon fruits, flowers and leaves, whilst larvae develop in rich organic matter. There are at least 46 genera and 240 species, which are widespread around the world although missing from Australia and Madagascar [177]. A species which can occasionally be found in the United Kingdom is *Gnorimus nobilis* or the Noble chafer (Figure 3.49).



Figure 3.49 – Photograph of a Gnorimus nobilis beetle from Poland.

3.5.4. Rutelinae

The subfamily Rutelinae is also known as the shining leaf chafers and has approximately 200 genera and 4,100 species and is distributed worldwide [180]. The adults feed upon leaves, flowers and flowering plants, some species such as *Popillia japonica* are considered agricultural pests [181]. This subfamily include several highly reflecting gold and silver species.

One of the optically more interesting rutelidae genera is *Chrysina* (Greek for gold) previously known as *Plusiotis*, which occurs with a variety of colours from simple green (Figure 3.50), purple, and red to more metallic reds, golds and silvers with over 100 known species [143],[182]. This genus contains such spectacular colours that the beetles are known as jewel scarabs. They range from the South West of the United States to Ecuador in the south [183]. Many species have distinct colour morphs such as *Chrysina chrysargyrea* in Figure 3.51. One of the more optically interesting species is *Chrysina boucardi*, which is usually low reflecting green, but has a golden colour morph (Figure 3.52). However, some colour forms are rarer at different locations than others, suggesting it is also genetic and area dependent [182]. The metallic colour forms tend to occur in tropical rainforests, where it is often wet and shiny, as the beetle's appearance acting as good camouflage, mirroring wet foliage. In the drier pine-oak forests of the southern US, the species are not nearly as highly reflecting. Some species have bright coloured or blue legs, which may be aposematic (warning colours). The genus is mostly active at night, and as such it is suggested that it is not useful in terms of mate recognition, with genitalia shape being a barrier to hybridization and pheromones being a form of communication [143].



Figure 3.50 – Photograph of a *Chrysina adelaida* beetle.

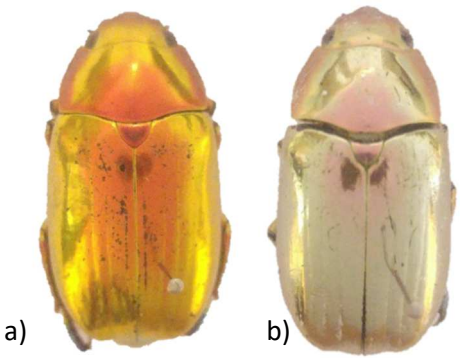


Figure 3.51 – a) Gold and b) silver colour morphs of *Chrysina chrysargyrea* from Costa Rica.

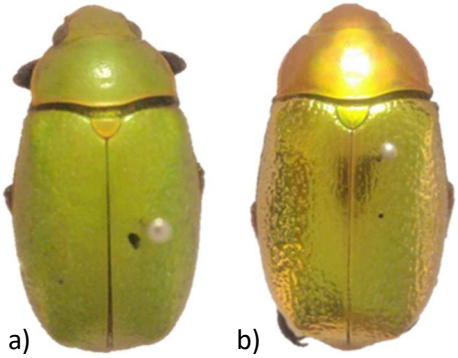


Figure 3.52 – a) Low reflecting green and b) high reflecting gold colour morphs of *Chrysina boucardi*.

The *Chrysina* species is not the only Rutelinae genus that contains broadband structural reflection, with similar reflection observed in several species of Australian genus *Anoplognathus*.

3.5.5. Phaenomeridinae

This subfamily of beetles is very small consisting of only two genera with two species of each and geographically located just within Africa [184]. One such example is a *Phaenomeris besckei* beetle (Figure 3.53).



Figure 3.53 – Photograph of a *Phaenomeris besckei* beetle from Tanzania.

3.5.6. Dynastinae

The dynastinae subfamily contains 196 genera and over 1,500 species. It is also present in all major regions of the world, excluding polar environments. The adults feed on fruits, nectar and leaves [184]. This subfamily contains the largest beetle in the family, the 'Hercules' beetle, reaching more than 170mm in length [52]. An image of a dynastinae beetle (whose shell contains circularly polarising structures) is seen in Figure 3.54.



Figure 3.54 – Photograph of an *Agaocephala urus* beetle from Brazil.

3.5.7. Melolonthinae

The melolonthinae subfamily is one of the largest in the Scarabaeoidae family, it has roughly 750 genera and almost 11,000 species worldwide [185]. The adults vary from 3mm to 58mm long. Many genera are damaging to both agriculture and gardens. The vast majority of melolonthinae are crepuscular or nocturnal [186]. An example of CP melolonthinae is shown in Figure 3.55.



Figure 3.55 – Photograph of a *Pyronota festiva* beetle from New Zealand, image from [187].

3.5.8. Euchirinae

The Euchirinae subfamily also known as long armed scarabs has three genera and 16 species, which are mostly found in Asia, with a single species in Cyprus and Egypt [184]. The beetles have gender dimorphism with the males having elongated forelegs as can be seen in Figure 3.56.



Figure 3.56 – Photograph of a Male of *Cheirotonus battareli* beetle from Vietnam.

3.5.9. Ceratocanthinae

Adult beetles of the Ceratocanthinae subfamily are easily recognisable compared to most other Coleoptera by the fact they can roll up into a near perfect ball (Figure 3.57). The subfamily is distributed in Australia, Afrotropical, Indomalaysia, Neotropical, Nearctic and Palearctic regions [188]. As of 2011 there were 43 genera and 355 species of Ceratocanthinae described [189]. The habitats of these beetles vary, some species being ground dwelling and flightless, while others fly between the canopies and can be found feeding on fungi and in dead trees. Several species have been found co-habiting with ants and termites. Many adults are bright, having an often metallic appearance, many species are small varying between two and 10mm.

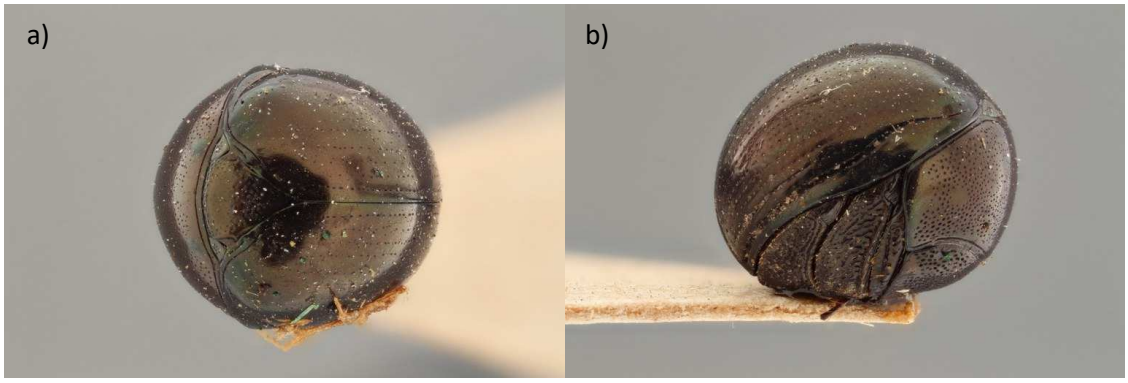


Figure 3.57 – *Ceratocanthus vicarious*, in a) dorsal and b) lateral views. From [190] under CC BY-NC-ND 4.0.

3.5.10. Summary

Whilst there are nine Coleopteran subfamilies that contain species which reflect CP light, the strength of reflection varies greatly, with the Cetoniinae and Rutelinae subfamilies containing some of the most intense, and hence easiest to study specimens. For this reason these two subfamilies are focused upon in this study, with a wide range of genera of Cetoniinae studied, whilst the primary focus of Rutelinae was upon the *Chrysina* genus.

3.6. References

[1] A. R. Parker, “Colour in Burgess Shale animals and the effect of light on evolution in the Cambrian,” *Proc. R. Soc. B Biol. Sci.*, vol. 265, no. 1400, pp. 967–972, 1998.

[2] A. R. Parker, “On the origin of optics,” *Opt. Laser Technol.*, vol. 43, no. 2, pp. 323–329, 2011.

[3] M. Doucet and M. G. Meadows, “Iridescence : a functional perspective,” *Interface Focus*, vol. 6, no. February, pp. S115–S132, 2009.

[4] M. E. McNamara, D. E. G. Briggs, P. J. Orr, H. Noh, and H. Cao, “The original colours of fossil beetles,” *Proc. R. Soc. B Biol. Sci.*, vol. 279, no. 1731, pp. 1114–1121, Mar. 2012.

[5] R. Hooke, *Micrographia*. London: Royal Society, 1665.

[6] I. Newton, *Opticks - ISBN:9780486602059*. New York: Dover (2012), 1704.

[7] A. L. Ingram and A. R. Parker, “A review of the diversity and evolution of photonic structures in butterflies , incorporating the work of John Huxley (The Natural History Museum , London from 1961 to 1990),” *Philos. Trans. R. Soc. Lond. B. Biol. Sci.*, no. March, pp. 2465–2480, 2008.

[8] T. F. Anderson, “An Electron Microscope Study of Some Structural Colors of Insects,” *J. Appl. Phys.*, vol. 13, no. 12, pp. 748–58, 1942.

[9] H. E. Hinton and D. F. Gibbs, “Diffraction gratings in gyrinid beetles,” *J. Insect Physiol.*, vol. 17, no. 6, pp. 1023–35, 1971.

[10] H. E. Hinton, “An Electron Microscope Study of The Gratings of Some Carabid Beetles,” *J. Insect Physiol.*, vol. 15, pp. 959–62, 1969.

[11] H. Hinton and D. Gibbs, “Diffraction Gratins in Phalacrid Beetles,” *Nature*, vol. 221, no. 8 March, pp. 953–4, 1969.

[12] A. E. Seago, P. Brady, J.-P. Vigneron, and T. D. Schultz, “Gold bugs and beyond: a review of iridescence and structural colour mechanisms in beetles (Coleoptera),” *J. R. Soc. Interface*, vol. 6 Suppl 2, pp. S165-84, Apr. 2009.

[13] E. Hecht, *Optics - ISBN:9781292021577*, 4th ed. Harlow: Pearson Education Limited, 2014.

[14] C. J. R. Sheppard, “Approximate calculation of the reflection coefficient from a stratified medium,” *J. Opt.*, vol. 4, pp. 665–9, Mar. 1995.

[15] D. G. Stavenga, B. D. Wilts, H. L. Leertouwer, and T. Hariyama, “Polarized iridescence of the multilayered elytra of the Japanese jewel beetle, Chrysochroa fulgidissima,” *Philos. Trans. R. Soc. Lond. B. Biol. Sci.*, vol. 366, no. 1565, pp. 709–23, Mar. 2011.

[16] P. Vukusic and D. G. Stavenga, “Physical methods for investigating structural colours in biological systems,” *J. R. Soc. Interface*, vol. 6 Suppl 2, no. January, pp. S133-48, 2009.

[17] T.-D. Nguyen and M. J. MacLachlan, “Biomimetic Chiral Nematic Mesoporous Materials from Crab Cuticles,” *Adv. Opt. Mater.*, vol. 2, no. 11, pp. 1031–1037, Nov. 2014.

[18] T. H. Chiou, S. Kleinlogel, T. Cronin, R. Caldwell, B. Loeffler, A. Siddiqi, A. Goldizen, and J. Marshall, “Circular Polarization Vision in a Stomatopod Crustacean,” *Curr. Biol.*, vol. 18, pp. 429–434, 2008.

[19] Y. Baar, J. Rosen, and N. Shashar, “Circular polarization of transmitted light by sapphirinidae copepods,” *PLoS One*, vol. 9, no. e86131, pp. 1–6, Jan. 2014.

[20] D. B. Shapiro, A. J. Hunt, M. S. Quinby-Hunt, and P. G. Hull, “Circular polarization effects in the light scattering from single and suspensions of dinoflagellates,” in *Proc. SPIE 1537, Underwater Imaging, Photography, and Visibility*, 1991, vol. 1537, no. 2, p. 30.

[21] S. Vignolini, P. J. Rudall, A. V. Rowland, A. Reed, E. Moyroud, R. B. Faden, J. J. Baumberg, B. J. Glover, and U. Steiner, “Pointillist structural color in Pollia fruit,” *Proc. Natl. Acad. Sci.*, vol. 109, no. 39, pp. 15712–15715, 2012.

[22] S. Vignolini, T. Gregory, M. Kolle, A. Lethbridge, E. Moyroud, U. Steiner, B. J. Glover, P. Vukusic, and P. J. Rudall, “Structural colour from helicoidal cell-wall architecture in fruits of Margaritaria nobilis,” *J. R. Soc. Interface*, vol. 13, no. 20160645, pp. 1–6, 2016.

[23] D. W. Lee, *Nature’s Palette - The Science of Plant Color - ISBN:C*. Chicago: The University of Chicago Press, 2007.

[24] R. M. Graham, D. W. Lee, and K. Norstog, “Physical and Ultrastructural Basis of Blue Leaf Iridescence in Two Neotropical Ferns,” vol. 80, no. 2, pp. 198–203, 1993.

[25] P. P. Shibayew and R. G. Pergolizzi, “The Effect of Circularly Polarized Light on the Growth of Plants,” *Int. J. Bot.*, vol. 7, no. 1, pp. 113–117, 2011.

[26] G. C. McLeod, “The Effect of Circularly Polarized Light on the Photosynthesis and Chlorophyll a Synthesis of Certain Marine Algae,” *Limnol. Oceanogr.*, vol. 2, no. 4, pp. 360–362, Oct. 1957.

[27] M. Kolle, P. M. Salgard-Cunha, M. R. J. Scherer, F. Huang, P. Vukusic, S. Mahajan, J. J. Baumberg, and U. Steiner, “Mimicking the colourful wing scale structure of the Papilio blumei butterfly,” *Nat. Nanotechnol.*, vol. 5, no. 7, pp. 511–5, 2010.

[28] P. Vukusic, J. R. Sambles, and C. R. Lawrence, “Colour mixing in wing scales of a butterfly,” *Nature*, vol. 404, no. 6777, p. 457, 2000.

[29] M. Crne, V. Sharma, J. Blair, J. O. Park, and C. J. Summers, “Biomimicry of optical microstructures of Papilio palinurus,” *Europhys. Lett.*, vol. 93, no. 14001, 2011.

[30] A. R. Parker, V. L. Welch, D. Driver, and N. Martini, “Structural colour: opal analogue discovered in a weevil,” *Nature*, vol. 426, no. 6968, pp. 786–787, 2003.

[31] J. W. Galusha, L. R. Richey, M. R. Jorgensen, J. S. Gardner, and M. H. Bartl, “Study of natural photonic crystals in beetle scales and their conversion into inorganic structures via a sol–gel bio-templating route,” *J. Mater. Chem.*, vol. 20, no. 7, pp. 1277–84, 2010.

[32] M. H. Bartl, J. W. Galusha, L. R. Richey, J. S. Gardner, and J. N. Cha, “Discovery of a diamond-based photonic crystal structure in beetle scales,” *Phys. Rev. E - Stat. Nonlinear, Soft Matter Phys.*, vol. 77, no. 5, pp. 2–5, 2008.

[33] G. S. He, H. Y. Qin, and Q. Zheng, “Rayleigh, Mie, and Tyndall scatterings of polystyrene microspheres in water: Wavelength, size, and angle dependences,” *J. Appl. Phys.*, vol. 105, no. 2, 2009.

[34] M. Burresi, L. Cortese, L. Pattelli, M. Kolle, P. Vukusic, D. S. Wiersma, U. Steiner, and S. Vignolini, “Bright-White Beetle Scales Optimise Multiple Scattering of Light,” *Sci. Rep.*, vol. 4, pp. 1–7, Aug. 2014.

[35] P. Vukusic, B. Hallam, and J. Noyes, “Brilliant whiteness in ultrathin beetle scales,” *Science*, vol. 315, no. 5810, p. 348, Jan. 2007.

[36] S. M. Luke, B. T. Hallam, and P. Vukusic, “Structural optimization for broadband scattering in several ultra-thin white beetle scales,” *Appl. Opt.*, vol. 49, no. 22, pp. 4246–4254, 2010.

[37] R. O. Prum and R. Torres, “Structural colouration of avian skin: convergent evolution of coherently scattering dermal collagen arrays,” *J. Exp. Biol.*, vol. 206, no. 14, pp. 2409–2429, 2003.

[38] R. O. Prum and R. H. Torres, “Structural colouration of mammalian skin: convergent evolution of coherently scattering dermal collagen arrays,” *J. Exp. Biol.*, vol. 207, no. 12, pp. 2157–2172, May 2004.

[39] R. O. Prum, J. A. Cole, and R. H. Torres, “Blue integumentary structural colours in dragonflies (Odonata) are not produced by incoherent Tyndall scattering,” *J. Exp. Biol.*, vol. 207, pp. 3999–4009, 2004.

[40] B. Michelsen, “Mandrill Photo,” 2016. [Online]. Available: https://commons.wikimedia.org/wiki/File:Mandrill_at_san_francisco_zoo.jpg. [Accessed: 12-Dec-2016].

[41] B. C. Tørrissen, “Chlorocebus Blue Scrotum,” 2016. [Online]. Available: https://commons.wikimedia.org/wiki/File:Chlorocebus-pygerythrus-private-parts.JPG. [Accessed: 12-Dec-2016].

[42] A. C, “Enallagma civile.” [Online]. Available: https://commons.wikimedia.org/wiki/File:Familiar_Bluet_(Enallagma_civile)_(15083515581).jpg. [Accessed: 12-Dec-2016].

[43] C. Pouya, D. G. Stavenga, and P. Vukusic, “Discovery of ordered and quasi-ordered photonic crystal structures in the scales of the beetle Eupholus magnificus,” *Opt. Express*, vol. 19, no. 12, pp. 11355–11364, 2011.

[44] R. Hanlon, “Cephalopod dynamic camouflage,” *Curr. Biol.*, vol. 17, no. 11, pp. 400–404, 2007.

[45] J. B. Messenger, “Cephalopod chromatophores : neurobiology and natural history,” *Biol. Rev*, vol. 76, pp. 473–528, 2001.

[46] L. M. Mäthger and R. T. Hanlon, “Malleable skin coloration in cephalopods: Selective reflectance, transmission and absorbance of light by chromatophores and iridophores,” *Cell Tissue Res.*, vol. 329, no. 1, pp. 179–186, 2007.

[47] L. M. Mäthger, G. R. R. Bell, A. M. Kuzirian, J. J. Allen, and R. T. Hanlon, “How does the blue-ringed octopus (Hapalochlaena lunulata) flash its blue rings?,” *J. Exp. Biol.*, vol. 215, pp. 3752–3757, 2012.

[48] D. G. Menter, M. Obika, T. T. Tchen, and J. D. Taylor, “Leucophores and iridophores of Fundulus heteroclitus: Biophysical and ultrastructural properties,” *J. Morphol.*, vol. 160, no. 1, pp. 103–119, Apr. 1979.

[49] E. Kreit, L. M. Mäthger, R. T. Hanlon, P. B. Dennis, R. R. Naik, E. Forsythe, and J. Heikenfeld, "Biological versus electronic adaptive coloration: how can one inform the other?," *J. R. Soc. Interface*, vol. 10, no. 20120601, pp. 1–13, 2012.

[50] J. Teyssier, S. V. Saenko, D. Van Der Marel, and M. C. Milinkovitch, "Photonic crystals cause active colour change in chameleons," *Nature*, pp. 1–7, 2015.

[51] D. G. DeMartini, A. Ghoshal, E. Pandolfi, A. T. Weaver, M. Baum, and D. E. Morse, "Dynamic biophotonics: female squid exhibit sexually dimorphic tunable leucophores and iridocytes," *J. Exp. Biol.*, vol. 216, no. 19, pp. 3733–3741, 2013.

[52] M. Rassart, J. F. Colomerl, T. Tabarrant, and J. P. Vigneron, "Diffractive hygrochromic effect in the cuticle of the hercules beetle Dynastes hercules," *New J. Phys.*, vol. 10, 2008.

[53] C. W. Mason, "Structural Colors in Insects. III," *J. Phys. Chem.*, vol. 31, no. 12, pp. 1856–1872, Jan. 1926.

[54] S. R. Mouchet, E. Van Hooijdonk, V. L. Welch, P. Louette, J.-F. Colomer, B.-L. Su, and O. Deparis, "Liquid-induced colour change in a beetle: the concept of a photonic cell," *Sci. Rep.*, vol. 6, no. 19322, pp. 1–10, 2016.

[55] M. Rassart, P. Simonis, A. Bay, O. Deparis, and J. P. Vigneron, "Scale coloration change following water absorption in the beetle Hoplia coerulea (Coleoptera)," *Phys. Rev. E - Stat. Nonlinear, Soft Matter Phys.*, vol. 80, no. 3, pp. 1–6, 2009.

[56] J. P. Vigneron, V. Lousse, J.-F. Colomer, and N. Vigneron, "Natural layer-by-layer photonic structure in the scales of Hoplia coerulea (Coleoptera)," *Phys. Rev. E*, vol. 6285, no. 72, pp. 628506-628506–5, Aug. 2006.

[57] J. P. Vigneron, J. M. Pasteels, D. M. Windsor, Z. Vértesy, M. Rassart, T. Seldrum, J. Dumont, O. Deparis, V. Lousse, L. P. Biró, D. Ertz, and V. Welch, "Switchable reflector in the Panamanian tortoise beetle Charidotella egregia (Chrysomelidae: Cassidinae)," *Phys. Rev. E - Stat. Nonlinear, Soft Matter Phys.*, vol. 76, no. 3, pp. 1–10, 2007.

[58] K. D. L. Umbers, "Turn the temperature to turquoise: Cues for colour change in the male chameleon grasshopper (Kosciuscola tristis) (Orthoptera: Acrididae)," *J. Insect Physiol.*, vol. 57, no. 9, pp. 1198–1204, 2011.

[59] K. Key and M. Day, "A temperature-controlled physiological colour response in the grasshopper Kosciuscola Tristis Sjost. (Orthoptera: Acrididae)," *Aust. J. Zool.*, vol. 2, no. 3, pp. 309–39, 1954.

[60] B. K. Filshie, M. F. Day, and E. H. Mercer, "Colour and colour change in the grasshopper, *Kosciuscola tristis*," *J. Insect Physiol.*, vol. 21, no. 11, pp. 1763–1770, 1975.

[61] A. Michelson, "On metallic colouring in birds and insects," *Philos. Mag.*, vol. 21, pp. 618–623, 1911.

[62] P. Gaubert, "Sur la polarisation circulaire de la lumiere reflechie pas les insectes," *Comptes Rendus*, vol. 179, pp. 1148–1150, 1924.

[63] H. Onslow, "On a Periodic Structure in Many Insect Scales, and the Cause of Their Iridescent Colours," *Philos. Trans. R. Soc. B*, vol. 211, pp. 1–74, 1923.

[64] J. Mathieu and N. Faraggi, "Étude de la lumière polarisée circulairement réfléchie far certains coléoptères," *Comptes Rendus*, vol. 205, pp. 1378–80, 1937.

[65] C. Robinson, "The Cholesteric Phase in Polypeptide Solutions and Biological Structures," *Mol. Cryst.*, vol. 1, no. 4, pp. 467–94, 1966.

[66] Y. Bouligand, "Twisted fibrous arrangements in biological materials and cholesteric mesophases," *Tissue Cell*, vol. 4, no. 2, pp. 189–217, 1972.

[67] A. C. Neville and S. Caveney, "Scarabaeid beetle exocuticle as an optical analogue of cholesteric liquid crystals," *Biol. Rev. Camb. Philos. Soc.*, vol. 44, pp. 531–562, 1969.

[68] S. Caveney, "Cuticle Reflectivity and Optical Activity in Scarab Beetles: The Role of Uric Acid," *Proc. R. Soc. B Biol. Sci.*, vol. 178, no. 1051, pp. 205–225, Jun. 1971.

[69] M. Xu, A. E. Seago, T. D. Sutherland, and S. Weisman, "Dual structural color mechanisms in a scarab beetle," *J. Morphol.*, vol. 271, no. 11, pp. 1300–5, Nov. 2010.

[70] A. C. Neville, "Metallic gold and silver colours in some insect cuticles," *J. Insect Physiol.*, vol. 23, no. 10, pp. 1267–74, 1977.

[71] A. Parker, D. McKenzie, and M. Large, "Multilayer reflectors in animals using green and gold beetles as contrasting examples," *J. Exp. Biol.*, vol. 1313, no. 1998, pp. 1307–1313, 1998.

[72] P. Vukusic, "Materials science. Evolutionary photonics with a twist," *Science*, vol. 325, no. 5939, pp. 398–9, Jul. 2009.

[73] W. E. Vargas, M. Hernández-Jiménez, E. Libby, D. E. Azofeifa, C. Barboza, and Á. Solis, "Light Reflection by Cuticles of Chrysina Jewel Scarabs: Optical Measurements, Morphology Characterization, and Theoretical Modeling," *Opt. Photonics J.*, vol. 6, no. 7, pp. 146–163, 2016.

[74] R. Yang, A. Zaheri, W. Gao, C. Hayashi, and H. D. Espinosa, "AFM Identification of Beetle Exocuticle: Bouligand Structure and Nanofiber Anisotropic Elastic Properties," *Adv. Funct. Mater.*, vol. 1603993, pp. 1–8, 2016.

[75] X. Wu, *Structure-property-relations of Cuticular Photonic Crystals Evolved by Different Beetle Groups (Insecta, Coleoptera) - ISBN:9783844294965*. Berlin: epubli GmbH, 2014.

[76] R. Ossikovski, M. Foldyna, C. Fallet, and A. De Martino, "Experimental evidence for naturally occurring nondiagonal depolarizers," *Opt. Lett.*, vol. 34, no. 16, pp. 2426–8, 2009.

[77] V. Sharma, M. Crne, J. O. Park, and M. Srinivasarao, "Structural origin of circularly polarized iridescence in jeweled beetles," *Science*, vol. 325, no. 5939, pp. 449–51, Jul. 2009.

[78] S. A. Jewell, P. Vukusic, and N. W. Roberts, "Circularly polarized colour reflection from helicoidal structures in the beetle Plusiotis boucardi," *New J. Phys.*, vol. 9, no. 99, pp. 1–10, Apr. 2007.

[79] V. Sharma, M. Crne, J. O. Park, and M. Srinivasarao, "Bouligand Structures Underlie Circularly Polarized Iridescence of Scarab Beetles: A Closer View," *Mater. Today Proc.*, vol. 1, pp. 161–171, 2014.

[80] L. McDonald, E. Finlayson, and P. Vukusic, "Untwisting the polarization properties of light reflected by scarab beetles," *SPIE BiOS*, vol. 9341, pp. 1–7, 2015.

[81] G. Agez, C. Bayon, and M. Mitov, "Multiwavelength micromirrors in the cuticle of scarab beetle Chrysina gloriosa," *Acta Biomater.*, vol. 48, pp. 357–367, Jan. 2017.

[82] D. Pye, *Polarised Light in Science and Nature - ISBN:9780750306737*. Bristol: IOP Publishing, 2001.

[83] L. De Silva, I. Hodgkinson, P. Murray, Q. H. Wu, M. Arnold, J. Leader, and A. Mcnaughton, "Natural and Nanoengineered Chiral Reflectors: Structural Color of Manuka Beetles and Titania Coatings," *Electromagnetics*, vol. 25, no. 5, pp. 391–408, Jul. 2005.

[84] M. Hernández-Jiménez, D. E. Azofeifa, E. Libby, C. Barboza-Aguilar, Á. Solís, L. Arce-Marenco, I. García-Aguilar, A. Hernández, and W. E. Vargas, "Qualitative correlation between structural chirality through the cuticle of Chrysina aurigans scarabs and left-handed circular polarization of the reflected light," *Opt. Mater. Express*, vol. 4, no. 12, pp. 2632–45, Nov. 2014.

[85] C. Campos-Fernández, D. E. Azofeifa, M. Hernández-Jiménez, A. Ruiz-Ruiz, and W. E. Vargas, "Visible light reflection spectra from cuticle layered materials," *Opt. Mater. Express*, vol. 1, no. 1, pp. 85–100, Apr. 2011.

[86] D. J. Brink, N. G. van der Berg, and L. C. Prinsloo, "The role of interface effects on the reflection of circularly polarised light from the thin-film structure of scarabus beetles," *Surf. Interface Anal.*, vol. 40, no. 3–4, pp. 769–771, Mar. 2008.

[87] S. Y. Ching, G. Li, H. L. Tam, D. T. P. Goh, J. K. L. Goh, and K. W. Cheah, "Chirality in Rhomborhina Gigantea beetle," *Opt. Mater. Express*, vol. 4, no. 11, pp. 2340–5, Oct. 2014.

[88] E. Libby, D. E. Azofeifa, M. Hernández-Jiménez, C. Barboza-Aguilar, A. Solís, I. García-Aguilar, L. Arce-Marenco, A. Hernández, and W. E. Vargas, "Light reflection by the cuticle of C. aurigans scarabs: a biological broadband reflector of left handed circularly polarized light," *J. Opt.*, vol. 16, no. 82001, pp. 1–7, Aug. 2014.

[89] D. J. Brink, N. G. Van Der Berg, L. C. Prinsloo, and I. J. Hodgkinson, "Unusual coloration in scarabaeid beetles," *J. Phys. D. Appl. Phys.*, vol. 40, no. 7, pp. 2189–2196, Apr. 2007.

[90] L. T. Mcdonald, T. A. Starkey, and P. Vukusic, "Photonic architectures in beetles: twists and iridescence," *Int. J. Des. Nat. Ecodynamics*, vol. 9, no. 4, pp. 266–275, Dec. 2014.

[91] J. D. Pye, "The distribution of circularly polarized light reflection in the Scarabaeoidea (Coleoptera)," *Biol. J. Linn. Soc.*, vol. 100, no. 3, pp. 585–596, Jun. 2010.

[92] T. Lenau and M. Barfoed, "Colours and Metallic Sheen in Beetle Shells — A Biomimetic Search for Material Structuring Principles Causing Light Interference," *Adv. Eng. Mater.*, vol. 10, no. 4, pp. 299–314, Apr. 2008.

[93] M. Srinivasarao, "Nano-optics in the biological world: beetles, butterflies, birds, and moths," *Chem. Rev.*, vol. 99, pp. 1935–1961, 1999.

[94] H. de Vries, "Rotatory power and other optical properties of certain liquid crystals," *Acta Crystallogr.*, vol. 4, no. 3, pp. 219–226, May 1951.

[95] W. John, W. Fritz, Z. Lu, and D. Yang, "Bragg reflection from cholesteric liquid crystals," *Phys. Rev. E*, vol. 51, no. 2, pp. 1191–1198, 1995.

[96] R. Dreher and G. Meier, "Optical Properties of Cholesteric Liquid Crystals," *Phys. Rev. A*, vol. 8, no. 3, pp. 1616–1623, Sep. 1973.

[97] A. C. Neville and B. M. Luke, "Molecular architecture of adult locust cuticle at the electron microscope level," *Tissue Cell*, vol. 1, no. 2, pp. 355–366, 1969.

[98] I. E. Carter, K. Weir, M. W. McCall, and A. R. Parker, "Variation in the circularly polarized light reflection of Lomaptera (Scarabaeidae) beetles," *J. R. Soc. Interface*, vol. 13, no. 120, pp. 1–9, Jul. 2016.

[99] D. E. Azofeifa, H. J. Arguedas, and W. E. Vargas, "Optical properties of chitin and chitosan biopolymers with application to structural color analysis," *Opt. Mater. (Amst).*, vol. 35, no. 2, pp. 175–183, Dec. 2012.

[100] H. Arwin, T. Berlind, B. Johs, and K. Järrendahl, "Cuticle structure of the scarab beetle Cetonia aurata analyzed by regression analysis of Mueller-matrix ellipsometric data," *Opt. Express*, vol. 21, no. 19, pp. 22645–22656, 2013.

[101] S. Nikolov, H. Fabritius, M. Petrov, M. Friák, L. Lymperakis, C. Sachs, D. Raabe, and J. Neugebauer, "Robustness and optimal use of design principles of arthropod exoskeletons studied by ab initio-based multiscale simulations," *J. Mech. Behav. Biomed. Mater.*, vol. 4, no. 2, pp. 129–145, 2011.

[102] M. Saba, B. D. Wilts, J. Hielscher, and G. E. Schröder-Turk, "Absence of circular polarisation in reflections of butterfly wing scales with chiral Gyroid structure," *Mater. Today Proc.*, vol. 1, no. March 2015, pp. 193–208, 2014.

[103] M. H. Song, B. C. Park, K. C. Shin, T. Ohta, Y. Tsunoda, H. Hoshi, Y. Takanishi, K. Ishikawa, J. Watanabe, S. Nishimura, T. Toyooka, Z. G. Zhu, T. M. Swager, and H. Takezoe, "Effect of phase retardation on defect-mode lasing in polymeric cholesteric liquid crystals," *Adv. Mater.*, vol. 16, no. 9–10, pp. 779–783, 2004.

[104] K. Jarrendahl and H. Arwin, "Polarizing Natural Nanostructures - ISBN:9783642401275," in *Springer Series in Surface Sciences:Ellipsometry of Functional Organic Surfaces and Films*, vol. 52, K. Hinrichs and K.-J. Eichhorn, Eds. Berlin: Springer, 2014, pp. 155–169.

[105] S. Lowrey, L. Silva, I. Hodgkinson, and J. Leader, "Observation and modeling of polarized light from scarab beetles," *JOSA A*, vol. 24, no. 8, pp. 2418–2425, 2007.

[106] I. Hodgkinson, S. Lowrey, L. Bourke, A. Parker, and M. W. McCall, "Mueller-matrix characterization of beetle cuticle: polarized and unpolarized reflections from representative architectures," *Appl. Opt.*, vol. 49, no. 24, pp. 4558–67, Aug. 2010.

[107] D. H. Goldstein, "Reflection properties of Scarabaeidae," in *Proceedings of SPIE*, 2005, vol. 5888, pp. 1–7.

[108] O. Arteaga, "Natural optical activity vs circular Bragg reflection studied by Mueller matrix ellipsometry," *Thin Solid Films*, vol. 617, pp. 14–19, 2016.
[109] R. Hegedüs, G. Szél, and G. Horváth, "Imaging polarimetry of the circularly polarizing cuticle of scarab beetles (Coleoptera: Rutelidae, Cetoniidae)," *Vision Res.*, vol. 46, pp. 2786–2797, 2006.
[110] H. Arwin, R. Magnusson, J. Landin, and K. Järrendahl, "Chirality-induced polarization effects in the cuticle of scarab beetles: 100 years after Michelson," *Philos. Mag.*, vol. 92, no. 12, pp. 1583–1599, Apr. 2012.
[111] R. Shamim, "Optical Studies of Nano-Structures in the Beetle Cetonia Aurata - MSc Thesis," Linköpings University, 2009.
[112] J. Gustafson, "Optical Studies and Micro-Structure Modeling of the Circular-Polarizing Scarab Beetles Cetonia aurata, Potosia cuprea, Liocola marmorata," Linköpings University, 2010.
[113] H. Arwin, R. Magnusson, L. Fernández del Río, J. Landin, A. Mendoza-Galván, and K. Järrendahl, "Exploring polarization features in light reflection from beetles with structural colors," *Proc. SPIE*, vol. 9429, no. 942909, pp. 1–13, Mar. 2015.
[114] A. Mendoza-Galván, E. Muñoz-Pineda, K. Järrendahl, and H. Arwin, "Evidence for a dispersion relation of optical modes in the cuticle of the scarab beetle Cotinis mutabilis," *Opt. Mater. Express*, vol. 4, no. 12, p. 2484, Nov. 2014.
[115] H. Arwin, L. Fernández del Río, and K. Järrendahl, "Comparison and analysis of Mueller-matrix spectra from exoskeletons of blue, green and red Cetonia aurata," *Thin Solid Films*, vol. 571, pp. 739–743, Nov. 2014.
[116] L. Fernández del Río, H. Arwin, and K. Järrendahl, "Polarizing properties and structural characteristics of the cuticle of the scarab Beetle Chrysina gloriosa," *Thin Solid Films*, vol. 571, pp. 410–415, Nov. 2014.
[117] L. Fernández del Río, H. Arwin, and K. Järrendahl, "Polarizing properties and structure of the cuticle of scarab beetles from the Chrysina genus," *Phys. Rev. E*, vol. 12409, pp. 1–9, 2016.
[118] C. Fallet, "Angle resolved Mueller polarimetry , applications to periodic structures) - PhD Thesis," École polytechnique, 2011.
[119] E. Muñoz-Pineda, K. Järrendahl, H. Arwin, and A. Mendoza-Galván, "Symmetries and relationships between elements of the Mueller matrix spectra of the cuticle of the beetle Cotinis mutabilis," *Thin Solid Films*, vol. 571, pp. 660–665, Nov. 2014.
[120] R. Magnusson, H. Arwin, E. Garcia-Caurel, K. Jarrendahl, and R. Ossikovski, "Sum regression decomposition of spectral and angle-resolved Mueller matrices from biological reflectors," *Appl. Opt.*, vol. 55, no. 15, pp. 4060–4065, 2016.
[121] H. Arwin, R. Magnusson, C. Fallet, K. Järrendahl, M. Foldyna, A. De Martino, and R. Ossikovski, "Sum decomposition of Mueller-matrix images and spectra of beetle cuticles," *Opt. Express*, vol. 23, no. 3, pp. 4558–4567, 2015.
[122] L. Fernández del Río, "An Investigation of the Polarizing Properties and Structural Characteristics in the Cuticles of the Scarab Beetles Chrysina gloriosa and Cetonia aurata - MSc Thesis," Linköpings University, 2012.
[123] L. Fernández del Río, "An Investigation of the Polarization States of Light Reflected from Scarab Beetles of the Chrysina Genus - BSc Thesis," Linköpings University, 2011.
[124] D. Pye, "Left-handed beetles," *Phys. World*, vol. 23, no. 8, pp. 52–52, Aug. 2010.
[125] O. F. Aguilar Gutierrez and A. D. Rey, "Chiral graded structures in biological plywoods and in the beetle cuticle," *Colloids Interface Sci. Commun.*, vol. 3, no. 2014, pp. 18–22, 2014.
[126] D. J. Brink, N. van der Berg, and L. Prinsloo, "Multi-color reflection from chiral thin-film stacks," *Proc. SPIE*, vol. 8094, no. 80940G, pp. 1–8, Sep. 2011.
[127] P. Hawkins, "Final year project A Study of Chiral Thin Films and their Occurrence in Nature - MSci Thesis," Imperial College, London, 2012.

[128] W. E. Vargas, M. Hernández-Jiménez, E. Libby, D. E. Azofeifa, Á. Solis, and C. Barboza-Aguilar, "Broadening of effective photonic band gaps in biological chiral structures: From intrinsic narrow band gaps to broad band reflection spectra," *EPL (Europhysics Lett.*, vol. 111, no. 64001, pp. 1–6, 2015.

[129] D. E. Azofeifa, M. Hernández-Jiménez, E. Libby, A. Solís, C. Barboza-Aguilar, and W. E. Vargas, "A quantitative assessment approach of feasible optical mechanisms contributing to structural color of golden-like Chrysina aurigans scarab beetles," *J. Quant. Spectrosc. Radiat. Transf.*, vol. 160, pp. 63–74, Jul. 2015.

[130] I. J. Hodgkinson, L. De Silva, P. Murray, Q. H. Wu, M. Arnold, and J. P. Leader, "Modeling optical reflectance from chiral micromirrors embedded in manuka beetles," in *Proceedings of SPIE*, 2004, vol. 5509, pp. 15–23.

[131] S. Valyukh, H. Arwin, and K. Järrendahl, "Simulation of light scattering from exoskeletons of scarab beetles," *Opt. Express*, vol. 24, no. 6, pp. 5794–808, 2016.

[132] A. Pace, "Cholesteric Liquid Crystal-Like Structure of the Cuticle of Plusiotis gloriosa," *Science (80-.).*, vol. 176, no. 4035, pp. 678–80, May 1972.

[133] R. Meister, M. Halle, H. Dumoulin, and P. Pieranski, "Structure of the cholesteric focal conic domains at the free surface," *Phys. Rev. E*, vol. 54, no. 4, pp. 3771–3782, 1996.

[134] R. Meister, H. Dumoulin, M. Hall, P. Pieranski, R. Meister, H. Dumoulin, and M. Hall, "The Anchoring of a Cholesteric Liquid Crystal at the Free Surface," *J. Phys. II*, vol. 6, no. 6, pp. 827–44, 1996.

[135] E. Loewen, M. Neviere, and D. Maystre, "Grating efficiency theory as it applies to blazed and holographic gratings," *Appl. Opt.*, vol. 16, no. 10, pp. 2711–2721, 1977.

[136] M. Y. Noh, S. Muthukrishnan, K. J. Kramer, and Y. Arakane, "Cuticle formation and pigmentation in beetles," *Curr. Opin. Insect Sci.*, vol. 17, no. May, pp. 1–9, 2016.

[137] A. Lequet, "La Cétoine Dorée (Cetonia aurata)!" [Online]. Available: https://www.insectes-net.fr/cetoine/cetoi3.htm. [Accessed: 17-Dec-2016].

[138] A. C. Neville, "A dermal light sense influencing skeletal structure in locusts," *J. Insect Physiol.*, vol. 13, pp. 933–939, 1967.

[139] B. Zelazny and A. C. Neville, "Endocuticle layer formation controlled by non-circadian clocks in beetles," *J. Insect Physiol.*, vol. 18, no. 10, pp. 1967–79, 1972.

[140] M. Kurachi, Y. Takaku, Y. Komiya, and T. Hariyama, "The origin of extensive colour polymorphism in Plateumaris sericea (Chrysomelidae, Coleoptera)," *Naturwissenschaften*, vol. 89, no. 7, pp. 295–298, 2002.

[141] A. L. V. Davis, "Functional implications of temperature-correlated colour polymorphism in an iridescent, scarabaeine," *Ecol. Entomol.*, vol. 33, pp. 771–779, 2008.

[142] M. E. Favila, G. Ruiz-Lizarraga, and J. Nolasco, "Inheritance of a red cuticular color mutation in the scarab beetle Canthon cyanellus cyanellus LeConte (Coleoptera : Scarabaeidae)," *Coleopt. Bull.*, vol. 54, no. 4, pp. 541–545, 2000.

[143] D. Hawks, "'The Eye of the Beholder' or 'They look really nice, but not very edible to me, and I have no idea what they look like to hawks, despite my name' or 'Color Variation and other stuff about Chrysina,'" *Scarabs*, vol. April, no. 26, 2008.

[144] H. F. Gleeson and H. J. Coles, "Optical Properties of Chiral Nematic Liquid Crystals," *Mol. Cryst. Liq. Cryst. Inc. Nonlinear Opt.*, vol. 170, no. 1, pp. 9–34, 1989.

[145] N. O. Young and J. Kowal, "Optically Active Fluorite Films," *Nature*, vol. 183, no. 4654, pp. 104–105, Jan. 1959.

[146] K. Robbie, M. J. Brett, and A. Lakhtakia, "Chiral sculptured thin films," *Nature*, vol. 384, no. 6610. pp. 616–616, 1996.

[147] A. Lakhtakia, M. W. McCall, J. A. Sherwin, Q. H. Wu, and I. J. Hodgkinson, "Sculptured-thin-film spectral holes for optical sensing of fluids," *Opt. Commun.*, vol. 194, no. 1–3, pp. 33–46, 2001.

[148] V. I. Kopp, V. M. Churikov, G. Zhang, J. Singer, C. W. Draper, N. Chao, D. Neugroschl, and A. Z. Genack, "Chiral fiber gratings: perspectives and challenges for sensing applications," 2007, vol. 6619, pp. 1–8.

[149] M. W. McCall and I. Hodgkinson, “Properties of partially polarized light remitted from lossless polarizing elements,” *Eur. J. Phys.*, vol. 30, no. 4, pp. S63–S80, 2009.
[150] H. Hepburn and A. Ball, “On the structure and mechanical properties of beetle shells,” *J. Mater. Sci.*, vol. 8, pp. 618–623, 1973.
[151] E. J. Warrant, “Polarisation vision: beetles see circularly polarised light.,” *Curr. Biol.*, vol. 20, no. 14, pp. R610-2, Jul. 2010.
[152] K. Allahverdyan and T. Galstian, “Could the Cuticle of Beetles Serve Also for Their Radiative Thermoregulation?,” *Opt. Photonics J.*, vol. 3, no. November, pp. 17–22, 2013.
[153] M. Dacke, P. Nordström, C. H. Scholtz, and E. J. Warrant, “A specialized dorsal rim area for polarized light detection in the compound eye of the scarab beetle Pachysoma striatum,” *J. Comp. Physiol. A Neuroethol. Sensory, Neural, Behav. Physiol.*, vol. 188, pp. 211–216, 2002.
[154] M. Dacke, P. Nordstrom, and C. Scholtz, “Twilight orientation to polarised light in the crepuscular dung beetle Scarabaeus zambesianus,” *J. Exp. Biol.*, vol. 206, no. 9, pp. 1535–1543, May 2003.
[155] M. Dacke, D. Nilsson, C. H. Scholtz, M. Byrne, and E. J. Warrant, “Insect orientation to polarized moonlight,” *Nature*, vol. 424, no. July, pp. 33–34, 2003.
[156] S. Kleinlogel and A. G. White, “The secret world of shrimps: Polarisation vision at its best,” *PLoS One*, vol. 3, no. 5, pp. 1–8, 2008.
[157] P. Brady and M. Cummings, “Differential response to circularly polarized light by the jewel scarab beetle Chrysina gloriosa,” *Am. Nat.*, vol. 175, no. 5, pp. 614–20, May 2010.
[158] G. Horváth, *Polarized Light and Polarization Vision in Animal Sciences - ISBN:9783642547171*, 2nd ed. Berlin, Heidelberg: Springer Berlin Heidelberg, 2014.
[159] N. Umow, “Chromatische depolarisation durch lichtzerstreuung,” *Phys. Zeitschrift*, vol. 6, pp. 674–676, 1905.
[160] M. Blahó, A. Egri, R. Hegedüs, J. Jósvai, M. Tóth, K. Kertész, L. P. Biró, G. Kriska, and G. Horváth, “No evidence for behavioral responses to circularly polarized light in four scarab beetle species with circularly polarizing exocuticle,” *Physiol. Behav.*, vol. 105, no. 4, pp. 1067–75, Feb. 2012.
[161] J. Miao, Y. Wu, K. Li, and Y. Jiang, “Evidence for Visually Mediated Copulation Frequency in the Scarab Beetle Anomala corpulenta,” *J. Insect Behav.*, vol. 28, no. 2, pp. 175–182, 2015.
[162] H. K. Snyder, R. Maia, L. D’Alba, A. J. Shultz, K. M. C. Rowe, K. C. Rowe, and M. D. Shawkey, “Iridescent colour production in hairs of blind golden moles (Chrysochloridae),” *Biol. Lett.*, vol. 8, no. 3, pp. 393–6, Jun. 2012.
[163] T. A. Retief, N. C. Bennett, A. A. Kinahan, and P. W. Bateman, “Sexual selection and genital allometry in the Hottentot golden mole (Amblysomus hottentotus),” *Mamm. Biol.*, vol. 78, no. 5, pp. 356–360, 2013.
[164] A. C. Neville, “the physics of helicoids,” *Phys. Bull.*, vol. 37, pp. 74–6, 1986.
[165] S. Clark, “Polarized starlight and the handedness of life,” *Am. Sci.*, vol. 87, no. 4, pp. 336–343, 1999.
[166] J. Bailey, “Astronomical sources of circularly polarized light and the origin of homochirality,” in *Origins of Life and Evolution of the Biosphere*, 2001, vol. 31, no. 1–2, pp. 167–183.
[167] M. Srinivasarao, “Chirality and polymerso,” *Curr. Opin. Colloid Interface Sci.*, vol. 4, no. 2, pp. 147–152, 1999.
[168] R. E. Woodruff, “Scarab Jewels,” *Scarabs*, vol. July, no. 41, pp. 1–12, 2009.
[169] N. E. Stork, J. McBroom, C. Gely, and A. J. Hamilton, “New approaches narrow global species estimates for beetles, insects, and terrestrial arthropods,” *Proc. Natl. Acad. Sci. U. S. A.*, vol. 112, no. 24, pp. 7519–23, 2015.
[170] P. Gullan and P. Cranston, *The Insects:An Outline of Entomology - ISBN:9781444330366*, 4th ed. Oxford: John Wiley and Sons, 2010.

[171] N. Fleming, "Which life form dominates Earth," *BBC News*, 10-Feb-2015. [Online]. Available: http://www.bbc.co.uk/earth/story/20150211-whats-the-most-dominant-life-form. [Accessed: 03-Mar-2016].

[172] K. Chung and J. H. Shin, "Range and stability of structural colors generated by Morpho-inspired color reflectors," *J. Opt. Soc. Am. A. Opt. Image Sci. Vis.*, vol. 30, no. 5, pp. 962–8, May 2013.

[173] I. E. Carter, K. Weir, and M. W. McCall, "Investigation of the Variation of Near-Circular Polarization in Scarabaeoidea Beetles," *Mater. Today Proc.*, vol. 4, no. 4, pp. 4942–4951, 2017.

[174] A. B. T. Smith, "A Review of the Family-group Names for the Superfamily Scarabaeoidea (Coleoptera) with Corrections to Nomenclature and a Current Classification," *Coleopt. Bull.*, vol. 60, no. sp5, pp. 144–204, 2006.

[175] A. B. T. Smith, D. C. Hawks, and J. M. Heraty, "An overview of the classificationand evolution of the major scarab beetle clades (Coleoptera: Scarabaeoidea)based on preliminary molecular analyses," *Coleopt. Soc. Monogr.*, pp. 35–46, 2006.

[176] B. D. Gill, "Generic Guide to New World Scarab Beetles-Scarabaeidae-Scarabaeinae Overview," *UNL State Museum - Division of Entomology*, 2005. [Online]. Available: http://museum.unl.edu/research/entomology/Guide/Scarabaeoidea/Scarabaeidae/Scarabaeinae/Scarabaeinae-Overview/ScarabaeinaeO.html.

[177] J. Krikken, "A new key to the suprageneric taxa in the beetle family Cetoniidae, with annotated lists of the known genera," *Zool. Verh.*, vol. 210, pp. 3–75, 1984.

[178] B. Ratcliffe, "Generic Guide to New World Scarab Beetles-Scarabaeidae-Cetoniinae Overview," *University of Nebraska State Museum - Division of Entomology*, 2005. [Online]. Available: http://museum.unl.edu/research/entomology/Guide/Scarabaeoidea/Scarabaeidae/Cetoniinae/Cetoniinae-Overview/CetoniinaeO.html.

[179] M. Moron, *Escarabajos, 200 millones de años de evolución*, no. 14. Mexico: Instituto de Ecologia, 1984.

[180] J. Machatschke, "Scarabaeoidea: Melolonthidae, Rutelinae," *Coleopt. Cat. Suppl.*, vol. 66, pp. 1–361, 1972.

[181] T. Ladd Jr, M. Jacobson, and C. Buriff, "Japanese Beetles: Extracts from Neem Tree Seeds as Feeding Deterrents," *J. Econ. Entomol.*, vol. 75, no. 5, pp. 810–3, 1978.

[182] D. Curoe, "An Annotated List of Some Species of Chrysina," *Scarabs*, vol. May, no. 27, pp. 1–22, 2008.

[183] D. B. Thomas, A. Seago, D. C. Robacker, and A. Poe, "Reflections On Golden Scarabs," *Am. Entomol.*, vol. Winter, pp. 224–230, 2007.

[184] J. Capinera, *Encyclopedia of Entomology*, 2nd ed. Springer, 2008.

[185] G. Cassis, W. Houston, T. Weir, and B. Moore, *Zoological Catalogue of Australia Vol. 9: COLEOPTERA:Scarabaeoidea - ISBN:9780644145961*. Canberra: Australian Government Publishing Service, 1992.

[186] A. Evans, "Generic Guide to New World Scarab Beetles- Scarabaeidae," *University of Nebraska State Museum - Division of Entomology*, 2005. [Online]. Available: http://museum.unl.edu/research/entomology/Guide/Scarabaeoidea/Scarabaeidae/Melolonthinae/Melolonthinae-Overview/MelolonthinaeO.html. [Accessed: 04-Mar-2016].

[187] MAF Plant Health & Environmental Laboratory, "Manuka Beetle (Pyronota festiva)," 2011. [Online]. Available: http://www.padil.gov.au/maf-border/pest/main/140414/30082.

[188] F. C. Ocampo, "Generic Guide to the New World Scarab Beetles-Hybosoridae-Ceratocanthinae," *University of Nebraska State Museum - Division of Entomology*, 2006. [Online]. Available: http://museum.unl.edu/research/entomology/Guide/Scarabaeoidea/Hybosoridae/Ceratocanthinae/CeratocanthinaeO.html. [Accessed: 04-Mar-2016].

[189] A. Ballerio, B. D. Gill, and V. V Grebennikov, “Illustrated overview and identification key to Cameroonian Ceratocanthinae beetles (Coleoptera: Scarabaeoidea: Hybosoridae) with description of four new species,” *Zootaxa*, vol. 24, no. 2892, pp. 1–24, 2011.

[190] Royal Belgian Institute of natural Sciences (RBINS), “Acanthocerus vicarius Bates, 1887.” [Online]. Available: http://virtualcollections.naturalsciences.be/virtual-collections/entomology/coleoptera/ceratocanthidae/ceratocanthus-vicarius. [Accessed: 11-Nov-2017].

Chapter 4 - Circularly Polarised Measurements

4.1. Introduction

Initially in this Chapter the method of identifying beetles which reflect CP light using passive 3D glasses is described. The photographing setup to capture images of the beetles using lenses from such CP glasses is then explained.

An experimental setup to measure the beetles was employed which could vary the handedness (between left and right) of the incoming and the analysis of the outgoing CP light over a wide range of wavelengths (450-1000nm). This built upon previous similar work at Imperial College [1] including the author's MRes Thesis [2], from where this setup which measures CP reflection was taken.

This setup had various problems which were overcome and the settings were optimised in order to obtain the best functioning system possible. Spectra were measured from many different specimens, firstly from typical examples of each of the nine subfamilies known to selectively reflect CP light. The variation in CP spectra of the *Chrysina* genus is discussed, including broadband and narrowband reflection, colour and intensity variations as well as variation in the handedness of reflection. The variation in large numbers of Cetoniinae were discussed, with some species having more variations and distinctive spectral shapes than others. In smaller sample sizes large variations in the CP wavelength were observed from blue to the NIR. Examples of single specimens with interesting LCP spectra are then presented, such as the colour mixing of red and blue wavelengths, resulting in a brilliant purple colour.

The *Rhomborhina gigantea* beetle was previously reported to have a CLC like structure, which was responsible for the shell's brilliant green colour. In this report, evidence is presented to the contrary.

Photographs of several selected beetles were taken to demonstrate the angular colour variation and also variation in unmeasured parts of the beetle including the underside of their shells.

4.2. Preliminary Work

4.2.1. Circularly Polarised Cinema Glasses

Further to past research which identified species which reflected CP light, a cheap and easy method of identifying other species with such properties was required. A solution was to use RealD 3D glasses which only allow LCP light to be transmitted through the left panel, and only

RCP light to be transmitted through the right panel. The glasses are created with a sheet quarter waveplate in front of the lens (further from the wearer's eye) and a sheet linear polariser behind. The angle between the transmission axis of the linear polariser and the fast axis of the quarter waveplate is ±45° for LCP and RCP light respectively. The glasses were analysed within the experimental setup shown in Figure 4.6. They were placed between the mirror and the collecting lens with the ray incident upon the front of the glasses as shown in Figure 4.1.



Figure 4.1 – The RealD 3D glasses in side profile, with the orientation of light propagation through them shown by the red arrow.

The transmission spectra of RCP and LCP light through the two lenses of the glasses can be seen in Figure 4.2, where it is demonstrated that using the correct polarised lens for each handedness of light results in approximately 65% of the light being transmitted. When using the opposite polariser (i.e. left circular polariser for RCP light and vice versa) only 5% transmission of light was achieved. It can be seen that the circular polariser worked well from the blue part of the visible spectrum (450nm) until approximately 750nm. At 750nm the transmission of all the polarisers and orientations tended towards full transmission. One feature which appeared consistently was an as yet small unexplained peaks at 660nm and 930nm.

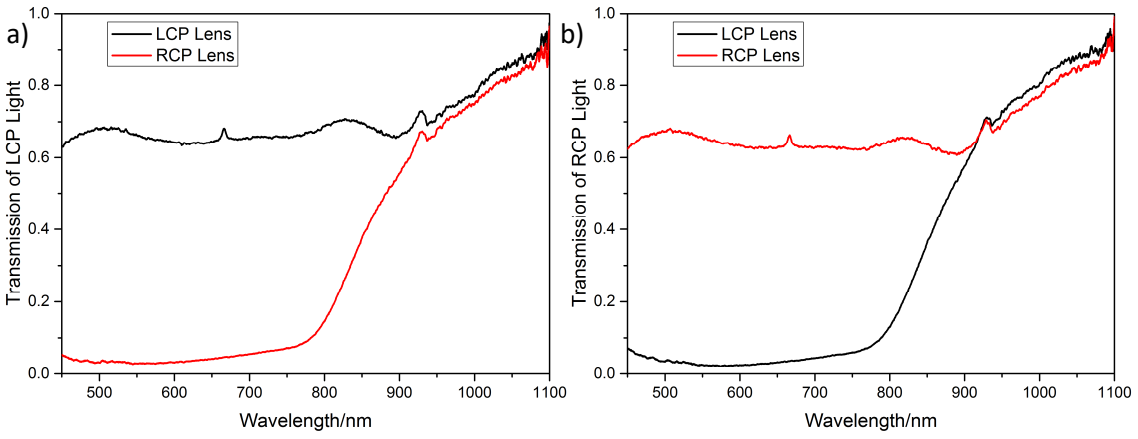


Figure 4.2 – Transmission of a) LCP light and b) RCP light through LCP and RCP lenses (filters), over the wavelength range 450nm to 1000nm.

The 3D glasses worked well with a ratio of 5% to 65% between the correct handed polariser and the opposite handed polariser. This would appear as an even stronger contrast to human eyes, since they work upon a logarithmic scale [3]. However, above 750nm the transmission tended towards 100% for both handed polarisers, meaning the glasses could not be used to study above this wavelength. It should be noted that human eyesight can only observe approximately 400-700nm [4] and any CP observation in the NIR would require a waveshifting device (such as a NIR camera) in order for the user to observe these wavelengths. (An example of a beetle specimen

which reflects LCP at these longer wavelengths from the *Cetonia aurata pisina* can be seen in Figure 4.78d).

The lenses from the 3D glasses were used with a camera in order to take photographs through the filters. In this report three photos of each beetle (when available) were taken in the following arrangements; through a LCP filter, a RCP filter and no filter at all. The setup for taking these photographs is described in Section 4.2.2.

4.2.2. Photographing Beetles

Photographs of each beetle specimen investigated in this section were taken through in three different filter settings (LCP filter, RCP filter and no filter). The setup used for taking these photographs can be seen in Figure 4.3. Several parts of the system were optimised in order to obtain the best photographs. Firstly a diffuse light source (Light box) was placed behind the camera to get a uniform light source and no high intensity 'white' spots from the beetles. Another method of reducing 'white' light spots was to put a sheet of white cardboard on top of the pinboard over the beetle to avoid direct lighting from ceiling lights and the use of a white cardboard iris also avoided this. The white cardboard iris (~2cm diameter) avoided the reflection of the camera and surroundings (such as the photographer appearing as an image) in the high metallic 'mirror-like' beetles.

The white pinboard was created from a rubberised board with a white sheet of paper in front. This setup gave the pictures a white background, which made it easier to remove the background from the images using Microsoft Word's in built function. The CP filters used were taken from a standard set of passive 3D cinema glasses and attached to the back of the cardboard iris (in the same orientation as in the glasses).

Photographs were taken using a phone (LG G4) mounted upon a tripod, to ensure stability.

The distance between the beetle and camera lens (with the cardboard iris moving with the camera) varied depending upon the size of the beetle. The photographs were captured at a distance where the smallest focal length from the camera lens arrangement meant the beetle filled the field of view. This required the distance between the camera and beetle to be larger in order to focus upon the bigger beetles.

The photograph settings (ISO, manual focus and white balance) for each beetle were the same for all of the images taken with each of the three filters arrangements (LCP/RCP/No filter). The settings were adjusted with no filter in place, adjusting the ISO settings to get the lightest images without the photograph becoming saturated. The white balance setting was also adjusted for

each beetle, in order for the background to look as white as possible for the slightly different lighting conditions (since the room had a window).

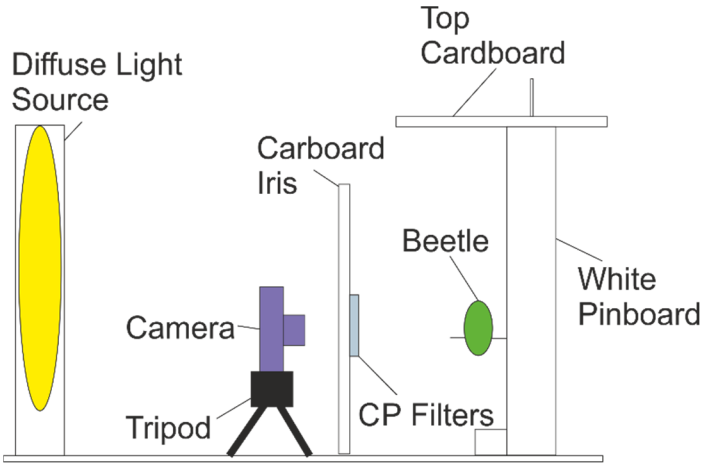


Figure 4.3 – Side view of the setup for photographing beetles through CP filters.

4.2.3. Reflection Position upon the Beetle

In the setup the intensity of reflected CP light was measured from the shell of the beetle. Initially the spot from which the light was reflected on the beetle was confined as much as possible to the scutellum, as shown in Figure 4.4. This part of the beetle was optically focused upon because it was relatively flat and focusing here was easily repeatable. This part of the beetle was focused upon for the *Lomaptera* genus from the Cetoniinae subfamily (Figure 4.5a).

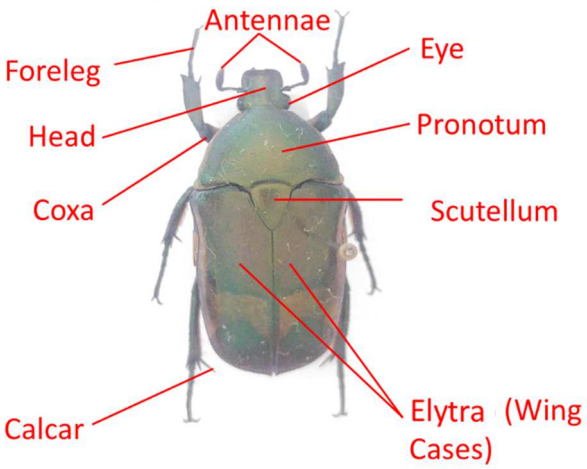
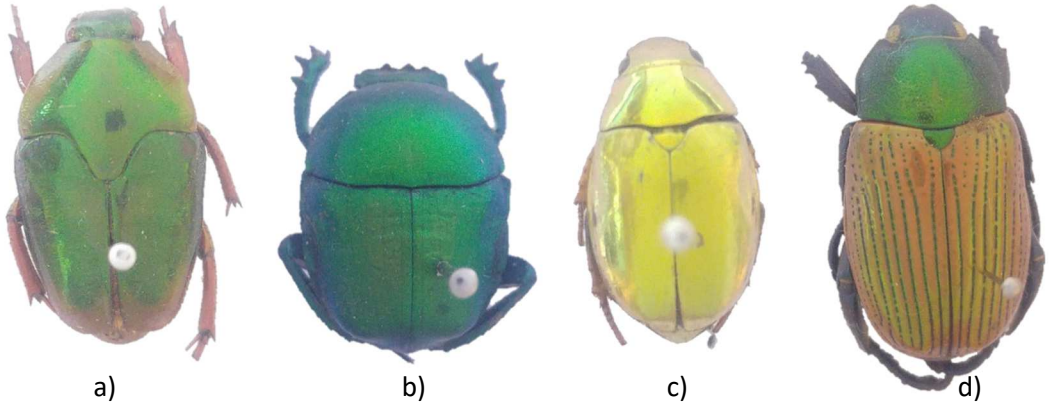


Figure 4.4 – Typical main body parts of a beetle (*Plaesiorrhinella plana cincta*). This photograph is taken without any filter.

Once the study was expanded to beetle species outside of the *Lomaptera* genus measuring from the scutellum was not practical and in many cases not possible. In some beetles the scutellum did not exist, particularly those of the subfamily Scarabaeinae (Figure 4.5b). In other beetles the scutellum was very small (due to the beetle size and also proportionally to the body) compared to the beam size, and as such it was not practical to reflect from there (Figure 4.5c). Due to these cases, the default measured reflection position became the top of the left elytra, and this was done for the majority of beetles. There were some exceptions such as Figure 4.5d, where the elytra did not reflect significant (or any) CP light and then reflection from the pronotum was measured.



a) b) c) d)

Figure 4.5 – Four typical beetles whose CP reflection were measured from a) the fused scutellum (Cetoniinae:*Lomaptera geelvinkiana*), b) top of the left elytra (Scarabaeinae:*Garreta azureus*), c) top of the left elytra (Rutelinae:*Anplognathus aereus*) and d) pronotum (Rutelinae:*Strigidia sanctijacobi*). These photographs were taken without any filters.

4.3. Experimental Setup

The experimental setup which was used to measure the broadband reflectance and polarisation of reflected CP light can be seen in Figure 4.6. This setup was based upon that of Tamara-Wicks [1] and is refined during the author's MRes Degree [2], from where the description of the setup in this section is taken.

The experimental setup had several requirements, including needing to work over a broad range of wavelengths (450nm-1000nm). A necessary requirement was being able to measure the intensity of a given circular polarisation in reflection. The two arms of the reflection setup (incoming and outgoing) had to have as small an angle between them as possible in order that the reflection on the beetle is as near to normal as possible. This meant that the path through the beetle's shell can be modelled more simply. The light beam (from the Ocean Optics DH2000-BAL light source) needed to be collimated to ensure that the light could be focused with a small spot size (diameter=2.0±0.5mm) on both the beetle and optical fibre (Ocean Optics QP600-2-SR-BX) which was linked to the Ocean Optics HR4000 spectrometer.

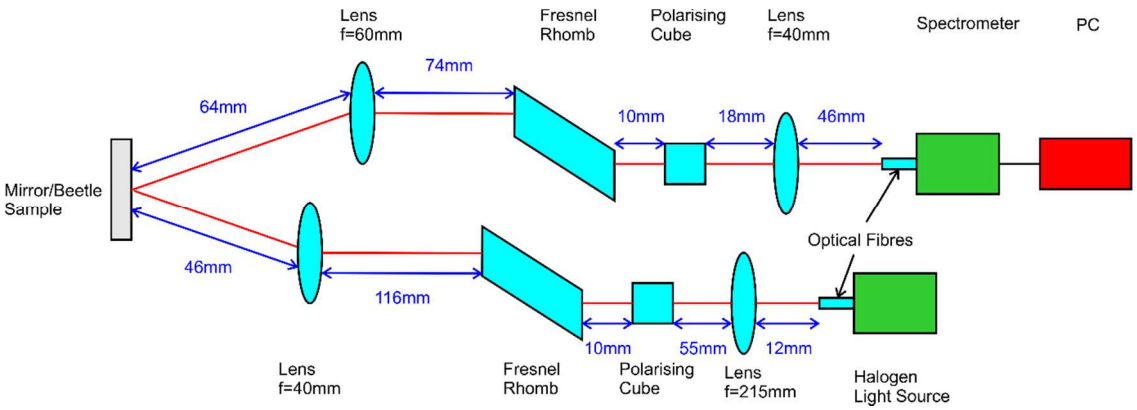


Figure 4.6 – The broadband experimental CP reflection setup using a beetle sample, with the full angle between the two arms being 22.5° (3sf), it should be noted that this diagram is not to scale and is a simplified schematic.

One limitation of the setup in Figure 4.6 cannot measure the ellipticity, an ellipsometer was necessary to do this as will be discussed in Chapter 6 using the MM algebra described in Chapter 2.

4.3.1. Polarising Cubes

In the experimental setup polarising cubes were used, these could be rotated in the plane that is perpendicular to the direction of the propagation of light. The polarising cubes could be configured to produce either +45° or -45° polarised light, which results in either LCP or RCP light being produced when the light passes through the Fresnel rhomb. The polarising cubes introduce a phase shift between the s- and p-polarised components of light, given as

$$\Delta\varphi = \frac{\pi}{2}. \tag{4.1}$$

The polarising cube splits light into the s and p polarisations which are orthogonally polarised with respect to each other as can be seen in Figure 4.7 [4]. The s polarised ray is totally reflected at the beamsplitter coating while the path of the p-polarised beam remains undeviated, effectively losing 50% of the signal at each trip through a beam splitter.

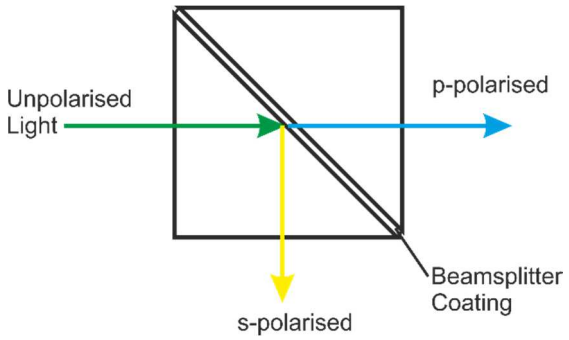


Figure 4.7 – Path of unpolarised light entering a polarising beamsplitting cube and being split into two perpendicular rays, the s-polarised and p-polarised rays.

4.3.2. Fresnel Rhomb

The Fresnel rhomb used in the experimental setup converts ±45° linearly polarised light (such that the x and y components are equal) into CP light, the process of which is shown in Figure 4.8. A 45° phase difference between the x and y components occurs at each total internal reflection within the rhomb. The s and p polarisations defined for the polarising beamsplitter such that they relate to the x (horizontal) and y (vertical) components respectively in this section.

A Fresnel rhomb is then used, which works over a wide range of wavelengths. In linearly polarised light the x and y electric field components are in phase. In CP light there is a ±90° phase difference between them.

As can be seen in Figure 4.8 there are two internal reflections within the Fresnel rhomb, with each reflection causing a phase shift of ±45° between the x and y components of the electric

field. The angle of the Fresnel rhomb is set to cause totally internal reflection (at an angle inducing the specified phase difference), the Fresnel rhomb is of higher refractive index than the surrounding air. The derivation from where the phase difference occurred was undertaken in the following way.

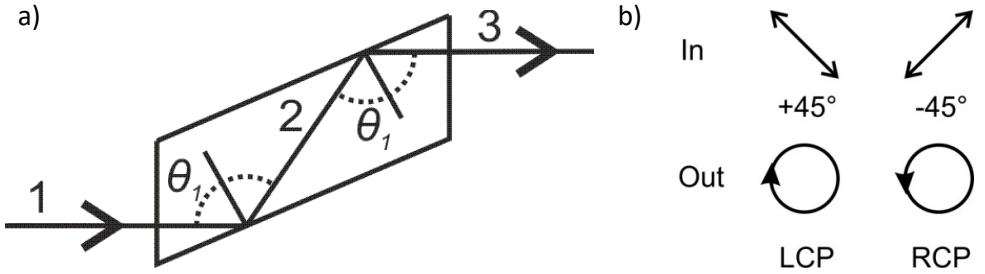


Figure 4.8 – a) The progression of light through the Fresnel rhomb. At position 1 linearly polarised light must be present with ±45° polarisation. It will then become elliptically polarised upon the first total internal reflection at position 2. Finally it will become CP at position 3 after the second total internal reflection. b) The input linear polarisations with the corresponding CP outputs are being shown on the left.

Firstly starting with Snell's law

$$\sin(\theta_2) = n\sin(\theta_1), \tag{4.2}$$

$$\cos(\theta_2) = \sqrt{1 - n^2\sin^2(\theta_1)}, \tag{4.3}$$

where the angle of incidence upon (or acceptance angle of) the rhomb is θ_2 and the angle from the side of the rhomb is defined as θ_1, n is the refractive index of the rhomb, and the refractive index of the surrounding medium, air is approximated as 1. The ratios of the magnitude of the electric field of the x and y components of light can be written as

$$\left.\frac{E_{0r}}{E_{0i}}\right|_x = -\frac{\sin(\theta_1 - \theta_2)}{\sin(\theta_1 + \theta_2)} = \frac{\cos(\theta_1) - i\sqrt{\sin^2(\theta_1) - \frac{1}{n^2}}}{\cos(\theta_1) + i\sqrt{\sin^2(\theta_1) - \frac{1}{n^2}}}, \tag{4.4}$$

$$\left.\frac{E_{0r}}{E_{0i}}\right|_y = -\frac{\tan(\theta_1 - \theta_2)}{\tan(\theta_1 + \theta_2)} = -\frac{\cos(\theta_1) - in^2\sqrt{\sin^2(\theta_1) - \frac{1}{n^2}}}{\cos(\theta_1) + in^2\sqrt{\sin^2(\theta_1) - \frac{1}{n^2}}}. \tag{4.5}$$

Equations 4.4 and 4.5 can be rearranged in terms of the form:

$$\frac{g^2 - h^2 - 2igh}{g^2 + h^2} \equiv e^{-i\varphi}, \tag{4.6}$$

where φ is the phase shift between the x and y components, using a tan expansion,

$$\tan(\varphi) = \tan\left(2\left(\frac{\varphi}{2}\right)\right) = \frac{2\tan\left(\frac{\varphi}{2}\right)}{1 - \tan^2\left(\frac{\varphi}{2}\right)} = \frac{2gh}{g^2 - h^2} = \frac{2\frac{h}{g}}{1 - \left(\frac{h}{g}\right)^2}. \tag{4.7}$$

It can be seen that

$$\tan\left(\frac{\varphi}{2}\right) = \frac{h}{g}. \tag{4.8}$$

The two different components of the electric field vector from equations 4.4 and 4.5 are put into equation 4.8 in terms of the respective phase shifts φ_x and φ_y.

$$\tan\left(\frac{\varphi_x}{2}\right) = \frac{\sqrt{\sin^2(\theta_1) - 1/n^2}}{\cos(\theta_1)} \tag{4.9}$$

$$\tan\left(\frac{\varphi_y}{2}\right) = \frac{n^2\sqrt{\sin^2(\theta_1) - 1/n^2}}{\cos(\theta_1)} \tag{4.10}$$

Finding the relative phase difference δ between the x and y phase shifts as

$$\tan\left(\frac{\varphi_x - \varphi_y}{2}\right) = \tan\left(\frac{\delta}{2}\right) = \frac{\tan\left(\frac{\varphi_x}{2}\right) - \tan(\frac{\varphi_y}{2})}{1 + \tan\left(\frac{\varphi_x}{2}\right)\tan(\frac{\varphi_y}{2})} = -\frac{\cos(\theta_1)\sqrt{n^2\sin^2(\theta_1) - 1}}{n\sin^2(\theta_1)}. \tag{4.11}$$

Then rearranging equation 4.11 to be able to calculate the phase difference as

$$\delta = 2\arctan\left(-\frac{\cos(\theta_1)\sqrt{n^2\sin^2(\theta_1) - 1}}{n\sin^2(\theta_1)}\right). \tag{4.12}$$

This equation has two solution angles which will produce the δ=45° as required. It can be seen that the phase difference is related to the angle of the Fresnel rhomb (θ_1) and also the refractive index of the material it is made from (n).

However, the refractive index of BK7 glass which the Fresnel rhomb is made of varies with wavelength as in the following Sellmeier relation,

$$n^2(\lambda) = 1 + \frac{B_1\,\lambda^2}{\lambda^2 - C_1} + \frac{B_2\,\lambda^2}{\lambda^2 - C_2} + \frac{B_3\,\lambda^2}{\lambda^2 - C_3}, \tag{4.13}$$

with the coefficients for the equation as given in Table 4.1.

The Sellmeier equation for BK7 in equation 4.13 along with the coefficents in Table 4.1 were plotted for wavelength against refractive index in Figure 4.9. It can be observed that the refractive index variation is relatively small over the observed spectrum from $n(\lambda$=400nm)=1.5309 to $n(\lambda$=1000nm)=1.5075.

Coefficient	Value (4dp)
B_1	1.0396
B_2	0.2318
B_3	1.0105
C_1	6.0007x$10^{-3}\mu m^2$
C_2	2.0018x$10^{-2}\mu m^2$
C_3	1.0356x$10^{2}\mu m^2$

Table 4.1 - Sellmeier coefficients for BK7 glass [5].

Incorporating the wavelength dependent refractive index, using equations 4.12 and 4.13 and using the manufacture's given value of the angle θ_1 as 55.33°±0.083° [6], the phase difference was plotted in Figure 4.10 over a range of wavelengths from 400nm to 1000nm. This illustrates the extent to which δ varied from 45°, which is required to obtain CP light from the rhomb. The code which was used to produce this plot can be found in [2] along with further modelling of

ideal Fresnel rhombs for varying angles, which are required to produce 45° phase differences upon each reflection.

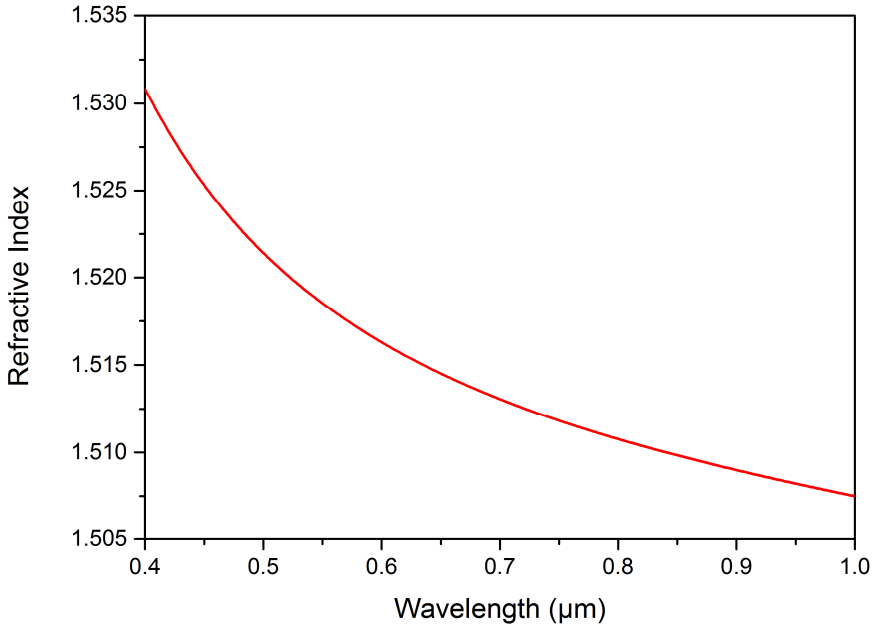


Figure 4.9 – Plot of the Sellmeier equation for wavelength between 400nm and 1000nm for BK7 glass.

From Figure 4.10, the maximum change in the modulus of ellipticity from 1 (circularly ellipticity) using minimum and maximum values of phase difference from the 55.33° curve were calculated as $|\Delta\xi(400nm)|$=0.02024 and as $|\Delta\xi(1000nm)|$=0.01814 using equation (4.14). As can be seen this error is only ~2% of that CP ellipticity and as such is considered not significant with respect to the experimental results.

$$\xi = \frac{b}{a}. \tag{4.14}$$

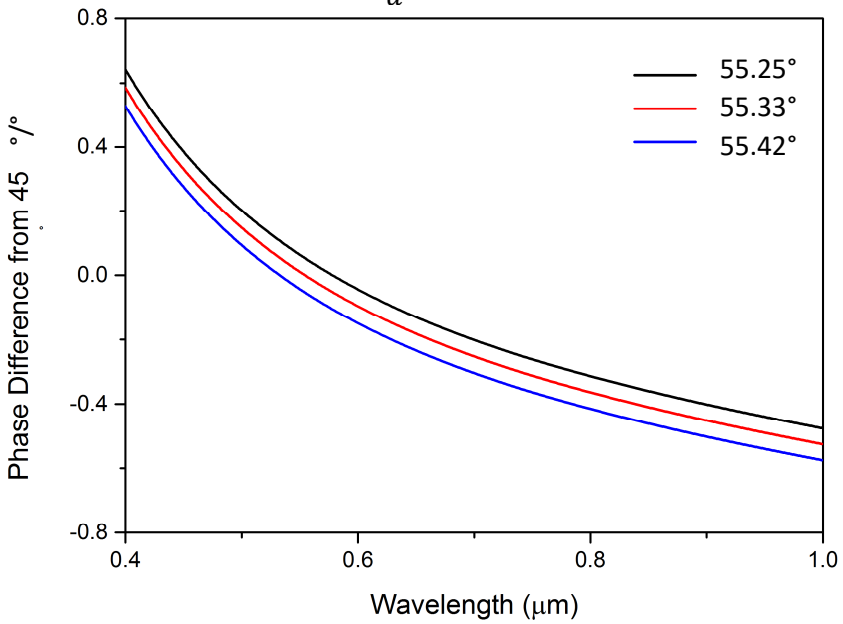


Figure 4.10 – Plot of the variation in the phase difference from 45° upon each reflection within the Fresnel Rhomb against wavelength, setting the internal angle of the Fresnel Rhomb as 55.33° (with an error of ±0.833°) as given by the manufacturer.

4.3.3. Calibration

The first stage of measuring the reflection spectra from the beetles was to align the system in order to obtain the best signal possible in terms of strength and minimised aberrations. The system was arranged as shown in Figure 4.6 and the mirror adjusted such that the spot reflected from the beetle went directly along the collection arm. The optical fibre position in the collecting arm was then finely adjusted to achieve the best signal. The input and output optical fibres were switched to see that the path of the light through the system was fully reversible and independent with respect to which end of the system the light was introduced. This ensured the system was aligned and errors reduced.

The system was adjusted such that the spot size upon the beetle was approximately 2.0±0.5mm diameter. It can be seen in Figure 4.11 that having this larger spot size produced a stronger signal. Since producing a smaller spot size required a shorter focal length lens, as such the two arms of the setup start to overlap, unless a greater angle between them is implemented. However, as previously stated the setup is required to have as near normal incidence as possible. Having a smaller focal length caused more scattering as reflection was at higher angles and this caused higher loss within the system. The spot size in the system was calculated in the author's masters study as 1.7mm [2], which was in the error of the experimental system.

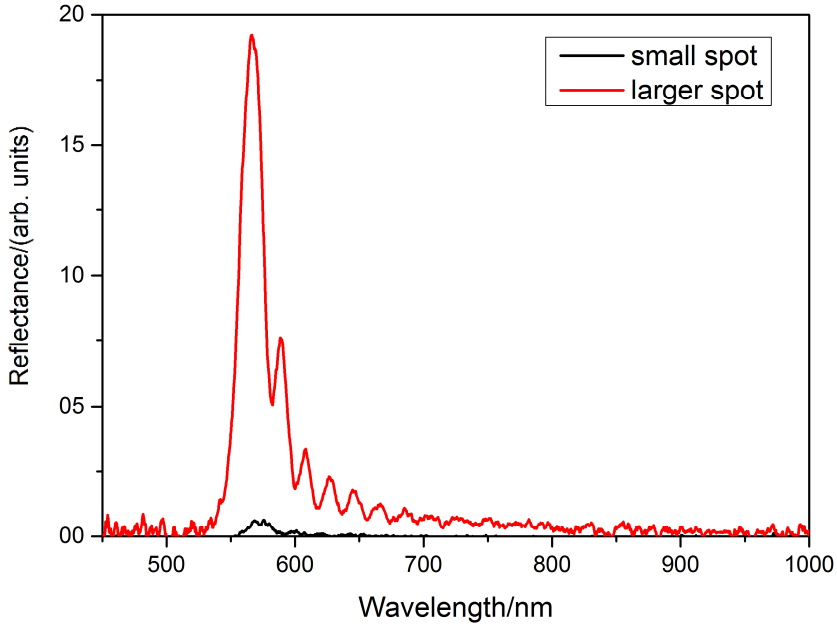


Figure 4.11 – LCP light input and response on a system configured using two different spot sizes, with a small spot of 1mm^2 (using a focusing lens of f=25mm focal length) and a larger spot of 2mm^2 (using a collecting lens of f=40mm) upon a *Lomaptera pseudodichropus* beetle.

The power of the Ocean Optics DH2000-BAL light source [7] was adjusted experimentally using a variable resistor. For all of the measurements of the beetle specimens, the light source was set to give the maximum intensity output in order to produce a higher signal to noise ratio which allowed for more defined features in reflection spectra to be observed.

In the setup the polarising cubes were rotated such that linearly polarised light transmitted through them is set to either ±(45±2.5°) polarisation, with the errors being observed experimentally within the setup. The two linearly polarising cubes in combination with the Fresnel rhombs could be set to allow LCP or RCP light to be incident upon the mirror or beetle sample and the reflected light's handedness to be measured. The following four combinations of LCP and RCP light in Table 4.2 were used within the system. It should be noted the angle of the dial of the second polarising cube is not the angle of the linear polarised transmission due to non-alignment of the dial.

Notation	Incident Circular Polarisation	Angle of Incident Polarising Cube Upon Dial	Reflected Circular Polarisation	Angle of Reflected Polarising Cube Upon Dial
LL	Left	45°±2.5°	Left	345°±2.5°
LR	Left	45°±2.5°	Right	75°±2.5°
RL	Right	135°±2.5°	Left	345°±2.5°
RR	Right	135°±2.5°	Right	75°±2.5°

Table 4.2 - Convention for CP light in system. It should be noted that due to the 180° symmetry of the polarising cubes, 135° orientation is equivalent to -45°.

4.3.4. Software Calibration

The software which was used to record the various reflection spectra was SpectraSuite by Ocean Optics. The three main variables which could be adjusted were the time base, the number of averages and the boxcar settings.

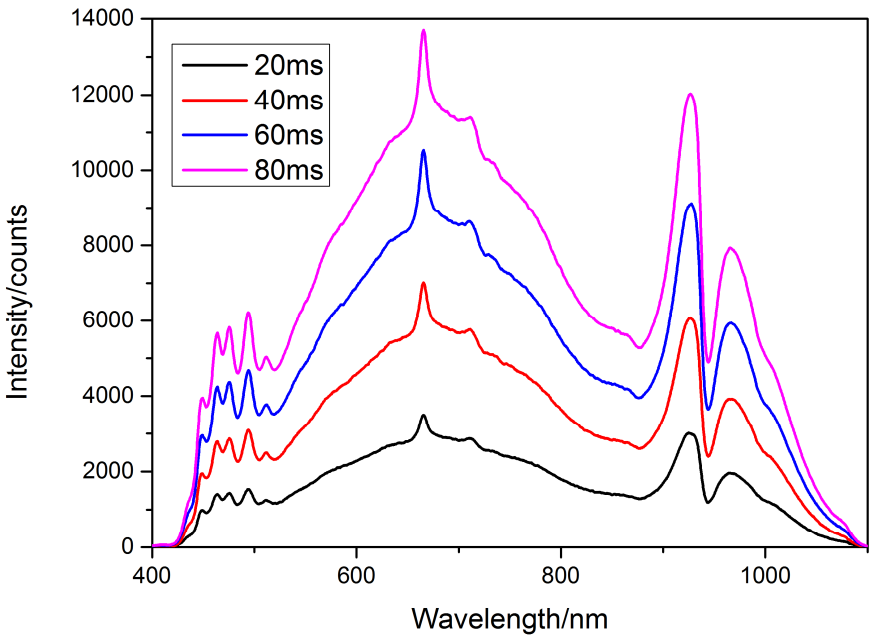


Figure 4.12 – Intensity plot from the system with a mirror in LR configuration, demonstrating the scaling of the graphs with increasing time base. Starting from an initial time base of 20ms increasing to 80ms at 20ms intervals and setting a boxcar of five and averaging of the spectra of one.

The time base is the time which is taken in order to obtain a spectrum reading. In general the longer the time base, the higher the number of counts. However, the spectrometer saturates at

an intensity of 16383 counts. The time base was chosen be as large as possible without saturating the spectrometer as can be seen in Figure 4.12. In the final experimental setup the time base used to achieve this was 100ms (unless stated). It should be noted that beetles with a very weak response used higher time bases in order to measure a clearer spectrum. Care was taken to ensure variation in the NIR peak at ~925nm with time was avoided, which is discussed later in Section 4.3.5.

The number of averages of spectra works by taking the average of consecutive spectra, the more averages the longer the overall reading takes. The smoothing which results from increasing the number of averages can be seen in Figure 4.13, however this also greatly increases in time needed to take a reading. As the boxcaring method was faster this was the used averaging method and the number of averages of spectra used in all readings was one.

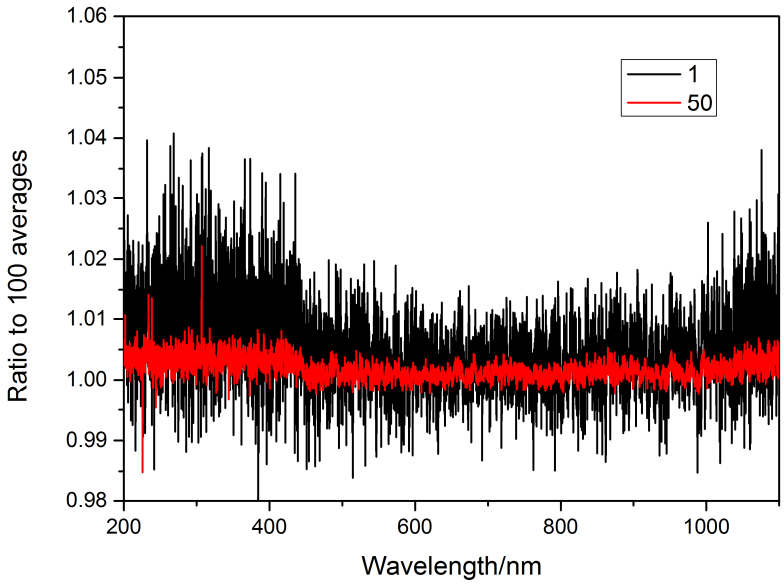


Figure 4.13 – Plot comparing the ratio of the signal for 1 and 50 averages compared to one of 100 averages (ie the signals divided by the 100 average signal), with a time base of 90ms and boxcar of zero.

The boxcar setting is the number of adjacent points that each point is averaged over, using the boxcar method resulted in smoother data, and unlike increasing the number of averages does not increase the time taken to obtain a reading. The boxcar setting used for all of the readings was either four or five, which can be seen to significantly decrease noise in Figure 4.14. The boxcar averaging can move the position of the spectral features, however this was avoided by using a very low boxcar (4 or 5) compared to the large number of data points (2,198) measured for each spectra (450-1000nm).

The software displays the intensity of the light signal in counts on the spectrometer which have been reflected from the mirror or beetle. The software can be used in order to produce reflection spectra which will be between zero (no reflection) and one (full reflection). A

reflection spectrum requires a reflection reading from the sample, a reference spectrum from a mirror and a background reading.

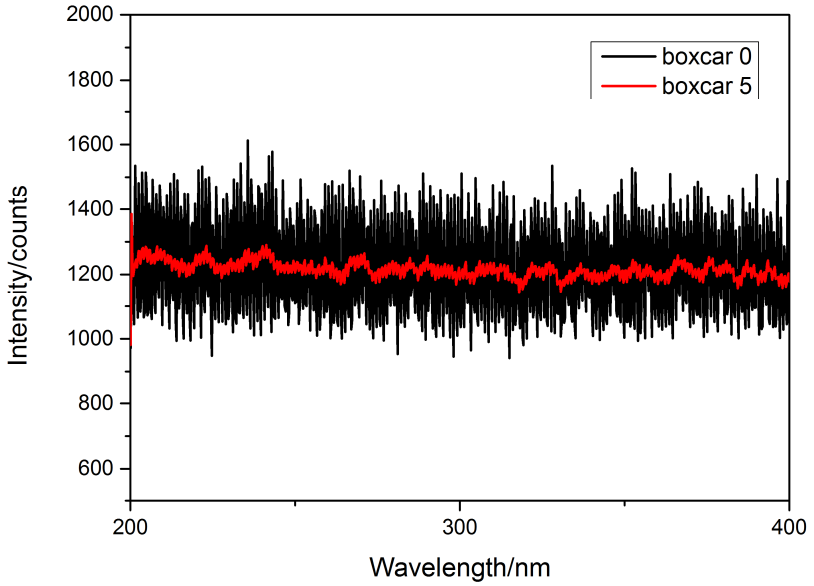


Figure 4.14 – Intensity plot of the background demonstrating the difference to the signal between not using the boxcar method (i.e. zero) and a boxcar of five adjacent points.

The reference sample is taken using a plane mirror, where the light in the incoming arm is CP. The CP handedness is reversed upon reflection. Hence the reference reading was taken in the LR (which was the same as RL) system setup. The background spectrum is recorded when the light source is blocked from propagating. The equation with which the reflectance spectra are calculated is

$$Reflectance\ (arbitary\ units) = 100\left(\frac{signal - background}{reference - background}\right). \quad (4.15)$$

It should be noted due to the shape of the beetle's exoskeleton not being flat, the measurements of reflectance are not absolute, since some light is scattered (more so the more curved a beetle's shell). The reflectance that is presented in this chapter is given in arbitrary units since losses are not taken into account for diffuse and divergent reflected light (though it gives some idea of the magnitude of reflectance, particularly between specimens of the same species and shape). It should be noted that equation 4.15 contains a factor of 100, since it could also be termed as the percentage of the light which is collected (but not totally reflected from the beetle, due to losses) compared to using the reference plane mirror.

4.3.5. Errors in Process

An issue was previously reported by Daly [8], where a feature appeared between 900nm and 950nm in reflection spectra. Several possible causes were suggested, firstly that it could be an issue with the light source warming up and therefore changing the reference spectrum. Secondly, that an error in the way in which the program calculates the reflection spectra occurred. An error in the detector being run for a long time was also another suggestion.

The system's stability with time was tested over a five hour period, using the reference system in LR configuration. As can be seen in Figure 4.15 the signal remained relatively constant and flat for the first two hours, then it appears to increase in the feature appearing between 900nm and 950nm. It is believed that this increase was mostly due to slight movement of the system as well as changes in temperature within the equipment. The software was also checked as a source of the error and found to be functioning correctly. This was done by performing the calculation in equation 4.15 manually.

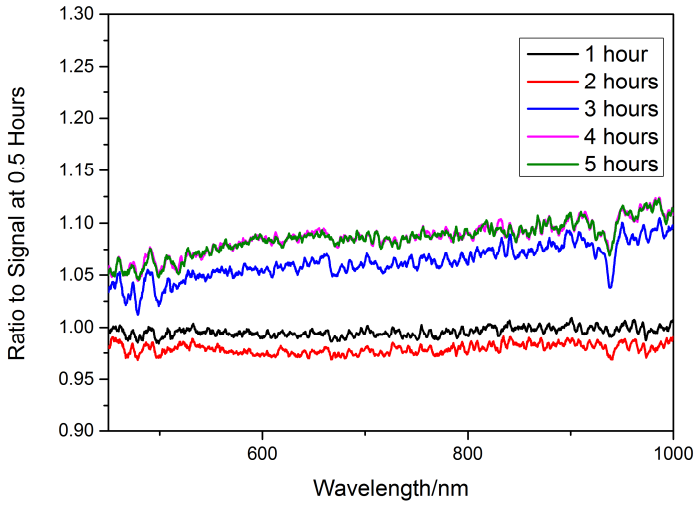


Figure 4.15 – Ratio of the LR signals varying with time from a reference system using a mirror. All are given as ratio to a signal reading which was taken at half an hour.

Upon further investigation the moving base (away from ~925nm) was seen to be caused by aberrations from slight movements within the alignment. The lenses in the system were singlets and as such chromatic aberration was thought to be dominant. Unfortunately, doublet lenses which could be used in the system were not available. It was also seen that there was some beam shifting occurring in the polarising prisms and Fresnel rhombs. The beam path was shifted by the polarising cube and once the beam was incident upon the Fresnel rhomb it became even further shifted.

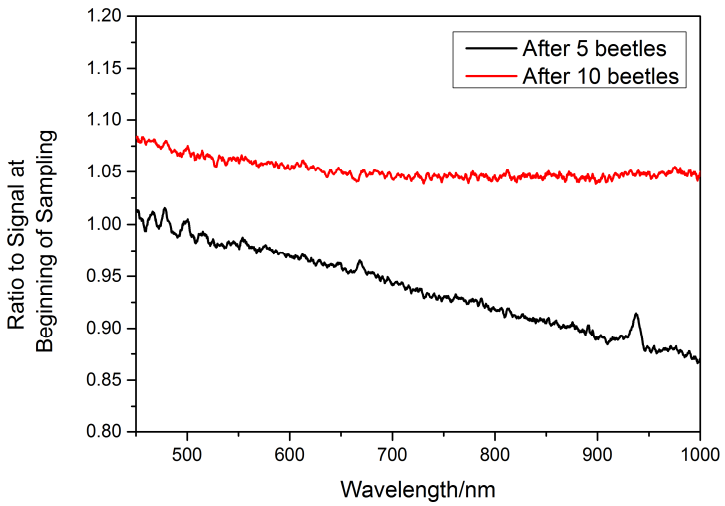


Figure 4.16 – The ratio of the LR signals varying with number of samples taken from a reference system using a mirror, all are ratios to the initial reading.

Due to movement of the equipment, each time a beetle's reading was taken the system was put in a slightly different position with a different amount of aberrations detected on the optical fibre, which is connected to the spectrometer. Hence a different reference signal was observed as seen in Figure 4.16. It should be noted that the time taken to obtain the ten beetles' readings in total was less than one hour, which is a much shorter time than previously discussed in the time stability graphs. Hence movement is the most likely cause, compounded by the aberrations which were present. There can also be seen a NIR peak which appears after five beetles, this was thought to be due to temperature variation in the light source. To avoid this, the light source reference signal was remeasured using the plane mirror after five beetle measurements.

4.3.6. Repeatability of Measurements

As shown in the results presented in Section 4.4 different parts of the beetle can have very pronounced differences in spectral response such in the species *Protaetia speciosa jousselini* (Figure 4.81). Further to these differences the repeatability of the measurements is discussed. One example of the repeatability is shown in Figure 4.17, where the measurements were taken a year apart on the same experimental setup reflecting from close to the same area on the same beetle. Figure 4.17a and b are very similar in terms of both reflectance intensity and the ratio of the different spectra. The LL peak was also at a very similar wavelength, being 9nm different, such a difference was put down to two factors, firstly a slightly different position of reflection upon the beetle's shell and also different angle of the incident beam with respect to the shell surface. It should be noted that if the difference in peak wavelengths of 9nm was purely due to angular variation this would relate to a 10° increase in the angle of the beetle's curvature from normal (at the measured point), (according to Equation 3.13).

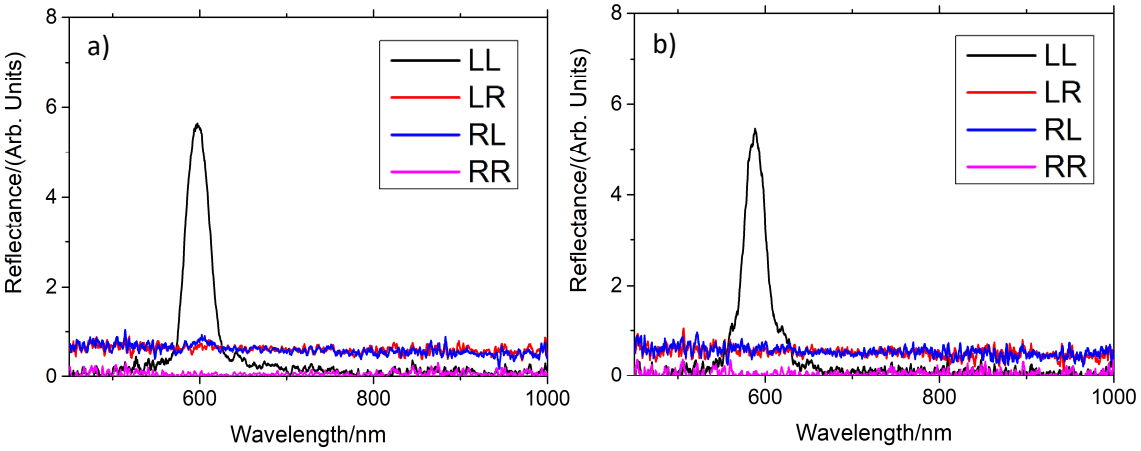


Figure 4.17 –Two sets of CP reflection spectra, a) and b) from the elytron of a red *Popillia* sp. beetle, collected from Mikumi National Park, Tanzania in 2013.

Two sets of spectra from a single specimen of *Chrysina resplendens* which were taken ~18 months apart can be seen in Figure 4.18. These two measurements have several differences. The two sets of spectra appear similar in terms of having two groups of peaks in the LL spectra

(with a discontinuity in between) and a RR spectra which peaks at the lower wavelength group of LL peaks.

There is a difference in the measured intensity of reflectance, Figure 4.18a is approximately twice the intensity of Figure 4.18b (though they are of the same order of magnitude). This variation in intensity can be linked to two things, firstly again a slightly different area of the beetle was measured, but also due to alignment of the beetle (and reference sample). If the reference sample (plane mirror) is not aligned well to get a high reference signal, the reflectance from the beetle in arbitrary units will be higher. In order to minimise this error the reference sample (plane mirror) was aligned until approximately the same intensity measurement was obtained. Another possible cause of the variation in reflection is if the beetle is not well aligned then then less light will be collected, in order to make this repeatable the beetle alignment was as close same position on the shell as possible and the angle with respect to the beam was also kept the same. Examples of the reflection spectra from specimens of the same species being of the same order of magnitude can be seen in Figure A 86 in the appendix.

There is also a slight difference in the ratio of the LL to RR spectra, again this was put down to a slightly different beam spot position and angle of the shell to the incident beam being used.

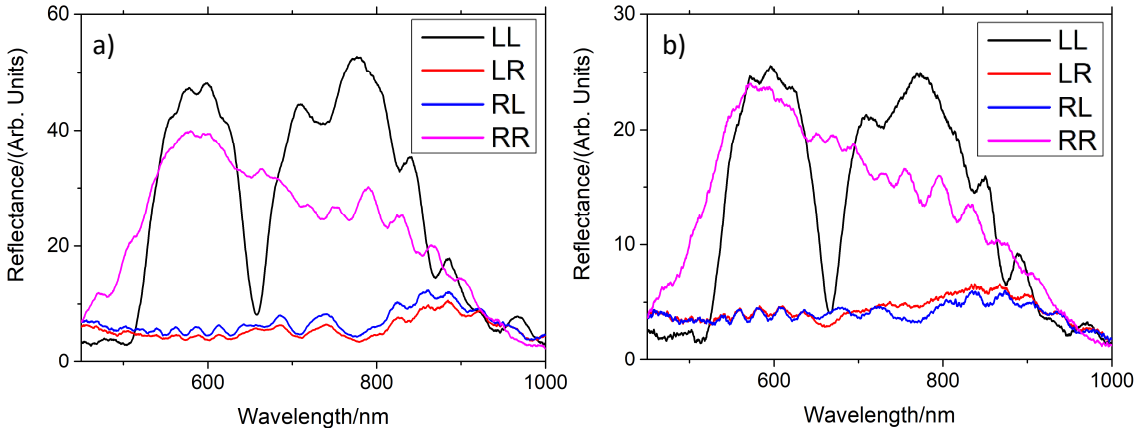


Figure 4.18 – Two sets of CP reflection spectra, a) and b) from the elytron of a *Chrysina resplendens* beetle, from Cerro Bellavista, Rio Guacimo, Costa Rica in 2015.

4.4. Circularly Polarised Reflection Spectra from Beetles

The setup which is described in the previous sections of this Chapter was used in order to obtain the optical spectra of reflected CP light from the beetles. This information could be used to help describe the optical structure of the beetles. One possible outcome of this research would be a method of classifying the beetles into taxonomic groups (e.g. subspecies, species, genus, etc). Previous work upon spectral classification was undertaken (as part of the author's Masters) upon the Cetoniinae genus *Lomaptera*, with more species of the genus being investigated as part of this study [2],[9]. In this section the variation in CP spectral response is investigated and discussed within and between species, genera, and subfamilies. There are many different

variations in shape, intensity and also handedness of light which is reflected from the beetles' shells.

A typical set of spectra (e.g. Figure 4.19), is one in which the LL (this notation is defined in Table 4.2) spectrum is the dominant (and most intense) feature. The LL spectrum varied both in intensity and shape between beetles. The basic single peaked CP feature was described previously in Section 3.4, it is caused by the helicoidal structure.

The LR and RL spectra in most species are due to impedance mismatch at the surface of the beetle. The surface acts as a weak mirror as such the values of these spectra are usually much lower than the LL. These spectra are typically flat, due to the refractive index of the surface being relatively wavelength independent in most species. In some beetle specimens which weakly reflect LCP light the main features were the LR and LR spectra, whilst other species had peaks in the LR and/or RL spectra.

The RR spectrum in most species is approximately zero, but varies slightly due to noise. Some *Chrysina* species as well as having significant LL there are also have significant RR responses.

It should be noted that in this section in the CP reflection spectra plots, the LL configuration is black, LR is red, RL is blue and RR is pink (unless otherwise explicitly stated). It should also be noted the photographs of beetles are labelled LF (through a LCP filter), RF (through a RCP filter) and NF (not filtered), if not labelled if should be assumed to be NF. The wavelength scale of each set of spectra is 450-1000nm (unless explicitly stated otherwise).

4.4.1. Typical Examples of Each Subfamily

In this section typical reflection spectra of one specimen from each of the nine different subfamilies which are known to reflect CP light (as identified by Pye [10] and discussed in Section 3.5) are discussed. It should be noted that while described as typical spectra there are large variations within the subfamilies, genera, and even species. Certain species in this report have known variations and some are mentioned. Due to space limitations reflection spectra from many other species are reported in Appendix A3. Many of the species presented in this study had multiple specimens investigate and only typical spectra (and perturbations) were shown. The gender of different specimens was not generally identified (expect for a few species with clear gender dimorphism, whose gender could be identified).

The first beetle presented is a Rutelinae:*Repsimus aeneus* beetle which has a typical example of a set of spectra, with a strong LL peak, negligible RR, and relatively low and flat of LR and RL spectra (Figure 4.19). Two clear LL peaks can be seen, the main being at 554nm, whilst a small resolvable peak can be seen at 586nm. This main peak produces the metallic green colour of the

beetle which can be observed. Two specimens were investigated, both of which had a strong main peak with another less intense peak at a higher wavelength. This specific species is also known to have blue and red variants, which will likely have different reflection spectra, due to reflection from shorter and longer pitches respectively.

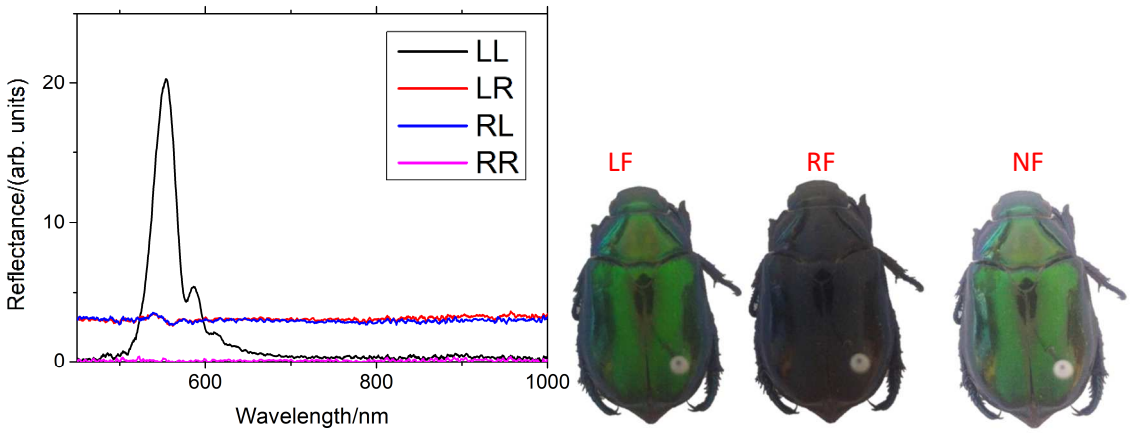


Figure 4.19 – CP reflection spectra from the elytron of a *Repsimus aeneus* beetle. This specimen was collected from Polly Creek, Garradunga, North Queensland, Australia in 2014. The specimen measures 24mm.

The Melolonthinae:*Melolontha melolontha* beetle is also known as the common European cockchafer, May bug or Doodlebug. In the reflection spectra from the beetle's pronotum in Figure 4.20 it can be observed that the LR and RL spectra are dominant. The low intensity LL spectra (relative to LR/RL) could be due to either a small helicoidal structure of only a few pitches, a low birefringence or a blocking structure on the surface. There is however a low intensity LL peak, which in this specimen was at a red wavelength. A colour change between the photographs through a LCP and RCP filter is not clearly visible in the inset picture, the LCP colour is more visible in another cockchafer specimen (with a green pronotum) (Figure 4.21). It was observed that only the pronotum and scutellum reflected significant amounts of CP light. From the five specimens investigated, variation in the colour of the sheen from green to red was observed.

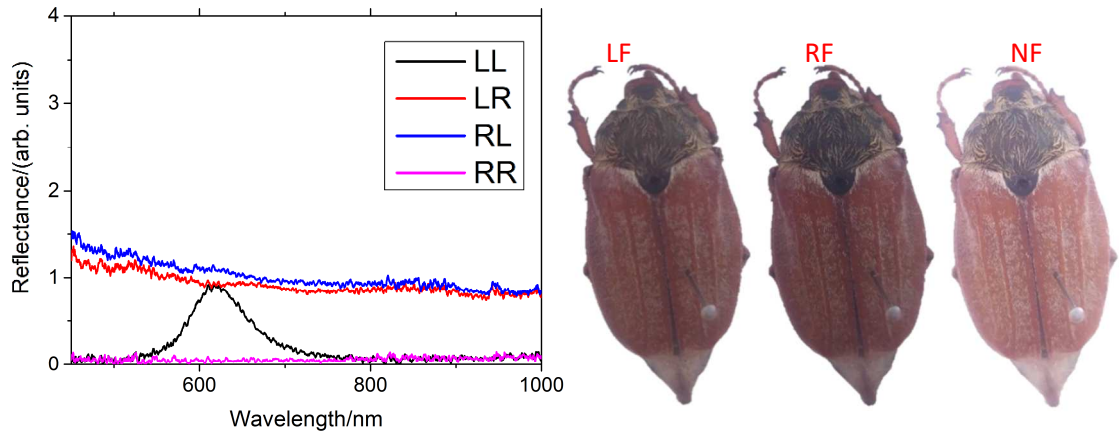


Figure 4.20 – CP reflection spectra from the pronotum of a *Melolontha melolontha* beetle. This specimen was collected from Bourg-le-Comte, Saone et Loire, France in 2013. The CP spectra were taken with an integration time of 500ms. The specimen measures 31mm.

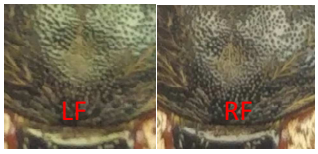


Figure 4.21 – The difference in colour of the pronotum of another *Melonontha melolontha* beetle through a LCP filter on the left and RCP filter on the right.

Reflection spectra from the Dynastinae:*Augoderia nitidula* beetle's pronotum (Figure 4.22) was very similar to that of the *Repsimus aeneus*, with a main peak bordering between the red and green wavelengths. It should be noted a similar spectra also exists for another specimen with a more green sheen (Appendix Figure A 120).

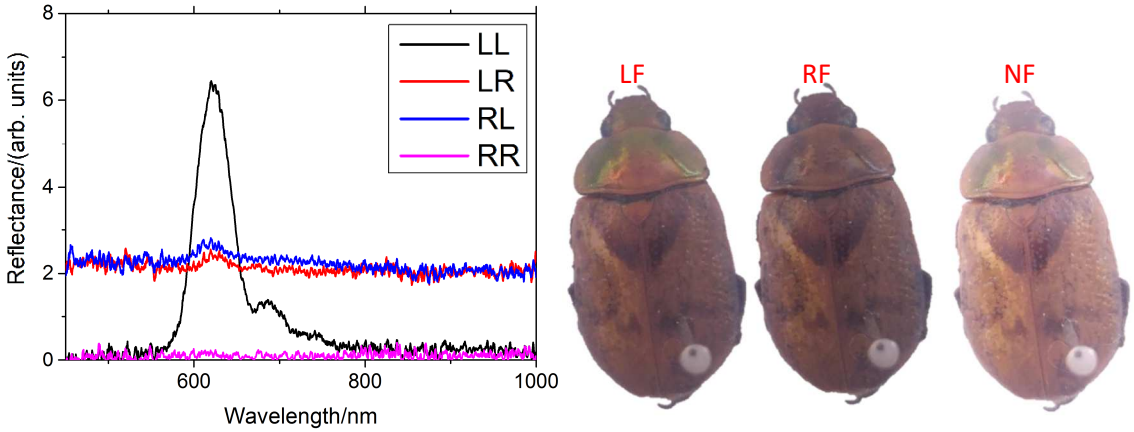


Figure 4.22 – CP reflection spectra from the pronotum of an *Augoderia nitidula* beetle. This specimen was collected from Nova Fiburgo, Rio de Janiero, Brasil in 2012. The specimen measures 19mm.

The Euchirinae:*Cheirotonus battareli* was the largest beetle measured in this study (with 52mm body length). The reflection spectra from the pronotum in Figure 4.23 shows the LL spectrum again the dominant feature, but instead of being a single peak or multiple peaks, has a smooth tail at higher wavelengths. From the inset photos the colour of the pronotum in the LCP filter can be seen to be redder in colour at normal incident, whilst at greater angles appears greener. The same LL spectral feature was present in all three specimens of the species which were investigated.

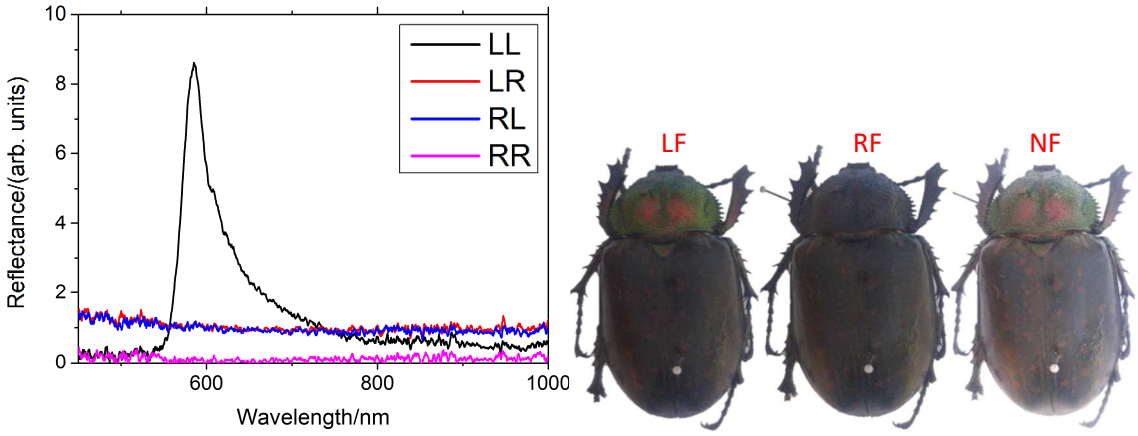


Figure 4.23 – CP reflection spectra from the pronotum of a female *Cheirotonus battareli* beetle. This specimen was collected from Sapa Mountain, Lao Cai, Vietnam in 2015. The specimen measures 54mm.

The LL spectrum of the Trichiinae:*Gnorimus nobilis* beetle (Figure 4.24) appears as a narrowband reflection which in this case borders between the red and green parts of the spectrum. From the three specimens which were investigated, similar spectra were observed. Though not measured in this experiment, this species is known to have many different colour forms as can be seen in Figure 4.25.

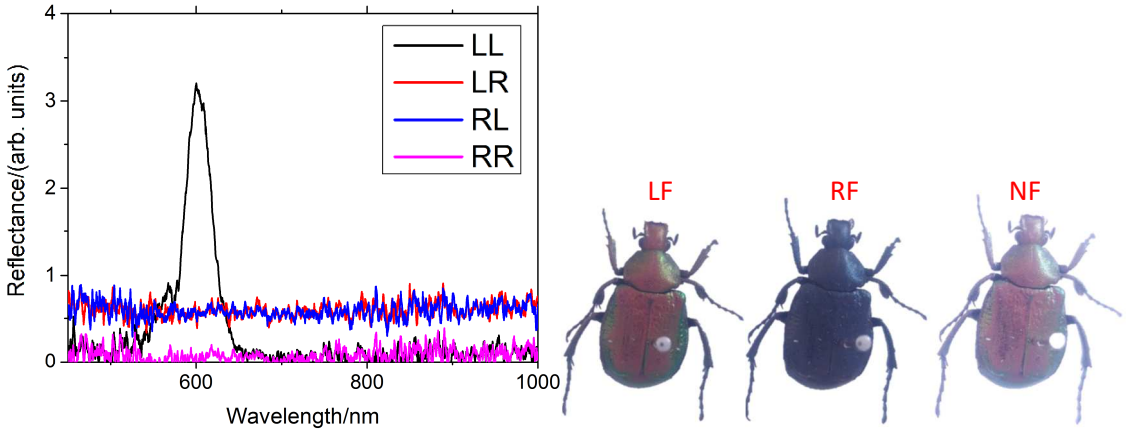


Figure 4.24 – CP reflection spectra from the elytron of a *Gnorimus nobilis* beetle. This specimen was collected from Poland in 2015. The specimen measures 19mm.

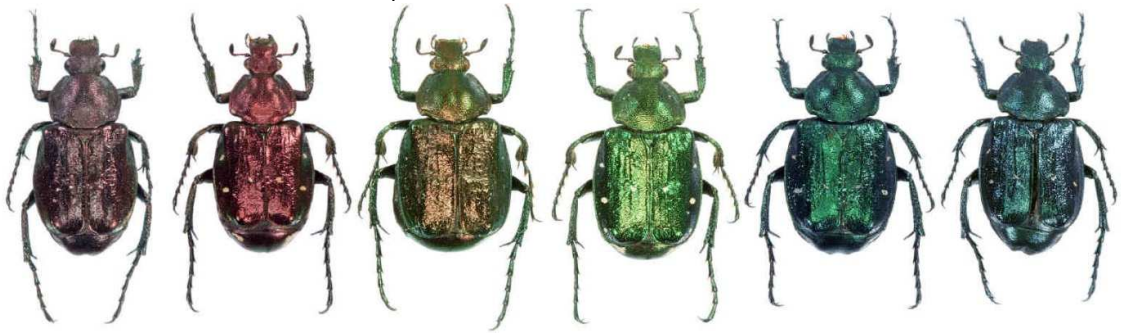


Figure 4.25 – Colour morphs of the species *Gnorimus nobilis*. Used with permission from [11].

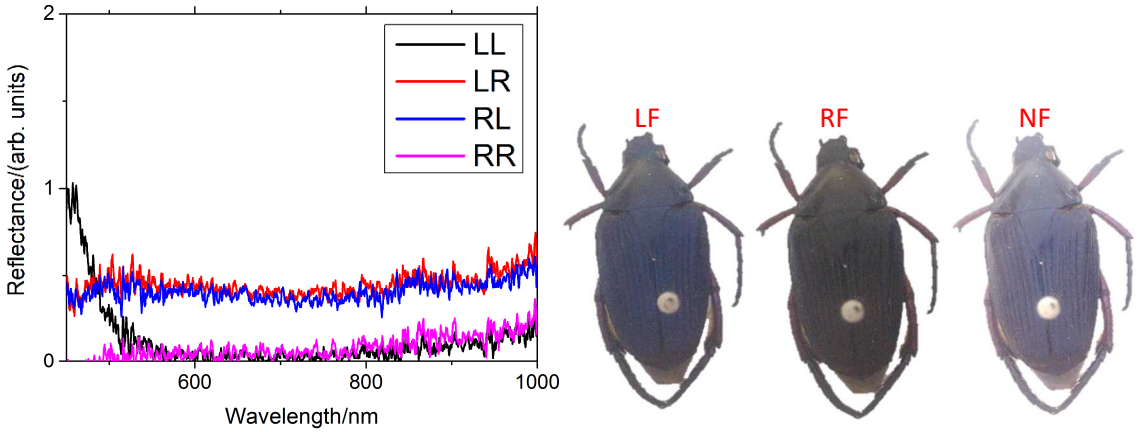


Figure 4.26 – CP reflection spectra from the elytron of a *Phaenomeris besckei* beetle. This specimen was collected from Mikumi-Udzungwa, Tanzania in 2009. The measured wavelength scale was 440-1000nm for this beetle. The CP spectra were taken with an integration time of 500ms. The specimen measures 21mm.

The Phaenomeridinae:*Phaenomeris besckei* beetle appears to be blue under a LCP filter and black under a RCP (Figure 4.26). The spectra (Figure 4.26), showed a single LL peak at ~450nm, with the LR and RL spectra half the value of the main peak. Three specimens all of different

colour variations were investigated these being blue, turquoise (Appendix Figure A 121) and green colours (Figure 4.93). The other colour variations had even weaker LL responses such that LR and RL spectra were dominant. This suggests a similar helicoidal structure to the Melolontha melolontha is responsible.

The Scarabaeinae:*Diabroctis mimas* beetle has variation in colour across the beetle's body with the elytra showing a dark green colour, whilst the front of the pronotum was golden in appearance. Reflection from the gold colour was measured and the LL spectrum can be observed in the LL spectrum in Figure 4.27. The reflection is more broadband than the previously typical beetles described in this thesis. Eight specimens of this species were investigated, all had broadband reflection and a golden appearance, the reflected band of wavelengths in the LL spectrum varied, but was consistently between the wavelength of 500nm (the lower limited for actual gold) and 800nm (the end of the visible wavelengths).

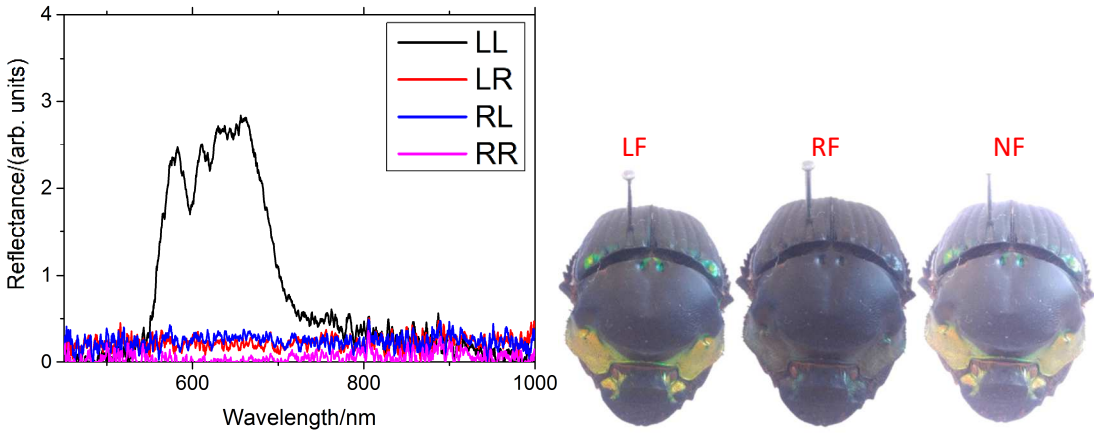


Figure 4.27 – CP reflection spectra from the gold part of the pronotum of a *Diabroctis mimas* beetle. This specimen was collected from Campo Zanja Moroti, Concepción, Paraguay in 2007. The specimen measures 31mm.

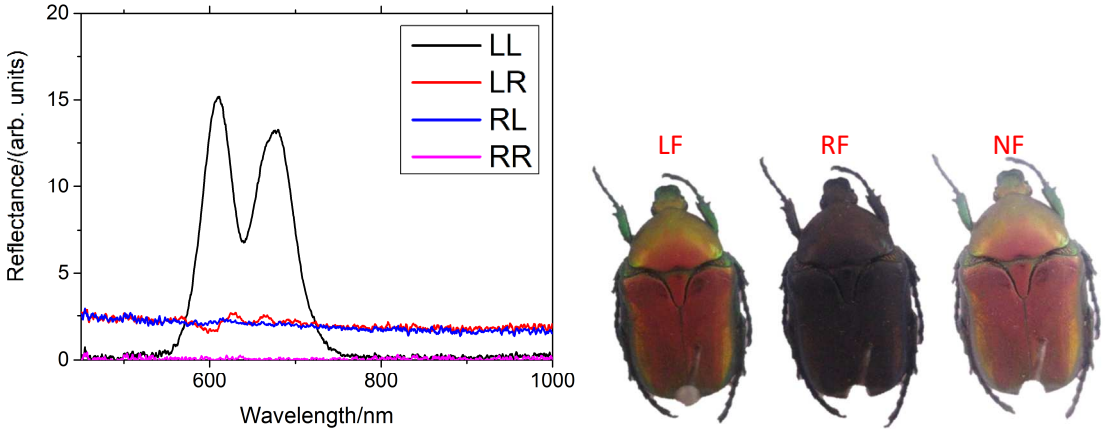


Figure 4.28 – CP reflection spectra from the elytron of a Protaetia angustata pyrodea beetle. This specimen was collected from Padau, Italy in 2012. The specimen measures 23mm.

The subfamily which was investigated in the greatest detail in this study is the Cetoniinae family. The Cetoniinae:*Protaetia angustata pyrodea* beetle has a red visual appearance both with and without a LCP filter and black (colourless) with a RCP filter (Figure 4.28). The LL spectrum (Figure

4.28) had a double peaked features which were close together (with a non-zero trough). The two peaks give rise to green and red colours, which can be observed in the beetles.

The Hybosoridae:Ceratocanthinae:*Ceratocanthopsis fulgida* beetle was one of the smallest (~2mm body length) and roundest beetles investigated, as such much light upon reflection was scattered. The LL spectrum in Figure 4.29 can clearly be seen to be dominant, with regular oscillating peaks (~30nm interval) at higher wavelengths than the main peak (691nm), which is at a red wavelength. It is worth noting that this beetle is from a different family to the other eight examples described previously.

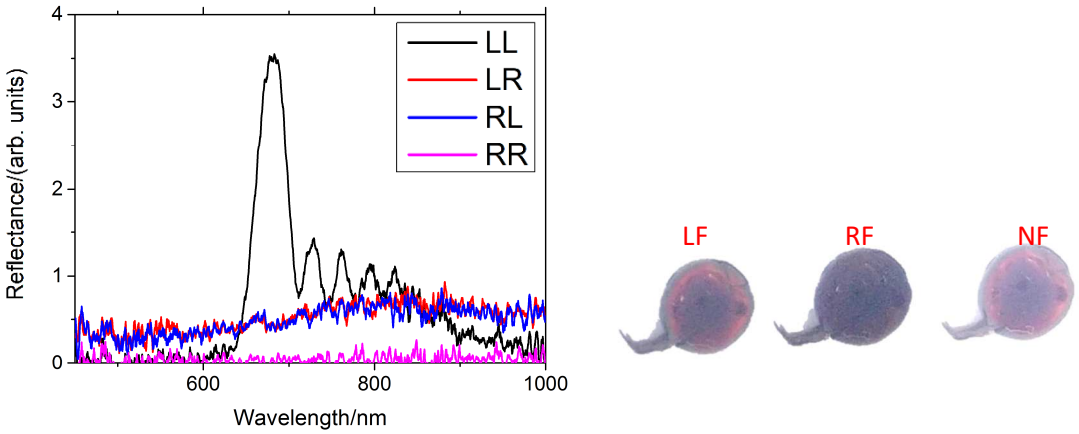


Figure 4.29 – CP reflection spectra from the elytron of a *Ceratocanthopsis fulgida* beetle. This specimen was collected from Belizon, French Guiana in 2015. The specimen measures 3mm.

Each of these beetles is just a single specimen from a single species of each subfamily and as such does not show the full diversity of CP spectra. From this section it can be seen there are similarities between the CP reflection spectra from specimens of some subfamilies (such as *Repsimus aeneus* and *Augoderia nitidula*), whilst some of the reflection spectra appear quite different (such as *Ceratocanthopsis fulgida*). The majority of the sets of reflection spectra have dominant LL reflection spectra, whilst others (such as *Melolontha melolontha*) have a weak LL spectra and dominant LR/RL spectra. The structural origin of these reflections is discussed in more detail in the modelling, ellipsometry and subwavelength imaging Chapters (Chapters 5, 6 and 7 respectively).

4.4.2. Rutelidae:Chrysina Genus

The *Chrysina* genus of the subfamily Rutelinae has long been a source of study since Michelson first investigated a *Chrysina resplendens* specimen. Their metallic appearance has attracted them to both collectors and researchers alike. Many investigations upon their structural colour and polarisation properties have been made. A full list of previous investigations can be found in Appendix A2. In this study the structural colour and polarisation properties of 28 different *Chrysina* species were investigated, many of which have not been optically studied previously.

The *Chrysina* genus had a great deal of variation, with the majority of *Chrysina* species having a LL spectrum which is dominant and shows a distinct peak at a green wavelength with another broader peak in the NIR. A good example of such a spectrum occurs from the reflection of a *Chrysina optima* (Figure 4.33). There are however many variations, including a lack of a NIR peak e.g. *Chrysina macropus* (Figure 4.40). There are also variations in the peak in the visible wavelength from the dominant green to other colours (wavelengths) both within and between species, one particular example is the green and brown *Chrysina tricolour* beetles variants (Figure 4.31). There are also variations in the intensity of the spectra between low reflecting species (e.g. *Chrysina modesta* (Figure 4.34)) and high reflecting species (e.g. *Chrysina limbata* (Figure 4.38)). There are also variations in intensity between specimens within a single species (e.g. *Chrysina boucardi* (Figure 4.35)). There are also species which reflected and preserve handedness of RCP light (i.e. a high RR spectral value) such as *Chrysina cupreomarginata* (Figure 4.30).

4.4.2.1. Species with RR and LL responses

To the best of this author's knowledge the *Chrysina resplendens* is the only species which has been discussed as reflecting both RCP and LCP light in published articles [12]–[24]. As described in Section 3.4, the reflection of both handednesses is caused by a uniaxial layer acting like a half-waveplate sandwiched between two helicoidal stacks.

In this study seven species of *Chrysina* were identified which selectively reflect both RCP and LCP light from the top side of their carapaces. They are grouped loosely into three different types. The first of which consists of two gold metallic species (*Chrysina resplendens* and *Chrysina cupreomarginata*) which reflected both LCP and RCP light of similar magnitudes. The second type is observed in three matt species (*Chrysina tricolour*, *Chrysina costatas*, *Chrysina alphabarreria*) which were all seen to reflect both LCP and RCP light, however the RCP light was only reflected at deep red to NIR wavelengths. The LCP light was also reflected at lower (visible) wavelenghts. A third type of RR/LL response was seen in two broadband metallic species (*Chrysina limbata*, *Chrsyina pastori*) where RCP light was still reflected but at a much lower intensity than LCP. While no quantitative measurements are made it can be seen in Section 4.4.1 that the underside of the *Chrysina cupreomarginata* specimen (Figure 4.100) largely appears to reflect LCP and not RCP light.

The first type of LL/RR reflection spectra was seen in *Chrysina cupreomarginata* and *resplendens*. The *Chrysina cupreomarginata* beetles which were investigated, had a large peak in the LL spectra at a green wavelength (Figure 4.30). Which was measured in eight specimens with the mean being 573.6nm and standard deviation 7.8nm. The RR spectra in these beetles is a similar shape to the *Chrysina resplendens* beetle (whose spectra and consistency can be seen in

Appendix Figures A 69 and A 88) in that it peaks at a green wavelength and gradually decreased towards the NIR. The *Chrysina cupreomarginata* beetle can be seen to have a greener appearance through a LCP filter and a more dull golden appearance through a RCP filter (Figure 4.30). This can be seen to relate to a much larger peak in the LL spectra (Figure 4.30).

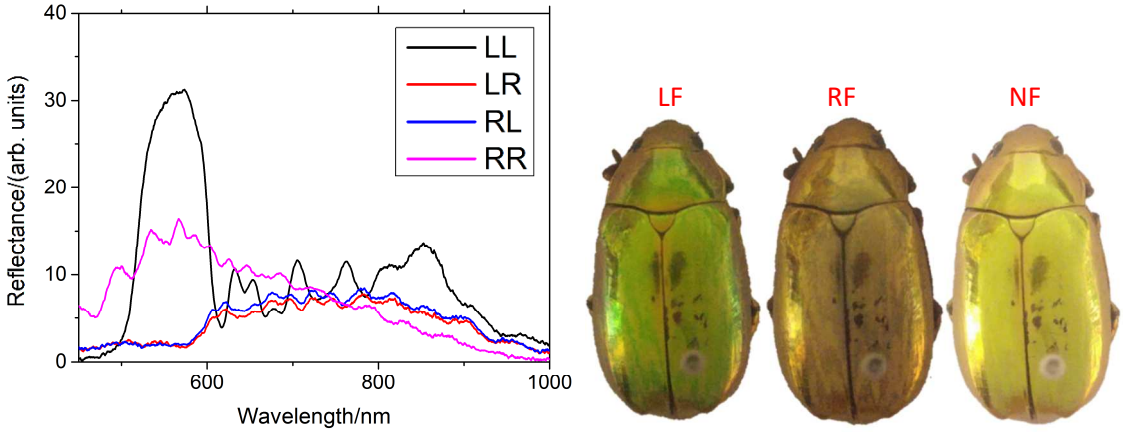


Figure 4.30 – CP reflection spectra from the elytron of a *Chrysina cupreomarginata* beetle. This specimen was collected from Cerro Chompipe, Costa Rica in 2015. The specimen measures 21mm.

An example of the second type of the LL/RR spectral response can be seen in the *Chrysina tricolour* species. The LL spectra of *Chrysina tricolour* beetles has two peaks, one in the visible range and one in the NIR. There are also LR, RL and RR peaks at the same wavelength as the LL in the NIR. Two different colour forms of the *Chrysina tricolour* species were investigated as part of this study, a brown and a green form. The brown form's LL reflection spectrum has a small peak in the visible range (at a red wavelength) and can be seen in the photographs to appear darker through the RCP filter than LCP filter (Figure 4.31a). The green form also has a smaller LL spectral peak in the visible wavelengths than that in the NIR, in this form the difference between a LCP and RCP filter is much stronger (Figure 4.31b). The green form varies in that the peaks in the NIR vary in relative intensity such the LL and LR spectra are the highest peaks in other specimens in Appendix Figure A 88. This second type of LL/RR spectral response was also observed in the *Chrysina costata* (Appendix Figure A 70) and *Chrysina alphabarreria* species (Appendix Figure A 71).

The last group of beetles which reflect both handednesses of CP light only reflect RCP with lower intensity to the LCP but of a non-negligible amount. The RR spectrum of the *Chrysina clypealis* specimen (Figure 4.32) is negligible in the blue wavelengths and gradually increases to peak around 700nm, in this way gold RCP light (albeit weakly) is reflected as can be seen through the RCP filter (Figure 4.32). It should be noted that the width of oscillations increases with wavelength in the LL spectrum, the oscillations however are relatively small in overall reflectance value and as such the beetle appears metallic silver through a LCP (Figure 4.32). In a previous study upon a specimen of *Chrysina clypealis* oscillations in the reflection LL spectrum

can be seen although their increasing nature is not as apparent due to measurements only being taken between 400nm and 700nm [19]. A similar but less intense response than the LL spectrum can be observed in the RR spectrum from a gold *Chrysina pastori* beetle (Appendix Figure A 72).

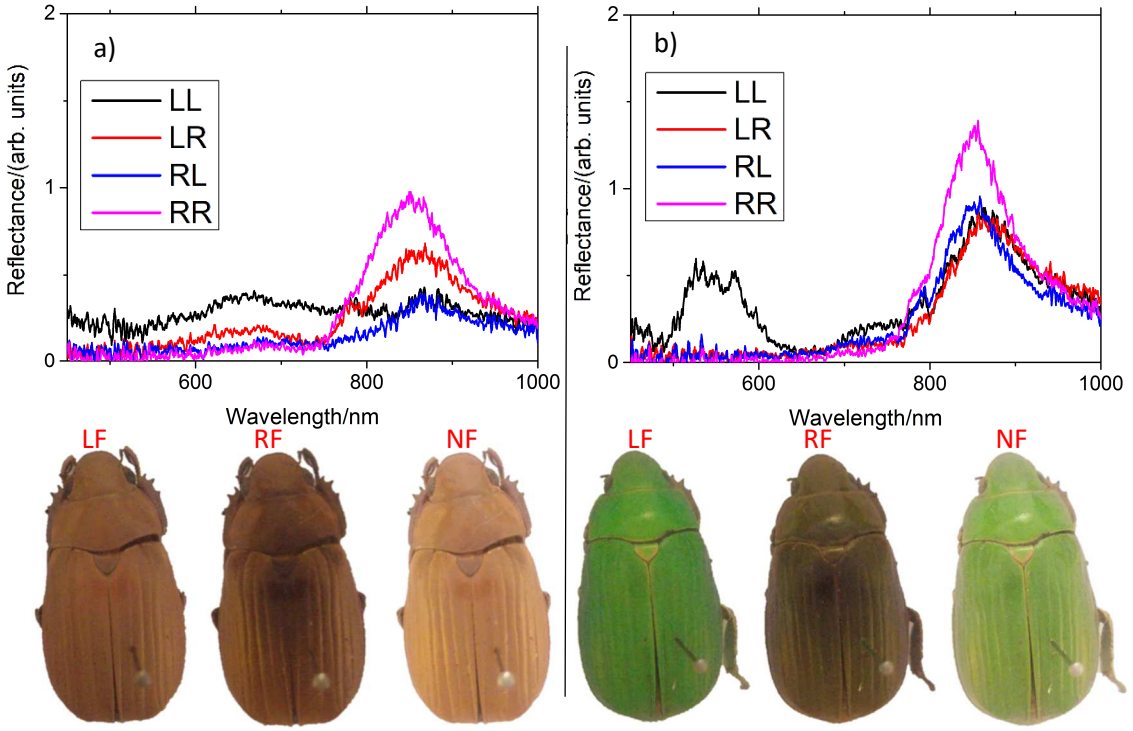


Figure 4.31 – CP reflection spectra from the elytron of a) a brown and b) a green *Chrysina tricolour* beetle. These specimens were collected from Cerro de la Muerta, Costa Rica in 2014 and 2013 respectively. The CP spectra were taken with an integration time of 500ms. The specimens measure a) 25mm and b) 25mm.

Three loose classifications of *Chrysina* which both selectively reflect LCP and RCP light were made. As discussed in Chapter 3.4 *Chrysina resplendens* (which would fall under the first type of LL/RR response) was seen to have such a response due to a uniaxial layer (acting as a half waveplate) between two helicoidal stacks. If the ratio of the helicoidal stacks either side of the uniaxial layer varies, then the ratio of the magnitude of the LL to RR response will also vary.

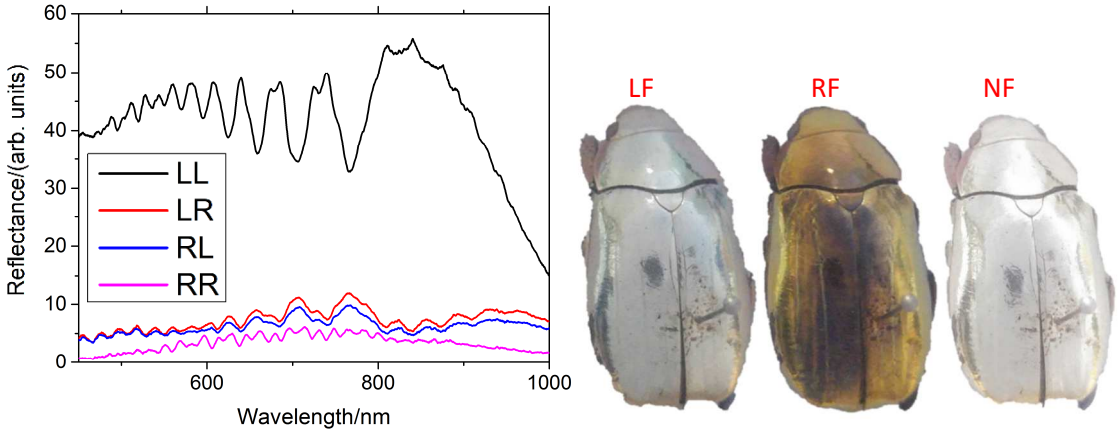


Figure 4.32 – CP reflection spectra from the elytron of a *Chrysina clypealis* beetle. This specimen was collected from Costa Rica in 2015. The specimen measures 24mm.

If the helicoidal stack near the surface contains more pitches than the one underneath the uniaxial layer (and all the helicoidal layers are optically reachable from the surface), then the LL

spectrum is likely higher than the RR. This structure could also be responsible for the third type of LL/RR response in *Chrysina clypealis*.

The second type of LL/RR response which only had a RR response in the NIR could be due to shorter pitched structures (visible wavelength relating) being nearer the surface and not below the helicoidal stack. Other possibilities include the uniaxial layer only working in a narrow wavelength band.

4.4.2.2. Measured Colour Variation

Further to measuring the reflection variation in RR spectra, there were clear variations in the visual appearance of *Chrysina* beetles through CP filters, which can be observed in photographs and also related to the LL spectra. Colour variation within species is discussed within this section, the first is the change in the colour of the beetles purely based upon wavelength change. Colour variation was seen in three species with metallic appearance, which have spectra consisting of larger peaks in the LL, negligible RR and low and relatively flat LR and RL spectra. It should be noted that variation was also observed in *Chrysina modesta* specimens which have a lower intensity reflection response. These variations in colour were previously described as being caused by different combinations of pitch thickness (see Section 3.4.7).

There have been several optical studies previously undertaken upon silver specimens of *Chrysina (Plusiotis) optima* [12],[14],[23],[25],[26]. The optima species has numerous other colour variations of red, gold, purple [27], green [28] and pink [29].

In this study variation in silver, gold and red *Chrysina optima* specimens were investigated. In terms of the LL reflection spectra all three colour morphs have a similar upper wavelength reflection limit, where the intensity decreases dramatically after 900nm. The silver morph's LL lower reflection limit is below what is measurable by the experimental setup (450nm) (Figure 4.33a) (previously reported to be below 400nm [25]). The gold colour morph's lower reflection limit is ~500nm (Figure 4.33b), meaning in the visible range blue wavelengths are not reflected. The lower reflection limit of the red colour morph is at ~600nm (Figure 4.33c). As with the other *Chrysina* colour variations the thicknesses of the pitches are suggested to change in order to produce different colour forms. The consistency of six silver *Chrysina optima* beetle is shown in the Appendix Figure A 87, noting that one of the specimens had much clearer oscillations in their spectra. This oscillating or ripple structure has been described as being caused by several possible mechanisms from the presence of graded or otherwise varying pitch values (in *Chrysina* species) [25],[30],[31]. One study in *Cetonia aurata* linked the oscillations to the overall thickness of the cuticle [32]. Similar colour variation can be seen from dark red to orange-red to yellow in *Chrysina aurigans* (Appendix Figure A 73) and from silver to orange-red in *Chrysina chrysargyrea* (Appendix A 74).

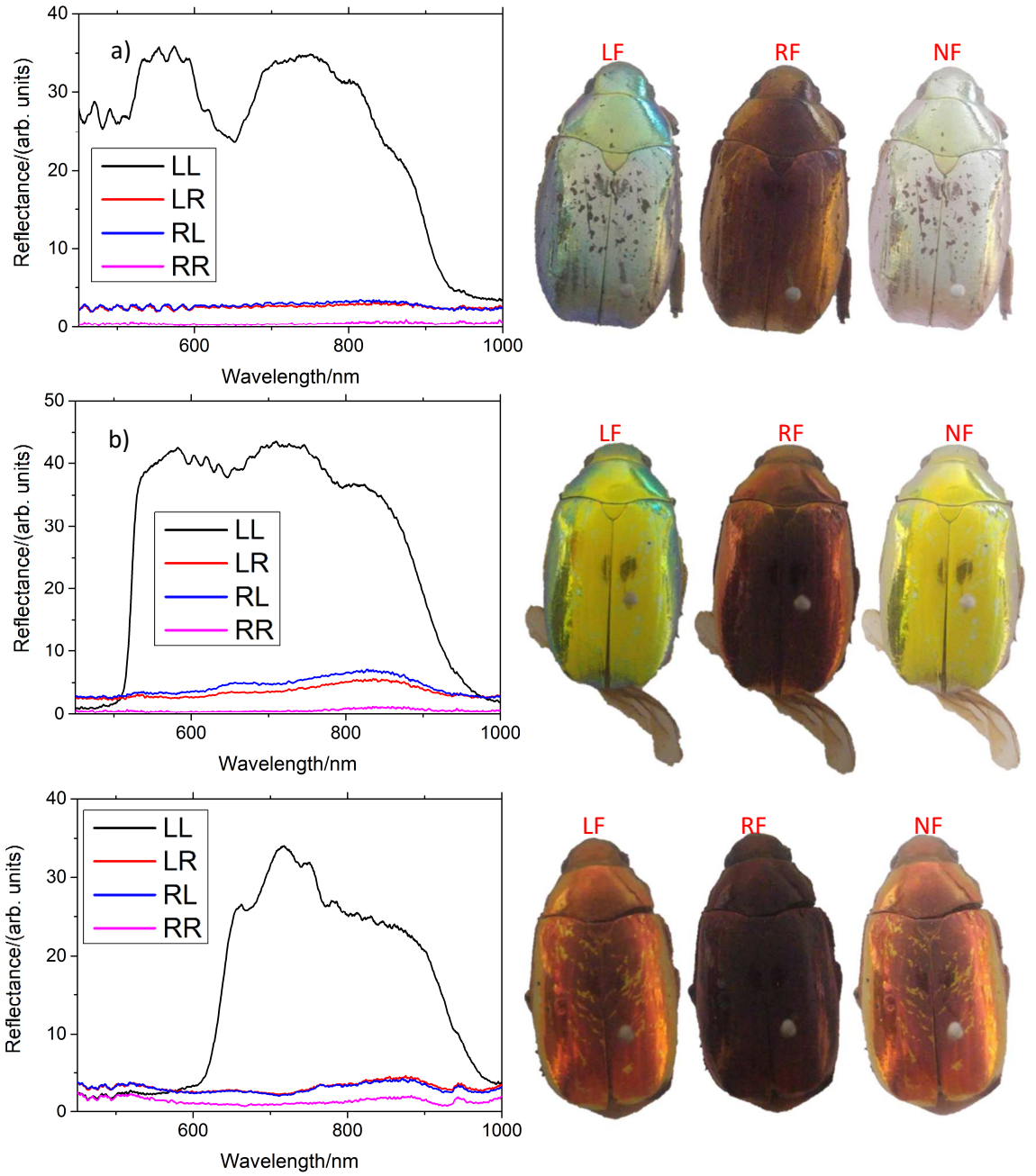


Figure 4.33 – CP reflection spectra from the elytron of a) a silver, b) a gold and c) a red *Chrysina optima* beetle. The silver specimen was collected from Cerro Chompipe, the gold specimen from Cartago, Orosi, and the red from Cerro las 3 Marias, all in Costa Rica in 2015. The specimens measure a) 24mm, b) 24mm and c) 26mm.

Green and brown colour variations of the non-metallic *Chrysina modesta* species were observed and their CP reflection spectra were measured (Figure 4.34). The green individual (Figure 4.34a) has a dominant green peak in the LL spectrum. The brown specimen (Figure 4.34b), had no dominant peaks in the LL spectrum, however this spectrum was non zero over the visible range, with LR and RL spectra being dominant. The photos of the brown *Chrysina modesta*, rather than a definitive colour change from the LCP filter and RCP filter, the beetle changed to a darker shade of brown. Both of the LL responses appear relatively weak, this is likely to relate to either to a helicoidal structure of a few layers or what is more likely the measured reflection is reduced by surface micromirrors.

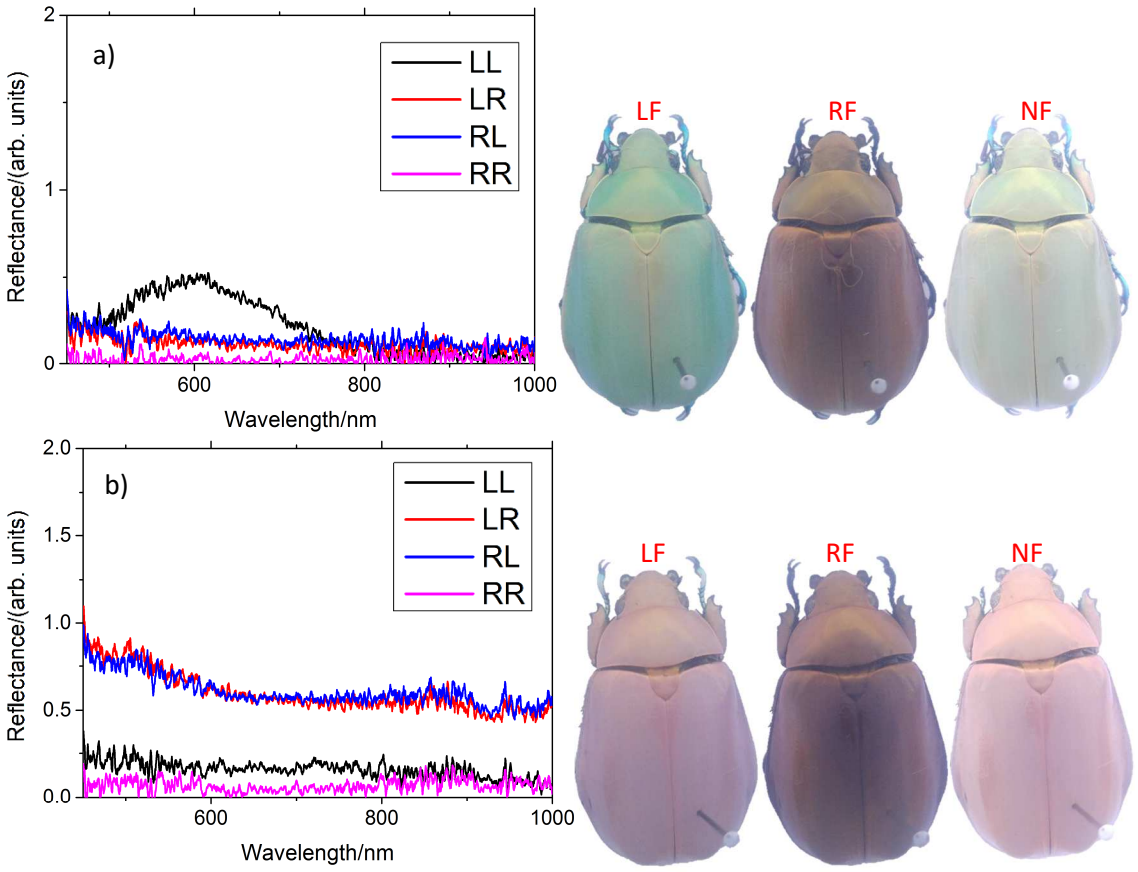


Figure 4.34 – CP reflection spectra from the elytron of a) a green and b) a brown *Chrysina modesta* beetle. The specimens were collected in Ville de Bravo, Mexico in 2016. The CP spectra were taken with an integration time of 500ms. The specimens measure a) 33mm and b) 34mm.

4.4.2.3. Variation in Intensity

Within the species *Chrysina boucardi* a variation in the measured intensity of reflection between specimens was observed. The variation between the LL spectra of the high (gold) (Figure 4.35a-b) and low (green) reflectance specimens (Figure 4.35c) is on an order of magnitude. The metallic specimen has a gold elytra and a red pronotum as viewed both with no filter and through a LCP filter. The magnitudes of the LL reflections from the gold and red parts of the specimen are similar, however the reflection from the red pronotum is much more narrowband with a peak in the NIR. The LL spectrum from the elytra of the gold *Chrysina boucardi* and the dull or matt green specimen both appear to be broadband over a similar wavelength range. In a previous study it was observed that reflection from matt green areas of the species *Chrysina gloriosa* became more polarised at off specular angles, whilst from metallic gold areas the reflection became less polarised at off specular angles [20].

In one entomological publication it was suggested that five or six distinct colour forms of *Chrysina boucardi* exist, but only one form has a metallic appearance [29]. Similarly the species *Chrysina karschi* from Honduras is known to have green, purple, pink, brown and a metallic gold form [33]. In the *Chrysina* family matt species (with a low reflectance) are known to have micro mirror surface structures which increase the angle range at which light is reflected (as they

curve) and can also mean the number chiral multilayers is reduced, in metallic species such surface structures are absent. Typical examples of the surface of a matt and metallic *Chrysina* species and their two surface structures are discussed in Section 3.4.5. A previous study on a green matt *Chrysina boucardi* beetle revealed the presence of chiral micromirrors as part of the optical structure [21].

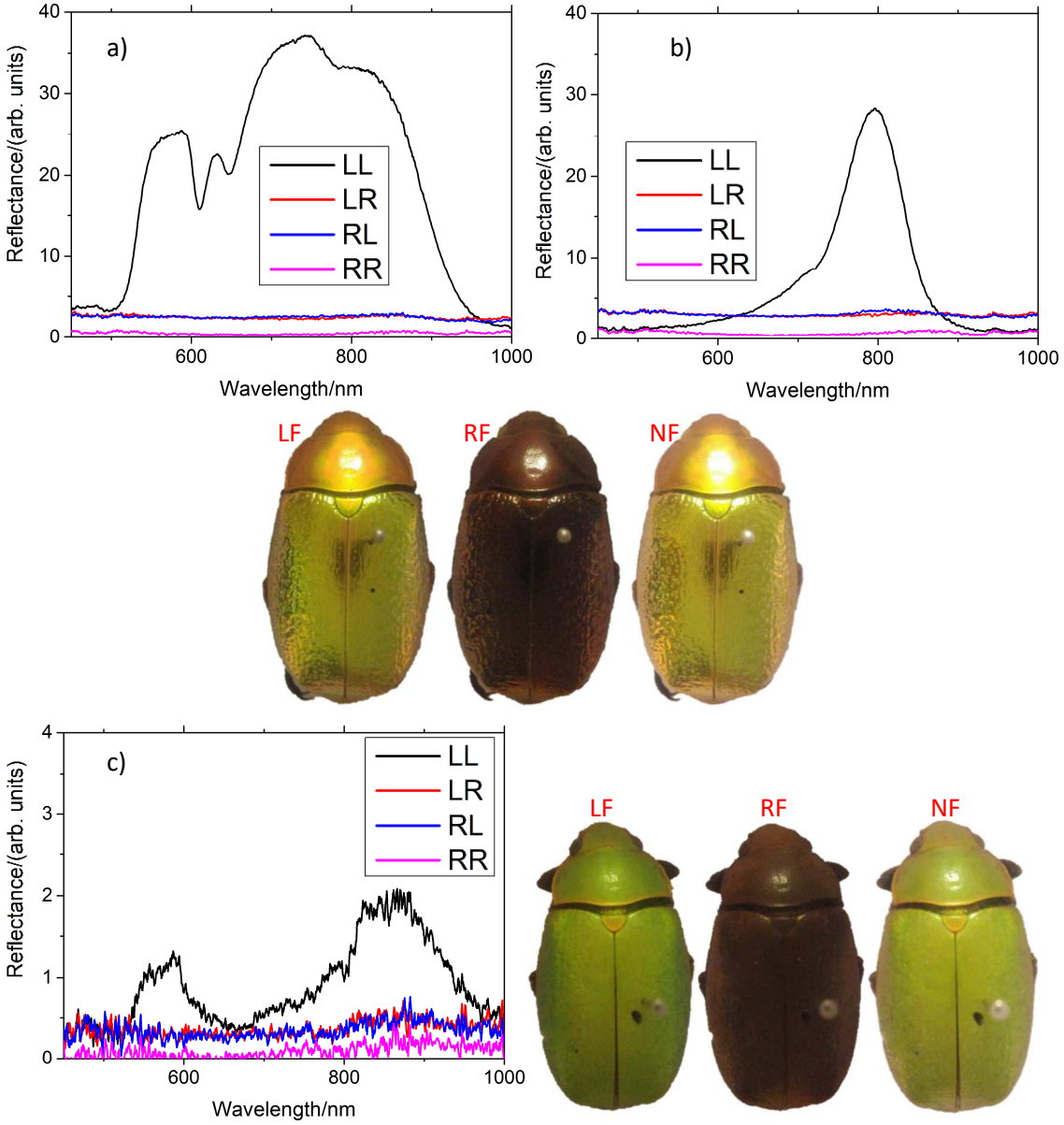


Figure 4.35 – CP reflection spectra from a) the golden elytron and b) red pronotum of a metallic and c) the elytron of a matt green *Chrysina boucardi* beetle. The gold specimen was collected from Caño Sucio, Chiriqui Grande, Bocas del Toro, Panama in 2012, whilst the green was collected from Limon, Costa Rica in 2015. The specimens measure a) 32mm and b) 29mm.

4.4.2.4. Variation in the Elytra and Pronotum

In this section examples of variation between and within elytra and pronotum reflections were measured experimentally. It should be noted that there are also clear variations in reflection and polarising properties on the underside of many beetle species in numerous species including *Chrysina*, examples of which can be seen in Section 4.5.1. Variation within other specimens were measured in depth as can be seen in Appendix A 77-9.

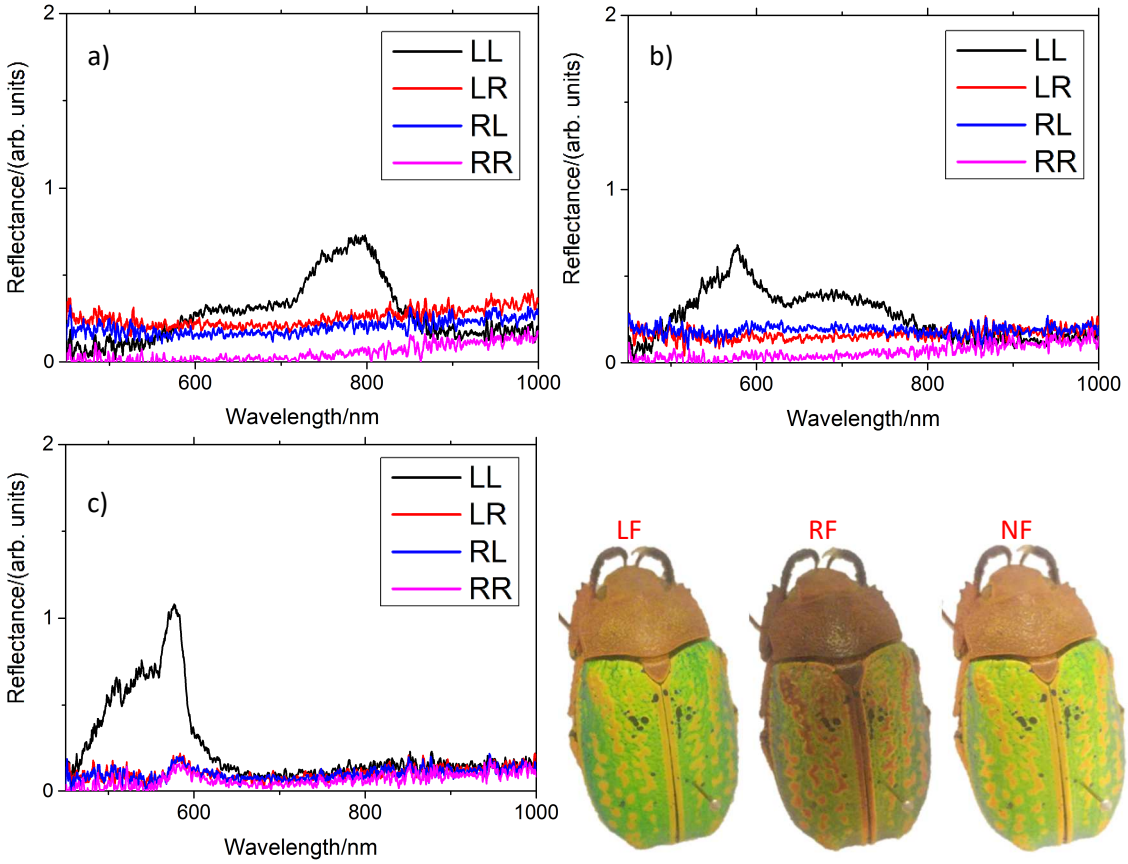


Figure 4.36 – CP reflection spectra from a) the red pronotum b) the predominantly red area of the elytron and c) the predominantly green area of the elytron of a *Chrysina vitoriana* beetle. This specimen was collected from Sierra de Juarez, Oaxaca, Mexico in 2013. The CP spectra were taken with an integration time of 500ms. The specimen measures 31mm.

Variation was observed in *Chrysina vitoriana*, where readings were taken primarily upon the red pronotum, green area of the elytra and red spots on the elytra. Due to the spot size in the experimental setup being ~2mm diameter reflection could not be exclusively taken from the green part or the red part of the elytra, instead primarily green and red areas were measured. Reflection spectra from the pronotum (Figure 4.36a) showed typical spectra where LL had the dominant feature that increased at red wavelengths and peaked in the NIR. Measurements from the mainly red and green areas of the elytra also showed peaks in the LL spectrum (Figure 4.36b and c). One difference between the spectra of the red and green areas of the beetle is that there appears to be a low intensity peak in the RR, RL and LR spectra in the green part of the elytron. This difference can be seen in the photographs of the beetle (Figure 4.36), with the red pronotum still appearing colourful (although less intense) through the RCP filter as well the LCP. The yellow-red areas upon the pronotum appear raised compared to green areas. The RR (and green colour through the RCP filter) indicate a uniaxial layer may be present in the green areas, although the peak is too week to conclude this. The other three variations, which differ greatly, from green elytra with gold spot in *Chrysina spectabilis*, to green elytra with metallic stripes in *Chrysina gloriosa* and *adelaida* are shown in Appendix Figure A 75-7 respectively.

4.4.2.5. Other Notable Species

Further to the variations in the *Chrysina* species already discussed, other notable species of *Chrysina* were also investigated optically.

The *Chrysina chalcothea* specimen is the only *Chrysina* species with a high reflecting green metallic appearance in this study (Figure 4.37). The LL spectrum has two dominant peaks, the lowest wavelength peak is relatively narrow and at a green wavelength, the highest peak is wider and in the NIR (Figure 4.37). Between these two main LL peaks oscillations of lesser intensity occur.

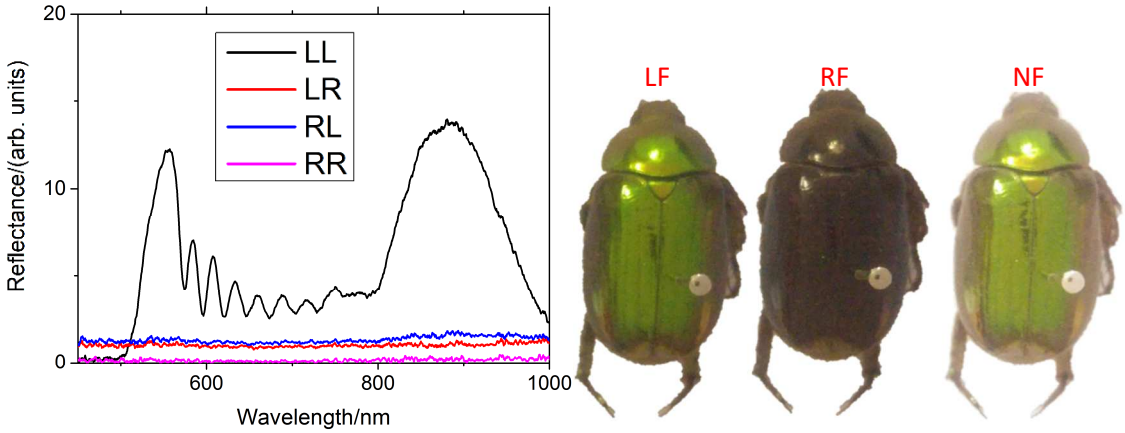


Figure 4.37 – CP reflection spectra from the elytron of a *Chrysina chalcothea* beetle. This specimen was collected from Cerro de la Muerta, Costa Rica in 2015. The specimen measures 25mm.

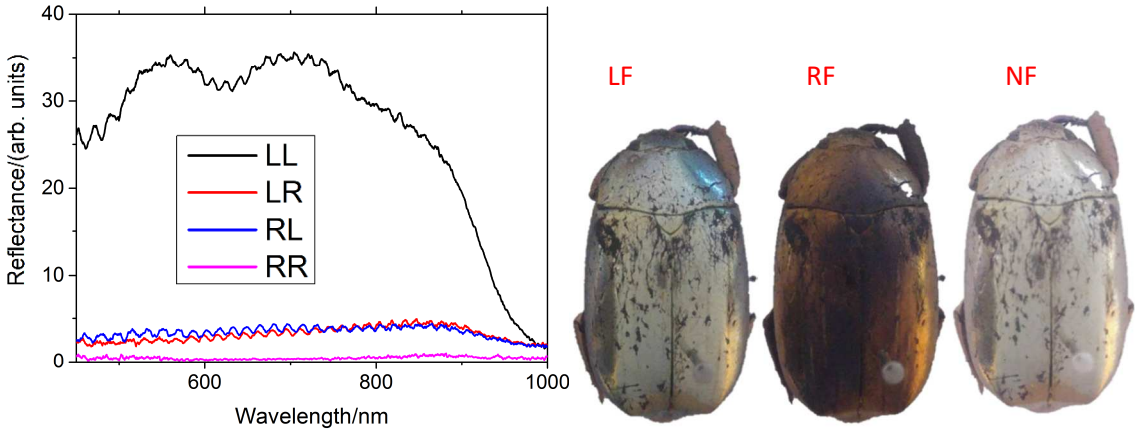


Figure 4.38 – CP reflection spectra from the elytron of a silver *Chrysina limbata* beetle. This specimen was collected from Costa Rica in 2015. The specimen measures 25mm.

The *Chrysina limbata* is a brilliant silver coloured beetle with a mirror-like appearance. The non-polarised response of *Chrysina limbata* has previously been investigated [34]. The LL spectrum is the dominant feature and is relatively flat (compared to other *Chrysina*) over the visible range, resulting in the silver colour (Figure 4.38). Oscillations in the LL, LR and RL spectra are quite visible although they are relatively small.

The *Chrysina turckheimi* beetle appears green with slightly white sheen (Figure 4.39) which gives a false sense of high reflectivity as it is relatively low reflecting. The LL reflectance spectrum is

the dominant feature being the largest feature at all wavelengths (450-1000nm) with a small peak around the green wavelength (Figure 4.39). In the NIR a large peak in the LL spectrum occurs, with small peaks in the LR and RL spectra with the RR reflection values too low to clearly observe any features which occur.

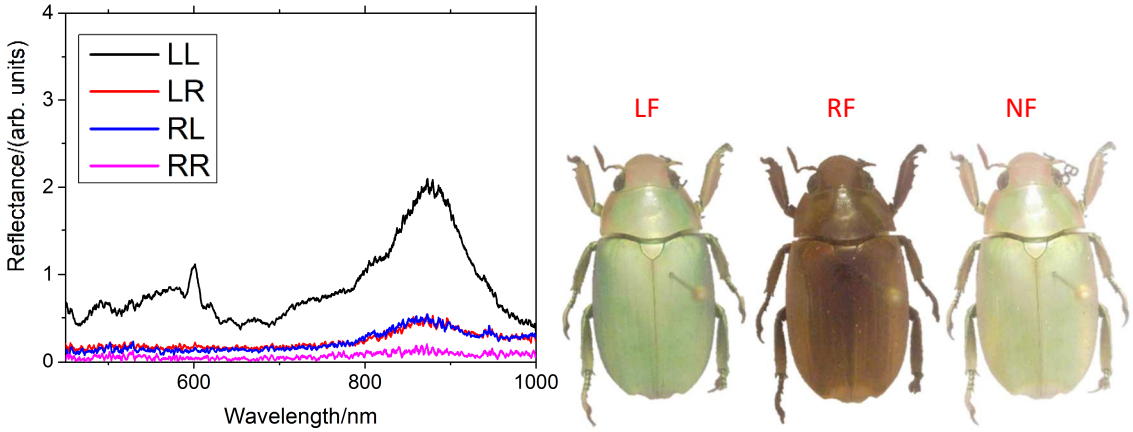


Figure 4.39 – CP reflection spectra from the elytron of a *Chrysina turckheimi* beetle. This specimen was collected from Camino La Fraternidad a El Bojonal, San Marcos, Guatemala in 2012. The CP spectra were taken with an integration time of 500ms. The specimen measures 24mm.

The optical properties of a *Chrysina macropus* have also previously been investigated [20],[22]. The *Chrysina macropus* beetle has a relatively weak LL spectrum, whose peak at a green wavelength is of a comparable value to the LR and RL spectra (Figure 4.40). The feature which is different to many other *Chrysina* is the absence of a NIR reflection peak in the LL spectrum.

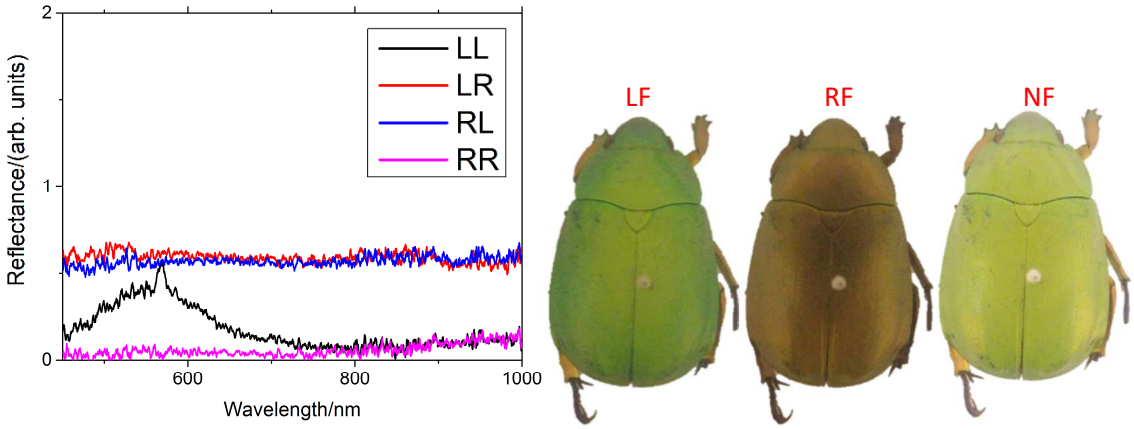


Figure 4.40 – CP reflection spectra from the elytron of a *Chrysina macropus* beetle. This specimen was collected from Venta Grande, Puebla, Mexico in 2004. The CP spectra were taken with an integration time of 500ms. The specimen measures 33mm.

4.4.2.6. Conclusion

In this section a wide range of different reflection properties can be seen within the *Chrysina* family, from matt green beetles to metallic silver, red and gold specimens to species which selectively reflect both LCP and RCP light. There are many other *Chrysina* species and colour morphs with interesting colourations whose optical properties have not been studied and the investigation of which could reveal interesting properties. Examples of such variations can be

seen in Figure 4.41 including red brown and purple species with gold patches and spots. Many other examples of *Chrysina* reflection can be found in Appendix A3.3.1.



Figure 4.41 – Photograph of a) a *Chrysina cunninghami*, b) a *Chrysina moroni* and c) a *Chrysina purulhensis* specimen. Used with permission from K. Robacker and also [35].

4.4.3. Cetoniinae In-Depth Variation Studies

Further to investigations upon the *Chrysina* genus, studies were made upon the CP reflection spectra of large numbers of specimens of several single species and genera in the Cetoniinae subfamily. It should be noted that a variety of individual species from the *Protaetia* genus can be found in the Appendix A3.2.8.

4.4.3.1. Lomaptera

Variation in the *Lomaptera* genus has been studied previously in the author's Master's thesis [2], with large numbers and more species being investigated as part of this thesis. Other studies have also investigated several species of *Lomaptera* [1],[8],[12].

Two hundred and eight *Lomaptera* specimens were optically investigated, although there were other *Lomaptera* species which could not be studied due to their very weak or non-visible LCP response. The LL spectra were seen to have the most intense features and were classified according to shape (Figure 4.41). The author identified six different classifications of single peaks (S), double peaks close together (DC), oscillations after the main peak, oscillations before the main peak, double peaks apart from each other (DA) and any that did not fit these groupings were not classified (NC). It should be noted that there was a wide range of shapes within the NC grouping. Modelling of a typical example of each of the spectral shapes will be discussed in Section 5.4.

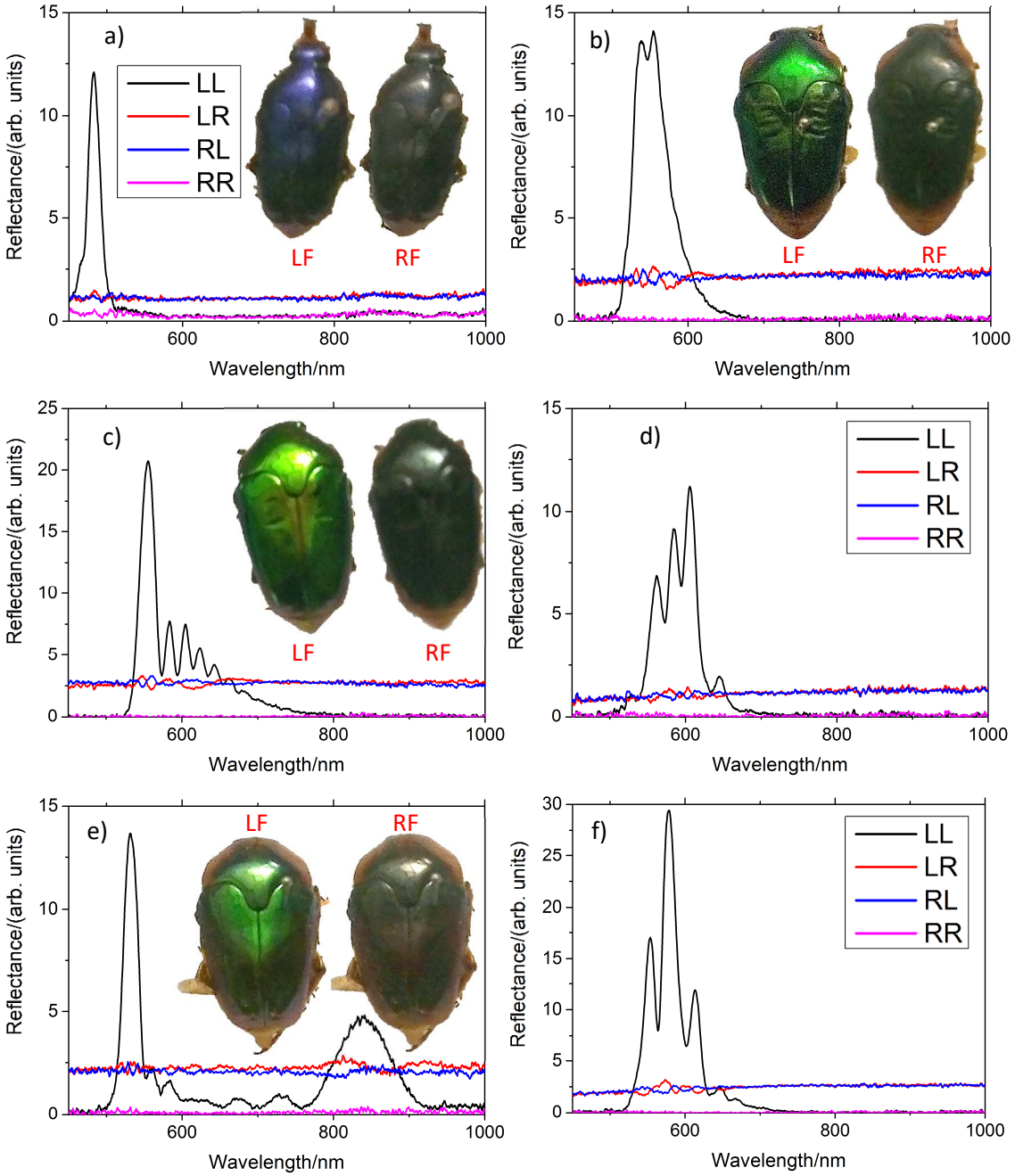


Figure 4.42 – CP spectra of *Lomaptera* species, where the LL spectrum is defined as a) Single peak (S) (*L. soror*), b) Double Close (DC) (*L. humeralis*), c) Oscillations After (OA) (*L. helleriana*), d) Oscillations Before (OB) (*L. soror*), e) Double Apart (DA) (*L. geelvinkiana*), f) Not Classified (NC) (*L. soror*).

The distribution of these classifications within and between *Lomaptera* species can be seen in Figure 4.43. This illustrates that some species are dominated by specific LL spectral shapes (such as OA in *L. helleriana, L. pseudodichropus* and L. *viridipes*), whilst other species are more mixed (such as *L. pygmaea*). This spectral distribution allows differentiation between some species such as the difference between *L. viridipes* and *L. gilnicki*. However there are some species which can be distinguished by LL spectral shape e.g. *L. pseudodichropus* and *L. helleriana*. So whilst this technique can be a useful tool in distinguishing species, it cannot be used as a standalone method and will need to be used in conjunction with other identification techniques.

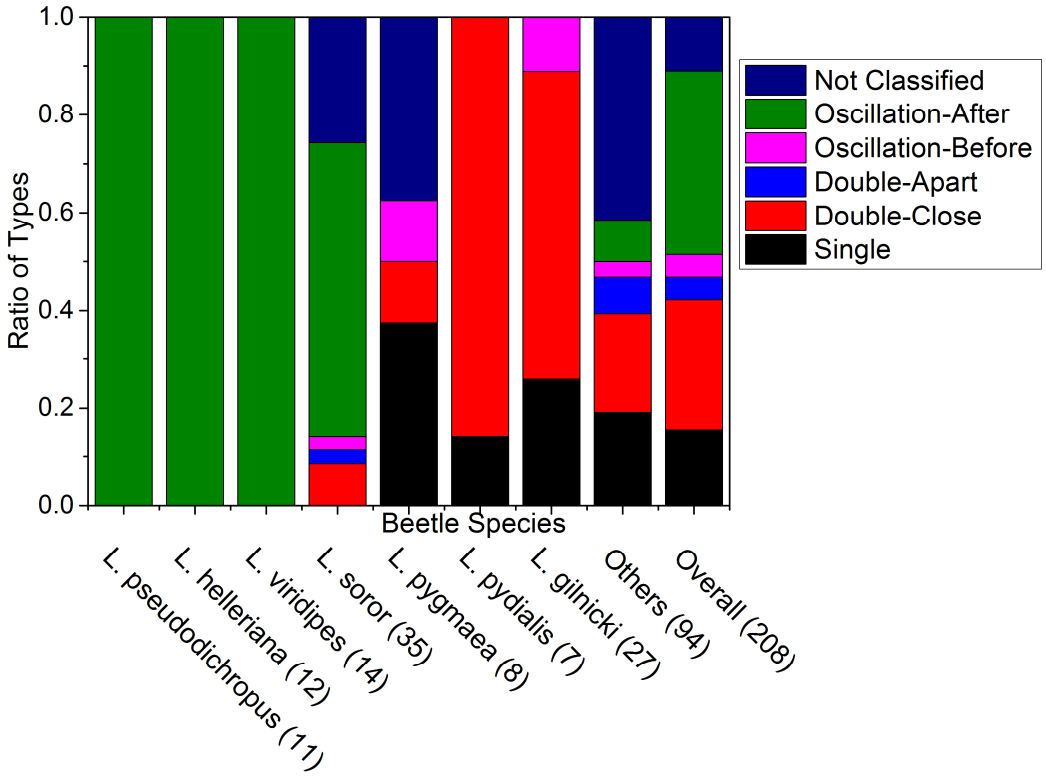


Figure 4.43 – Ratios of LL spectral shape variation within and between different species of the *Lomaptera* genus. The number in brackets denotes the number of specimens investigated.

Further to the distribution of spectral shapes variation in the wavelength of the LL peaks was calculated, in this genus this was done in terms of pitch using equations 3.14 and 3.15. Variation between spectral shapes mean pitch values can be seen in Figure 4.44, where the average pitch related to a green-yellow wavelength (577nm). It can also be seen there is less variation in the single and double close variations than in the other classifications. It should be noted that for oscillations before and oscillations after spectra only the largest peak was considered for the analysis.

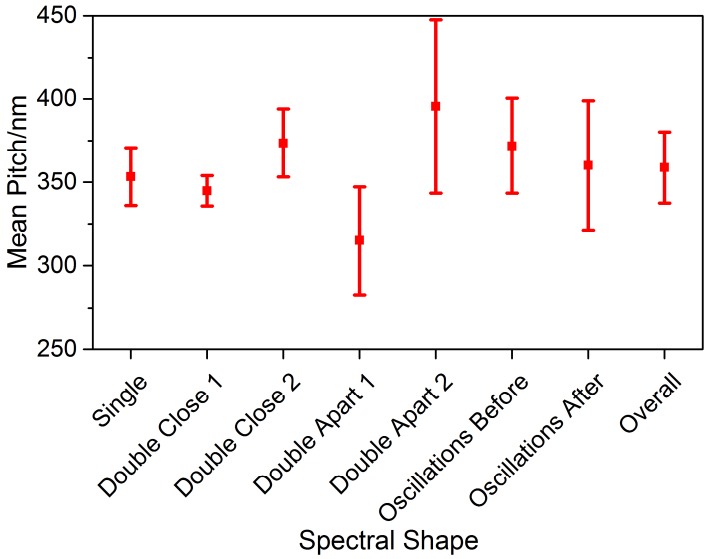


Figure 4.44 – Calculated mean pitch variations (from the reflection spectra peaks) with standard deviation error bars of the beetles of different spectral shapes in the *Lomaptera* genus, where 1 and 2 after double close and apart labels relate to the lower and higher peaks respectively.

Variations in pitch value between different *Lomaptera* species also occurs (Figure 4.45) and certain species have a much lower variation (such as *L. pseudodichropus*), whilst others have much greater variations (such as *L. soror*). In the appendix variation in the *L. soror* species from green to red to the NIR can be seen (Appendix Figure A 61).

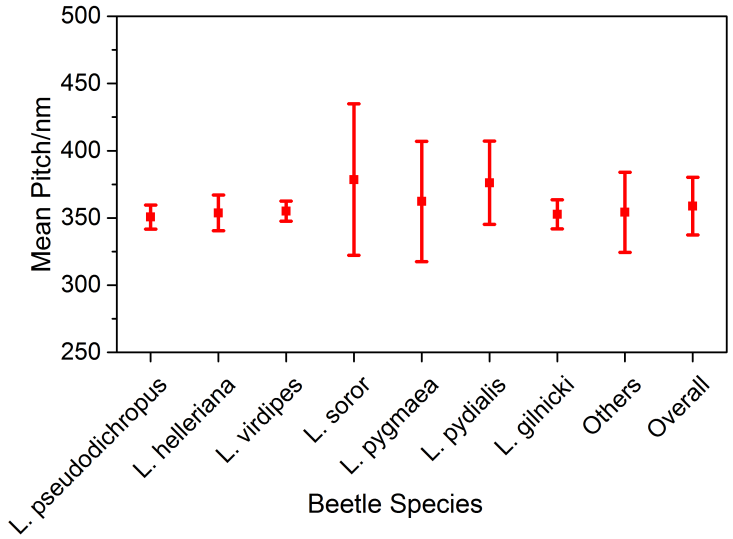


Figure 4.45 – Calculated mean pitch variations (from the reflection spectra peaks) with standard deviation error bars of different species from the *Lomaptera* genus.

4.4.3.2. Mycterophallus duboulayi

The *Mycterophallus duboulayi* species is sometimes known as *Lomaptera duboulayi* and previous optical studies have been made [1],[36]. The distribution of the spectra of these species was also discussed as part of the author's MRes thesis [2].

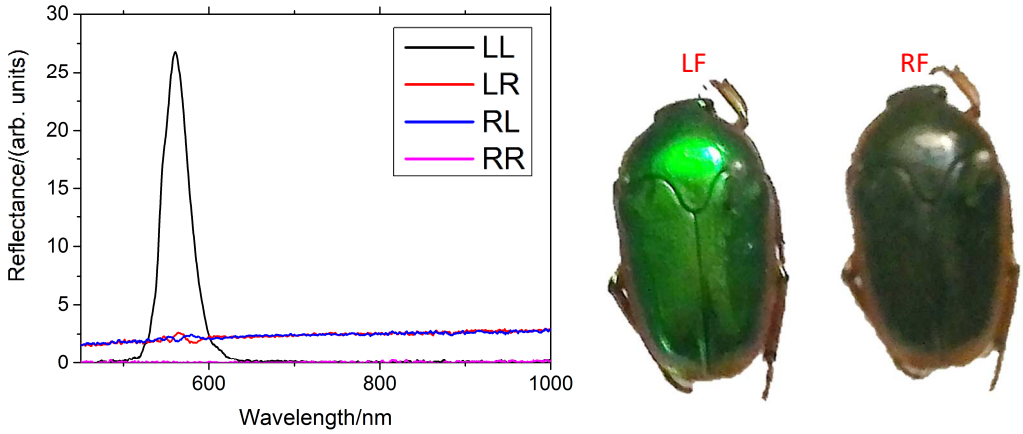


Figure 4.46 – CP reflection spectra from the elytron of a *Mycterophallus duboulayi* beetle.

A typical set of spectra for the species can be seen in Figure 4.46, where the LL spectrum was the dominant feature and demonstrates the ratio to the other CP spectra combinations.

The same classification of LL spectra as used with the *Lomaptera* genus (Section 4.4.3.1) was implemented for analysis of this species, however the double apart shape of the LL spectrum was not observed in this species. Examples of each LL spectrum and its classification can be seen in Figure 4.47.

The spectral type distribution of 49 specimens (Figure 4.48), shows that there are two dominant classifications, the first being double close (DC) and the second spectral type was more complex and could not be classified simply (NC).

The mean peak values of the different spectral types in Figure 4.49 show relations between the lowest double peak close together (DC1) and the oscillation after (OA) values. There can also be seen to be a relation between the highest double peaks close together (DC2) and the oscillation before (OB) values. The single peak mean peak value appears to be between the DC1 and DC2 values (and OA and OB values). This suggests the peaks (and pitch values) diverge both to lower and higher wavelengths for the DC peaks. The OB has on average higher and OA a lower wavelength main peaks, which suggests perturbations of longer pitches (OB) and shorter pitches (OA).

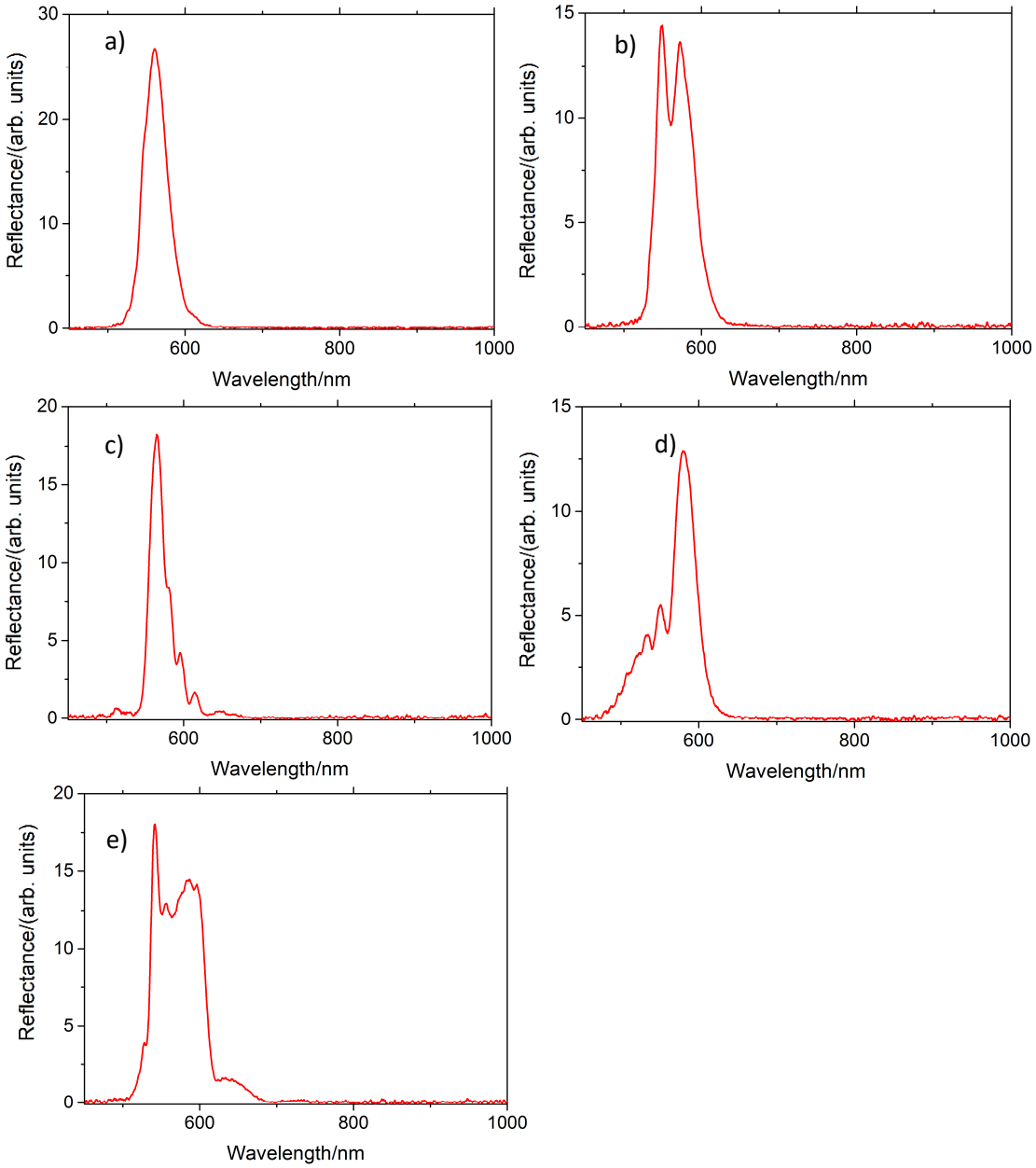


Figure 4.47 – LL CP spectra of *Mycterophallus duboulayi*, the spectral shapes are defined as a) Single (S), b) Double Close (DC), c) Oscillations After (OA), d) Oscillations Before (OB) and e) Not Classified (NC).

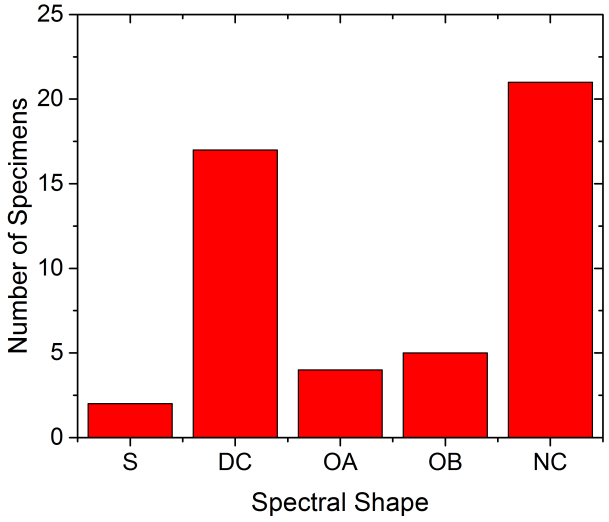


Figure 4.48 – Distribution of the LL spectral type of *Mycterophallus duboulayi* beetles.

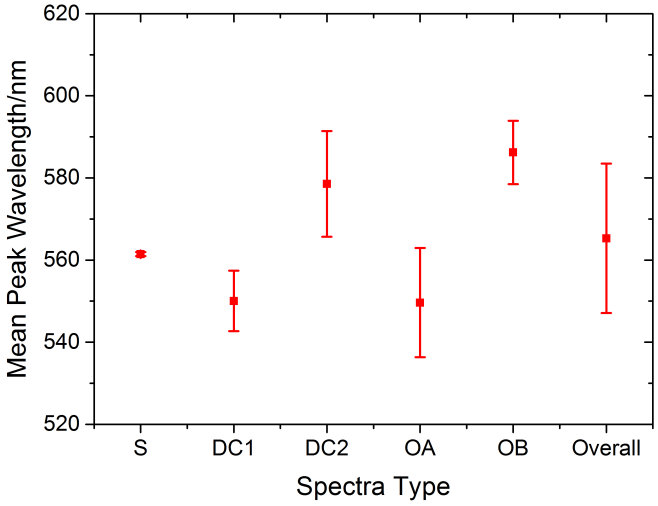


Figure 4.49 – Distribution of mean peak wavelength values with standard deviation errors of the main peak in the LL spectrum by spectral type for *Mycterophallus duboulayi* beetles.

4.4.3.3. Thaumastopeus pugnator

Sixty *Thaumastopeus pugnator* specimens were investigated which had a dominant LL spectra that consisted of multiple peaks which were close together. A typical set of CP spectra from this species is shown in Figure 4.50.

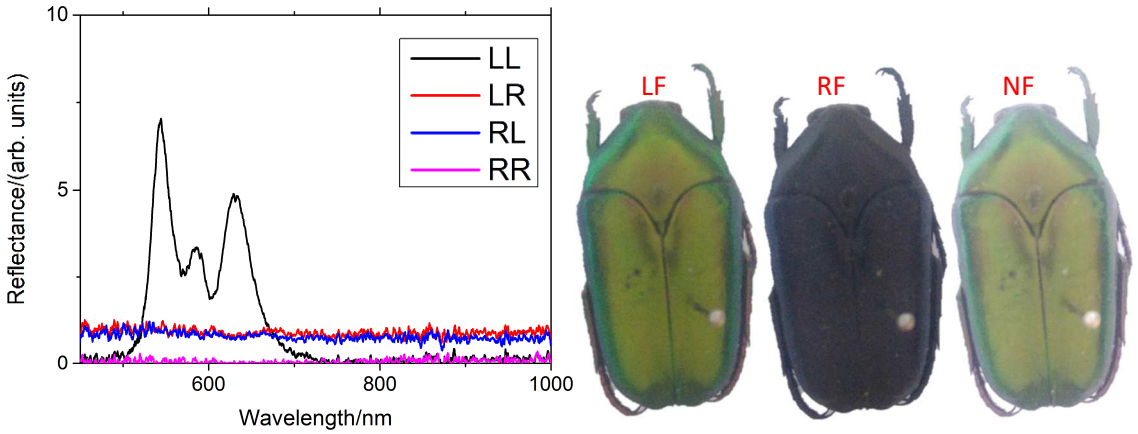


Figure 4.50 – CP reflection spectra from the elytron of a *Thaumastopeus pugnator* beetle. This specimen was collected from Mount Talang, West Sumatra, Indonesia in 2015. The species measures ~34mm.

The LL spectra typically have two, three or four peaks, an example of each can be seen in Figure 4.51.

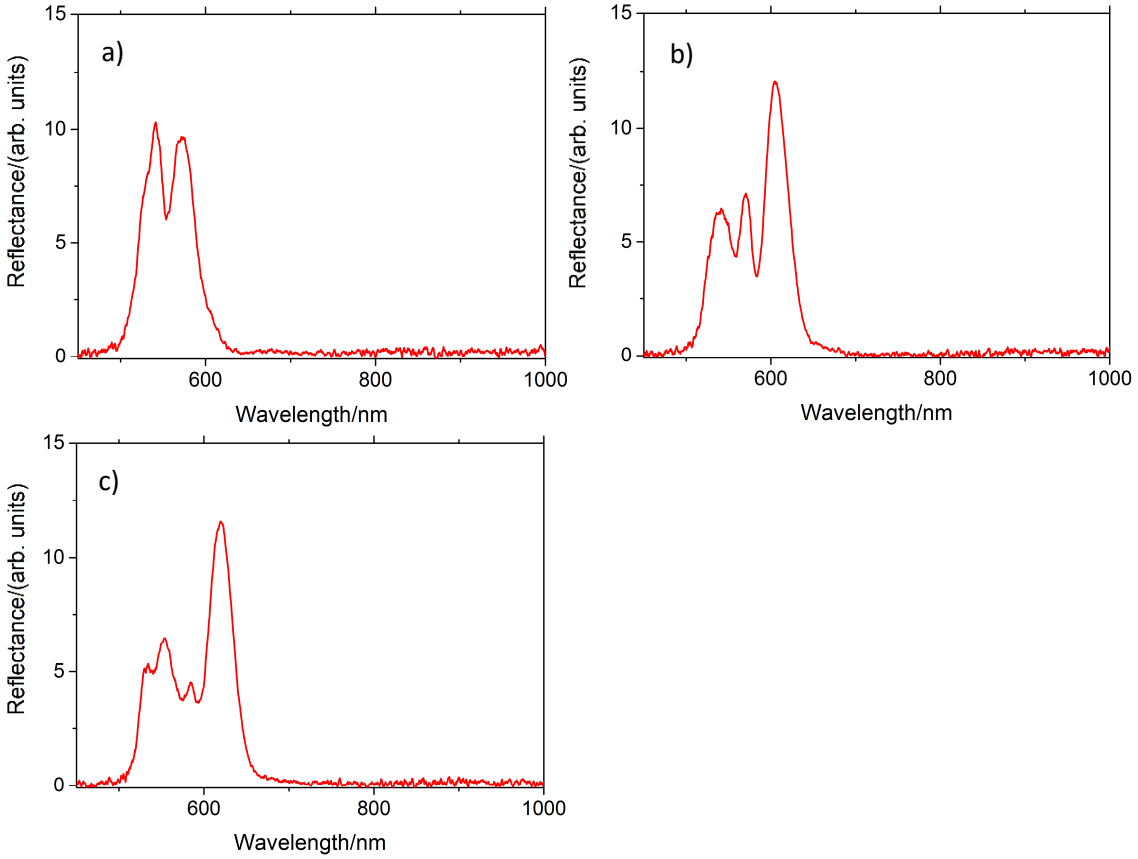


Figure 4.51 – LL CP spectra of *Thaumastopeus pugnator* specimens, where the spectra have a) two, b) three and c) four peaks.

The distribution of the number of pitches (Figure 4.52) shows that LL spectra with two peaks are most common followed by four, with three (triple) being the least common.

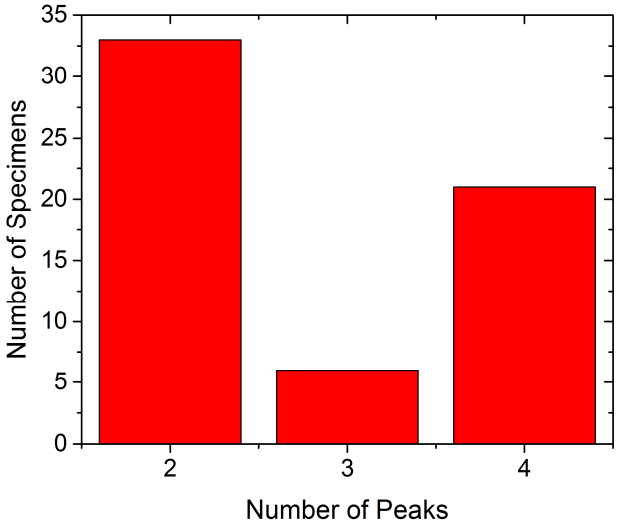


Figure 4.52 – LL spectral distribution of numbers of peaks of *Thaumastopeus pugnator* beetles.

The mean peak wavelengths of the different spectral types showed a small increase in mean peak value of the higher peak as the number of peaks increased (Figure 4.53). There was also a larger decrease in mean peak value of the lower peak as the number of peaks increased.

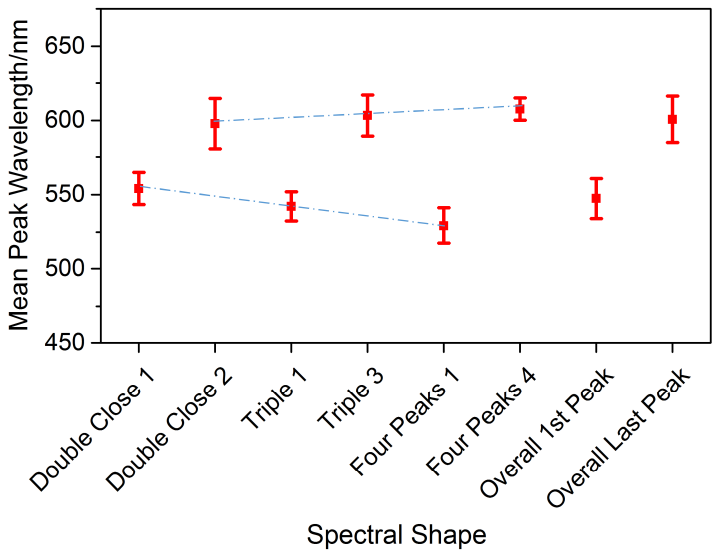


Figure 4.53 – Distribution of mean peak wavelength values with standard deviation errors of the highest and lowest peaks in the LL spectrum of each number of peaks for the *Thaumastopeus pugnator* beetles. The number 1 corresponds to the lowest peak and the higher number corresponds to the highest peak value of each spectral shape. Dashed lines were added to highlight the trends of the lower and upper peaks.

4.4.3.4. Protaetia brevitarsis

Sixty-three *Protaetia brevitarsis* specimens were studied, a typical example of a set of CP spectra can be observed in Figure 4.54. The typical LL spectrum consists of the highest and lowest wavelength peaks being of greater intensity values than the peaks in between. Each LL spectrum contained between three and nine distinguishable peaks (Figure 4.55).

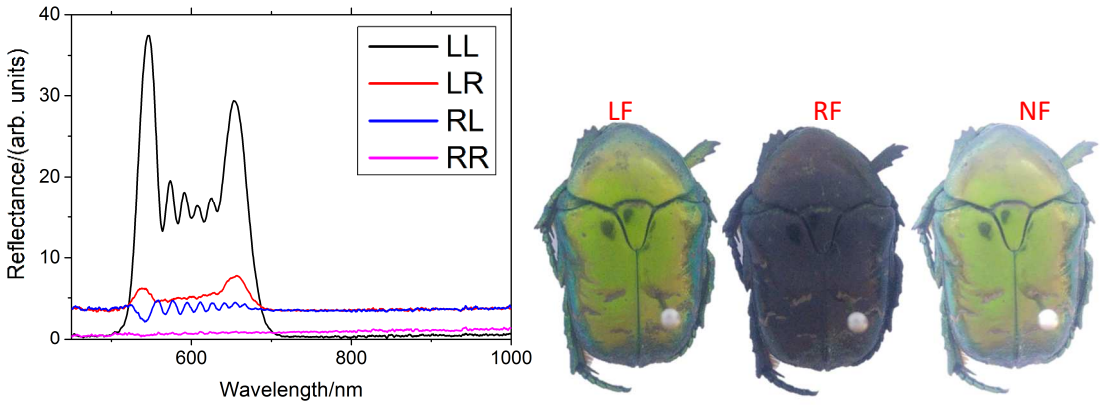


Figure 4.54 – CP reflection spectra from a green part of the elytron of a *Protaetia brevitarsis* beetle. This specimen was collected in Hubei, China in 2013. The species measures ~24mm.

The distribution of the number of peaks (Figure 4.56) showed that three, four, five and six peaked LL spectra occurred with between 10 and 20 specimens of each type. The number of specimens with seven, eight or nine peaks in the LL spectra was much smaller.

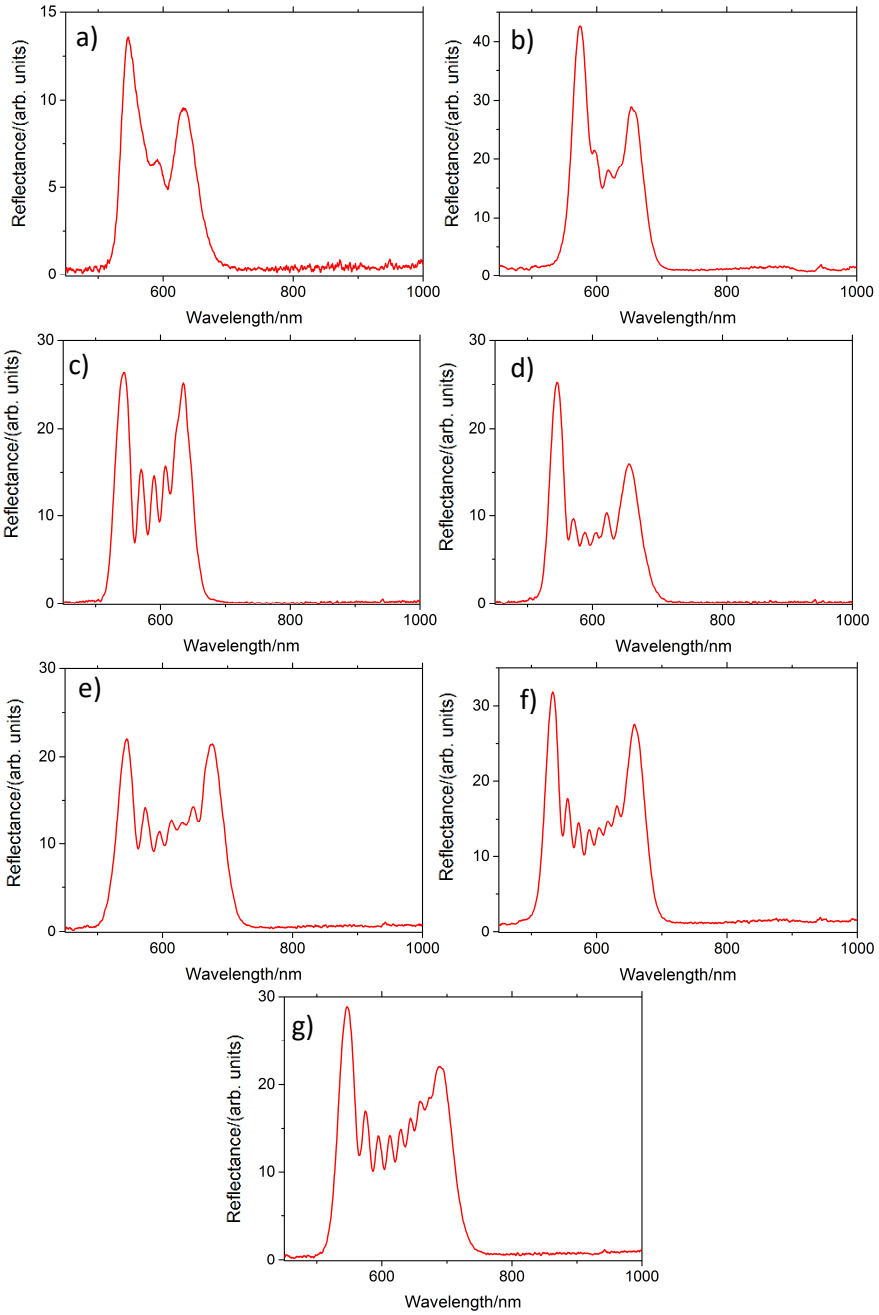


Figure 4.55 – LL CP spectra of *Protaetia brevitarsis* specimens, where the spectra have a) three, b) four, c) five, d) six, e) seven, f) eight and g) nine peaks.

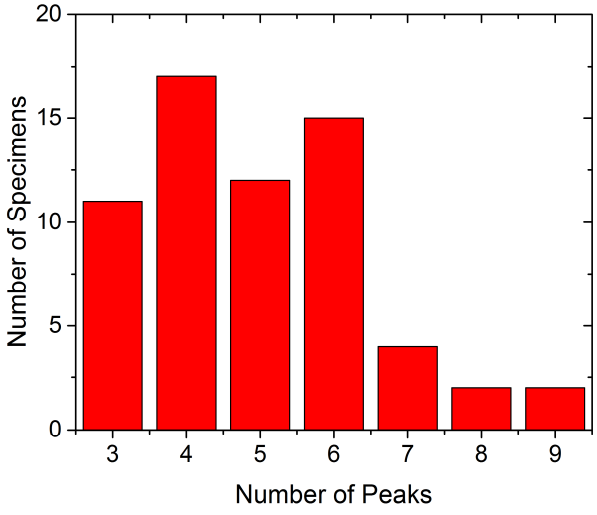


Figure 4.56 – LL spectral distribution of numbers of peaks of *Protaetia brevitarsis* beetles.

The mean wavelength was found for the lowest and highest peaks of each spectral shape (Figure 4.57). It was found that as the number of peaks in the LL spectrum increased the mean wavelength of the highest peak dramatically increased, whilst the lowest mean peak value had a much smaller increase. The dominant colour of all specimens was at green wavelengths.

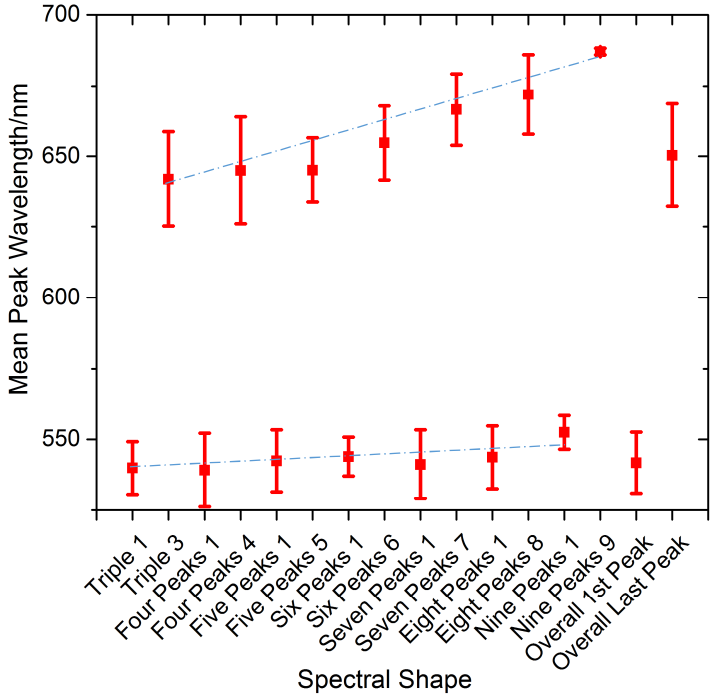


Figure 4.57 – Distribution of mean peak wavelength values with standard deviation errors of the highest and lowest peaks in the LL spectrum of each number of peaks for the *Protaetia brevitarsis* beetles. The number 1 corresponds to the lowest peak and the higher number corresponds to the highest peak value of each spectral shape. Dashed lines were added to highlight the trends of the lower and upper peaks.

4.4.3.5. Cetonia aurata aurata

All 191 *Cetonia aurata aurata* reported in this section were collected in Poland and Romania in 2014/5. The CP reflection spectra were taken from the top of the beetles' right elytra. Six different LL spectral classifications were made within the species (Figure 4.58). These spectral shapes include two addition classifications compared to the *Lomaptera* genus (triple peaks (T), and oscillations between two peaks (X)). It should also be noted that the not classified (NC) became labelled as unclassified (UC). With the exception of beetles with oscillations between two main peaks (X) the beetles appear very similar upon visual examination.

In the spectral shape distribution (Figure 4.59) it can be seen the OA spectral shape is the most common followed by DC and then T. It demonstrates that the single peak LL reflection spectrum shape is not the dominant feature and more complex shapes dominate.

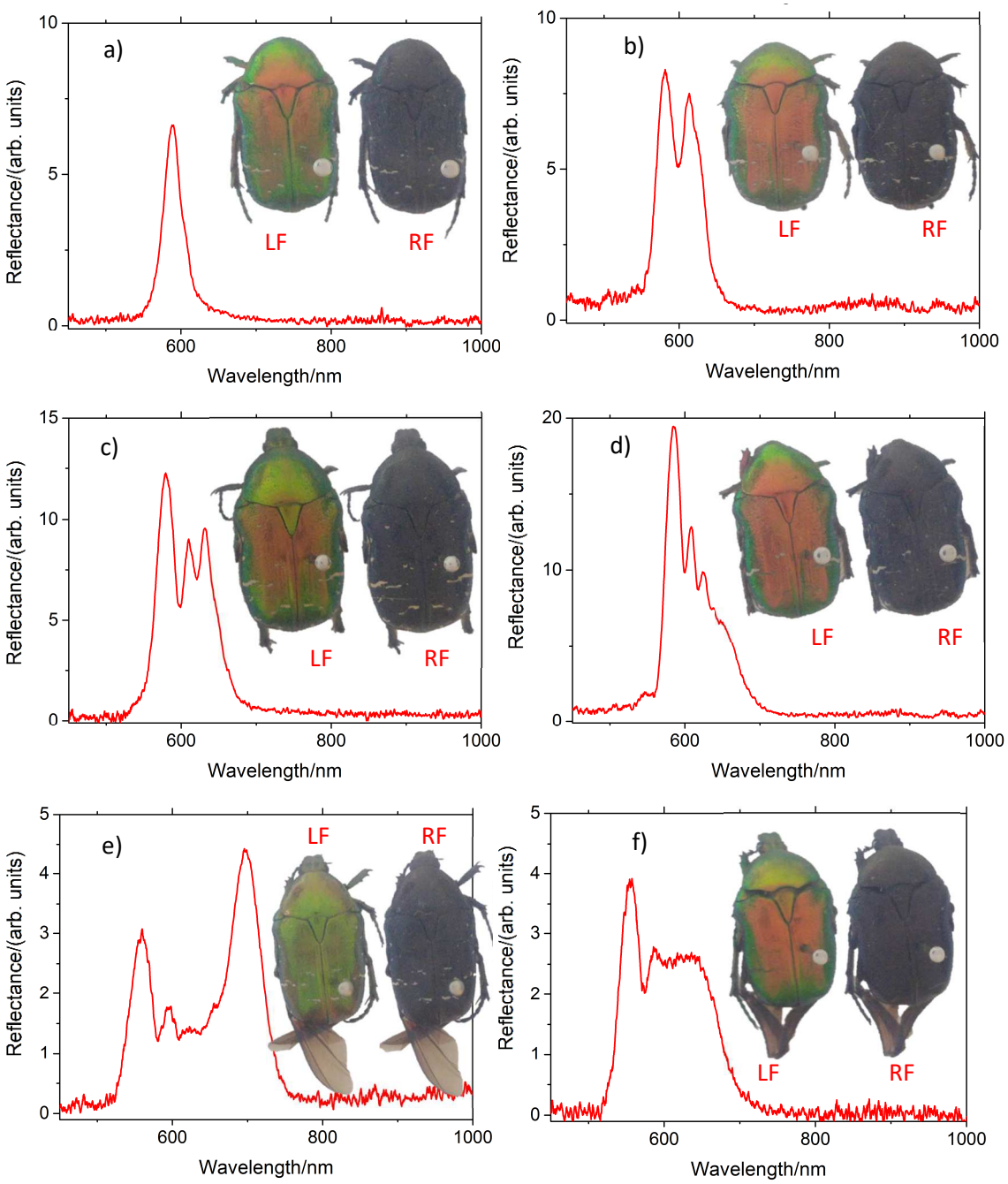


Figure 4.58 – LL CP spectra of *Cetonia auruata aurata* specimens, where the LL spectra are defined as a) Single peak (S), b) Double Close (DC), c) Triple (T), d) Oscillations After (OA), e) Oscillations between peaks (X), f) Unclassified (UC). The specimens in this study were measured as ~20mm.

The distrubtion of mean pitches for different spectral types (Figure 4.60) shows smaller variation between the S, DC, T and OA spectra, but with the higher value in the X spectra (Xf) value appears much larger. It should be noted the DC1 and DC2 peaks have similar distributions to T1 and T2 peaks, however the T3 peak appears at a higher wavelength. It should also be noted the S peak value is similar to that of DC1, T1 and OA, with additional peaks occuring at higher wavelengths.

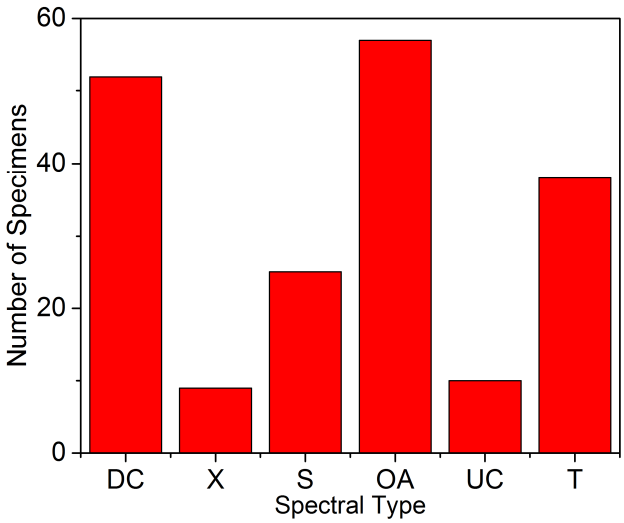


Figure 4.59 – Distribution of the LL spectral types of *Cetonia aurata* beetles. Published by the author in [37].

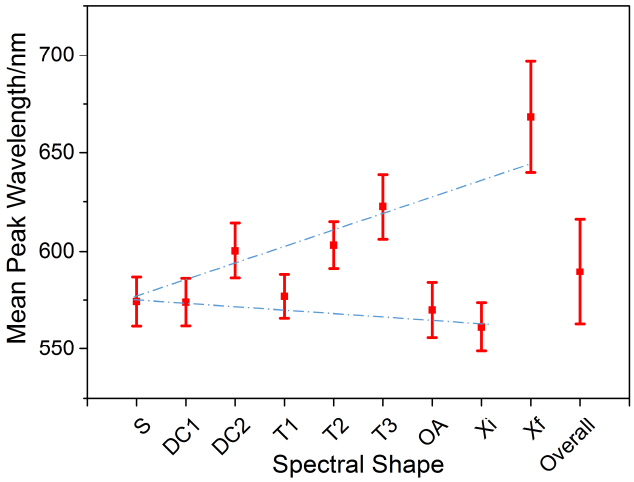


Figure 4.60 – Mean peak wavelength variations with standard deviation error bars of the beetles of different spectral shapes in the species *Cetonia aurata aurata*. The 1, 2 and 3 after DC and T correspond to the first, second and third peaks respectively. The Xi and Xf represent the initial and final peaks in the X shaped spectra. Dashed lines were added to highlight the trends of the lower and upper peaks.

4.4.3.6. Ischiopsopha aruensis

CP reflection spectra were measured from 210 *Ischiopsopha aurensis* specimens. A typical CP spectra of this species can be seen in Figure 4.61 where LL is the dominant spectra. This species had a small variation in the number of LL peaks with two, three, four and five peaks being seen (Figure 4.62). Since in the five peaks spectra the peaks were unclear and there were so few spectra, they were grouped with four peaks in the category 4+ peaks. The distribution of the number of peaks (Figure 4.63) showed that three peaks was the dominant type with two peaks being the least common.

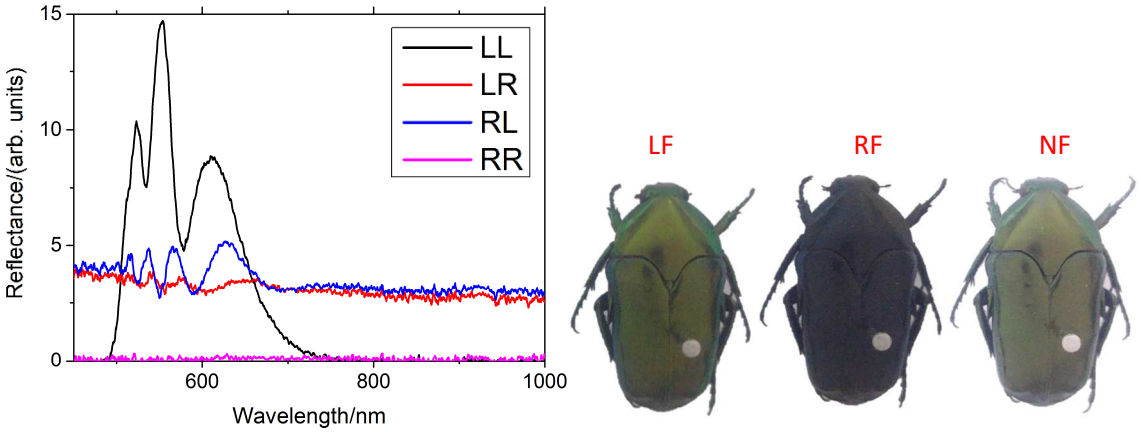


Figure 4.61 – CP reflection spectra from the right elytron of an *Ischiopsopha aruensis* beetle. This specimen was collected from Kai Besar Island, Indonesia in 2014. The species measures ~24mm.

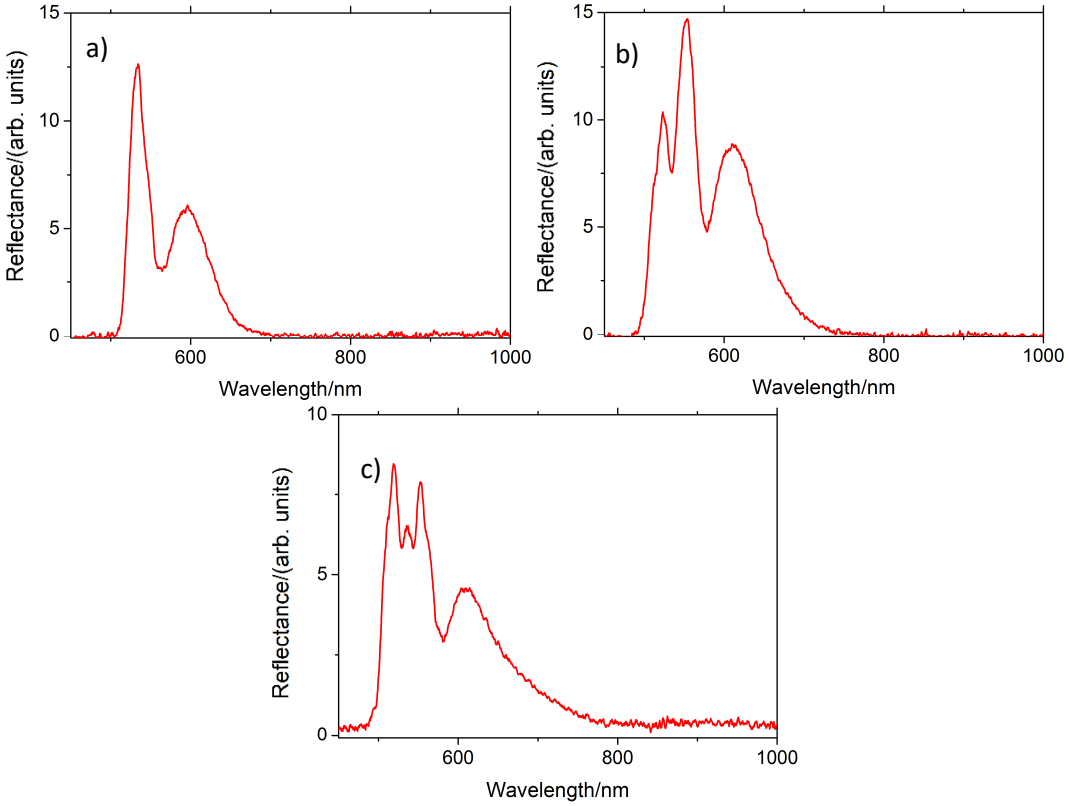


Figure 4.62 – LL CP spectra of *Ischiopsopha aruensis* specimens, where the spectra have a) two, b) three and c) four peaks.

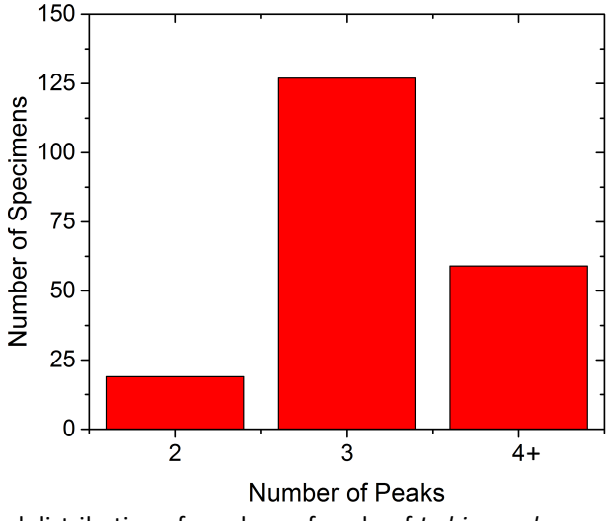


Figure 4.63 – LL spectral distribution of numbers of peaks of *Ischiopsopha aruensis* beetles.

The variation in mean reflection wavelength of each spectra type shows as more peaks occur, the wavelength of the first peak decreases (Figure 4.64). Also as the number of peaks increases there is a small increase (of a similar magnitude) in the higher mean peak wavelength. One of the more notable features is the large variation in the lower wavelength mean peak of the triple LL spectral shape.

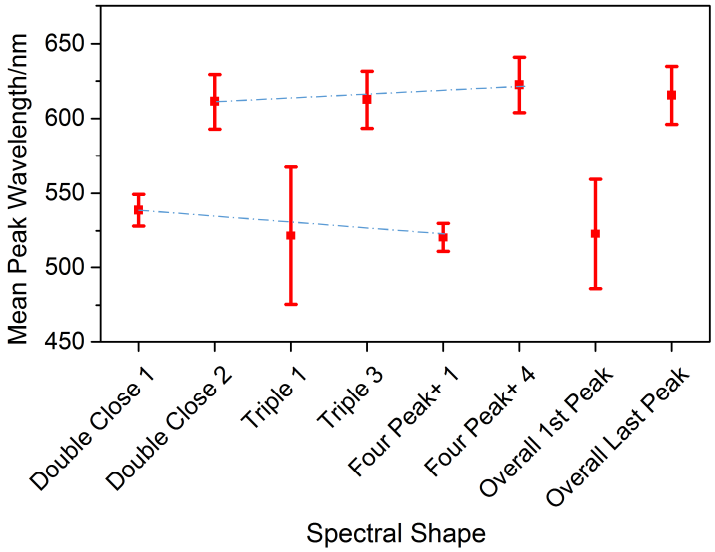


Figure 4.64 – Distribution of mean peak wavelength values with standard deviation errors of the highest and lowest peaks in the LL spectrum of each number of peaks for the *Ischiopsopha aruensis* beetles. The number 1 corresponds to the lowest peak and the higher number corresponds to the highest peak value of each spectral shape. Dashed lines were added to highlight the trends of the lower and upper peaks.

4.4.3.7. Agestrata luzonica

The *Agestrata luzonica* beetles investigated had a highly metallic orange-green appearance. These beetles were reasonably large, being over 40mm in length. A typical CP spectra (Figure 4.65) shows a large dominant LL response. The LL spectral shape contained between two and seven peaks (Figure 4.66).

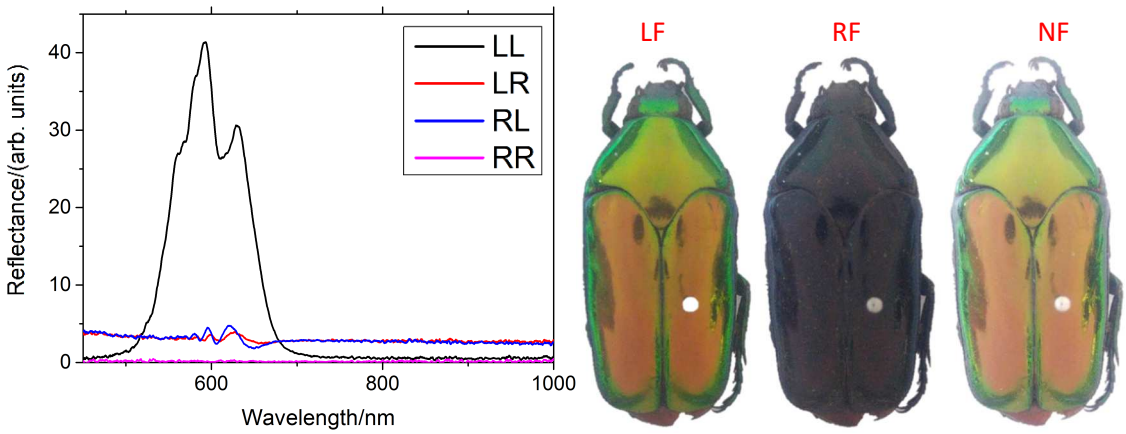


Figure 4.65 – CP reflection spectra from the right elytron of an *Agestrata luzonica* beetle. This specimen was collected from the Philippines in 2014. The species measures ~37mm.

The distribution of the numbers of peaks in the LL spectra of thirty-one *Agestrata luzonica* beetles with different number of peaks (Figure 4.67) shows the majority of spectra had between four and six distinguishable peaks.

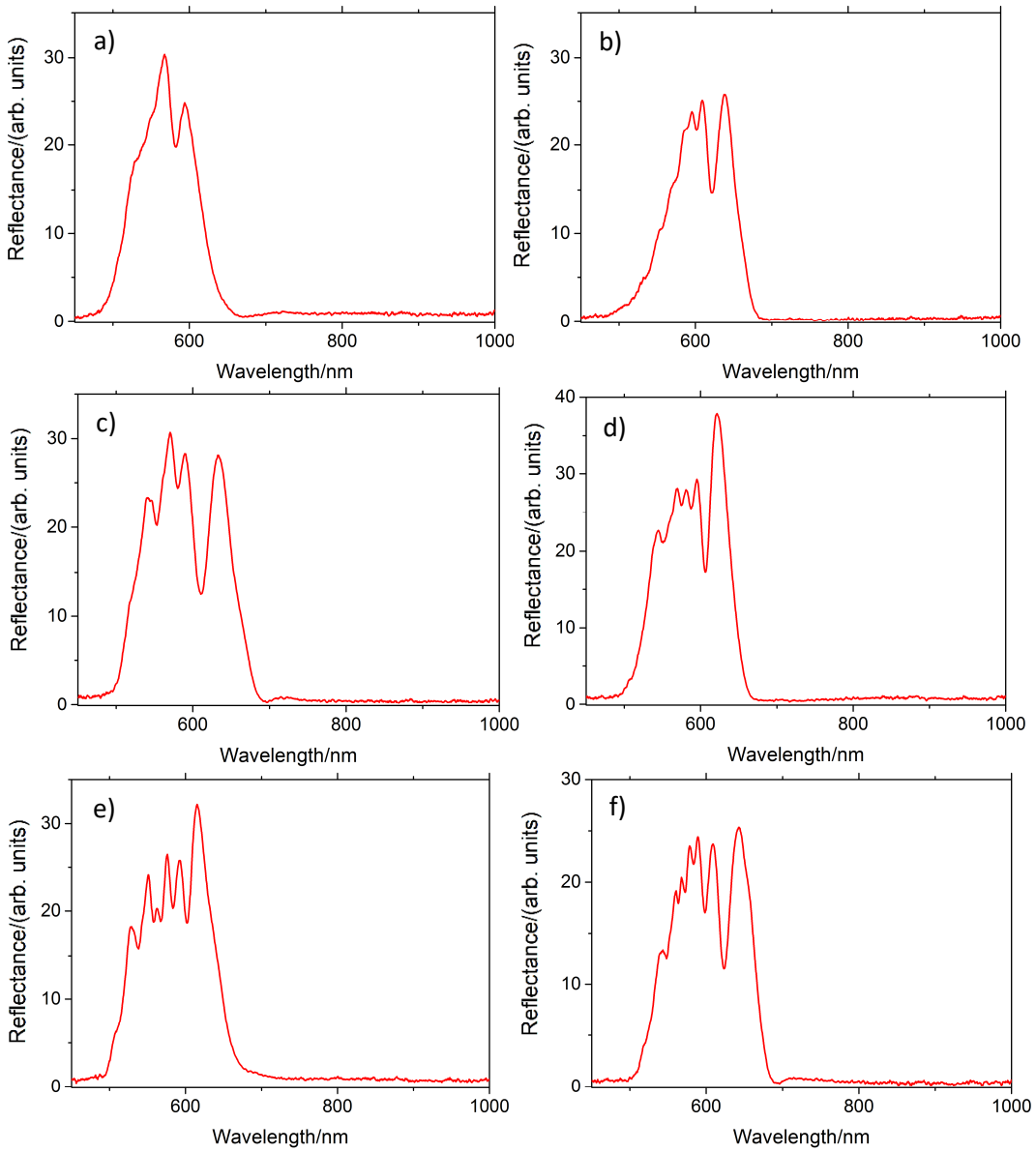


Figure 4.66 – LL CP spectra of *Agestrata luzonica* specimens, where the spectra have a) two, b) three, c) four, d) five, e) six and f) seven peaks.

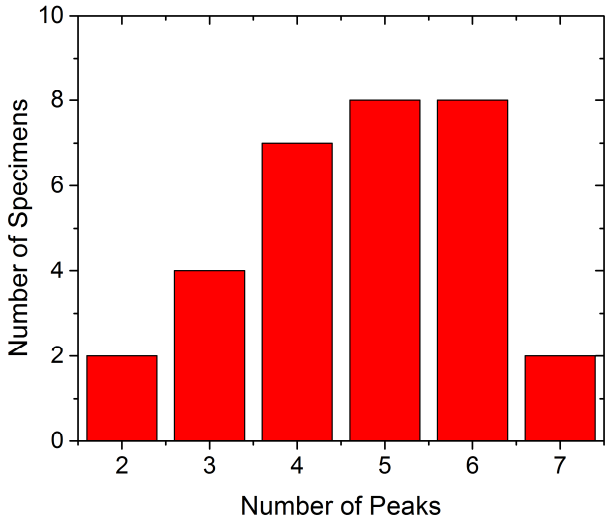


Figure 4.67 – LL spectral distribution of numbers of peaks of *Agestrata luzonica* beetles.

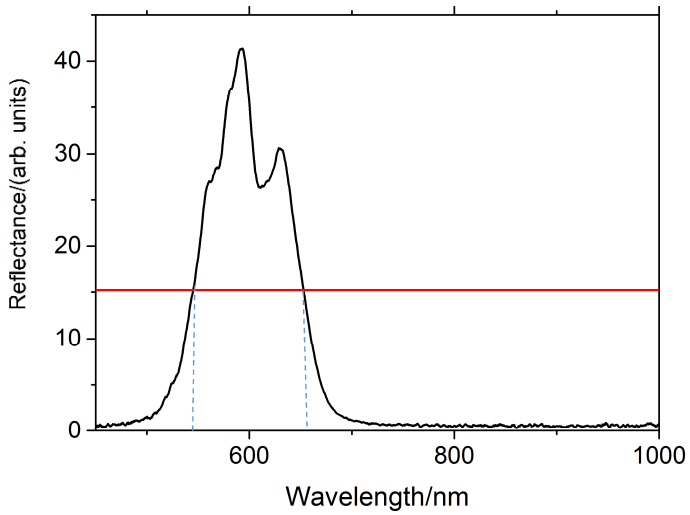


Figure 4.68 – *Agestrata luzonica* LL spectra (Black) and the line of the maximum peak intensity/exp(1) (red), with the intersections between the two shown with a dashed blue line.

The reflected spectral wavelengths were found using a different method to previous species studied in this thesis. This method was chosen due to peaks being closer together and harder to measure using the peak finding function than other species. A line was plotted in the y-axis, whose value was the maximum value of the peak in LL spectrum divided by exp(1), the lower and upper wavelength intersects of this line with the LL spectrum were then recorded (as in Figure 4.68). The distribution of the lower and upper bounds of each of the spectral types (numbers of peaks) is shown in Figure 4.69, where it can be seen the upper bound varies more than the lower. The variation of both the upper and lower limit is small, with the upper limit increasing a greater amount than the lower limit decreases.

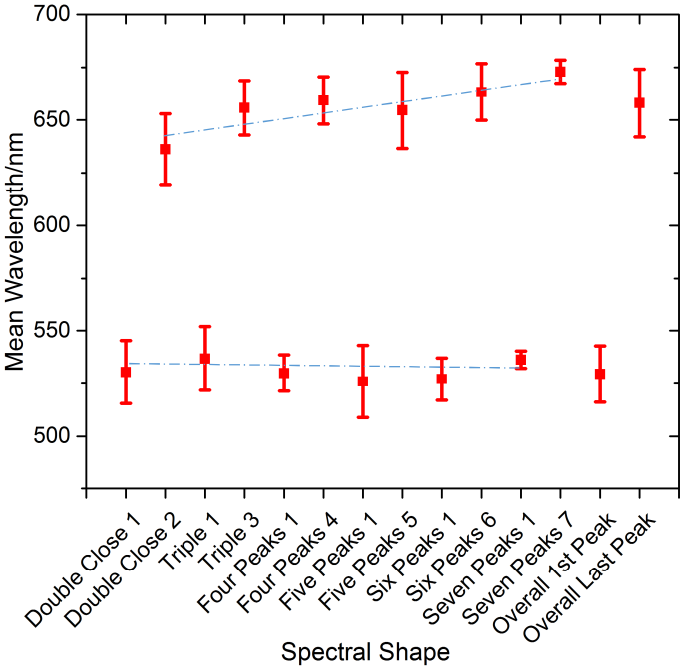


Figure 4.69 – Distribution of mean wavelength intersect values with standard deviation errors of the highest and lowest peaks in the LL spectrum of each number of peaks for the *Agestrata luzonica* beetles. The number 1 corresponds to the lower boundary and the higher number corresponds to the higher boundary of each spectral shape. Dashed lines were added to highlight the trends of the lower and upper peaks.

4.4.3.8. Protaetia himalayana

The reflection spectra of 18 captive bred *Protaetia himalayana* were measured. A typical set of CP spectra (Figure 4.70), shows a dominant LL spectrum with multiple peaks.

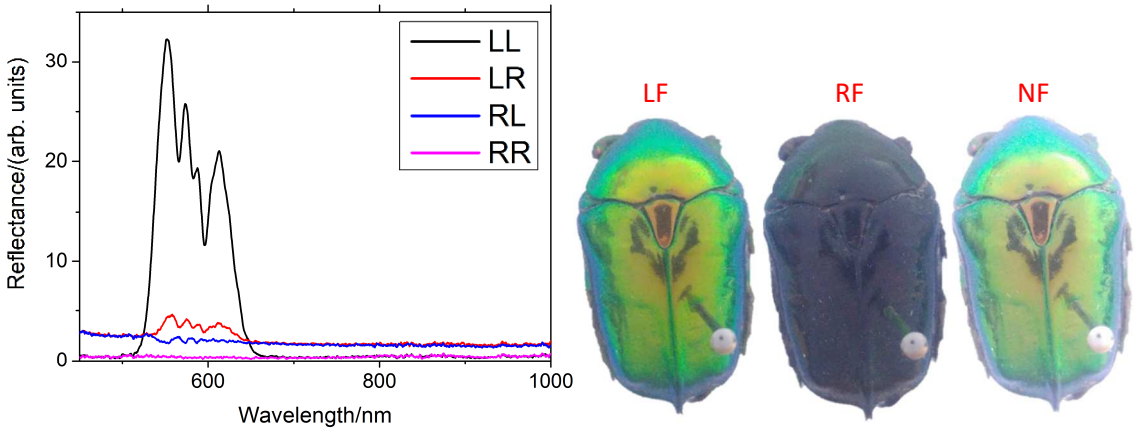


Figure 4.70 – CP reflection spectra from the scutellum of a *Protaetia himalayana* beetle. This was a captive bred specimen from 2015, which originated from Thailand. The species measures ~21mm.

One unusual specimen, which had a blue appearance was found not fully developed (and dead) in the pupae stage. The CP spectra were taken of this specimen (Figure 4.71), which showed a LL spectrum which had peaks in the blue region. This may suggest the development produces shorter pitches at a younger age, which increase with age, or the refractive index may gradually change as the colour structure develops. It should be noted the numerical and spectral shape analysis excluded this blue beetle.

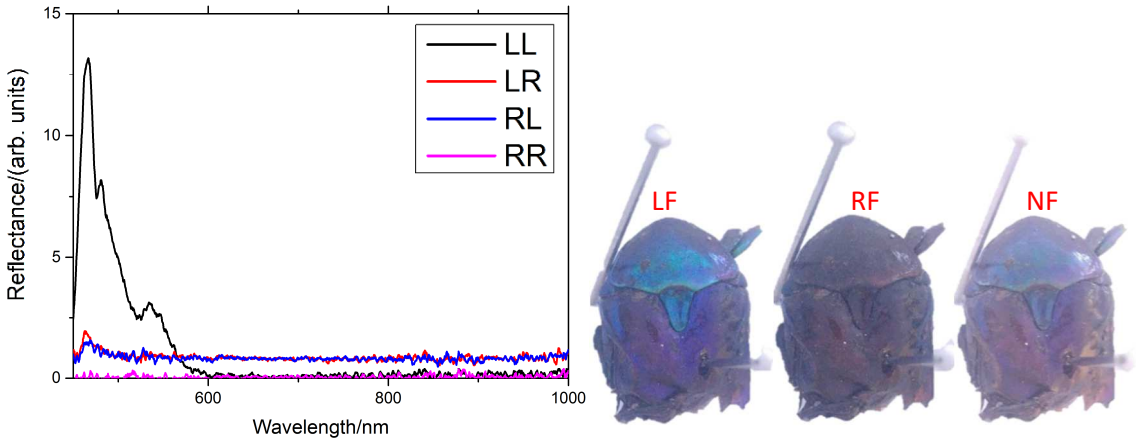


Figure 4.71 – CP reflection spectra from the scutellum of an under developed *Protaetia himalayana* beetle. This was a captive bred specimen from 2015, which originated from Thailand.

The LL spectral shape varied from two to four peaks (Figure 4.72), with the distribution of the number of peaks (Figure 4.73) showing that four peaks was the dominant type.

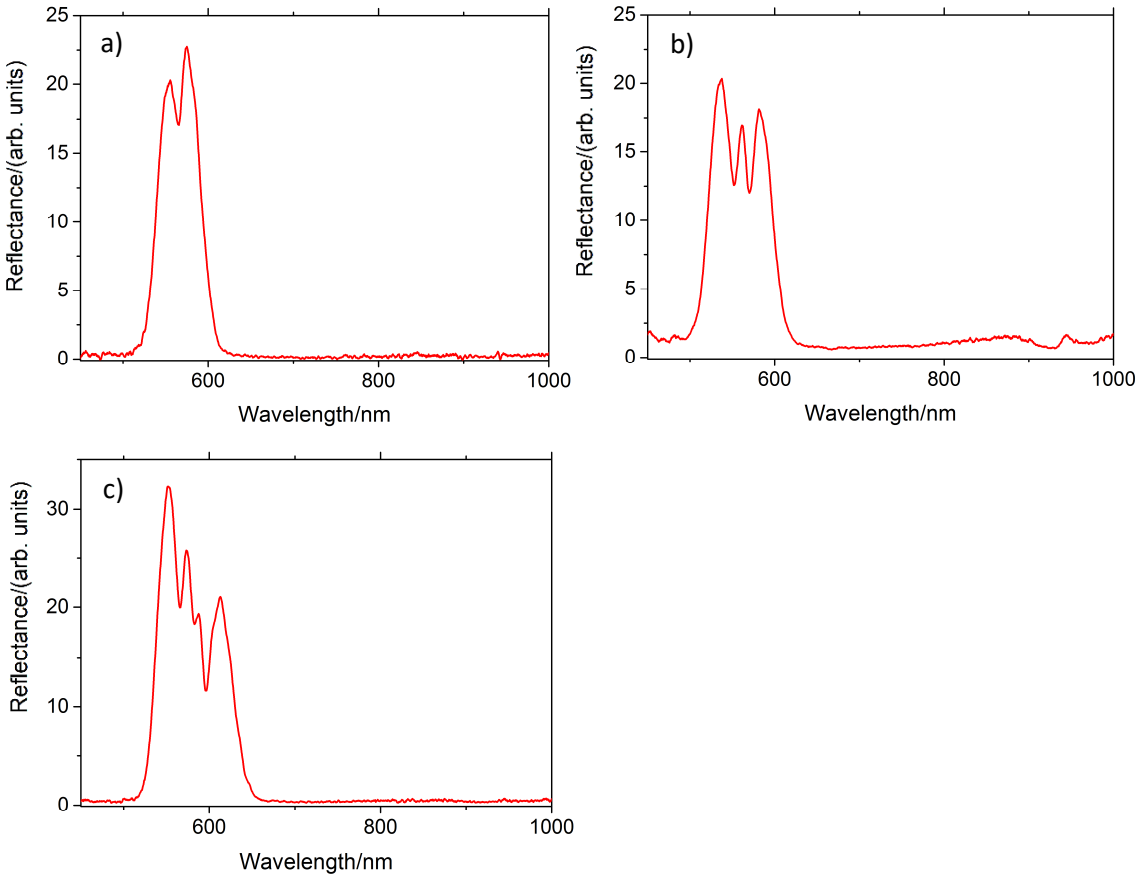


Figure 4.72 – LL CP spectra of *Protaetia himalayana* specimens, where the spectra have a) two, b) three and c) four peaks.

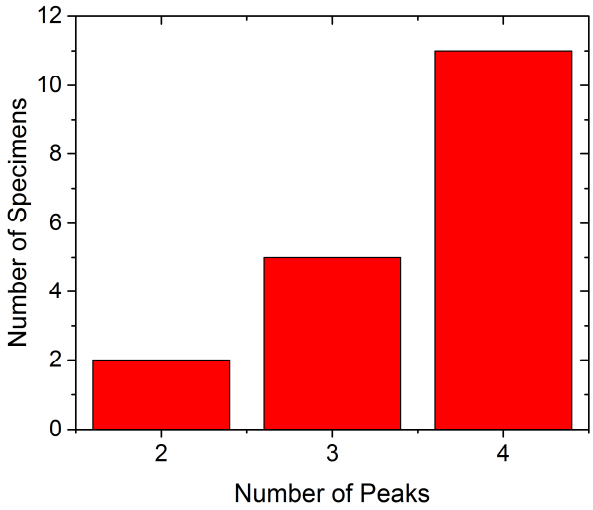


Figure 4.73 – LL spectral distribution of numbers of peaks of *Protaetia himalayana* beetles.

The mean wavelength values of the highest and lowest peaks of each spectral shape were calculated and the variation was shown in Figure 4.74. It can be seen that as the number of peaks increases the highest peak increases, whilst the lowest peak decreases in wavelength by a smaller amount.

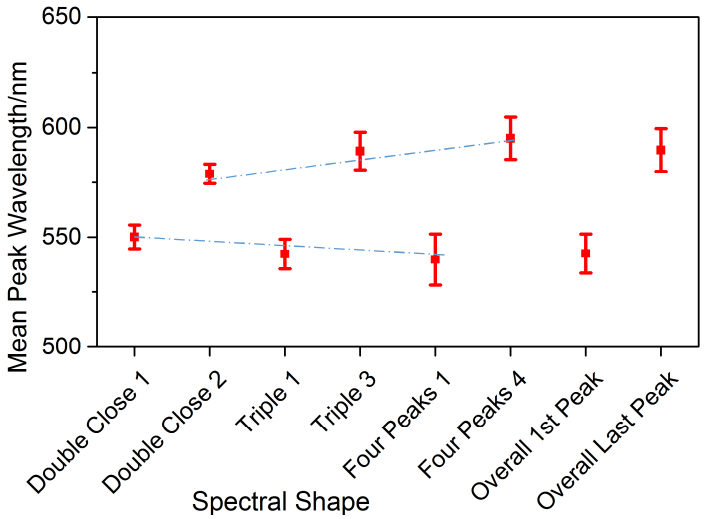


Figure 4.74 – Distribution of mean peak wavelength values with standard deviation errors of the highest and lowest peaks in the LL spectrum of each number of peaks for the *Protaetia himalayana* beetles. The number 1 corresponds to the lowest peak and the higher number corresponds to the highest peak value of each spectral shape. Dashed lines were added to highlight the trends of the lower and upper peaks.

4.4.3.9. Conclusion

Variation in the spectral responses of a significant number of specimens over seven species and one genus has been presented. There can be seen to be greater variation in some species (such as *Cetonia aurata aurata*) than others (such as *Ischiosopha aruensis*). There is a range of LL spectral shapes in different beetle species. For many species as the number of peaks within a LL spectrum became larger, the upper wavelength peak also increased in intensity. It is difficult to draw significant conclusions upon the response within these beetles, due to how they were selected. It does not take into account other variables such as if they were all collected at the same time and from exactly the same area. Another problem is the preference of the person who collected them, if they deliberately collected a certain look or colour of beetle, in which case there will be induced variation. There are other variations with smaller numbers of specimens in both the Appendix A3 and also Section 4.4.4.

4.4.4. Variation in other Species

Further to investigation of variations of large numbers of Cetoniinae, smaller numbers of specimens with variations from other Cetoniinae and Rutelinae are considered in this section.

4.4.4.1. Popillia

Four different variations of 103 specimens of the Rutelinae:*Popillia* genus based upon colour (blue, green, red, and a light green) from the same location in Tanzania in the same year were studied. It should be noted that the distribution of colours presented in this study may not be an accurate representation of their occurrence in nature and may be as a result of the collector's choice of colours. The spectra for each variation can be seen in Figure 4.75. It is not known if the beetles are the same species or different species. One other point to note was that the elytra of

the light green *Popillia species (sp.)* does not appear black through the RCP filter, whilst the other three variations do.

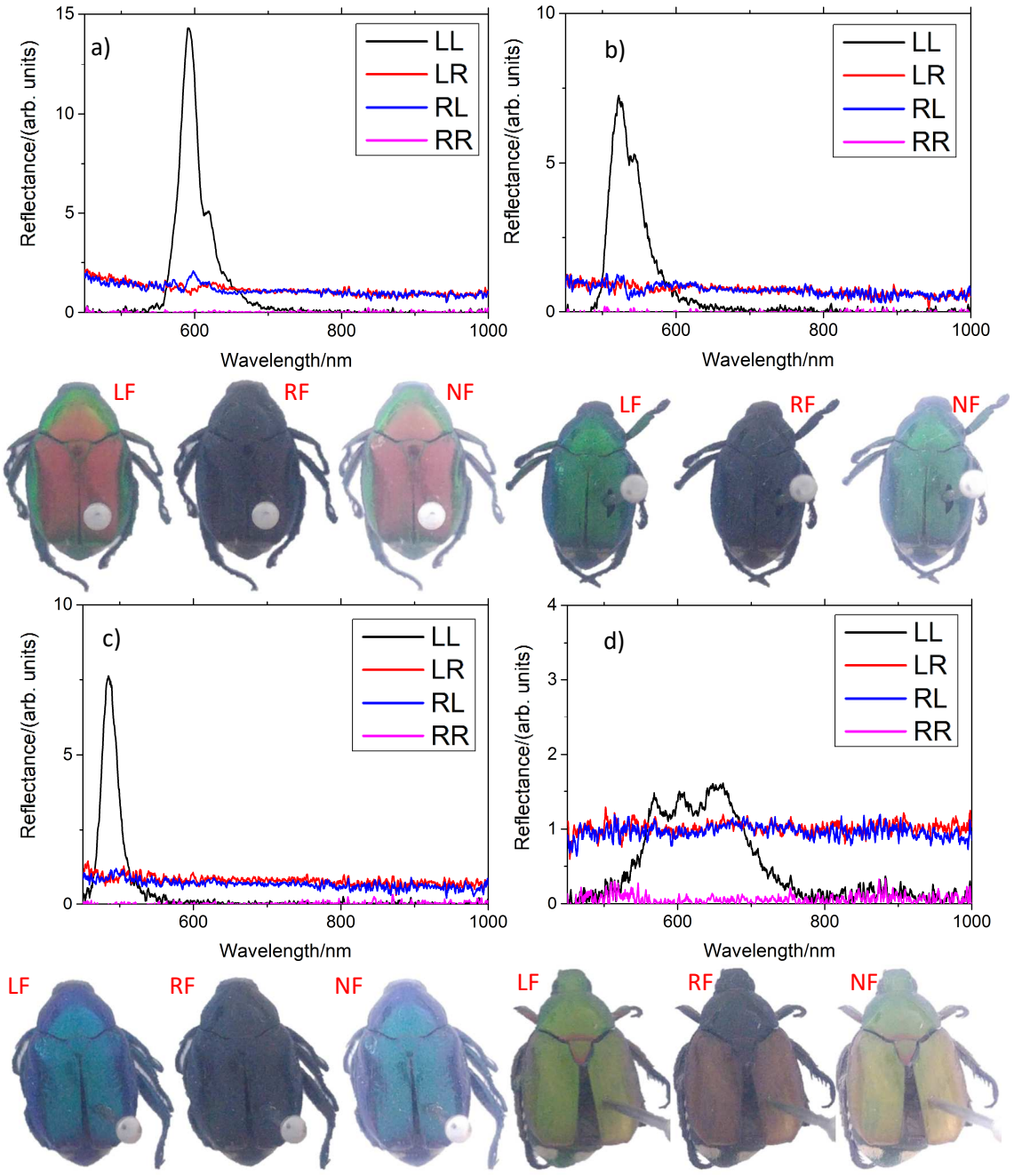


Figure 4.75 – CP reflection spectra from the elytron of an a) red, b) green, c) blue and d) light green *Popillia sp.* beetles. These specimens were collected from Mikumi National Park, Tanzania in 2013. The sizes of the different coloured popillia were a) ~12mm, b) ~13mm, c) ~11mm and d) ~11mm.

Of the 103 beetles the breakdown of different colours is shown in Figure 4.76. As can be seen the dominant colour is the red type *Popillia sp*.

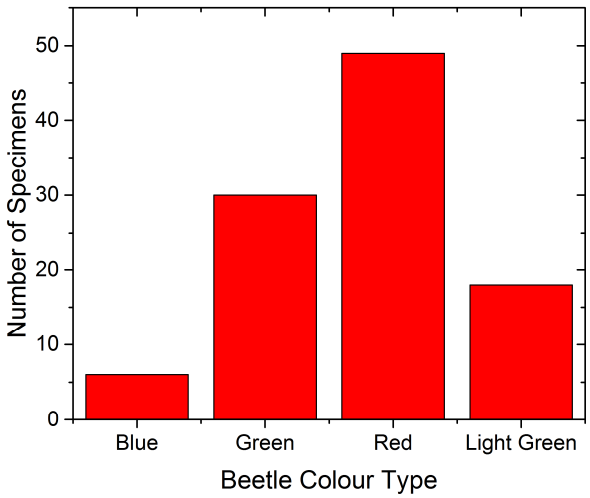


Figure 4.76 – Distribution of different colours of *Popillia sp* from Mikumi National Park, Tanzania.

The distribution of the main peak wavelengths in the LL spectra of each of the four colours were made in Figure 4.77, where it can be seen there are clear differences between the four colour classifications. The red beetles has consistently higher peak wavelength values than the green and blue variations. The light green variation lower peak mean varies far less than the upper peak value. The species of each colour form still need to be identified and as such the classification system could be a helpful tool in the process. It is especially promising in that there is such a definite difference between the four colour classifications.

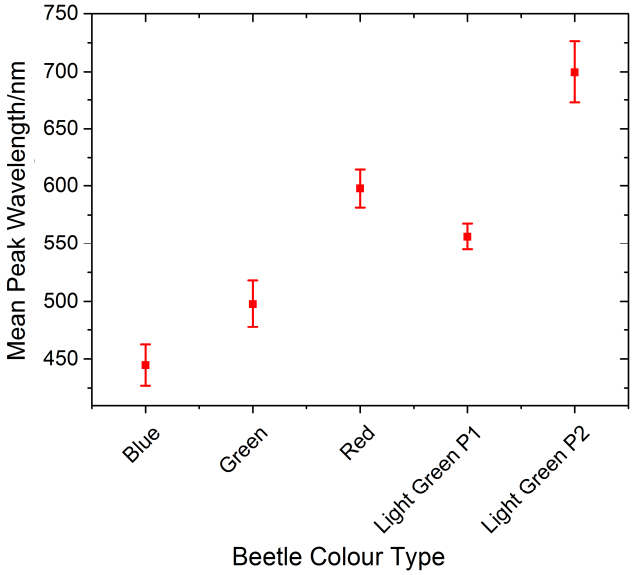


Figure 4.77 – Distribution of the main peaks in the LL spectra of the blue, green and red *Popillia sp*, whilst the lowest peak (P1) and highest peak (P2) of the light green *Popillia sp* are analysed. The mean values are calculated and standard deviation used in the error bars.

4.4.4.2. Cetonia aurata pisina

Unlike the variation in the previous section (4.4.3), which studied large numbers of specimens, spectra from four Cetoniinae:*Cetonia aurata pisina* specimens are presented (Figure 4.78).

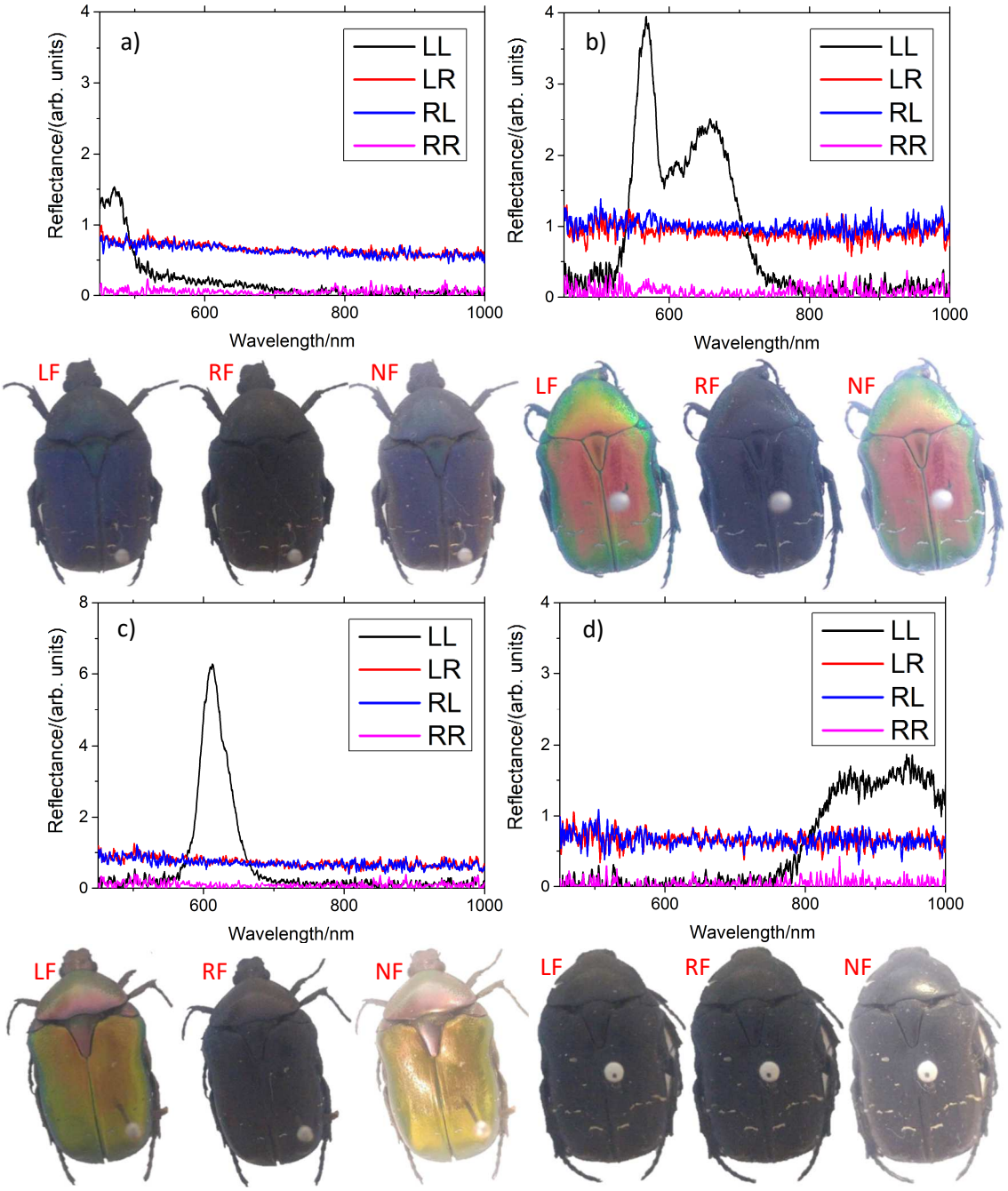


Figure 4.78 – CP reflection spectra from the elytra of a) a blue, b) a green-red, c) yellow-purple and d) black *Cetonia aurata pisina* beetles. These specimens were collected from Venaco, Haute-Corse, France in 2015. The specimens measure a) 21mm, b) 17mm, c) 20mm, and d) 20mm.

The four *Cetonia aurata pisina* beetles were all collected at the same collecting location in France upon the same day. These four specimens demonstrate a huge variation in the reflected wavelengths from blue (Figure 4.78a) to the NIR (Figure 4.78d). Though none of the specimens investigated in the study presented evidence of reflecting UV light, it is possible such species occur in nature. There can also be seen to be variation (although not presented) within a single species between the purple head and yellow elytra of the specimen in Figure 4.78c. As with *Cetonia aurata aurata* (a different subspecies) there is variation in the shape of the LL spectrum as well as the wavelength value. This variation in the shape and wavelength are very large which relate to large variations in pitches.

4.4.4.3. Cetonia carthami

As with the Cetoniinae:*Cetonia aurata pisina*, the four *Cetonia cathimi* specimens shown (all collected in Sardinia) demonstrate large variation within the species (Figure 4.79).

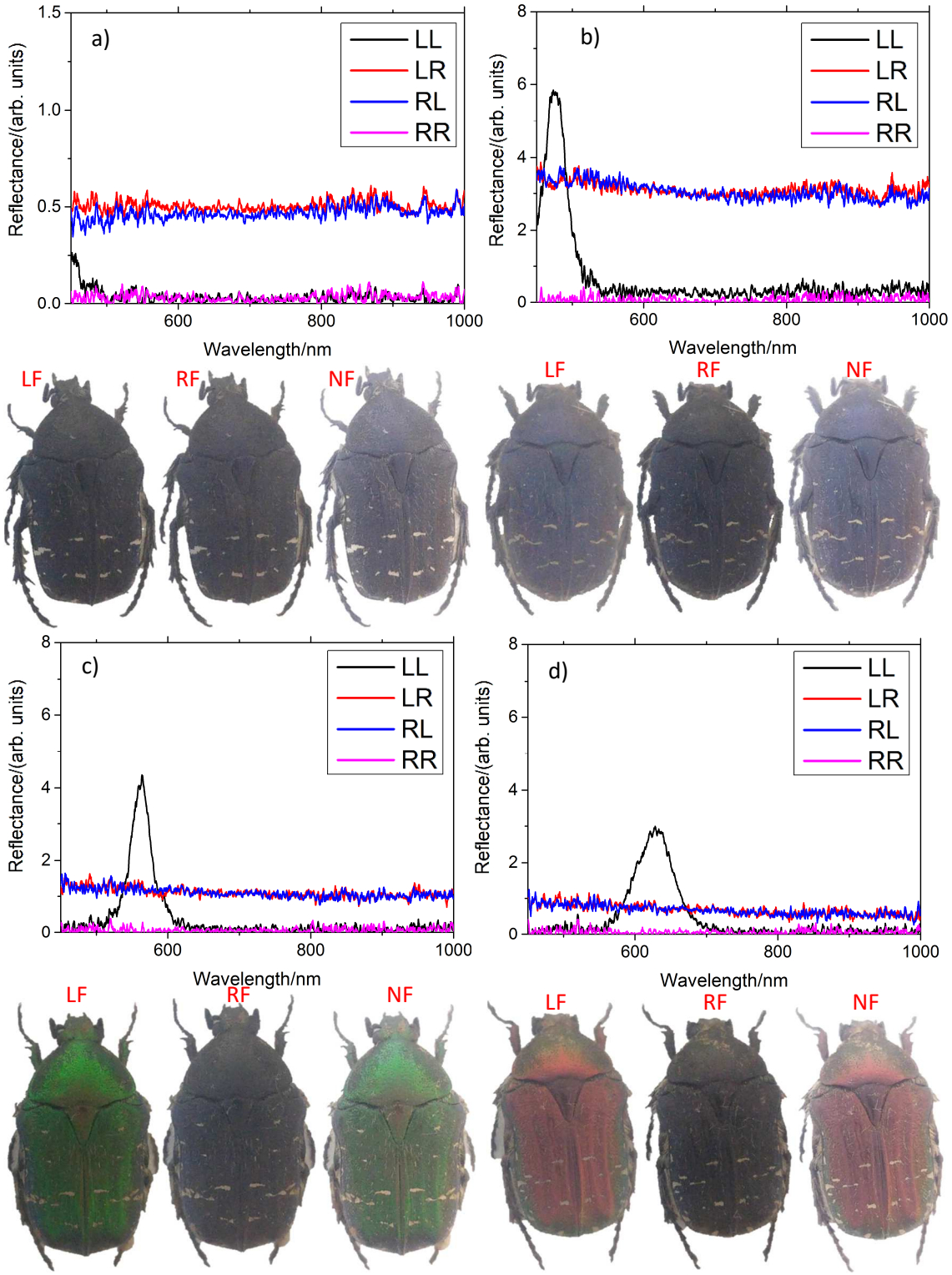


Figure 4.79 – CP reflection spectra from the elytra of black, blue, green and red *Cetonia carthami* beetles. These specimens were collected from Iglesias, Sardinia, Italy in 2013. a) and b) were taken with an integration time of 500ms and c) and d) with an integration time of 100ms. The specimens measure a) 16mm, b) 16mm, c) 16mm and d) 16mm.

Unlike the *Cetonia aurata* subspecies, variation in the shape of the LL peaks of *Cetonia cathimi* was not observed with single peaks occurring (although the LL peak cannot be observed in the

first specimen). Variation from blue to red was observed in the colours, with the first specimen's peak (Figure 4.79a) not being observable due to it being beyond the wavelengths recorded (<450nm). This specimen's LL spectrum (Figure 4.79a) can be seen to be increasing in a tail like way, suggesting the peak is at a lower wavelength, possibly in the UV. *Cetonia carthami* have previously been brought to the attention of CP study by Tamura-Wick in a Masters study [1], who found the peaks in blue, green and red specimens. The variations in the peaks in the LL reflection spectra relate to variation in the helicoidal pitch size.

4.4.4.4. Other Species

Two specimens of the Rutelinae:*Viridimicus cyanochlorus* were investigated, the first which was a male specimen, which under normal lighting conditions appeared to have a green pronotum and scutellum and a blue elytra for which single peaks can be seen in the LL spectra (Figure 4.80a and b).

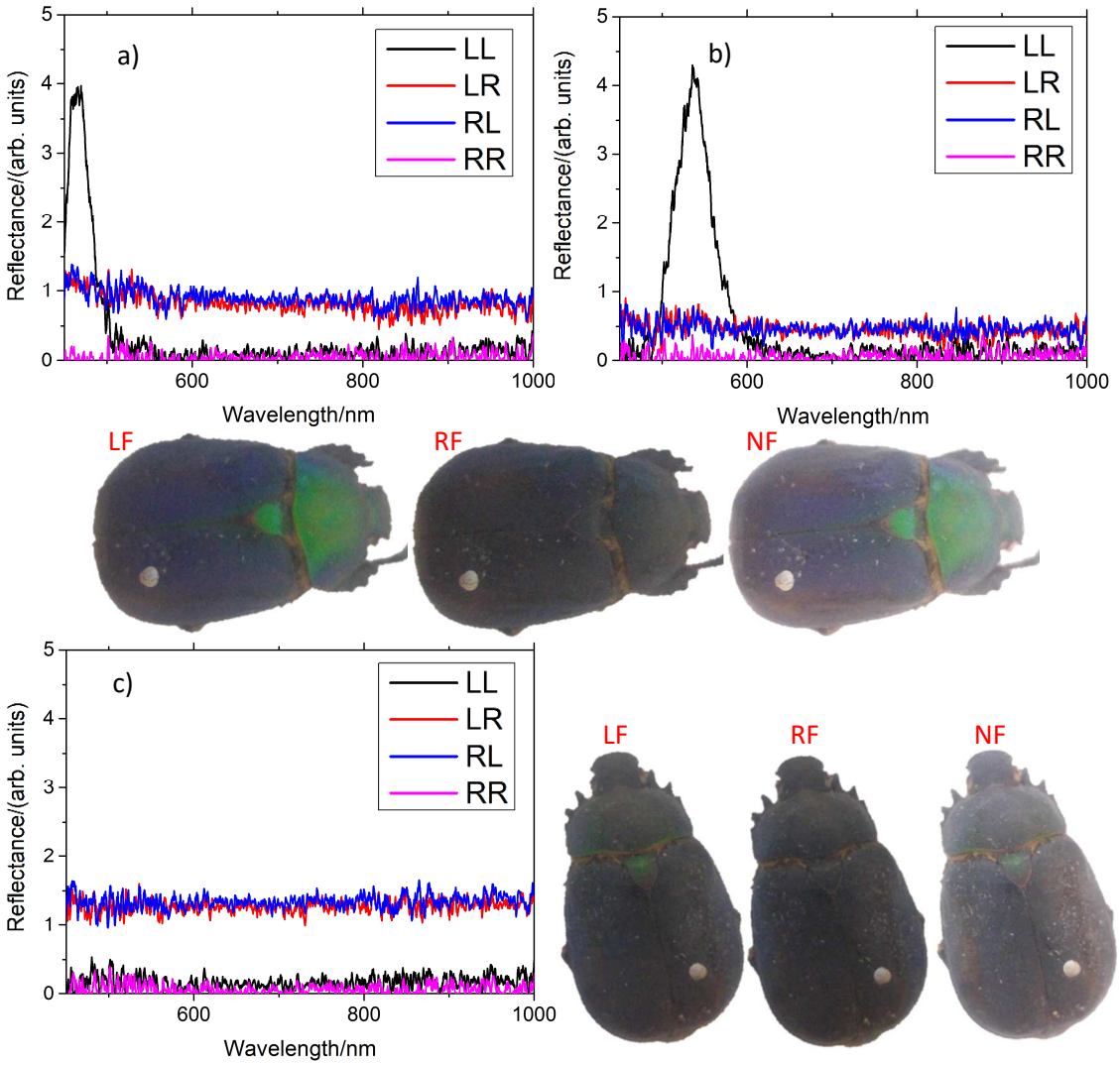


Figure 4.80 – CP reflection spectra from the a) elytron and b) pronotum of a male and c) the elytron of a female *Viridimicus cyanochlorus* beetles. These specimens were collected from San Sebastian, Oaxaca, Mexico in 2013. The specimens measure a) 27mm and c) 23mm.

The second specimen was a female whose appearance without a filter was completely black except the scutellum which was green (Figure 4.80c). The spectra from the elytra of the black

specimen showed no peaks in the LL spectrum (Figure 4.80c). Either there is a lack of helicoidal layers, melanin is in front of the helicoidal layers, or the pitches are at wavelengths beyond the visible range (most likely in the UV).

4.4.5. Notable Single Species Studied

In this section CP reflection spectra of species with notable CP spectra are presented, it should also be noted that there are measurements from many other species in Appendix A3.

4.4.5.1. Cetoniinae

The *Protaetia mirifica* beetle was a brilliant purple colour, this colour can be seen to be a result of the selective reflection of LCP light at two distinct wavelengths (Figure 4.81). This colour mixing occurs from a narrow intense peak in the blue wavelength mixing with a less intense but wider peak at red wavelengths. It should be noted that this species like many others in this study had measurements from multiple specimens. Multiple spectra were only presented when there was significant variations.

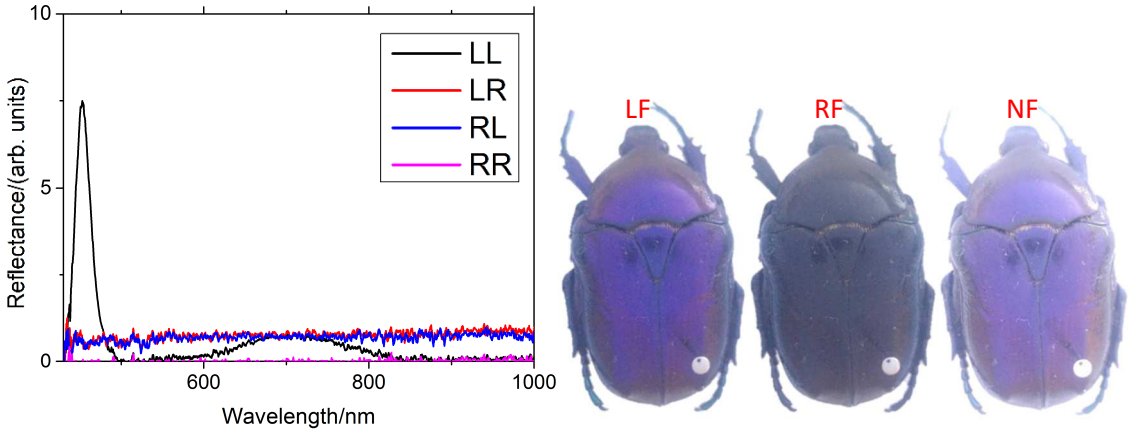


Figure 4.81 – CP reflection spectra from the elytron of a *Protaetia mirifica* beetle. This specimen was collected from Bois de Païolive, Ardèche France in 2013. The specimen measures 26mm.

As with the *Melolontha melolontha* beetle (Figure 4.20), the reflection spectra from the elytra of a *Plectrone tristis* beetle had dominant LR and RL spectra and a small LL peak. The peak in the LL spectrum occurred at a blue wavelength (Figure 4.82), however the colour difference between the beetle through a LCP and RCP is very subtle.

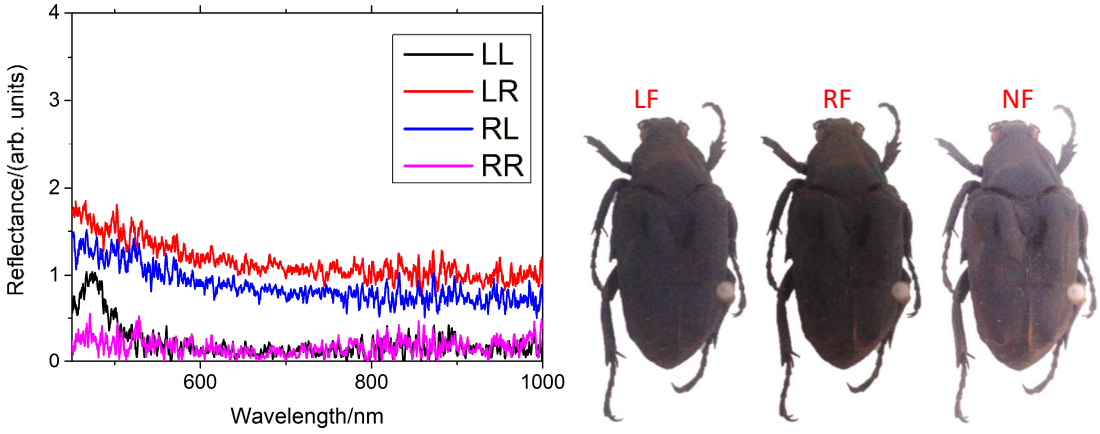


Figure 4.82 – CP reflection spectra from a green part of the elytron of a *Plectrone tristis* beetle. This specimen was collected in Sancary, Java, Indonesia in 2008. The specimen measures 27mm.

There were also variations within individual specimens of Cetoniinae, the first of which is a *Protaetia speciosa jousselini* beetle. A previous study took various polarisation images of this beetle [15]. The beetle has a red pronotum and blue-green elytra, the LL reflection spectra from these areas are single peaks (Figure 4.83).

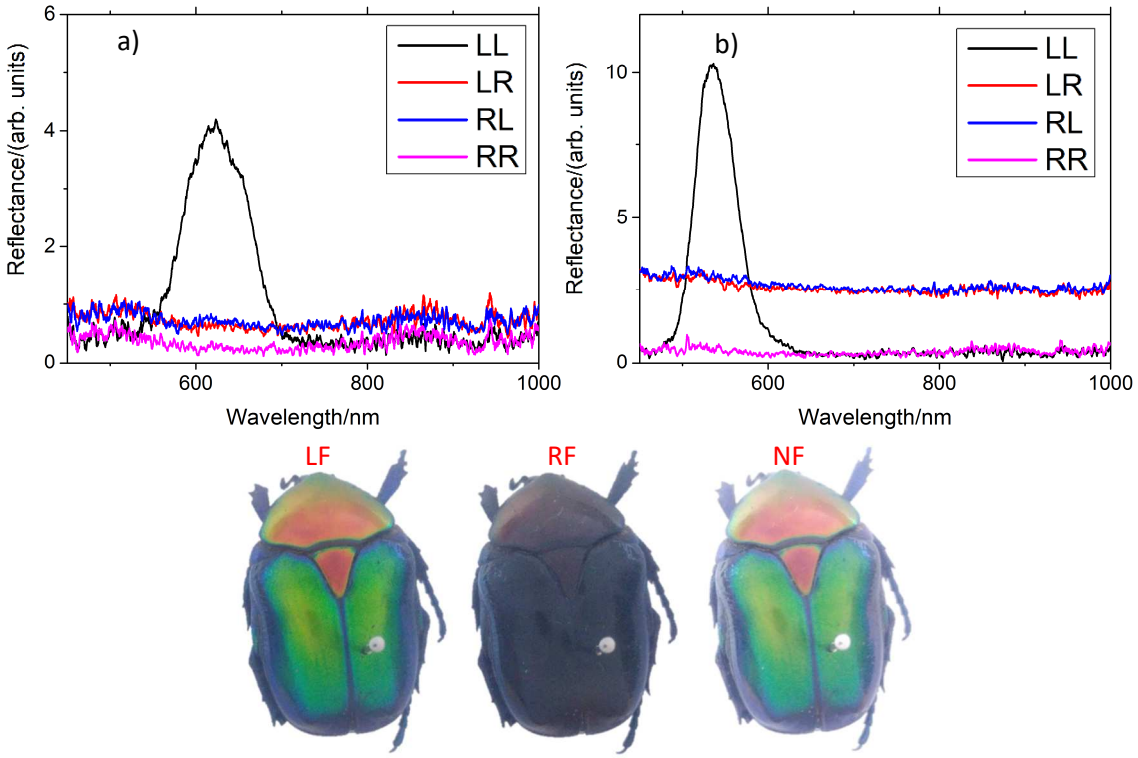


Figure 4.83 – CP reflection spectra from a) the red pronotum and b) the blue-green elytron of a *Protaetia speciosa jousselini* beetle. The specimen was collected from Turkey in 2014. The specimen measures 28mm.

Another variation of this species exists, where all the colours are blue shifted, where the elytra is blue and the pronotum and scutellum are orange-yellow (Figure 4.84).

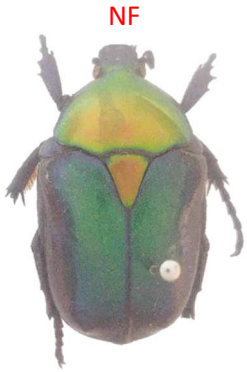


Figure 4.84 – Photograph of a variation of a *Protaetia speciosa jousselini* beetle which has blueshifted colours. The specimen measures 27mm.

Ischiopsopha (Lomaptera) jamesi (green form) [12] and the *Ischiopsopha (Lomaptera) jamesi coerulea* (blue form) [23], were previously mentioned in studies. This beetle was unusual in that there were three colours upon the elytra (being blue, green and orange) (Figure 4.85). The reflection spectra were relatively weak with the LR and RL spectra in the orange region being

larger than the LL spectrum, which has a small peak at an orange wavelength. Reflection from the blue region was much weaker, but the LL spectrum was dominant.

The orange area on the elytra, is surrounded by an outline of green, the orange colour is very angularly dependent in the photographs (Figure 4.85). This can be seen to be very similar to the angular dependence of the *Heterorrhina sexmaculata* beetle (Figure 4.86), whose optical structure has been described in great detail [38]. It should be noted the *Hetterorrhina sexmaculata* beetle does not selectively reflect CP light. This suggests that since there is a peak in the LL reflection spectrum from the orange part of the *Ischiosopha jamesi coerulea* elytra, there are also helicoidal structures in this region.

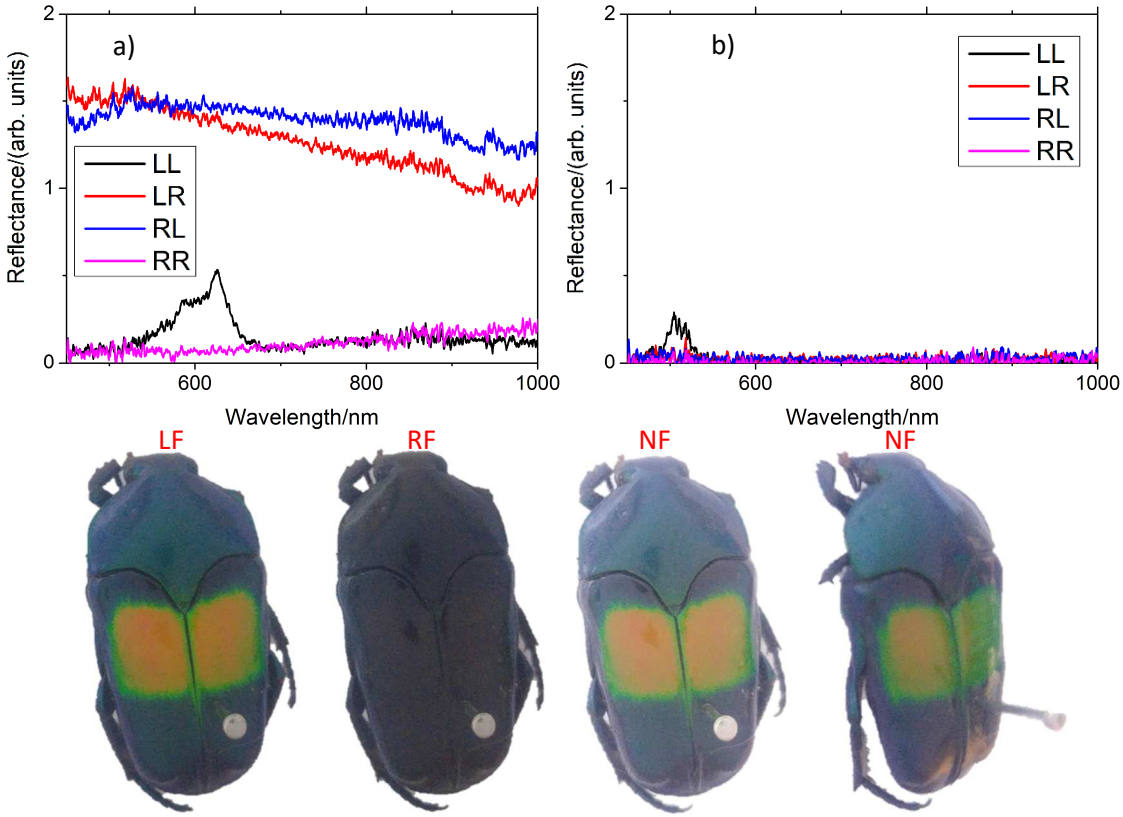


Figure 4.85 – CP reflection spectra from the right elytron in the orange part a) and the blue part b) of an *Ischiopsopha jamesi coerulea* beetle. This specimen was collected from Papau New Guinea in 2014. The CP spectra were taken with an integration time of 500ms. The specimen measures 27mm.

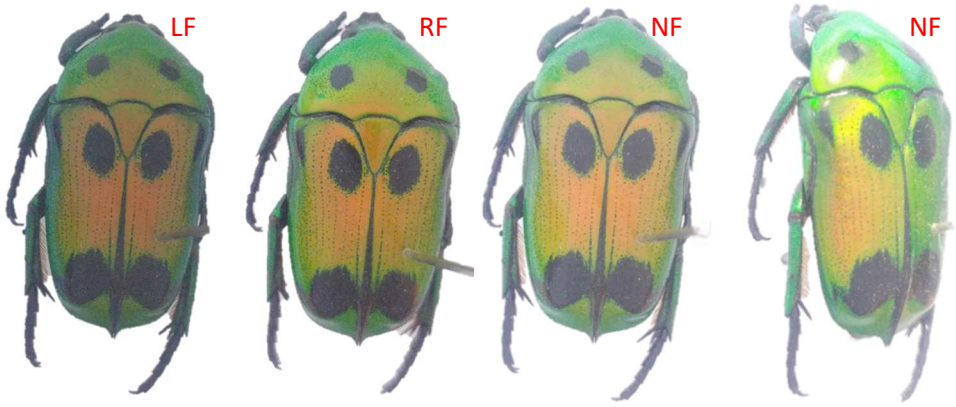


Figure 4.86 – Photographs of *Heterorrhina sexmaculata*, through a range of CP filters. The last photograph demonstrates the large angular variation in colour of this beetle. The specimen measures 26mm.

4.4.5.2. Rutelinae

The *Anoplognathus* aureus beetle was very similar in appearance (albeit half the size) to many of the metallic gold *Chrysina* beetles. Previous studies have been carried out upon this species [39],[40] and several others have been published upon other species of this genus [12],[14],[17],[23],[41]. This beetle had a strong LL response with weaker LR and RL responses and a negligible RR response (Figure 4.87).

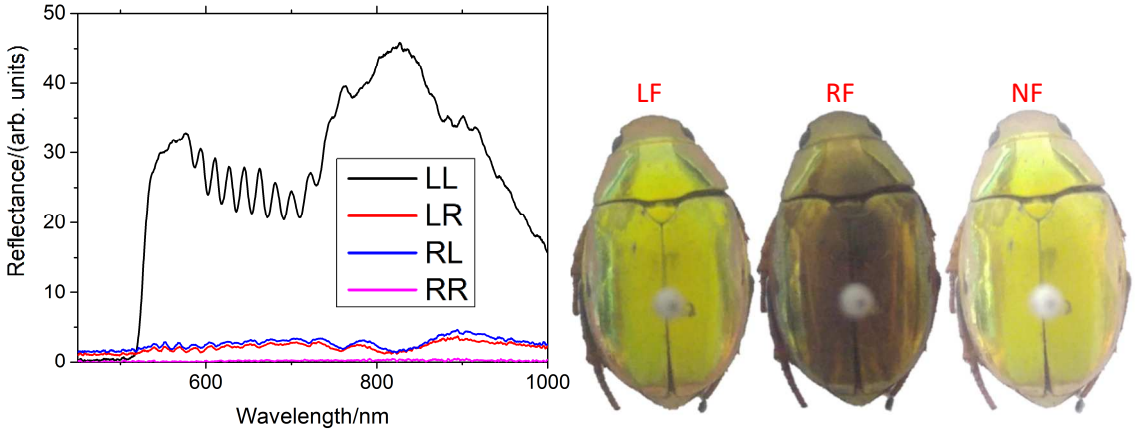


Figure 4.87 – CP reflection spectra from the elytron of an *Anoplognathus aureus* beetle. This specimen was collected from Polly Creek, Garradunga, North Queensland, Australia in 2015. The specimen measures 17mm.

The three *Anoplognathus porosus* beetles studied all had a green pronotum and scutellum with the elytra visually appearing to reflect very little LCP as can be seen in the inset photos (Figure 4.88). Unlike the *Anoplognathus aureus* beetle, this species has a narrowband response in the green wavelength with a double peaks together in the LL spectrum (Figure 4.88). The appearance of this beetle suggests a large reduction in the helicoidal structure upon the elytra compared to the pronotum and scutellum.

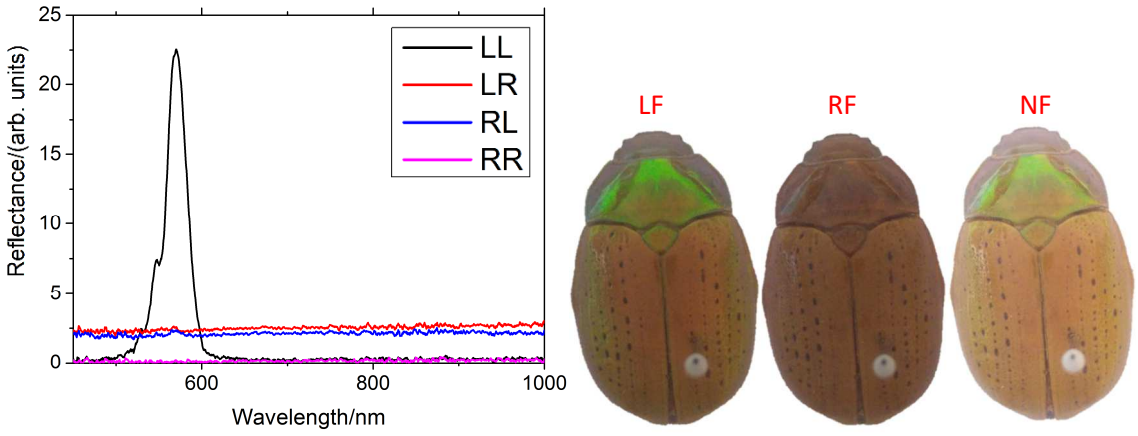


Figure 4.88 – CP reflection spectra from the pronotum of an *Anoplognathus porosus* beetle. This specimen was collected from Polly Creek, Garradunga, North Queensland, Australia in 2015. The specimen measures 18mm.

The *Chysophora chrysochlora* species has elytra which is more 'textured'. This texturing leads to a more diffuse reflection, which makes for a much lower measured intensity LL spectrum (Figure 4.89). Previous experiments upon *Chrysophora chrysochlora* have been undertaken, including

imaging [15] and measurement of the polarised reflection [42] which had more peaks than the LL response in Figure 4.89.

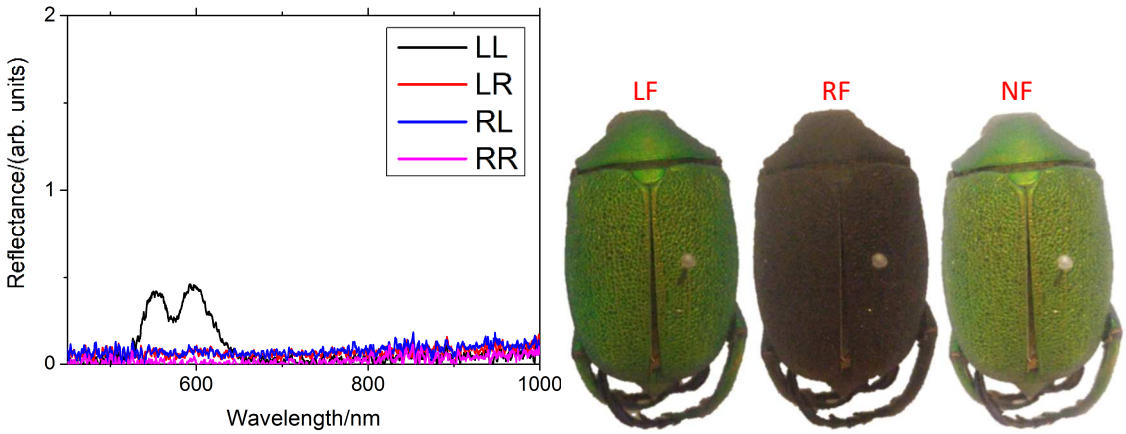


Figure 4.89 – CP reflection spectra from the elytron of a *Chrysophora chrysochlora* beetle. This specimen was collected in Peru in 2015. The CP spectra were taken with an integration time of 500ms. The specimen measures 29mm.

Unlike the *Anoplognathus porosus* species, which had a colourful pronotum and dull elytra, the *Rutela laeta* beetle has a colourful elytra, but dull scutellum and pronotum (Figure 4.90). The LL spectrum in Figure 4.90 has numerous peaks or both sides of the main peak which is at a green wavelength. The pronotum can be seen to have two colours (black and brown), which are known colours of melanin.

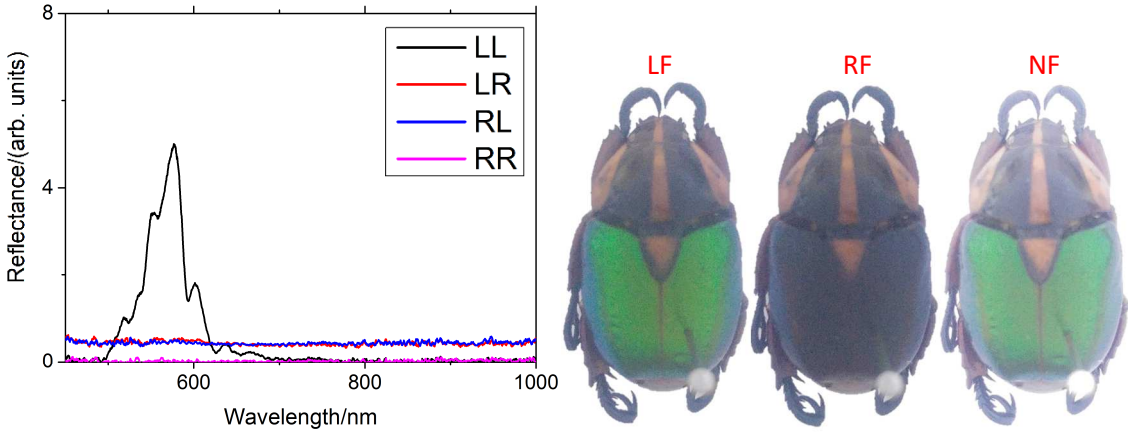


Figure 4.90 – CP reflection spectra from the elytron of a *Rutela laeta* beetle. This specimen was collected from San Fernando de Apure, Venezuela in 2016. The CP spectra were taken with an integration time of 500ms. The specimen measures 21mm.

In the species *Mimela ohausi* the colour varies over the body with blue on the scutellum to green, red and yellow on the elytra. The variation in the colours in the elytra was measured and can be observed in the LL spectra in the predominantly green (Figure 4.91a) and red areas (Figure 4.91b). These variations are likely due to variations in the helicoidal pitch. This example is unusual in that the variation in the elytra is more gradual than other species.

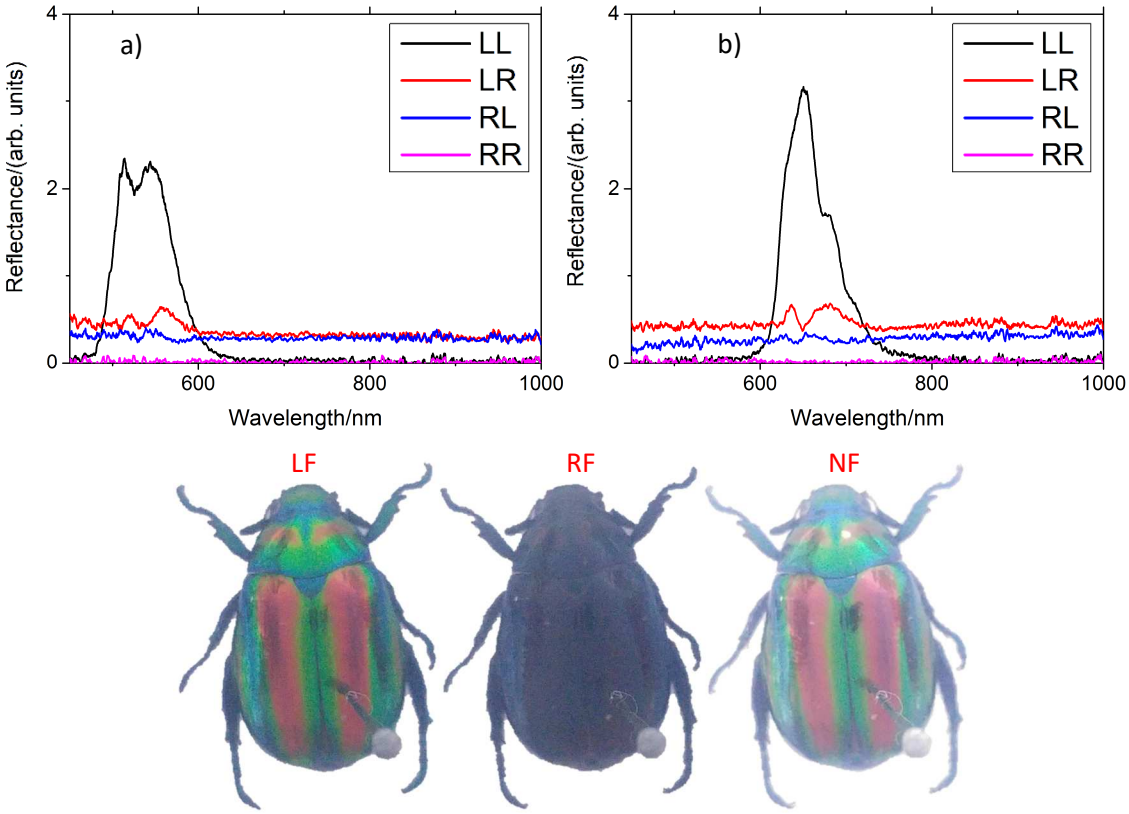


Figure 4.91 – CP reflection spectra from a) the green part and b) the red part of the elytron of a *Mimela ohausi* beetle. This specimen was collected from Phou Pane Mountain, Houaphanh, Laos in 2012. The CP spectra were taken with an integration time of 500ms. The specimen measures 17mm.

4.4.5.3. Scarabaeinae

In addition to the Scarabaeinae beetle with a broadband gold reflection in the LL spectrum (Figure 4.27), there are also species which reflect more narrowband spectral peaks such as the *Phaneus mexicanus* (Figure 4.92).

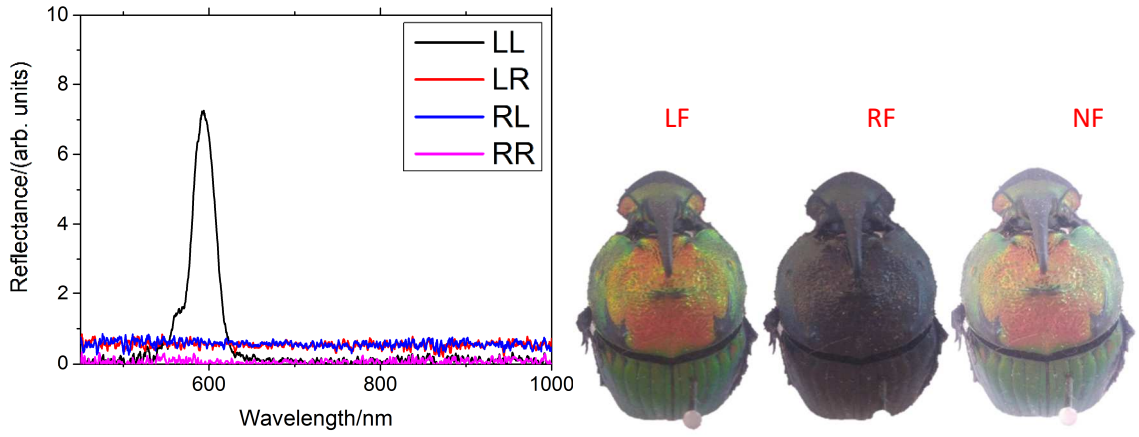


Figure 4.92 – CP reflection spectra from the pronotum of a male *Phanaeus mexicanus* beetle. This specimen was collected from Catemaco, Veracruz, Mexico in 2004. The specimen measures 23mm.

4.4.5.4. Phaenomeridinae

Further to the blue specimen in Figure 4.26, other colour variations of the *Phaenomeris besckei* beetle were investigated including green (Figure 4.93) and turquoise examples (Appendix Figure

A 121). Unlike the blue specimen the LL spectra in the green and turquoise specimens are not the dominant spectra.

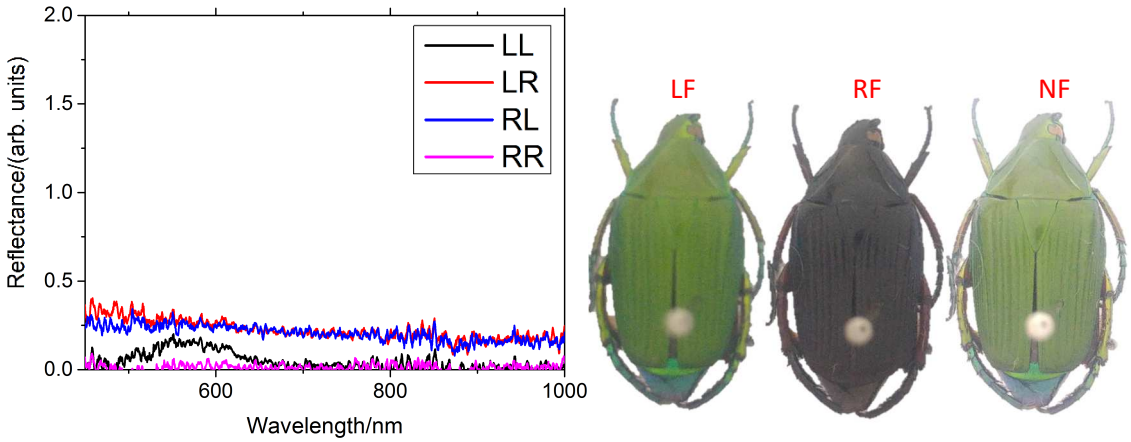


Figure 4.93 – CP reflection spectra from the scutellum of a green *Phaenomeris besckei* beetle. This specimen was collected from Tanzania. The CP spectra were taken with an integration time of 500ms. The specimen measures 20mm.

4.5. Lack of Circularly Polarised Response in Rhomborhina gigantea

It has been reported that the optical response and colour of the *Rhomborhina gigantea* beetle was due to a structure which is a biological analogue to a CLC [43] (also previously in a brief report [44]). However from the data presented in this section it will be shown that this is not the case.

In [43] it was stated "Scarabaeid beetles are similar to CLCs optically, such as selective reflection of LCP light and brilliant metallic appearance [12]". Whilst true that there are numerous examples of Scarabaeidae beetles which do have such structures (and reflect CP light), many species do not [10]. The paper by Ching *et al* also stated:

"The fact that the cross-section of the elytron of *R. Gigantea* (Fig. 2(a)) resembled to that of *Dynastes Hercules* [45], which is also a species of the family Scarabaeidae, implicates that *R. Gigantea* could also possess optical chirality analogues to CLCs."

The *Dynastes hercules* is however not very colourful and also not identified by Pye as selectively reflecting CP light, despite being present in the Natural History Museum collection he investigated (CP light) [10]. Further to this the reference to a discussion of *Dynastes hercules* structure [45], describes the hygrochromic effect in the cuticle and makes no mention of any CLC like structure. As such suggesting that *R. Gigantea* has a similar structure to *Dynastes hercules* does not imply that it could possess a chiral analogue to CLCs. It is worth noting that other structure colours (other than helicoidal) produce green colours in the Cetoniinae subfamily such as *Heterorrhina sexmaculata* (Figure 4.86).

Experimentally the first indicator that *R. Gigantea* does not reflect CP light is that in the photographs of the beetle taken through LCP and RCP filters are of the same appearance (and colour) (Figure 4.94). A beetle whose colour is caused by a CLC like structure will generally appear colourful through a LCP filter and dull through a RCP filter (e.g. Figure 4.19). There are uncommon exceptions to this indicator, which have been observed in *Chrysina (Plusiotis) cupreomarginata* specimens (Figure 4.30), where both LCP and RCP light are selectively reflected due to a half waveplate like layer between chiral stacks of chitin [14]. (It should be noted that there are beetles with CLC-like structures that do not reflect visible CP light either due to a layer of melanin near the surface (giving a pigmentary brown or black colour and potentially blocking colour structures behind) [36] or reflecting in the NIR [9]).

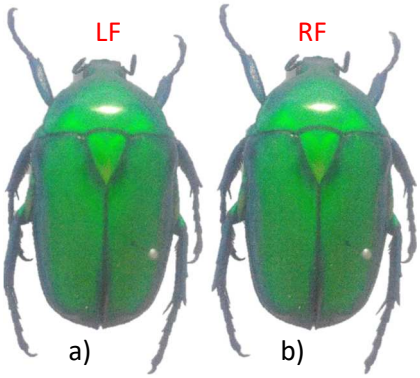


Figure 4.94 – Photographs of a Cetoniinae:*Rhomborhina gigantea* beetle through a) a left circularly polarised filter, b) a right circularly polarised filter. The specimen measures 37mm.

In order to determine if the *Rhomborhina gigantea* selectively reflects any CP light, spectra were taken using a setup described at the start of this section.

The typical reflection spectra from a beetle which has a simple CLC-like stack of a relatively finite pitch value can be seen earlier in this chapter, with a dominant LL spectrum. Reflection spectra from the *Rhomborhina gigantea* beetle were taken with the same setup. However when aligning the specimen in the system it was observed that the reflected beam appeared an intense white-red in the centre and green around the outside (Figure 4.95).

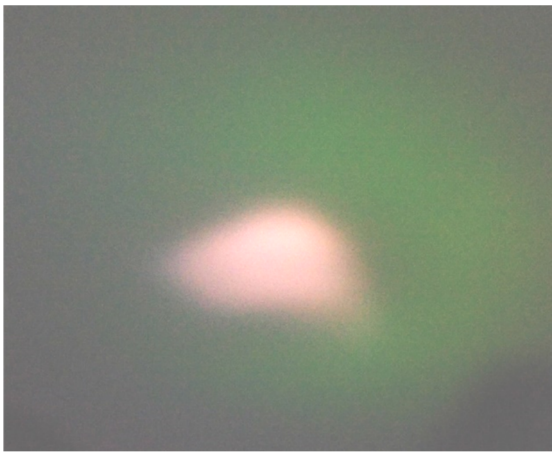


Figure 4.95 – Photograph of the reflected spot from the scutellum of a *Rhomborhina gigantea* beetle.

The white-red centre reflection spectra (Figure 4.96a) acted as a weak mirror with the LL and RR spectra being negligible and the LR and RL being non zero and relatively flat. The green halo however had a different response in that all the spectra were flat and negligible except LR and RL, where a similar small peak occurred in both at green wavelengths (Figure 4.96b). The halo around a mirror-like spot suggests some structural reflection, which was described from the SEM by Ching *et al* as being formed "by layers parallel to the outer surface and an array of perpendicular ridges supported by vertical columns (diameter ~0.55 µm)" [43]. It can be concluded however that a chiral stack is not responsible for the green appearance of the beetle with no CP light being selectively reflected (Figure 4.96b).

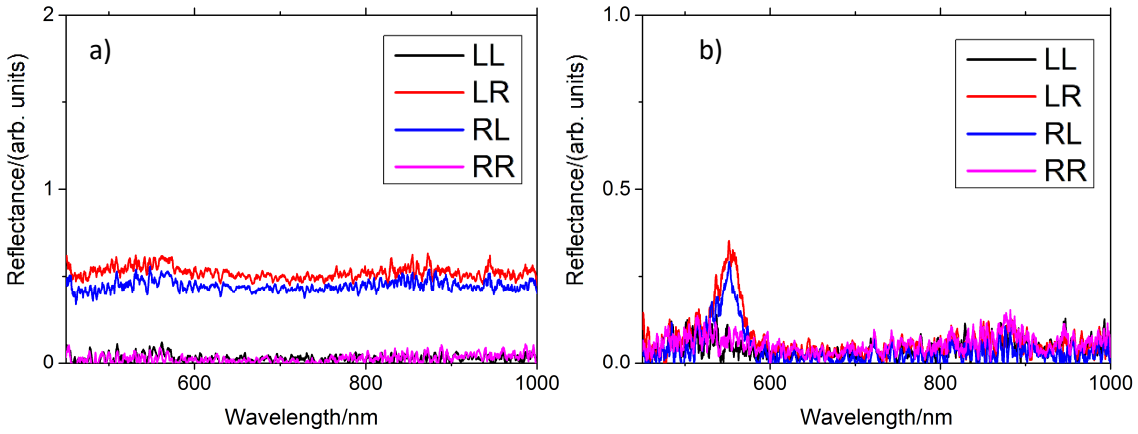


Figure 4.96 – CP relectance spectra from the scutellum of a *Rhomborhina gigantea* beetle from a) the centre reflection spot and b) the green halo. The black spectra is LL, red is LR, blue is RL and pink is RR. The CP spectra were taken with an integration time of 500ms.

4.6. Other Observed Variations

4.6.1. Variation on the Underside

As well as variations in the top side of the beetles which have been previously discussed in this section, there are differences to the underside in terms of both colour and intensity. This variation was not experimentally measured, but was simply observed by taking photographs through CP filters.

The first type of variation, observed in *Plectrone endroedii* has an underside which is a similar colour to the topside (Figure 4.97), with LCP reflection occurring in both the top and underside of the beetle. The next type of variation is when the colour is of the underside is different to that of the topside. In Protaetia cuprea cuprea (Figure 4.98) the top side is green whilst the underside is purple. In some species such as *Chrysina chrysargyrea* the topside is a uniform colour, whilst the underside and legs vary in colour, in this species an almost rainbow variation in colour occurs (Figure 4.99). One of the starkest changes between the upperside and underside are in the metallic *Chrysina* species which reflect a significant amount of RCP light (Section 4.4.2.1). An example of this occurred in *Chrysina cupreomarginata*, which is colourful in both LCP and RCP filters on the upper side, whilst duller in the RCP filter in the underside (Figure 4.100). Though

not pictured the same CP response from *Chrysina resplendens* was observed (Appendix Figure A 127) and measurements of the underside have been studied [46]. Other examples are also shown in Appendix A3.10. The reason for the underside and upper side being different are not completely clear. The upper side is often more visible in the natural environment than the underside, so could be due to some optical function.

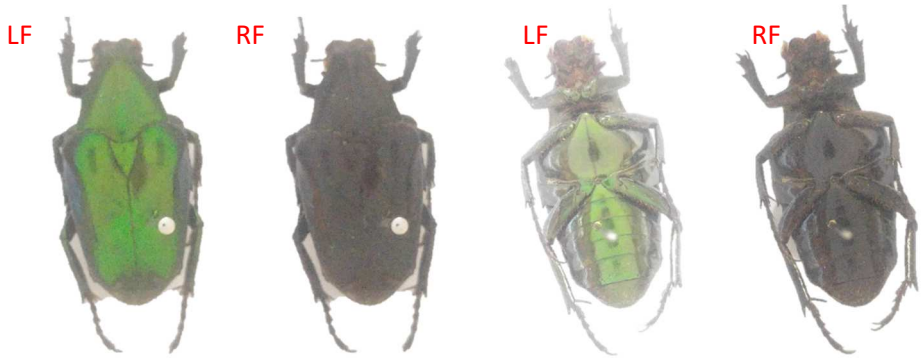


Figure 4.97 – Photographs with CP filters of the upper side and underside of a *Plectron endroedii* beetle.

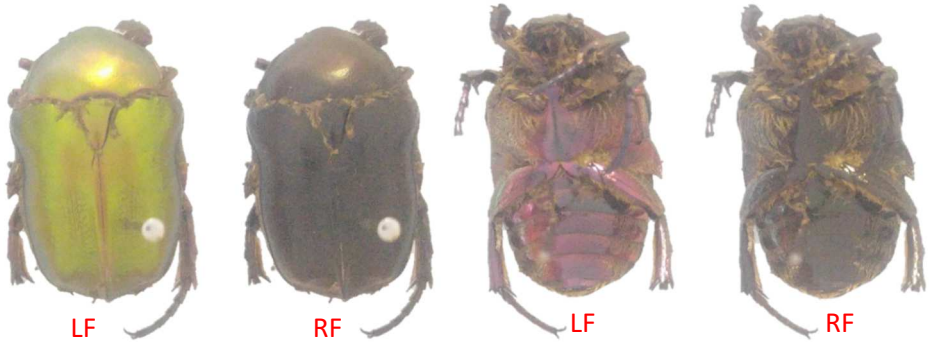


Figure 4.98 – Photographs with CP filters of the upper side and underside of a *Protaetia cuprea cuprea* beetle.

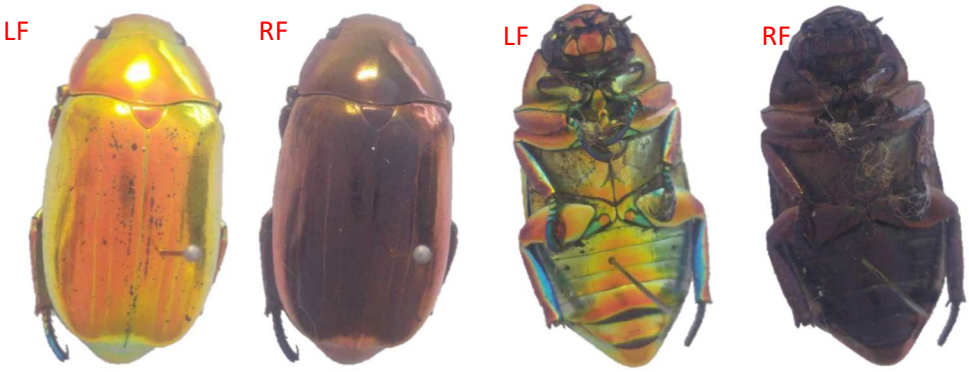


Figure 4.99 – Photographs with CP filters of the upper side and underside of a *Chrysina chrysargyrea* beetle.

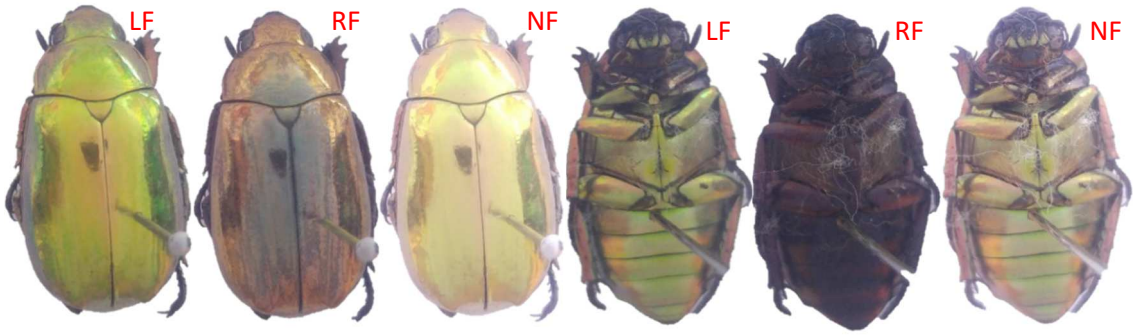


Figure 4.100 – Photographs with and without CP filters of the upper side and underside of a *Chrysina cupreomarginata* beetle.

4.6.2. Angle Variation

As discussed in Section 3.4.1 and from equation 3.13, it can be seen that the optical responses from the helicoidal structure within the beetles' shells are angularly dependent. There are several examples of angular dependence in beetles in this section. The first example is a *Protaetia speciosa jousselini* beetle whose appearance changes in the pronotum from orange-red (at near normal incidence) to a more yellow colour (as the viewing angle increases) (Figure 4.101). The same blueshift appears upon the elytra with the green-blue colour becoming a darker blue at a larger viewing angle. The *Chrysina curoei* beetle is a broadband reflector, however at normal incidence a pink colour is visible, this becomes a more yellow or golden shade at wider reflection angles (Figure 4.102). The *Garreta azureus* beetle has lower CP reflection and as such the angular dependence is not so visible (Figure 4.103). Further examples of angular variation are shown in Appendix A3.11.

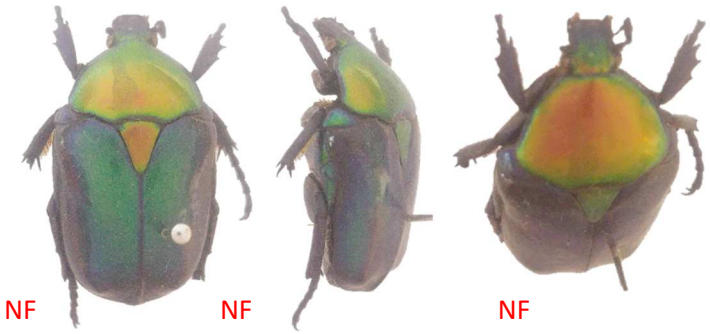


Figure 4.101 – Photographs without a filter of a *Protaetia speciosa jousselini* specimen at different angles.

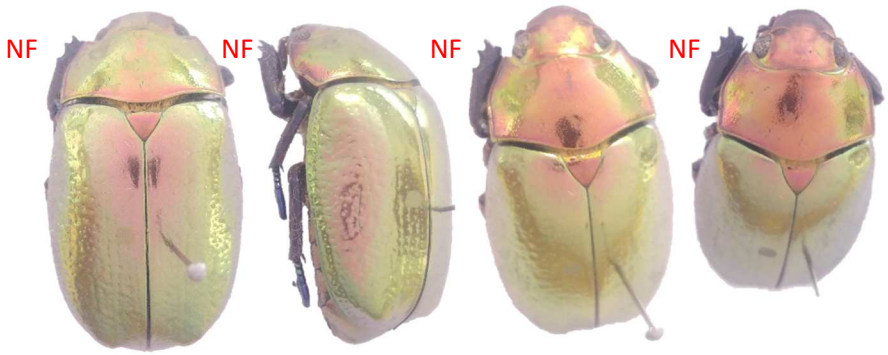


Figure 4.102 – Photographs without a filter of a *Chrysina curoei* specimen at different angles.



Figure 4.103 – Photographs without a filter of a *Garreta azureus* specimen at different angles.

4.7. Conclusion

In this Chapter the development and refinement of a setup to measure the CP reflection response from various beetles was made. As well as a technique of using passive 3D cinema glasses to broadly identify specimens which selectively reflect CP light, an imaging setup was created in order to take photographs of CP reflection from the beetle using lenses from the 3D glasses.

Further to the development of the experimental setup characteristics measurements of the reflection responses from the shells of the beetles were made. A wide degree of variation in the CP spectra was observed. In this study typical CP reflection spectra from nine different subfamilies were taken to demonstrate the wide ranging spectral types from a taxonomic point of view.

The *Chrysina* genus had both broadband (e.g. *Chrysina limbata*) and more narrowband (e.g. *Chrysina macropus*) LCP reflection responses. The difference in spectral reflection width has been previously shown to be due to different pitch values in the helicoidal structure. Variations in the intensity of CP responses also occurred with less intense beetles (typically green) as well as more intense metallic reflections occurred (typically gold and silver). The intensity variation occurs between species such as *Chrysina limbata* (high intensity reflection) and *Chrysina macropus* (low intensity reflection) and within the species *Chrysina boucardi*. The variation between the high and low intensity reflection in this species has been discussed as being due to a surface mirror like structure. Colour variation also occurred in the broadband high intensity spectra of *Chrysina optima* (from red to gold and silver) and in the more narrowband *Chrysina modesta* (with green and brown forms). The colour variation in both species appears to be the removal of lower reflection wavelengths, which was shown in previous studies of *Chrysina aurigans* and *chrysargyrea* to be due to variation in the helicoidal pitch thickness.

Building upon a large number of previous studies of *Chrysina resplendens* beetles, several other *Chrysina* species were found to reflect both LCP and RCP light. These were divided into three

distinct categories, the first of which included *Chrysina cupreomarginata* and had high intensity reflection in the LL and RR on a similar order of magnitude at most wavelengths. The second contained lower reflecting specimens (such as *Chrysina tricolour*), which reflected LCP light in the visible range and both LCP and RCP light in the NIR. The third classification (e.g. *Chrysina clypealis*) was similar to the first in the high metallic and broadband response, the difference being that the RCP response was of an order of magnitude lower than the LCP. These differences were suggested to be due to the variation in the location of a half waveplate uniaxial layer in relation to the helicoidal stacks.

Other variations in *Chrysina* were also discussed such as in different body parts of *Chrysina vitoriana*.

The variation of larger numbers of Cetoniinae specimens in a genus (*Lomaptera*) and then in single species was considered. In the *Lomaptera* genus various spectral shapes were observed from single peaks to multiple peaks both close together and further apart. It was observed that the single peak was not the dominant feature.

Within some individual species less LL spectral variation occurred, with the *Protaetia brevitarsis* species having variations with a larger number of peaks. It was interesting to note as the number of peaks increased the highest wavelength in the LL spectra also did, whilst the lower wavelength peaks decreased (but at a smaller rate). Such variation in the reflected wavelength implies complex pitch structures. Other Cetoniinae were also investigated including large numbers of other species, this included *Protaetia himalayana*. An underdeveloped specimen of this species was measured and was seen to be blue shifted compared to the normal green colour of an adult beetle's shell.

Variation was also observed in four colour forms of *Popillia sp*. from the same location. Analysis of the LL reflection spectra from the four colour variations showed distinct peaks, leading to the possibility of using the CP response as a classification technique. In the species *Cetonia aurata pisina* reflected LL wavelength variation occurred from blue to the NIR. It is also worth noting that *Cetonia cathimi* appeared to have a specimen whose reflection wavelength was lower than measurable by the setup (450nm) and it is suggested some beetles may reflect in the UV.

Other striking optical examples were discussed, such as the colour mixing in LL spectrum (of a narrow intense blue peak and less intense but wider red peak) in a purple *Protaetia mirifica*. The beetle *Mimela ohausi* had a large colour variation across all of the visible spectrum within the elytra, which suggests a huge variety in pitch value. Another variation was in *Ischiosopha jamesi coerulae*, which appeared to have both helicoidal colour structures and a surface structure whose optical structures vary with angle.

An investigation of the *Rhomborhina gigantea* beetle showed that it did not reflect CP light. This finding was contrary to a previous study which suggested the colour was due to a CLC like structure.

Photographs were taken which demonstrate angular variation in several beetles, which resulted in a blue shift when viewed away from normal incidence. Finally, CP photographs were taken of the variation in the underside of various beetles. The most interesting was *Chrysina cupreomarginata* which is known to reflect both LCP light from the top and bottom of the shell, but only appears to significantly reflect RCP from the top.

4.8. References

[1] H. Tamura-Wicks, "Final Report : Polarised Light in Nature An Experimental Assessment of Beetles - MSci Thesis," Imperial College, London.

[2] I. E. Carter, "A Study of the Polarising Properties and Structural Characteristics of the Shells of Several Species of Scarab Beetles of the Genus Lomaptera - MRes Thesis," Imperial College London, 2013.

[3] S. Hecht, "The Visual Discrimination of Intensity and the Weber-Fechner Law," *J. Gen. Physiol.*, vol. 7, no. 2, pp. 235–267, 1924.

[4] E. Hecht, *Optics - ISBN:9781292021577*, 4th ed. Harlow: Pearson Education Limited, 2014.

[5] M. Polyanskiy, "Refractive Index of N-BK7." [Online]. Available: http://refractiveindex.info/?group=SCHOTT&material=N-BK7. [Accessed: 08-Aug-2013].

[6] Comar Optics, "Comar Optics: Achromatic Retarder." [Online]. Available: http://www.comaroptics.com/components/filters/retarders/achromatic-retarders.

[7] Ocean Optics, "DH-2000 BAL." [Online]. Available: http://oceanoptics.com/product/dh-2000-bal/. [Accessed: 20-Apr-2016].

[8] I. Daly, "Polarised Light in Nature An Experimental Assessment of Beetles - MSci Thesis," Imperial College, London, 2012.

[9] I. E. Carter, K. Weir, M. W. McCall, and A. R. Parker, "Variation in the circularly polarized light reflection of Lomaptera (Scarabaeidae) beetles," *J. R. Soc. Interface*, vol. 13, no. 120, pp. 1–9, Jul. 2016.

[10] J. D. Pye, "The distribution of circularly polarized light reflection in the Scarabaeoidea (Coleoptera)," *Biol. J. Linn. Soc.*, vol. 100, no. 3, pp. 585–596, Jun. 2010.

[11] S. Peslier, "Note de chasse à Kalesmeno (Grèce), localité… très colorée," *R.A.R.E*, vol. XVII, no. 1, pp. 38–39, 2008.

[12] A. C. Neville and S. Caveney, "Scarabaeid beetle exocuticle as an optical analogue of cholesteric liquid crystals," *Biol. Rev. Camb. Philos. Soc.*, vol. 44, pp. 531–562, 1969.

[13] L. T. Mcdonald, T. A. Starkey, and P. Vukusic, "Photonic architectures in beetles: twists and iridescence," *Int. J. Des. Nat. Ecodynamics*, vol. 9, no. 4, pp. 266–275, Dec. 2014.

[14] S. Caveney, "Cuticle Reflectivity and Optical Activity in Scarab Beetles: The Role of Uric Acid," *Proc. R. Soc. B Biol. Sci.*, vol. 178, no. 1051, pp. 205–225, Jun. 1971.

[15] R. Hegedüs, G. Szél, and G. Horváth, "Imaging polarimetry of the circularly polarizing cuticle of scarab beetles (Coleoptera: Rutelidae, Cetoniidae)," *Vision Res.*, vol. 46, pp. 2786–2797, 2006.

[16] G. W. Kattawar, "A Search for Circular Polarization," *Opt. Photonics News*, no. September, pp. 42–43, 1994.

[17] I. Hodgkinson, S. Lowrey, L. Bourke, A. Parker, and M. W. McCall, "Mueller-matrix characterization of beetle cuticle: polarized and unpolarized reflections from representative architectures," *Appl. Opt.*, vol. 49, no. 24, pp. 4558–67, Aug. 2010.

[18] D. B. Thomas, A. Seago, D. C. Robacker, and A. Poe, “Reflections On Golden Scarabs,” *Am. Entomol.*, vol. Winter, pp. 224–230, 2007.

[19] D. H. Goldstein, “Polarization properties of Scarabaeidae,” *Appl. Opt.*, vol. 45, pp. 7944–7950, 2006.

[20] L. Fernández del Río, H. Arwin, and K. Järrendahl, “Polarizing properties and structure of the cuticle of scarab beetles from the Chrysina genus,” *Phys. Rev. E*, vol. 12409, pp. 1–9, 2016.

[21] S. A. Jewell, P. Vukusic, and N. W. Roberts, “Circularly polarized colour reflection from helicoidal structures in the beetle Plusiotis boucardi,” *New J. Phys.*, vol. 9, no. 99, pp. 1–10, Apr. 2007.

[22] L. Fernández del Río, “An Investigation of the Polarization States of Light Reflected from Scarab Beetles of the Chrysina Genus - BSc Thesis,” Linköpings University, 2011.

[23] A. C. Neville, “Metallic gold and silver colours in some insect cuticles,” *J. Insect Physiol.*, vol. 23, no. 10, pp. 1267–74, 1977.

[24] A. Michelson, “On metallic colouring in birds and insects,” *Philos. Mag.*, vol. 21, pp. 618–623, 1911.

[25] L. McDonald, E. Finlayson, and P. Vukusic, “Untwisting the polarization properties of light reflected by scarab beetles,” *SPIE BiOS*, vol. 9341, pp. 1–7, 2015.

[26] B. D. Wilts, H. M. Whitney, B. J. Glover, U. Steiner, and S. Vignolini, “Natural helicoidal structures: morphology, self-assembly and optical properties,” *Mater. Today Proc.*, vol. 1S, pp. 177–185, 2014.

[27] A. Solís, “Chrysina de Costa Rica,” *InBio*. [Online]. Available: http://www.inbio.ac.cr/papers/Plusiotis/Clave.html.

[28] F. Stumpe, “INTERINSECTS Felix Stumpe.” [Online]. Available: http://chrysina.com/. [Accessed: 18-Dec-2016].

[29] D. Curoe, “An Annotated List of Some Species of Chrysina,” *Scarabs*, vol. May, no. 27, pp. 1–22, 2008.

[30] W. E. Vargas, M. Hernández-Jiménez, E. Libby, D. E. Azofeifa, C. Barboza, and Á. Solis, “Light Reflection by Cuticles of Chrysina Jewel Scarabs: Optical Measurements, Morphology Characterization, and Theoretical Modeling,” *Opt. Photonics J.*, vol. 6, no. 7, pp. 146–163, 2016.

[31] E. Libby, D. E. Azofeifa, M. Hernández-Jiménez, C. Barboza-Aguilar, A. Solís, I. García-Aguilar, L. Arce-Marenco, A. Hernández, and W. E. Vargas, “Light reflection by the cuticle of C. aurigans scarabs: a biological broadband reflector of left handed circularly polarized light,” *J. Opt.*, vol. 16, no. 82001, pp. 1–7, Aug. 2014.

[32] H. Arwin, L. Fernández del Río, and K. Järrendahl, “Comparison and analysis of Mueller-matrix spectra from exoskeletons of blue, green and red Cetonia aurata,” *Thin Solid Films*, vol. 571, pp. 739–743, Nov. 2014.

[33] D. Hawks, “‘The Eye of the Beholder’ or ‘They look really nice, but not very edible to me, and I have no idea what they look like to hawks, despite my name’ or ‘Color Variation and other stuff about Chrysina,’” *Scarabs*, vol. April, no. 26, 2008.

[34] C. Campos-Fernández, D. E. Azofeifa, M. Hernández-Jiménez, A. Ruiz-Ruiz, and W. E. Vargas, “Visible light reflection spectra from cuticle layered materials,” *Opt. Mater. Express*, vol. 1, no. 1, pp. 85–100, Apr. 2011.

[35] K. Robacker, “Chrysina Gallery,” *University of Nebraska State Museum - Division of Entomology*. [Online]. Available: http://museum.unl.edu/research/entomology/Guide/Scarabs Gallery/Chrysina Gallery/index.html. [Accessed: 18-Dec-2016].

[36] M. Xu, A. E. Seago, T. D. Sutherland, and S. Weisman, “Dual structural color mechanisms in a scarab beetle,” *J. Morphol.*, vol. 271, no. 11, pp. 1300–5, Nov. 2010.

[37] I. E. Carter, K. Weir, and M. W. McCall, “Investigation of the Variation of Near-Circular Polarization in Scarabaeoidea Beetles,” *Mater. Today Proc.*, vol. 4, no. 4, pp. 4942–4951, 2017.

[38] F. Liu, B. Dong, F. Zhao, X. Hu, X. Liu, and J. Zi, "Ultranegative angular dispersion of diffraction in quasiordered biophotonic structures," *Opt. Express*, vol. 19, no. 8, pp. 7750–5, 2011.

[39] H. Arwin, R. Magnusson, L. Fernández del Río, J. Landin, A. Mendoza-Galván, and K. Järrendahl, "Exploring polarization features in light reflection from beetles with structural colors," *Proc. SPIE*, vol. 9429, no. 942909, pp. 1–13, Mar. 2015.

[40] H. Arwin, R. Magnusson, J. Landin, and K. Järrendahl, "Chirality-induced polarization effects in the cuticle of scarab beetles: 100 years after Michelson," *Philos. Mag.*, vol. 92, no. 12, pp. 1583–1599, Apr. 2012.

[41] A. Parker, D. McKenzie, and M. Large, "Multilayer reflectors in animals using green and gold beetles as contrasting examples," *J. Exp. Biol.*, vol. 1313, no. 1998, pp. 1307–1313, 1998.

[42] S. Lowrey, L. Silva, I. Hodgkinson, and J. Leader, "Observation and modeling of polarized light from scarab beetles," *JOSA A*, vol. 24, no. 8, pp. 2418–2425, 2007.

[43] S. Y. Ching, G. Li, H. L. Tam, D. T. P. Goh, J. K. L. Goh, and K. W. Cheah, "Chirality in Rhomborhina Gigantea beetle," *Opt. Mater. Express*, vol. 4, no. 11, pp. 2340–5, Oct. 2014.

[44] Suet Ying Ching, Gui Xin Li, Hoi Lam Tam, D. T. P. Goh, J. K. L. Goh, and K. W. Cheah, "Photonic nano-structure of R. Gigantea," in *2010 3rd International Nanoelectronics Conference (INEC)*, 2010, pp. 1360–1361.

[45] M. Rassart, J. F. Colomerl, T. Tabarrant, and J. P. Vigneron, "Diffractive hygrochromic effect in the cuticle of the hercules beetle Dynastes hercules," *New J. Phys.*, vol. 10, 2008.

[46] E. D. Finlayson, L. T. McDonald, and P. Vukusic, "Optically ambidextrous circularly polarized reflection from the chiral cuticle of the scarab beetle Chrysina resplendens," *J. R. Soc. Interface*, vol. 14, no. 131, 2017.

Chapter 5 - Modelling of Circularly Polarised Reflection

5.1. Introduction

In this Chapter the beetles' CP spectra models are shown. They were achieved by adapting the thin film toolbox written by Hodgkinson and McCall in whose book a fuller derivation of the code can be found [1]. The thin films toolbox uses Berreman calculus in order to calculate the CP reflection. A transfer matrix approach is used in order to transfer the input to output parameters.

After the coding method is fully described, the modelling is applied to the LL spectra of various beetles. These models were used to demonstrate possible optical structures which produce such a LL response. The modelling introduced two main perturbations to an otherwise single pitch structures. These were multiple pitches and sudden jumps in the helicoidal rotation. The multiple pitch perturbations have been observed in electron micrographs in previous studies (as gradual [2] and more sudden changes [3]). The sudden jump or angular discontinuity in a helicoidal structure has been shown in liquid crystals [4]. The multiple pitch values lead to multiple reflection wavelengths and the sudden jump in the helical rotation of the layers of chitin leads to troughs in the reflection spectra.

The models were applied to variations of LL spectra in the *Lomaptera* genus, the species *Cetonia aurata aurata*, examples from each of the nine subfamilies known to selectively reflect CP light and the broadband responses in *Chrysina optima* (from Section 4.4).

5.2. Background

The derivation within this section is based upon sections of the book by McCall *et al* [1].

The physical setup the model is representing consists of an isotropic substrate with a multiple chiral structures (of varying pitch) on top (which consist of many birefringent layers (ie individual layers where all the chitin molecules are in the same direction) of a fixed height), further on top of this an isotropic cover layer could be applied.

The basic outline of the model is as follows. Berreman calculus was used in the code, with a 4x4 field matrix being defined, as a set of four basis vectors which represent waves propagating the fields between biaxial layers. The field matrix then calculates the polarisation eigenmodes between the helicoidal stack and the surrounding media (i.e. the transfer of fields across the interface between the surface and the bottom of the chiral structure). The 4x4 characteristic matrix of a chiral thin film was then calculated. As a discrete individual layer thickness within the

helix is used, the characteristic matrix of layers is used. The characteristic matrix of individual layers defines the propagation through a single layer of birefringent film, it was then used in combination with is the rotation matrix (between adjacent rotated individual layers). Once the individual characteristic matrices were combined the overall characteristic matrix was used in order to calculate the reflectance of CP light from the structure (with the reflect function).

In order to run the code the follow inputs need to be defined: the refractive index of the surroundings (incident medium cover and substrate), the birefringent refractive indices of the helical stack, the initial angle of rotation and final angle, the number of layers in the helical stack and the wavelength of the Bragg resonance. As the number of rotations and number of individual layers can be input, the modelling is of a discrete structure. The refractive indices can be made complex in order to include absorption. The code scales wavelength to the Bragg wavelength, (which is input separately).

5.2.1. Maxwell's Equations – Electromagnetics

To understand how the model works, Maxwell's equations must be satisfied for electromagnetic waves propagating through an isotropic, uncharged, nonmagnetic, and nonconducting medium. The vector forms Maxwell's equations are

$$\nabla \times \mathbf{E} = -\mu_0 \frac{\partial \mathbf{H}}{\partial t}, \tag{5.1}$$

$$\nabla \times \mathbf{H} = \varepsilon_0 \varepsilon \frac{\partial \mathbf{E}}{\partial t}, \tag{5.2}$$

$$\nabla . \mathbf{E} = 0, \tag{5.3}$$

$$\nabla . \mathbf{H} = 0. \tag{5.4}$$

Where $\mathbf{E}$ is the electric field vector, $\mathbf{H}$ is the magnetic field, where ε is the relative permittivity, ε_0 is the permittivity of a vacuum and μ_0 is the permeability of vacuum. When considering propagating in a medium the electric field is related to the electric displacement, $\mathbf{D}$ as

$$\mathbf{D} = \varepsilon_0 \varepsilon \mathbf{E}, \tag{5.5}$$

The direction and power flow per unit area perpendicular to direction of flow is given by the Poynting vector $\mathbf{S}$ as

$$\mathbf{S} = \mathbf{E} \times \mathbf{H}. \tag{5.6}$$

5.2.2. Propagating Waves

Consider a single plane wave propagating in the x-y plane perpendicularly incident upon a biaxial medium (of parallel layers) of average refractive index, n. This single plane wave is considered to initiate four plane waves in a biaxial medium. The co-ordinate system which is used in this system is shown in Figure 5.1.

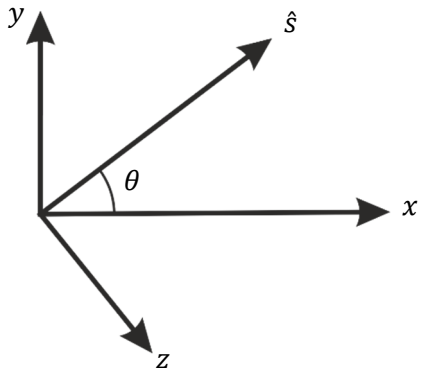


Figure 5.1 – Co-ordinate system used in this derivation.

The four waves have linear polarisation, with directions which are described by the **D** field. All four have the same Snell's law value as in:

$$\beta = n\sin(\theta), \tag{5.7}$$

where the different directions of each of the four waves is defined by θ. It can also be stated for each of the four waves that

$$\alpha = n\cos(\theta). \tag{5.8}$$

Then Maxwell's equations (equations 5.1 and 5.2) can be represented in column vector form for plane harmonic waves become

$$n\hat{s}\vec{E} = z_0\vec{H}, \tag{5.9}$$

$$n\hat{s}\vec{H} = -\frac{1}{z_0}\,\hat{\varepsilon}\vec{E}, \tag{5.10}$$

where $\vec{\ }$ denotes column vectors, $\hat{\ }$ denotes matrices, z_0 is the impedance of the vacuum and n the refractive index. $\hat{\varepsilon}$ is the relative permittivity matrix given in the Cartesian propagation frame as

$$\hat{\varepsilon} = \begin{bmatrix} \varepsilon_{xx} & \varepsilon_{xy} & \varepsilon_{xz} \\ \varepsilon_{xy} & \varepsilon_{yy} & \varepsilon_{yz} \\ \varepsilon_{xz} & \varepsilon_{yz} & \varepsilon_{zz} \end{bmatrix}. \tag{5.11}$$

If the individual plane waves propagate in the x-y plane, $\hat{s}$ is a 3x3 matrix is defined as

$$\hat{s} = \begin{bmatrix} 0 & 0 & s_y \\ 0 & 0 & -s_x \\ -s_y & s_x & 0 \end{bmatrix}. \tag{5.12}$$

Setting equation 5.7 and 5.8 equal to ns_x and ns_y respectively the following is obtained

$$n\hat{s} = \begin{bmatrix} 0 & 0 & \beta \\ 0 & 0 & -\alpha \\ -\beta & \alpha & 0 \end{bmatrix}. \tag{5.13}$$

Combining with equations 5.9, 5.10, 5.11 and 5.12 to give

$$\begin{bmatrix} 0 & 0 & \beta \\ 0 & 0 & -\alpha \\ -\beta & \alpha & 0 \end{bmatrix} \begin{bmatrix} E_x \\ E_y \\ E_z \end{bmatrix} = z_0 \begin{bmatrix} H_x \\ H_y \\ H_z \end{bmatrix}, \tag{5.14}$$

and

$$-z_0\begin{bmatrix}0 & 0 & \beta\\ 0 & 0 & -\alpha\\ -\beta & \alpha & 0\end{bmatrix}\begin{bmatrix}H_x\\ H_y\\ H_z\end{bmatrix}=\begin{bmatrix}\varepsilon_{xx} & \varepsilon_{xy} & \varepsilon_{xz}\\ \varepsilon_{xy} & \varepsilon_{yy} & \varepsilon_{yz}\\ \varepsilon_{xz} & \varepsilon_{yz} & \varepsilon_{zz}\end{bmatrix}\begin{bmatrix}E_x\\ E_y\\ E_z\end{bmatrix}. \quad (5.15)$$

This then leads to six equations. However two of them can be used in order to eliminate the electric and magnetic fields in the x direction (which is normal to the interfaces) and so required for boundary condition matching. We have

$$E_x=-(\varepsilon_{xy}E_y+\varepsilon_{xz}E_z+z_0\beta H_z)/\varepsilon_{xx}, \quad (5.16)$$

$$H_x=\left(\frac{\beta}{z_0}\right)E_z. \quad (5.17)$$

This then allows the representation as an eigenequation:

$$\hat{L}\begin{bmatrix}E_y\\ H_z\\ E_z\\ H_y\end{bmatrix}=\alpha\begin{bmatrix}E_y\\ H_z\\ E_z\\ H_y\end{bmatrix}, \quad (5.18)$$

where the auxiliary matrix $\hat{L}$ is set to,

$$\hat{L}=\begin{bmatrix}-\frac{\beta\varepsilon_{xy}}{\varepsilon_{xx}} & z_0-\frac{z_0\beta^2}{\varepsilon_{xx}} & -\frac{\beta\varepsilon_{xz}}{\varepsilon_{xx}} & 0\\ \frac{\varepsilon_{yy}}{z_0}-\frac{\varepsilon_{xy}^2}{z_0\varepsilon_{xx}} & -\frac{\beta\varepsilon_{xy}}{\varepsilon_{xx}} & \frac{\varepsilon_{yz}}{z_0}-\frac{\varepsilon_{xy}\varepsilon_{xz}}{z_0\varepsilon_{xx}} & 0\\ 0 & 0 & 0 & -z_0\\ -\frac{\varepsilon_{yz}}{z_0}+\frac{\varepsilon_{xy}\varepsilon_{xz}}{z_0\varepsilon_{xx}} & \frac{\beta\varepsilon_{xz}}{\varepsilon_{xx}} & \frac{\beta^2}{z_0}-\frac{\varepsilon_{xz}^2}{z_0\varepsilon_{xx}}-\frac{\varepsilon_{zz}}{z_0} & 0\end{bmatrix}. \quad (5.19)$$

5.2.3. Field Matrix

The eigenequation (equation 5.18) can then be stated as

$$\hat{L}\vec{F}=\alpha\vec{F}, \quad (5.20)$$

where $\vec{F}$ is a matrix where columns are the electric vectors called the Field matrix,

$$\hat{F}=\begin{bmatrix}E_{y1}^+ & E_{y1}^- & E_{y2}^+ & E_{y2}^-\\ H_{z1}^+ & H_{z1}^- & H_{z2}^+ & H_{z2}^-\\ E_{z1}^+ & E_{z1}^- & E_{z2}^+ & E_{z2}^-\\ H_{y1}^+ & H_{y1}^- & H_{y2}^+ & H_{y2}^-\end{bmatrix}, \quad (5.21)$$

where the + and - indices represent forwards and backwards propagating waves and the subscript 1 and 2 represent the outer and inner sheets (which refer to the refractive index surfaces of the cover and substrate mediums). The diagonal matrix contains the corresponding eigenvalues and is defined as

$$\hat{\alpha}=\begin{bmatrix}\alpha_1^+ & 0 & 0 & 0\\ 0 & \alpha_1^- & 0 & 0\\ 0 & 0 & \alpha_2^+ & 0\\ 0 & 0 & 0 & \alpha_2^-\end{bmatrix}. \quad (5.22)$$

The matrix form of equation 5.20 can be given as

$$\hat{L}\hat{F}=\hat{F}\hat{\alpha}. \quad (5.23)$$

In the code, the function `fmat` gives the field matrix $\hat{F}$, a row vector with the four α values and a 3x4 matrix of the electric field components and magnetic field components in the x, y and z

directions. fmat takes the birefringent refractive indices and angle of rotation as inputs. Firstly define

$$\gamma_p = H_z^+/E_y^+ = -H_z^+/E_y^- = n/z_0\cos\theta\,, \tag{5.24}$$

$$\gamma_s = H_y^+/E_z^+ = -H_y^-/E_z^- = -n\cos\theta/z_0. \tag{5.25}$$

The Field matrix can be changed to have an elliptical basis for an isotropic medium using linear sums of the linear polarised basis vectors as

$$\hat{F} = \begin{bmatrix} cos\theta(\cos\phi + ie\sin\phi) & cos\theta(cos\phi - iesin\phi) & -cos\theta(\sin\phi + ie\cos\phi) & -\cos\theta(\sin\phi - ie\cos\phi) \\ \gamma_p\cos\theta(\cos\phi + ie\sin\phi) & -\gamma_p cos\theta(cos\phi - ie\sin\phi) & -\gamma_p cos\theta(\sin\phi + ie\cos\phi) & \gamma_p\cos\theta(\sin\phi - ie\cos\phi) \\ (\sin\phi - ie\cos\phi) & (sin\phi + ie\cos\phi) & (\cos\phi - ie\sin\phi) & (\cos\phi + ie\sin\phi) \\ \gamma_s(\sin\phi - ie\cos\phi) & -\gamma_s(\sin\phi + ie\cos\phi) & \gamma_s(\cos\phi - ie\sin\phi) & -\gamma_s(\cos\phi + ie\sin\phi) \end{bmatrix} \tag{5.26}$$

where e is the ellipticity parameter and ϕ the inclination angle of the major axis of the ellipse. If a material is isotropic, such as a substrate or cover using s and p polarisation denotations (in the subscript) the form can be given as

$$\hat{F} = \begin{bmatrix} 1 & 1 & 0 & 0 \\ \gamma_p & -\gamma_p & 0 & 0 \\ 0 & 0 & 1 & 1 \\ 0 & 0 & \gamma_s & -\gamma_s \end{bmatrix}. \tag{5.27}$$

The reciprocal field matrix in an isotropic medium has the form

$$\hat{F}^{-1} = \frac{1}{2}\begin{bmatrix} 1 & 1/\gamma_p & 0 & 0 \\ 1 & -1/\gamma_p & 0 & 0 \\ 0 & 0 & 1 & 1/\gamma_s \\ 0 & 0 & 1 & -1/\gamma_s \end{bmatrix}. \tag{5.28}$$

Berreman calculus is employed as a transfer matrix, taking an input vector and transforming it to the output vector based upon the system the input vector goes through.

5.2.4. Field Coefficients

The next variable defined is a field coefficient column vector $\vec{a}$. In a biaxial layer the four waves propagate with multiple reflections and transmissions. Each field is multiplied by a complex amplitude. The column vector of amplitude is given in terms of coefficients as:

$$\vec{a} = \begin{bmatrix} a_1^+ \\ a_1^- \\ a_2^+ \\ a_2^- \end{bmatrix} \tag{5.29}$$

5.2.5. Total Field

The total field column vector, $\vec{m}$ must be preserved to do a transformation across an interface. It is given as

$$\vec{m} = \begin{bmatrix} E_y \\ H_z \\ E_z \\ H_y \end{bmatrix} = \begin{bmatrix} a_1^+E_{y1}^+ + a_1^-E_{y1}^- + a_2^+E_{y2}^+ + a_2^-E_{y2}^- \\ a_1^+H_{z1}^+ + a_1^-H_{z1}^- + a_2^+H_{z2}^+ + a_2^-H_{z2}^- \\ a_1^+E_{z1}^+ + a_1^-E_{z1}^- + a_2^+E_{z2}^+ + a_2^-E_{z2}^- \\ a_1^+H_{y1}^+ + a_1^-H_{y1}^- + a_2^+H_{y2}^+ + a_2^-H_{y2}^- \end{bmatrix}. \tag{5.30}$$

It can be seen that the total field vector is a product of the field matrix and field coefficient column vector, i.e.

$$\hat{F}\vec{a} = \vec{m}. \tag{5.31}$$

This can be rearranged in order to find the field coefficients.

$$\hat{F}^{-1}\vec{m} = \vec{a}. \tag{5.32}$$

5.2.6. Phase Matrix

The phases of the four travelling wave fields change with displacement in the x-direction. The phase changes are defined by the phase matrix. For a distance from $x = x_0$ to $x = x_0 - d$. Where d is the physical thickness of the material, the Phase matrix is defined as

$$\hat{A}_d = \begin{bmatrix} \exp(-i\phi_1^+) & 0 & 0 & 0 \\ 0 & \exp(-i\phi_1^-) & 0 & 0 \\ 0 & 0 & \exp(-i\phi_2^+) & 0 \\ 0 & 0 & 0 & \exp(-i\phi_2^-) \end{bmatrix}. \tag{5.33}$$

Where

$$\phi_{1,2}^{\pm} = k\alpha_{1,2}^{\pm} d. \tag{5.34}$$

Here k is the wavenumber. The phase matrix transforms the field coefficients between two points in the same layer (Figure 5.2).

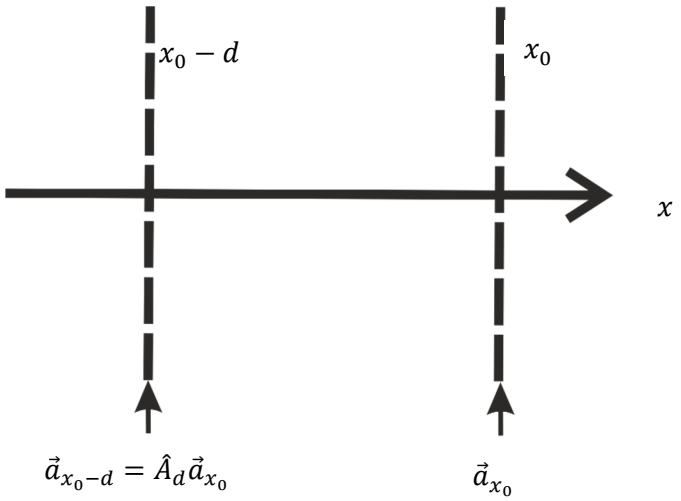


Figure 5.2 – Showing two planes distance d apart, with the field coefficients $\vec{a}$ between them being transformed by the phase matrix $\hat{A}_d$. Based upon Figure 4.4 from [1], with permission.

This transformation can be written as

$$\vec{a}_{x_0-d} = \hat{A}_d\vec{a}_{x_0}. \tag{5.35}$$

5.2.7. Characteristic Matrix

The phase matrix is used in combination with the field matrix in order to calculate the Characteristic Matrix as

$$\widehat{M} = \hat{F}\hat{A}_d\hat{F}^{-1}. \tag{5.36}$$

The Characteristic Matrix can be used to transform the total field between two planes within a biaxial layer via

$$\vec{m}_{x_0-d} = \widehat{M}\vec{m}_{x_0}. \tag{5.37}$$

The Characteristic Matrix can be defined with any two planes, but in the code the convention is to use it to transform the total field from the right hand interface of the layer to the left hand and is described as the Characteristic Matrix of the layer. The transformation as performed by the Characteristic Matrix over a single layer is shown in Figure 5.3. The transformation can be considered between layers (noted by subscripts of substrate, S and cover, C) as

$$\vec{m}_C = \hat{M}\vec{m}_S. \tag{5.38}$$

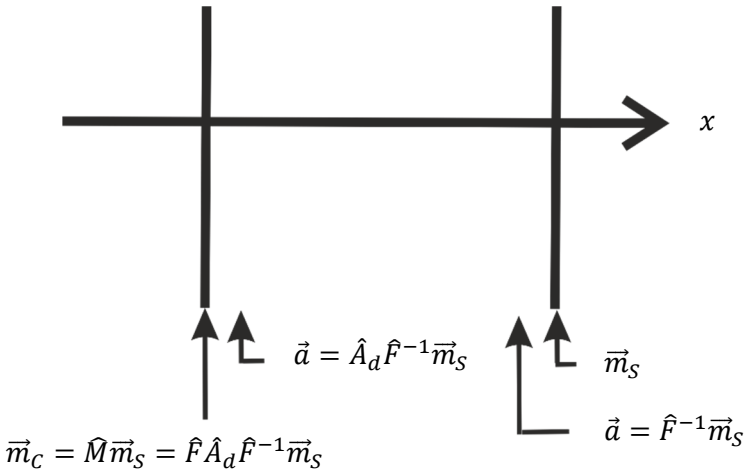


Figure 5.3 – Showing the tranformation of the total field across the layer, by the characteristic matrix of that layer. Based upon Figure 4.5 from [1], with permission.

If a stack of a number (*N*) of layers is used, the Characteristic Matrix for the overall structure can be calculated as a product of Charactristic Matrices of the individual layers as

$$\hat{M} = \hat{M}_1\hat{M}_2..\hat{M}_N. \tag{5.39}$$

Figure 5.4 shows a stack of N layers which is surrounded by a cover and substrate. This function (equation 5.39) is equivalent to calculating the difference between individual layers using the function within the code (`hmat` or `cmat`).

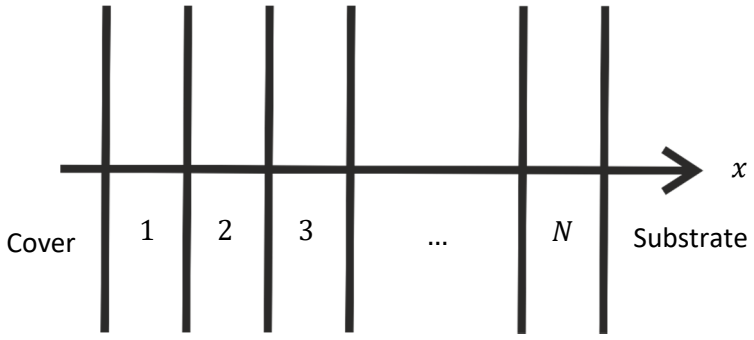


Figure 5.4 – Stack of N Biaxial layers. Based upon Figure 4.6 from [1], with permission.

The system matrix $\hat{A}$ is 4x4 and used when a layered structure is between a cover medium and a substrate. It is defined as

$$\hat{A} = \hat{F}_C^{-1}\hat{M}\hat{F}_S. \tag{5.40}$$

Where $\hat{F}_C$ and $\hat{F}_S$ are the field matrices of the cover medium and substrates respectively. The system matrix can be used to relate the fields between the cover and substrate field coefficients

in equation 5.41. This starts from the field coefficients of the substrate $\vec{a}_S$ to the right of the last layer substrate interface (Figure 5.5), then three matrix transformations occur, the first being the field coefficients in the substrate, to the total fields at the substrate, to the total field at the cover to finally the field coefficients just inside the cover as in the relation

$$\vec{a}_C = \hat{A}\vec{a}_S. \tag{5.41}$$

It will be shown that $\hat{A}$ is useful in calculating the reflectance and transmission.

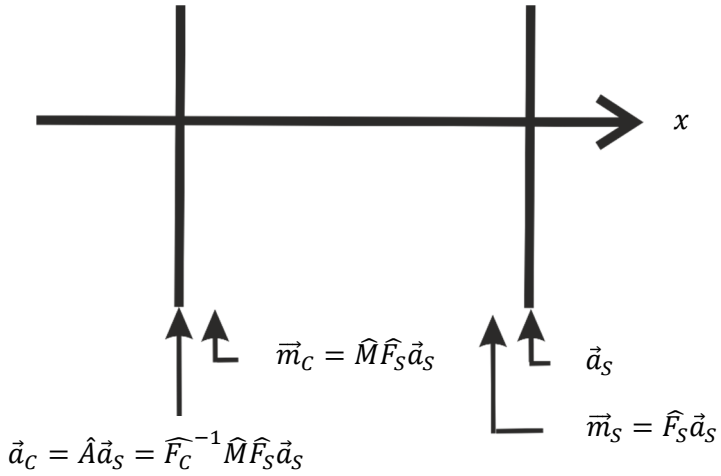


Figure 5.5 – Showing the tranformation of the total field across the layer, by the characteristic matrix of that layer. Based upon Figure 4.7 from [1], with permission.

5.2.8. Rotation Matrix

The azimuthal rotation in multilayer structures can be taken into account by using the rotation matrix $\hat{R}_b(\varsigma)$, where ς is the azimuthal angle, given by

$$\hat{R}_b(\varsigma) = \begin{bmatrix} \cos\varsigma & 0 & -\sin\varsigma & 0 \\ 0 & \cos\varsigma & 0 & \sin\varsigma \\ \sin\varsigma & 0 & \cos\varsigma & 0 \\ 0 & -\sin\varsigma & 0 & \cos\varsigma \end{bmatrix}. \tag{5.42}$$

This can be used to calculate the change in the Characteristic Matrix to take into account the azimuthal rotation as

$$\hat{M}(\varsigma) = \hat{R}_b(\varsigma)\hat{M}(0)\hat{R}_b(-\varsigma), \tag{5.43}$$

where $\hat{M}(0)$ is the Characteristic Matrix for an unrotated medium. Propagation through a chiral layered film (of uniform rotation) with finite individual layer thickness (of thickness d) with birefringent axis perpendicular to propagation (labelled 2 and 3) is considered. Where the axis 2 makes an azimuth angle ς_1 with respect to the y-axis at the cover-chiral layers interface and an angle of ς_2 with respect to the chiral layers-substrate interface. At normal incidence the characteristic matrix for a continuous chiral structure is defined as

$$\hat{M} = \hat{R}_b(\varsigma_1)\left[\hat{m}\hat{R}_b(\Delta\varsigma)\hat{m}\right]^N\hat{R}_b(-\varsigma_2), \tag{5.44}$$

where $\Delta\varsigma = (\varsigma_2\text{-}\varsigma_1)/N$ is the difference in azimuth angle per finite layer. The biaxial layers were of thickness $d/2N$, where N is the number of layers and $\hat{m}$ is the Characteristic Matrix of an individual (sub)layer.

5.2.9. Helix Definitions

The number of individual (sub)layers in one half pitch (the perpendicular distance that it takes for 180° rotation in chitin molecules orientation in plane in the chiral structure to occur) (κ) is equal to the dielectric half pitch divided by the thickness of each individual layer (Δd) (or π divided by the rotation of a individual layer ($\Delta\xi$)) as in

$$N_s = \frac{\kappa}{\Delta d} = \frac{\pi}{\Delta\varsigma}. \tag{5.45}$$

As mentioned earlier (in Chapter 3), the peak reflected (Bragg) wavelength (λ_{Br}) is related to the average refractive index of the helicoidal stack (n_{av}) as

$$\lambda_{Br} = 2n_{av}\kappa. \tag{5.46}$$

The spectral width of the reflection band is given as

$$\Delta\lambda_{Br} = 2\Delta n\kappa. \tag{5.47}$$

The average refractive index of the stack is related to the birefringent refractive indices (n_2) and (n_3) as

$$n_{av} = (n_2 + n_3)/2, \tag{5.48}$$

and the birefringence of the stack in plane

$$\Delta n = n_3 - n_2. \tag{5.49}$$

A dimensionless variable G is used to describe the modelling in a more general manner and is related to the wavelength and Bragg wavelength as

$$G = \frac{\lambda_{Br}}{\lambda}, \tag{5.50}$$

$$\frac{\Delta G}{G} = \frac{\Delta\lambda_{Br}}{\lambda_{Br}}. \tag{5.51}$$

In order to run the model, the birefringent refractive indices, the start and final angles of rotation, the number of individual (sub)layers and number of pitches, the refractive indices of the incident medium and substrate must be given in order to model the reflectance.

5.2.10. Reflection and Transmission

5.2.10.1. All Biaxial Structures

The optical reflection and transmission coefficients of layered biaxial media were obtained in order to model the CP spectra.

Initially consider the general case in which the cover, layers and substrate may all be birefringent. The solution consists of a 4x4 matrix $\hat{r}$, which contains a ratio of field coefficients (discussed later in this section). The arrangement of layers is shown in Figure 5.6. The field coefficients for incident and outgoing waves are considered where the + superscript indicates right going waves and – relates to left going waves (as Figure 5.6). The subscripts 1 and 2 refer to the cover and 3 and 4 to the substrate.

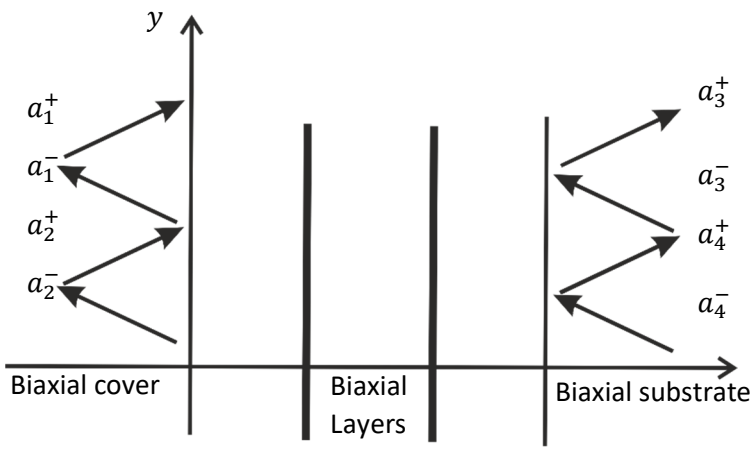


Figure 5.6 – Labelling scheme used for the amplitudes of the four basis vectors that propagate in the cover and the amplitudes of the four basis vectors in the substrate. Based upon Figure 5.1 from [1], with permission.

To calculate the reflectance and transmittance the field strengths in the cover and substrate need to be known, (which requires the field matrix and field coefficients for the cover and substrate). The set of field coefficients for a wave travelling towards the layers are regarded as an input as

$$\begin{bmatrix} a_1^+ \\ a_2^+ \\ a_3^- \\ a_4^- \end{bmatrix}. \tag{5.52}$$

For the output wave the set of field coefficients becomes

$$\begin{bmatrix} a_1^- \\ a_2^- \\ a_3^+ \\ a_4^+ \end{bmatrix}. \tag{5.53}$$

At the interface between the stack of anisotropic films and anisotropic cover and substrate, the boundary conditions become satisfied when the total field at the cover is equal to the result of transferring the total field in the substrate to the cover. i.e.

$$\hat{F}_C \vec{a}_C = \hat{M} \hat{F}_S \vec{a}_S. \tag{5.54}$$

Combining equations 5.52 and 5.53 with the system matrix (equation 5.41) which can be rewritten as

$$\begin{bmatrix} a_1^+ \\ a_1^- \\ a_2^+ \\ a_2^- \end{bmatrix} = \begin{bmatrix} A_{11} & A_{12} & A_{13} & A_{14} \\ A_{21} & A_{22} & A_{23} & A_{24} \\ A_{31} & A_{32} & A_{33} & A_{34} \\ A_{41} & A_{42} & A_{43} & A_{44} \end{bmatrix} \begin{bmatrix} a_3^+ \\ a_3^- \\ a_4^+ \\ a_4^- \end{bmatrix}, \tag{5.55}$$

allows this to be rearranged to place the output field coefficients on the left hand side and input on the right hand side as

$$\begin{bmatrix} 0 & 0 & -A_{11} & -A_{13} \\ 1 & 0 & -A_{21} & -A_{23} \\ 0 & 0 & -A_{31} & -A_{33} \\ 0 & 1 & -A_{41} & -A_{43} \end{bmatrix} \begin{bmatrix} a_1^- \\ a_2^- \\ a_3^+ \\ a_4^+ \end{bmatrix} = \begin{bmatrix} -1 & 0 & A_{12} & A_{14} \\ 0 & 0 & A_{22} & A_{24} \\ 0 & -1 & A_{32} & A_{34} \\ 0 & 0 & A_{42} & A_{44} \end{bmatrix} \begin{bmatrix} a_1^+ \\ a_2^+ \\ a_3^- \\ a_4^- \end{bmatrix}. \tag{5.56}$$

This can then be rewritten as

$$\begin{bmatrix} a_1^- \\ a_2^- \\ a_3^+ \\ a_4^+ \end{bmatrix} \equiv \hat{r} \begin{bmatrix} a_1^+ \\ a_2^+ \\ a_3^- \\ a_4^- \end{bmatrix}, \tag{5.57}$$

where $\hat{r}$ is the intermediary matrix stated as

$$\hat{r} \equiv \begin{bmatrix} r_{11} & r_{12} & t_{13} & t_{14} \\ r_{21} & r_{22} & t_{23} & t_{24} \\ t_{31} & t_{32} & r_{33} & r_{34} \\ t_{41} & t_{42} & r_{43} & r_{44} \end{bmatrix} = \begin{bmatrix} 0 & 0 & -A_{11} & -A_{13} \\ 1 & 0 & -A_{21} & -A_{23} \\ 0 & 0 & -A_{31} & -A_{33} \\ 0 & 1 & -A_{41} & -A_{43} \end{bmatrix}^{-1} \begin{bmatrix} -1 & 0 & A_{12} & A_{14} \\ 0 & 0 & A_{22} & A_{24} \\ 0 & -1 & A_{32} & A_{34} \\ 0 & 0 & A_{42} & A_{44} \end{bmatrix}. \tag{5.58}$$

The intermediary matrix elements contain ratios of field coefficients, as

$$\begin{aligned} r_{11} &= a_1^-/a_1^+ \quad r_{12} = a_1^-/a_2^+ \quad t_{13} = a_1^-/a_3^- \quad t_{14} = a_1^-/a_4^- \\ r_{21} &= a_2^-/a_1^+ \quad r_{22} = a_2^-/a_2^+ \quad t_{23} = a_2^-/a_3^- \quad t_{24} = a_2^-/a_4^- \\ t_{31} &= a_3^+/a_1^+ \quad t_{32} = a_3^+/a_2^+ \quad r_{33} = a_3^+/a_3^- \quad r_{34} = a_3^+/a_4^- \\ t_{41} &= a_4^+/a_1^+ \quad t_{42} = a_4^+/a_2^+ \quad r_{43} = a_4^+/a_3^- \quad r_{44} = a_4^+/a_4^- \end{aligned}. \tag{5.59}$$

The irradiance reflectance and transmittance coefficients are in the matrix

$$\hat{R} \equiv \begin{bmatrix} R_{11} & R_{12} & T_{13} & T_{14} \\ R_{21} & R_{22} & T_{23} & T_{24} \\ T_{31} & T_{32} & R_{33} & R_{34} \\ T_{41} & T_{42} & R_{43} & R_{44} \end{bmatrix}. \tag{5.60}$$

The terms are defined in relation to power flows in the x-direction such

$$\hat{R} = \begin{bmatrix} |r_{11}|^2|p_1^-/p_1^+| & |r_{12}|^2|p_1^-/p_2^+| & |r_{13}|^2|p_1^-/p_3^-| & |r_{11}|^2|p_1^-/p_4^-| \\ |r_{21}|^2|p_2^-/p_1^+| & |r_{22}|^2|p_2^-/p_2^+| & |r_{23}|^2|p_2^-/p_3^-| & |r_{11}|^2|p_2^-/p_4^-| \\ |t_{31}|^2|p_3^+/p_1^+| & |r_{32}|^2|p_3^+/p_2^+| & |t_{33}|^2|p_3^+/p_3^-| & |r_{11}|^2|p_3^+/p_4^-| \\ |t_{41}|^2|p_4^+/p_1^+| & |r_{42}|^2|p_4^+/p_2^+| & |t_{43}|^2|p_4^+/p_3^-| & |r_{11}|^2|p_4^+/p_4^-| \end{bmatrix}. \tag{5.61}$$

The p's are the power carried by basis vectors in the x-direction, which can be found using the equation to find the Poynting flux in the x direction as

$$p_x = \frac{1}{2}\Re\{E_y H_z^* - E_z H_y^*\}, \tag{5.62}$$

This requires elements from the field vector. Cyclic variations can also be obtained from p_y and p_z.

5.2.10.2. Isotropic Cover and Substrate

The model used in this study involved an isotropic cover and substrate. For the cover,

$$\vec{a}_C = \begin{bmatrix} a_1^+ \\ a_1^- \\ a_2^+ \\ a_2^- \end{bmatrix} = \begin{bmatrix} E_{Cy}^+ \\ E_{Cy}^- \\ E_{Cz}^+ \\ E_{Cz}^- \end{bmatrix}, \tag{5.63}$$

and for the substrate

$$\vec{a}_s = \begin{bmatrix} a_3^+ \\ a_3^- \\ a_4^+ \\ a_4^- \end{bmatrix} = \begin{bmatrix} E_{Sy}^+ \\ E_{Sy}^- \\ E_{Sz}^+ \\ E_{Sz}^- \end{bmatrix}. \tag{5.64}$$

It is assumed the light is incident upon the cover, i.e. $E_{sy}^- = 0 = E_{sz}^-$, which then leads to

$$E_{cy}^- = \frac{(A_{21}A_{33} - A_{23}A_{21})E_{Cy}^+ + (A_{11}A_{23} - A_{13}A_{21})E_{Cz}^+}{A_{11}A_{33} - A_{13}A_{31}}, \tag{5.65}$$

$$E_{cz}^{-} = \frac{(A_{33}A_{41} - A_{31}A_{43})E_{Cy}^{+} + (A_{11}A_{43} - A_{13}A_{41})E_{Cz}^{+}}{A_{11}A_{33} - A_{13}A_{31}}, \tag{5.66}$$

$$E_{sy}^{-} = \frac{A_{33}E_{Cy}^{+} - A_{13}E_{Cz}^{+}}{A_{11}A_{33} - A_{13}A_{31}}, \tag{5.67}$$

$$E_{sz}^{-} = \frac{-A_{31}E_{Cy}^{+} - A_{11}E_{Cz}^{+}}{A_{11}A_{33} - A_{13}A_{31}}. \tag{5.68}$$

Using the equation $\hat{A} = \hat{F}_C^{-1}\hat{M}\hat{F}_S$, to give the elements $\hat{A}$ and $\hat{M}$,

$$\hat{A} = \frac{1}{2}\begin{bmatrix} 1 & 1/\gamma_{Cp} & 0 & 0 \\ 1 & -1/\gamma_{Cp} & 0 & 0 \\ 0 & 0 & 1 & 1/\gamma_{Cs} \\ 0 & 0 & 1 & -1/\gamma_{Cs} \end{bmatrix}\begin{bmatrix} M_{11} & M_{12} & M_{13} & M_{14} \\ M_{21} & M_{22} & M_{23} & M_{24} \\ M_{31} & M_{32} & M_{33} & M_{34} \\ M_{41} & M_{42} & M_{43} & M_{44} \end{bmatrix}\begin{bmatrix} 1 & 1 & 0 & 0 \\ \gamma_{Sp} & -\gamma_{Sp} & 0 & 0 \\ 0 & 0 & 1 & 1 \\ 0 & 0 & \gamma_{Ss} & -\gamma_{Ss} \end{bmatrix}, \tag{5.69}$$

where the equating coefficient of $\hat{A}$ in columns 1 are written as

$$A_{11} = (M_{11} + \gamma_{Sp}M_{12} + M_{21}/\gamma_{Cp} + \gamma_{Sp}M_{22}/\gamma_{Cp})/2, \tag{5.70}$$

$$A_{21} = (M_{11} + \gamma_{Sp}M_{12} + M_{21}/\gamma_{Cp} - \gamma_{Sp}M_{22}/\gamma_{Cp})/2, \tag{5.71}$$

$$A_{31} = (M_{31} + \gamma_{Sp}M_{32} + M_{41}/\gamma_{Cs} + \gamma_{Sp}M_{42}/\gamma_{Cs})/2, \tag{5.72}$$

$$A_{41} = (M_{31} + \gamma_{Sp}M_{32} + M_{41}/\gamma_{Cs} - \gamma_{Sp}M_{42}/\gamma_{Cs})/2, \tag{5.73}$$

and for column 3 as

$$A_{13} = (M_{13} + \gamma_{Ss}M_{14} + M_{23}/\gamma_{Cp} + \gamma_{Ss}M_{24}/\gamma_{Cp})/2, \tag{5.74}$$

$$A_{23} = (M_{13} + \gamma_{Ss}M_{14} - M_{23}/\gamma_{Cp} - \gamma_{Ss}M_{24}/\gamma_{Cp})/2, \tag{5.75}$$

$$A_{33} = (M_{33} + \gamma_{Ss}M_{34} + M_{43}/\gamma_{Cs} + \gamma_{Ss}M_{42}/\gamma_{Cs})/2, \tag{5.76}$$

$$A_{43} = (M_{33} + \gamma_{Ss}M_{34} - M_{43}/\gamma_{Cs} - \gamma_{Ss}M_{42}/\gamma_{Cs})/2. \tag{5.77}$$

5.2.10.3. Amplitude Reflection and Transmission Coefficients

From this the amplitude reflection and transmission coefficients can be put in terms of $\hat{A}$ as

$$\begin{bmatrix} r_{pp} & r_{ps} \\ r_{sp} & r_{ss} \end{bmatrix} \equiv \begin{bmatrix} r_{11} & r_{12} \\ r_{21} & r_{22} \end{bmatrix} = \begin{bmatrix} E_{Cy}^{-}/E_{Cy}^{+} & E_{Cy}^{-}/E_{Cz}^{+} \\ E_{Cz}^{-}/E_{Cy}^{+} & E_{Cz}^{-}/E_{Cz}^{+} \end{bmatrix} = \begin{bmatrix} A_{21}A_{33} - A_{23}A_{21} & A_{11}A_{23} - A_{13}A_{21} \\ A_{33}A_{41} - A_{31}A_{43} & A_{11}A_{43} - A_{13}A_{41} \end{bmatrix} / \begin{bmatrix} A_{11} & A_{13} \\ A_{31} & A_{33} \end{bmatrix}. \tag{5.78}$$

Similarly the transmission amplitude coefficients are

$$\begin{bmatrix} t_{pp} & t_{ps} \\ t_{sp} & t_{ss} \end{bmatrix} \equiv \begin{bmatrix} t_{11} & t_{12} \\ t_{21} & t_{22} \end{bmatrix} = \begin{bmatrix} E_{Sy}^{+}/E_{Cy}^{+} & E_{Sy}^{+}/E_{Cz}^{+} \\ E_{Sz}^{+}/E_{Cy}^{+} & E_{Sz}^{+}/E_{Cz}^{+} \end{bmatrix} = \begin{bmatrix} A_{33} & -A_{13} \\ -A_{31} & A_{11} \end{bmatrix} / \begin{bmatrix} A_{11} & A_{13} \\ A_{31} & A_{33} \end{bmatrix} = \begin{bmatrix} A_{11} & A_{13} \\ A_{31} & A_{33} \end{bmatrix}^{-1} \tag{5.79}$$

5.2.10.4. Irradiance Reflectance and Transmittance Coefficients

The irradiance reflection coefficients are calculated from the amplitude coefficients, where the reflectance coefficients for the cover are

$$\begin{bmatrix} R_{pp} & R_{ps} \\ R_{sp} & R_{ss} \end{bmatrix} \equiv \begin{bmatrix} R_{11} & R_{12} \\ R_{21} & R_{22} \end{bmatrix} = \begin{bmatrix} |r_{pp}|^2 & -|r_{pp}|^2\gamma_{Cp}/\gamma_{Cs} \\ -|r_{sp}|^2\gamma_{Cs}/\gamma_{Cp} & |r_{ss}|^2 \end{bmatrix}, \tag{5.80}$$

and the transmission coefficients are given by

$$\begin{bmatrix} T_{pp} & T_{ps} \\ T_{sp} & T_{ss} \end{bmatrix} \equiv \begin{bmatrix} T_{31} & T_{32} \\ T_{41} & T_{42} \end{bmatrix} = \begin{bmatrix} |t_{pp}|^2 \gamma_{Sp}/\gamma_{Cp} & -|t_{ps}|^2 \gamma_{Sp}/\gamma_{Cs} \\ -|t_{sp}|^2 \gamma_{Ss}/\gamma_{Cp} & |t_{ss}|^2 \gamma_{Ss}/\gamma_{Cs} \end{bmatrix}. \quad (5.81)$$

It should be noted that in this model the rotation of the helix was set to right handed with respect to the code, such that the R_{11} where the first subscript number relates to the handedness of the incoming light and the second relates to that of the outgoing. The number 1 related to reflected RCP, 2 to reflected LCP. The numbers in transmission 3 and 4 refer to transmitted polarisation of RCP and LCP respectively. In effect the modelling was done such involving RCP light upon a RCP structure, which gives the same results as LCP light upon a left circularly polarising structure.

5.3. Modelling Method

The altering of the parameters in the model (birefringence, number of pitches and thickness of the individual (sub)layers) was shown in Appendix A4. From these variations it can be seen that the higher the birefringence the more intense the peaks. The larger the number of pitches the narrower and more intense the reflection peak becomes. The number of individual (sub)layers of chitin molecules of the same orientation (in the range used) did not appear to alter the reflection spectra, as such they are not stated for the models in this section.

An example of the model in use, fitted to a *Popillia sp.* beetle is shown in Figure 5.7. The parameters of birefringence and number of layers were iteratively adjusted within the acceptable range of parameters given from previous experiments (Section 3.4.1). No quantitative measurements of the degrees of fit were taken as part of the study and the models were used to demonstrate such a structure with physically realistic parameters. It should be noted that in this study the LL spectra were focused upon in the modelling. The LR and RL spectra were chromatic invariant and the reflectance intensity (relative to LL) could be changed by altering the change in refractive index between cover, (average) chiral layer and substrate. In all models the RR spectra had intensity of zero. In the presented results the substrate was index matched to the average index of the birefringent layers, whilst the cover medium in all the models (except Figure 5.7) were modelled with a refractive index matched to air.

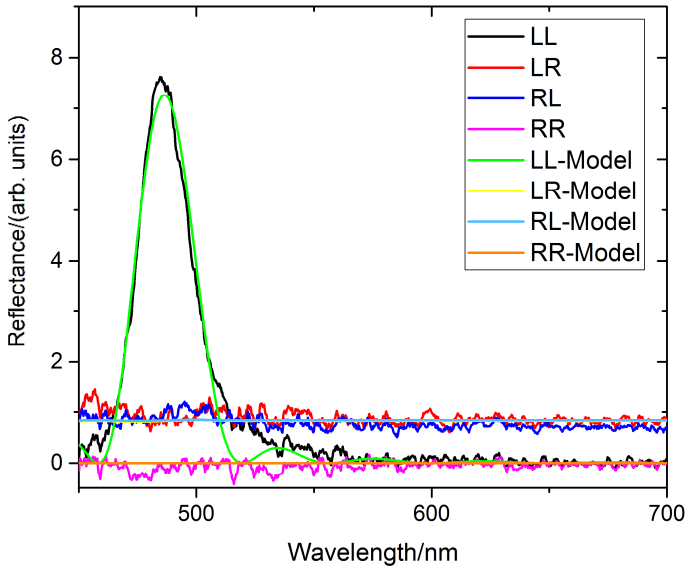


Figure 5.7 - Experimental and modelled CP spectra from a *Popillia sp.* beetle. It should be noted the LR/RL in the model overlay each other as well at the RR model being absolutely zero. The structure was modelled as eight pitches thick and birefringent refractive indices of 1.434 and 1.45, having the cover medium as a refractive index as n=1.2 in order to take into account the waxy cuticle.

The models in this Chapter are comparisons to experimental results and demonstrate a probable structure that is responsible for the spectra within the beetles. The models use experimentally determined values of variables from previous publications, which makes them realistic representations of such structures. These variables include the average refractive indices, birefringence, number of pitches and individual chitin individual (sub)layer thicknesses and are stated in Section 3.4. The robustness of the models has been shown in [1].

5.4. Different Basic Lomaptera Modelling Types

In Section 4.3.3.1 the *Lomaptera* genus was categorised into six different LL reflection shapes (single peaked, double peaks close, double peaks further apart, peaks with oscillations before the mean peak, oscillations after the main peak and not classified). These six different LL shapes have been modelled to complement the experimental data. The figures in this section are from modelling completed by the author [5].

5.4.1. Single Pitch

The simplest LL model was based upon a structure with a single pitch (such as in Figure 3.23). From equation 3.14a, a single peaked structure results in a single peak at one wavelength. The fit can be seen in Figure 5.8.

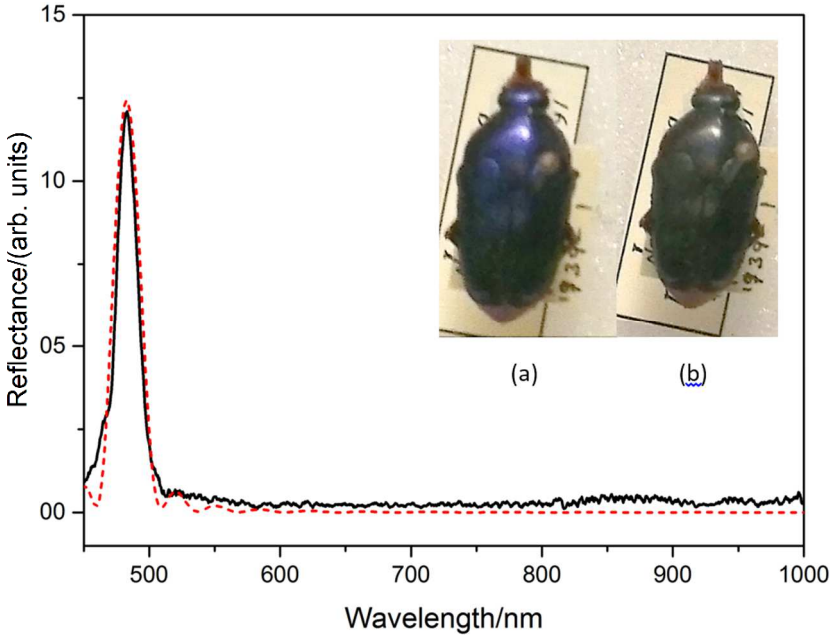


Figure 5.8 - Single peak LL reflection graph with a clear single peak from a *L. pygmaea* specimen (black curve). The inset photographs show the appearance of the specimen through (a) left and (b) right circular polarisers. The red-dashed plot shows a theoretical plot of the Left-through-Left reflectivity of ten pitches thick with each individual chitin layer of 20nm and birefringent refractive indices of 1.475+0.008i and 1.50+0.008i. From the authors paper [5].

5.4.2. Double Peak Close

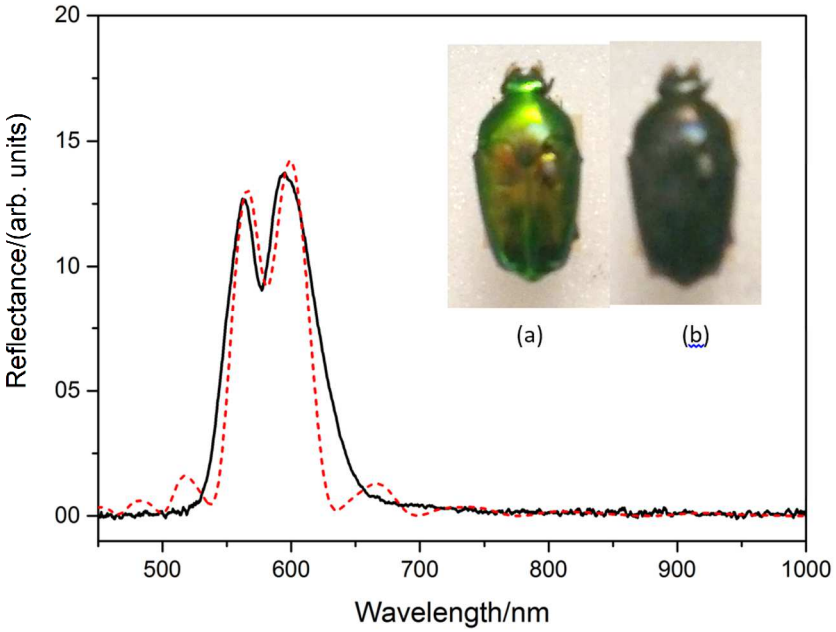


Figure 5.9 – Double peak LCP reflection graph with a small trough from a beetle of the species *L. pygmeae* (black curve). The insets show the appearance of the specimen through (a) left and (b) right circular polarisers. The red-dashed theoretical curve is modelled upon a discontinuity in the pitch of 8/15 π, using complex birefringent refractive indices, of 1.46+0.025i and 1.52+0.025i to simulate absorption, and a layer of 11 pitches thickness in total. From the authors paper [5].

The second *Lomaptera* classification, which had a double peak close together LL spectrum was modelled using a discontinuity in the helical rotation as shown in Figure 3.25c. This feature was modelled with a sudden jump of (8/15) π in the orientation of the molecules within the helix (Figure 5.9). The phase of the sudden jump was chosen in order to obtain the asymmetry

between the peak reflection values. A sudden jump in the helix was also seen in the *Chrysina resplendens* beetle [6], although unlike the beetle in this study the *C. resplendens* also contains a uniaxial layer. Twist defects without uniaxial layer have been observed in other chiral structures [7].

5.4.3. Double Pitches Further Apart

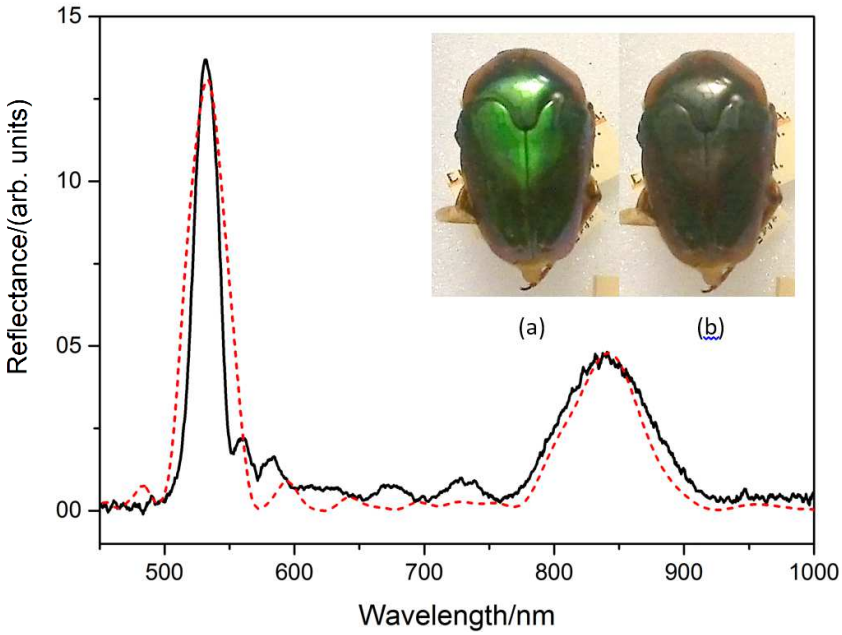


Figure 5.10 – Double peak LL reflection graph with two clearly distinct peaks from a *L. geelvinkiana* specimen (black curve). The inset photographs show the appearance of the specimen through (a) left and (b) right circular polariser. The red-dashed theoretical curve is modelled upon two distinct pitch values, using complex birefringent refractive indices of 1.485+0.01i and 1.52+0.01i and having a thickness of 12.5 pitches in total. From the authors paper [5].

The double pitches which are further apart were modelled as two different and distinct pitches with the stack with the shorter pitch nearer the surface. The basis for the structure used in the model is demonstrated in Figure 3.25a. The two stacks with different pitches, results in two distinct pitches at different wavelengths. The model shows oscillations between the two main peaks, which also occur in the experimental results (Figure 5.10). This double peak structure and model was also supported by an SEM of the *Mycterophallus validipies* beetle (Figure 7.1), which also had a LL spectrum with double peaks apart from each other.

5.4.4. Multiple Discontinuity

The last three classifications were all modelled using multiple discontinuities in the helix rotation. The 'oscillation after' spectral type (Figure 5.11) was modelled using two discontinuities of (1/6)π and (1/2)π.

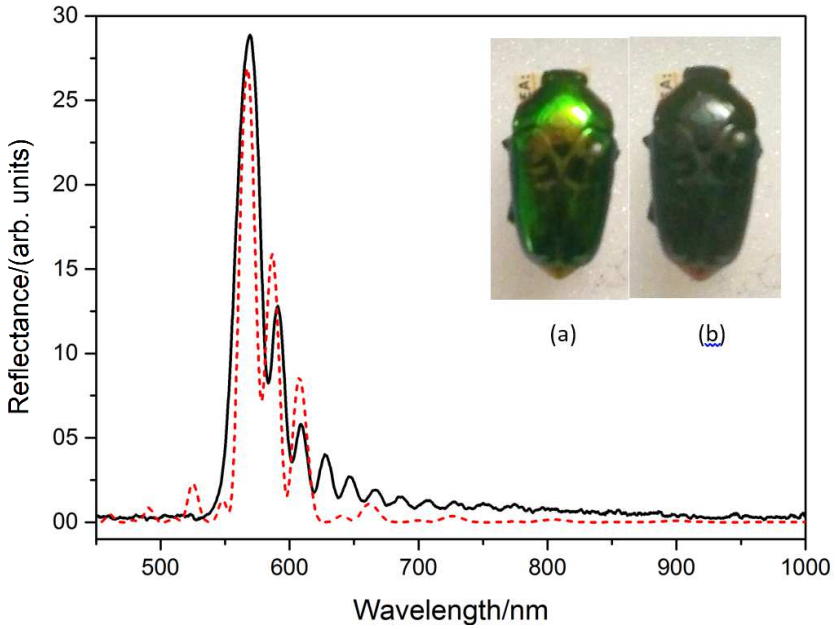


Figure 5.11 – LL reflectance spectrum with gradually reducing oscillations at higher wavelengths of a beetle of *L. pseudodichropus* (black curve). The insets show the appearance of the specimen through (a) left and (b) right circular polarisers. The red-dashed theoretical curve is based upon a model of a structure of 19.5 pitches thick and discontinuities in the pitch of (1/6)π and (1/2)π, using complex birefringent refractive index of 1.498+0.002i and 1.52+0.002i. From the authors paper [5].

The model with oscillations before the main peak had two discontinuities of (5/6)π and (3/2)π (Figure 5.12). It should be noted that previously it was stated that oscillations before or after the main peak had been described as being caused by a chirped structure by Parker *et al* [8].

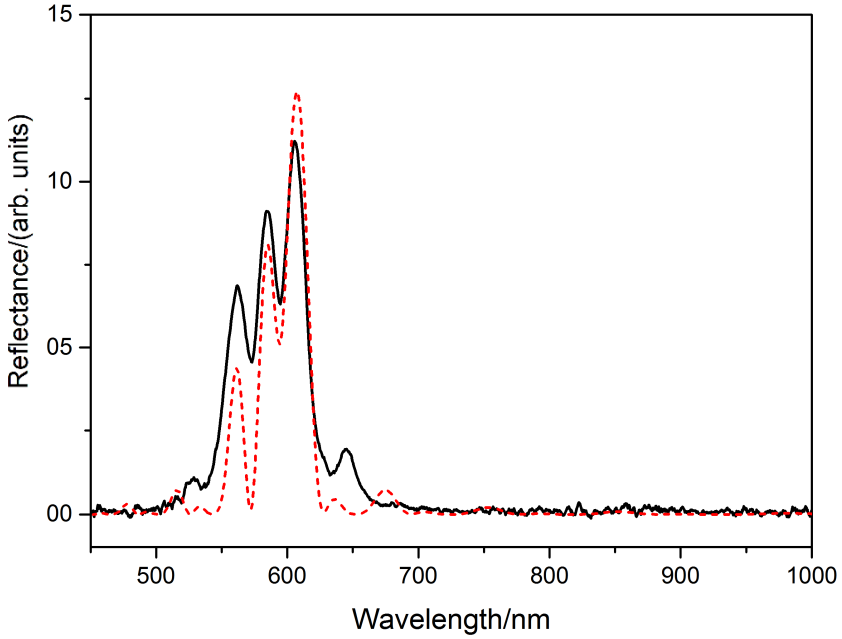


Figure 5.12 – Experimental LCP reflectance spectrum with gradually increasing oscillations before the main peak of a beetle of *L. soror* (black curve). The red-dashed curve is based upon a theoretical model with two different twist defects. The model is based on a structure of 16.5 pitches thick structure with discontinuities in the pitch of (5/6)π and (3/2)π, using complex birefringent refractive indices of 1.498+0.006i and 1.52+0.006i. From the authors paper [5].

An unclassified spectral shape was more complex and was also modelled using two discontinuities of (1/15)π and (17/24)π (Figure 5.13). It should be noted the unclassified spectra

shapes varied greatly in shape and wavelength and this is shown as an example of how a model can be applied.

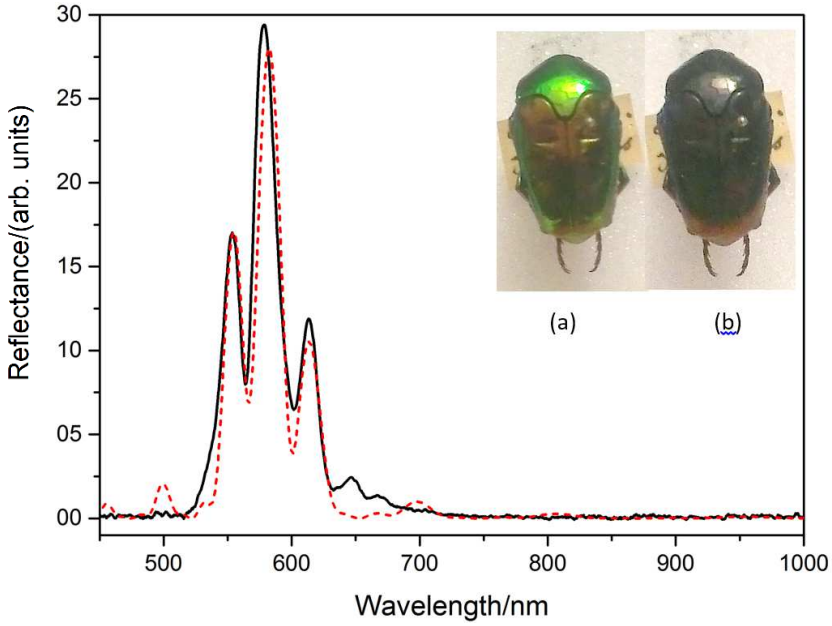


Figure 5.13 – A plot of a LCP spectrum, this being one from a *L. soror* beetle, showing a response which could not be placed into the five chosen classifications (black curve). The red-dashed theoretical curve is from a model based upon a structure 13.5 pitches thick with discontinuities in the pitch of (1/15)π and (17/24)π, using complex birefringent refractive indices of 1.49+0.001i and 1.52+0.001i. From the authors paper [5].

5.5. Modelled Cetonia aurata aurata

As with the *Lomaptera* genus (Section 5.4) variations in the LL spectral shape in *Cetonia aurata aurata* beetles were modelled. The variation of these LL spectral shapes and distribution of those shapes was analysed in Section 4.3.3.5. The models for these spectral shapes were based upon a single pitch value (Figure 5.14a), pitch rotation defects (Figure 5.14b-d) and multiple pitch values (Figure 5.14e-f). The details of the variables used in these models can be seen in Table 5.1 with a more detailed description in Appendix Table A 1. These models with the more complete fits were the single (Figure 5.14a), double close (Figure 5.14b) and unclassified spectra (5.14f). The triple (Figure 5.14c), oscillations after (Figure 5.14d) and double apart (Figure 5.14e) spectra had some agreement, though the oscillation features were less perfect fits with more notable troughs in the models than the experimental spectra.

Average refractive index	Minimum birefringence	Maximum birefringence	Mean extinction coefficient	Range of extinction coefficient	Mean total thickness in pitches
1.51	0.02	0.08	0.012	0.0243	15.8

Table 5.1 – Minimum and maximum input parameters used in the models in Figure 5.14.

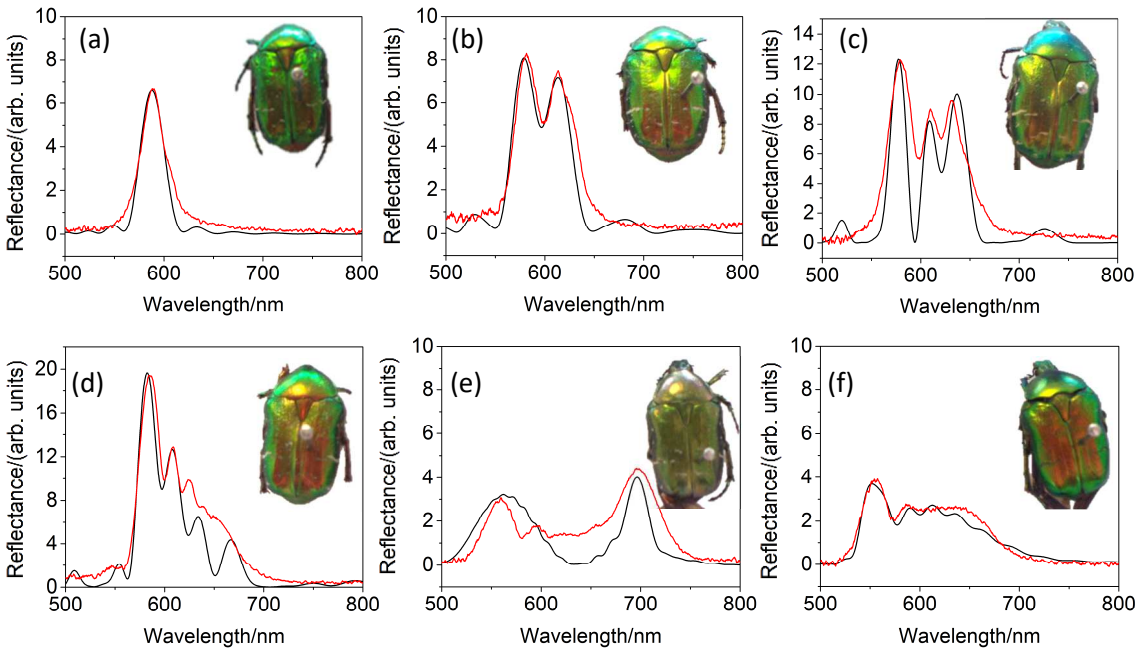


Figure 5.14 - LL spectral responses of *Cetonia aurata aurata* specimens with, described as (a) single peak (S), (b) double close (DC), (c) triple (T), (d) oscillations after (OA), (e) double apart (X) and (f) unclassified (U). The red lines are experimental data and the black are modelled. The inset photographs are of beetles through a LCP filter. Published by the author in [9].

5.6. Modelled Examples from Each of the Nine Subfamilies

Further to the *Lomaptera* family, models were applied to an example of each of the nine subfamilies which reflect CP light. These models were fitted in various different and often more complex ways.

As can be seen in Figure 5.15 there is a wide variation in different spectral shapes. The models for which were based upon the three basic variations mentioned in Section 5.3. The models in Figure 5.15d-h were based upon a single pitch, Figure 5.15a and i were based upon multiple pitches, Figure 5.15c was based upon defects only and Figure 5.15b was a combination of defects and pitches. The details of the variables used in these models can be seen in Table 5.2 with a more detailed description in Appendix Table A 2. The single peak LL models (Figure 5.15d-h) and the model with a tail (Figure 5.15i) had better degree of fits, than the multiple peaked LL spectrum Figure 5.15a-c which had less defined experimental troughs than the models.

Average refractive index	Minimum birefringence	Maximum birefringence	Mean extinction coefficient	Range of extinction coefficient	Mean total thickness in pitches
1.495	0.013	0.069	0.009	0.0202	7.8

Table 5.2 – Minimum and maximum input parameters used in the models in Figure 5.15.

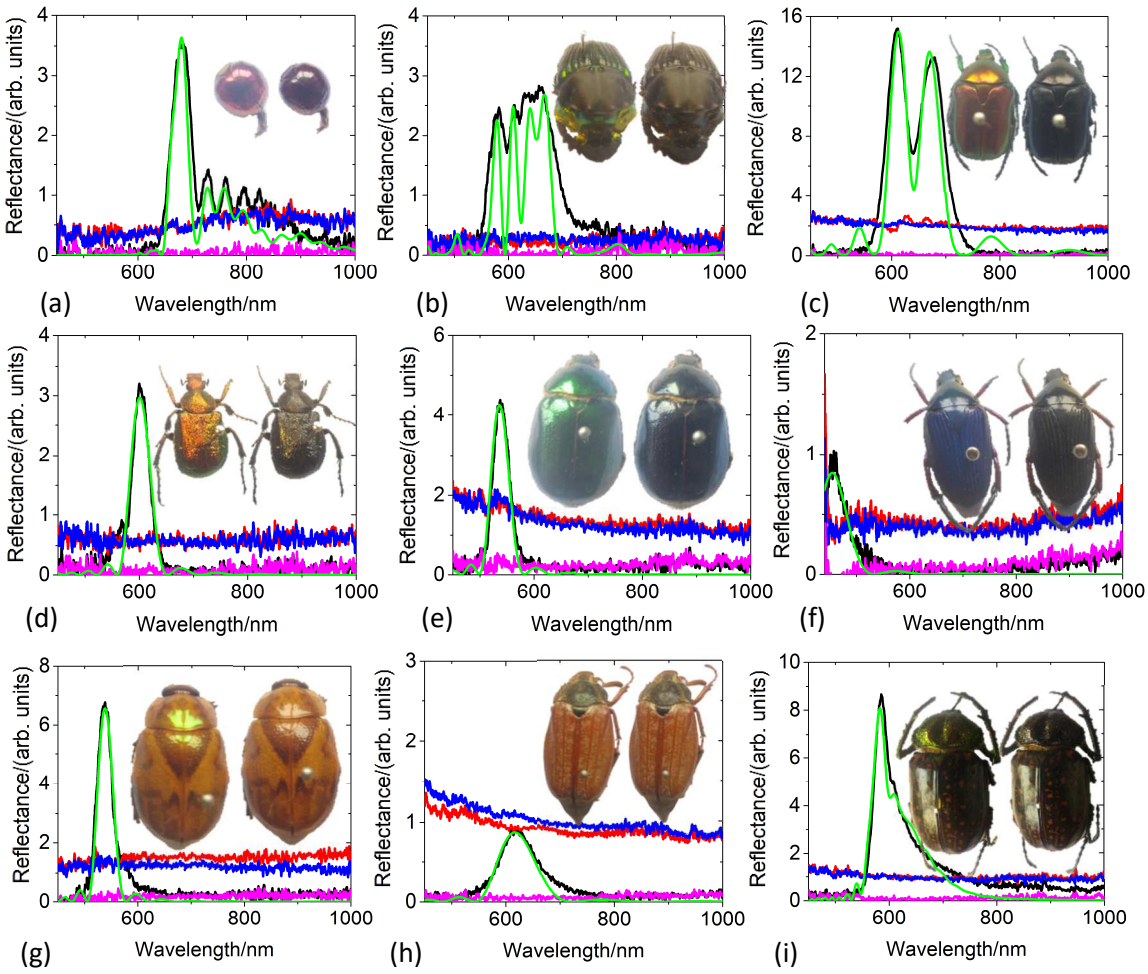


Figure 5.15 - CP reflection spectra with inset LCP (left) and RCP (right) filtered photographs of (a) Ceratocanthinae:*Ceratocanthopsis fulgida* (b) Scarabaeinae:*Diabroctis mimas* (pronotum) (c) Cetoniinae:*Protaetia angustata pyrodera*. (d) Trichiinae:*Gnorimus nobilis*. (e) Rutelinae:*Viridimicus aurescens*. (f) Phaenomeridinae:*Phaenomeris besckei*. (g) Dynastinae:*Augoderia nitidula* (pronotum). (h) Melolonthinae:*Melolontha melolontha* (pronotum). (i) Euchirinae:*Cheirotonus battareli* (pronotum). Experimental LL spectra are black, LR are red, RL are blue, RR are pink and modelled LL spectra are green. Published by the author in [9].

5.7. Broadband Model

A broadband model was developed for the LL spectra of three colour variations of the *Chrysina optima* beetle (Figure 5.16). The difference in colour forms is due to the lower wavelength boundary of reflection. The model for these beetles was based upon the structure observed in the closely related *Chrysina aurigans*, where the pitch decreases exponentially from the surface [10]. The details of the variables used in these models can be seen in Table 5.3 with a more detailed description in Appendix Table A 3. These model fits were successful defining the lower bandwidth limits of the LL reflection spectra seen in the experimental data. The oscillations in the model were more wavelength dependent and as with the previous models the troughs were better defined than the experimental data. It should also be noted that the reflectance percentage between the different coloured *Chrysina optima* specimens did not vary in the model as it did in the experimental data.

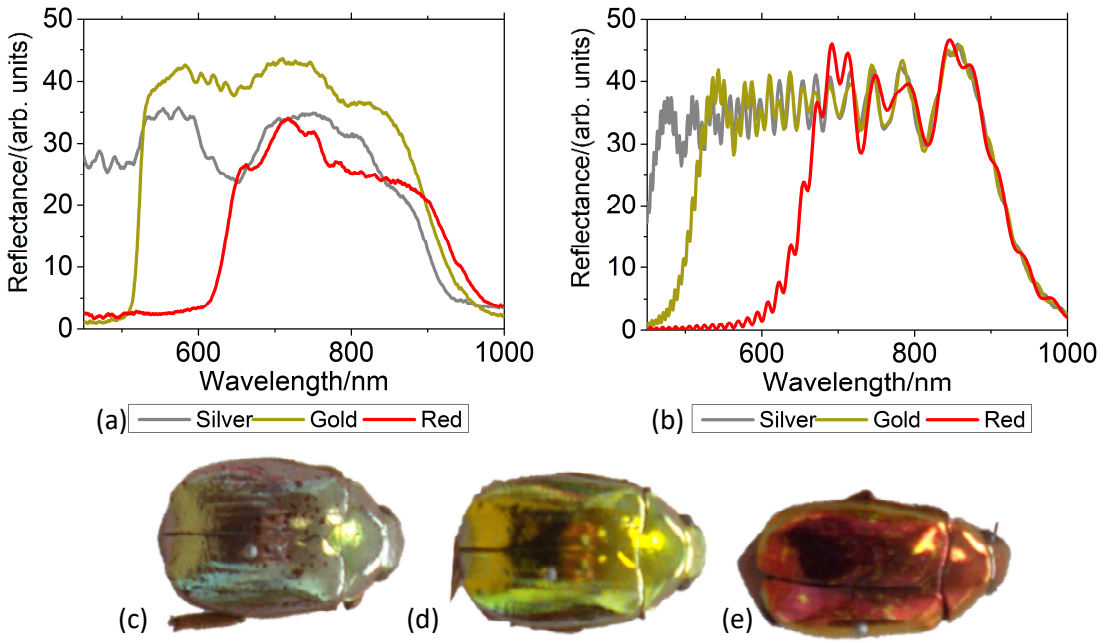


Figure 5.16 - *Chrysina optima* (a) experimental CP spectral responses (b) modelled spectra responses and photographs through a LCP filter of (c) the silver form, (d) the gold form and (e) the red form. Published by the author in [9].

Average refractive index	Minimum birefringence	Maximum birefringence	Mean extinction coefficient	Range of extinction coefficient	Mean total thickness in pitches
1.54	0.08	0.08	0.0007	0	61.5

Table 5.3 – Minimum and maximum input parameters used in the models in Figure 5.16.

5.8. Conclusion

The method in which the code works using Berreman calculus in a layer by layer matrix response is discussed in detail. Once the description of the working of the code is developed the application to modelling experimental CP reflection spectra from beetles is then made. The models were used to demonstrate likely structures which produce the experimental LL spectra. Whilst the structures modelled were not certain to be the exact structures within the beetles' shells they were created using experimentally obtained parameters (such as birefringences, refractive index and number of layers) and structural descriptions.

Examples of different spectral shapes of the LL spectra from the genus *Lomaptera* were modelled. This was done using a combination of two main perturbations to the single pitch structure, which were multiple pitches values and sudden jumps in the helicoidal rotation of layered molecules. A similar modelling process was done for the six typical LL spectral shapes in the species *Cetonia aurata aurata*.

This modelling was further expanded to typical LL spectra from nine specimens each of a different subfamily known to selectively reflect CP light. These examples demonstrated a wide and varied range of LL spectra and hence a large variation to the single pitch helicoidal structure.

In this Chapter several models have been made of many varying LL spectra. Three basic structure models (single pitches, multiple pitches and rotation discontinuities) have been considered in this both alone and also in combinations.

The final model type was upon the broadband response from three *Chrysina optima* colour variations (silver, gold and red). This was the most complex model using an exponential model of pitch thickness variation.

The LL reflection spectra models in this Chapter incorporated experimentally published optical parameters. Twenty five different LL models have been developed, based upon both individual and as combinations of the three basic structures (single pitch, multiple pitches and rotation discontinuity). Modelling using combinations (and perturbations) of these basic structures could be applied to a much wider range of other beetles which reflect LCP light than presented in this study.

5.9. References

[1] M. W. McCall, I. J. Hodgkinson, and Q. H. Wu, *Birefringent Thin Films and Polarizing Elements: 2nd Edition - ISBN:9781783265350*. London: Imperial College Press, 2015.

[2] W. E. Vargas, M. Hernández-Jiménez, E. Libby, D. E. Azofeifa, C. Barboza, and Á. Solis, "Light Reflection by Cuticles of Chrysina Jewel Scarabs: Optical Measurements, Morphology Characterization, and Theoretical Modeling," *Opt. Photonics J.*, vol. 6, no. 7, pp. 146–163, 2016.

[3] D. J. Brink, N. G. Van Der Berg, L. C. Prinsloo, and I. J. Hodgkinson, "Unusual coloration in scarabaeid beetles," *J. Phys. D. Appl. Phys.*, vol. 40, no. 7, pp. 2189–2196, Apr. 2007.

[4] J.-Y. Chen and L.-W. Chen, "Defect modes in a stacked structure of chiral photonic crystals," *Phys. Rev. E*, vol. 71, no. 6, p. 61708, Jun. 2005.

[5] I. E. Carter, K. Weir, M. W. McCall, and A. R. Parker, "Variation in the circularly polarized light reflection of Lomaptera (Scarabaeidae) beetles," *J. R. Soc. Interface*, vol. 13, no. 120, pp. 1–9, Jul. 2016.

[6] M. H. Song, B. C. Park, K. C. Shin, T. Ohta, Y. Tsunoda, H. Hoshi, Y. Takanishi, K. Ishikawa, J. Watanabe, S. Nishimura, T. Toyooka, Z. G. Zhu, T. M. Swager, and H. Takezoe, "Effect of phase retardation on defect-mode lasing in polymeric cholesteric liquid crystals," *Adv. Mater.*, vol. 16, no. 9–10, pp. 779–783, 2004.

[7] V. I. Kopp, V. M. Churikov, G. Zhang, J. Singer, C. W. Draper, N. Chao, D. Neugroschl, and A. Z. Genack, "Chiral fiber gratings: perspectives and challenges for sensing applications," 2007, vol. 6619, pp. 1–8.

[8] A. Parker, D. McKenzie, and M. Large, "Multilayer reflectors in animals using green and gold beetles as contrasting examples," *J. Exp. Biol.*, vol. 1313, no. 1998, pp. 1307–1313, 1998.

[9] I. E. Carter, K. Weir, and M. W. McCall, "Investigation of the Variation of Near-Circular Polarization in Scarabaeoidea Beetles," *Mater. Today Proc.*, vol. 4, no. 4, pp. 4942–4951, 2017.

[10] D. E. Azofeifa, M. Hernández-Jiménez, E. Libby, A. Solís, C. Barboza-Aguilar, and W. E. Vargas, “A quantitative assessment approach of feasible optical mechanisms contributing to structural color of golden-like Chrysina aurigans scarab beetles,” *J. Quant. Spectrosc. Radiat. Transf.*, vol. 160, pp. 63–74, Jul. 2015.

Chapter 6 - Ellipsometry

6.1. Introduction

In this Chapter the description of how a polarimeter was designed and employed in order to measure the MM of any beetle in reflection is presented. The polarimeter setup basic operation had two arms, an incoming arm with known polarisation and an output arm, which analysed the polarisation of the reflected light. It should be noted that in this study the terms ellipsometer/ellipsometry and polarimeter/polarimetry are used interchangeably, with ellipsometry being the study of thin films using polarimetry. Such measurements will allow a more detailed description of the polarisation of reflected beetles than the setup in Chapter 4 allowed. MM calculus is employed, as described in Section 2.3, which allows a detailed description of the polarisation in terms of ellipticity, azimuth angle and degree of polarisation. Several different polarimeter arrangements were considered, with the final setup having sheet polarisers in the input arm and LCVRs in the output arm.

In the experimental results the MMs were normalised in the following way due to the beetles curved shells introducing loss in the measured spectrum. The maximum single value over all wavelengths (A_{00}) of the MM element M_{00} (which is a column vector) was found. Then each MM element M_{mn}, was then divided by A_{00} as in equation 6.1 below. Normalising the MM to have maximum value of 1 for each set of measurements made the results between specimens more easily comparable.

$$\frac{1}{A_{00}}\begin{bmatrix} M_{00} & M_{01} & M_{02} & M_{03} \\ M_{10} & M_{11} & M_{12} & M_{13} \\ M_{20} & M_{21} & M_{22} & M_{23} \\ M_{30} & M_{31} & M_{32} & M_{33} \end{bmatrix} \tag{6.1}$$

6.2. Retarder Types

In order to measure the optical structure using polarisation changes upon reflection from the beetle, the experimental setup required retarders to control polarisation in the input and analyse polarisation in the output. In this study various retarders were considered for use in creating a MM ellipsometer. These include sheet waveplates, Babinet-Soleil compensators and Fresnel rhombs. Table 6.1 discusses the advantages and disadvantages of each of them [1],[2].

Using this knowledge, several MM systems were investigated. The first setups that were considered involved the use of Fresnel rhombs. The setup involving a Fresnel rhomb and the results are discussed in Appendix A5.1. This setup encountered numerous problems including it having to be adjusted manually for different polarisation inputs, due to the geometry of the Fresnel rhombs, which led to the introduction of alignment errors.

The next setup which was considered using a LCVR on the input and output paths using the same method. However this meant MM element M_{33} could not be calculated due the use of a single LCVR at the input (or output) stage (Appendix A5.2).

RETARDER TYPE	ADVANTAGES	DISADVANTAGES
Waveplates	• Fixed retardance	• Not achromatic
Babinet-Soleil compensators	• Achromatic	• Needs to be adjusted for every wavelength
Fresnel Rhombs	• Achromatic	• Difficult to rotate due to symmetry
Cholestric Liquid Crystal Retarders	• No moving parts • Relatively fast • Retardance can be kept constant for minutes and hours	• Temperature dependence • Not fully stable with time (weeks) • Variable retardance over wavelengths for one driving voltage
Piezo-optic modulators	• No moving parts • Highly stable • Fast modulation	• Modulation only for short time (ms) • Not achromatic
Electro-optic modulators	• No moving parts • Highly stable • Fast modulation	• Modulation only for short time (ms) • High driving voltages required • Not achromatic

Table 6.1- Advantages and disadvantages of different retarders, which were considered for use in a MM ellipsometer.

The method which will be discussed in detail in this report involved calibration using two LCVRs in the analysing arm and sheet Quarter Waveplate (QP) and sheet Linear Polariser (LP) in the input arm. It should also be noted this was compared to using sheet polarisers in both arms (Appendix A5.3).

6.3. Mueller Matrix Method

A calibration method was employed, in which only the input arm was of known polarisation. The setup was created using two LCVRs in the analysing arm, whilst using a QP and sheet LP in various orders in the incident arm. This setup is similar to one described previously by Ramella-Roman *et al* [3]. The calibration of this setup was based upon a previous study by Boulbry *et al*, which was at a single wavelength for each measurement [4].

Initially this setup was used in transmission over a broadband range in order to be able to calibrate and test the system using a sheet LP as a sample.

In the input arm a sheet LP and a sheet QP was used in combination to produce six different but known input states of polarisation (it is possible to use four and cover all polarisation states

required to fully define the MMs, but using six reduces noise). The QP placed before the LP 1, in position 1 (Figure 6.1a) the linear polarisation states could be produced (-45°, 0°, 45°, and 90°). When LP 1 is placed before the QP (Figure 6.1b), LCP and RCP light can be produced.

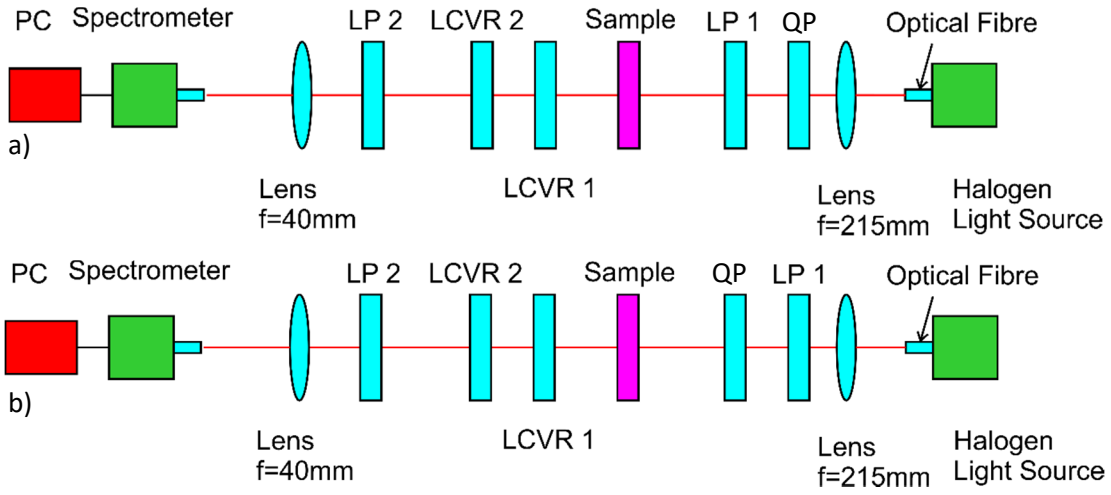


Figure 6.1 – Transmission ellipsometer setup, in position a) 1 and b) 2, with linear polarisers (LP1, 2), quarter waveplate (QP) liquid crystals (LCVR1, 2).

In the analysing arm LP 2 is set to 90° with respect to the other LPs, LCVR 1 is set to two different voltages whilst LCVR 2 is set to three different voltages leading to six different voltage combinations.

The system works by first taking a reference measurement without a sample in place, using known polarisation inputs and different voltages in the LCVR in the output arm. From this reference measurement the output arms response can be calibrated. When a sample is placed in the system the same measurement process is undertaken and from this the MM of the sample can be calculated.To minimise errors, calibration of the system is defined by the equation 6.2.

$$B = WMI, \tag{6.2}$$

where B is the measured output intensity matrix (of dimension jxk), W is the matrix of the analysing arm (kx4), M is the MM of the sample (4x4), I is a matrix of input Stokes vectors (4xj). Where j is the number of different input polarisation states and k is the number of different retardance combinations of the LCVR's used. In the final setup k and j were both equal to six.

The first stage is to acquire the matrix of the analysing arm through calibration. This was done with no sample in the system such the MM was a 4x4 identity matrix in the transmission setup (in the reflection setup the MM of a mirror must be taken into account). With rearranging equation 6.2 becomes

$$W = B_0 I^{-1} M^{-1} = B_0 I^{-1}, \tag{6.3}$$

where B_0 is the output intensity matrix with no sample in the setup. As W is now known, the MM of a sample in the system can then be calculated with the measured output intensity matrix with a sample B_s, as

$$M = W^{-1}B_s I^{-1}. \quad (6.4)$$

It should be noted that this calculation of the MM is performed at 0.25nm intervals between 450nm and 750nm.

6.4. Calibration

6.4.1. Liquid Crystal Variable Retarder Calibration

In order to obtain a functional setup, basic calibration of the LCVRs retardances is required. This was achieved using the method as described by Bueno [5]. A LCVR was placed between two crossed LPs with the fast axis of the LCVR at 45° to the first LP 1 (as in Figure 6.2). Two different LCVRs were used, the first was a digital LCVR (ThorLabs LCC1223-A and the second was [6]) an analogue LCVR (ARCoptix [7]).

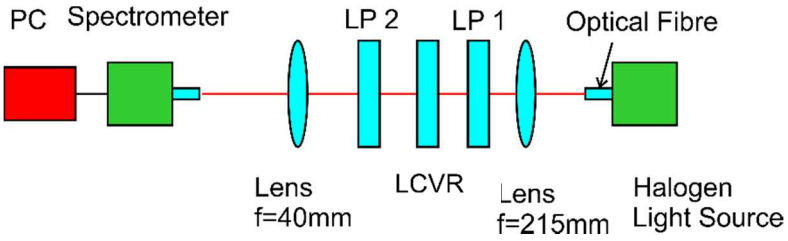


Figure 6.2 – LCVR calibration setup.

The intensity of the light reaching the detector, when the two LPs are crossed $I_{crossed}$, is given by equation 6.5. The intensity of light which passes through two parallel LP's (without the LCVR) with the transmission of both the analogue and digital LCVRs (Figure 6.3) also taken into account is given as I_p, where δ is the phase difference as an angle and equation 6.5 can be rearranged in order to find δ, equation 6.6.

$$I_{crossed} = I_p \sin^2\left(\frac{\delta}{2}\right) \quad (6.5)$$

$$\delta = 2\arcsin\left(\sqrt{\frac{I_{crossed}}{I_p}}\right) \quad (6.6)$$

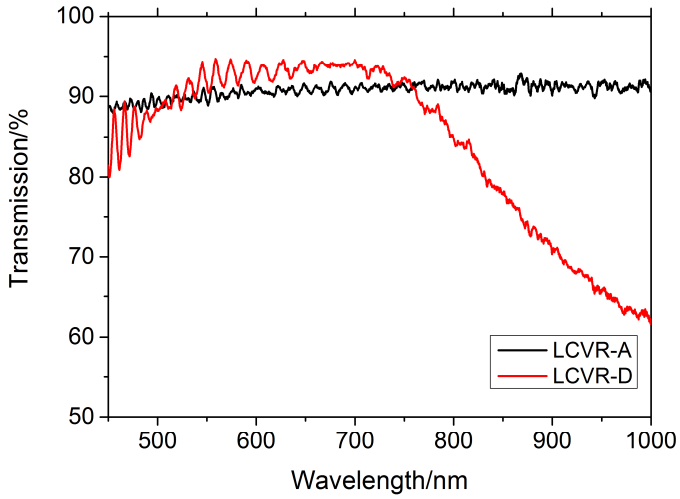


Figure 6.3 – The transmission of the analogue (LCVR-A) and digital (LCVR-D) LCVRs.

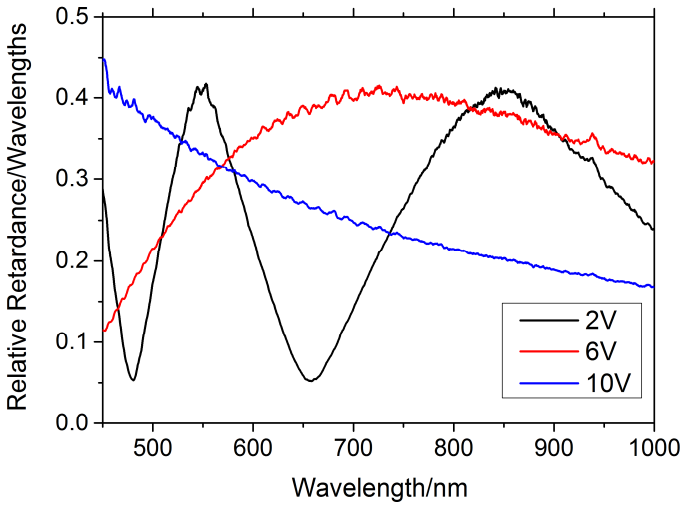


Figure 6.4 – The relative retardance of a LCVR at different driving voltages over the wavelength range available.

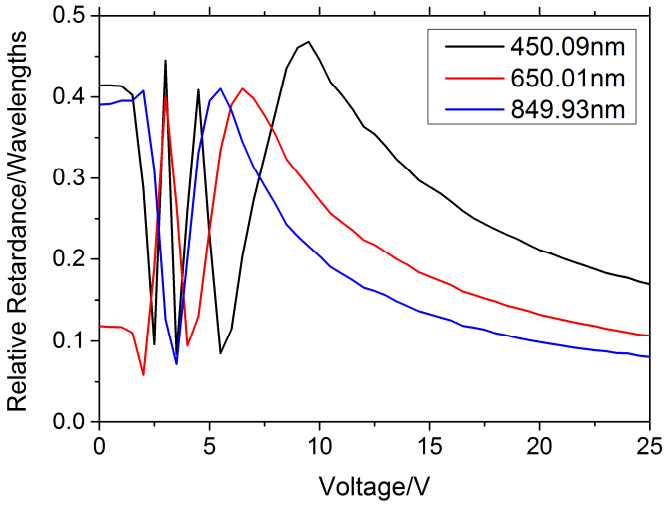


Figure 6.5 – The relative retardance of a LCVR at different wavelengths across the driving voltage range.

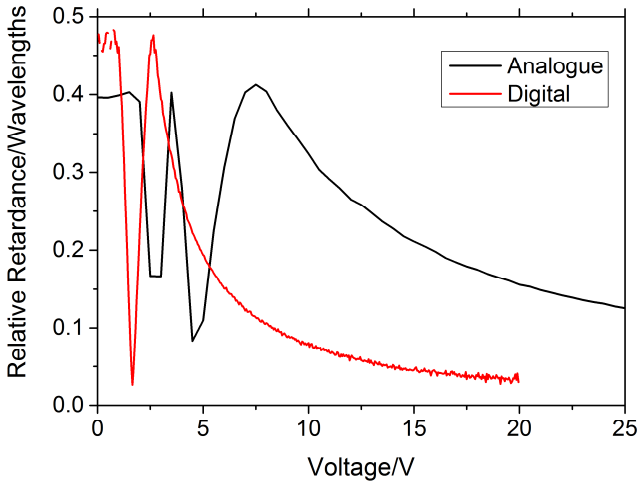


Figure 6.6 – Relative retardance of the two different LCVRs at different driving voltages at 750nm.

Using equation 6.6, the setup described (Figure 6.2) and the LCVR manufactured by ThorLabs (LCC1223-A), the retardances were found for multiple applied voltages (Figure 6.4) and multiple wavelengths (Figure 6.5). The multiple wavelength measurements (Figure 6.5) were taken using a program written in LabView with the help of Dr. S. Kumar, Imperial College.

In the final setup the digital and an analogue LCVRs were used and the retardances of each was plotted over a range of input voltages at the wavelength 750nm (Figure 6.6). Relative retardance of the LCVRs were given rather than absolute retardances. The relative retardances have turning points when they tend to the minimum (0 wavelengths) and maximum (0.5 wavelengths) retardances. It can be seen in Figure 6.6 that the digital LCVR is much more voltage sensitive than the analogue. It should be noted the LCVRs are time and temperature dependent (Appendix 4.5.4), this is overcome by recalibrating the full MM every few hours when measurements are made and also using more LCVR driving voltage combinations than necessary.

In the final setup the angle of the LCVR's fast axis were set to 72.4° (LCVR digital) and 27.4° (LCVR analogue) which optimised the system. Driving voltages were initially chosen to give two retardances at 650nm on each of the LCVRs of δ_1=(135+v90)° and δ_2=(315+v90)°, where v is an integer. The optimum choices of these parameters were taken from previous studies to ensure enough independent polarisation states could be analysed in order to fully define the calibration matrix of the analysing arm, W [8].

The minimum number of input polarisations required for the polarimeter to be able to produce the full MM is four; (0°), (45° or -45°), (90°) and (LCP or RCP). However, a greater accuracy is given by six polarisations as can be seen in Figure 6.7, and so this number was used. It should be noted that there is a delta-like function at ~500nm due to retardance degeneracy. This is discussed further in Section 6.4.5.

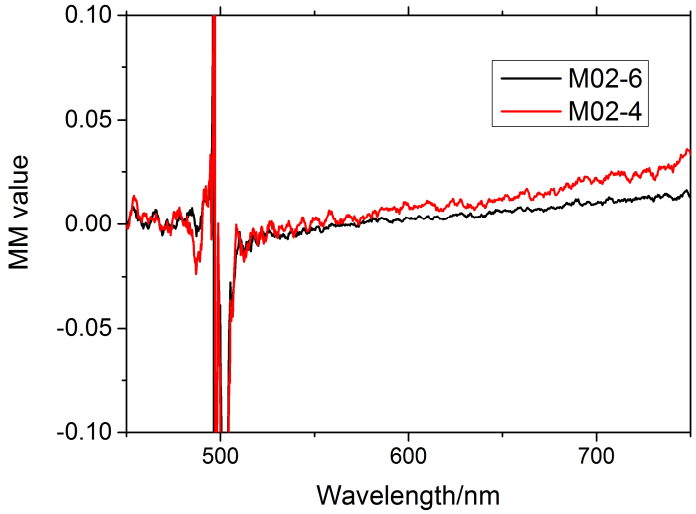


Figure 6.7 – The difference in the MM element M02 for four and six polarisation inputs (which should ideally be close zero for a LP at 86°).

In the input arm linear and circular polarisers used in the system were also analysed in order to determine the useable wavelength range of the system.

6.4.2. Linear Polarisers

The usable wavelength range of the LP was the first component to be analysed. The transmission through two LPs was measured in both parallel and perpendicular configurations (Figure 6.8). From this the upper wavelength boundary of measurements was established as 750nm, since above this in the perpendicular configuration the light is longer extinguished. As in Chapter 4, the halogen light source works stably above 450nm, so this defined the lower wavelength limit.

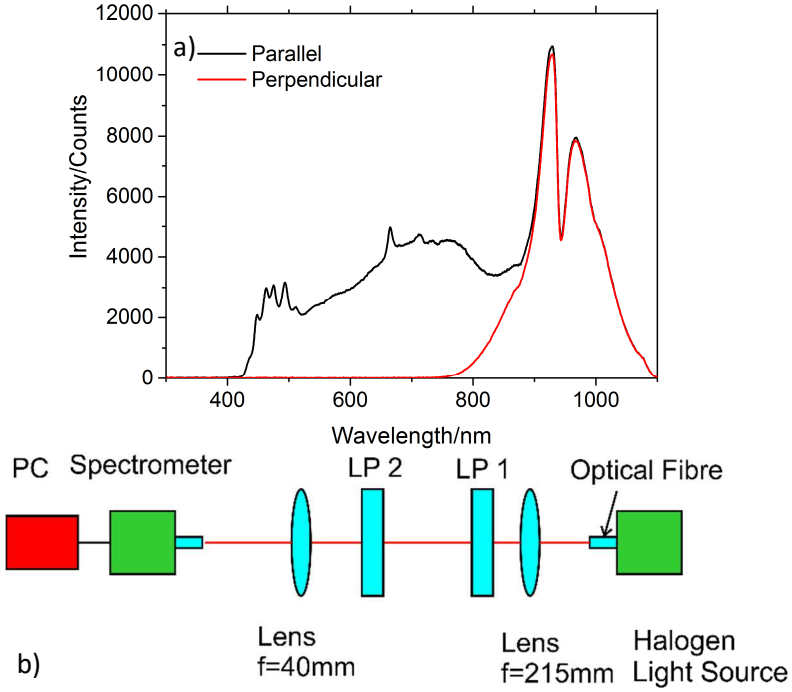


Figure 6.8 – a) Intensity spectra of parallel and perpendicular LP configurations, with boxcar of 5, average of 1 and integration time of 40ms, with b) the experimental arrangement depicted below of two LPs (LP 1 and LP 2).

The transmission spectra of unpolarised light through both linear and circular polarisers were determined (Figure 6.9). The spectra from the circular polariser is relatively flat, transmission through the LPs varies more with wavelength (Figure 6.10). It should also be noted that transmission was high for the circular polariser at ~0.83 (or ~83%), compared to the LPs which were much lower at ~0.3 (or ~30%). The transmission of LP on a rotating mount was slightly less than that of the non-rotating, due to the fact the rotating LP was attached to glass, which absorbs a small amount of the light.

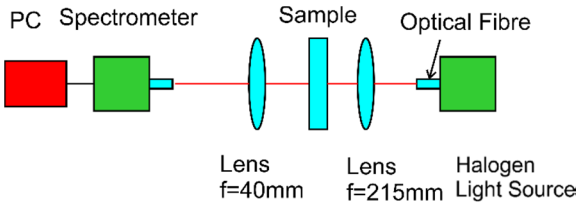


Figure 6.9 - A diagram of the experimental arrangement for measuring the transmission of optical components.

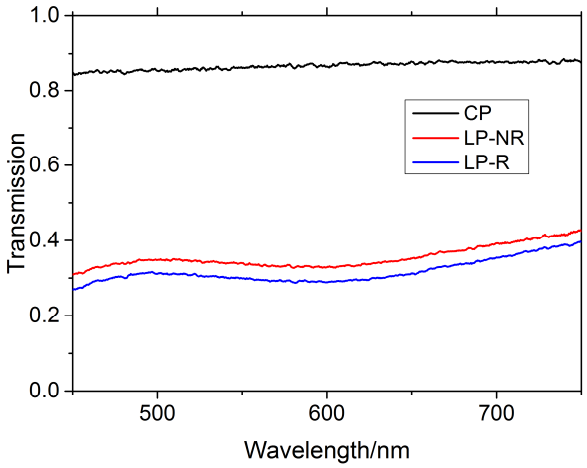


Figure 6.10 – Transmission (between 0 and 1) of linear polarisers (LP), non-rotating (NR) and rotating (R) and quarter waveplate (CP), with boxcar of 5, average of 1 and integration time of 40ms.

6.4.3. Testing the System

In order to test the system, a LP, which was at approximately 86° was used as the sample. The ideal MM of this sample taking into account the average transmission of the LP was calculated as:

$$\begin{bmatrix} 0.3600 & -0.3565 & 0.0501 & 0 \\ -0.3565 & 0.353 & -0.0496 & 0 \\ 0.0501 & -0.0496 & 0.007 & 0 \\ 0 & 0 & 0 & 0 \end{bmatrix}. \quad (6.7)$$

When the system was measured using six input polarisation states and four different LCVR voltage combinations, there was seen to be several problems with the MM (Figure 6.11). The first of which is in the MM elements M_{03} and M_{13} are non-zero and vary with wavelength. The second can clearly be seen as a delta-like function at ~500nm across all the MM elements.

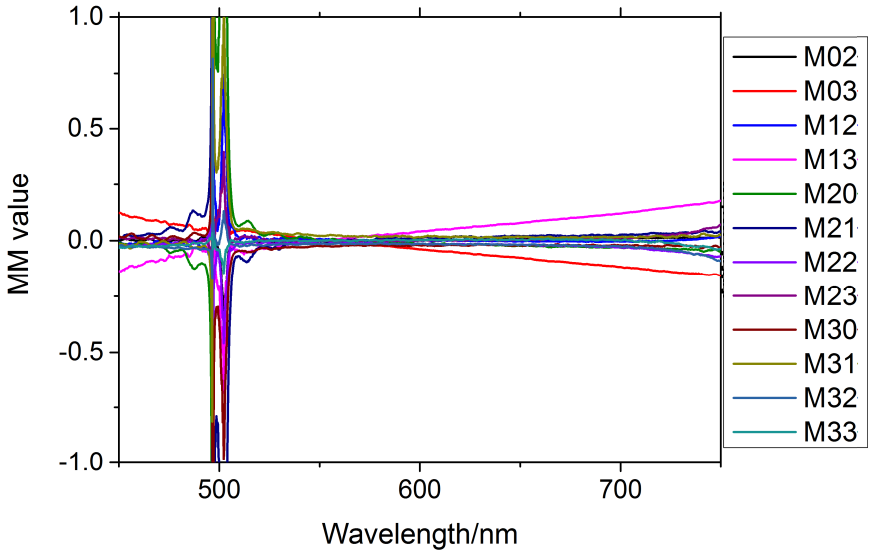


Figure 6.11 – Plot of the MM elements from a LP at 86°, which should ideally be negligible.

6.4.4. Quarter Waveplate Variation

The achromatic variation of MM elements M_{03} and M_{13} was due to the QP being used. This QP only acted as such at 560nm (the specified working wavelength). In order to correct this, the

variation from circular polarisation states in terms of the ideal Stokes vectors of $[1, 0, 0, \pm 1]^T$ must first be found. This was done by considering the polarisation ellipse (Chapter 2), where a is the major axis, b the minor axis and θ is the angle of the major axis. The Stokes vectors can be represented in equation 6.8a-d, from [9].

$$S_0 = |E_x|^2 + |E_y|^2 = a^2 + b^2, \quad (6.8a)$$

$$S_1 = |E_x|^2 - |E_y|^2 = (a^2 - b^2)\cos 2\theta, \quad (6.8b)$$

$$S_2 = 2\mathrm{Re}(E_x E_y^*) = (a^2 - b^2)\sin 2\theta, \quad (6.8c)$$

$$S_3 = 2\mathrm{Im}(E_x E_y^*) = 2abh, \quad (6.8d)$$

where (h=±1) is the handedness of CP light.

Experimentally the QP variation was investigated using the setup in Figure 6.12, where LP 1 is set at ±45° to the fast axis of the QP, in order to produce RCP and LCP light respectively. LP 2 was rotated from 0° to 180°. It would be expected if the LP1-QP arrangement produced perfectly CP light the intensity output would be independent of the angle of LP 2.

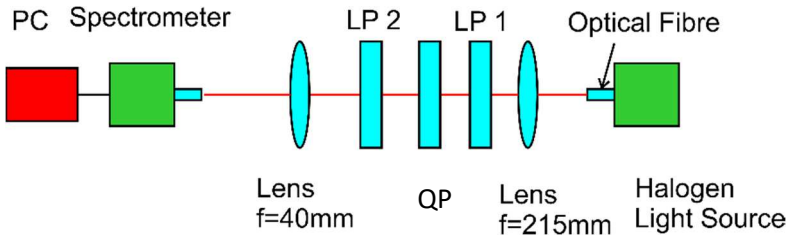


Figure 6.12 – Experimental setup to measure the chromatic variation of a circular polariser.

This setup was configured in both the LCP and RCP arrangements. In Figure 6.13 the output of the system when set to the RCP configuration is shown. This output varies in intensity with LP angle away from the designed wavelength (560nm). This shows that at a wavelength of 560nm, the light is closest to being almost perfect circular polarisation. Away from this wavelength, the light produced becomes more elliptical and hence the transmission becomes dependent upon the angle of LP2.

In order to account for this the following procedure was used. The angle of the second LP at which the maximum transmission ratio occurred was the azimuth angle θ. The value of the major axis (a) of the polarisation ellipse was found from the square root of the maximum value of a ratio of transmission intensity (to the response at 560nm) for each wavelength (Figure 6.14). The value of the minor axis, (b) was found from the square root of the minimum value of the transmission ratio. The handedness was taken as ±1 for RCP and LCP configurations respectively. These parameters were used to calculate the Stokes vectors using equations 6.7a-d, which are then normalised at all wavelengths, such that S_0 is always equal to one.

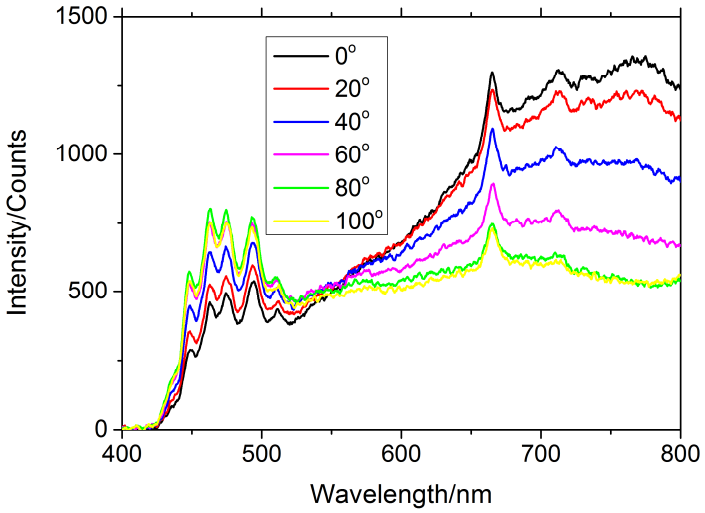


Figure 6.13 – Intensity spectra of light generated from a QP sheet with a LP at 45° to the fast axis, with rotating analysing linear polariser (LP 2) at different angles, with boxcar of 5, average of 1 and integration time of 40ms.

When the adjusted Stokes vectors for the LCP and RCP positions over the working wavelength range (450nm-750nm) were obtained they were then used in recalculating the MM of the LP at 86°. These could be seen to correct the MM elements M_{03} and M_{13} (Figure 6.15). These MM elements (away from the delta like function at 500nm) can be seen to be close to zero with little chromatic variation.

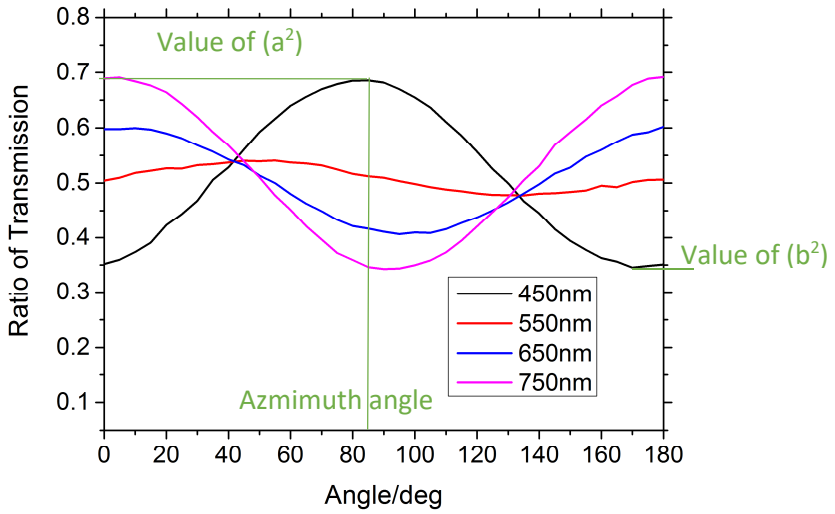


Figure 6.14 – The ratio of transimission compared to the light source for the QP sheet set to RCP output, over 180° on the LP2 for 450nm, 550nm, 650nm and 750nm. The major axis, minor axis and azimuth angles are labelled for 450nm in green.

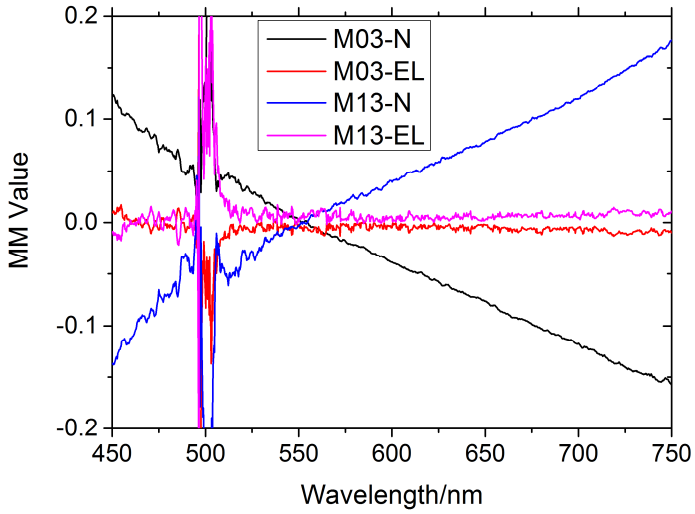


Figure 6.15 – Elliptical fix (EL) applied to the data compared to non-corrected (N) data for the MM elements M_{03} and M_{13} using an 86° LP.

6.4.5. Delta-like Function – Retardance Degeneracy

A minimum of four voltage combinations are required for the LCVR's in order to produce four independent polarisation analysis states in the output arm. However, as broadband polarimetry was employed and the LCVR's retardance is wavelength dependent, degeneracy occurred at some wavelengths. This was caused by the four voltage combinations (of the digital LCVR-D and analogue LCVR-A) producing less than four different polarisation states at certain wavelengths, leading to delta like function (Figure 6.16). The wavelength at which the delta function occurs can be varied by altering the input voltage as shown Figure 6.17. In order to avoid this delta like function and achieve at least four independent polarisation states for every wavelength six voltage combinations were used (Figure 6.18). It is possible to use a combination of four or five voltages (See Appendix A5.5), as the LCVR is temperature and slightly time dependent six voltages combinations must be used in order to compensate for this and avoid degeneracy.

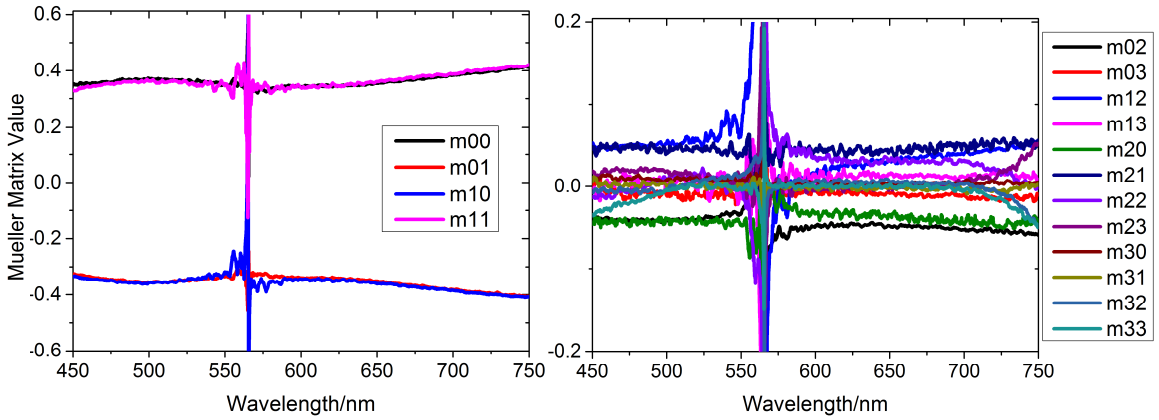


Figure 6.16 – MM values of a LP at 86° using four driving voltages of LCVR-D and LCVR-A combinations (2.277V, 6.6V), (6.494V, 6.6V), (6.494V, 25.0V) and (3.777V, 6.6V).

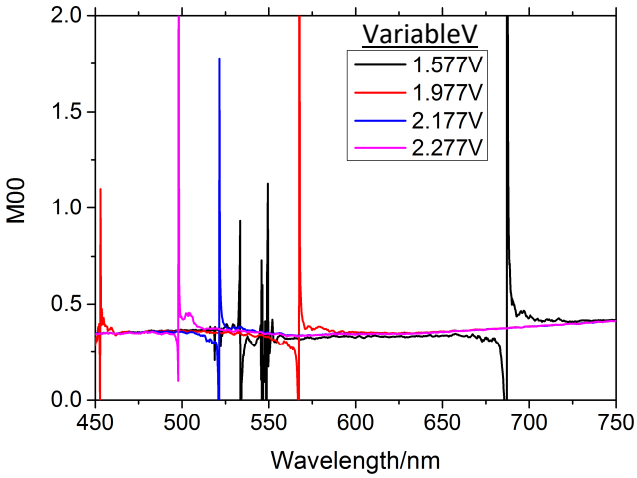


Figure 6.17 – M_{00} element values of a LP sample at 86°. One of the two driving voltages upon the LCVR-D is varied. The driving voltages combinations of the LCVR-D and LCVR-A were (VariableV, 6.6V), (VariableV, 25.0V), (6.494V, 6.6V) and (6.494V, 25.0V). The variable voltage (VariableV) values are stated in the inset key.

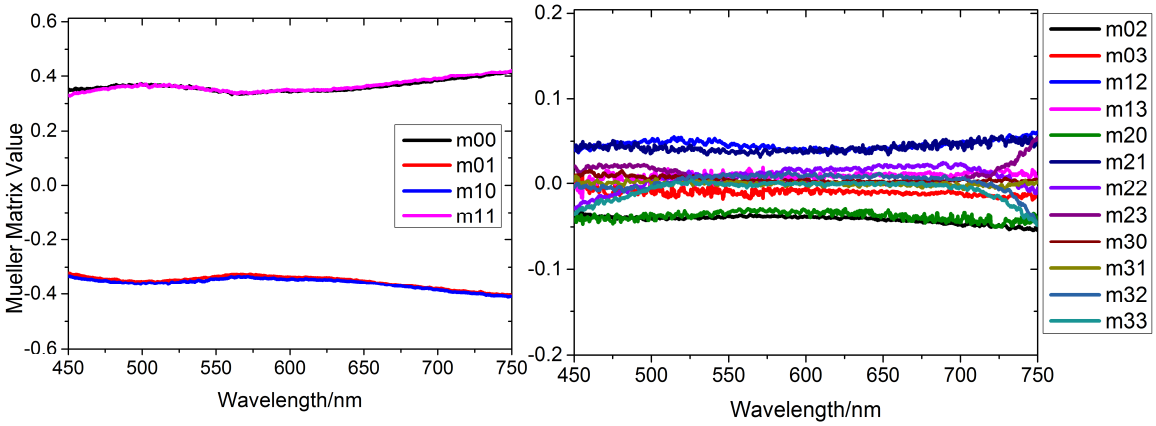


Figure 6.18 – MM values of a LP at 86° using six driving voltages combinations of on the LCVR-D and LCVR-A respectively as (2.277V, 6.6V), (2.277V, 25.0V), (6.494V, 6.6V), (6.494V, 25.0V), (3.777V, 6.6V) and (3.777V, 25.0V).

At this stage a fully working broadband transmission MM ellipsometer was developed using two LCVRs in the analysing arm using six voltage combinations.

6.5. Reflection Mode

The calibration was done in transmission mode and the MM values were seen to reproduce those of a LP at 86° (Figure 6.18). The system was then altered to operate in reflection mode (Figure 6.19), in order to measure the beetles' optical MMs. The angle between the two arms was 30°, making the incident angle 15°.

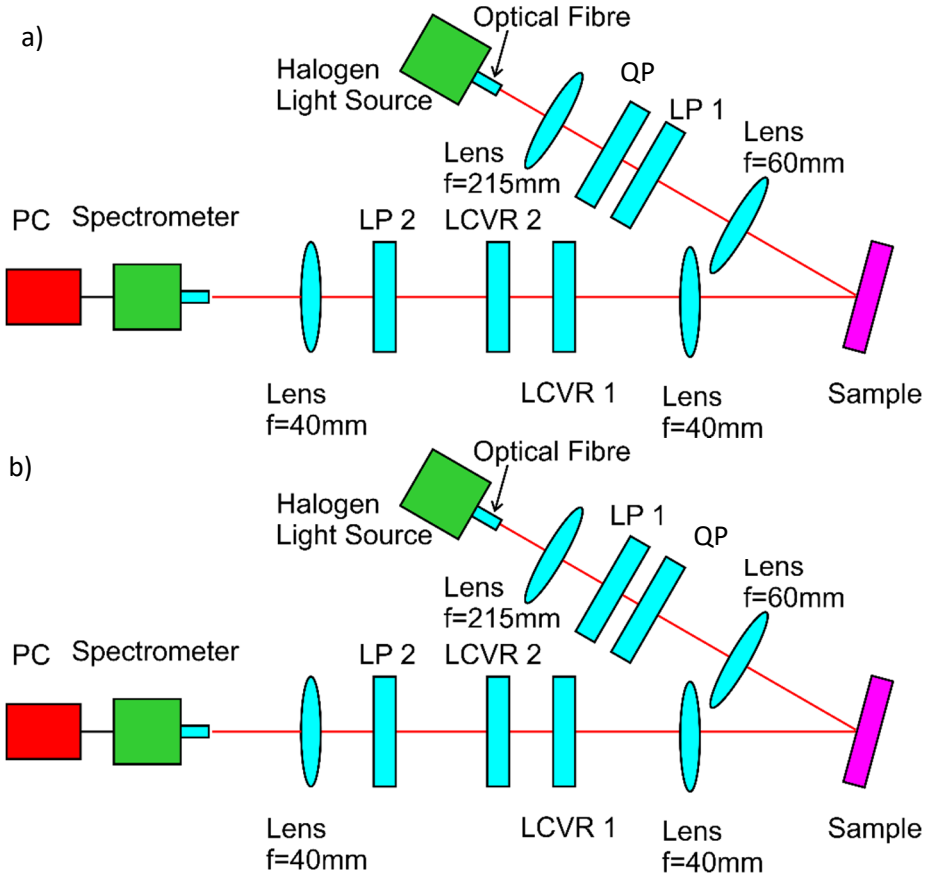


Figure 6.19 – Reflection ellipsometer setup, in a) position 1 and b) position 2, with linear polarisers (LP 1, 2), quarter waveplate (QP) and liquid crystals (LCVR 1, 2).

The reflection system functioned in the same manner as the transmission setup. However in order to calibrate this system a mirror was used and the matrix of the analysing arm was found using equation 6.3, where the MM of an ideal mirror (equation 2.40) was included in the calculation. This mirror was placed in the position labelled sample in Figure 6.19. The beam spot size was the same as in the CP setup in Chapter 4 (~2mm diameter).

6.6. Beetle Reflection Mueller Matrices

Using the reflection setup and method described in the previous sections, MM measurements of beetles were taken and normalised using Equation 6.1. The main variations in the reflection of MM is highlighted in this section, with further example shown in Appendix A5.6. For these MM measurements using the equations in Chapter 2, the ellipticity (equation 2.51), reflection of polarised light (equation 2.47), the azimuth angle (equation 2.52) and the degree of polarisation (equation 2.49) were obtained and plotted against wavelength.

6.6.1. Single Peak

A *Repsimus aeneus* beetle with a single peaked LL CP reflection spectrum (Figure 4.19) identified in Chapter 4 was selected to have its reflection MM measured. This gave rise to the first type of reflection MM (Figure 6.20), where there was a single peak observed in the M_{00} and M_{33} elements, whilst there was the inverse structure peak in the M_{03} and M_{30} elements. The MM

corner elements of the reflection have peaks which are the dominant feature. These peaks are similar to those in the LL spectra. The MM corner elements peaks (which related to the reflection of CP light) appear similar to that of a perfect left circular polariser (equation 2.43).

Along the negative diagonal (M_{00}, M_{11}, M_{22}, M_{33}), the elements can be seen to be acting as a mirror (equation 2.40), but this is not the dominant feature. The mirror-like properties of this are demonstrated in that the element M_{00}'s (and M_{11}'s) baseline are greater than zero and M_{33}'s (and M_{22}'s) are less than zero.

There also seem to be smaller peaks/inverse peaks in the outside non corner elements (M_{01}, M_{02}, M_{10}, M_{13}, M_{20}, M_{23}, M_{31}, and M_{32}), which appear more as oscillations than single peaks.

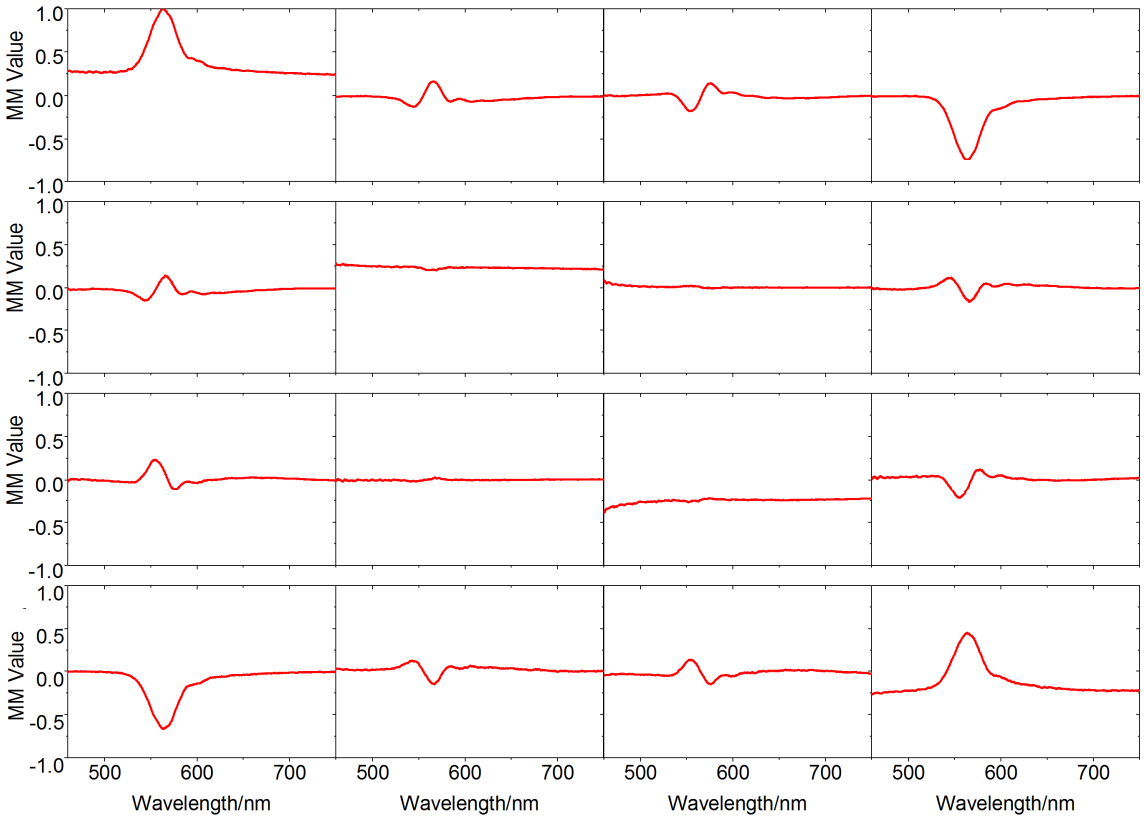


Figure 6.20 – Normalised MM of reflection from the elytron of a *Repsimus aeneus* beetle.

It can also be seen that the ellipticity (Figure 6.21a) reaches the negative extreme (close to -1, which is LCP) at a wavelength which corresponds to the peaks in the polarised reflection (Figure 6.21b) and degree of polarisation (Figure 6.21d). The peaks in the polarised reflection and degree of polarisation, are dominant and make up most of the reflected light (almost 75%). The azimuth angle (Figure 6.21c) goes to extreme values at the same wavelengths as the peak in the polarised reflection (flipping between the negative and positive values due to the polarisation being so close to CP that a very small amount of variation in the x or y values can alter this greatly). The ellipticity values near the peaks is close to -1.0 (which corresponds perfectly LCP light) this means that the azimuth angle at these wavelengths is more prone to errors.

These calculated values of ellipticity, degree of polarisation and azimuth angle (Figure 6.21) from measured data appear similar to the measurements of the *Cetonia aurata* beetle presented in a previous study in Figure 3.27 (when considering the lowest incident angle). This is likely to relate to a comparable number of pitches of similar size, resulting in the same colour of beetle observed.

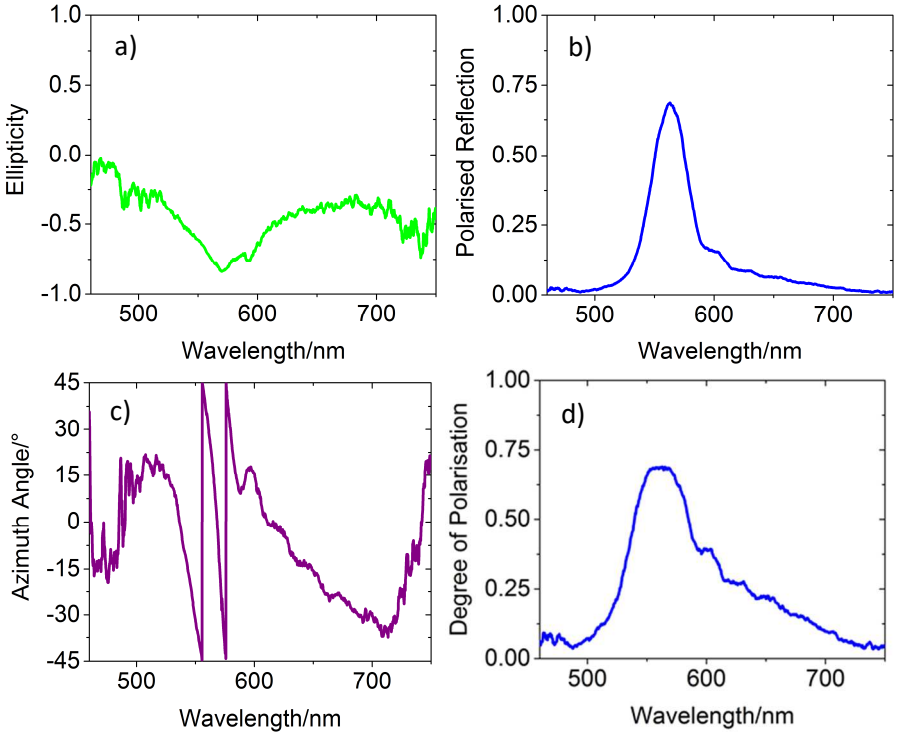


Figure 6.21 – Wavelength variation from the reflection on the elytron of a *Repsimus aeneus* beetle of a) the ellipticity, b) the polarised reflection, c) the azimuth angle and d) the degree of polarisation.

In order to test the MM of the beetle, the reflection Stokes vectors of the system discussed in Chapter 4 were calculated (R_{out}) (equation 6.9). The reflection was calculated using the MMs of a ±45 LP($M_{LP\pm45°}$) (equation 2.41), a QP with fast axis vertical (M_{QWP}) (equation 2.42) and the beetle itself (M_{beetle}). A factor of 0.5 is in front of M_{beetle} to ensure the S_0 element of R_{out} does not exceed 1, since M_{beetle} is normalised to 1 (at the highest value over all wavelengths) and mostly reminiscent of a left circular polariser (equation 2.43).

$$R_{out} = M_{LP\pm45°} M_{QWP} (0.5 M_{beetle}) S_{LCP/RCP} \tag{6.9}$$

Equation 6.9 is used to calculate the four CP spectra combination in Chapter 4, due to the fact the two variables ($M_{LP\pm45}$ and $S_{LCP/RCP}$) each have two configurations. The similarity between the calculated relative reflectance and the experimental CP measurement can be seen in Figure 6.22. This shows the validity of the of the MM measurements, there is however a few small differences between the two sets of spectra. Firstly due to the angle between the two arms being larger for the simple CP setup than the ellipsometer the CP measurement (Figure 6.22a) is slightly blue shifted compared to the ellipsometrically measurement (Figure 6.22b). Another difference is the secondary peaks in the ellipsometric measurement are also less pronounced,

this too may have to do with the incident angle difference. Finally there is a slight difference between the LR and RL measurements, with the ellipsometric measurement having a peak also in the LR measurement.

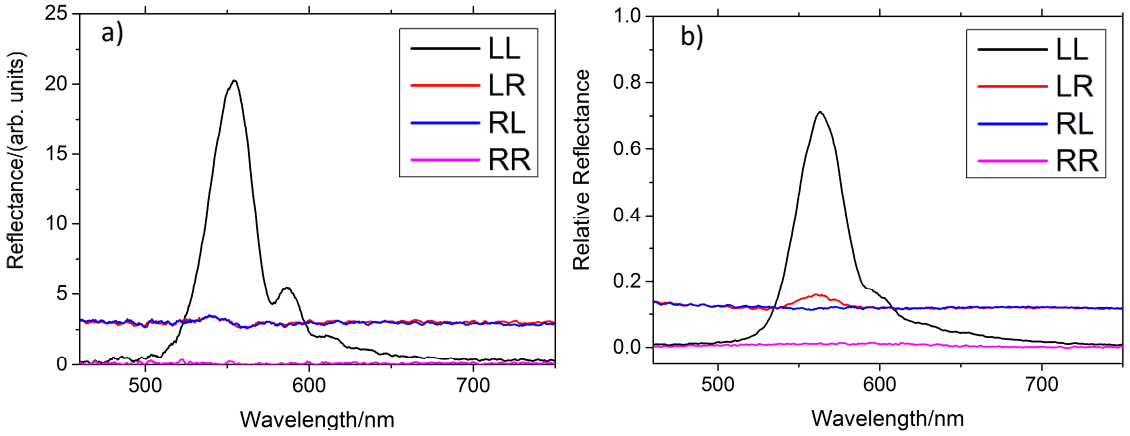


Figure 6.22 – CP reflectance from a) the experimental setup in Chapter 4 (From Figure 4.19) and b) calculated from the measured MM from the beetle.

6.6.2. Non Dominant LL Peak

Another type of beetle's reflection MM was measured from a specimen upon which the selective reflection of CP light occurs, but was not the dominant feature. An example of this type can be seen from a *Melolontha melolontha* specimen (Figure 4.20). Here the corner MM elements have peaks in them, but these are not the dominant feature. The dominant feature of this beetle's MM corresponds to that of mirror's MM (equation 2.40), which can be observed in the negative diagonal MM elements (Figure 6.23).

The ellipticity measurement (Figure 6.24a) again goes to a minimum value close to -1.0 (LCP) at a wavelength that corresponds to the peak in the polarised reflection (Figure 6.24b) and degree of polarisation (Figure 6.24d). The polarised reflection and degree of polarisation peaks are relatively low due to the fact the main reflection component is from the refractive index mismatch of the surface and the helicoidal structure reflection contribution is relatively weak. The azimuth angle (Figure 6.24c) again reaches the extreme values around the wavelength of the peaks in the other calculated variables.

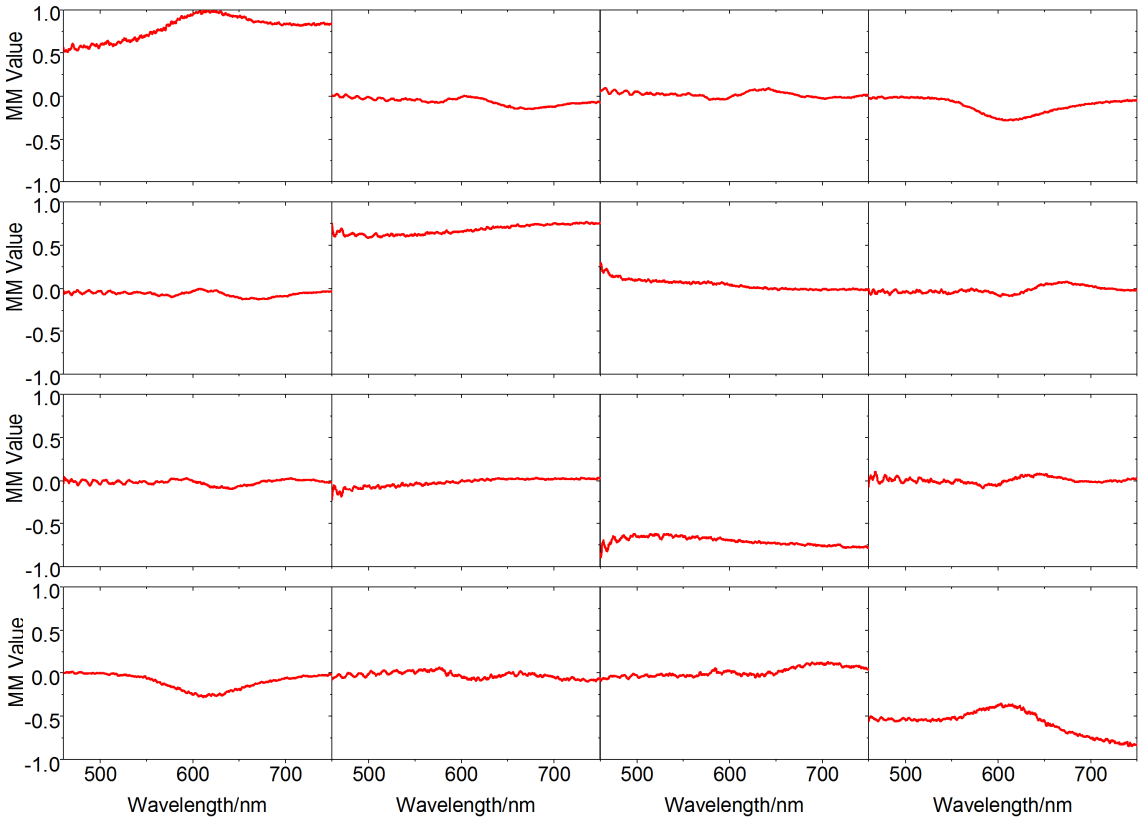


Figure 6.23 – Normalised MM of reflection from the pronotum of a *Melolontha melolontha* beetle.

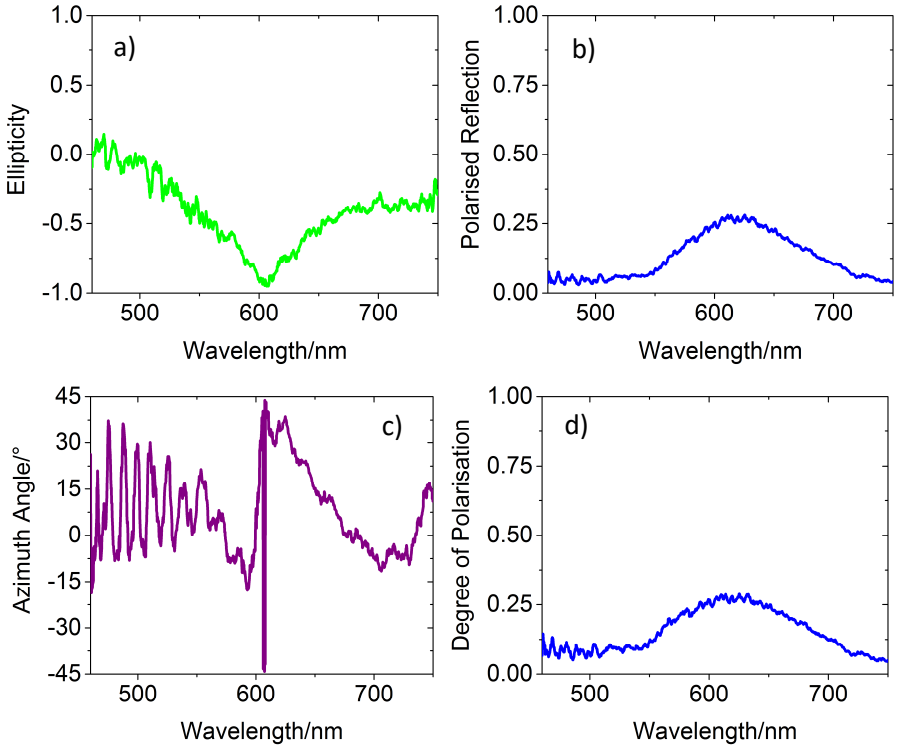


Figure 6.24 – Wavelength variation from the reflection on the pronotum of a *Melolontha melolontha* beetle of a) the ellipticity, b) the polarised reflection, c) the azimuth angle and d) the degree of polarisation.

6.6.3. Multiple Peaks

There are other reflection MMs from beetle specimens which had complex dominant peaks of near LCP reflection. A specific example was the measured MM reflection from the scutellum of

a *Protaetia himalayana* beetle (Figure 6.25). A different specimen of this species was observed to be a metallic green colour with similar multiple peaks in the LL spectra (Figure 4.70). Multiple dominant peaks were observed as the dominant shapes in the corner MM elements. However in the non-corner outside MM elements there appear to have more oscillations in them, which decreased in intensity with wavelength. The non-corner outside MM elements related to the overall thickness of the material [10], since the structure is more complex than a simple helicoidal stack the calculation becomes more difficult (and was not calculated in this study). In the normalised negative diagonal mirror-like MM elements are less pronounced due to the strong reflection by the helicoidal structure.

The oscillations are also visible in the ellipticity (Figure 6.26a) and azimuth angle (Figure 6.26c). However they are less pronounced in the polarised reflection (Figure 6.26b) and even less so in the degree of polarisation (Figure 6.26d).

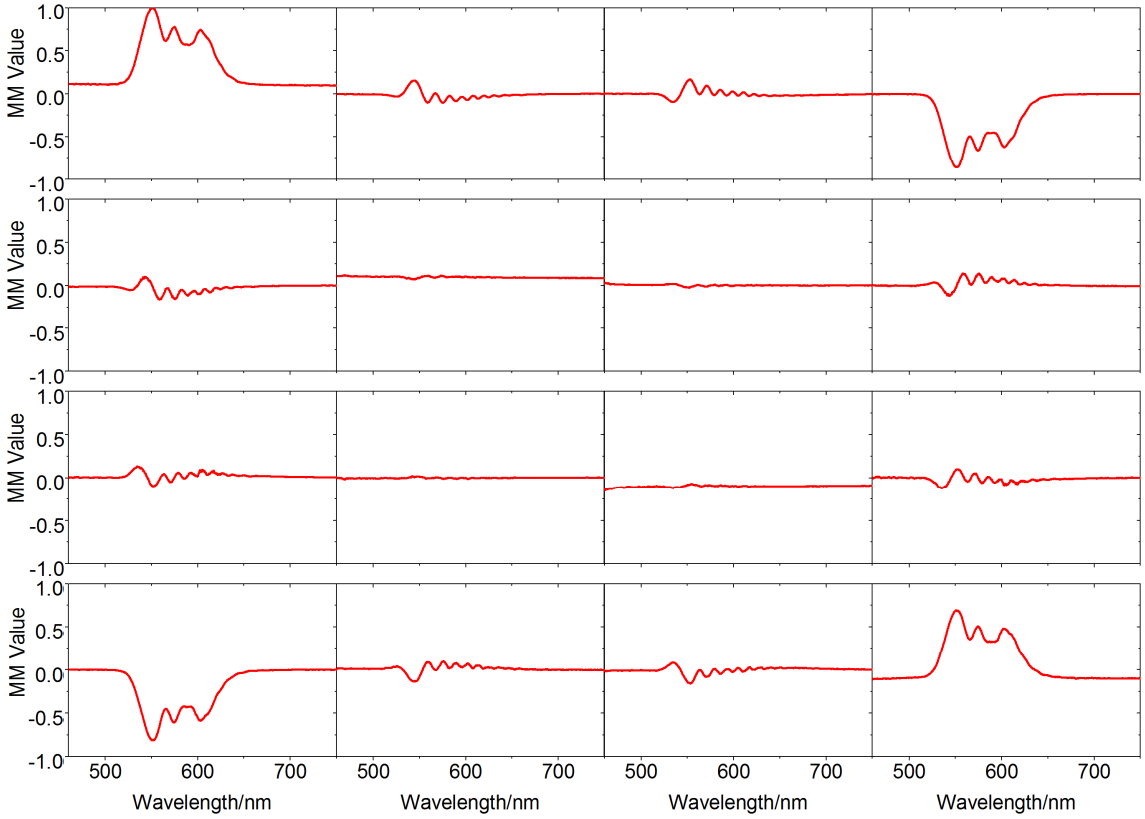


Figure 6.25 – Normalised MM of reflection from the scutellum of a *Protaetia himalayana* beetle.

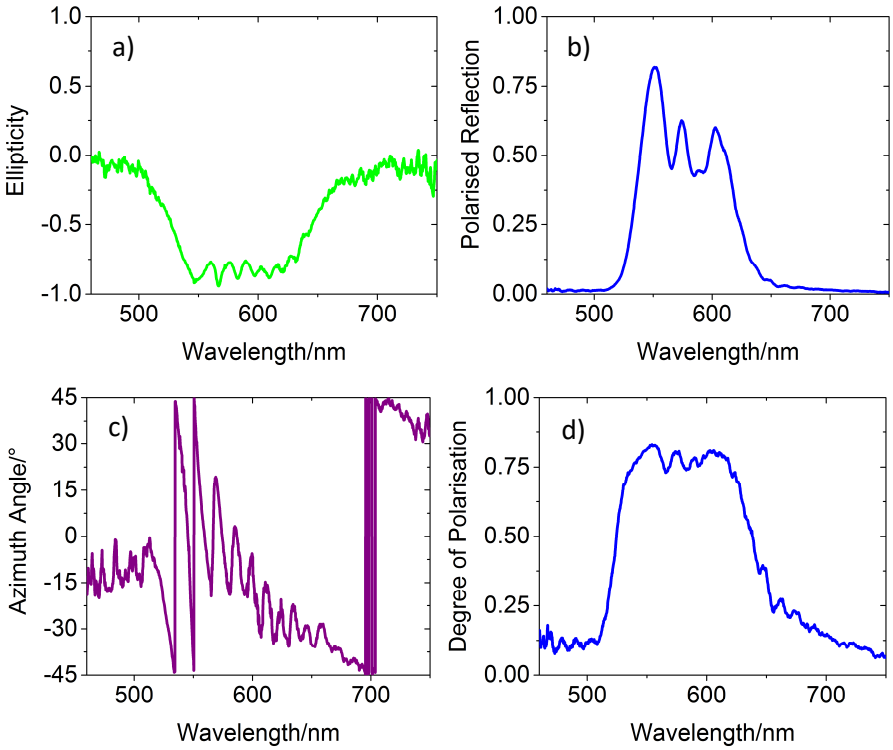


Figure 6.26 – Wavelength variation from the reflection on the scutellum of a *Protaetia himalayana* beetle of a) the ellipticity, b) the polarised reflection, c) the azimuth angle and d) the degree of polarisation.

6.6.4. Colour Variation

The next type of MM considered is from the broadband reflecting beetles of the *Chrysina* genus. There were three metallic *Chrysina optima* colour variations (silver, gold and red), which were seen in Figure 4.33 each had their reflection MM spectra taken.

The MM from the silver specimen (Figure 6.27) as with the majority of previous MM measurements from beetles had dominant corner elements, with oscillations in the non-corner outside elements. These oscillations appear to have two different periods, with a longer period below 600nm. Oscillations were also visible in the ellipticity (Figure 6.28a) and azimuth angle calculations (Figure 6.28c). There was also a large variation between the polarised reflection (Figure 6.28b) and the degree of polarisation (Figure 6.28d), due to the non-uniform spectrum in M_{00}.

Similarly to the silver specimen the gold had oscillations in the outside non-corner MM elements with two distinct periods (Figure 6.29). Unlike the silver specimen the corner elements had LCP-like MM properties only at wavelengths above 500nm. The oscillations are in the ellipticity (Figure 6.30a), but are not as visible as in the azimuth angle (Figure 6.30c). The degree of polarisation was very high (~80%) with few visible oscillations (Figure 6.30d), these oscillations are more visible in the polarised reflection (Figure 6.30b)

The red *Chrysina optima* specimen from the previous reflection CP analysis showed little reflection below 600nm (Figure 6.31). As with the other two colour variations oscillations are

visible (but much wider) in the outer non-corner MM elements. In both the ellipticity (Figure 6.32a) and azimuth angle (Figure 6.32c), oscillations are not visible. The degree of polarisation (Figure 6.32d) increases dramatically below 600nm, although less spectacularly than the polarised reflection (Figure 6.32b).

Between the three colour forms, there can be seen a difference in the lower end of the spectrum reflectance, with silver having a lower reflection bound than the gold, which in turn is higher than the red. The mirror like MM elements (on the negative diagonal) appear very weak due to the overwhelming reflection of the helicoidal structures, which can be seen in the corner elements. The oscillations in the outside non-corner MM elements also vary between the three colour forms, with the widening of the oscillation period relating to the increase in lower bound. As mentioned previously this is (at least in part) related to the overall thickness of the structure.

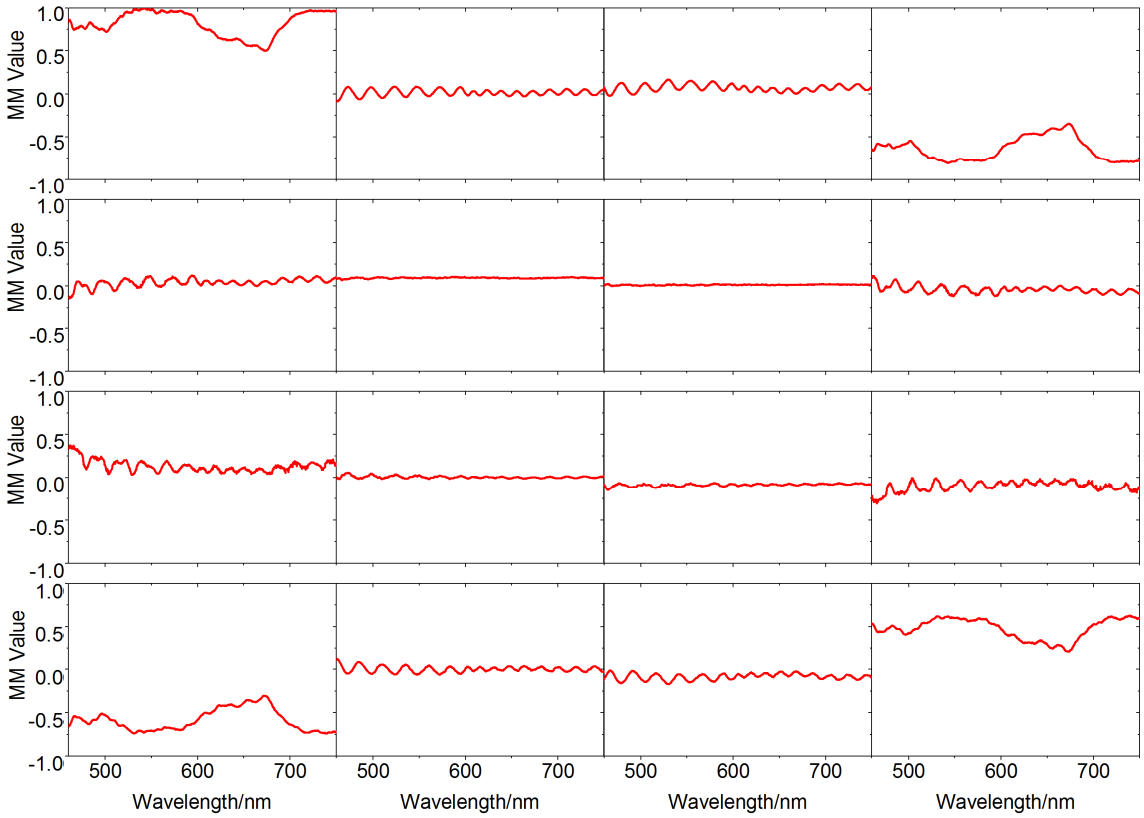


Figure 6.27 – Normalised MM of reflection from the elytron of a silver *Chrysina optima* beetle.

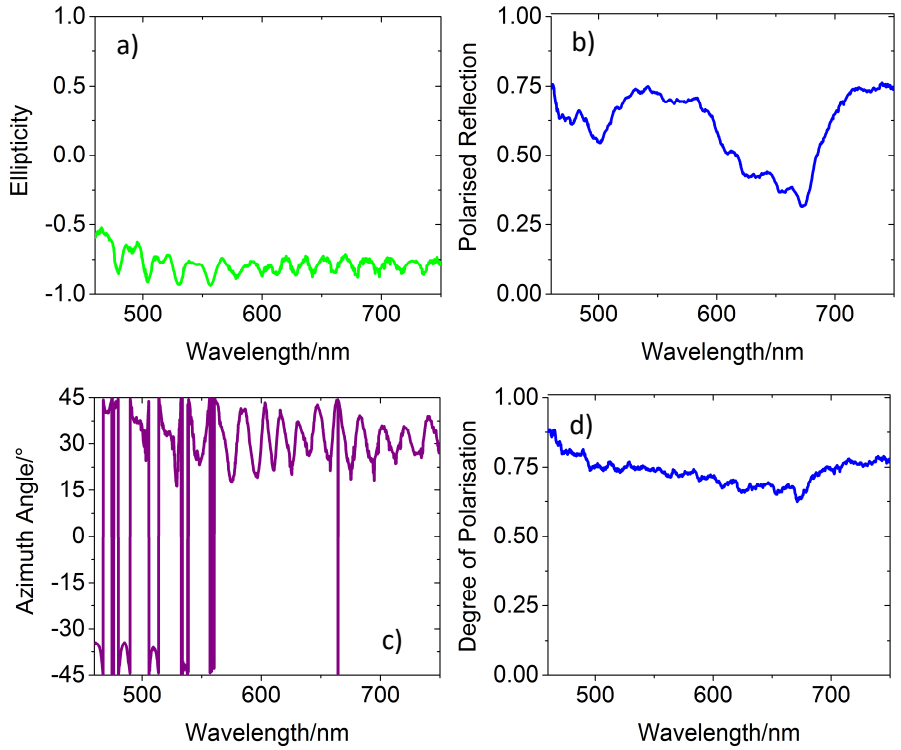


Figure 6.28 – Wavelength variation from the reflection on the elytron of a silver *Chrysina optima* beetle of a) the ellipticity, b) the polarised reflection, c) the azimuth angle and d) the degree of polarisation.

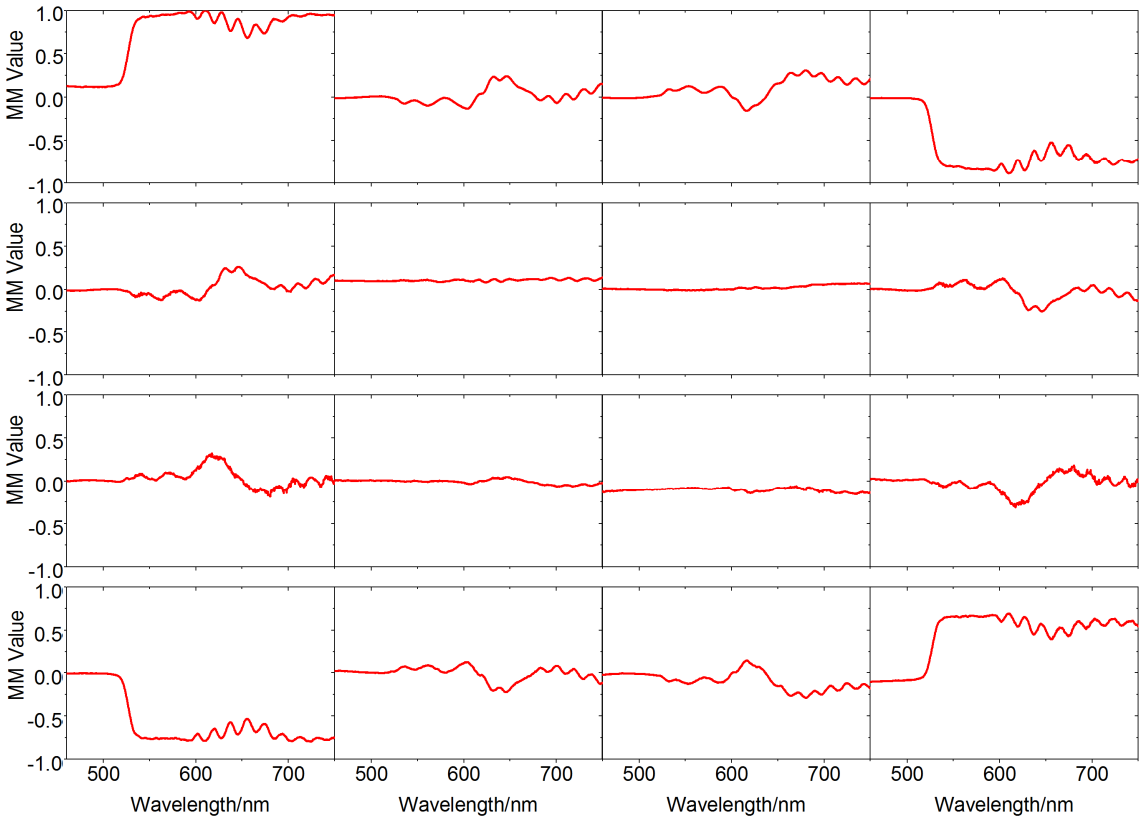


Figure 6.29 – Normalised MM of reflection from the elytron of a gold *Chrysina optima* beetle.

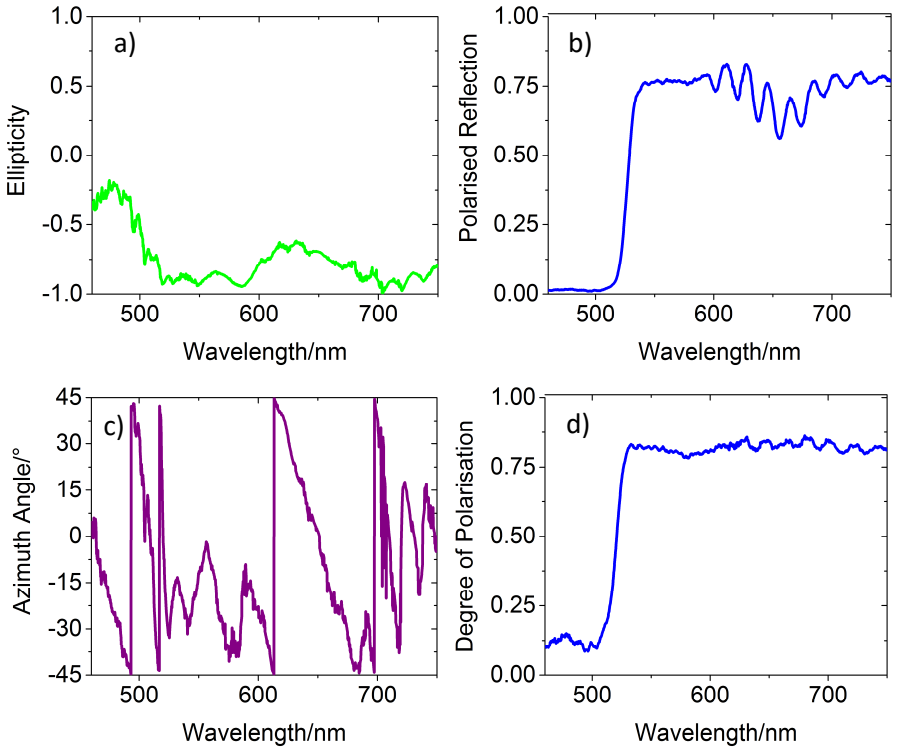


Figure 6.30 – Wavelength variation from the reflection on the elytron of a gold *Chrysina optima* beetle of a) the ellipticity, b) the polarised reflection, c) the azimuth angle and d) the degree of polarisation.



Figure 6.31 – Normalised MM of reflection from the elytron of a red *Chrysina optima* beetle.

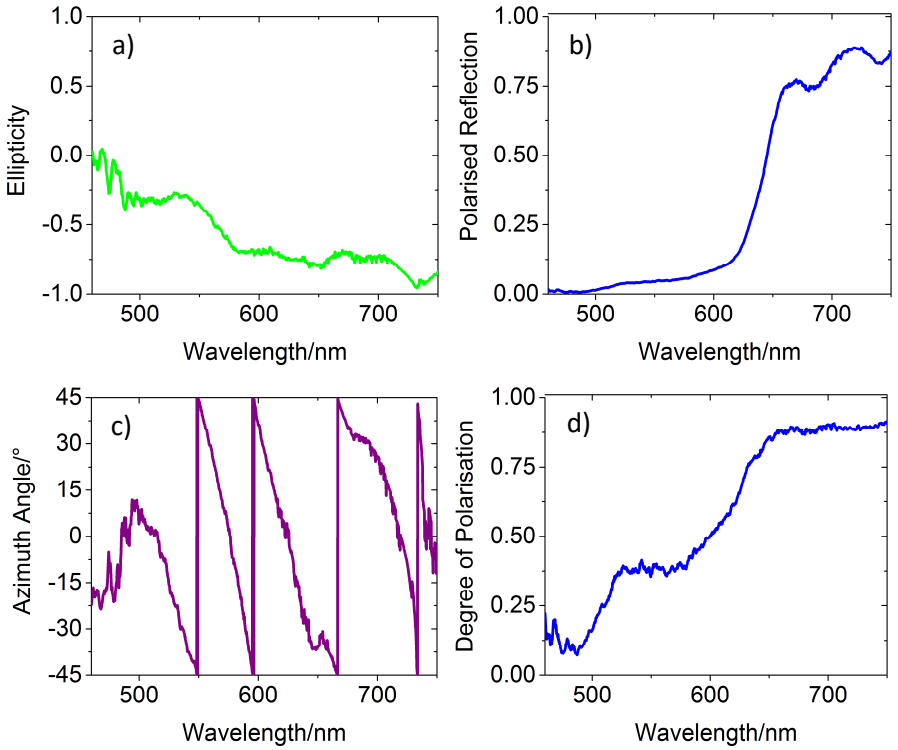


Figure 6.32 – Wavelength variation from the reflection on the elytron of a red *Chrysina optima* beetle of a) the ellipticity, b) the polarised reflection, c) the azimuth angle and d) the degree of polarisation.

6.6.5. Intensity Reflection

Another variation which was observed was in intensity within a species, this was seen in a *Chrysina boucardi* CP spectra (Figure 4.35). The first specimen studied was the dull matt green specimen. As the MM was normalised the low reflection value cannot be observed as clearly (Figure 6.33). The mirror-like MM elements on the diagonal are quite apparent compared to the corner CP-like MM elements.

The ellipticity appears to be quite close to being LCP (Figure 6.34a), whilst the azimuth angle only varies slightly (Figure 6.34c). The degree of polarisation (Figure 6.34d) and polarised reflection (Figure 6.34b) appear to be quite low. This corresponds to the CP spectra, where the refractive index mismatch reflection (LL/LR spectra) is/are comparable in intensity to that from the helicoidal layer reflection.

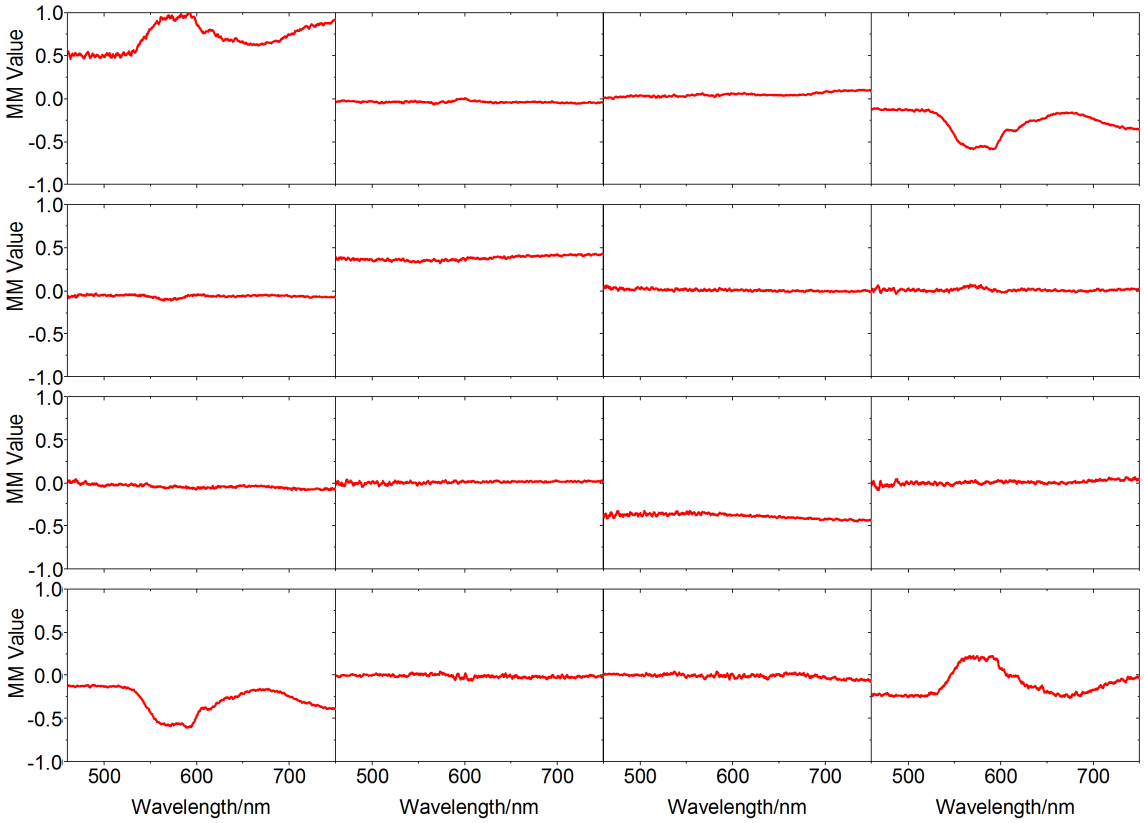


Figure 6.33 – Normalised MM of reflection from the elytron of a matt green *Chrysina boucardi* beetle.

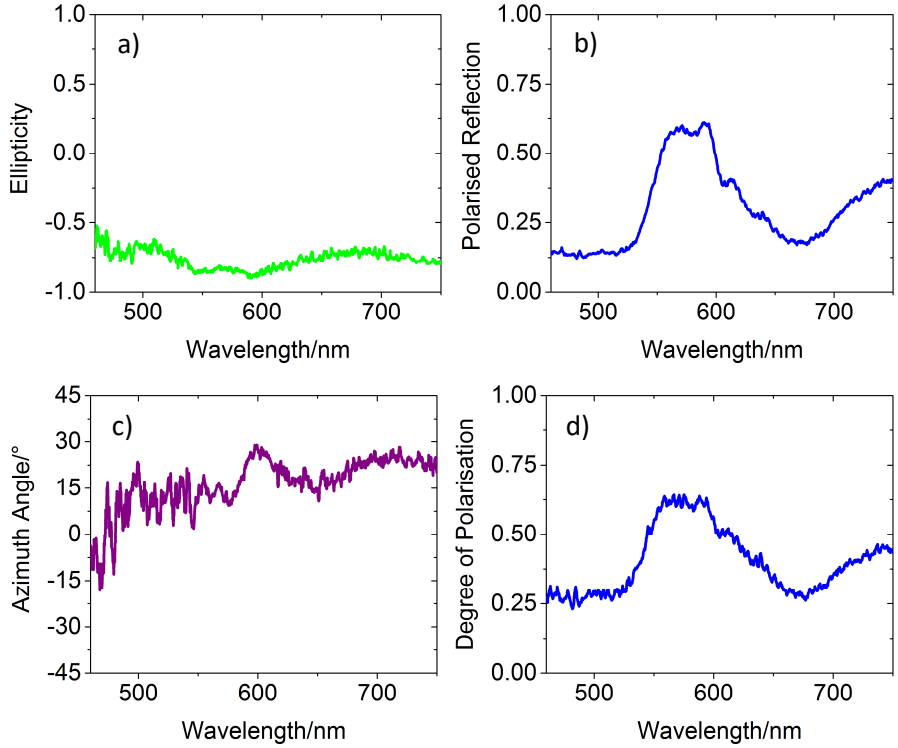


Figure 6.34 – Wavelength variation from the reflection on the elytron of a matt green *Chrysina boucardi* beetle of a) the ellipticity, b) the polarised reflection, c) the azimuth angle and d) the degree of polarisation.

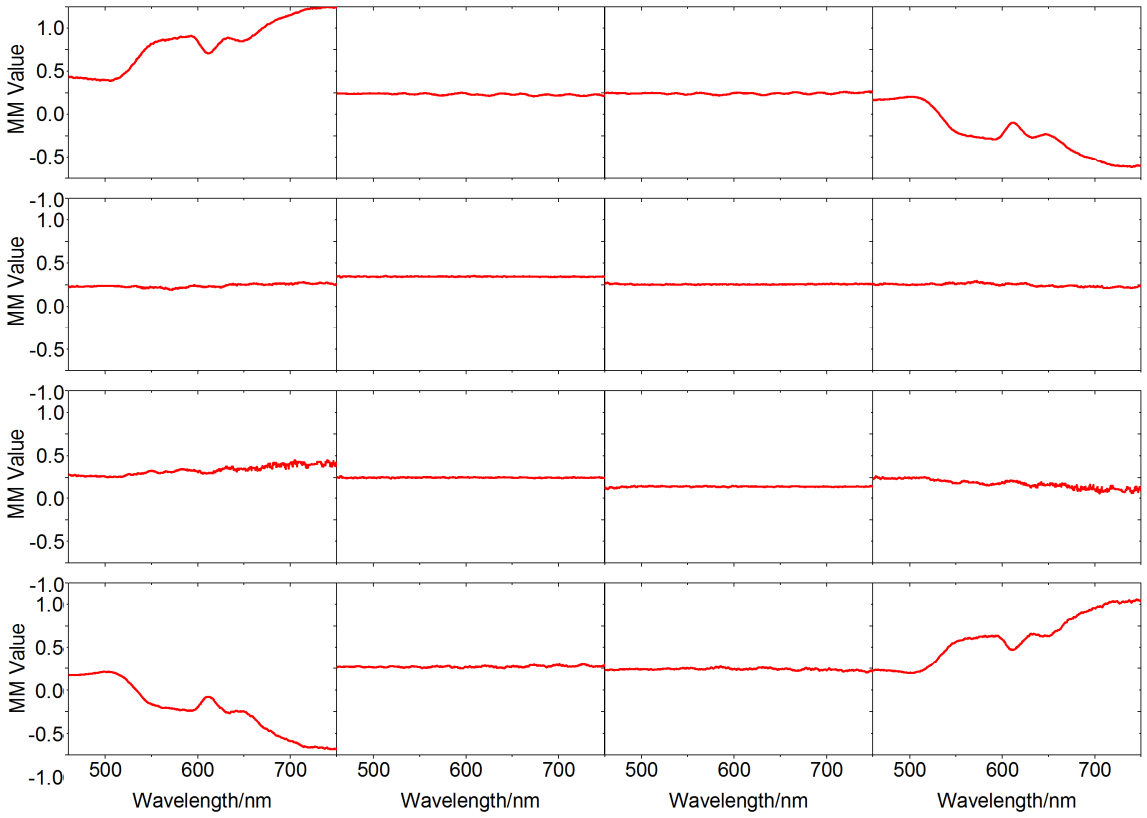


Figure 6.35 – Normalised MM of reflection from the elytron of a metallic gold *Chrysina boucardi* beetle.

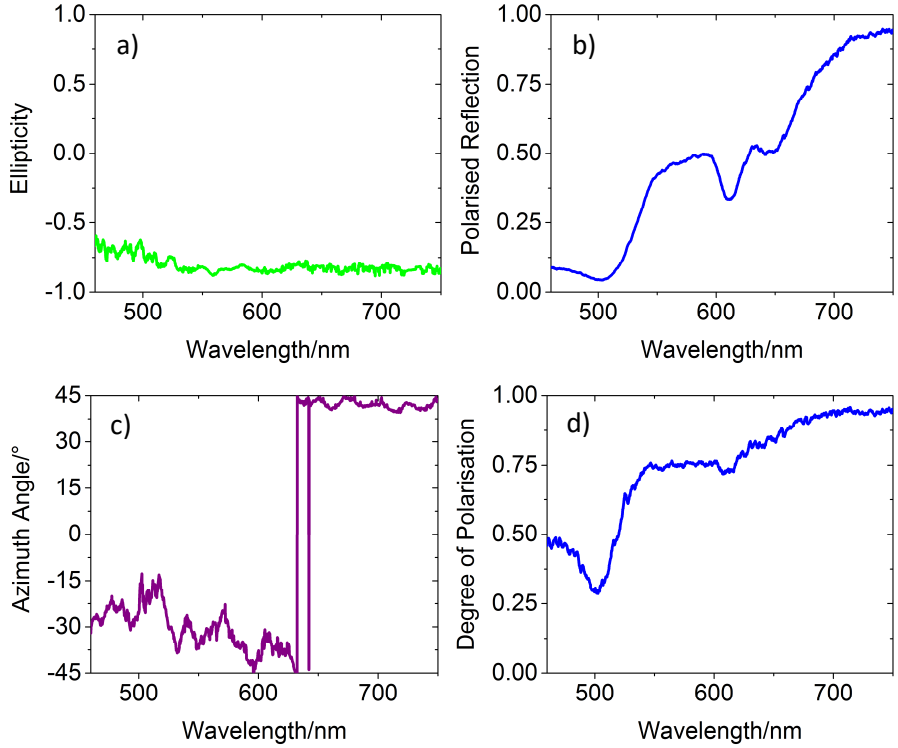


Figure 6.36 – Wavelength variation from the reflection on the elytron of a metallic gold *Chrysina boucardi* beetle of a) the ellipticity, b) the polarised reflection, c) the azimuth angle and d) the degree of polarisation.

The reflection MM from the metallic gold specimen (Figure 6.35) can be seen to have less defined mirror like MM elements (on the diagonal) in comparison to the LCP-like (corner) MM

elements. Another feature in the normalised MM is the LCP-like corner elements that varies from the matt green specimen is at lower MM values at shorter wavelengths.

The metallic gold specimen has a much higher degree of polarisation than the green, particularly at higher wavelengths (Figure 6.36b). One feature which was absent in both specimens was a lack of oscillations in the ellipticity (Figure 6.36a) and azimuth angle (Figure 6.36c).

The difference in the calculated variables (ellipiticity and degree of polarisation) can be seen to be similar to *Chrysina macropus* (Figure 3.28) for the matt specimen and similar to *Chrysina chrysargyrea* (Figure 3.29) for the gold specimen. It should be noted that the matt *Chrysina boucardi* specimen has a more broadband response than the *Chrysina macropus*.

6.6.6. RR Reflection

Another feature observed was selectively reflecting both LCP and RCP light as seen in Section 4.4.2.1. The MM of one such metallic *Chrysina* beetle species is shown in this section. The MM of the *Chrysina cupreomarginata* (Figure 6.37), had clear oscillations in the outside non-corner MM elements. The corner MM elements however vary from positive to negative with wavelength, with a large peak corresponding to a mainly LCP-like reflector at around 570nm. It should be noted a different specimen (but with a similar spectrum) to that in Figure 4.30 was used in the ellipsometer. From the ellipticity calculation (Figure 6.38a), it can be seen that the ellipticity is left handed from 530nm to 610nm, whilst at other wavelengths right handed dominates (although is far from perfectly circular). The degree of polarisation (Figure 6.38d) can also be seen to be low compared to previous MMs in this chapter. The azimuth angle (Figure 6.38c) appears to oscillate between the extremes particularly when the ellipticity is close to -1 (at 530nm-610nm).

This beetle has similar MM calculated variables to the *Chrysina resplendens* from previous work (Figure 3.30). There are however some differences, in the *Chrysina cupreomarginata* beetle the ellipiticity tends to RCP (+1) both at high and low wavelengths (and LCP (-1) between 530nm and 610nm), whilst in the *Chrysina resplendens* only tends to RCP at high wavelengths.

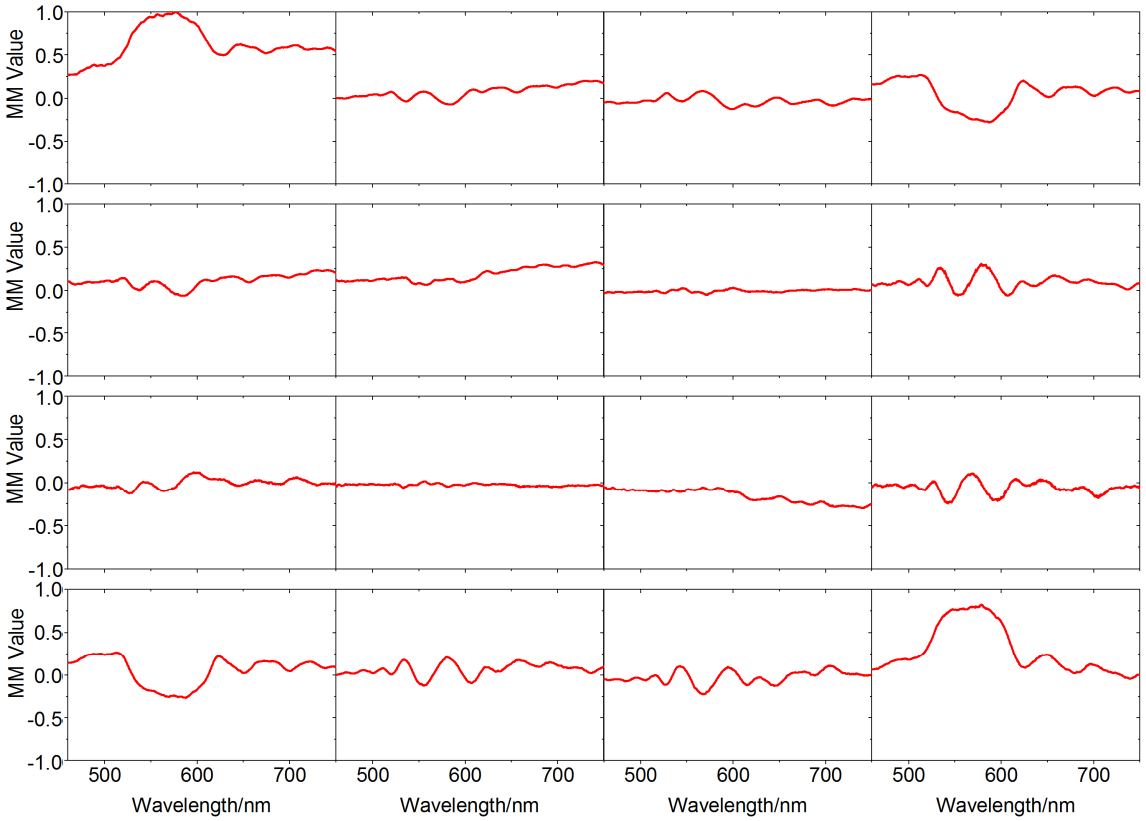


Figure 6.37 – Normalised MM of reflection from the elytron of a *Chrysina cupreomarginata* beetle.

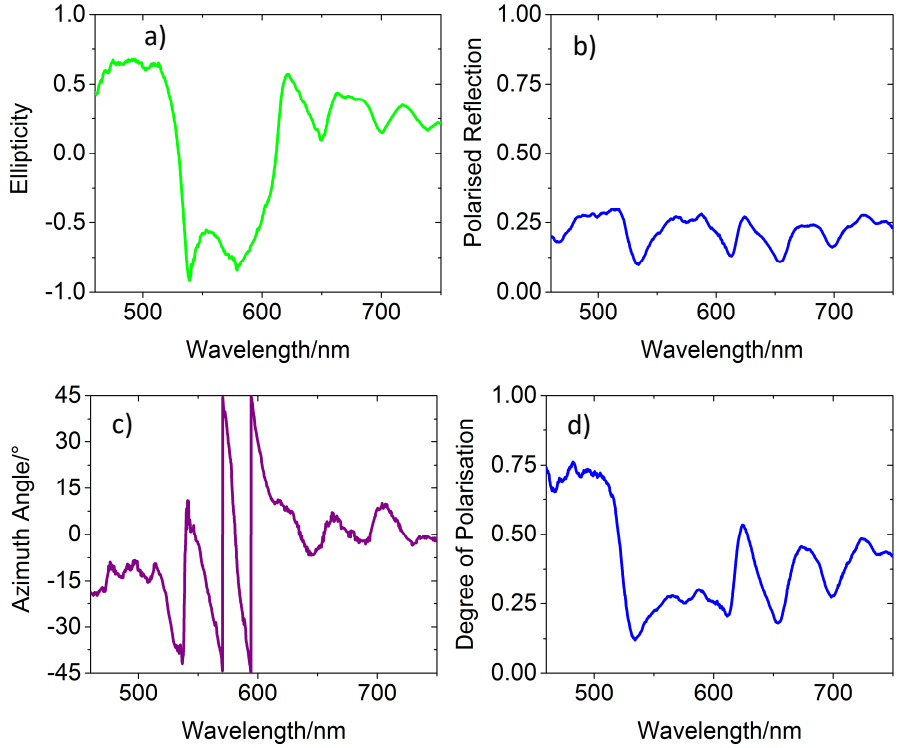


Figure 6.38 – Wavelength variation from the reflection on the elytron of a *Chrysina cupreomarginata* beetle of a) the ellipticity, b) the polarised reflection, c) the azimuth angle and d) the degree of polarisation.

6.6.7. Minor RR

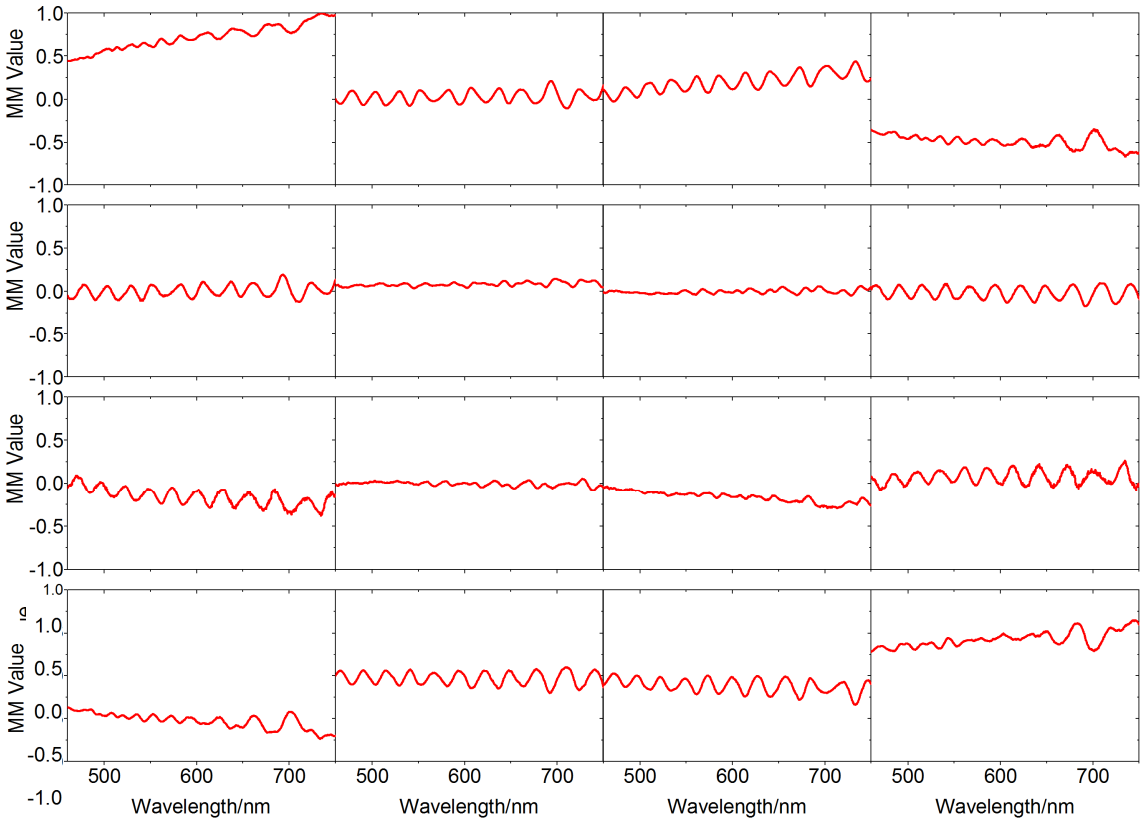


Figure 6.39 – Normalised MM of reflection from the elytron of a *Chrysina clypealis* beetle.

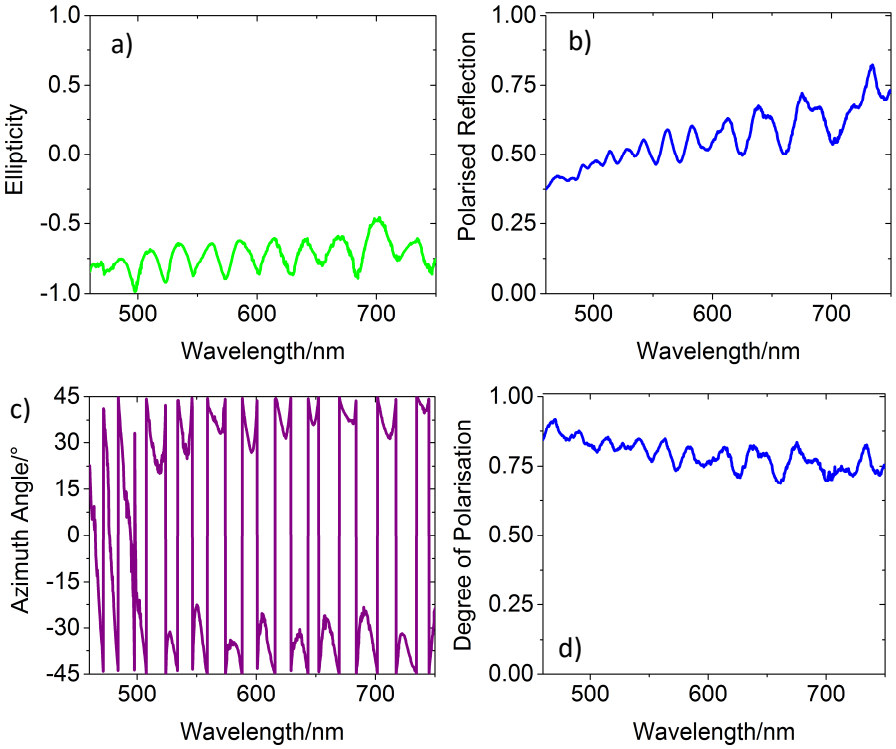


Figure 6.40 – Wavelength variation from the reflection on the elytron of a *Chrysina clypealis* beetle of a) the ellipticity, b) the polarised reflection, c) the azimuth angle and d) the degree of polarisation.

The last variation within the *Chrysina* genus predominantly reflected LCP light, with only a small amount of RCP. The specimen studied was of the *Chrysina clypealis* species, the reflection MM

(Figure 6.39) has oscillations in the non-corner elements, which have larger periods than the silver *Chrysina optima*. The MM corner elements appear to be close to that of a LCP reflector.

As with previous *Chrysina* which reflect only LCP light selectively, the ellipticity is close to -1 and has oscillations (Figure 6.40a) as does the azimuth angle (Figure 6.40c). The degree of polarisation is also very large (Figure 6.40d). The features of the MM *Chrysina clypealis* beetle do not vary greatly from a *Chrysina* which selectively reflects only LCP light. This MM analysis compares well to the previous studies made upon this beetle [11].

Further examples of MM and their analysis from other beetle species can be seen in Appendix A5.6.

6.7. Conclusion

This Chapter has discussed the development of a broadband ellipsometer system using two LCVRs and a calibration method. Overcoming the LCVR degeneracy and correction for the elliptical response over a broadband range of the QP was implemented. A fully functioning fixed angle reflection MM spectroscopic ellipsometer was created.

Some general points were noticed about the reflection MMs from the beetles. There were three main element groups of the MMs which vary. Firstly the four corner elements (M_{00}, M_{03}, M_{30} and M_{33}) relate to the reflection of CP light and hence the helicoidal structure. Secondly the negative diagonal elements (M_{00}, M_{11}, M_{22} and M_{33}) relate to a mirror-like response, from the refractive index mismatch between the beetle's shell and the air. The last is the outside non corner MM elements, which are non-zero and often contain oscillations.

Several different MM corner element (with wavelength) shapes and variations have been shown in this Chapter. It was seen that some had simple single peaks and reflected very close to near CP light (e.g. *Repsimus aeneus*), whilst others had less dominant selective reflection of LCP light (e.g. *Melolontha melolontha*). Variations in intensity (*Chrysina boucardi*) and colour (*Chrysina optima*) within species were also investigated. The selective reflection of the RCP and LCP light has also been observed with a specimen of *Chrysina cupreomarginata* and *Chrysina clypealis*, which had their reflection MMs measured. The results presented in this section appear to agree with previous work discussed in Section 3.4.2

The calculated variables which also relate to the MM (of ellipiticity, degree of polarisation and azimuth angle) were discussed within this Chapter. The ellipticity can be seen to be mostly negative and close to -1 (except *Chrysina cupreomarginata*). The azimuth angle can also be seen to reach extreme values (a consequence of the light being near CP), which corresponds with ellipticity peaks. The degree of polarisation and polarised reflection can also be seen to relate in wavelength to the ellipticity. The value of degree of polarisation and polarised reflection

strength can be seen to vary from being very strong in metallic beetles such as the gold *Chrysina optima*, to being much weaker in duller beetles such as *Melolontha melolontha*.

The MM measurements in this Chapter give additional information to the CP measurements from Chapter 4. These include the oscillations in the outside non-corner elements being visible, which may allow the calculation of the thickness of the optical structures (although this is still to be determined from the measurements of this study). The MM measurements allowed calculation of the degree of polarisation, which determines the amount the light is polarised at different wavelengths. The ellipticity was also investigated, which showed how close to CP the reflected light from the beetles was rather than simply measuring the LCP and RCP as in Chapter 4. From the reflection MM measurements the difference between the CP (corner elements) and mirror like (negative diagonal elements) could also to be seen.

6.8. References

[1] C. U. Keller, "Lecture 8: Variable Retarders (University of Leiden) - Slides," *International Summer School On Solar Polarization - The South Sichuan's Bamboo Sea, Sichuan Province, China*, 2011. [Online]. Available: http://home.strw.leidenuniv.nl/~keller/Teaching/China_2011/China2011_L09_VariableRetarders.pdf. [Accessed: 13-Aug-2013].

[2] O. Arteaga, "Mueller Matrix Ellipsometry Tutorial Slides," *9th Workshop of Ellipsometry at Utwente*, 2015. [Online]. Available: http://www.mmpolarimetry.com/wp-content/uploads/2015/02/MMEllipsometry_Oarteaga_WSE2015.pptx. [Accessed: 09-Sep-2016].

[3] J. C. Ramella-Roman, A. Nayak, and S. A. Prahl, "Spectroscopic sensitive polarimeter for biomedical applications," *J. Biomed. Opt.*, vol. 16, no. 47001, pp. 1–7, 2011.

[4] B. Boulbry, J. C. Ramella-Roman, and T. A. Germer, "Improved method for calibrating a Stokes polarimeter," vol. 46, no. 35, pp. 8533–8541, 2007.

[5] J. Bueno, "Polarimetry using liquid-crystal variable retarders: theory and calibration," *J. Opt. A Pure Appl. Opt.*, vol. 2, pp. 216–222, 2000.

[6] Thorlabs, "Full-Wave Liquid Crystal Variable Retarders." [Online]. Available: https://www.thorlabs.com/newgrouppage9.cfm?objectgroup_id=6339. [Accessed: 04-Dec-2015].

[7] ARC Optix, "ARCoptix Achromatic switchable polarization rotator." [Online]. Available: http://www.arcoptix.com/polarization_rotator.htm. [Accessed: 12-Jun-2016].

[8] P. Terrier, J. M. Charbois, and V. Devlaminck, "Fast-axis orientation dependence on driving voltage for a Stokes polarimeter based on concrete liquid-crystal variable retarders.," *Appl. Opt.*, vol. 49, no. 22, pp. 4278–83, 2010.

[9] A. G. Santos, Q. M. Sugon, Jr., and D. J. McNamara, "Polarization ellipse and Stokes parameters in geometric algebra," *J. Opt. Soc. Am. A*, vol. 29, no. 1, p. 89, 2012.

[10] D. G. Stavenga, "Thin film and multilayer optics cause structural colors of many insects and birds," *Mater. Today Proc.*, vol. 1, pp. 109–121, 2014.

[11] D. H. Goldstein, "Polarization properties of Scarabaeidae," *Appl. Opt.*, vol. 45, pp. 7944–7950, 2006.

Chapter 7 - Imaging the Optical Structures

In this study two methods of imaging the optical structures were used, using a SNOM and EMs. These images offer confirmation of the origin of structures responsible for the polarisation responses measured in Chapters 4 and 6. This imaging could lead to understanding how the structures are formed, which will first allow more accurate modelling and also the possibility to artificially create similar structures. The EM images were obtained with collaboration with Dr D. Prentner at Imperial College, and the SNOM images as part of a collaboration with William Hart, also of Imperial College. The results presented here are as a demonstration of each technique used, contrasting the images and results obtained.

7.1 Electron Micrographs

Images were taken of a *Mycterophallus validipes* beetles which is a very close relative of the *Lomaptera* family. Two different microscopes were used in the imaging, firstly a two-beam Zeiss Auriga SEM device with an Orsay gallium ion gun and also a Helios NanoLab 600, both of which are located in the Department of Materials, Imperial College London.

The process to obtain the images was as follows. Initially a small sample of the beetle's scutellum was placed into the Helios NanoLab 600, where images of the surface were taken with both the Focused Ion Beam (FIB) and also using a scanning electron beam. A Pt strip (25 (length) x 2.5 (width) x 1 (depth) μm) was then Ion-beam deposited upon the sample using a 30kV 0.46nA beam for 4:30 minutes (Figure 7.1a). A trench was then milled (26 (length) x 20 (width) x 12 (depth) μm) using Si which took 20 minutes (Figure 7.1b).

The sample was then transferred to the Auriga for cross-sectional viewing of the structure at an angle of 54° from normal incidence (the angle was corrected for by considering the geometry and taking into account the tilt of the vertical axis of the image), using a SEM beam of 30kV, 50pA. An example can be seen in Figure 7.2a, where alternating layers of chitin are clearly visible.

As mentioned in Chapter 5 LL reflection spectra which have two distinct peaks (in terms of wavelength) (such as Figure 7.2c) were suggested to be due to two different pitch thicknesses within the beetle's shell. In the cross section SEM of a *Mycterophallus validipes* beetle (Figure 7.2a), clear dark and light bands can be seen. The light and dark bands correspond to difference in refractive index from rotation of the birefringent chitin molecules. The distance between two dark bands corresponds to a half pitch thickness. A profile across the grey scale image of the

Mycterophallus beetle was taken (along the yellow line in Figure 7.2a), and normalised (in order to take into account contrast variation across the image) in Figure 7.2b.

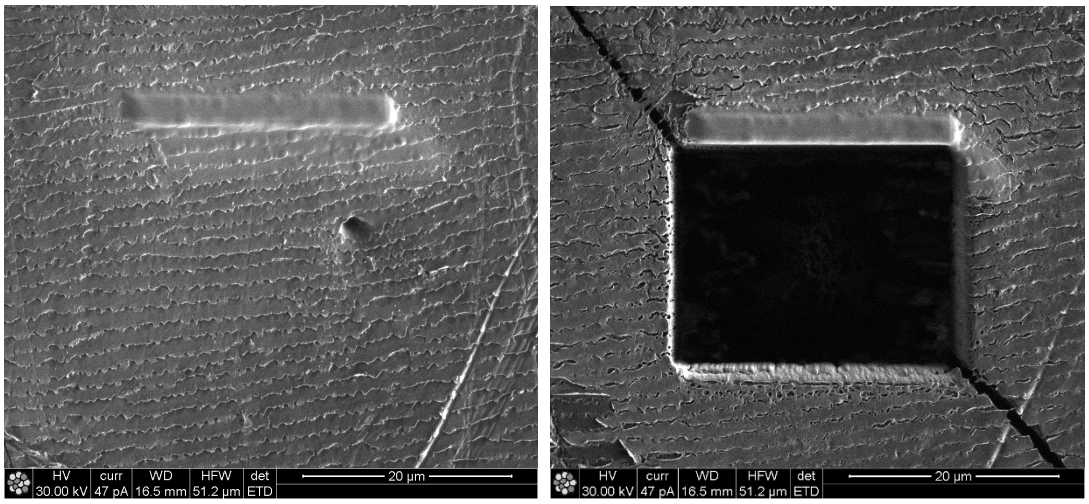


Figure 7.1 –SEM images obtain with the Pt strip deposited on the left and then the trench milled on the right, where the sample can be seen to have fractured. Where HV is the high voltage applied to the ions and curr the current, WD the working distance, HFW the horizontal field width, while the det noted the detection method, which in this case was an Everhart-Thornley Detector ETD.

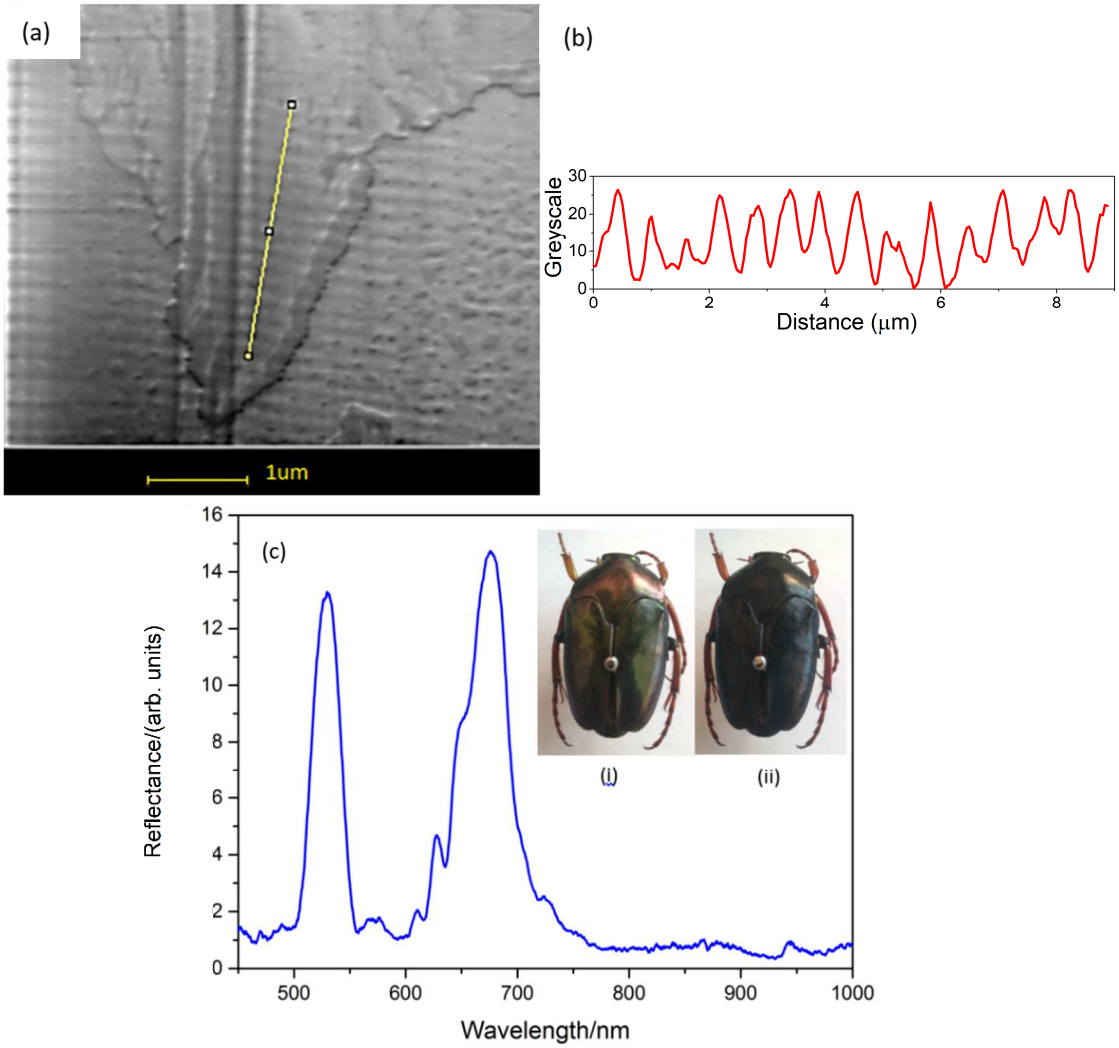


Figure 7.2 – (a) SEM image cross section of the *Mycterophallus validipes* beetle's scutellum. (b) A greyscale profile taken along the line on the image in (a), (c) the associated LL optical spectrum with insect image of beetle through (i) LCP filter and (ii) RCP filter. Taken from the author's publication [1].

The pitches taken from the greyscale plot (Figure 7.2b) were corrected for non-normal incidence and analysed using the Sellmeier relation (equation 3.15) and the reflection wavelengths are shown in Table 7.1. From this table it can be seen that the pitches alternate in thickness (excluding separation 10) relating to the lower and higher wavelength peaks seen in the LL spectrum in Figure 7.2c. These separations correspond to mean wavelength of 531nm and 682nm, which are compared to the peak wavelengths of the LL spectrum of 528nm and 673nm. This interstitial arrangement is rather unusual and could be related to the circadian rhythm as discussed in Section 3.4.7. The interstitial arrangement has not been measured using the model in Chapter 5, the difficulty arises in modelling either sudden changes in the rotation the molecules orientation between adjacent layers or gradual variation.

Further to measuring the helicoidal structure in a cross section of the *Mycterophallus validipes* cuticle, several SEM's of the surface structure were taken. A blaze-grating like structure was observed, which can be seen in Figure 7.3. The blazed period was found by taking a cross section (yellow line) along the surface (Figure 7.3). The blazed grating structure is discussed in Section 3.4.6.

Separation	Wavelength/nm	Separation	Wavelength/nm
1	586	2	628
3	544	4	670
5	544	7	670
6	502	9	754
8	502	10	670
11	586	12	712
13	461		
Average 1st	531	Average 2nd	682
standard deviation/nm	43		39

Table 7.1 – The reflection wavelength data arranged in alternating separations from the SEM in Figure 7.2, the lower the separation numbering the nearer to the surface of the cuticle the layer is.

The cross sectional line from Figure 7.3 was analysed in terms of greyscale value, where the higher greyscale values correspond to the white edges of the blazed gratings and hence the blaze grating period. These blazed grating periods were plotted (Figure 7.4) and the average was found to be 1.38µm with a standard deviation of 0.39µm.

A cross section of the surface structure was also taken in order to obtain the blaze angle value of the structure. The blaze angle was obtained using the angle finding function within the ImageJ software.

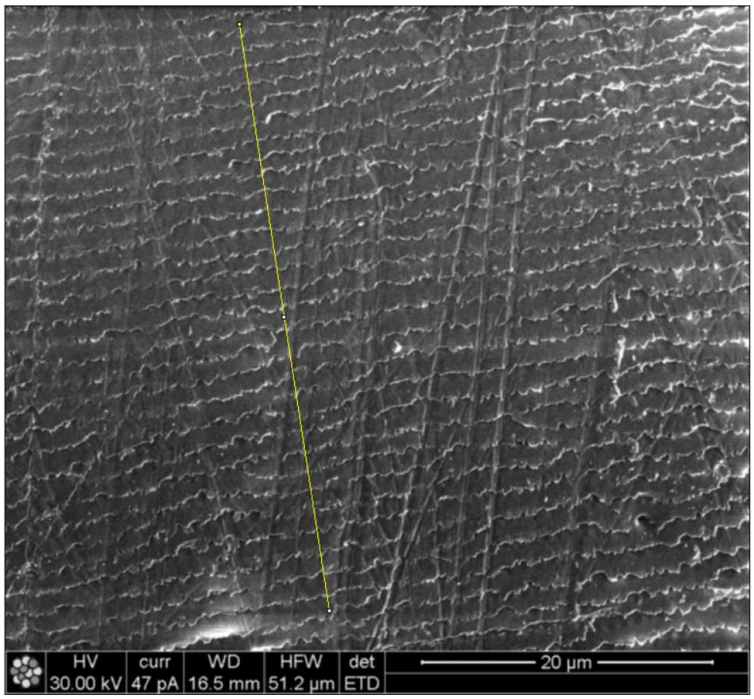


Figure 7.3 – Surface SEM of *Mycterophallus validipes* beetle, with a yellow perpendicular cross section line.

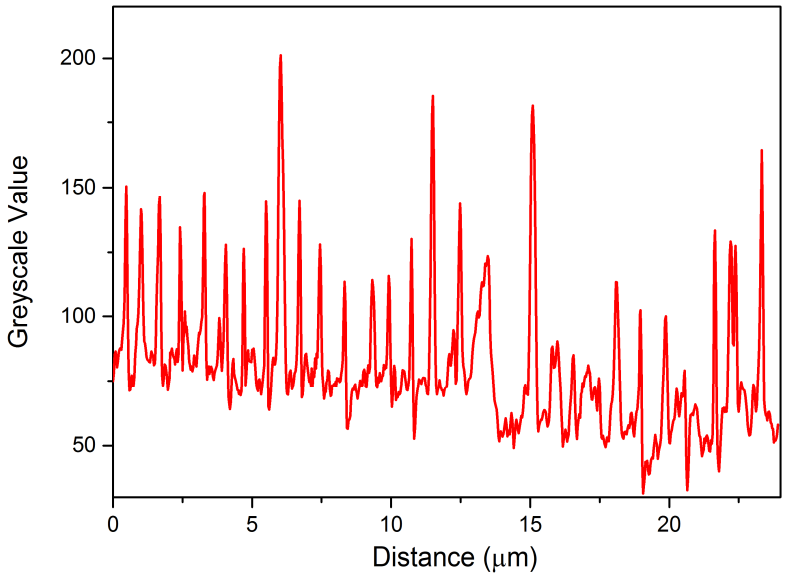


Figure 7.4 – A grayscale profile taken along the line on the surface SEM of the *Mycterophallus* beetle's shell.

Equation 3.17 was rearranged in terms of wavelength for the lowest order (m=1), and using the grating separation along the line in Figure 7.3 and a blazed angle of 9° from Figure 7.5 the mean blazed grating peak was calculated as 431.5nm with a standard deviation of 121.7nm. As only the lowest order was considered, and the colour varies with angle, it is very likely this colour adds to the overall (but not CP) colour reflection. A small amount of colour is seen on the pronotum of the beetle in the inset photograph through a RCP filter in Figure 7.2c.

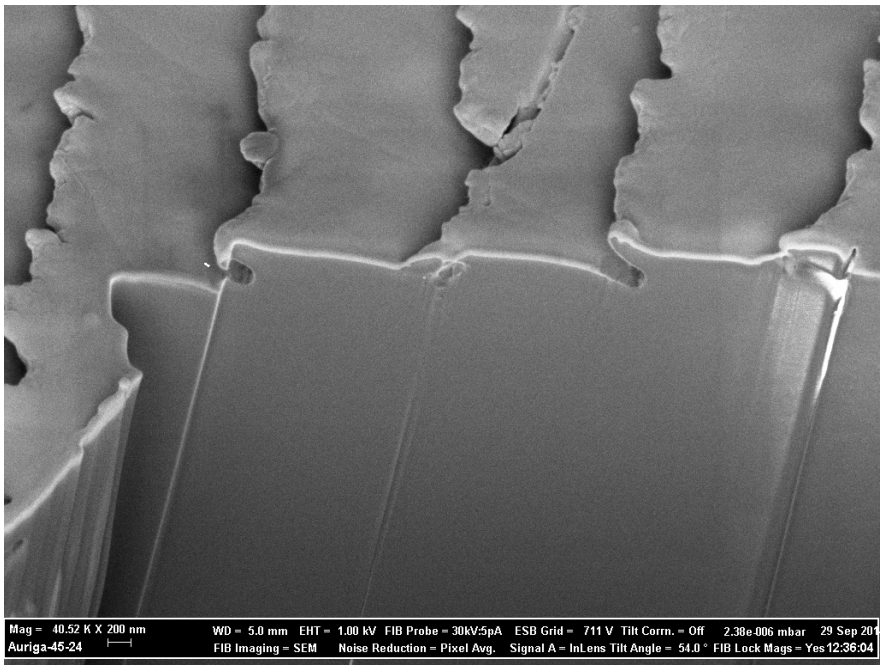


Figure 7.5 – SEM Cross section of the blaze-grating like structure of the *Mycterophallus validipes* beetle.

7.2. Scanning Nearfield Optical Microscopy/Atomic Force Microscopy

The second method of imaging the beetles' optical structures was also attempted, using an Infrared s-SNOM. This method was done in collaboration with William Hart of Imperial College London. A large part of the description and the images are taken from the publication [2].

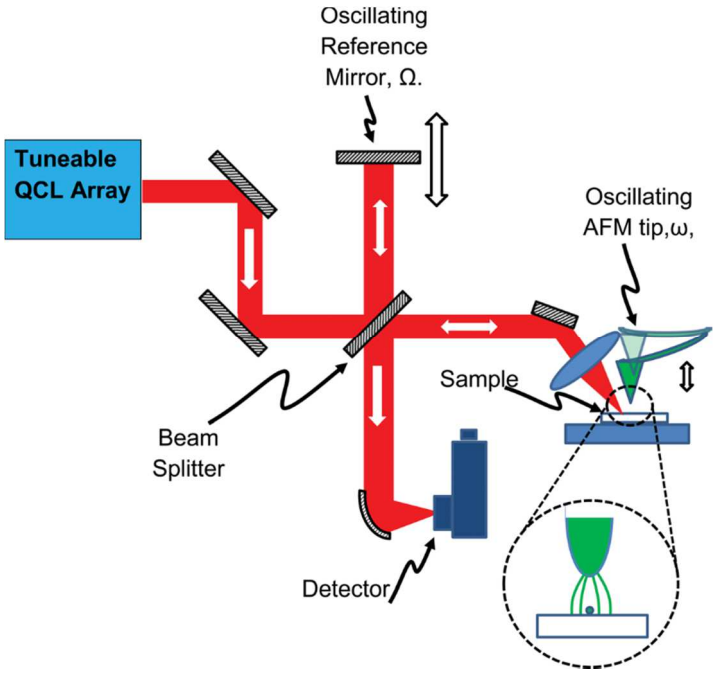


Figure 7.6 – Schematic of the mode of operation of a "scattering-type Scanning Near-field Optical Microscope" (s-SNOM). An AFM tip hovers close to the sample surface and vibrates, vertically, at a frequency ω. IR laser light is focused onto the tip region, and concentrated, into a spatial area roughly corresponding to the tip diameter (inset), by the "lightning rod" effect. By detecting the portion of the backscattered light fluctuating at 3ω (i.e. a harmonic of the tip vibration), the light backscattered from this small region can be isolated. An interferometer (with a reference mirror oscillating at $\Omega << \omega$) is used to measure both the amplitude and phase of the backscattered light, from which the optical properties of the very small sample area that is interacting with the AFM tip can be inferred. An image is assembled by rastering the AFM tip across the sample in the usual way. Figure and caption from publication by the author [2].

The s-SNOM works on the principle that the incoming Infrared (IR) beam is focused upon the end of the Atomic Force Microscope (AFM) tip, which is in contact with the sample and the light which scattered is then analysed. The setup used to take images of the structures within the beetle is shown and described in Figure 7.6. The s-SNOM technique can offer a spatial resolution of ~10nm.

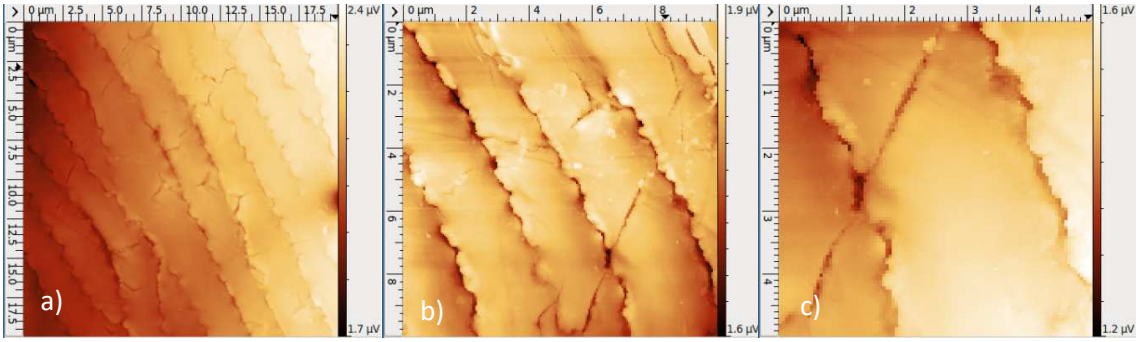


Figure 7.7 – AFM image of the surface of a *Mycterophallus validipes* beetle with imaging areas of a) 20x20um, b) 10x10um, and c) 5x5um.

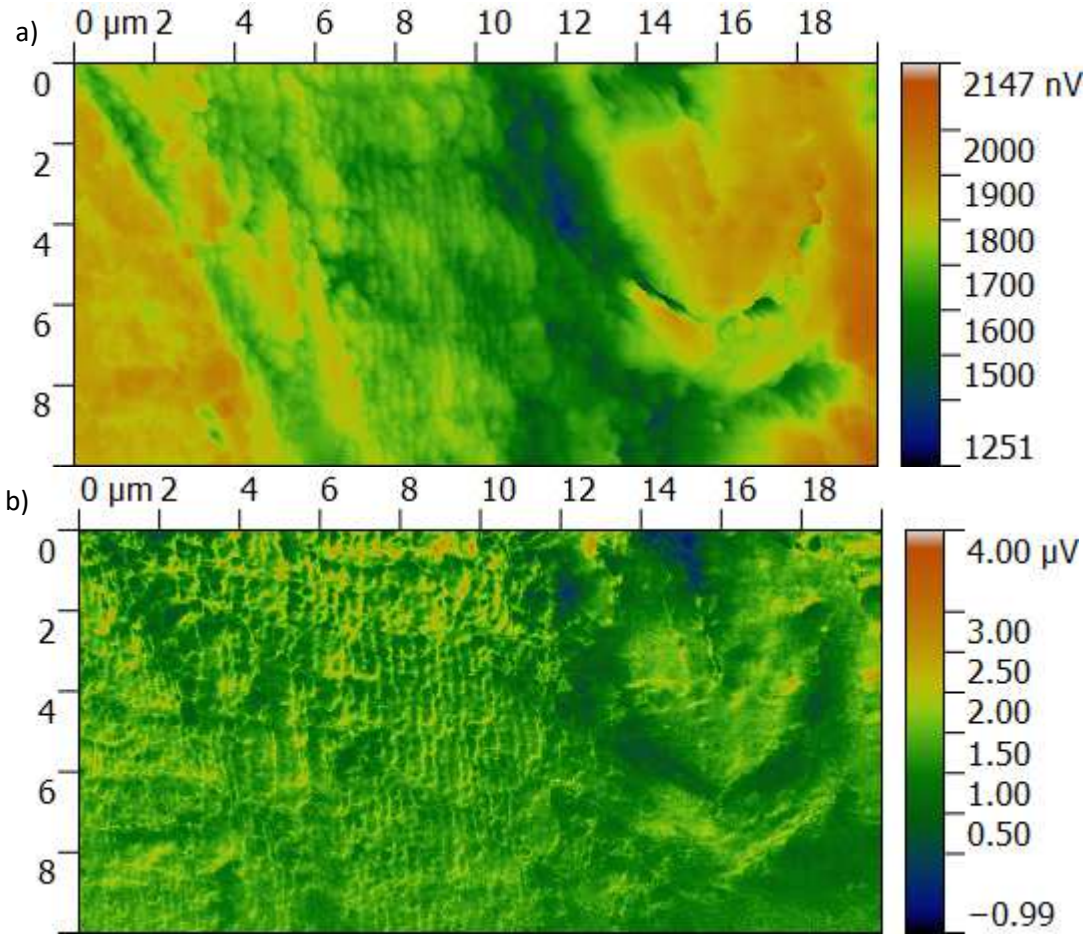


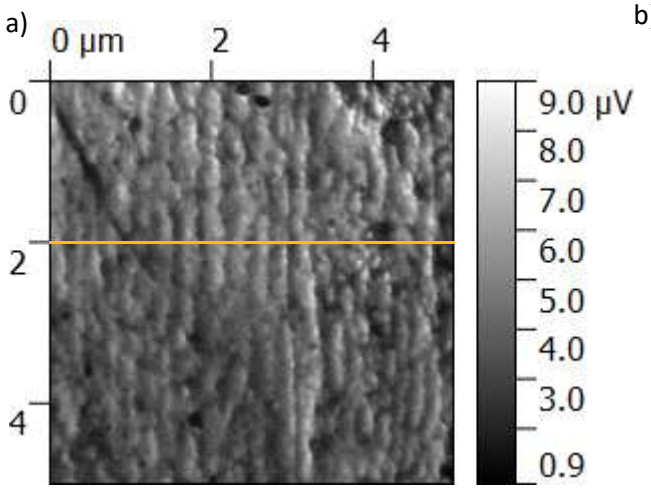
Figure 7.8 – a) AFM topography and b) operating wavelength λ=10.21um s-SNOM scattered amplitude image of a *Mycterphallus validipes* beetle. The voltage corresponds to the signal measured upon the detector. The s-SNOM image has given the chemical contrast of the components that make up the multilayers in the insect shell. In order to generate the shell's interference features in the visible part of the spectrum, the concentrations of these components vary on a sub-micron length scale, and only the s-SNOM can deliver chemical images at this resolution. The surface of the beetle being upon the left hand side. Taken from a publication by the author [2].

The AFM mode of this setup was used in order to first image the surface of the beetle's structure, where the blaze-like grating were observed (Figure 7.7). The image however appears to give twice the value in period of the SEM image produced. One factor that could cause this difference is that the vacuum imaging within the SEM could reduce the period of the structure, whilst the AFM was taken in non-vacuum conditions. Another possibility is that a different area of the beetle was viewed.

The sample was then microtomed, the cross section polished and was then imaged. This was then imaged as an AFM image (Figure 7.8a) and s-SNOM amplitude image (Figure 7.8b). The layered structure can be seen, which relates to the helicoidal structure pitches. The s-SNOM imaging can be seen to offer a great improvement in resolution over the AFM.

The contrast variation (which is reminiscent of a helicoidal structure) is more visible using the s-SNOM amplitude data than the AFM and as such the cross section on a greyscale image was analysed (Figure 7.9). From the table in Figure 7.9b, two distinct periods relating to two wavelength values (calculated using the same method as the EM image) cannot be seen and often the period doubles in value. The image was also not as clear as the SEM. There are several possible reasons for this including, as already discussed, the non-vacuum nature of the AFM/SNOM. In Figure 7.8b it can be seen that the apparent helicodal period appears to get thinner nearer the surface and it is possible the analysed image came from deeper within the structure and is so deep it does not substantially contribute to the optical response.

a)



b)

Amplitude Separation/nm	Wavelength/nm
175	555.1
200	634.4
350	1110.2
350	1110.2
350	1110.2
550	1744.6
300	951.6
250	793
275	872.3
375	1189.5
300	951.6
200	634.4
425	1348.1
250	793

Figure 7.9 – a) A s-SNOM amplitude image of 5x5µm of the *Mycterophallus validipes* beetle with the profile examined across the yellow line. b) The corresponding peak amplitude separation and wavelength.

The potential to use the s-SNOM system to image the helicoidal optical structures within Scarabaeoidae beetles can clearly be seen, with a vast improvement in resolution over using an

AFM. There are still some issues and calibration to be overcome, in terms of comparing non vacuum structural images with those taken in a vacuum. This also includes taking a smaller defined section of the beetles shell.

7.3. Conclusion

The optical structures of a *Mycterophallus validipes* beetle was investigated in this section. From the SEM images a link was made between the LL optical response and the period of the optical structure. The measured LCP optical response had two peaks at distinct wavelengths of 528nm and 673nm, this compared to the calculated values from the EM image of 531nm and 682nm.

The s-SNOM/AFM technique was shown to be able to image these optical structures within the *Mycterophallus validipes* beetle (although not as with as much resolution). The AFM and s-SNOM images had larger period values within them than the SEM images. There are several explanations for this, including the way in which the samples were prepared. The cross section SEM images were prepared by ion-beam milling, whilst the s-SNOM cross section images were microtomed. The AFM/SNOM images were also done in normal atmospheric conditions, whilst the SEM were done in vacuum conditions, this could lead to some period contraction. Another possibility is that slightly different regions of the beetle were investigated in the two different methods.

7.4. References

[1] I. E. Carter, K. Weir, M. W. McCall, and A. R. Parker, “Variation in the circularly polarized light reflection of Lomaptera (Scarabaeidae) beetles,” *J. R. Soc. Interface*, vol. 13, no. 120, pp. 1–9, Jul. 2016.

[2] H. Amrania, L. Drummond, R. C. Coombes, S. Shousha, L. Woodley-Barker, K. Weir, W. Hart, I. Carter, and C. C. Phillips, “New IR imaging modalities for cancer detection and for intra-cell chemical mapping with a sub-diffraction mid-IR s-SNOM,” *Faraday Discuss.*, vol. 187, pp. 539–553, 2016.

Chapter 8 - Future Research and Applications

There are many areas which are worthy of future research. Firstly, finding the purpose of the beetle shell needs to be investigated:

- One area of research, which is discussed earlier is the CP sensitivity in the vision of Scarabaeidae beetles. Several experiments have been done on this topic with no conclusive results. A wider selection of beetles should be investigated, in terms of variations in reflection of CP from elytra, geographic distribution and also taxonomic families. Their responses can be investigated using behavioural studies and also electrophysiology, which has previously been applied to Stomatopods.
- From a biology/entomology view point research into the genetics could help to find the evolutionary origin of such a structure and this may help with beetle classification. Such genetic classification has previously been undertaken in several species by Vogler and described in [1].

More research into how the CP structures form in these beetles, building on the work by Neville *et al* [2] could be done. Hopefully this would lead to some understanding of the system and perhaps the development of novel self-assembly optical structures.

There have been many CP reflection measurements taken and other non-purely optical techniques are required in order to determine the structure responsible. This includes taking images of the structures responsible for the optical response (using EMs or SNOMs) in order to verify the origin of such responses of the beetles. More in-depth modelling should also be carried out which takes into account layers other than the helicoidal ones, such as the waxy cuticle on the surface as well as surface structures.

A wider ellispometric study would be useful, taking into account variation with angle, extending the studies by Fernandez et al [3], which would help in making a better description and understanding of the polarising properties of such structures.

Another topic worthy of further investigation is the MM imaging of smaller areas of the beetle (for a large number of beetles) than the current beam size such as has been shown Figure 8.1.

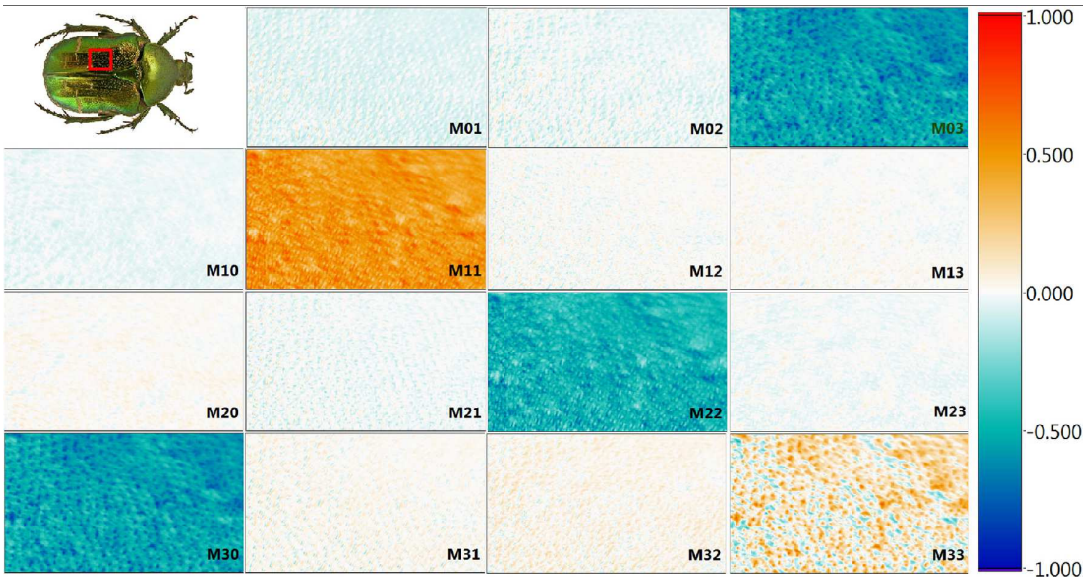


Figure 8.1 – Mueller matrix of a *Cetonia aurata* over an area 350µm x 220µm at 535nm. Used with permission, from [4].

Polarimetry imaging of the whole beetle (also at different angles) could be done (Figure 8.2), in order to view variations across the beetles' bodies without having to take many images. However, this requires separate images for every wavelength to be taken.

Investigation upon other parts of the beetle's body (than the top surface) could yield useful results with preliminary photographs of the underside of the beetles shown in Chapter 4.5.1. For example in these photographs it can be seen that there are beetles which reflect both LCP and RCP light only appear to reflect LCP upon the underside.

Much further research should also be done into the manufacturing of structures which mimic the CP properties of these beetles.

There are wide and varied applications which have been inspired by the helicoidal structures within the beetle's shells. The highly reflective and sometimes broadband metallic colours seen in some of the beetles have many advantages over using metals, such as a relatively short decomposition time so are not a pollutant and also not a good electrical or thermal conductor [5]. If such materials could be manufactured, then this could lead to a plethora of uses.

Potential other uses include structurally coloured fibres which can be used in textiles, such as those which have been inspired by the blue *Morpho* butterfly [6],[7].

Several attempts have been made to make materials inspired by the beetles' shells, one such example was done by Srinivasarao, who doped nematic crystals with a chiral material [8]. It was found that altering the dopant concentration could change the pitch and hence colour produced. Deparis et al also created TiO_2 and SiO_2 multilayered films [9]. This is discussed in greater depth in Section 3.4.8 and also in [10].

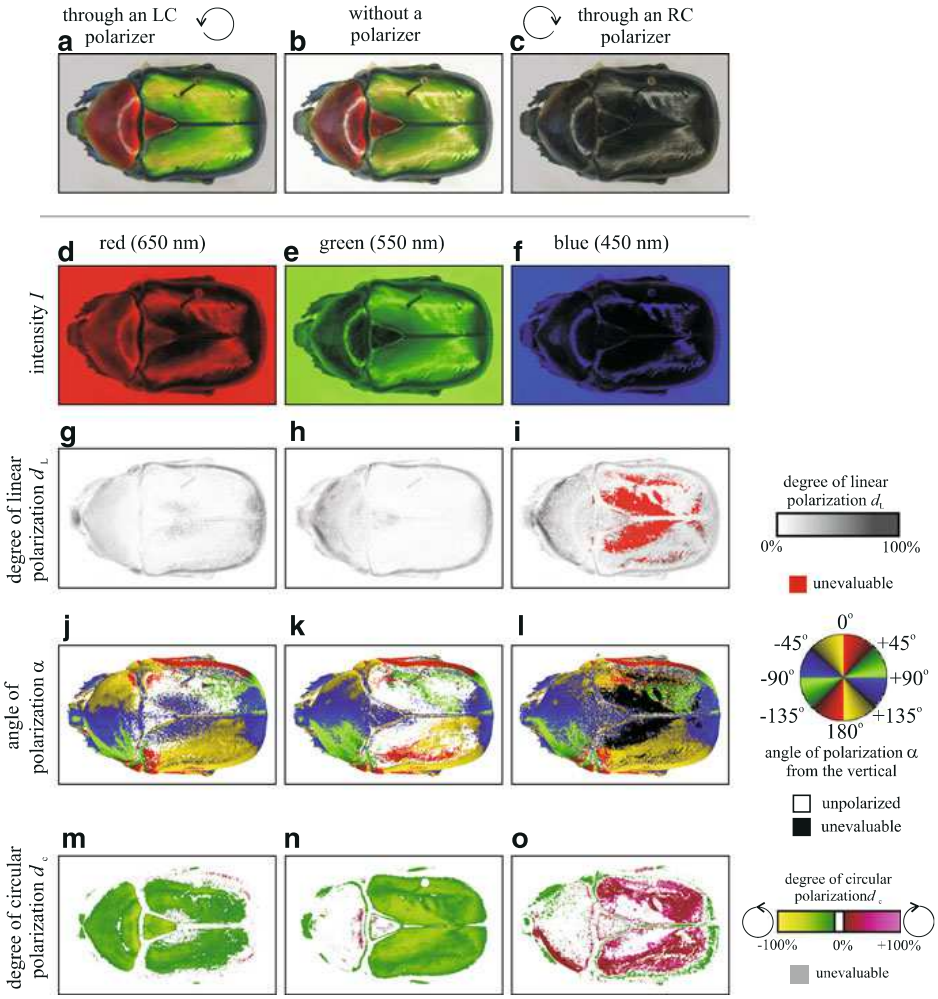


Figure 8.2 – Linear and circular polarisation patterns of the flower chafer, *Protaetia jousselini*, measured by imaging polarimetry at red (650 nm), green (550 nm) and blue (450 nm) wavelengths. The upper row shows the appearance through an LC polariser (a), an RC polariser (c) and without a polariser (b). The circular arrows here show the handedness of CP light transmitted by the polarisers. Below a–c, the panels are sorted by wavelength (650, 550, 450 nm). Rows d–f, g–i, j–l, m–o display the intensity I, degree of linear polarisation d_L, angle of polarisation α (measured clockwise from the vertical) and degree of circular polarisation d_c. Used with permission, from [11].

Paint pigment which is similar in appearance to rose chafer has been produced and commercially sold [12].

Other more exotic uses have been discussed, such as broadband silver beetle (*Chrysina chrysargyrea*) being studied for inspiration as coatings in aircraft and satellites and it has been proposed to send the beetles into space [13].

The use of structures such as those found in *Chrysina resplendens* which reflect both LCP and RCP light, have inspired laser designs with defect modes [14]. The beetle also inspired a diode whose polarisation is directionally dependent, with RCP generated in forward propagation and LCP in the other [15]. Chiral lasers have been produced, with the beetle structure inspiring further research [16]. There is continuing development in such a topic.

There is the potential to create more efficient electronic chips, optical filters, sensors and various displays [17].

One potential use is based upon the ability to generate CP light directly rather than having to convert it with a filter. This would mean much more efficient, simplistic, compact and cheaper devices. Chiral molecules have been suggested for use in a OLEDs as a screen backlight, which would produce CP light, as used in some 3D televisions and cinemas [18].

The use of such a device in quantum optical communication could enable a base three system to be used instead of the on-off binary, it would be on-left, on-right and off, effectively increasing the capacity [19].

8.1. References

[1] L. Jolin, "The Animals Went in Two by Two," *Imperial Magazine*, London, pp. 12–17, 2016.

[2] B. Zelazny and A. C. Neville, "Endocuticle layer formation controlled by non-circadian clocks in beetles," *J. Insect Physiol.*, vol. 18, no. 10, pp. 1967–79, 1972.

[3] L. Fernández del Río, H. Arwin, and K. Järrendahl, "Polarizing properties and structure of the cuticle of scarab beetles from the Chrysina genus," *Phys. Rev. E*, vol. 12409, pp. 1–9, 2016.

[4] O. Arteaga, "Natural optical activity vs circular Bragg reflection studied by Mueller matrix ellipsometry," *Thin Solid Films*, vol. 617, pp. 14–19, 2016.

[5] T. Lenau and M. Barfoed, "Colours and Metallic Sheen in Beetle Shells — A Biomimetic Search for Material Structuring Principles Causing Light Interference," *Adv. Eng. Mater.*, vol. 10, no. 4, pp. 299–314, Apr. 2008.

[6] M. Yoshimura, "Structural-Colored Fiber (Morphotex®)," *Kobunshi*, vol. 52, no. 11, pp. 826–828, 2003.

[7] K. Iohara, M. Yoshimura, H. Tabata, and S. Shimizu, "Structurally Colored Fibers," *Chem. Fibers Int.*, vol. 50, pp. 38–39, 2000.

[8] M. Srinivasarao, "Nano-optics in the biological world: beetles, butterflies, birds, and moths," *Chem. Rev.*, vol. 99, pp. 1935–1961, 1999.

[9] O. Deparis, M. Rassart, C. Vandenbem, V. Welch, J. P. Vigneron, and S. Lucas, "Structurally tuned iridescent surfaces inspired by nature," *New J. Phys.*, vol. 10, no. 13032, pp. 1–11, Jan. 2008.

[10] L. De Silva, I. Hodgkinson, P. Murray, Q. H. Wu, M. Arnold, J. Leader, and A. Mcnaughton, "Natural and Nanoengineered Chiral Reflectors: Structural Color of Manuka Beetles and Titania Coatings," *Electromagnetics*, vol. 25, no. 5, pp. 391–408, Jul. 2005.

[11] R. Hegedüs, G. Szél, and G. Horváth, "Imaging polarimetry of the circularly polarizing cuticle of scarab beetles (Coleoptera: Rutelidae, Cetoniidae)," *Vision Res.*, vol. 46, pp. 2786–2797, 2006.

[12] J. Heinlein and M. Kasch, "Pigment offer color effects matched only by nature," *Paint Coatings Ind.*, vol. 15, no. 8, p. 58, 1999.

[13] A. M. Vargas, M. Rojas, J. Solis, R. Aguilar, M. Jimenez, and M. Hernandez, "Design of a Nanolab to Monitor the Elytra of a Chrysina Beetle at the International Space Station," in *66th International Astronautical Congress*, 2015, pp. 1–13.

[14] M. H. Song, B. C. Park, K. C. Shin, T. Ohta, Y. Tsunoda, H. Hoshi, Y. Takanishi, K. Ishikawa, J. Watanabe, S. Nishimura, T. Toyooka, Z. G. Zhu, T. M. Swager, and H. Takezoe, "Effect of phase retardation on defect-mode lasing in polymeric cholesteric liquid crystals," *Adv. Mater.*, vol. 16, no. 9–10, pp. 779–783, 2004.

[15] J. Hwang, M. H. Song, B. Park, S. Nishimura, T. Toyooka, J. W. Wu, Y. Takanishi, K. Ishikawa, and H. Takezoe, "Electro-tunable optical diode based on photonic bandgap liquid-crystal heterojunctions," *Nat. Mater.*, vol. 4, no. 5, pp. 383–387, 2005.

[16] R. D. M. Topf and M. W. McCall, "Modes of structurally chiral lasers," *Phys. Rev. A - At. Mol. Opt. Phys.*, vol. 90, no. 53824, pp. 1–5, 2014.

[17] A. Lakhtakia, "Toward optical sensing of metal nanoparticles using chiral sculptured thin films," *J. Nanophotonics*, vol. 1, no. 19502, pp. 1–6, Jun. 2007.

[18] Y. Yang, R. C. da Costa, D.-M. Smilgies, A. J. Campbell, and M. J. Fuchter, "Induction of circularly polarized electroluminescence from an achiral light-emitting polymer via a chiral small-molecule dopant," *Adv. Mater.*, vol. 25, no. 18, pp. 2624–8, May 2013.

[19] J. F. Sherson, H. Krauter, R. K. Olsson, B. Julsgaard, K. Hammerer, I. Cirac, and E. S. Polzik, "Quantum teleportation between light and matter," *Nature*, vol. 443, no. 7111, pp. 557–60, Oct. 2006.

Chapter 9 – Conclusion, Publications and Conferences

9.1. Conclusion

For over 100 years the study of the selective reflection of CP light from Scarabaeoidae beetles has been an area of study which has attracted great interest from a variety of disciplines. The majority of this thesis deals with this phenomenon. The reflection of CP light has a physical origin in a helicoidal structure consisting of layers of birefringent thread like molecules of chitin. In a single layer within the helicoidal structure the molecules all have the same orientation, this orientation changes by a few degrees between consecutive layers. The length taken for the molecules to rotate a full 360° orientation between single layers is known as a pitch and is related to the reflected wavelength at normal incidence by the average refractive index of the beetles' helicoidal structures.

The study focused upon the variation in the CP response from Scarabaeoidae beetles within and between species, genera and subfamilies (Chapter 4). A broadband setup (450nm-1000nm) with Fresnel rhombs was used in order to measure this CP response. One hundred and seventy eight species of beetle which selectively reflect CP light were investigated in the report (and the appendix). CP spectra from nine subfamilies were investigated, with vast variations. Most of the CP spectra in this study have a dominant LCP reflection response, from a pitch structure (e.g. *Repsimus aeneus*), whilst others had more mirror like responses due to the refractive index mismatch of the shell and air (e.g. *Melolontha melolontha*).

This study includes twenty eight species from the much studied *Chrysina* genus; which had variation in colour, intensity and handedness of CP light within and between species. Many new optical variations have been uncovered for the first time to the author's knowledge. These include typical colour variation in *Chrysina optima* where all the forms selectively reflected LCP light by similar amounts where the lower reflection limit decreased between the silver, gold and red metallic morphs respectively. This colour change was suggested to be due to the variation in the pitch structure, with the gold and red forms lacking the shorter pitches within the silver variant. Two forms of the *Chrysina boucardi* beetle (a metallic gold and matt green form) were investigated and had an order of magnitude difference between the LL spectra of the two, this was thought to be due to a micro mirror-like surface structure in the green form disrupting the helicoidal structure. Within the genus both broadband (e.g. *Chrysina limbata*) and narrowband reflections (e.g. *Chrysina macropus*) were observed. New Chrysina species which reflect both

LCP and RCP light have been uncovered both being metallic (*Chrysina cupreomarginata*) and matt (e.g. *Chrysina costata*). From previous research this is thought to be due to uniaxial layer that acts as a half waveplate. Variation also occurred in individual beetles such as *Chrysina vitoriana*, which had a red pronotum and green elytra with red spots again thought to be due to variation in pitch thickness.

This study looked at reflected spectral polarisation variation within larger numbers of beetles than previous studies. This included a study of the LCP spectral shape of 208 specimens of the *Lomaptera* genus and showed some species had very consistent spectral shapes (such as *Lomaptera pseudodichropus*), whilst other species (such as *Lomaptera soror*) had more variation.

Some single species within this study had a great deal of variation in the LCP spectra such as a study of 191 *Cetonia aurata aurata*. Another study of 210 *Ischiosopha aruensis* had less variation, only varying slightly in both pitch shape and reflected wavelength.

Variations with smaller numbers of beetles were also investigated, including the species *Cetonia aurata pisina*, whose specimens were collected at the same location on the same date had wavelength variation in the LCP spectra response from blue to the NIR. Such a large variation in single peaks has not been reported previously. In the majority of specimens studied green was the dominant colour and as such is suggested to be a useful camouflage amongst green vegetation. A noticeable colourful specimen was the bright purple colour observed in the *Protaetia mirifica* as a combination of an intense narrow peak in the blue and weaker wider peak at a red wavelength, relating to short and long pitch values within the beetles shell. Other variations also occurred within single species such as *Protaetia speciosa jousselini*, which had blue elytra and a red pronotum.

The Cetoniinae *Rhomborhina gigantea* was previous reported to produce colour from a chiral structure, in this thesis the response was shown not to selectively reflect CP light.

Further to the experimental measurements of LCP light reflection, modelling of several spectral shapes was also carried out in Chapter 5. The model used Berreman calculus in a layer-by-layer transfer matrix approach, using previously published experimentally obtained variables such as refractive index, number of pitches, birefringence and chitin molecule size. The spectral shapes of the *Lomaptera* genus and *Cetonia aurata* were chosen to be modelled. The models were created as variations and combinations of two basic perturbations to the otherwise single pitch value. The first perturbation type uses multiple pitches values resulting in multiple wavelength reflection. The second perturbation type is sudden jumps in the orientation of individual layers of chitin molecules in the helicoidal structure, which results in a trough in the peak. More

complex combinations of model perturbations were used for an example of each of the nine subfamilies investigated. The use of many pitch perturbations allowed the modelling of broadband reflection of the three *Chrysina optima* colour variations (silver, gold and red).

In order to further understand the origin of the CP response, images of the helicoidal structures (as well as surface structures) were taken using Electron Microscopy and Scanning Near-field Optical Microscopy. From the electron micrographs taken of a *Mycterophallus validipes* beetle pitch values were obtained which corresponded to peaks in an experimental LL spectrum with two distinct wavelength peaks. The pitch values were seen to be in an interstitial arrangement, alternating in value as to which peak they corresponded to as the distance increased from the surface. A blazed grating like structure was also observed on the surface of this beetle.

To fully describe the polarising properties of reflection from the beetles, a broadband MM polarimetry/ellipsometry system was developed. This involved using LCVRs in the output arm of the system and used a calibration method, which did not require full knowledge of the LCVR's retardances. Several issues were overcome in the setup, including using a sheet QP which introduced chromatic variation and retardance degeneracy at some wavelengths with the used LCVR voltage combinations.

Using the ellipsometry setup MMs of a selection beetles with different spectra (as identified in Chapter 4) were taken. These included a simple dominant LCP single peaks, multiple peaked and broadband reflection as well as less dominant LCP peaks and beetles with both LCP and RCP reflection. MM of colour variation and intensity variation in *Chrysina* were also taken. The main two features of the MMs were mirror-like elements (on the negative diagonal) and CP elements (in the corners of the MM). From the MMs the degree of polarisation, azimuth angle and ellipticity were calculated. It was seen that some beetles such as *Melolontha melolontha* had a low degree of polarisation and acted more mirror-like than circular polarisers. Most of the beetles had ellipiticty that was close to that of a left circular polariser (-1) at the reflected peak values, whilst a few of the *Chrysina* beetles which reflect RCP light had a larger variation of this parameter. Many of the beetles had oscillations within the ellipiticity (and various MM elements). This was suggested to be related to the overall thickness of the beetles' shells, the oscillations increased in period with wavelength as the pitch value of the beetle got larger.

A plethora of uses have been suggested for the manufacturing of circularly polarising structures, such as in aesthetic applications, where the colour is metallic but not a good conductor of heat or electricity. The advantage of using such a material would be that it would only require a single material (rather than multiple layered materials) and could potentially self-assemble. Other more technical uses have been suggested such as chiral lasers or 3D screens and displays. Future

research in the topic still needs to be done including more electron micrographs of the actual optical structures, finding techniques in which to manufacture such structures and understanding the biologic processes and purposes (which may lead to novel self-assembly techniques).

This thesis presents polarisation studies of many species of Scarabaeoidae beetle, which to the author's knowledge have not been optically studied previously. This revealed a wide variety of different spectral distributions and over a wide range of wavelengths from blue to the NIR (even within a single species, *Cetonia aurata pisina*). A wide range of reflection bandwidths were observed from very narrowband to broadband (over the entire optical range, resulting in a silver colour). The wide range of variations within some species demonstrates the care that needs to be taken when presenting results from a single specimen.

9.2. Publications

- I. E. Carter, K. Weir, M. W. McCall, and A. R. Parker, "Variation in the circularly polarized light reflection of Lomaptera (Scarabaeidae) beetles," *J. R. Soc. Interface*, vol. 13, no. 120, pp. 1–9, Jul. 2016.
- H. Amrania, L. Drummond, R. C. Coombes, S. Shousha, L. Woodley-Barker, K. Weir, W. Hart, I. Carter, and C. C. Phillips, "New IR imaging modalities for cancer detection and for intra-cell chemical mapping with a sub-diffraction mid-IR s-SNOM," *Faraday Discuss.*, vol. 187, pp. 539–553, 2016.
- I. E. Carter, K. Weir, and M. W. McCall, "Investigation of the Variation of Near-Circular Polarization in Scarabaeoidea Beetles," *Mater. Today Proc.*, vol. 4, no. 4, pp. 4942–4951, 2017.

9.3. Talks

- Carter, I.E., Weir, K. and McCall, M.W. (September 2014) 'The Circularly Polarised Response of Lomaptera Beetles', Photon14. (London, UK)
- Carter, I.E., Weir, K. and McCall, M.W. (June 2016) 'Investigating the Variation in the Polarisation of Reflected light in Optically Active Scarabaeidae', Imperial College London Seminar. (London, UK)
- Carter, I.E., Weir, K. and McCall, M.W. (September 2016) 'Polarisation variation in reflected light from Scarabaeidae beetles', Photon16. (Leeds, UK)
- Carter, I.E., Weir, K. and McCall, M.W. (February 2017) 'Wide variation in near-circular polarisation reflection in Scarabaeidae beetles', Optical Biomimetics. (London, UK)

9.4. Posters

- Carter, I.E., Weir, K. and McCall, M.W. (May 2016) 'Investigation of the Variation of Near-Circular Polarisation in Scarabaeoidea Beetles', Living Light 2016. (San Diego, USA)

9.5. Notable Outreach

- Jointly designed and took part in "The Wonderful World of Polarisation" as an exhibition at the Imperial College Festival. (April 2015, London, UK).
- Presented and organised a polarisation exhibition at the Natural History Museum event called "Colour and Vision Lates". (July 2016, London, UK).

Appendix

Table of Contents

INTRODUCTION 207
A1 - Beetles in Popular Culture 207
A2 - List of previous studies by species 208
A3 - CP Spectra 210
A3.1 – Scarabaeinae 210
A3.2 – Cetoniinae 212
A3.2.1 - Single species 212
A3.2.2 - Poecilopharis 216
A3.2.3 - Agestrata 217
A3.2.4 - Jumnos 218
A3.2.5 - Mycterophallus 219
A3.2.6 - Ischiopsopha 220
A3.2.7 - Plaesiorhinella 221
A3.2.8 – Protaetia 223
A3.2.9 – Lomaptera 231
A3.3 - Rutelinae 239
A3.3.1 - Chrysina 239
A3.3.2 - Single Species 249
A3.3.3 – Anomala 255
A3.3.4 - Pelidnota 257
A3.3.5 - Strigidia 258
A3.4 – Trichiinae 259
A3.5 - Melolonthinae 259
A3.6 - Euchirinae 260
A3.7 -Dynastinae 260
A3.8 - Phaenomeridinae 261
A3.9 - Ceratocanthinae 262
A3.10 – Underside Photographs 262
A3.11 – Angular Variation 264
A4 - Modelling 264
A4.1 - Modelling Parameters 265
A5 – Mueller Matrix Ellipsometer Alternative Methods 266
A5.1 - Fresnel rhombs 267
A5.2 - LCVR in one side-air 267
A5.3 - Rotating only waveplates 268
A5.4 - Stability of LCVR 269
A5.5 - LCVR MM Setup Delta Function 270
A5.6 – Beetle MM 272
A5.6.1 - Typical species from each subfamily 272
A5.6.2 - Cetonia aurata aurata 279
A5.6.3 - Chrysina 285
A5.6.4 - Other Cetoniidae 298
A5.6.5 - Other Rutelidae 302
A5.6.6 - Other Phaenomeridae 303
References 304

Introduction

In this appendix there are photographs of beetles taken through CP filters (Section A1). Followed by list of previous species which have been investigated with referenced articles in Section A2. This is then followed by a reference library of CP spectra from different beetle species (Section A3). The parameters which were used to model the spectra in the main text were discussed and given in Section A4. In Section A5 other setups for measuring MMs were discussed and demonstrated. This is followed by another reference library this time of MMs of some of the beetles in Section A5.6.

A1 - Beetles in Popular Culture



Figure A 1 – Keyrings and pendants of beetles; 1-*Chalcothea resplendens*, 2-*Mimela splendens*, 3-*Popillia mutans*, 4-*Popillia mongolica*, 5-*Popillia flavosellata*, 6- *Mimela splendens*, 7-*Protaetia brevaitis*, through a) a LCP filter and b) a RCP filter.

A2 - List of previous studies by species

The following section contains a list of previous publications upon the circularly polarised reflection response of beetles. This list does not include the 19,000 species investigated by Pye, or any of the authors own publications.

Scarabaeidae

Cetoniinae

Agestrata orichalcea[1]
Cetonia aurata[1]–[20]
Cetonia carthami [1]
Chalcothea (*Calcothea*) affinis [2]
Cotinus (*Cetonia*) mutabilis [2],[17],[21]–[23]
Ischiopsopha (Lomaptera) jamesi [3],[24]
Ischiopsopha bifasciata [25]
Liocola marmorata [11]
Lomaptera sp. [3]
Lomaptera helleriana [12]
Lomaptera lomapteroides [12]
Lomaptera soroi [1],[12]
Lomaptera viridipes [12]
Mycterophallus sp. [26]
Mycterophallus duboulayi [1],[26]
Protaetia aeruginosa (*Potosia speciosissima*) [2],[3],[24],[27]
Protaetia (*Potosia*) cuprea [1],[3],[5],[10],[11]
Protaetia (Cetonischema) speciosa jousselini [28]
Pseudochalcothea auripes[10]
[1]Rhomborhina gigantea [29]

Scarabaeinae

Canthon smaragdulus (Goniocanthon smaragdulus) [3]
Gymnopleurus virens [30],[31]
Gymnopleurus humanus[32]
Onitis sp. [3]
Oxysternon festivum (Phanaeus festivus) [3]
Phanaeus sallei [3]
Phanaeus vindex [33]
Proagoderus brucei [34]
Sulcophanaeus carnifex (Phanaeus carnifex) [3]
Sulcophanaeus imperator (Phanaeus imperator) [3]

Rutelinae

Anomala aenea[35]
Anomala albopilosa [2],[36]
Anomala dimidiata [37]
Anomala dubia [3],[5]
Anomala motschulskyi (motschilskyi) [2]
Anomala viridis [2]
Anomala vitis [5]

[1]Note this species previous was noted to have chiral structure responsible for colour, but in this thesis this was shown not to be the case.

Anoplognathus aureus [6],[17]
Anoplognathus parvulus (parvalus) (mastersi) [3],[24],[27],[38],[39]
Anoplognathus viridiaeneus[3],[24],[27]
Calloodes grayanus [38],[39]
Chrysina alticola [40]
Chrysina (Plusiotis) adelaida [27],[41],[42]
Chrysina (Plusiotis) alphabarrerai [43]
Chrysina (Plusiotis) peruviana (amena) [35]
Chrysina argentola [10],[17],[18],[20],[42],[44]
Chrysina aurigans [19],[40],[45]–[50]
Chrysina aurora [42]
Chrysina (Plusiotis) boucardi [43]
Chrysina chrysargyrea [40],[42],[44],[46]
Chrysina costatas [24]
Chrysina (Plusiotis) clypealis [41]
Chrysina (Plusiotis) gloriosa [14],[24],[27],[37],[40]–[42],[44],[51]–[56]
Chrysina gordo [40]
Chrysina limbata [47]
Chrysina macropus [40],[42],[44]
Chrysina (Plusiotis) optima [3],[24],[27],[37],[57]
Chrysina purulhensis [40]
Chrysina peruviana [42],[44]
Chrysina (Plusiotis) resplendens [3],[19],[24],[27],[28],[33],[39]–[44],[58],[59]
Chrysina (Plusiotis) sallei [43]
Chrysina strasseni [57]
Chrysina (Plusiotis) woodi [25],[33],[42],[52]
Chrysina xalisteca [40]
Chrysophora chrysochlora [25],[28]
Macrapsis lucida [4]
Pelidnota chamaeleon ignita [3]
Pelidnota cyanitarsis [3]
Pelidnota ignita [3]
Pelidnota sumptuosua [2],[3]
Phyllopertha horticola [3]

Trichiinae
Gnorimus variabilis [3]

Melolonthinae
Melolontha melolontha [3]
Stethaspis pulcher [60]
Pyronota festiva [61],[62]

Euchirinae
-
Dynastinae
-
Phaenomeridinae
-

Hybosoridae

Ceratocanthinae

A3 - CP Spectra

This section contains a number of typical CP spectra from various subfamilies, genera and species.

A3.1 – Scarabaeinae

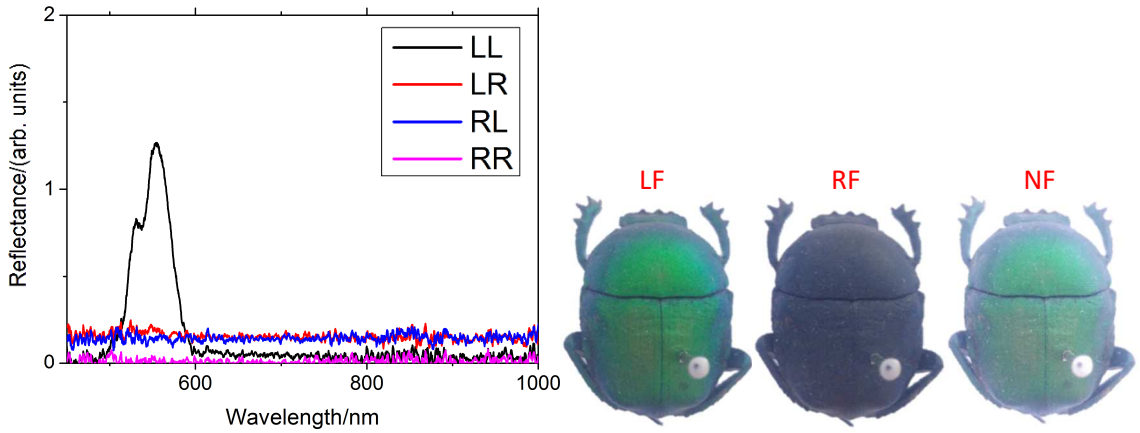


Figure A 2 – CP reflection spectra from the elytron of a *Garreta azureus* beetle. This specimen was collected from South Africa in 2014. Taken with an integration time of 500ms. The species measures ~18mm.

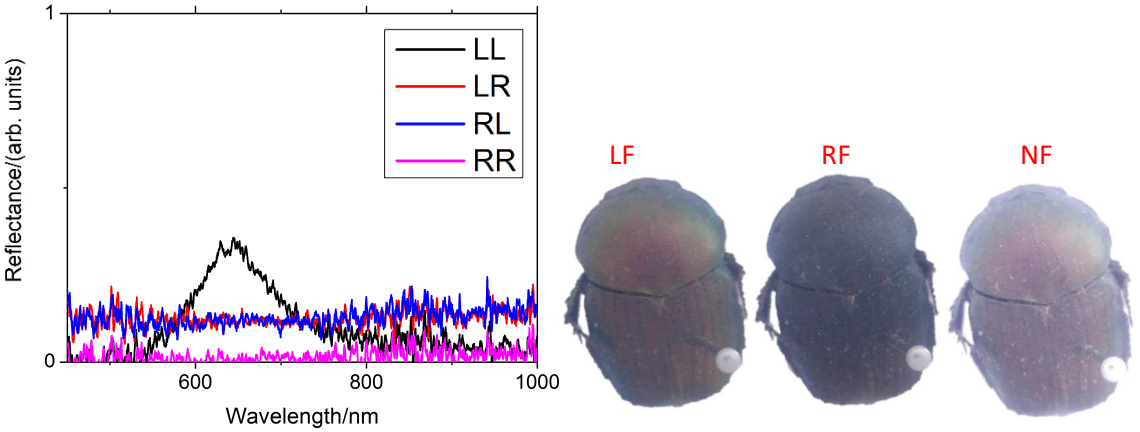


Figure A 3 – CP reflection spectra from the pronotum of an *Ontis Sp*. beetle. This specimen was collected from South Africa in 2014. Taken with an integration time of 500ms. The species measures ~16mm.

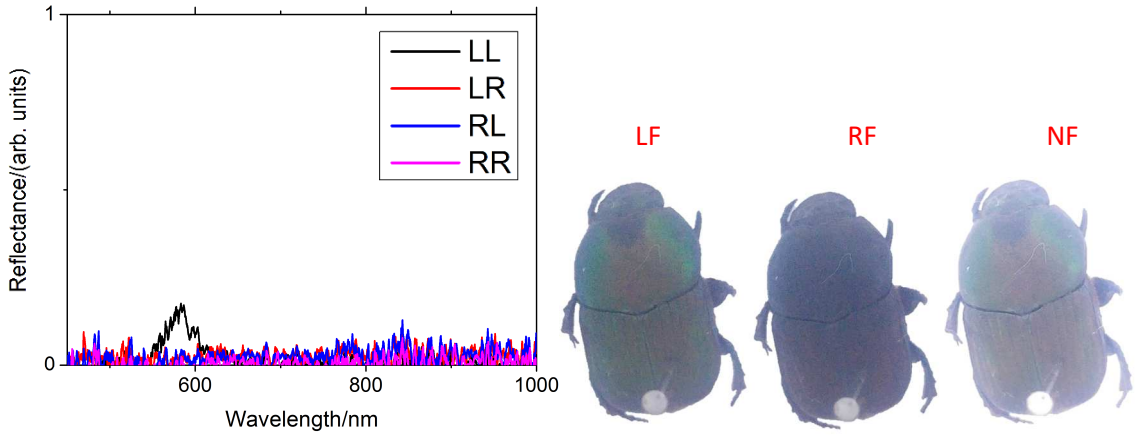


Figure A 4 – CP reflection spectra from the pronotum of an *Ontis alexis* beetle. This specimen was collected from Moshi, Kilimanjaro, Tanzania in 2016. Taken with an integration time of 500ms. The species measures ~17mm.

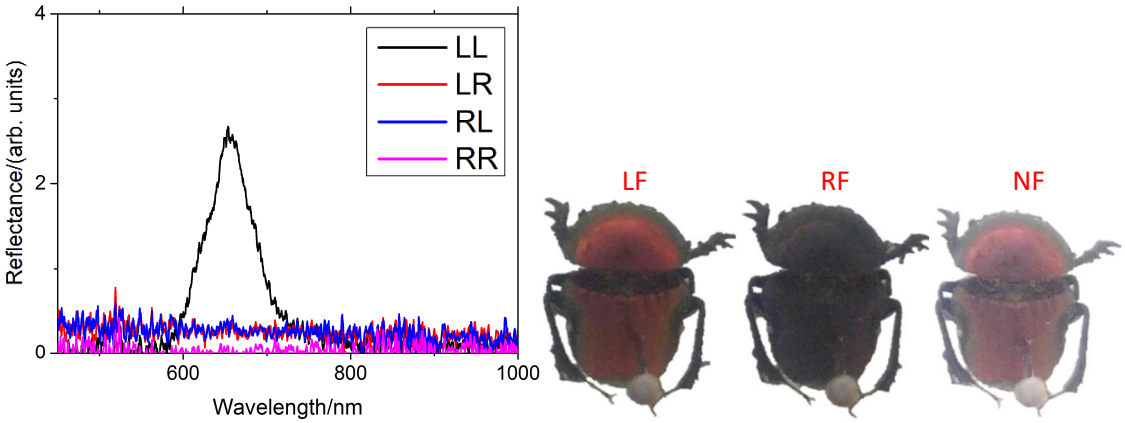


Figure A 5 – CP reflection spectra from the prontum of a *Gymnopleurus sp* beetle. This specimen was collected from Uluguru Mountains, Tanzania in 2007. The specimen measures 9mm.

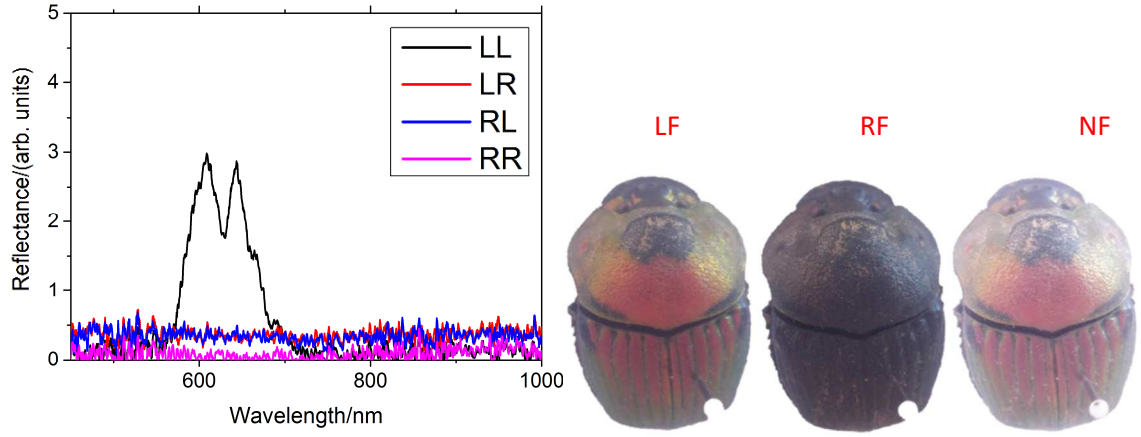


Figure A 6 – CP reflection spectra from the pronotum of a female *Phanaeus mexicanus* beetle. This specimen was collected from Catemaco, Veracruz, Mexico in 2004. The specimen measures 22mm.

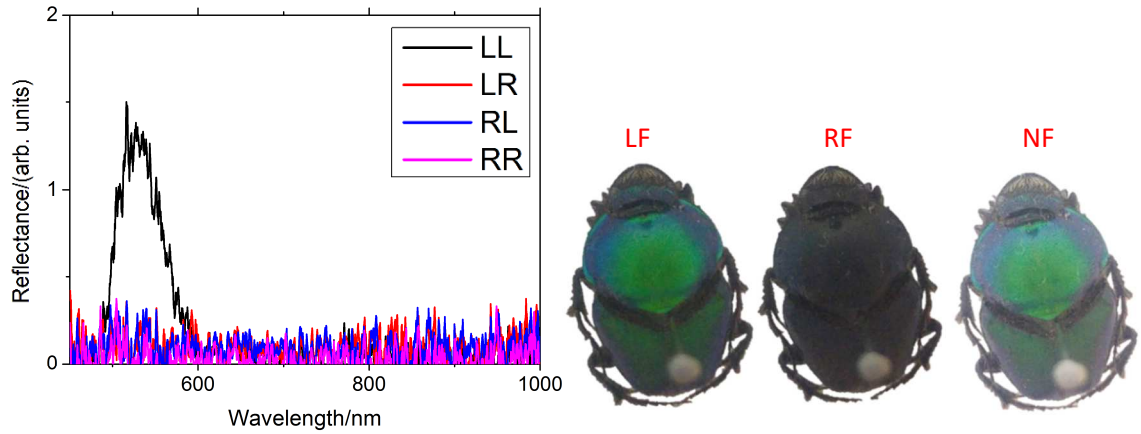


Figure A 7 – CP reflection spectra from the pronotum of an *Onthophagus (Proagoderus) rangifer* beetle. This specimen was collected from Uluguru Mountains, Tanzania in 2012. The specimen measures 12mm.

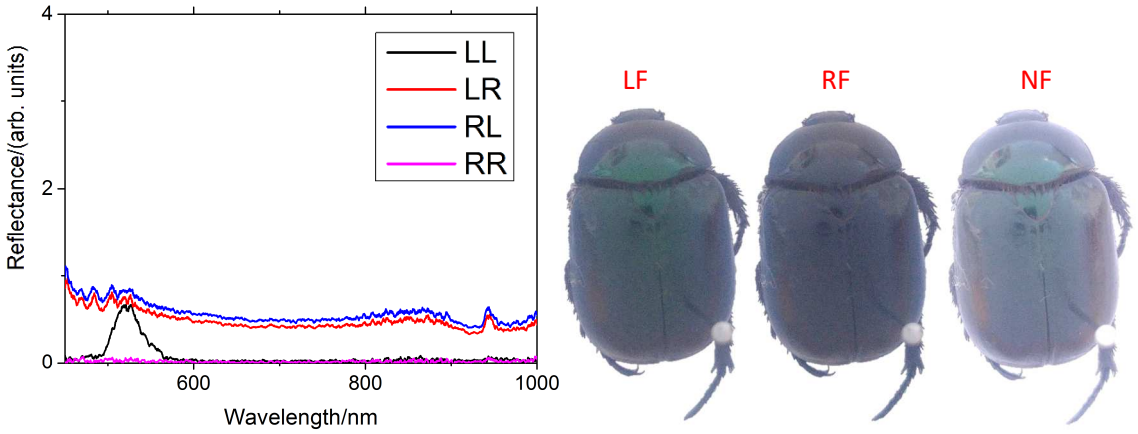


Figure A 8 – CP reflection spectra from the pronotum of an *Oogenius chilensis* beetle. This specimen was collected from El Canelo, Cordillera, Chile 2016. Taken with an integration time of 2000ms. The specimen measures 22mm.

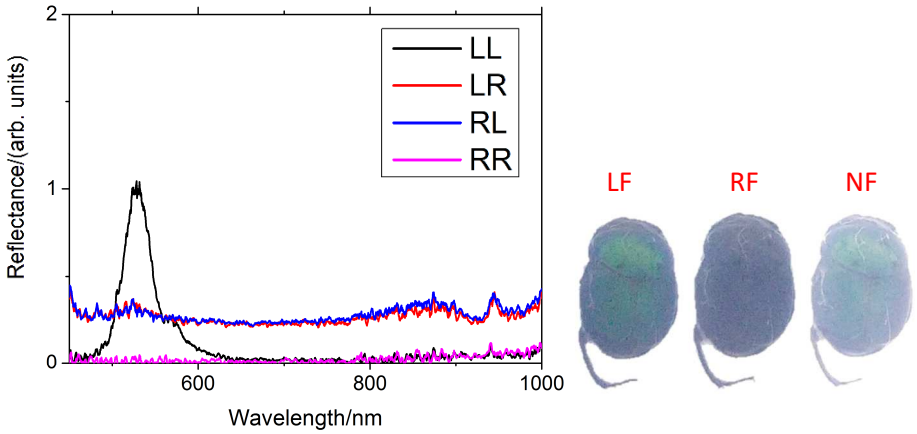


Figure A 9 – CP reflection spectra from the pronotum of a *Canthon Sp.* beetle. This specimen was collected from Santa Maria, Catamarca, Argentina in 2017. Taken with an integration time of 2000ms. The specimen measures 6mm.

A3.2 – Cetoniinae

A3.2.1 - Single species

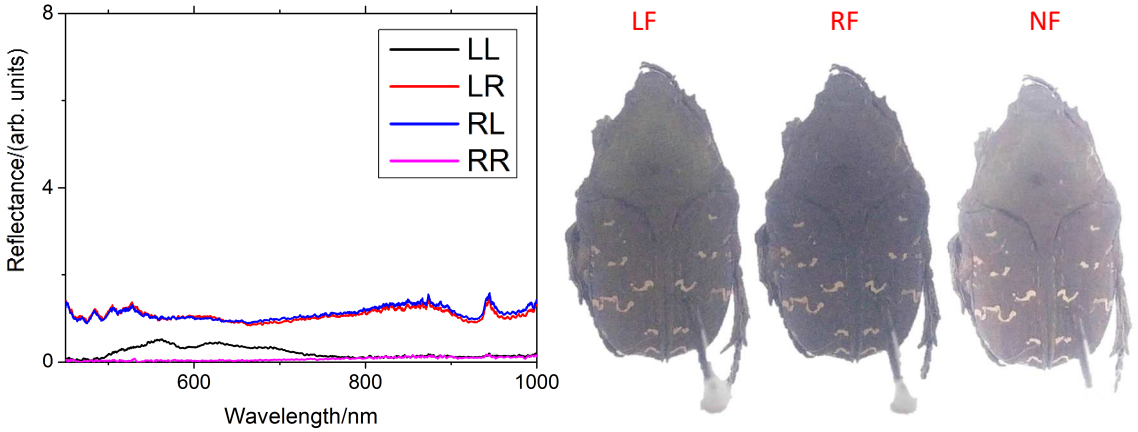


Figure A 10 – CP reflection spectra from the elytron of a *Euphoria leucographa* beetle. This specimen was collected from Cusco Cortes, Honduras in 2016. Taken with an integration time of 2000ms. The specimen measures 14mm.

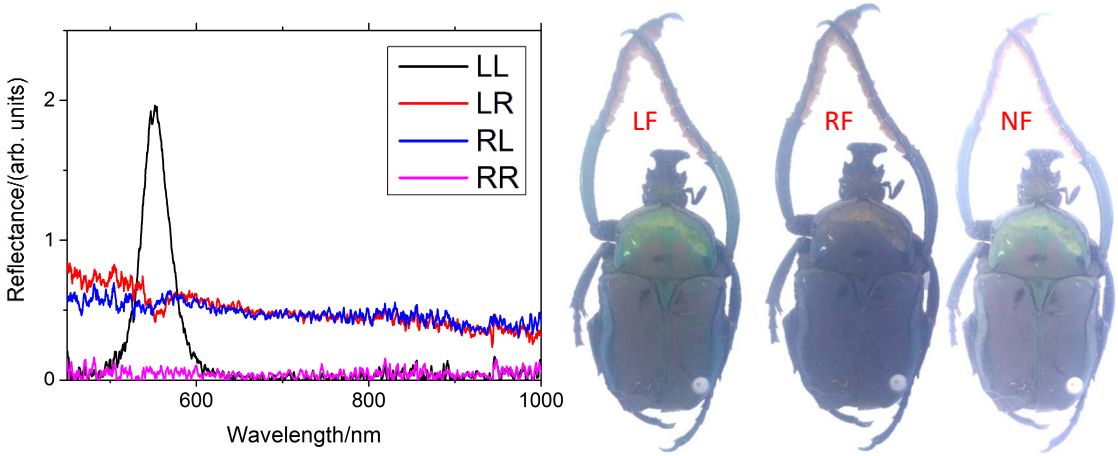


Figure A 11 – CP reflection spectra from the elytron of a *Neoscelis dohrni* beetle. This beetle was collected in Potrerillos, Sinaloa, Mexico in 2008. Taken with an integration time of 500ms. The specimen measures 28mm.

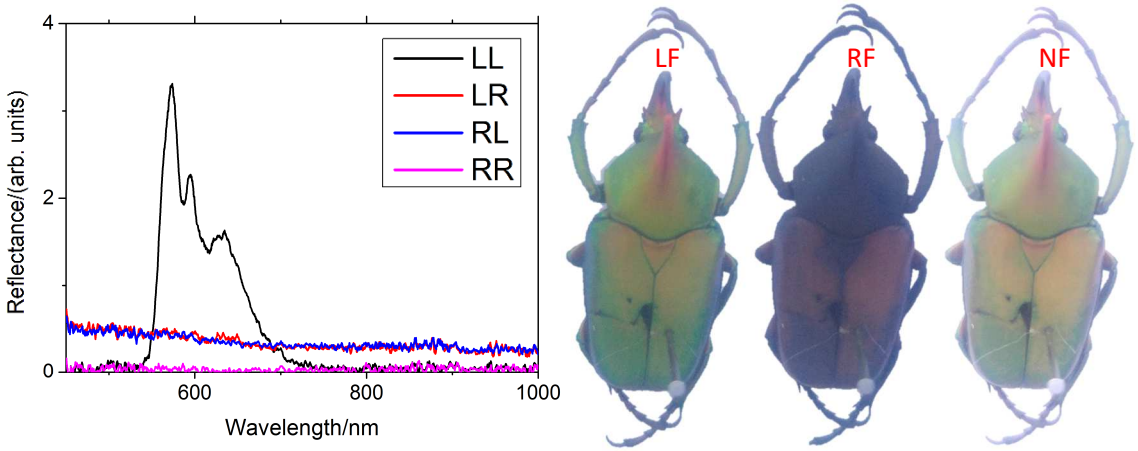


Figure A 12 – CP reflection spectra from the pronotum of a *Theodosia rodriguezi* beetle. This beetle was collected in Palawan, Philippines in 2012. The specimen measures 28mm.

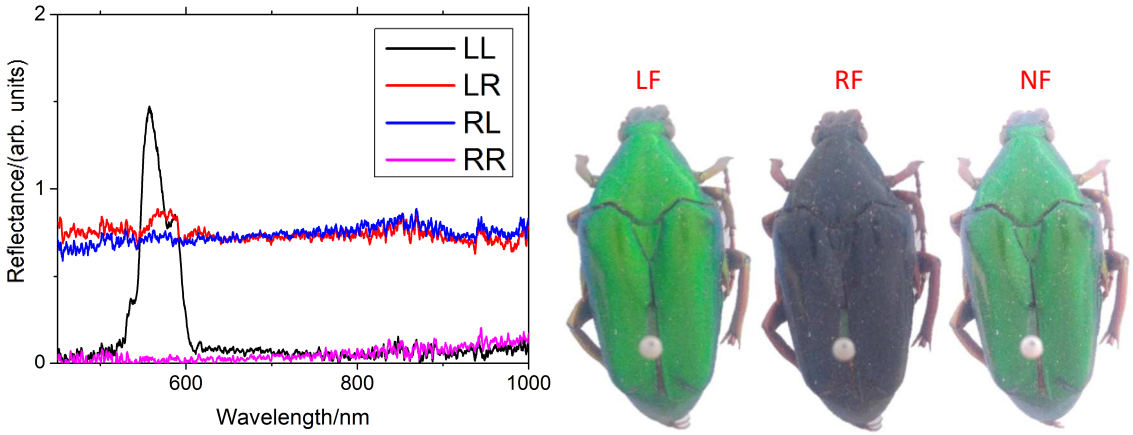


Figure A 13 – CP reflection spectra from the elytron of a *Hemichalca inermis* beetle. This beetle was collected in Malaysia in 2013. Taken with an integration time of 500ms. The species measure ~28mm.

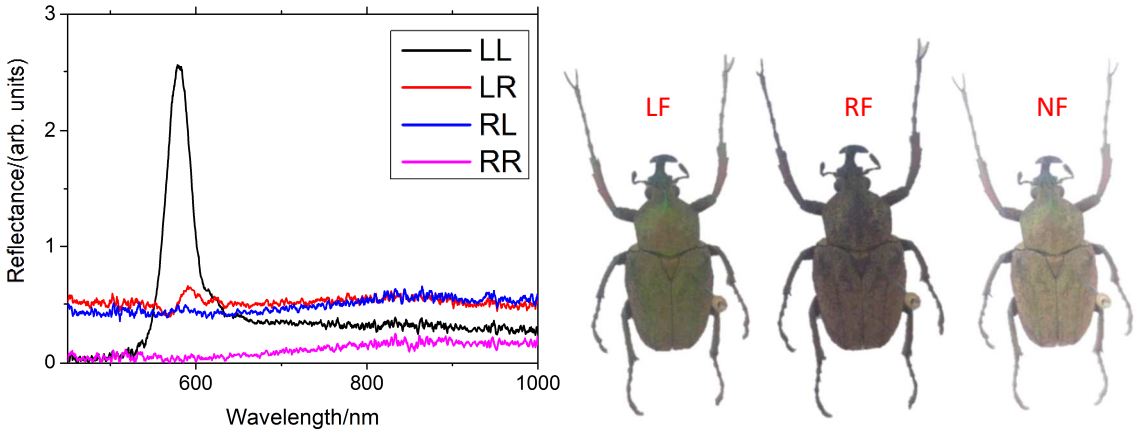


Figure A 14 – CP reflection spectra from the pronotum of a *Mycteristes rhinophyllus* beetle. This specimen was collected from East Java, Indonesia in 2012. Taken with an integration time of 500ms. The specimen measures 21mm.

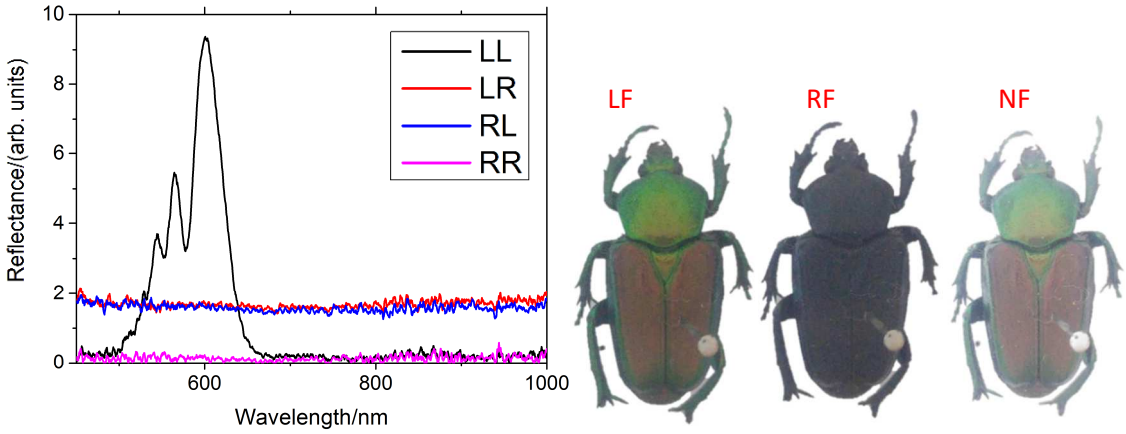


Figure A 15 – CP reflection spectra from the pronotum of a *Phaedimus howdeni* beetle. This specimen was collected from Salvador Benedicto, Philippines in 2015. The specimen measures 21mm.

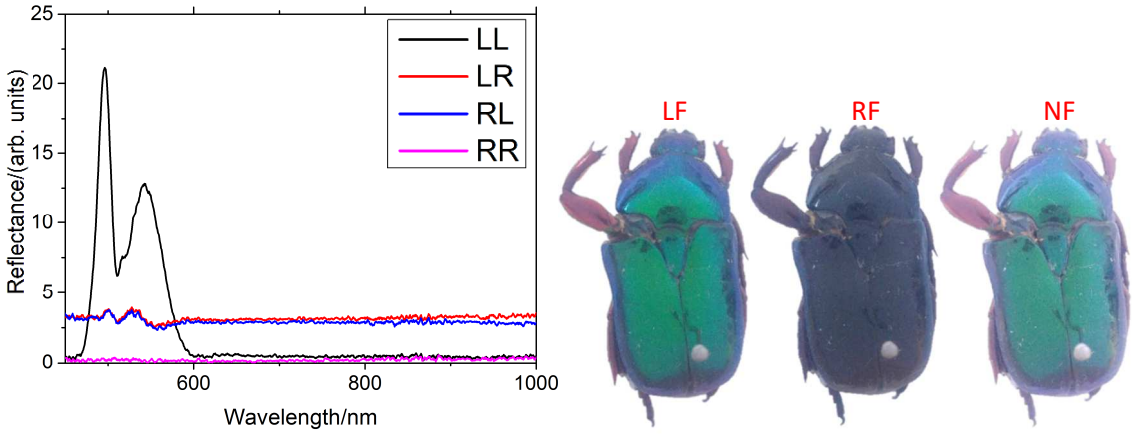


Figure A 16 – CP reflection spectra from the elytron of an *Anacampthorrhina ignipes* beetle. This beetle was collected in Indonesia in 2013. The specimen measures 22mm.

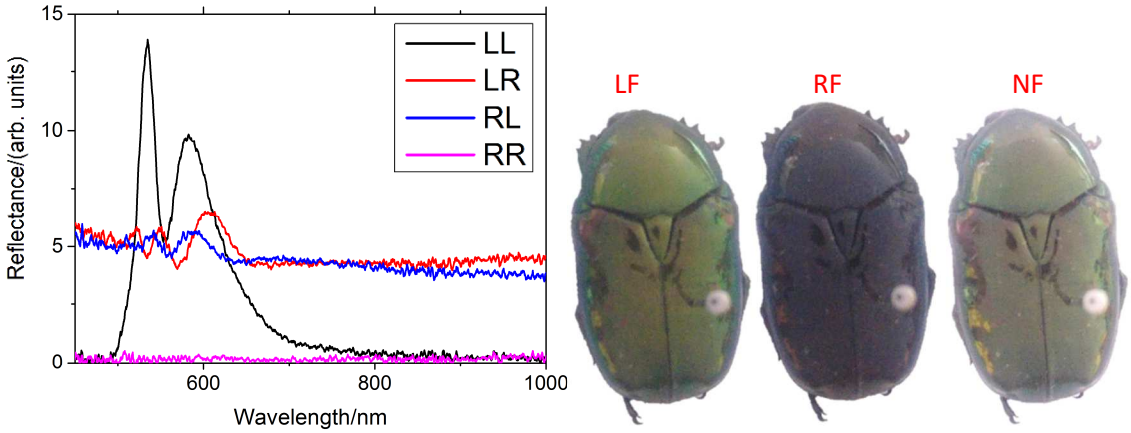


Figure A 17 – CP reflection spectra from the elytron of a *Diplognatha viridula* beetle. This specimen was collected from Morogoro, Mikumi National Park, Tanzania in 2013. The specimen measures 24mm.

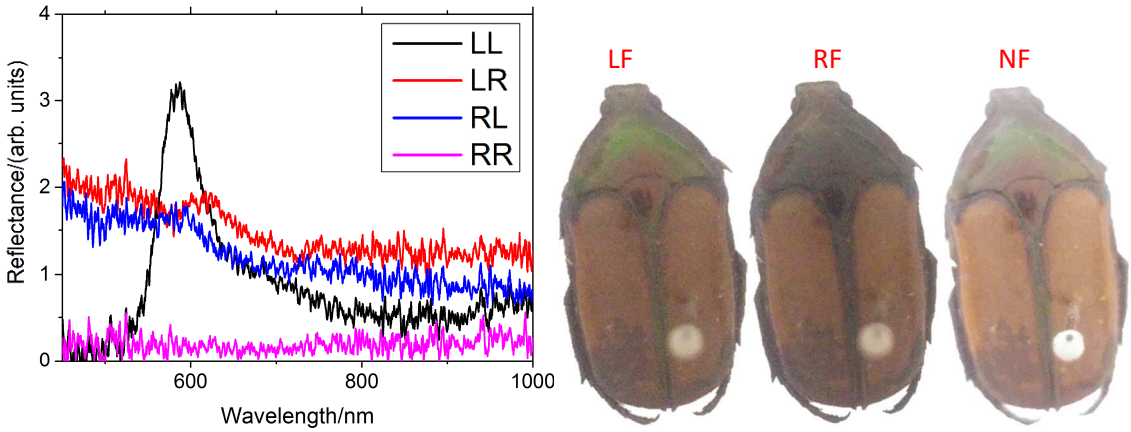


Figure A 18 – CP reflection spectra from the pronotum of a *Pedinorrhina viridicollis* beetle. This specimen was collected from Ebogo, Cameroon in 2013. The specimen measures 20mm.

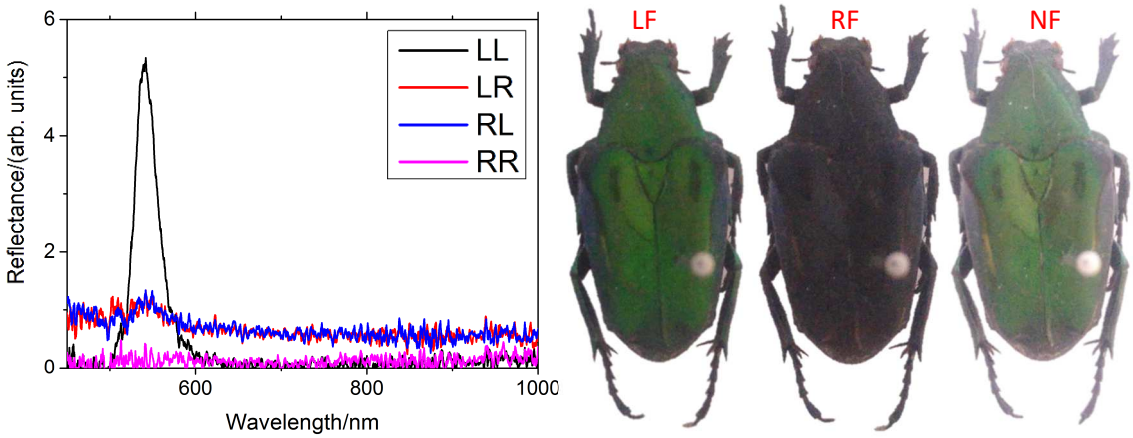


Figure A 19 – CP reflection spectra from the elytron of a *Plectrone endroedii* beetle. This specimen was collected from Surigao del Sur, Philippines in 2012. The specimen measures 27mm.

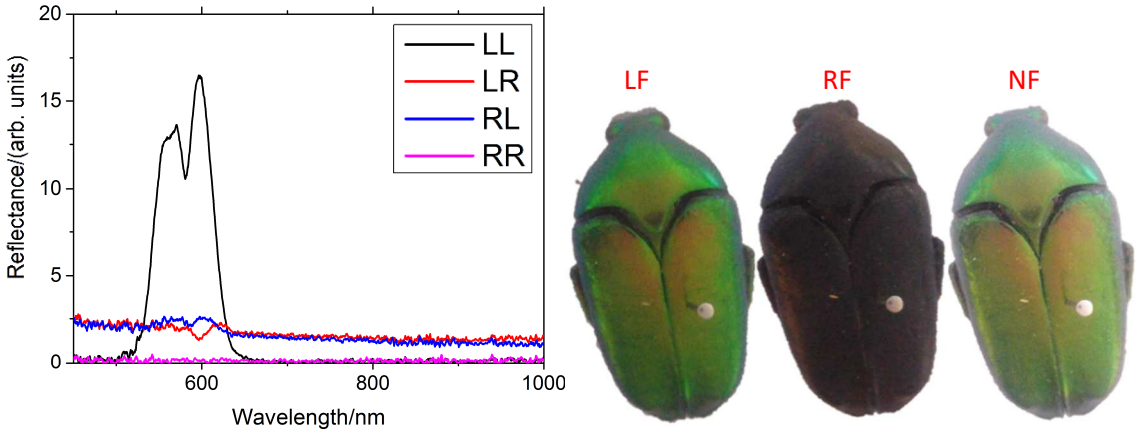


Figure A 20 – CP reflection spectra from the elytron of a *Thaumastopeus striatus* beetle. This specimen was collected from Tapah Hills, Perak, Malaysia in 2014. The specimen measures ~32mm.

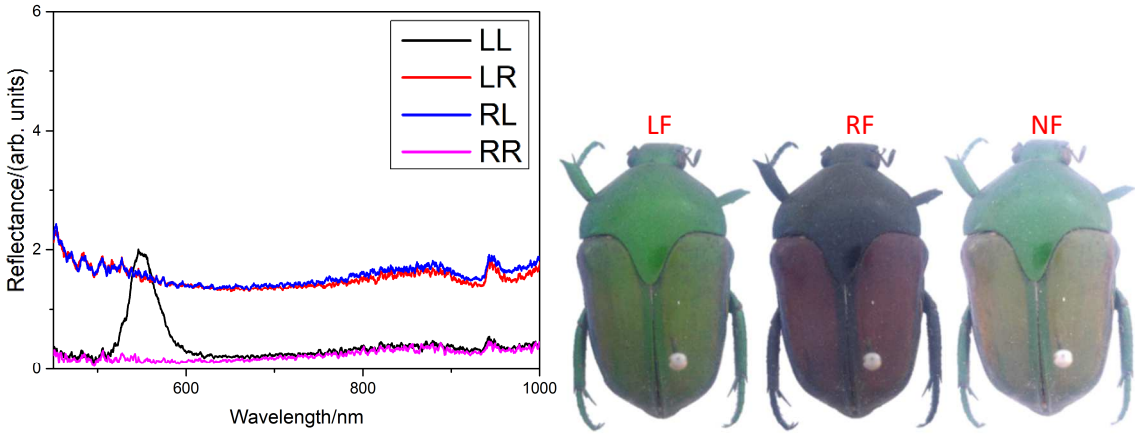


Figure A 21 – CP reflection spectra from the pronotum of a *Megaphonia adolphinae* beetle. This beetle was collected in Indonesia in 2013. Taken with an integration time of 500ms. The specimen measures 35mm.

A3.2.2 - Poecilopharis

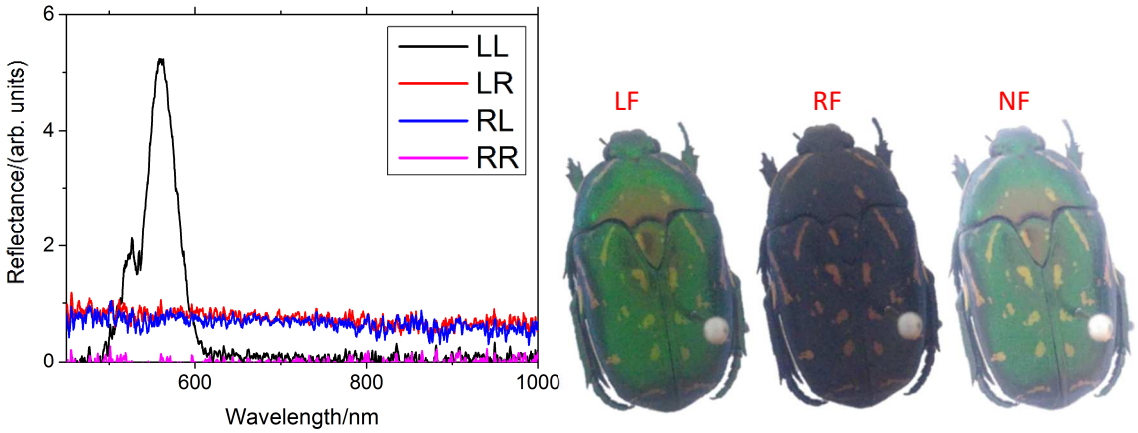


Figure A 22 – CP reflection spectra from a green part of the elytron of a *Poecilopharis truncatipennis* beetle. This beetle was collected in Elat, Kei Besar, Indonesia in 2014. The species measures ~20mm.

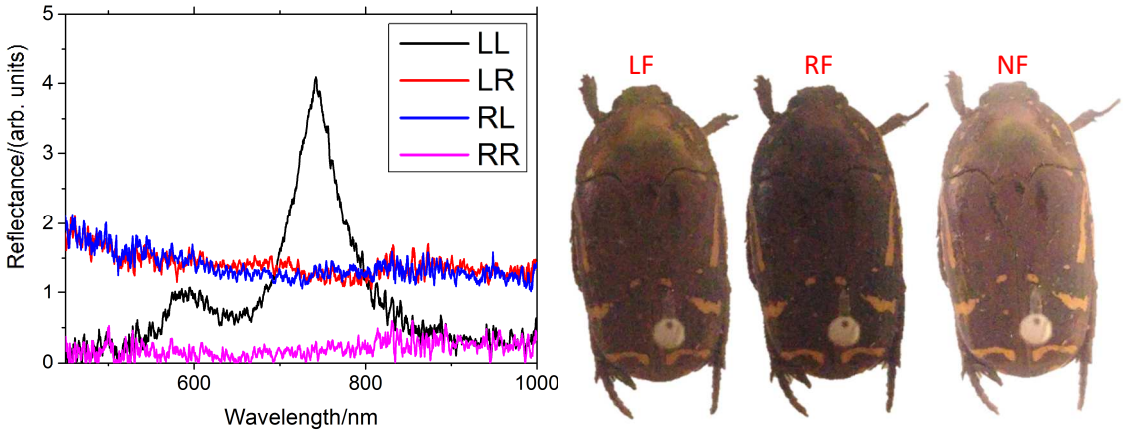


Figure A 23 – CP reflection spectra from the elytron of a *Poecilopharis schochi* beetle. This beetle was collected in Naibre, Indonesia in 2008. The specimen measures 18mm.

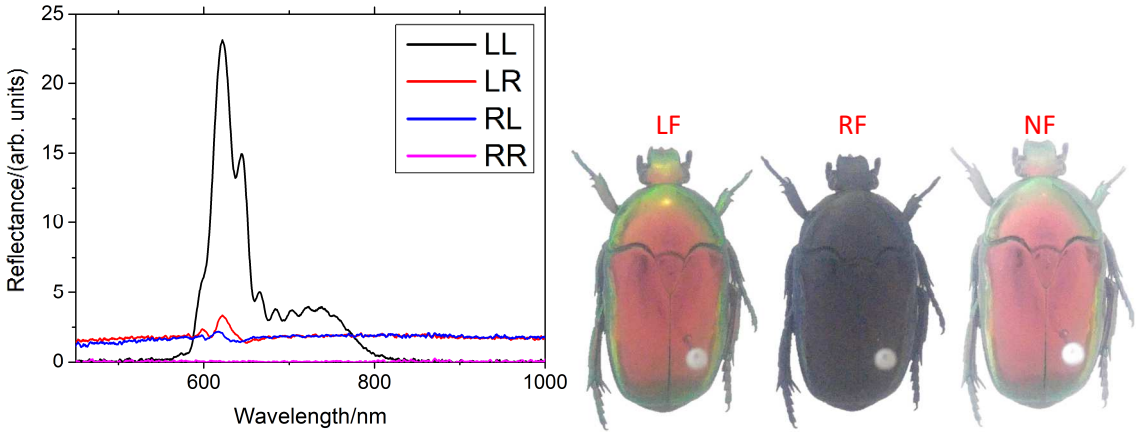


Figure A 24 – CP reflection spectra from the elytron of a *Poecilopharis curtisi* beetle. This specimen was collected from Lorulun, Yamdena, Tanimbur, Indonesia in 2007. Taken with an integration time of 200ms. The specimen measures 22mm.

A3.2.3 - Agestrata

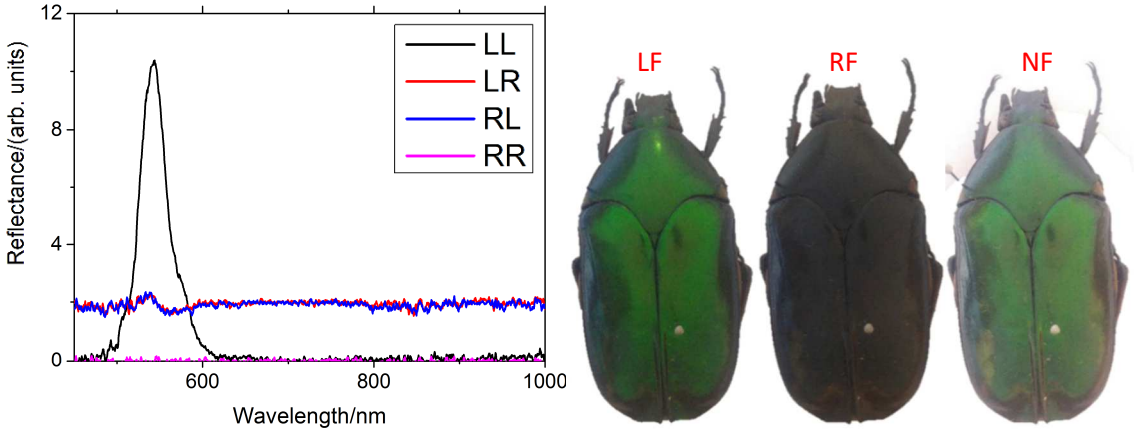


Figure A 25 – CP reflection spectra from the elytron of an *Agestrata orichalca* beetle. This specimen was collected from Chiang Mai, Thailand in 2015. The specimen measures 49mm.

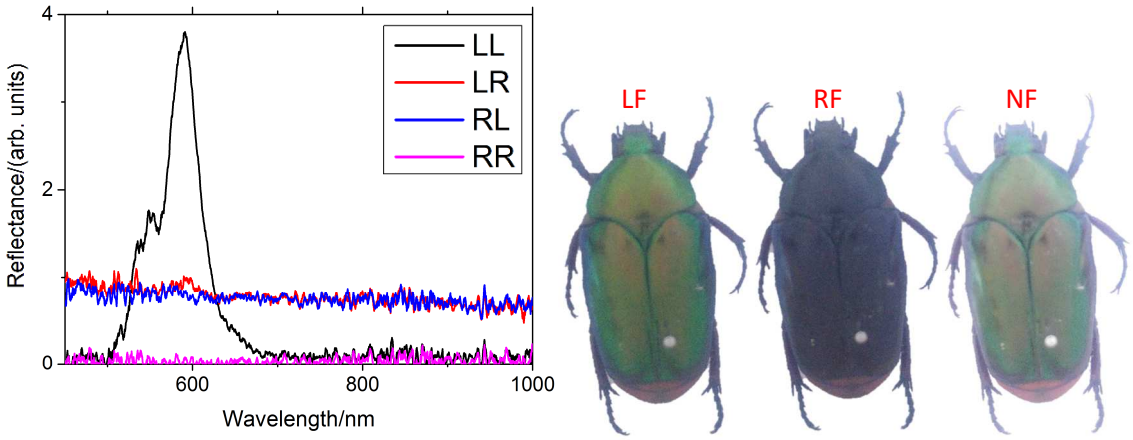


Figure A 26 – CP reflection spectra from the elytron of an *Agestrata punctatastriata* beetle. This specimen was collected from Lombok, Indonesia in 2006. Taken with an integration time of 200ms. The specimen measures 44mm.

A3.2.4 - Jumnos

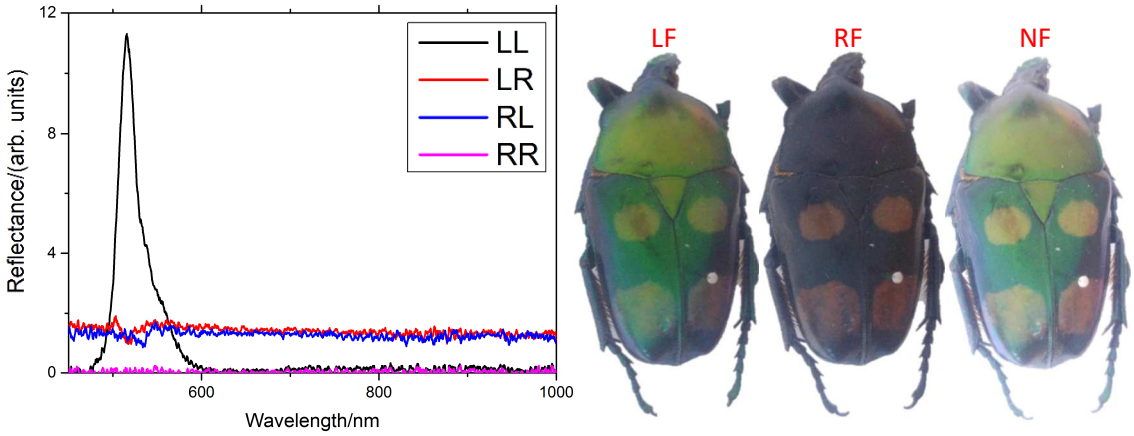


Figure A 27 – CP reflection spectra from a green part of the elytron of a *Jumnos ruckeri ruckeri* beetle. This beetle was collected in Vietnam in 2015. The specimen measures 51mm.

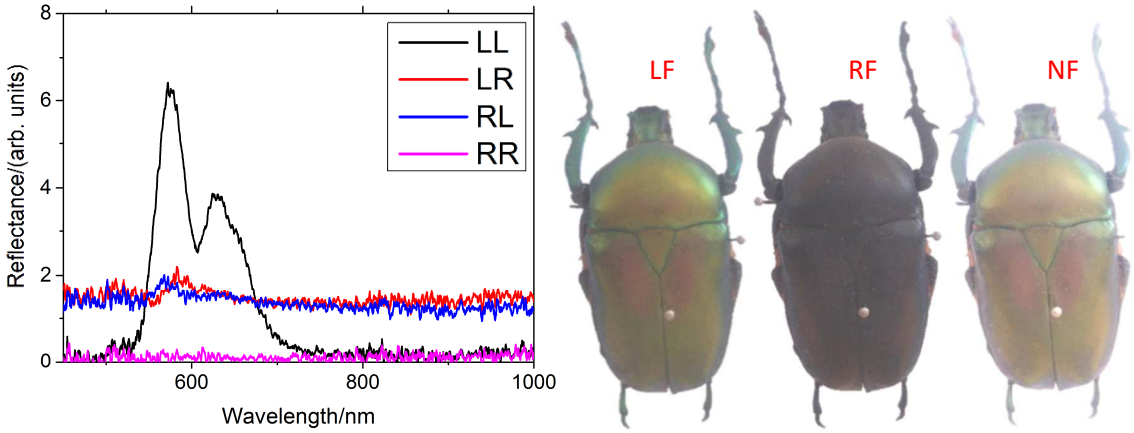


Figure A 28 – CP reflection spectra from the elytron of a *Jumnos ferroiminettiique* beetle. This specimen was collected from Fang, Thailand in 2010. The specimen measures 43mm.

A3.2.5 - Mycterophallus

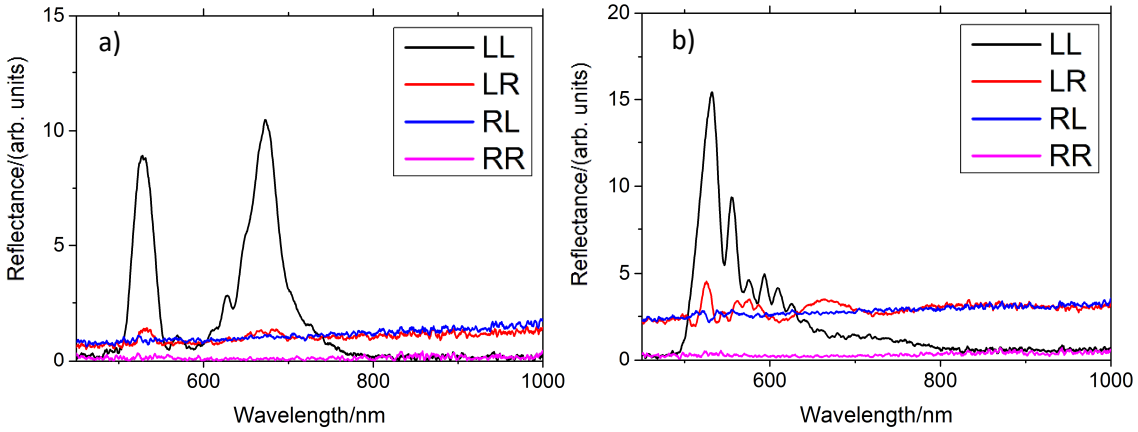


Figure A 29 – CP reflection spectra from the elytron of a *Mycterophallus validipes* beetle. This specimen was collected from Aru Island, Indonesia.

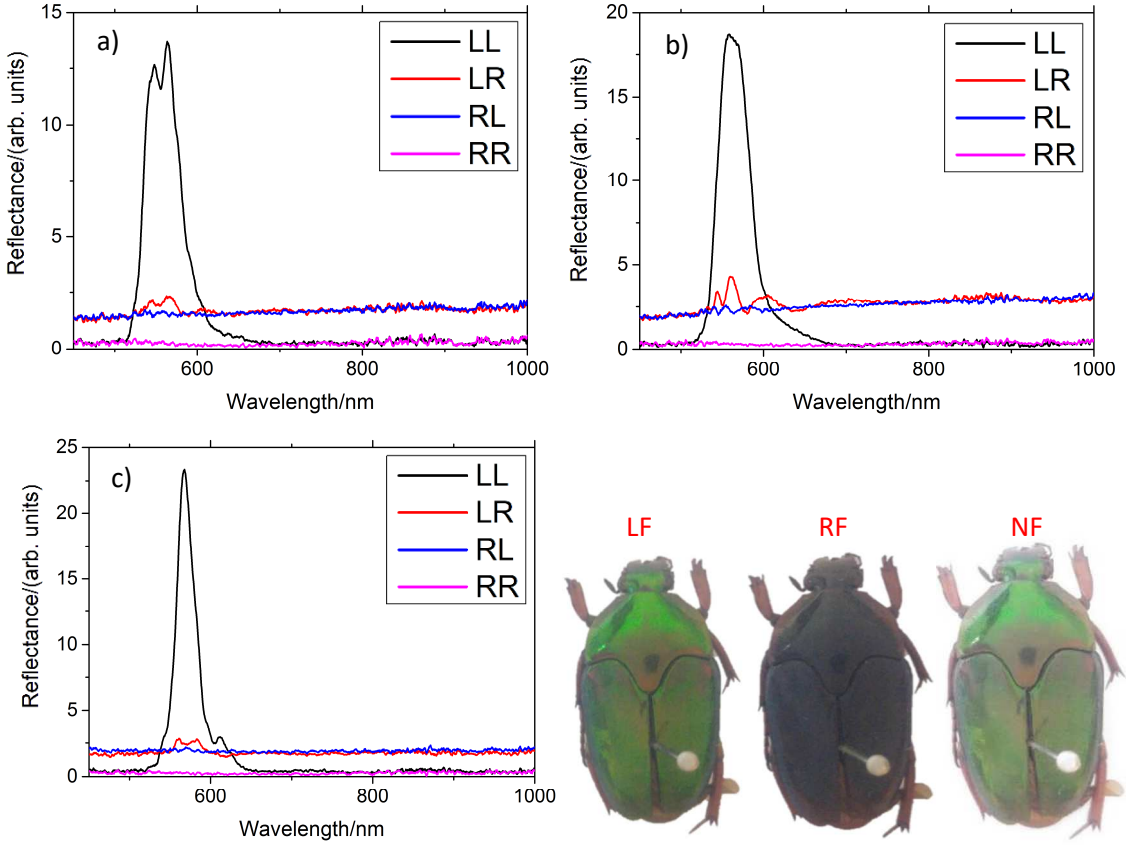


Figure A 30 – CP reflection spectra from the elytron of a *Mycterophallus xanothopus* beetle. This specimen was collected from Naibre, Indonesia.

A3.2.6 - Ischiopsopha

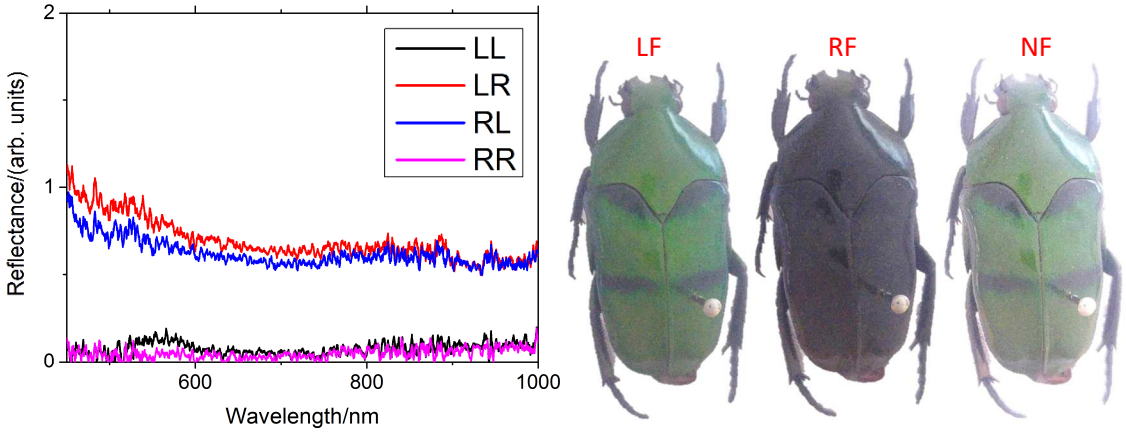


Figure A 31 – CP reflection spectra from the elytron of an *Ischiopsopha bifasciata* beetle. This beetle was collected in Indonesia in 2014. Taken with an integration time of 500ms. The specimen measures 29mm.

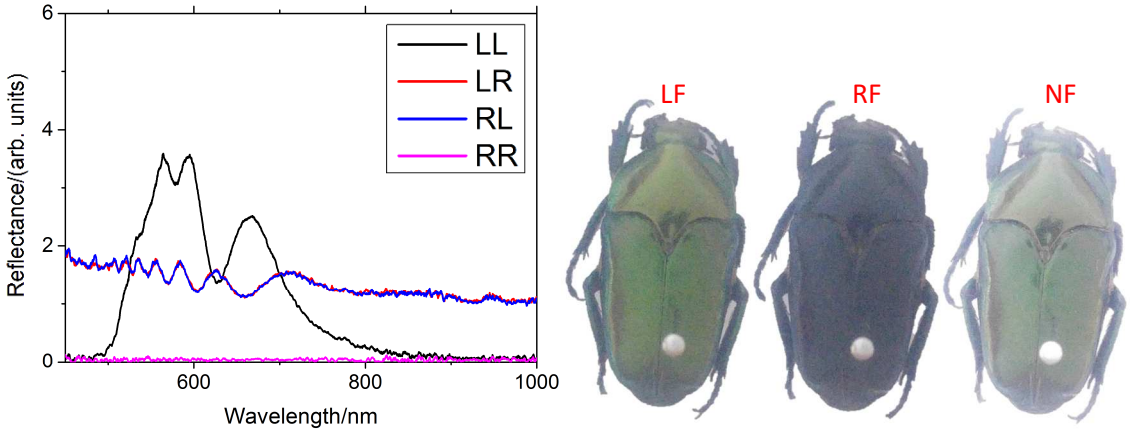


Figure A 32 – CP reflection spectra from the elytron of an *Ischiopsopha cetamensis* beetle. This specimen was collected from Seram, Indonesia in 2006. The specimen measures 23mm.

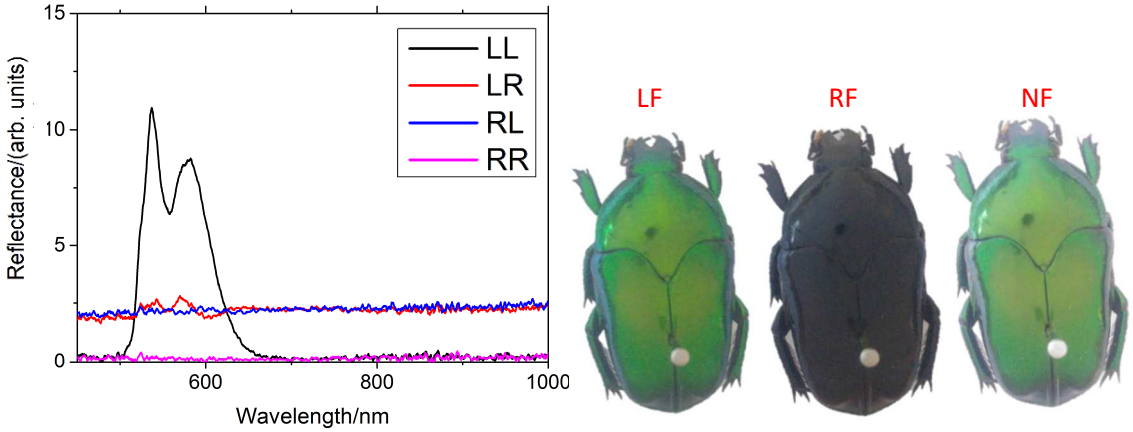


Figure A 33 – CP reflection spectra from the elytron of an *Ischiopsopha ritsmae* beetle. This specimen was collected from Sumatra, Indonesia. The specimen measures 27mm.

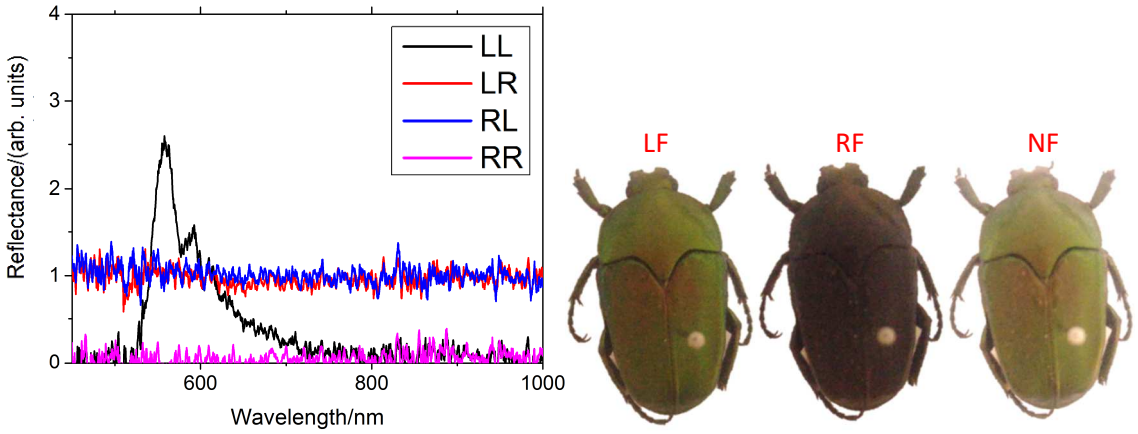


Figure A 34 – CP reflection spectra from the elytron of an *Ischiopsopha plana* beetle. This specimen was collected from Ambon, Indonesia in 2012. The specimen measures 27mm.

A3.2.7 - Plaesiorhinella

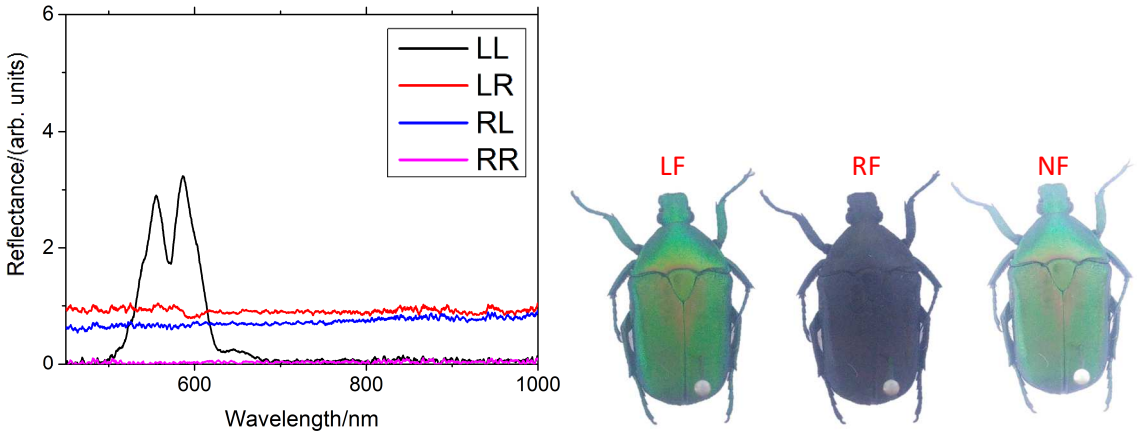


Figure A 35 – CP reflection spectra from the elytron of a *Plaesiorhinella recurve* beetle. This specimen was collected from Wome, Togo in 2016. Taken with an integration time of 500ms. The specimen measures 24mm.

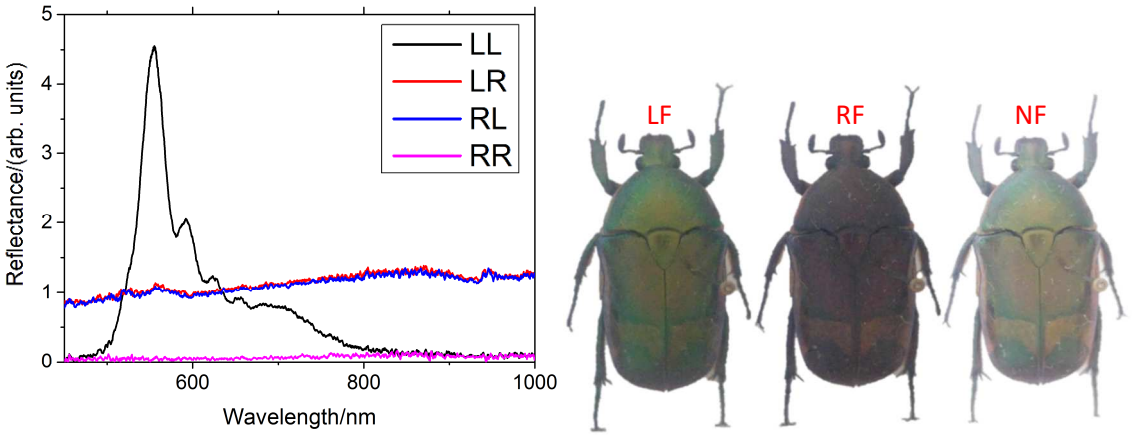


Figure A 36 – CP reflection spectra from the elytron of a *Plaesiorrhina plana cincta* beetle. This beetle was collected in Western Uganda in 2001. The specimen measures 25mm.

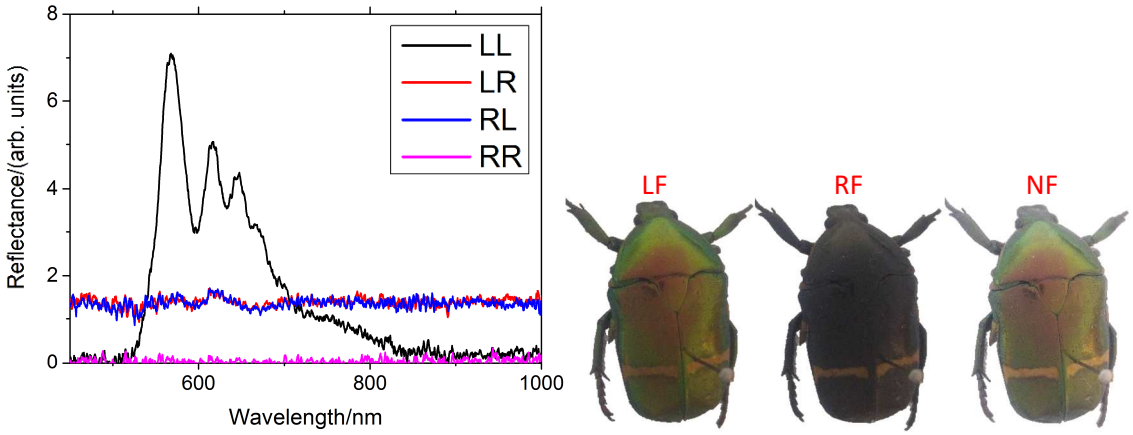


Figure A 37 – CP reflection spectra from the elytron of a *Plaesiorrhina plana* beetle. This beetle was collected in Cameroon in 2014. The specimen measures 23mm.

A3.2.8 – Protaetia

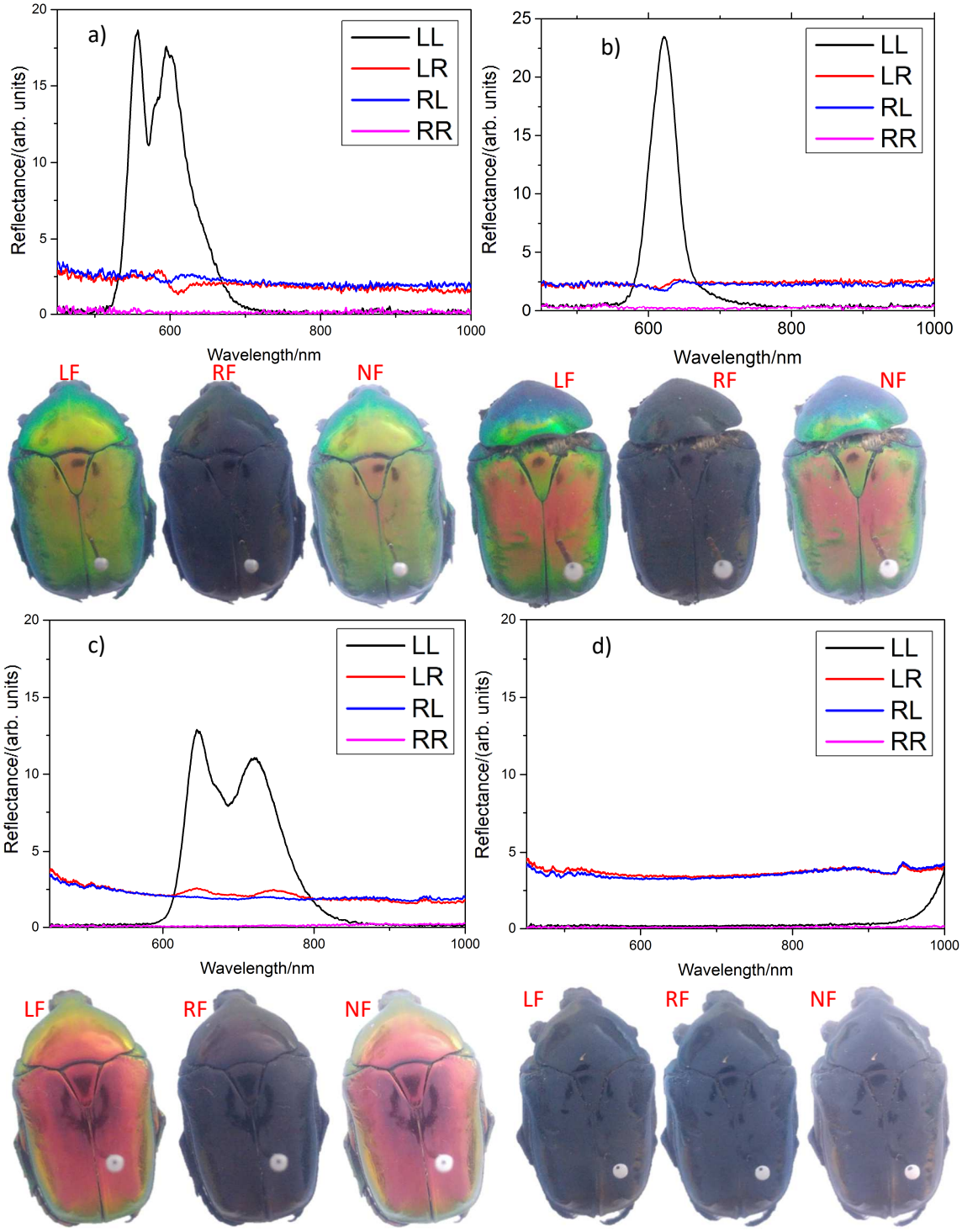


Figure A 38 – CP reflection spectra from the elytron a) of green-yellow, b) green-orange, c) red and black *Protaetia aerguinosa* beetles. These specimens were from captive bred beetles originally descended from specimens collected in a) Czech Republic, b) France, c) and d) from Croatia in 2015. a) and b) were taken with an integration time of 100ms and c) and d) with an integration time of 500ms. The specimens measured a) 24mm, b) 23mm , c) 25mm, d) 27mm.

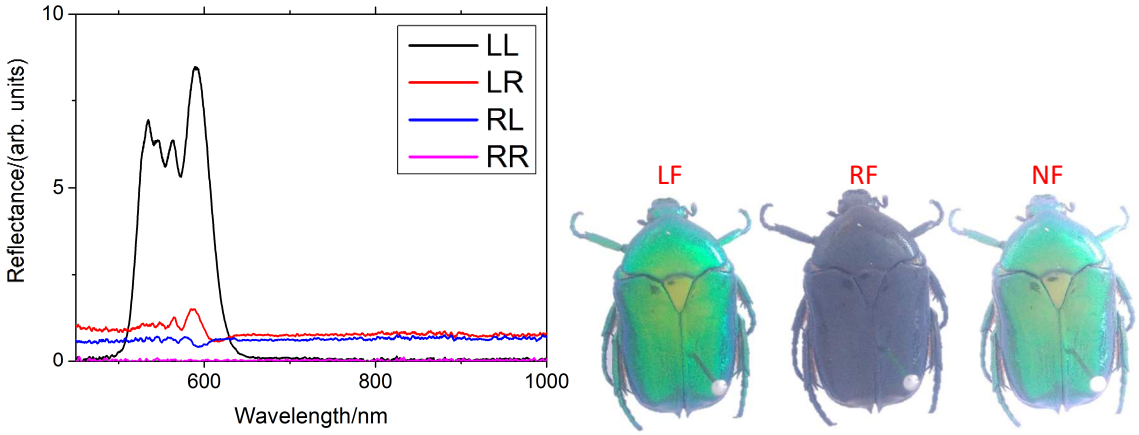


Figure A 39 – CP reflection spectra from the elytron of a *Protaetia timorensis* beetle. This specimen was collected from Oemelu, Timor, Indonesia in 2009. Taken with an integration time of 500ms. The specimen measured 24mm.

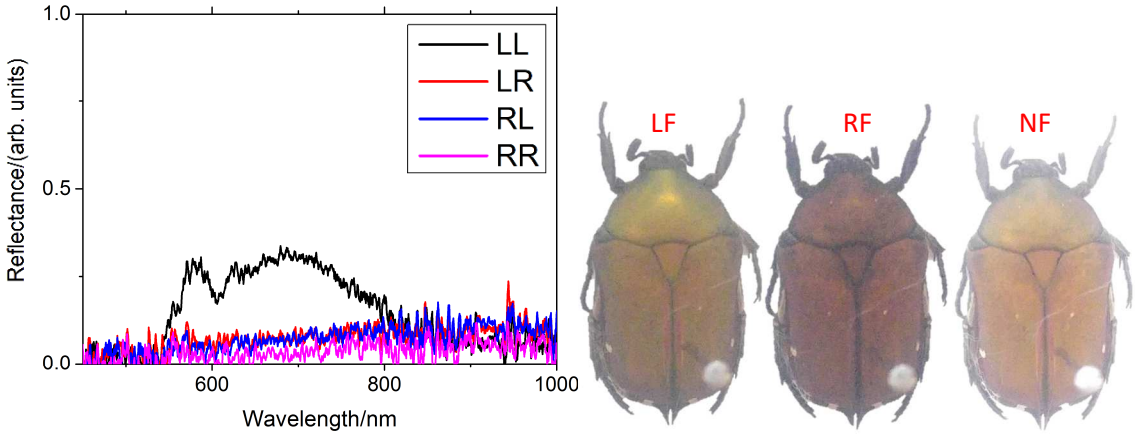


Figure A 40 – CP reflection spectra from the elytron of a *Protaetia bipunctata* beetle. This specimen was collected from Puncak Palopo, South Sulawesi, Indonesia in 2012. Taken with an integration time of 500ms. The specimen measured 17mm.

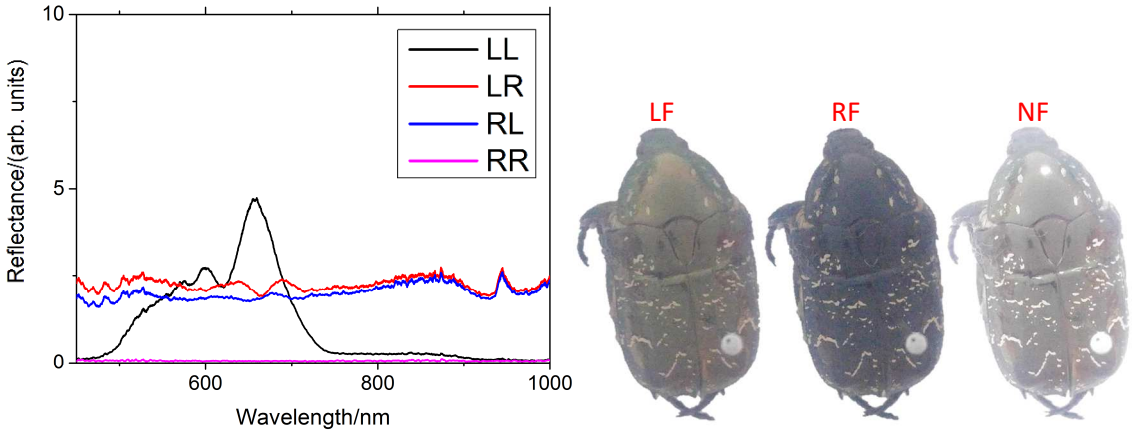


Figure A 41 – CP reflection spectra from the elytron of a *Protaetia lugbris* beetle. This specimen was collected from Orneta, Poland in 2016. The specimen measured 22mm.

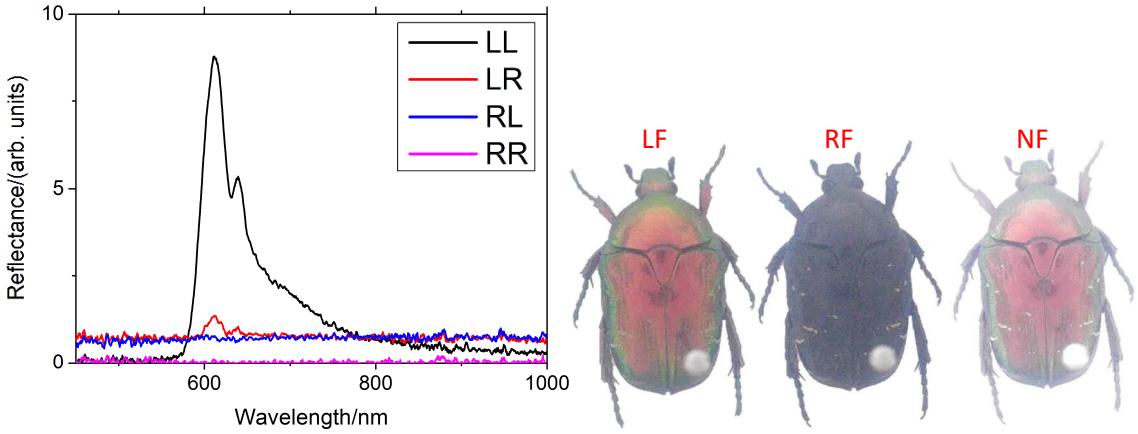


Figure A 42 – CP reflection spectra from the elytron of a *Protaetia multifoveolata* beetle. This specimen was collected from Siping, Sichuan, China in 2005. Taken with an integration time of 200ms. The specimen measured 16mm.

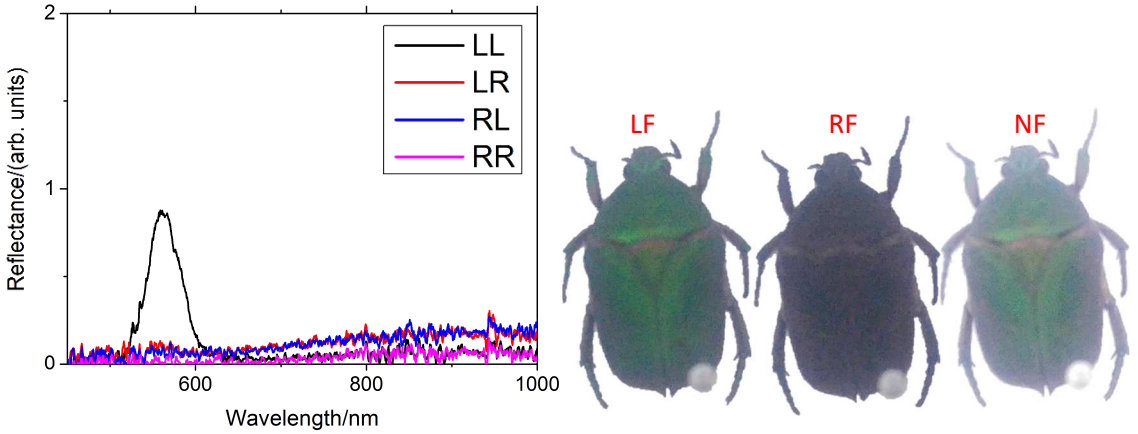


Figure A 43 – CP reflection spectra from the elytron of a *Protaetia salomoensis* beetle. This specimen was collected from Barana, Guadalcanal, Solomon Islands in 2013. Taken with an integration time of 500ms. The specimen measured 21mm.

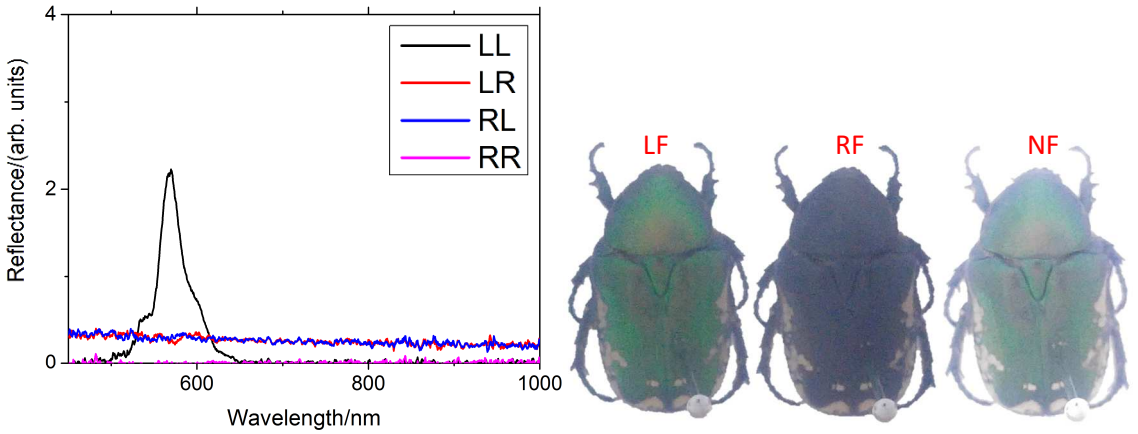


Figure A 44 – CP reflection spectra from the elytron of a *Protaetia trojana godeti* beetle. This specimen was collected from Aragatsotn, Arailer Mountain, Amenia in 2007. Taken with an integration time of 500ms. The specimen measured 17mm.

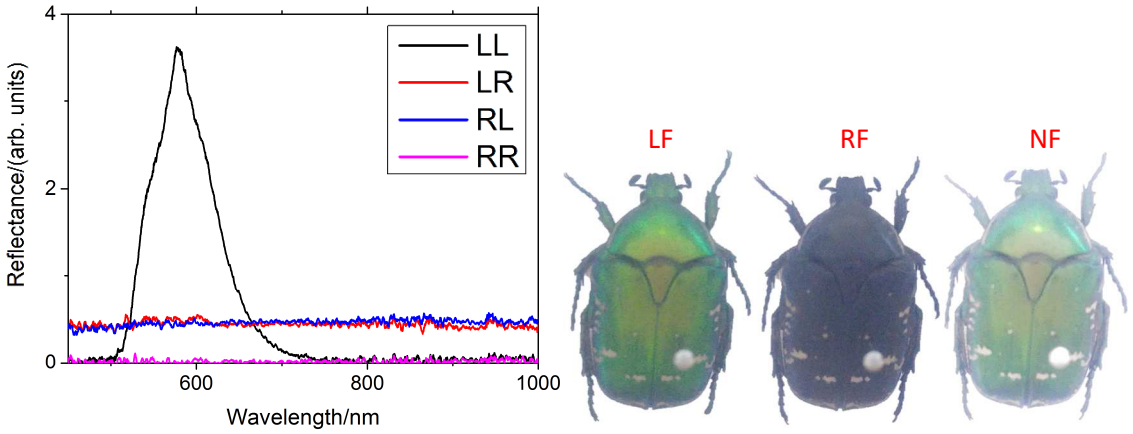


Figure A 45 – CP reflection spectra from the elytron of a *Protaetia marginicollis* beetle. This specimen was collected from Budula, Kazakhstan in 2013. Taken with an integration time of 500ms. The specimen measured 22mm.

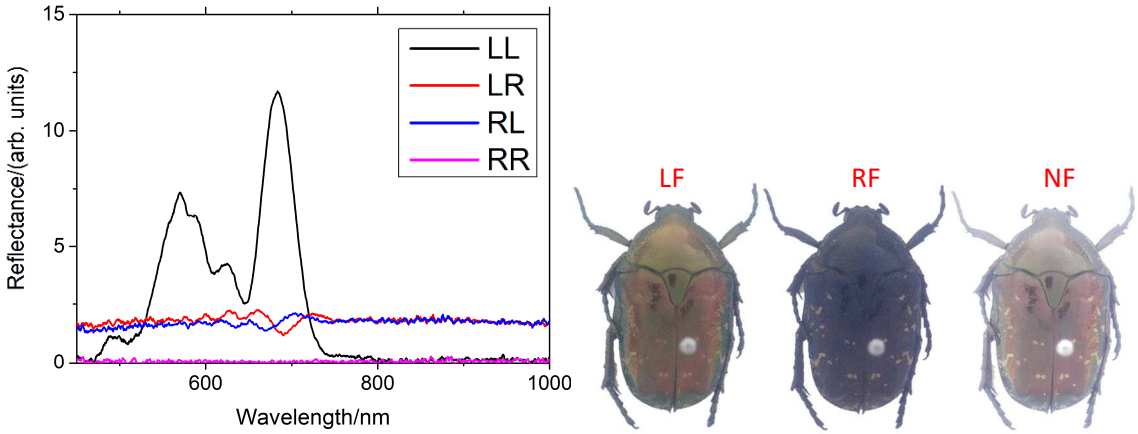


Figure A 46 – CP reflection spectra from the elytron of a *Protaetia orientalis* beetle. This specimen was collected from Wuxi, Jiangsu, China in 2006. Taken with an integration time of 200ms. The specimen measured 23mm.

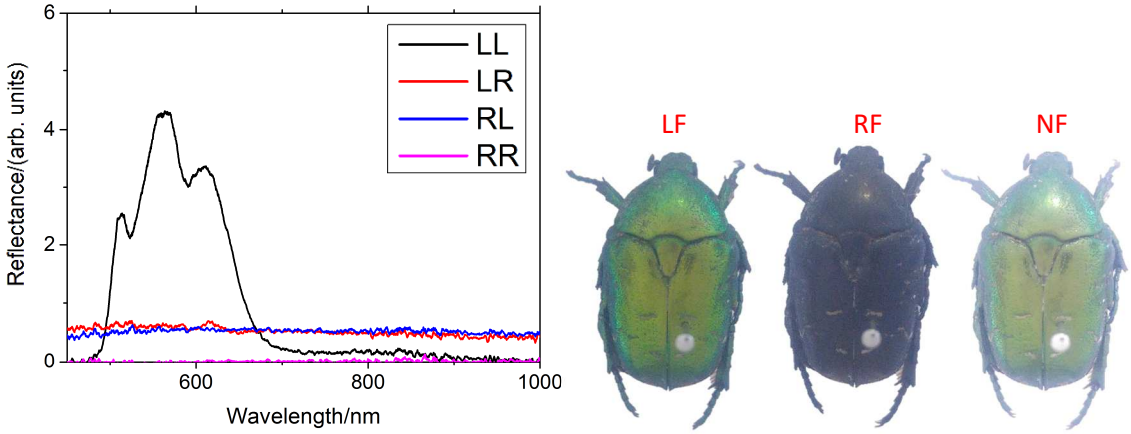


Figure A 47 – CP reflection spectra from the elytron of a *Protaetia mandshuriensis dumonti* beetle. This specimen was collected from Shang Guan, Liupan Mountains, Gansu, China in 2011. Taken with an integration time of 500ms. The specimen measured 23mm.

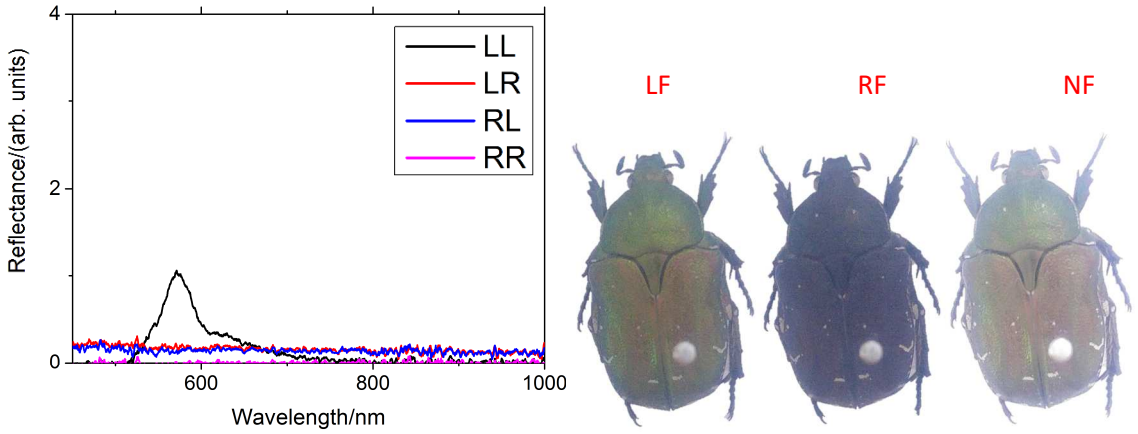


Figure A 48 – CP reflection spectra from the elytron of a *Protaetia expansia expansia* beetle. This specimen was collected from Naze-Paikum, Amami city, Amami city, Kagoshima, Japan in 2011. Taken with an integration time of 500ms. The specimen measured 22mm. There was also a duller less intensely reflecting specimen (Figure A 49).

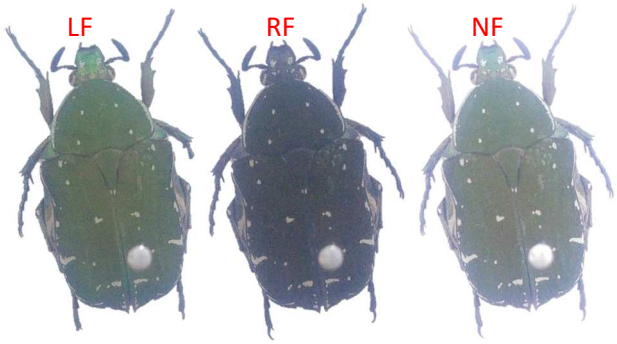


Figure A 49 – Photographs of a dull *Protaetia expansia expansia* specimen taken through a LCP (left), RCP (centre) and no filter (right). This specimen was collected from Naze-Paikum, Amami city, Amami city, Kagoshima, Japan in 2011. The specimen measured 20mm. This specimen had reflection intensity which was so low that its CP spectra could not be measured with the experimental setup. The difference between the two variants of the specimen can be seen best in natural daylight as in Figure A 50.



Figure A 50 – Photographs of a metallic and dull *Protaetia expansia expansia* through no filter in natural daylight.

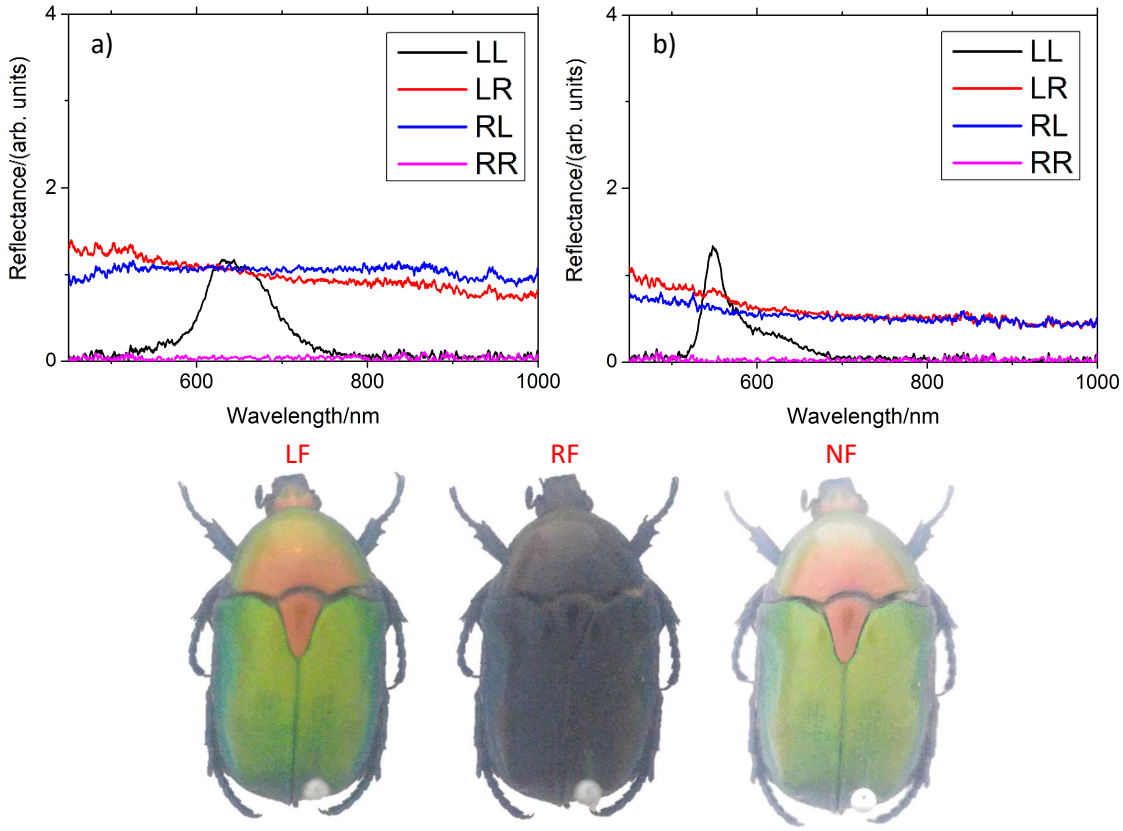


Figure A 51 – CP reflection spectra from a) the red part and b) the green part of the elytron of a *Protaetia cuprea ignicollis* beetle. This specimen was collected from Israel in 2014. Taken with an integration time of 500ms. The specimen measured 23mm.

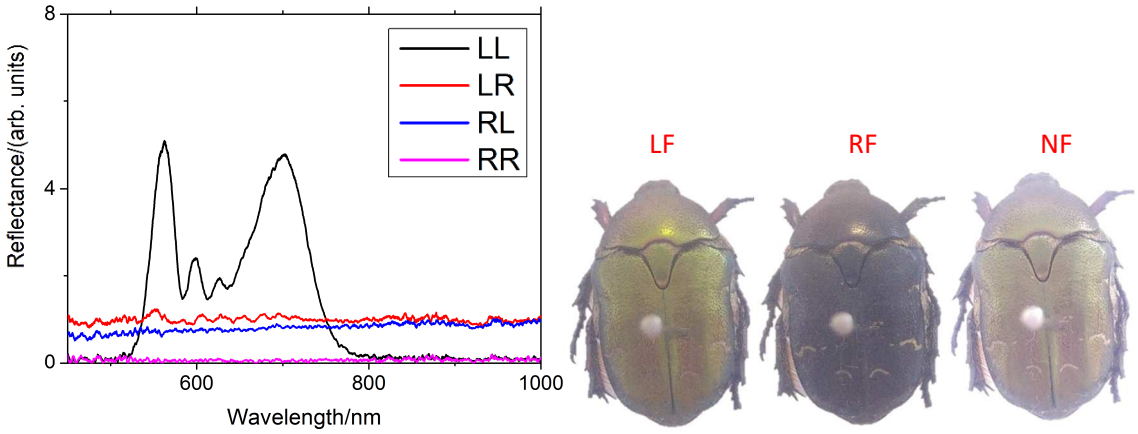


Figure A 52 – CP reflection spectra from the elytron of a *Protaetia cuprea metallica* beetle. This beetles was originally collected in Koljala, Saaremaa, Estonia in 2014. Taken with an integration time of 500ms. The specimen measured 22mm.

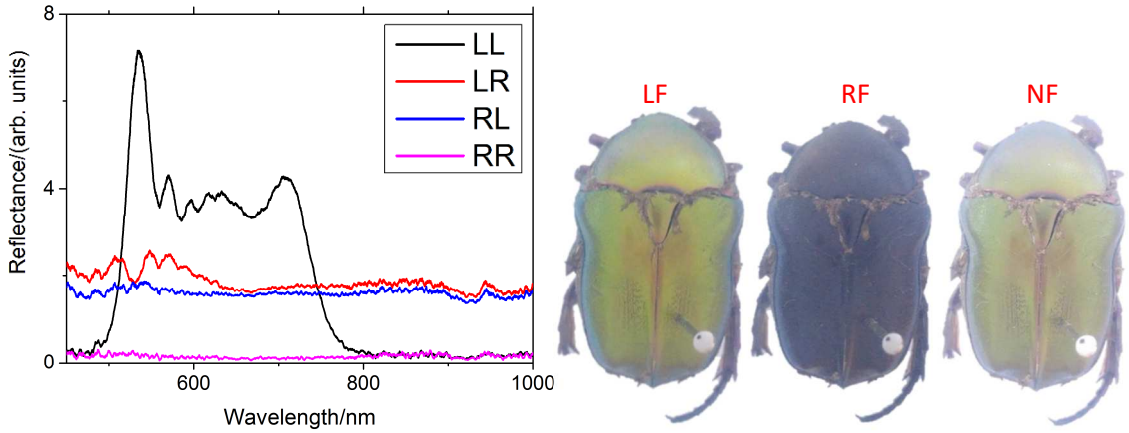


Figure A 53 – CP reflection spectra from the elytron of a *Protaetia cuprea cuprea* beetle. This beetle was captive bred, from beetles originally from France. Taken with an integration time of 500ms. The specimen measured 22mm.

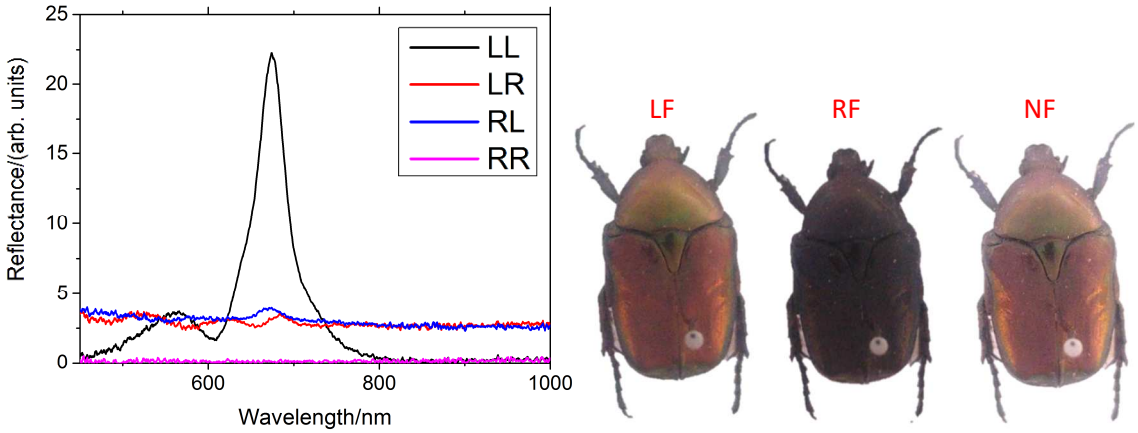


Figure A 54 – CP reflection spectra from the elytron of a *Protaetia (Potosia) besucheti* beetle. This beetle was collected in Fithiye, Turkey in 2012. The specimen measured 23mm.

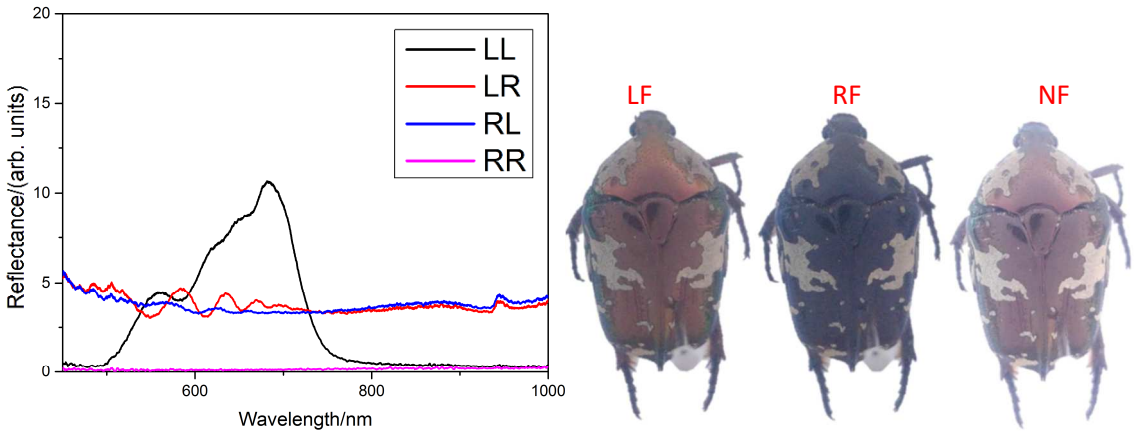


Figure A 55 – CP reflection spectra from the elytron of a *Protaetia aurichalcea* beetle. This beetle was collected in Reunion Island in 2014. Taken with an integration time of 500ms. The specimen measured 17mm.

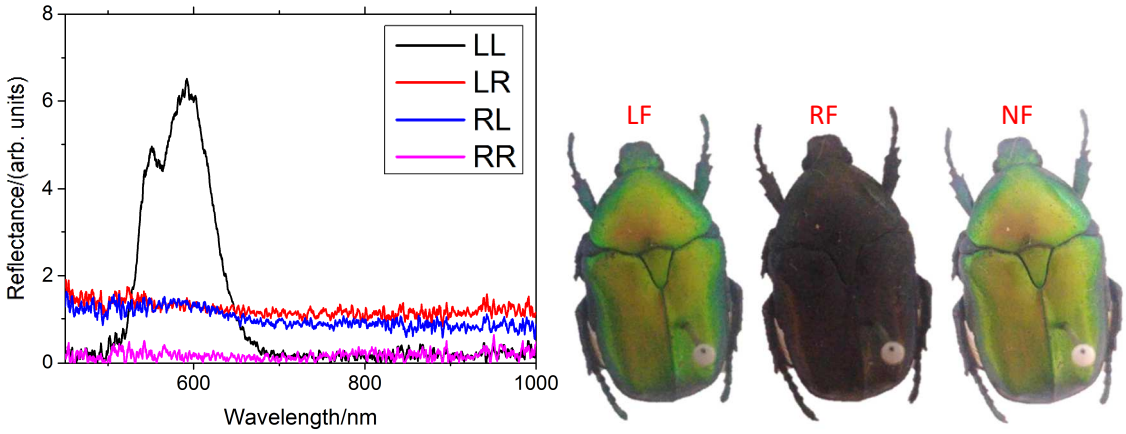


Figure A 56 – CP reflection spectra from the elytron of *Protaetia (eupotosia) affinis* beetle. This specimen was collected from Anege, France in 2008. The specimen measured 22mm.

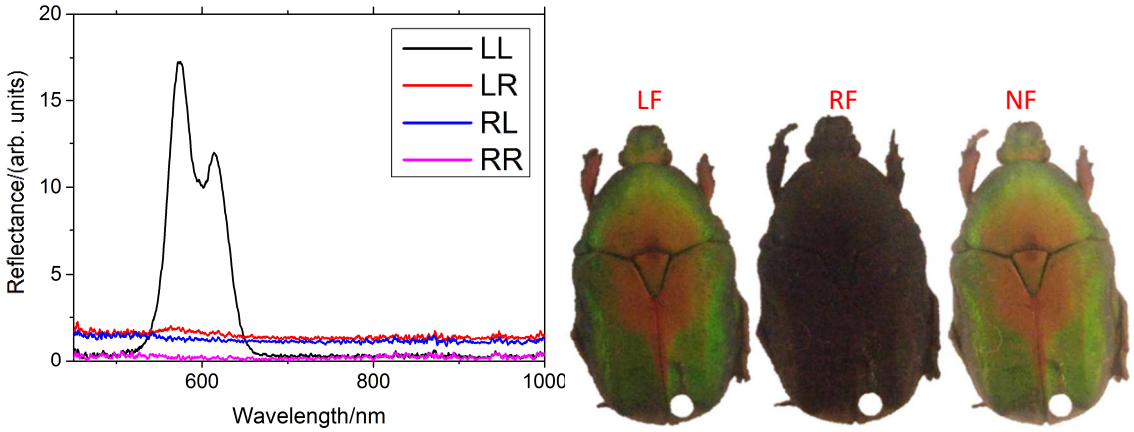
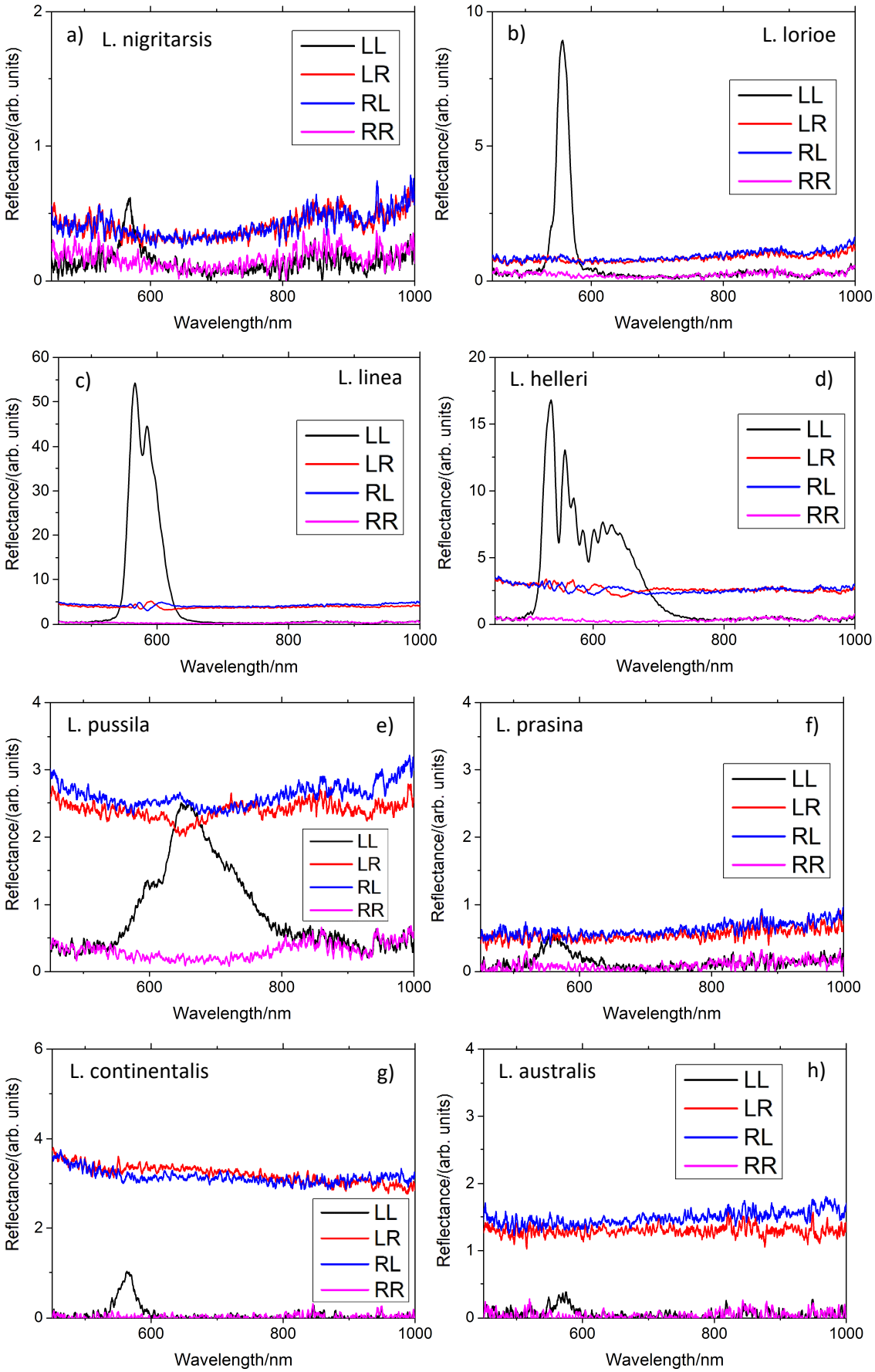
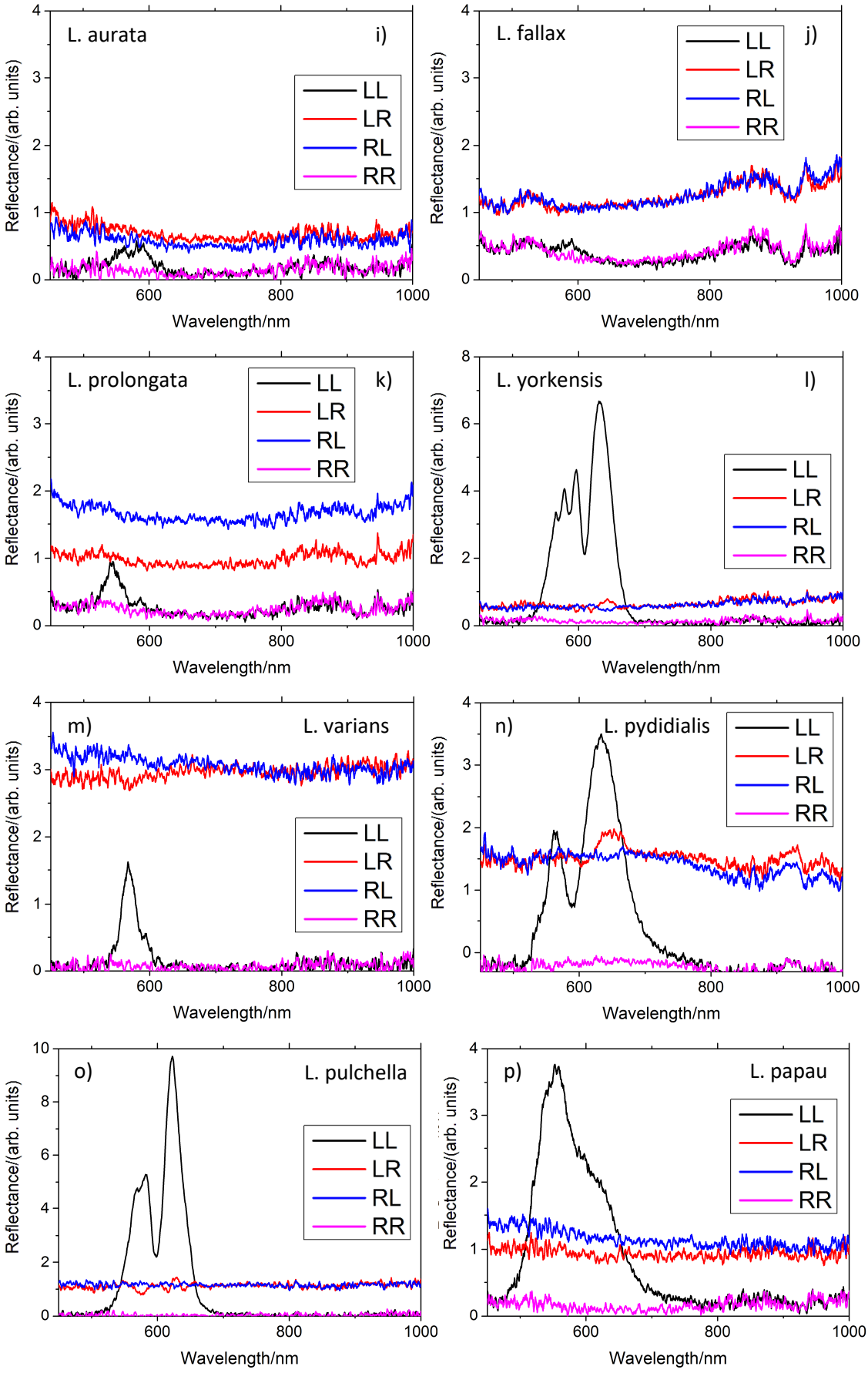
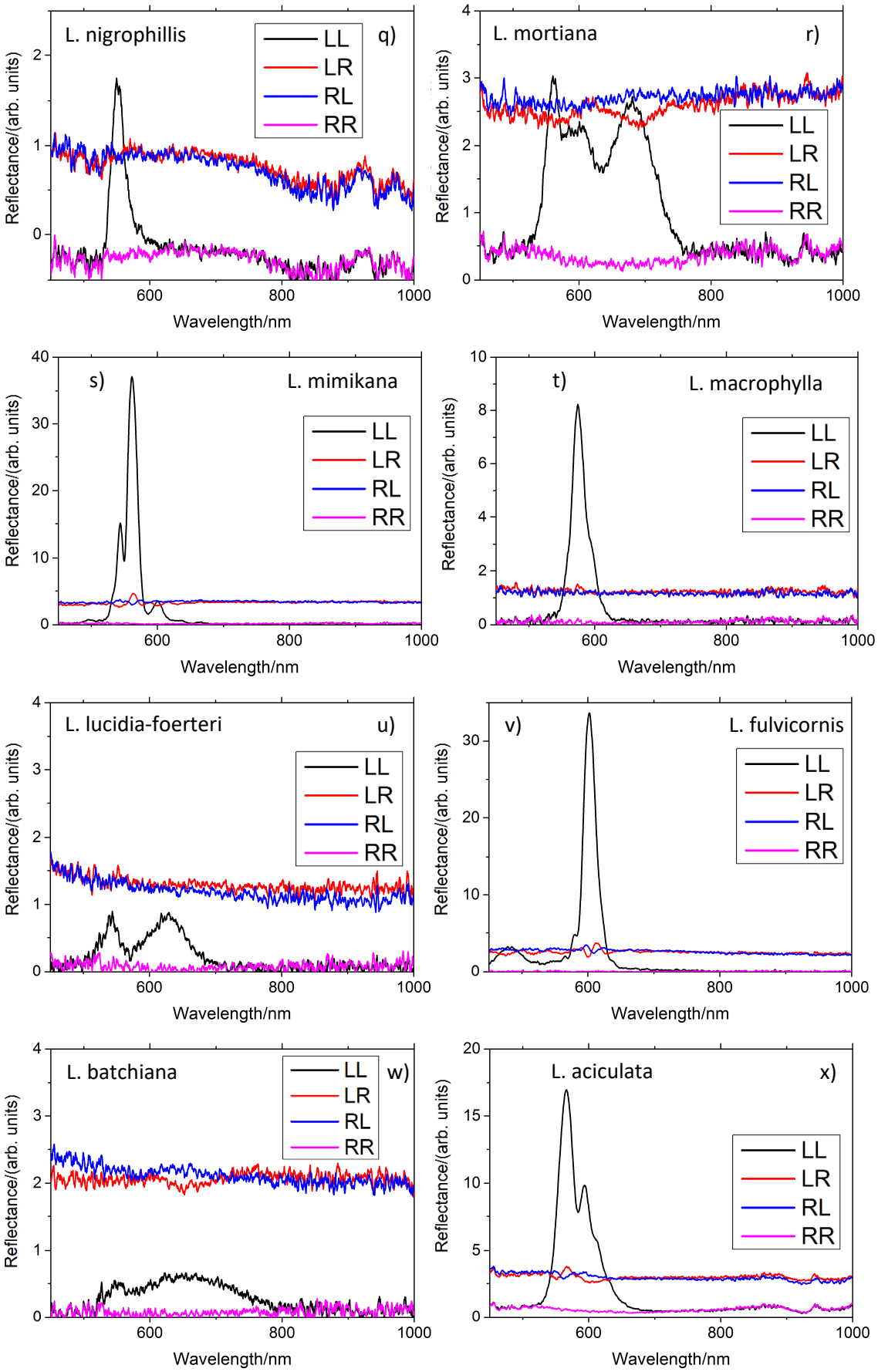


Figure A 57 – CP reflection spectra from the elytron of *Protaetia pryeri pryeri* beetle. This specimen was collected from Zamami, Okinawa, Japan in 1997. The specimen measured 26mm.

A3.2.9 – Lomaptera




i)
L. aurata
j)
L. fallax
k)
L. prolongata
l)
L. yorkensis
m)
L. varians
n)
L. pydidialis
o)
L. pulchella
p)
L. papau
LL
LR
RL
RR
Reflectance/(arb. units)
Wavelength/nm


L. nigrophillis
q)
LL
LR
RL
RR
Reflectance/(arb. units)
Wavelength/nm
L. mortiana
r)
s)
L. mimikana
t)
L. macrophylla
L. lucidia-foerteri
u)
v)
L. fulvicornis
L. batchiana
w)
L. aciculata
x)

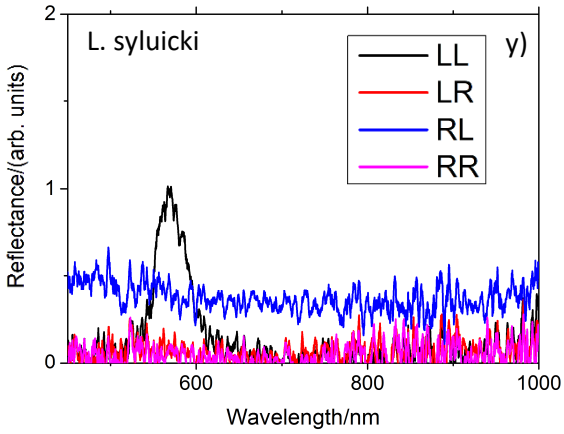


Figure A 58 – CP reflection spectra from the various species of the *Lomaptera* genus.

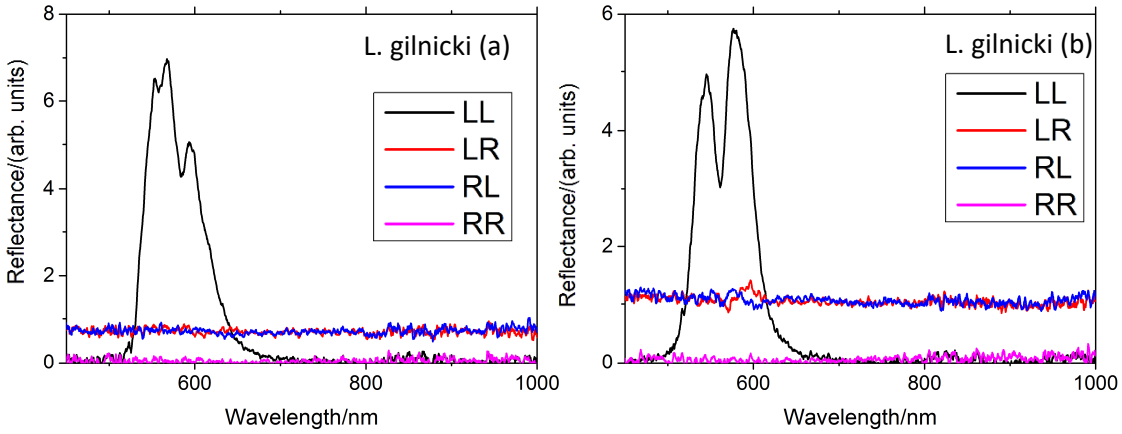


Figure A 59 – CP spectra variation in the *Lomaptera gilnicki*.

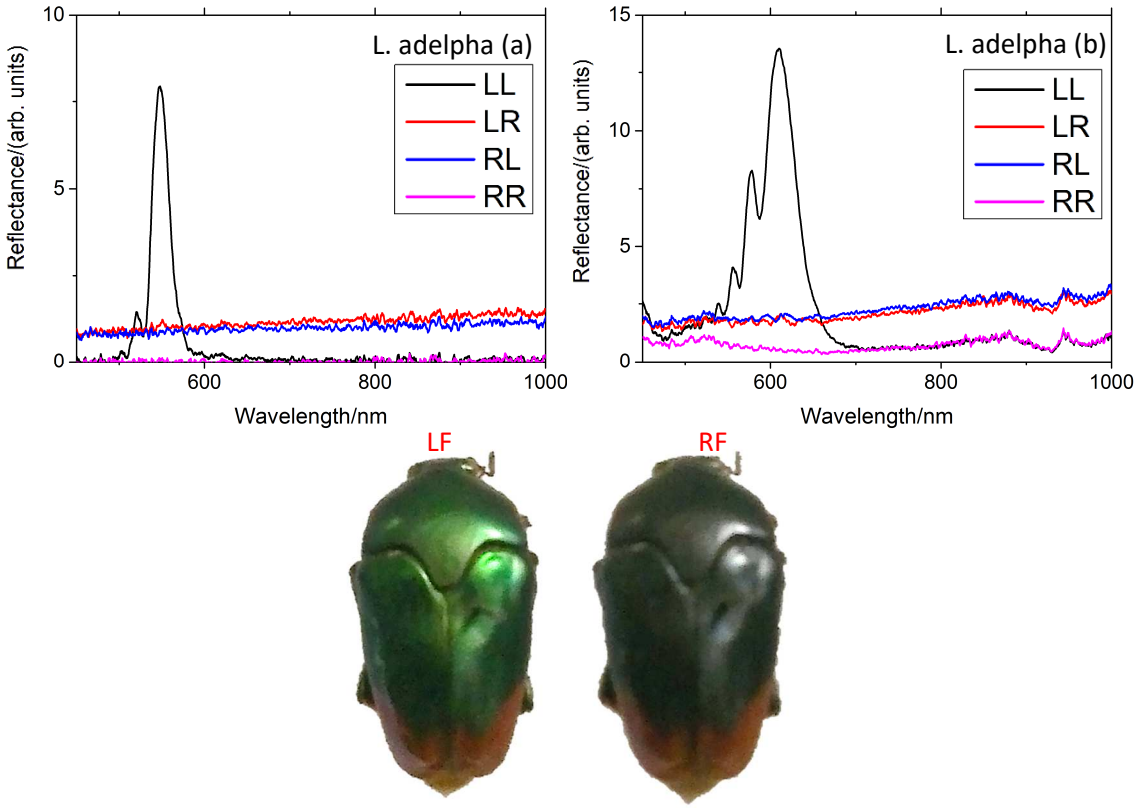


Figure A 60 – CP spectra variation in the *Lomaptera adelpha* beetle. The photographs of a typical specimens were taken through CP filters.

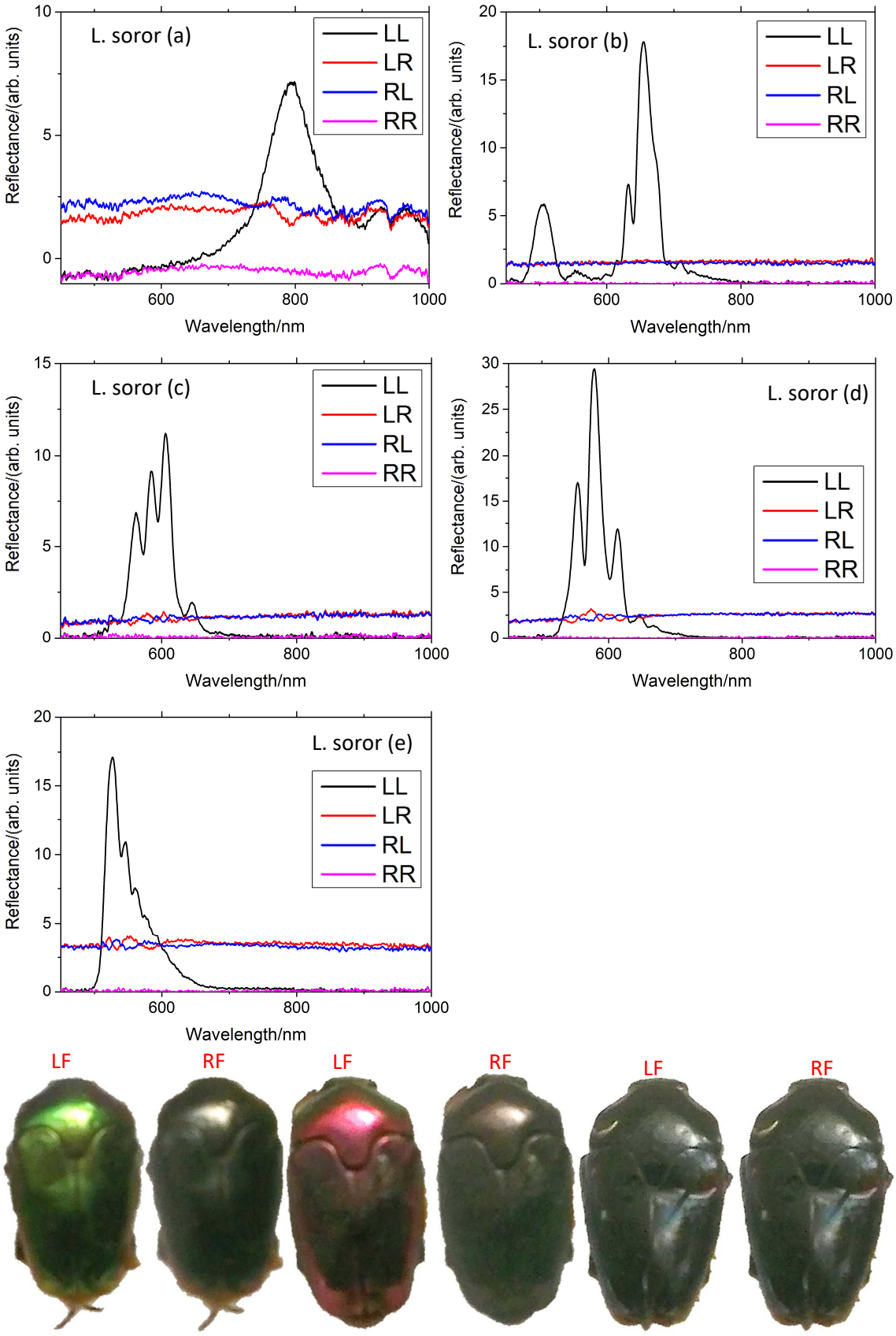


Figure A 61 – CP spectra variation in the *Lomaptera soror* beetle. There are photographs of three typical colour variations in the species through CP filters (which do not correspond directly to the spectra presented)

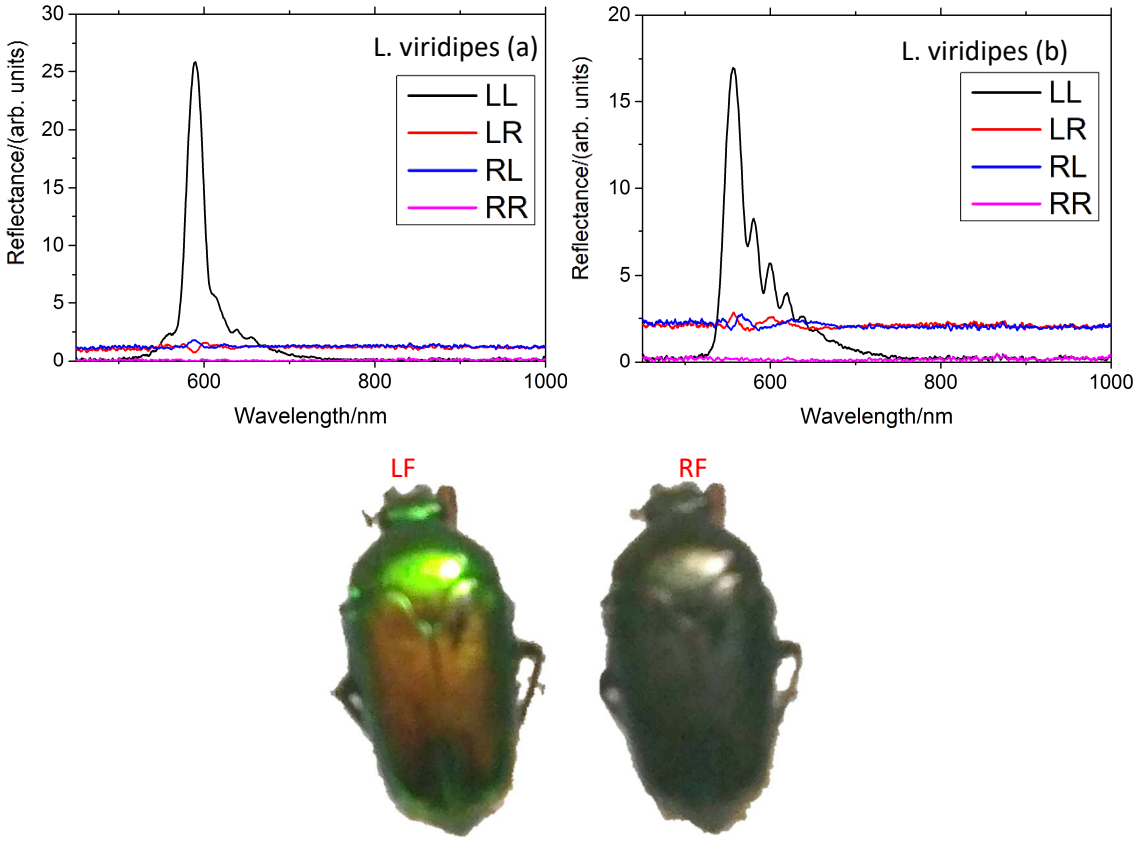


Figure A 62 – CP spectra variation in the *Lomaptera viridipes* beetle. There are examples typical of the family photographed through CP filters.

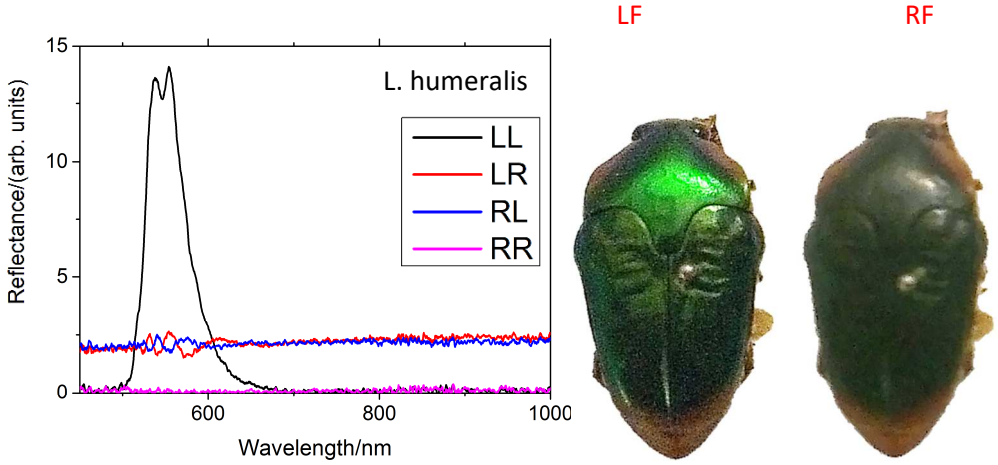


Figure A 63 – CP spectra variation in the *Lomaptera humeralis* beetle.

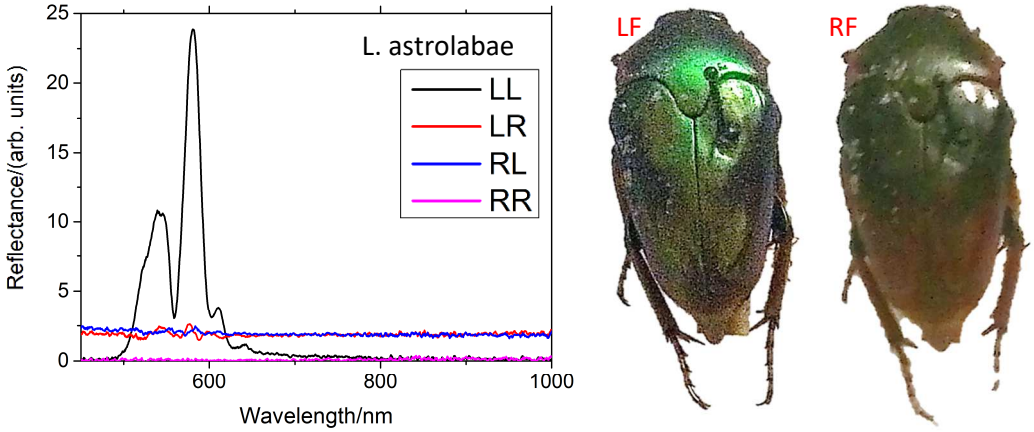


Figure A 64 – CP spectra of the *Lomaptera astrolabae* beetle.

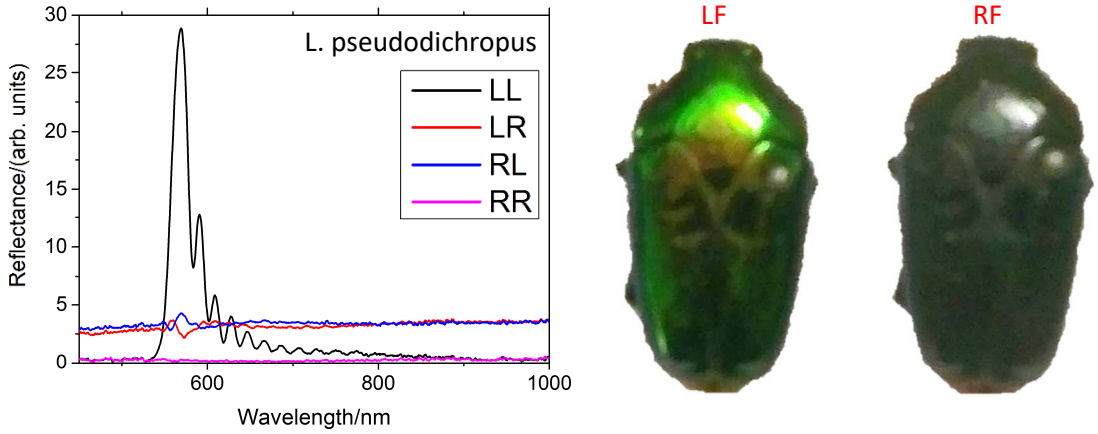


Figure A 65 – CP spectra of the *Lomaptera pseudodichropus* beetle.

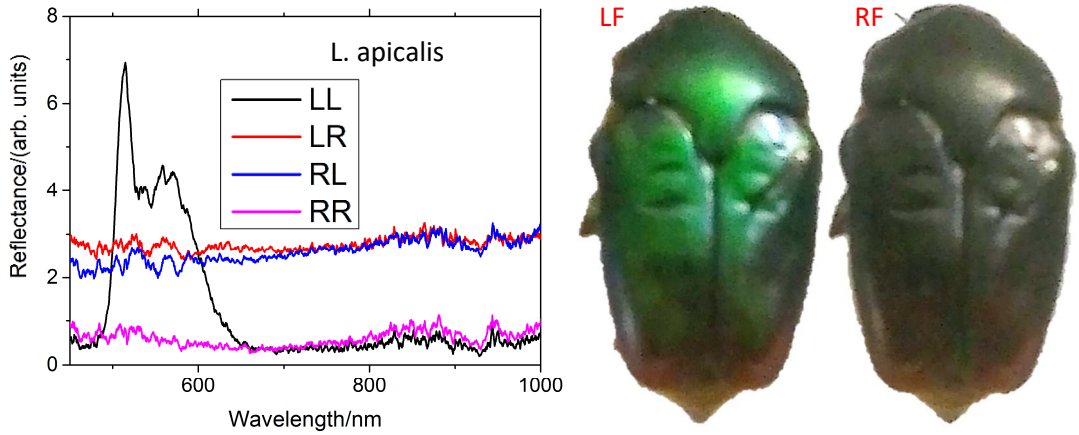


Figure A 66 – CP spectra of the *Lomaptera apicalis* beetle.

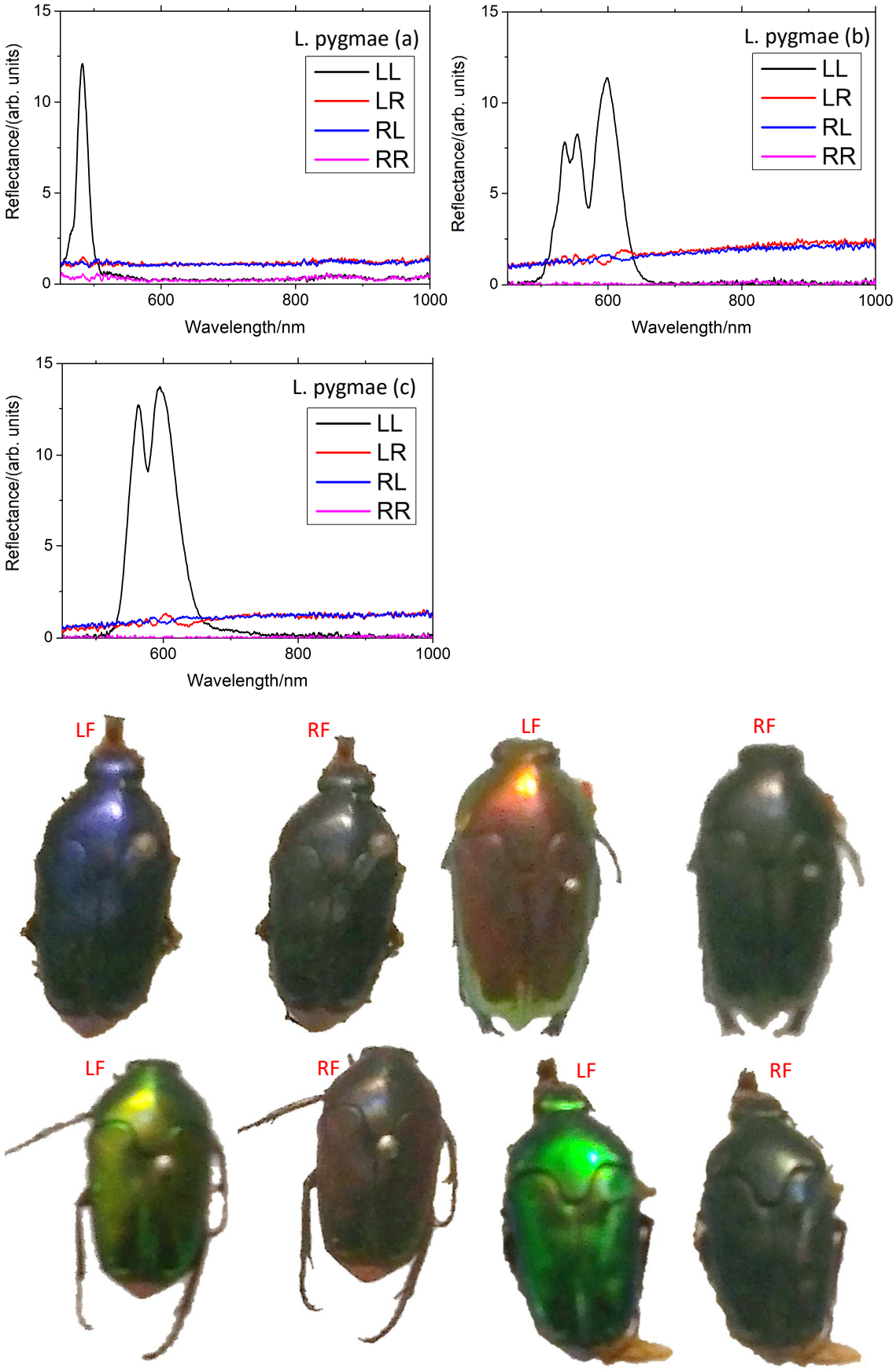


Figure A 67 – CP spectra of the *Lomaptera pygmae* beetle. The photographs were taken of four colour variations (blue, red, yellow and green) through CP filters (note these photos of beetles do not directly relate to the spectra, except the blue one which relates to spectra a).

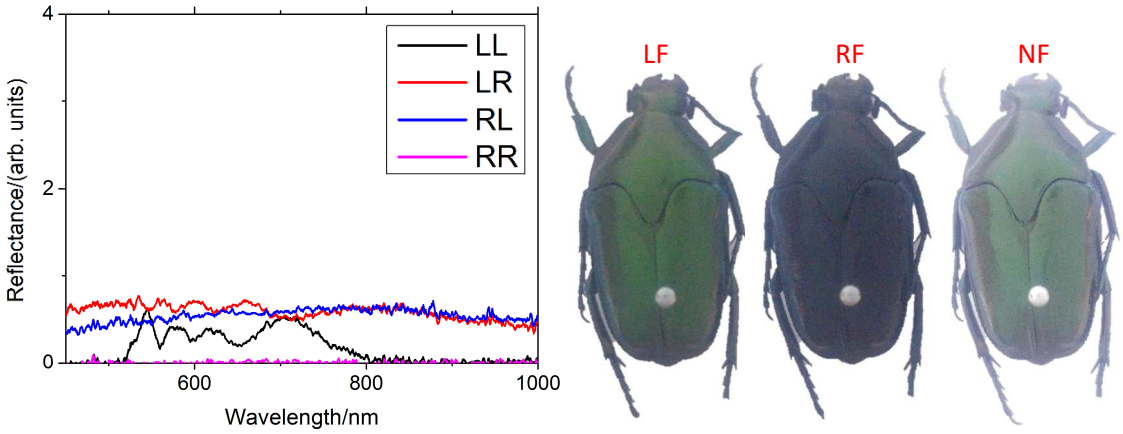


Figure A 68 – CP spectra from a *Lomaptera kaestneri* beetle. This specimen was collected from Tapaya, Obi Island, Moluccas, Indonesia in 2009. The specimen measures 24mm.

A3.3 - Rutelinae

A3.3.1 - Chrysina

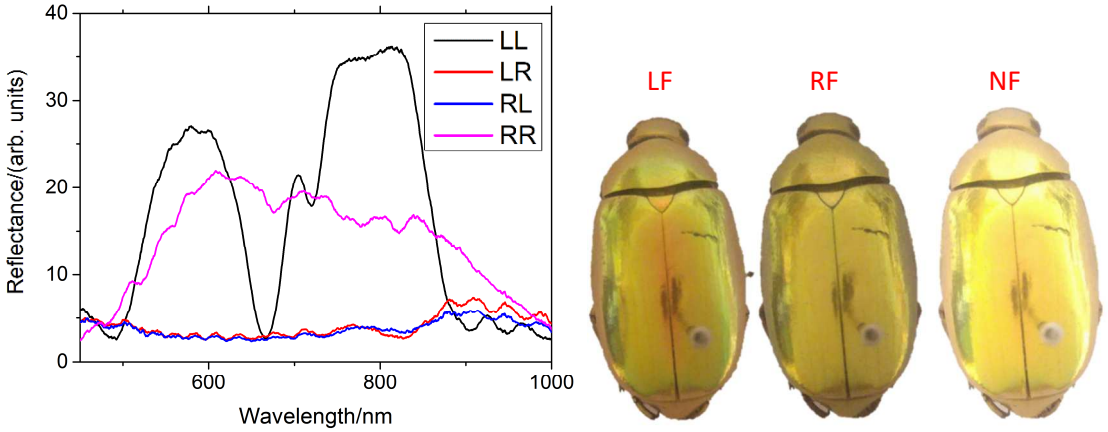


Figure A 69 – CP reflection spectra from the elytron of a gold *Chrysina resplendens* beetle. This specimen was collected from Cerro Bellavista, Rio Guacimo, Costa Rica in 2015. The species measures ~23mm.

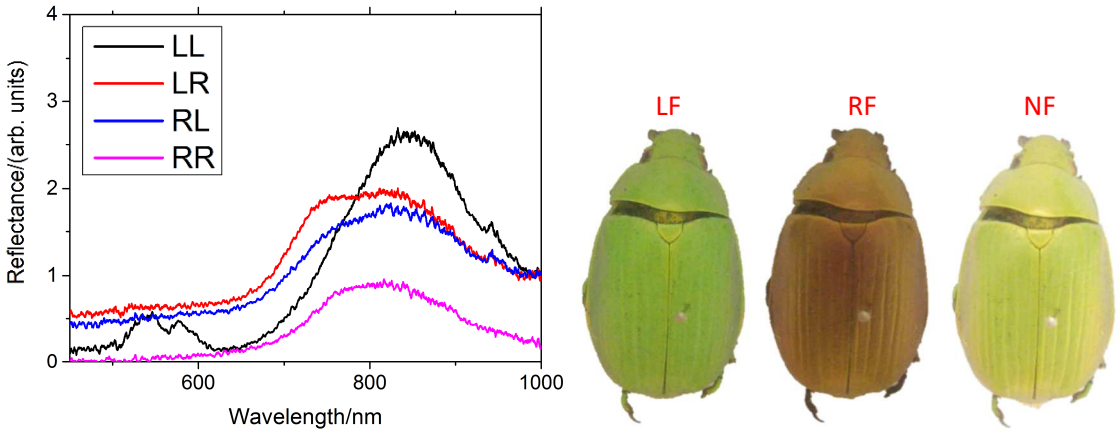


Figure A 70 – CP reflection spectra from the elytron of a *Chrysina costata* beetle. This specimen was collected from Huauchinango, Puebla, Mexico in 2011. The CP spectra were taken with an integration time of 500ms. The specimen measures 33mm.

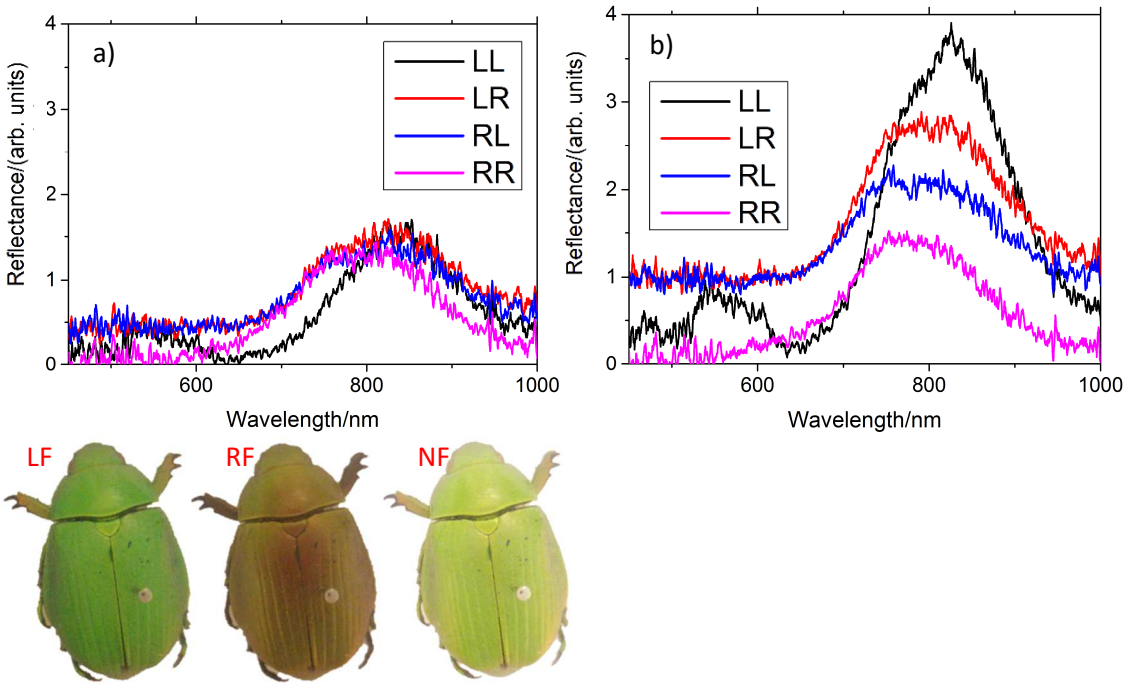


Figure A 71 – CP reflection spectra from the elytron of two *Chrysina alphabarreria* beetles a) and b). These specimens were collected from Santa Martha, Veracruz, Mexico in 2005. Although not measured experimentally colour variations of *Chrysina alphabarreria* are known to exist. The species measures ~27mm.

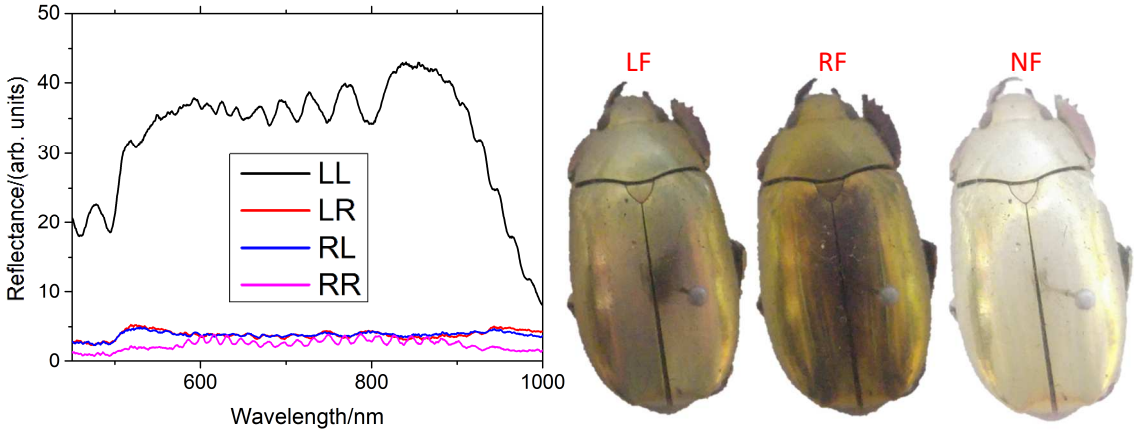


Figure A 72 – CP reflection spectra from the elytron of a *Chrysina pastori* beetle. This specimen was collected from Merendon, Honduras in 2015. The specimen measures 24mm.

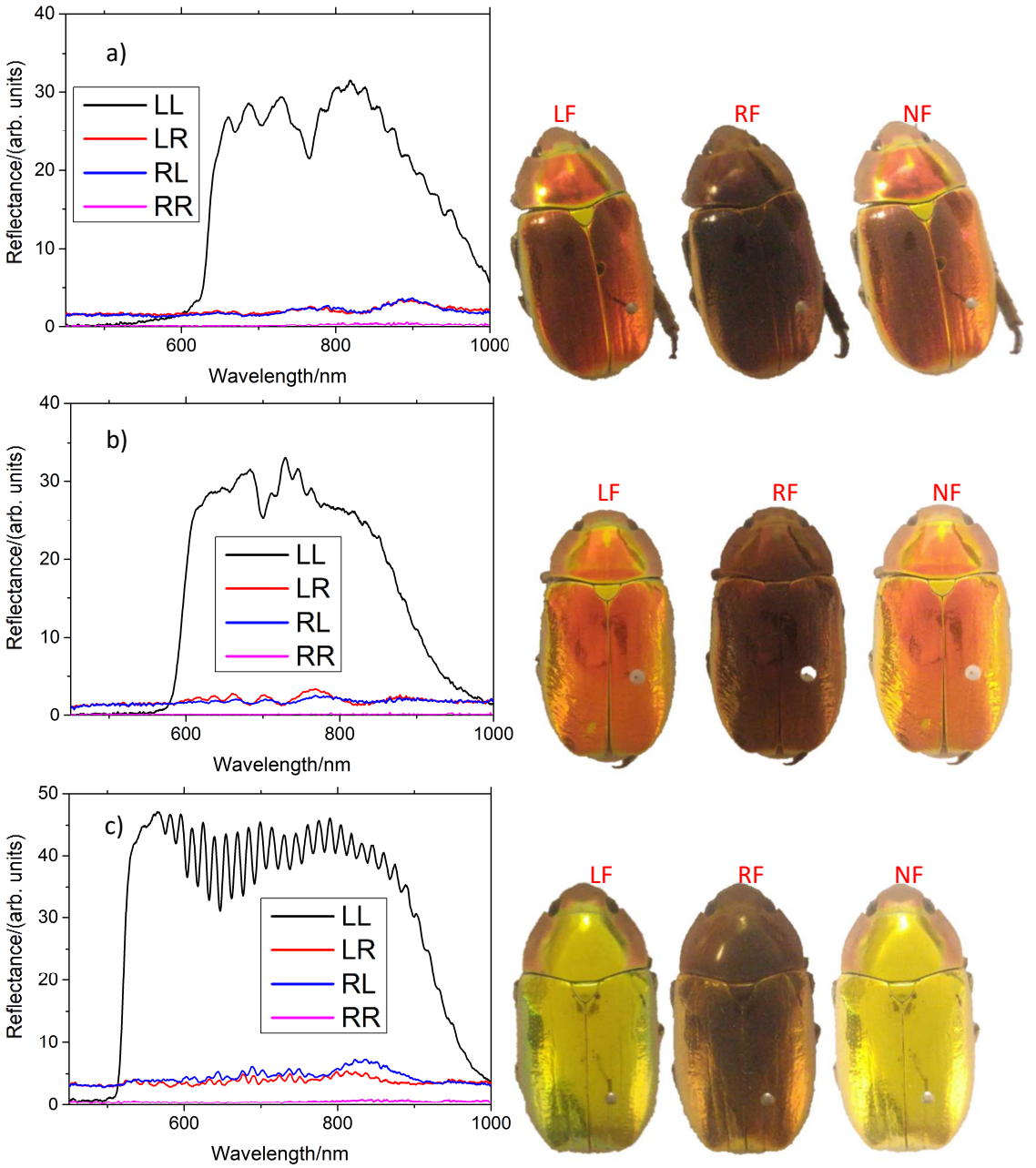


Figure A 73 – CP reflection spectra from the elytra of an a) dark red, b) light red and c) gold *Chrysina aurigans* beetle. This specimen was collected from Cerro Bellavista, Rio Guacimo, Costa Rica in 2015. The specimens measure a) 28mm, b) 28mm and c) 29mm.

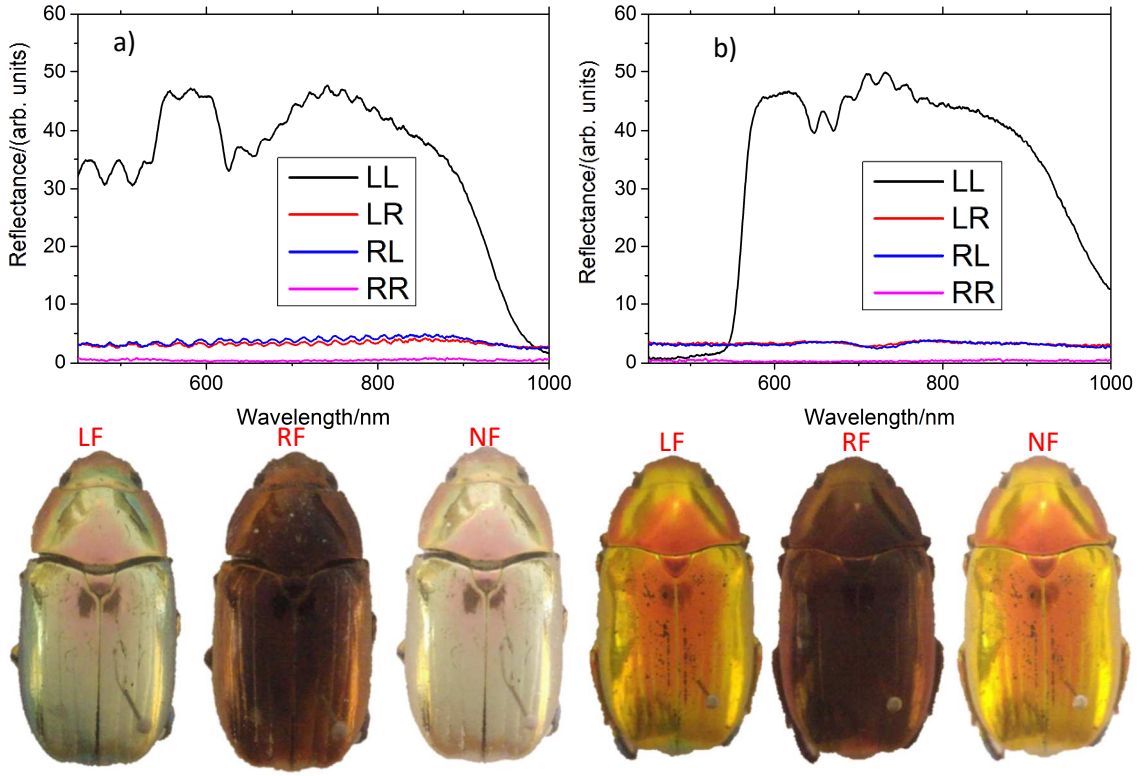


Figure A 74 – CP reflection spectra from the elytron of a) a silver and b) a gold *Chrysina chrysargyrea* beetle. The silver beetle was collected from Cerro Bellavista, Rio Guacimo, Costa Rica in 2015 and the gold was collected from Cerro de la Meurte, Costa Rica in 2014. The specimens measure a) 29mm and b) 29mm.

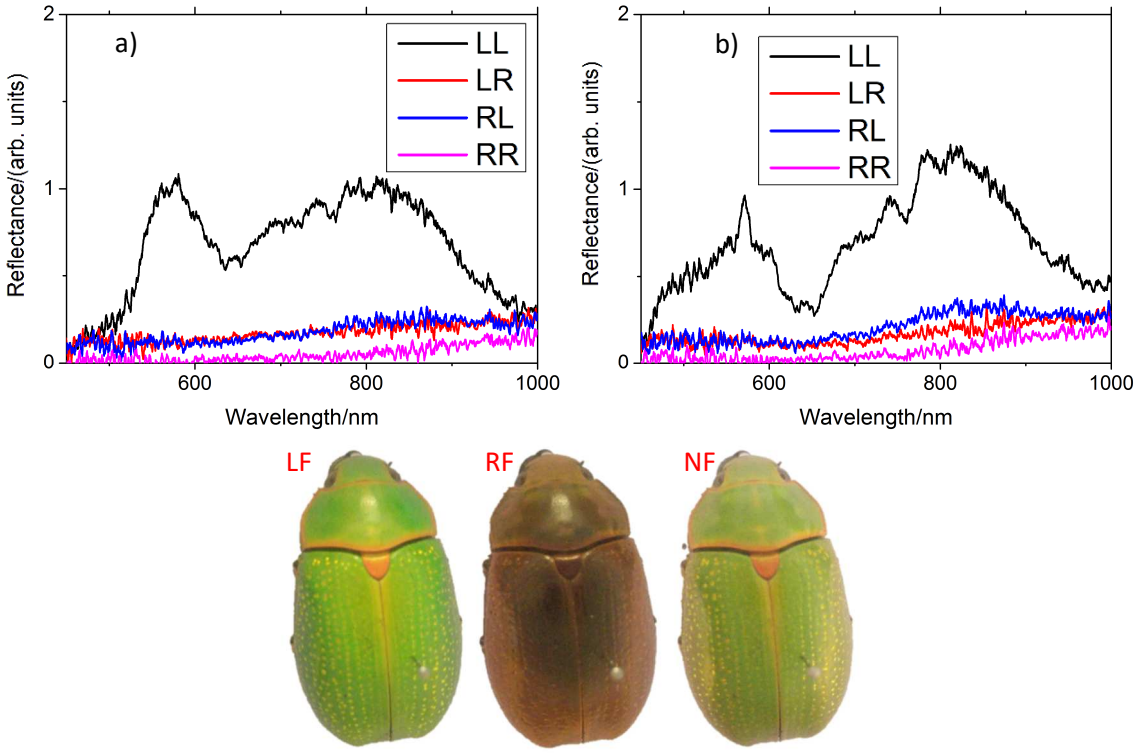


Figure A 75 – CP reflection spectra from a beam spot which focused upon a region with a) a gold spot in and b) a predominately green part of the elytron of a *Chrysina spectabilis* beetle. This specimen was collected from Cusuco National Park, Honduras in 2012. The specimen measures 35mm.

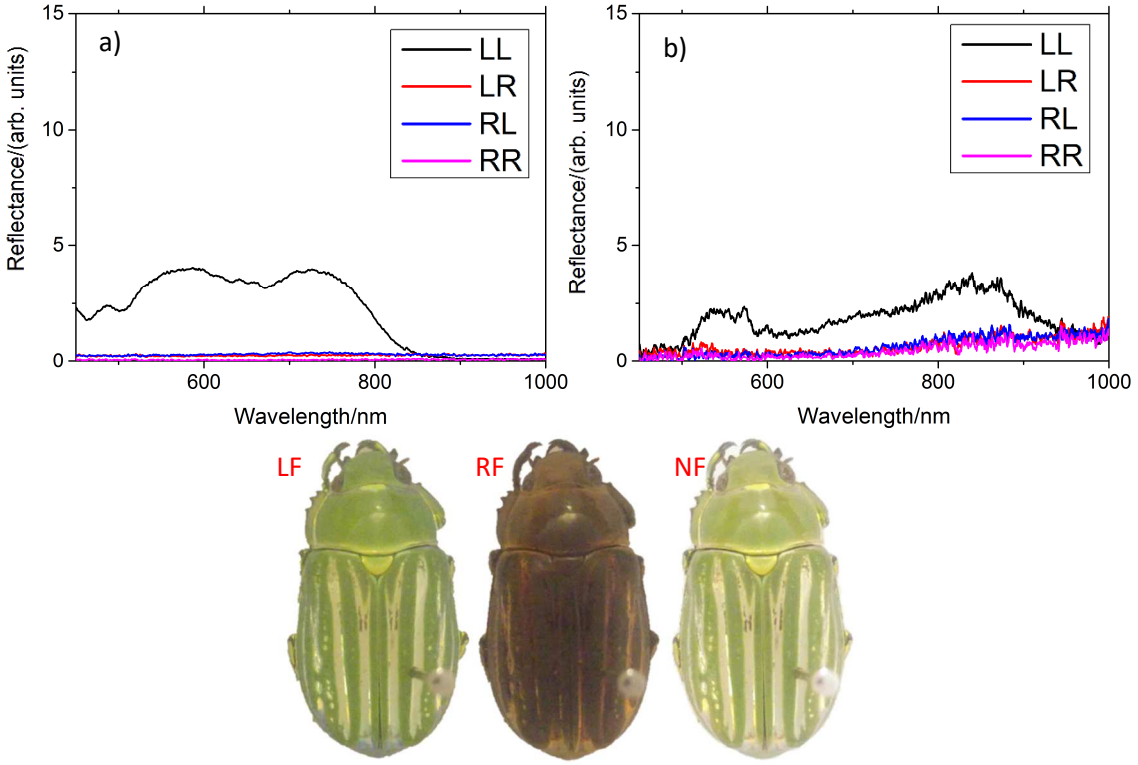


Figure A 76 – CP reflection spectra from predominately a) the green region on the pronotum and b) the gold area of elytron of a *Chrysina gloriosa* beetle. This specimen was collected from Huachuca Mountains, Life Canyon, Sanata Cruz, Arizona, USA in 1999. a) was taken with an integration time of 500ms whilst b) with 100ms. The specimen measures 23mm.

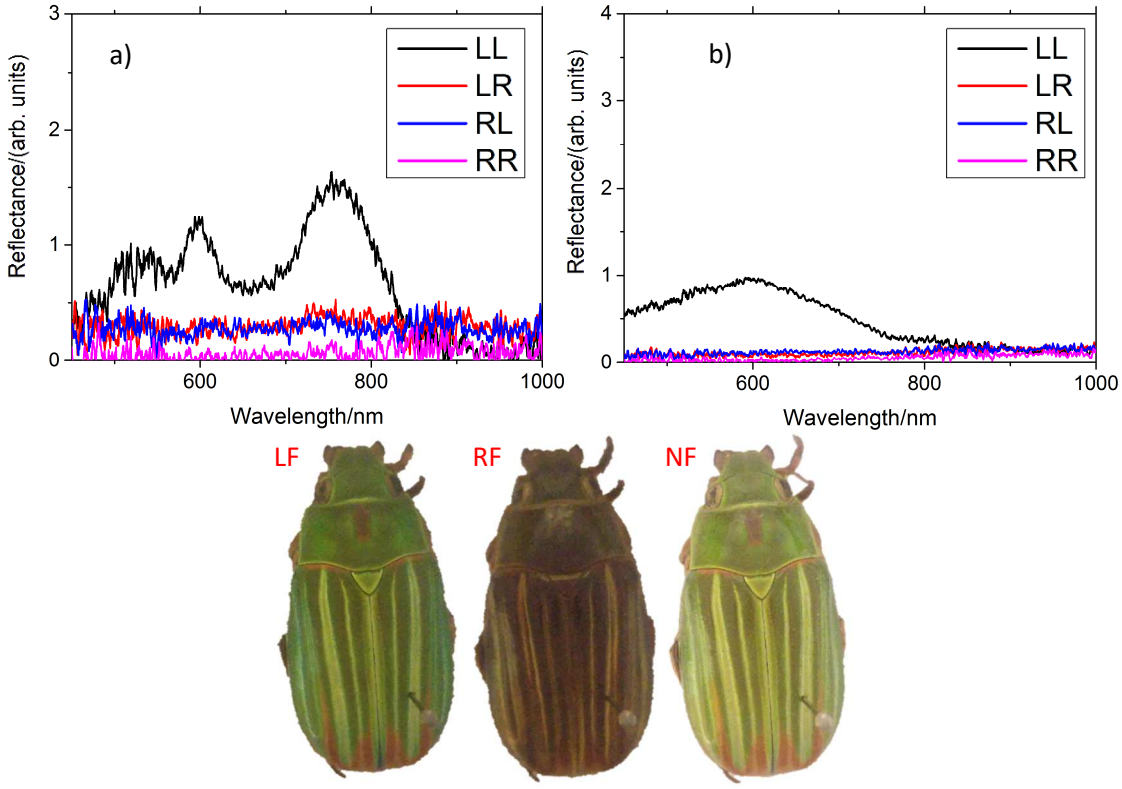


Figure A 77 – CP reflection spectra focused upon a) the golden stripes on the elytron and b) the pronotum of a *Chrysina adelaida* beetle. This specimen was collected from San José del Pacífico, Mexico in 2015. b) was taken with an integration time of 500ms whilst a) with 100ms. The specimen measures 26mm.

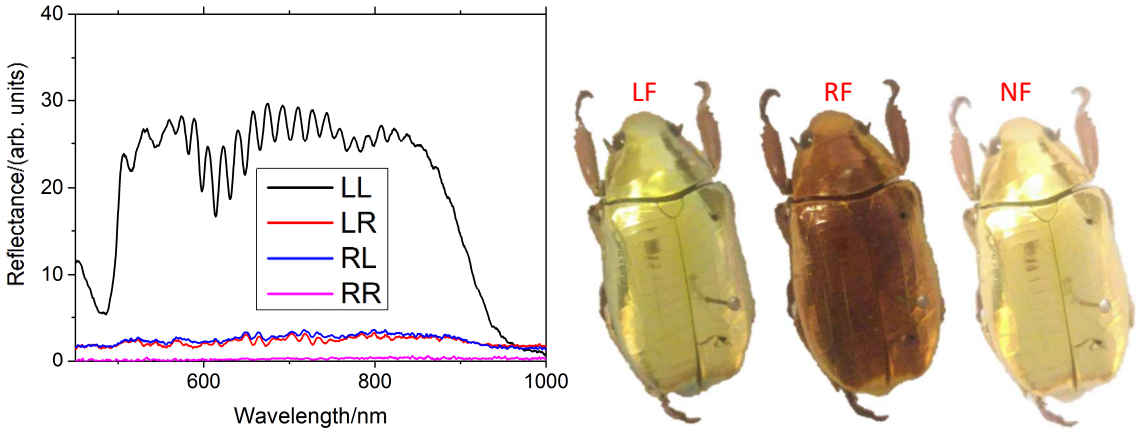


Figure A 78 – CP reflection spectra from the elytron of a *Chrysina argenteola* beetle. This specimen was collected from Ecuador in 2012. The specimen measures 29mm.

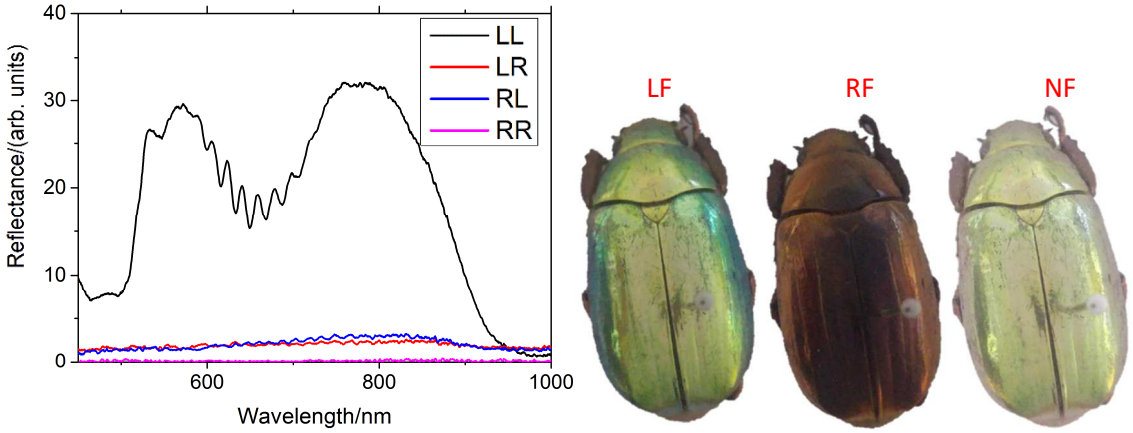


Figure A 79 – CP reflection spectra from the elytron of a *Chrysina batesi* beetle. This specimen was collected from Cerro de la Muerta, Costa Rica in 2015. The specimen measures 31mm.

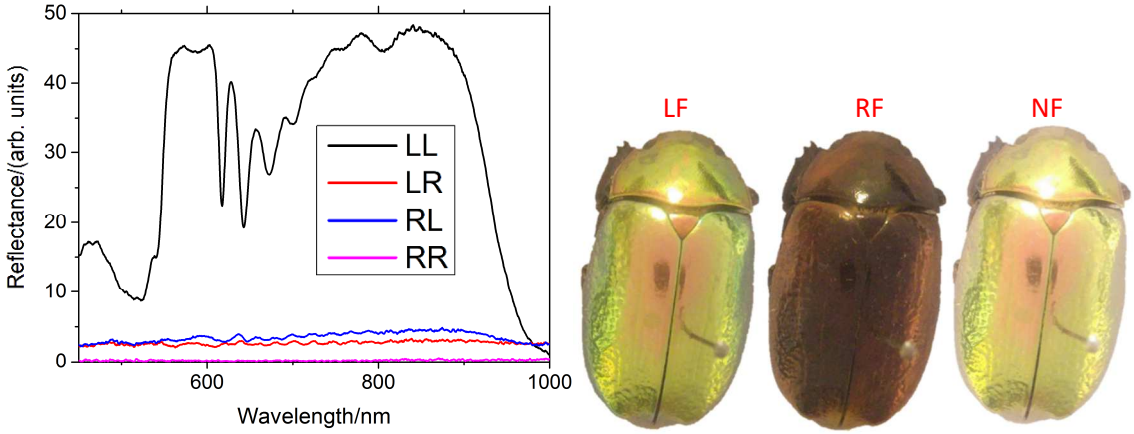


Figure A 80 – CP reflection spectra from the elytron of a *Chrysina curoei* beetle. This specimen was collected from Costa Rica in 2015. The specimen measures 27mm.

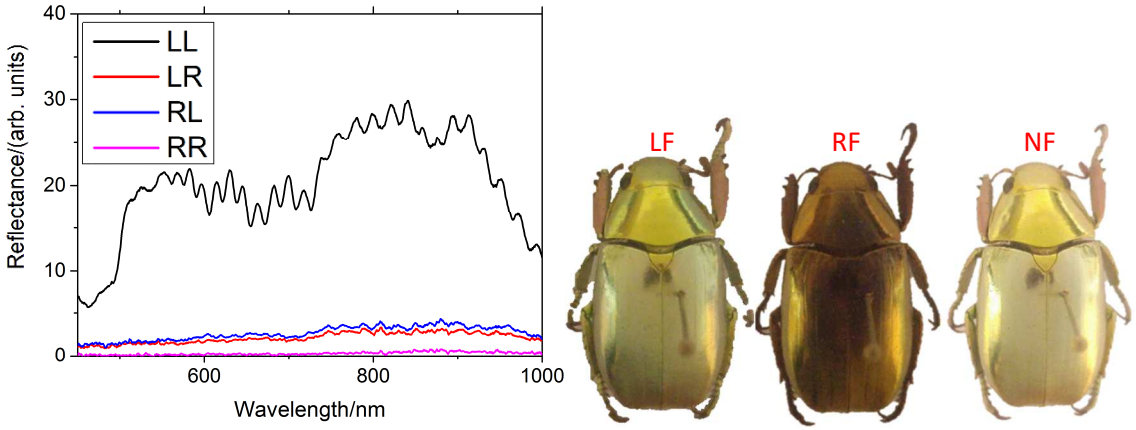


Figure A 81 – CP reflection spectra from the elytron of a *Chrysina strasseni* beetle. This specimen was collected from Cusuco National Park, Cortes, Honduras in 2015. The specimen measures 25mm.

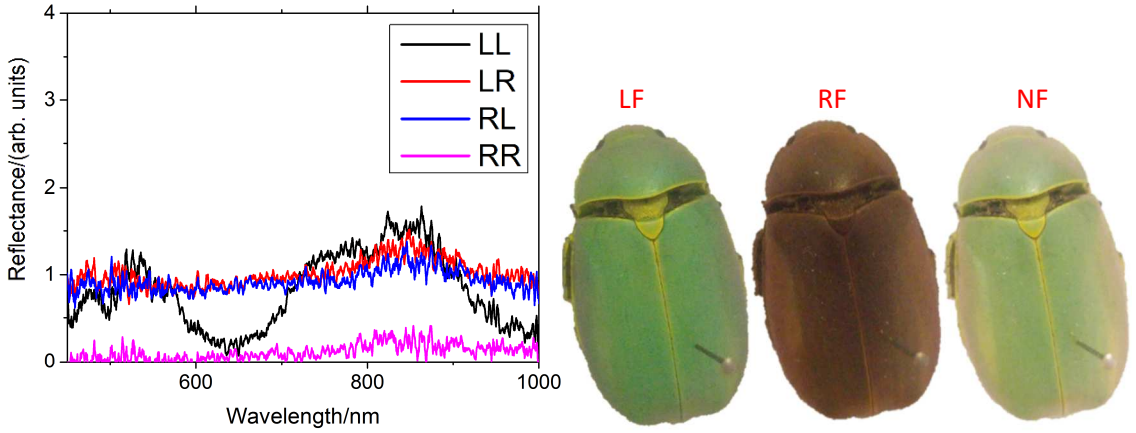


Figure A 82 – CP reflection spectra from the elytron of a *Chrysina aurora* beetle. This specimen was collected from Cost Rica in 2014. The specimen measures 27mm.

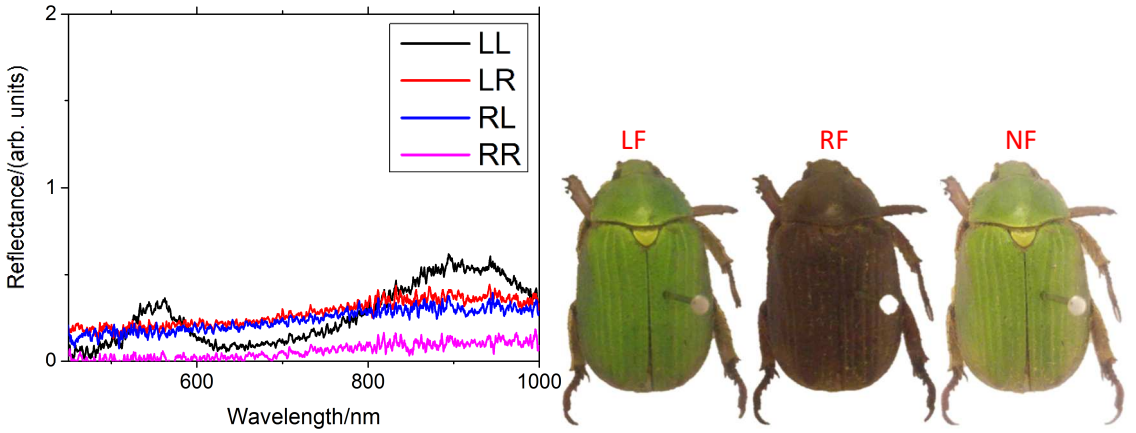


Figure A 83 – CP reflection spectra from the elytron of a *Chrysina leconti* beetle. This specimen was collected from El Salto, Durango, Mexico in 2007. The CP spectra were taken with an integration time of 500ms. The specimen measures 23mm.

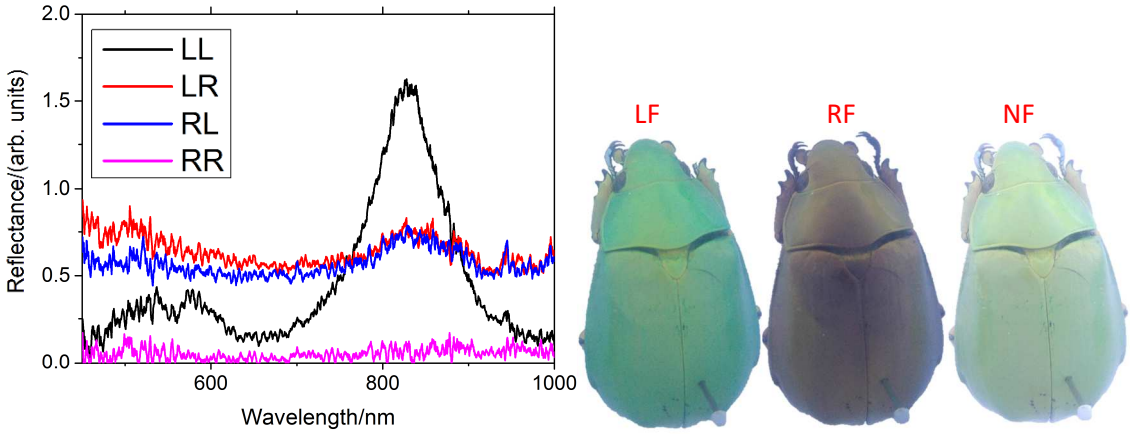


Figure A 84 – CP reflection spectra from the elytron of a green *Chrysina karschi* beetle. This beetle was collected in Merendon, Cortes, Honduras in 2011. The CP spectra were taken with an integration time of 500ms. The specimen measures 24mm.

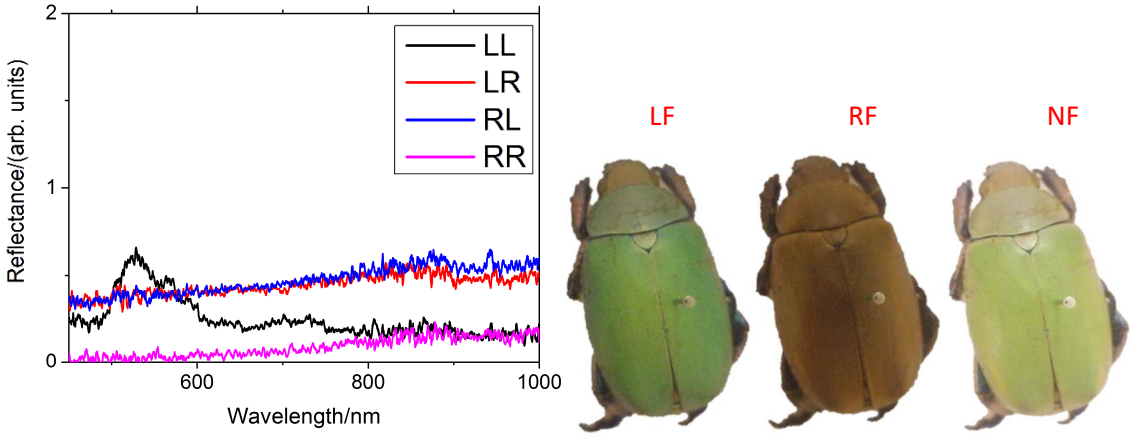


Figure A 85 – CP reflection spectra from the elytron of a *Chrysina erubescens* beetle. This specimen was collected from El Salto, Durango, Mexico in 2007. The CP spectra were taken with an integration time of 500ms. The specimen measures 36mm.

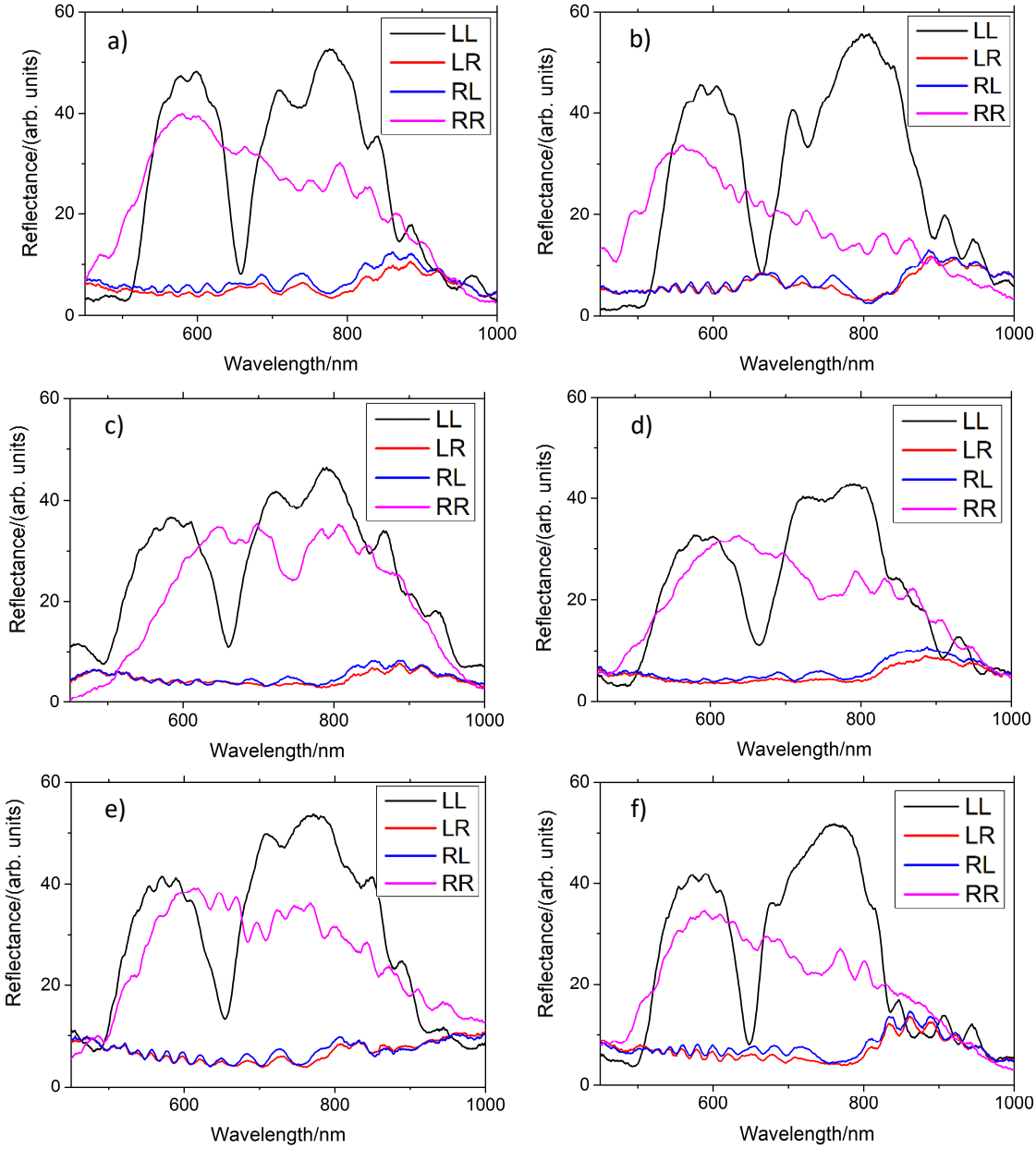


Figure A 86 – Consistency in six sets of CP spectra of beetles from the *Chrysina resplendens* species.

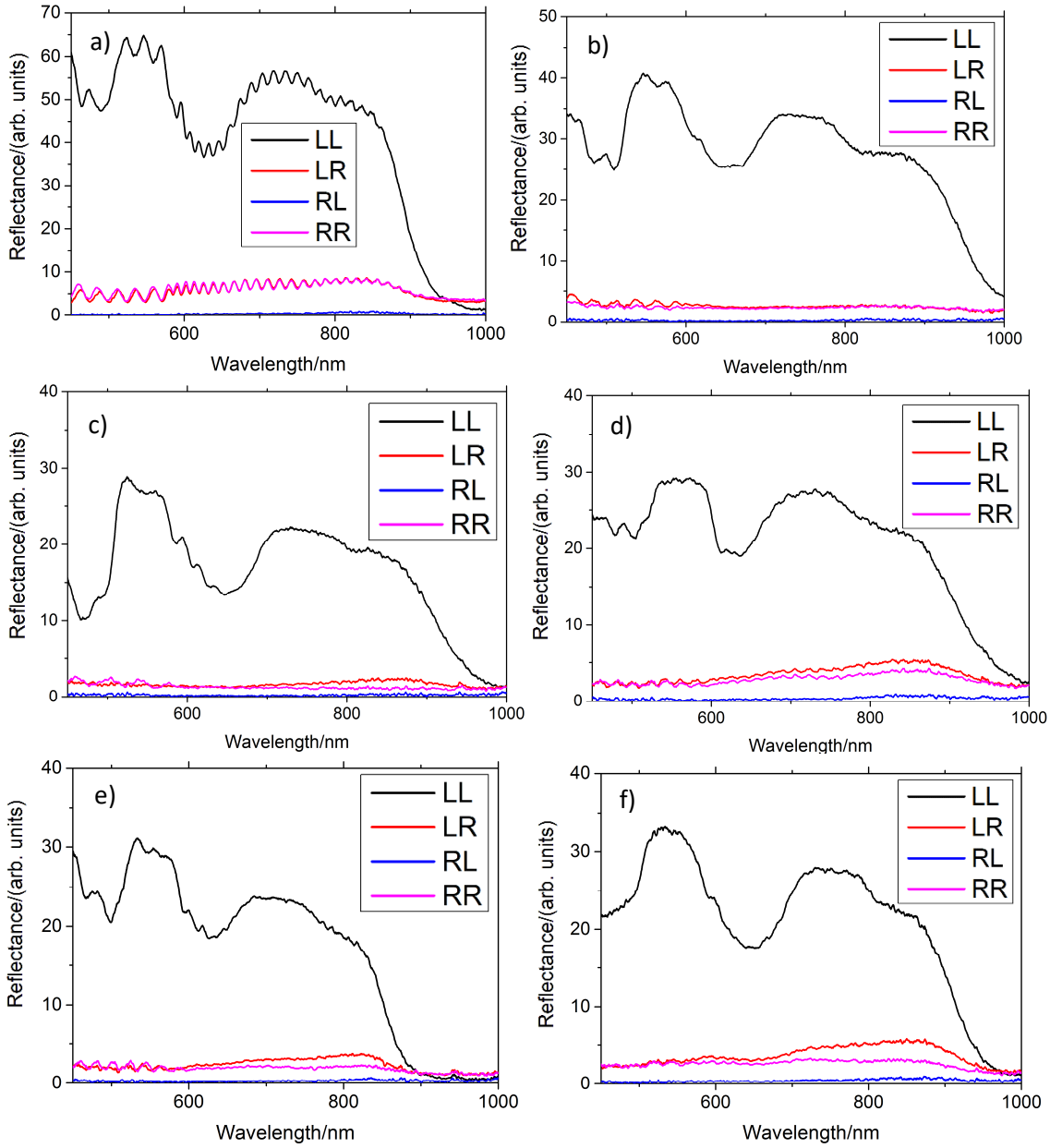


Figure A 87 – Consistency in six sets of the CP spectra of *Chrysina optima* beetles.

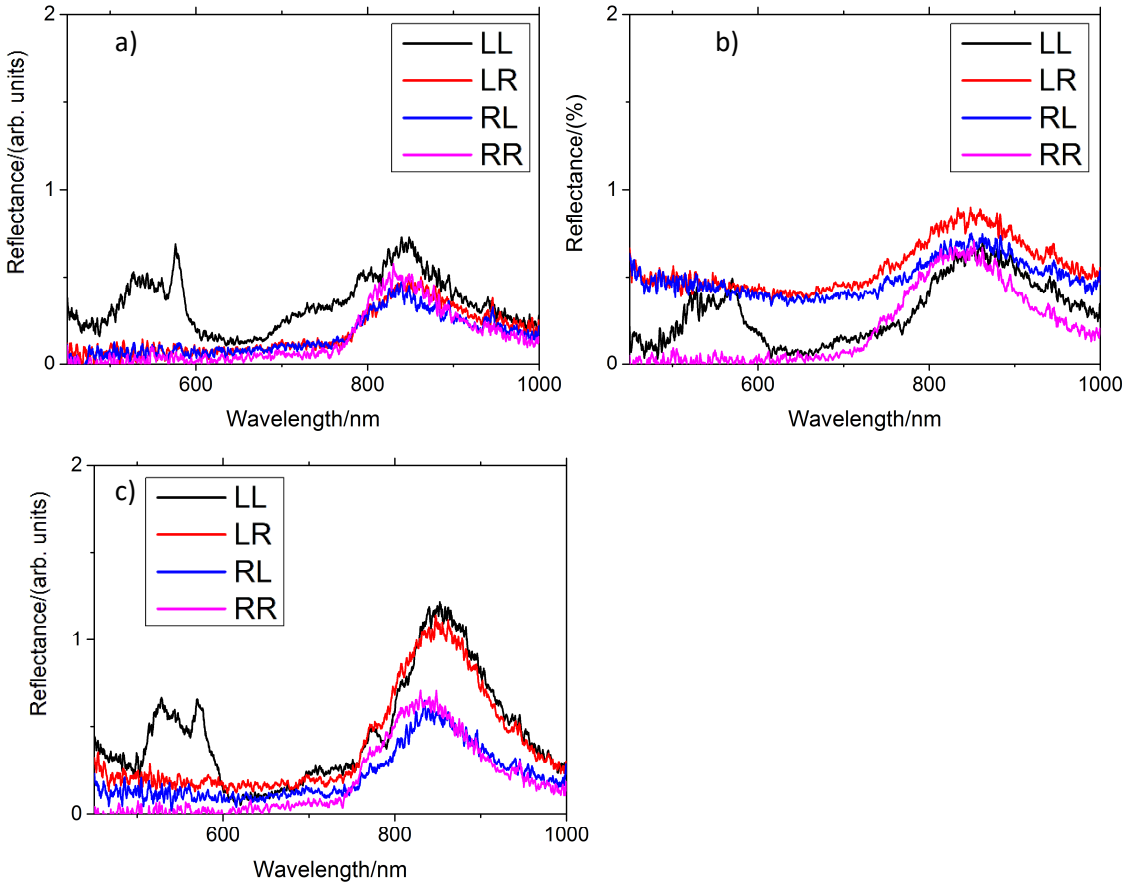


Figure A 88 – Variation in CP reflection spectra from the elytron of three green *Chrysina tricolour* beetles. These specimens were collected from Cerro de la Muerta, Costa Rica in 2013. There are four spectral CP configurations which are LL (black), LR (blue), RL (red) and RR (pink). Taken with an integration time of 500ms.

A3.3.2 - Single Species

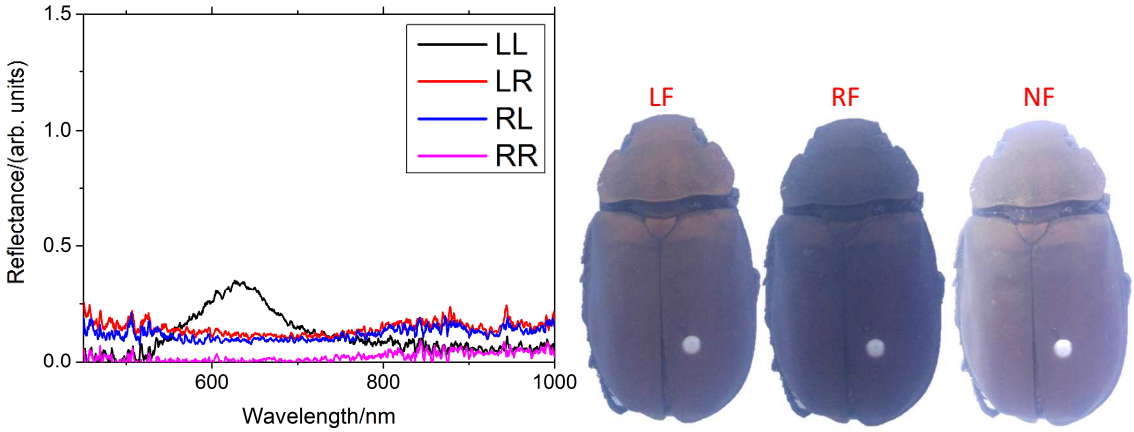


Figure A 89 – CP reflection spectra from the elytron of a *Spodochlamys cupreola* beetle. This beetle was collected in Guapiles, Limon Province, Costa Rica in 2012. Taken with an integration time of 2000ms. The specimen measures 29mm.

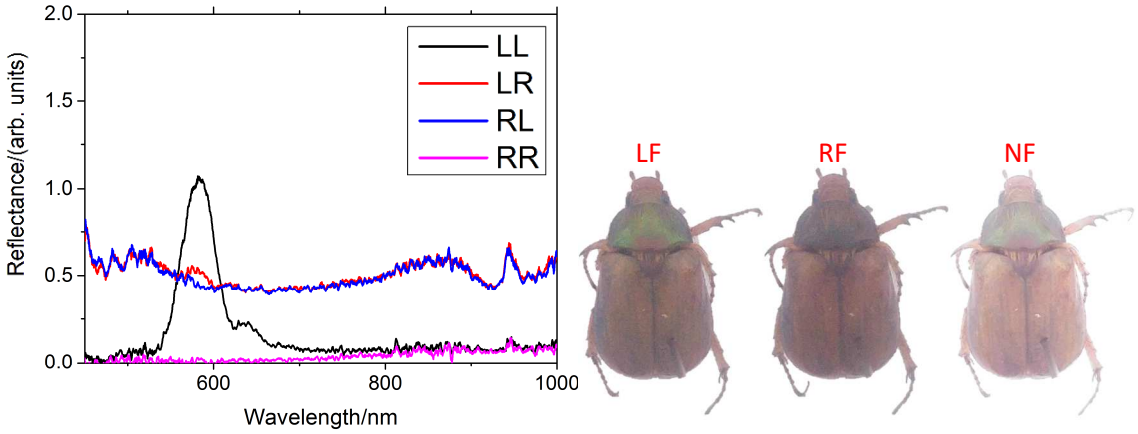


Figure A 90 – CP reflection spectra from the pronotum of an *Aulacopalpus aconcaguensis* beetle. This beetle was collected in Laguna Verde, Valparaiso, Chile in 2016. Taken with an integration time of 2000ms. The specimen measures 15mm.

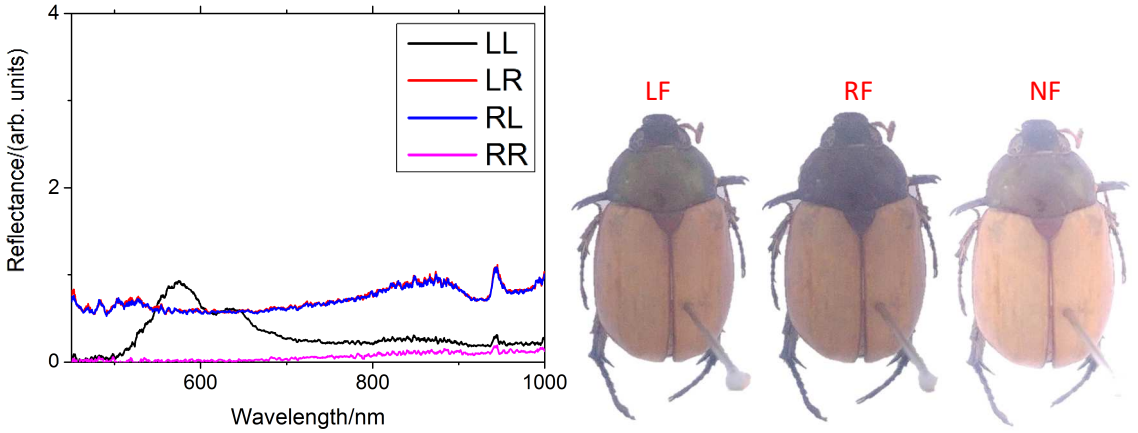


Figure A 91 – CP reflection spectra from the pronotum of a *Rutelidae sp* beetle. This specimen was collected from Piura, Peru in 2017. Taken with an integration time of 500ms. The specimen measures 16mm.

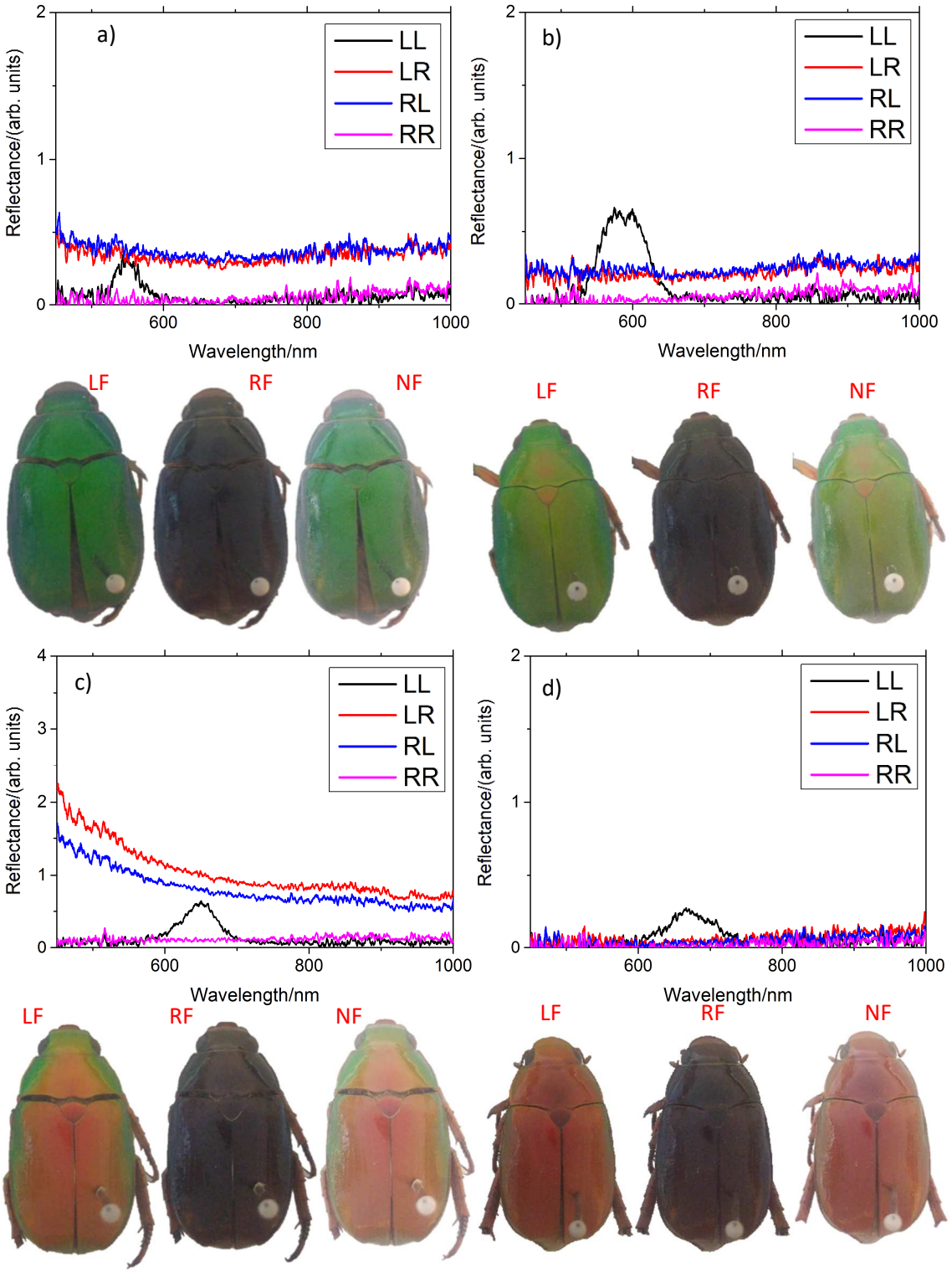


Figure A 92 – CP reflection spectra from the elytron of 4 colour variants of *Anoplognathus smaragdinus* beetles. These specimens were collected from Polly Creek, Garrandunga, North Queensland Australia in 2015. Taken with an integration time of 500ms. The specimens measure a) 23mm, b) 20mm, c) 19mm and d) 20mm.

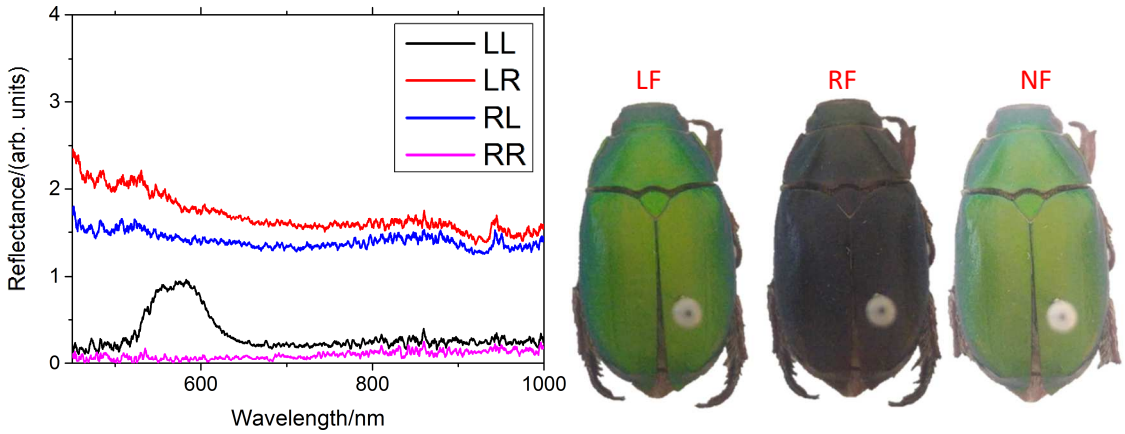


Figure A 93 – CP reflection spectra from the elytron of a *Calloodes rayneri* beetle. This specimen was collected from Mount Garnet, North Queensland Australia in 2014. Taken with an integration time of 500ms. The specimen measures 18mm.

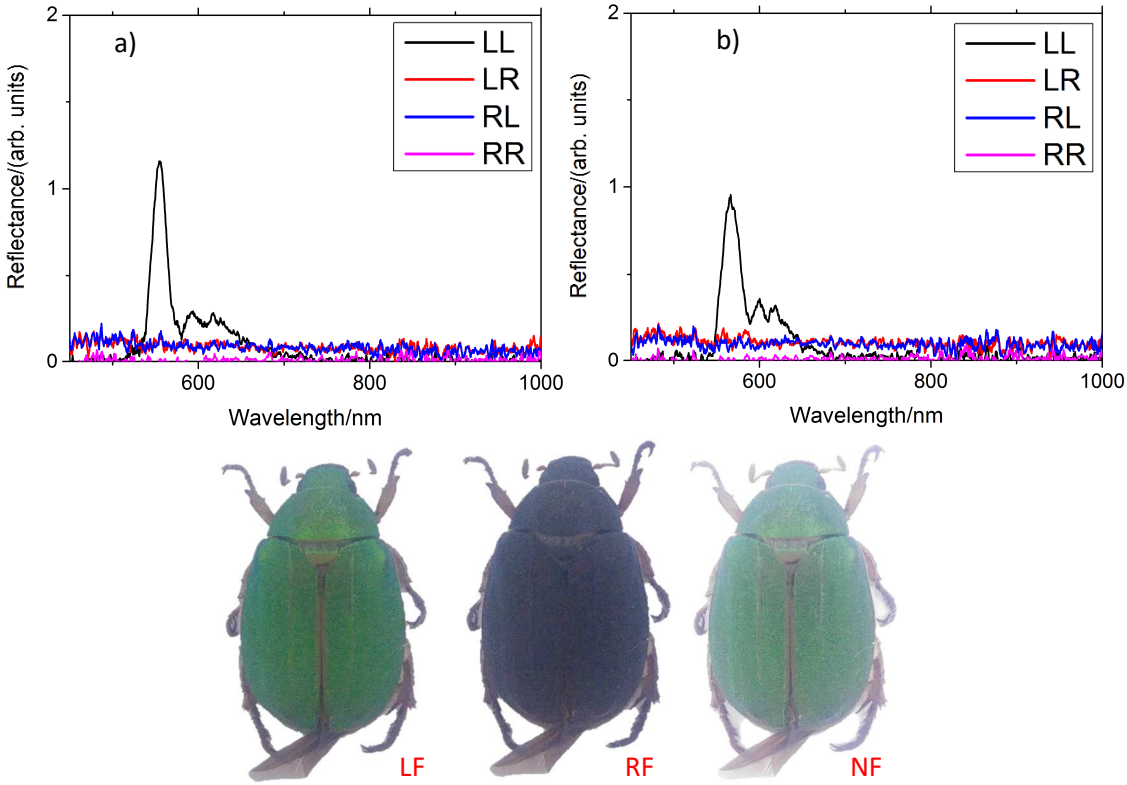


Figure A 94 – CP reflection spectra from a) the pronotum and b) the elytra of a *Mimela holosericea* beetle. This specimen was collected from Partizansk, Russia in 2015. The specimen measures 20mm.

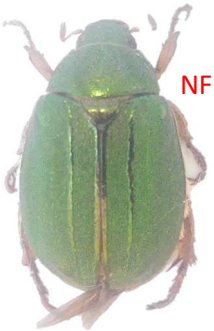


Figure A 95 – Photograph of a *Mimela holosericea* beetle taken in natural (less diffuse) light which highlights its more highly reflecting stripes.

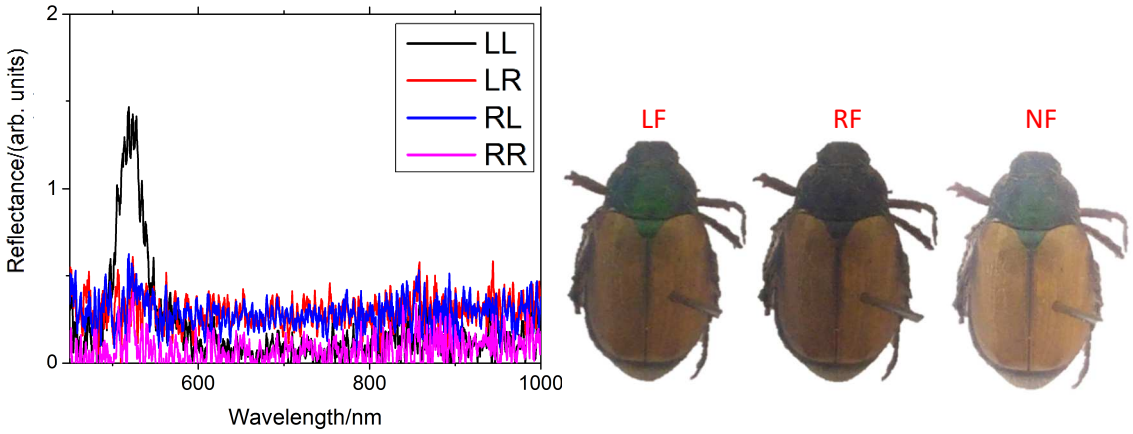


Figure A 96 – CP reflection spectra from the pronotum of a *Phyllopertha horticola* beetle. This specimen was collected from Ahja, Estonia in 2005. The specimen measures 11mm.

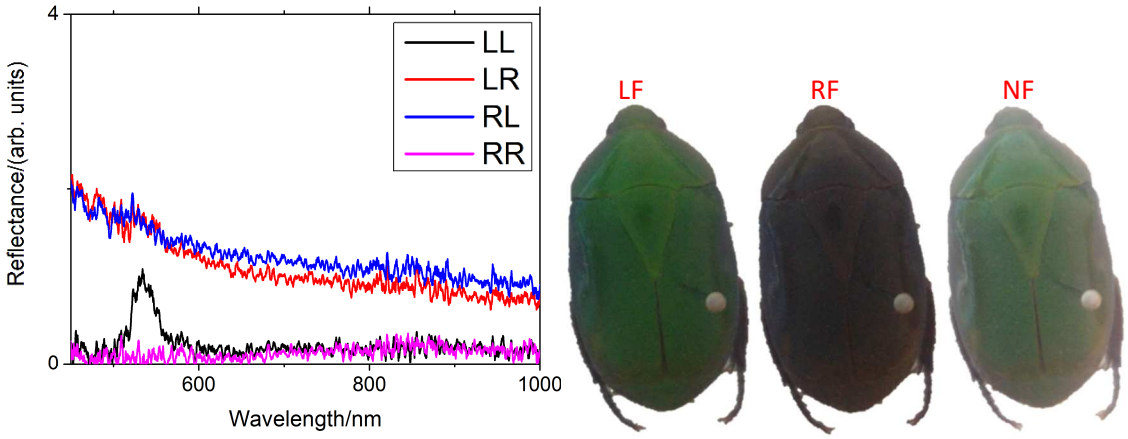


Figure A 97 – CP reflection spectra from the elytron of a *Pseudomacrapsis affinis* beetle. This specimen was collected from Satipo, Huanuco, Peru in 2014. Taken with an integration time of 500ms. The specimen measures 24mm.

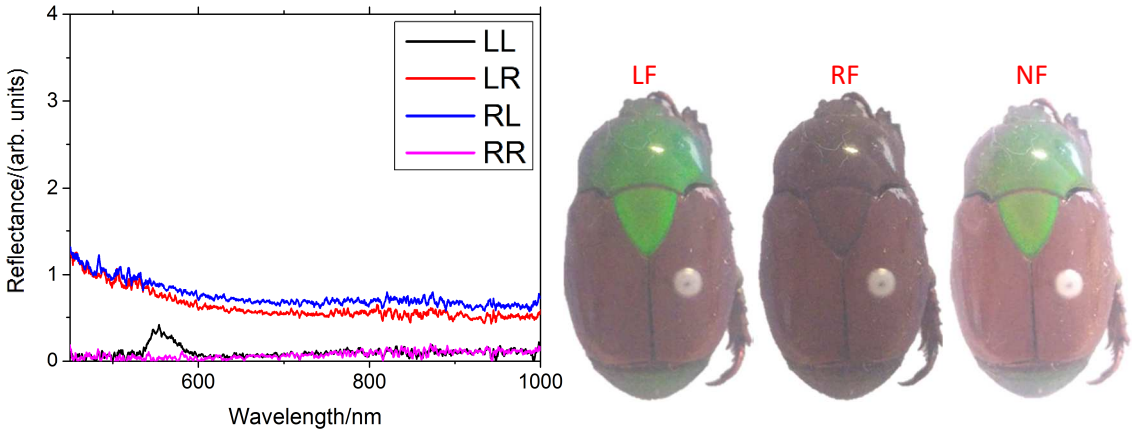


Figure A 98 – CP reflection spectra from the elytron of a *Calomacrapsis haroldi* beetle. This specimen was collected from Los Tuxtlas, Veracruz, Mexico in 2010. Taken with an integration time of 500ms. The specimen measures 19mm.

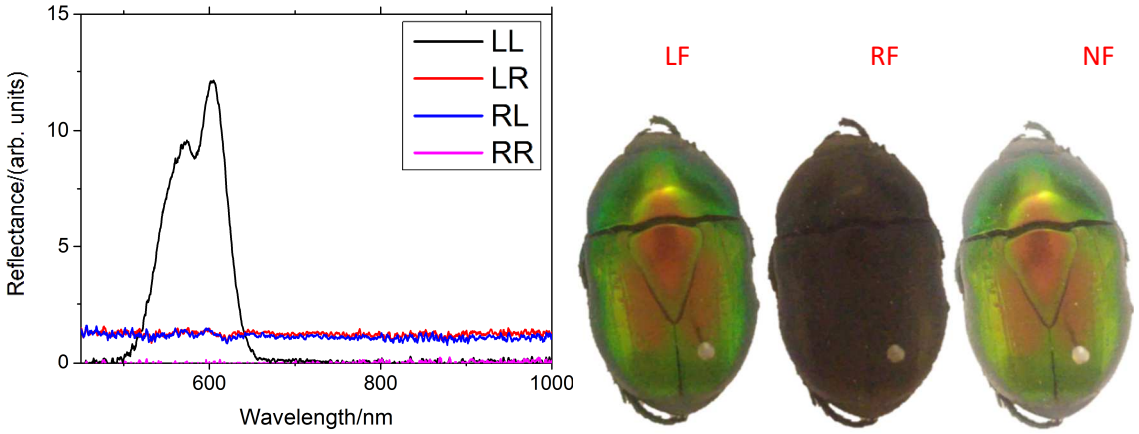


Figure A 99 – CP reflection spectra from the scutellum of a *Macrapsis lucida* beetle. This specimen was collected from Los Tuxtlas, Veracruz. Mexico in 2014. The specimen measures 26mm.

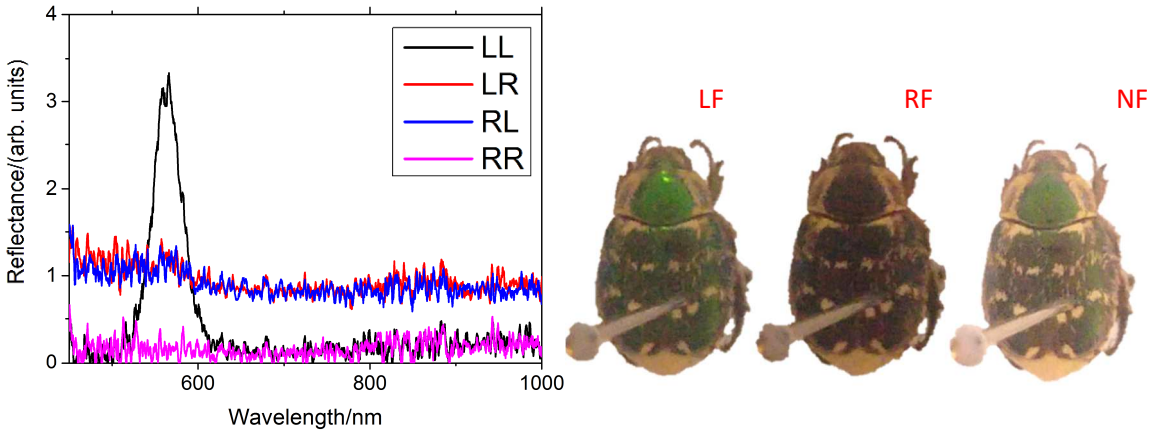


Figure A 100 – CP reflection spectra from the elytron of a *Mimadoretus niveosquamosus* beetle. This specimen was collected from Polly Creek, Garradunga, North Queensland, Australia in 2014. The specimen measures 9mm.

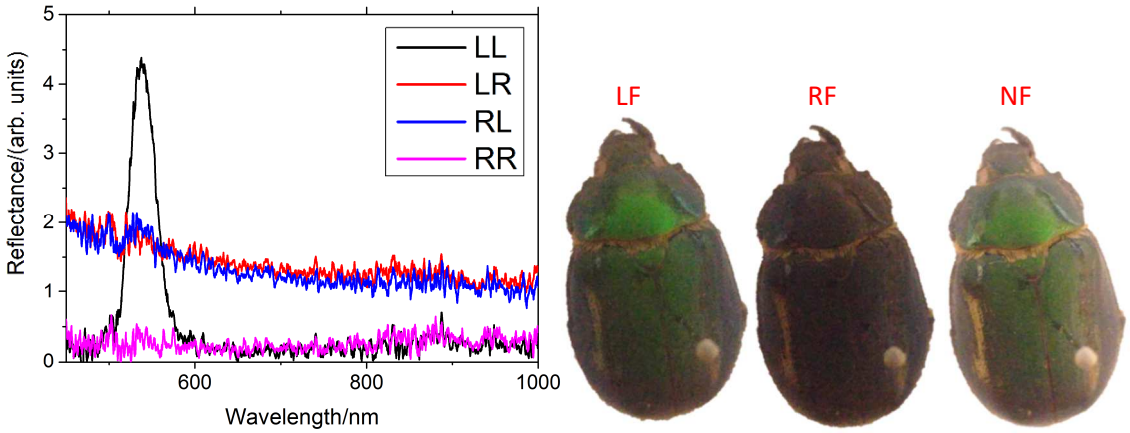


Figure A 101 – CP reflection spectra from the elytron of a *Viridimicus aurescens* beetle. This specimen was collected from San Cristobal de las Casas, Chiapas, Mexico in 2013. The specimen measures 21mm.

A3.3.3 – Anomala

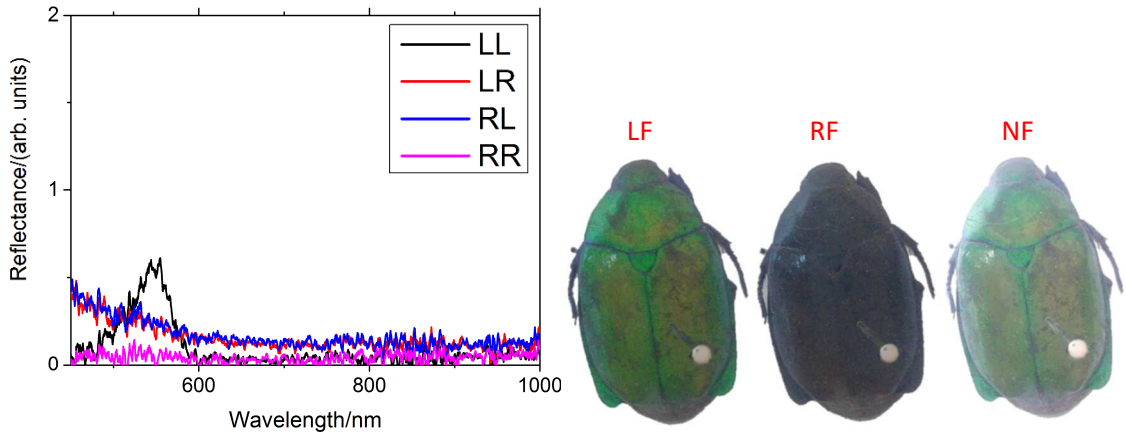


Figure A 102 – CP reflection spectra from the elytron of an *Anomala expansa* beetle. This specimen was collected from Nam-To, Taiwan in 2006. Taken with an integration time of 500ms. The specimen measures 25mm.

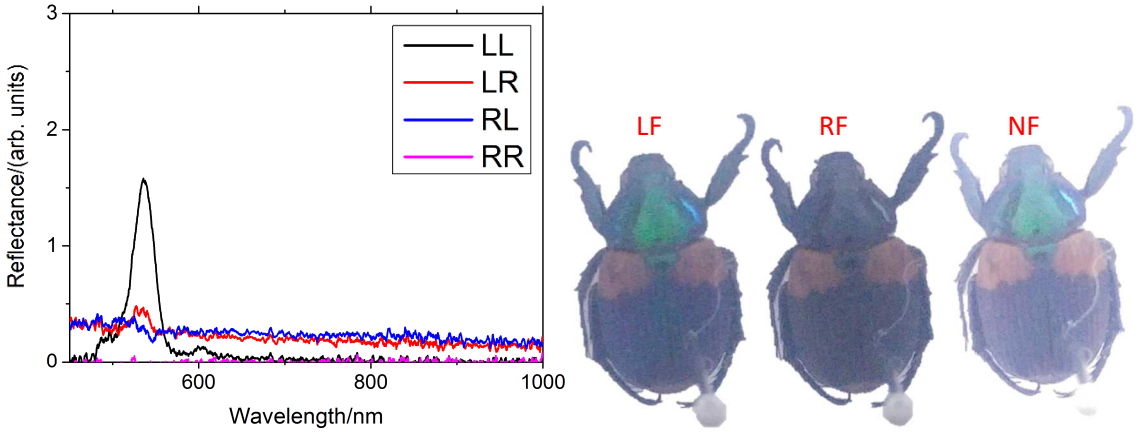


Figure A 103 – CP reflection spectra from the pronotum of an *Anomala basalis* beetle. This specimen was collected from Isimani, Iringa, Tanzania in 2014. Taken with an integration time of 500ms. The specimen measures 11mm.

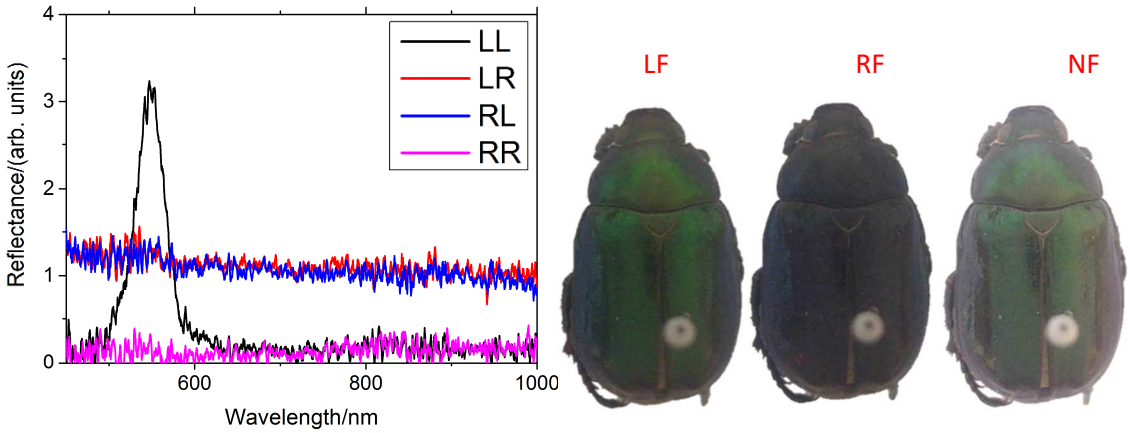


Figure A 104 – CP reflection spectra from the scutellum of an *Anomala antiqua* beetle. This specimen was collected from 38km West of Mount Garent, North Queensland, Australia in 2014. The specimen measures 17mm.

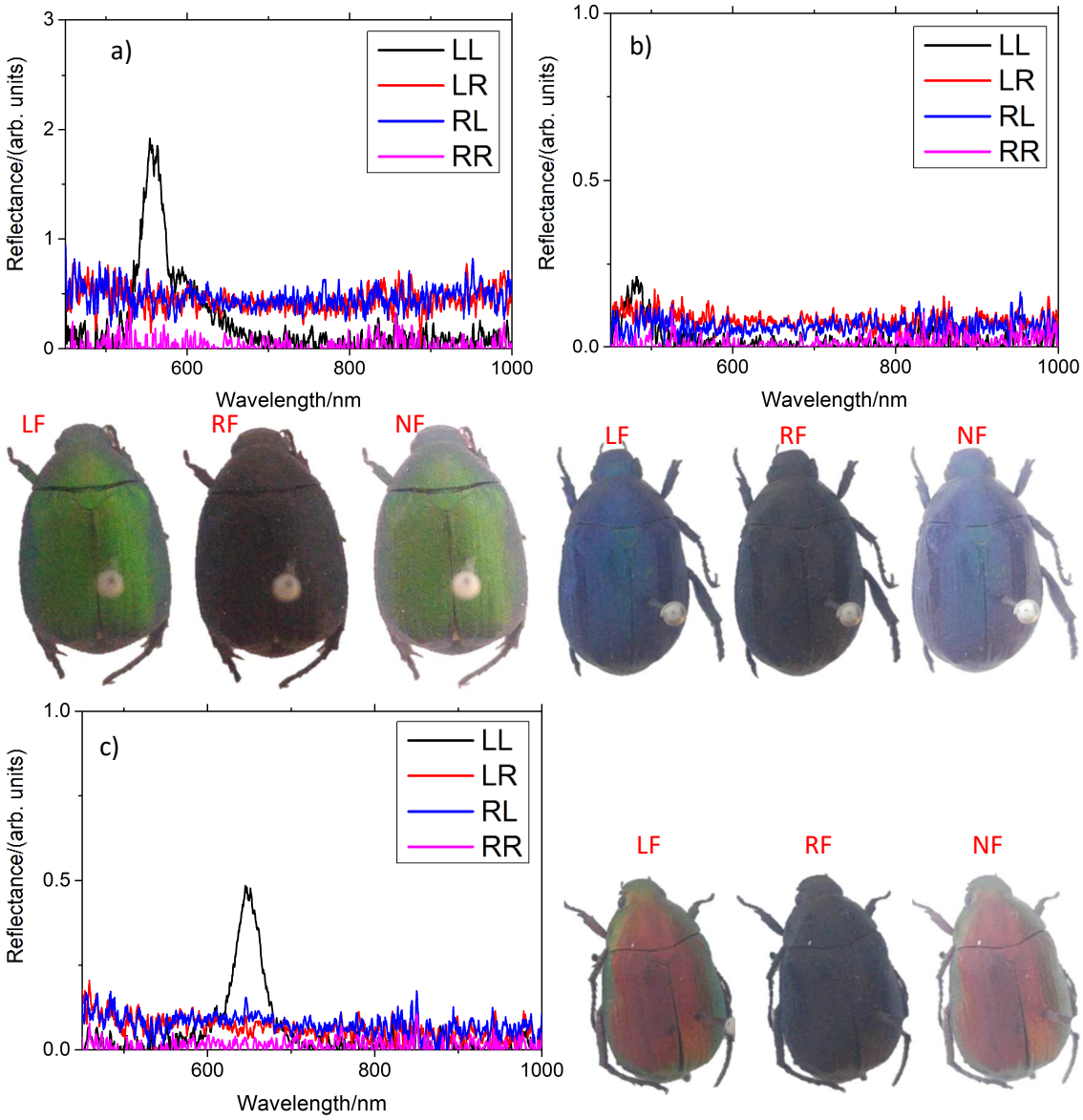


Figure A 105 – CP reflection spectra from the elytron of a) a green, b) a blue and c) a red *Anomala vitis* beetle. These specimens were collected from a) Cartura, Padua, Italy, b) and c) from Velika, Greece in 2015. Taken with an integration time of 500ms. The specimens measure a) 15mm, b) 18mm and c) 17mm.

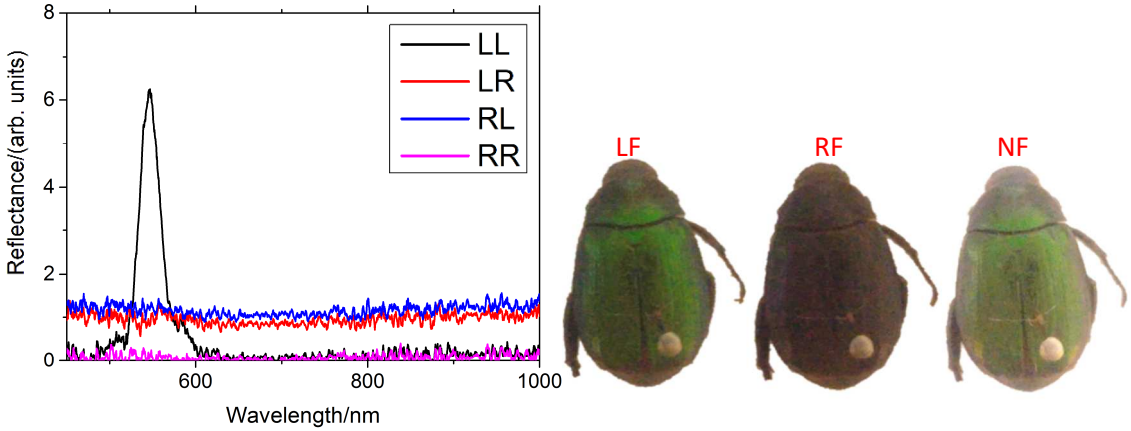


Figure A 106 – CP reflection spectra from the elytron of an *Anomala rufocuprea* beetle. This specimen was collected from Shibusawa, Kanagawa Prefecture, Japan. The specimen measures 15mm.

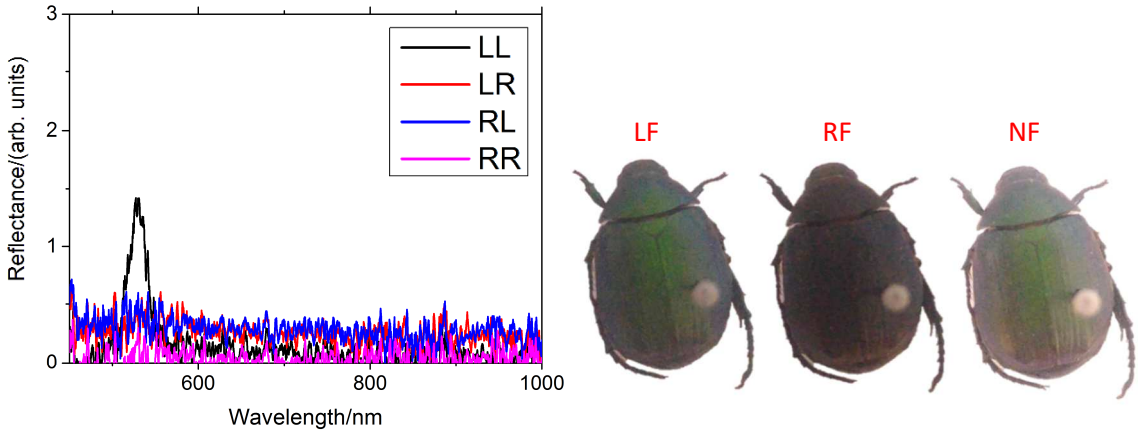


Figure A 107 – CP reflection spectra from the elytron of an *Anomala ausonia* beetle. This specimen was collected from Rosolina, Padua, Italy in 2012. The specimen measures 15mm.

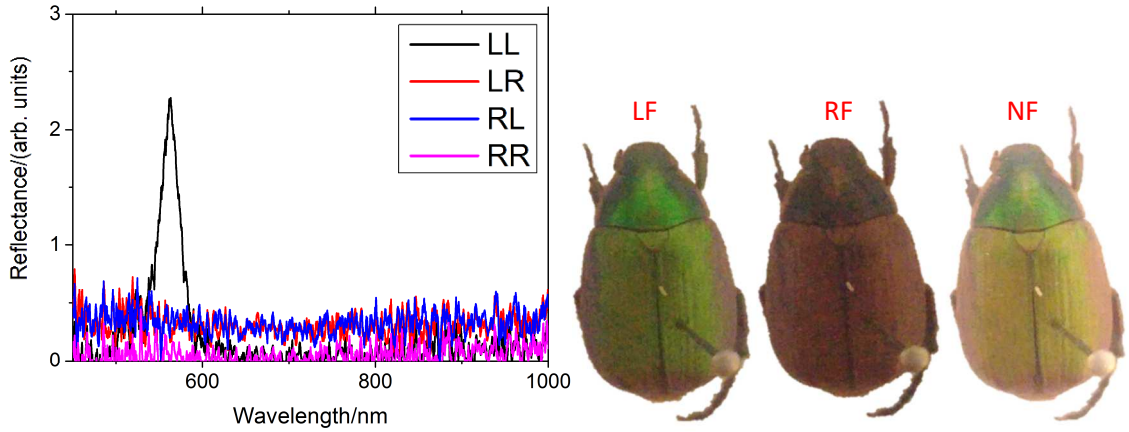


Figure A 108 – CP reflection spectra from the elytron of an *Anomala solida* beetle. This specimen was collected from Kesan, Edirne, Turkey in 2011. The specimen measures 14mm.

A3.3.4 - Pelidnota

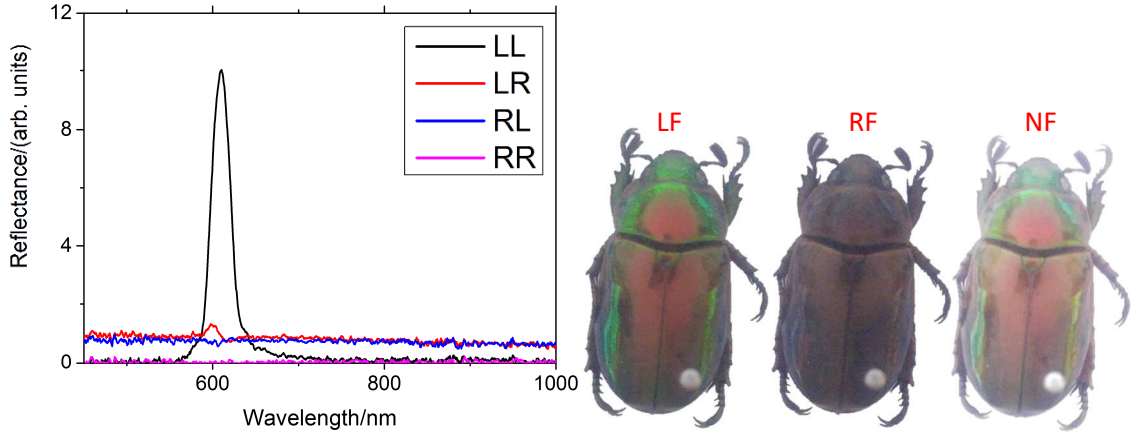


Figure A 109 – CP reflection spectra from the pronotum of a *Pelidnota punctata* beetle. This specimen was collected from Chiapa de Corzo, Mexico in 2016. Taken with an integration time of 200ms. The specimen measures 24mm.

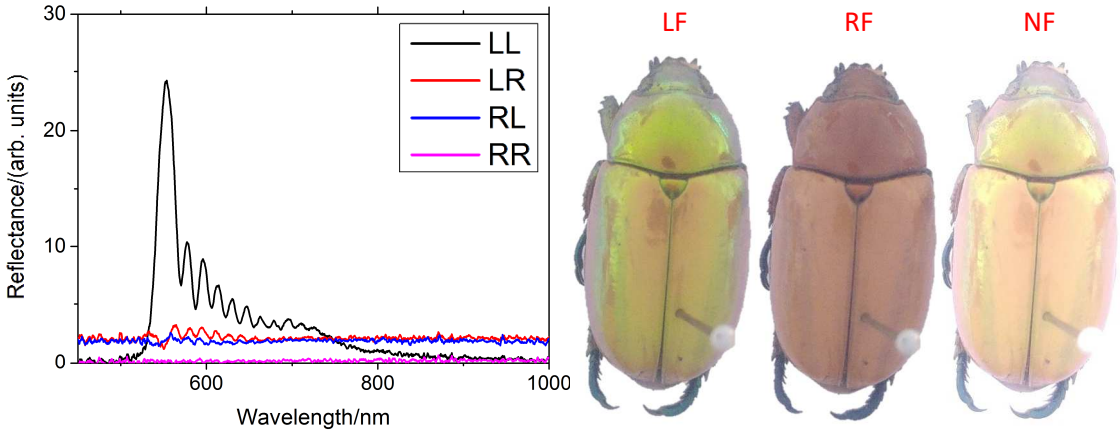


Figure A 110 – CP reflection spectra from the pronotum of a *Pelidnota testaceovirens* beetle. This specimen was collected from Nor Yungas, Bolivia in 2010. The specimen measures 25mm.

A3.3.5 - Strigidia

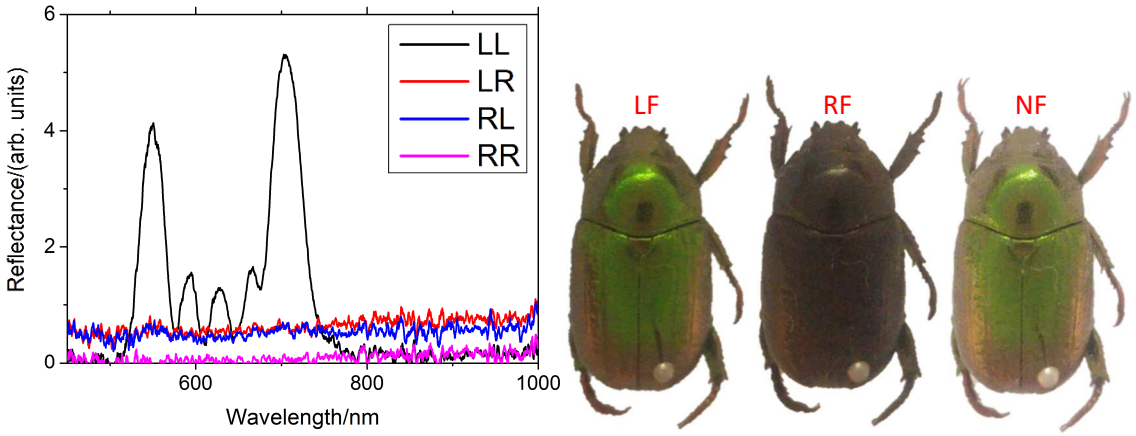


Figure A 111 – CP reflection spectra from the elytron of a *Strigidia granulata* beetle. This specimen was collected from the Petit-Saut Dam, French Guiana in 2013. The specimen measures 20mm.

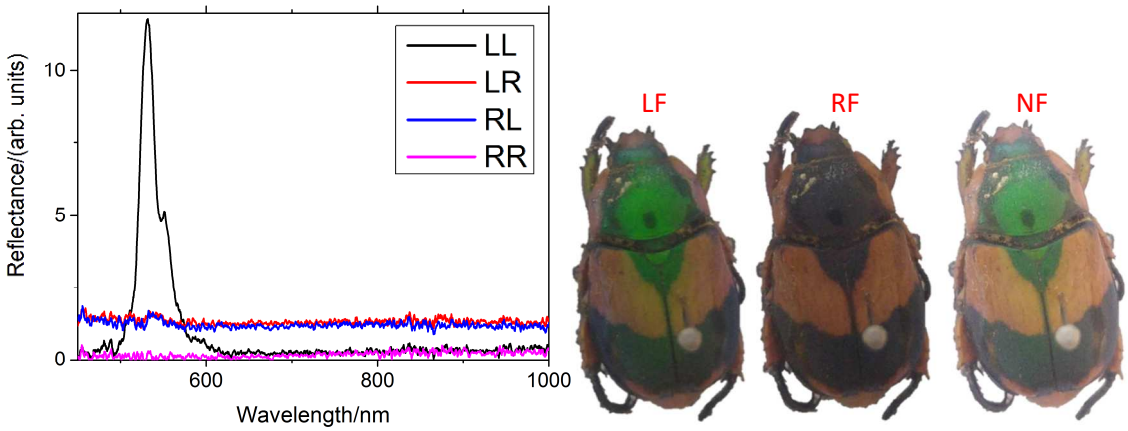


Figure A 112 – CP reflection spectra from the pronotum of a *Strigidia pulchella* beetle. This specimen was collected from Dos de Mayo, Misiones, Argentina in 2012. The specimen measures 18mm.

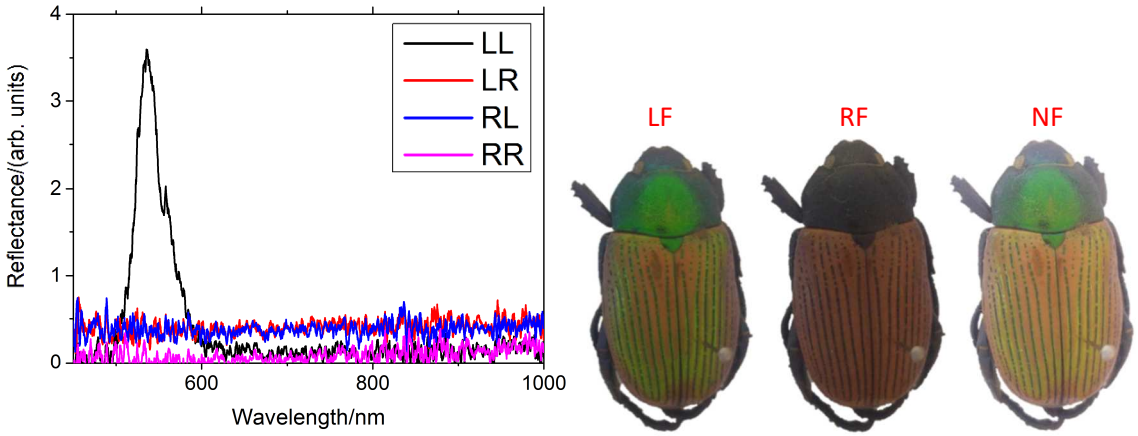


Figure A 113 – CP reflection spectra from the pronotum of a *Strigidia sanctijacobi* beetle. This specimen was collected from Ulapes, la Riojas, Argentina in 2015. The specimen measures 26mm.

A3.4 – Trichiinae

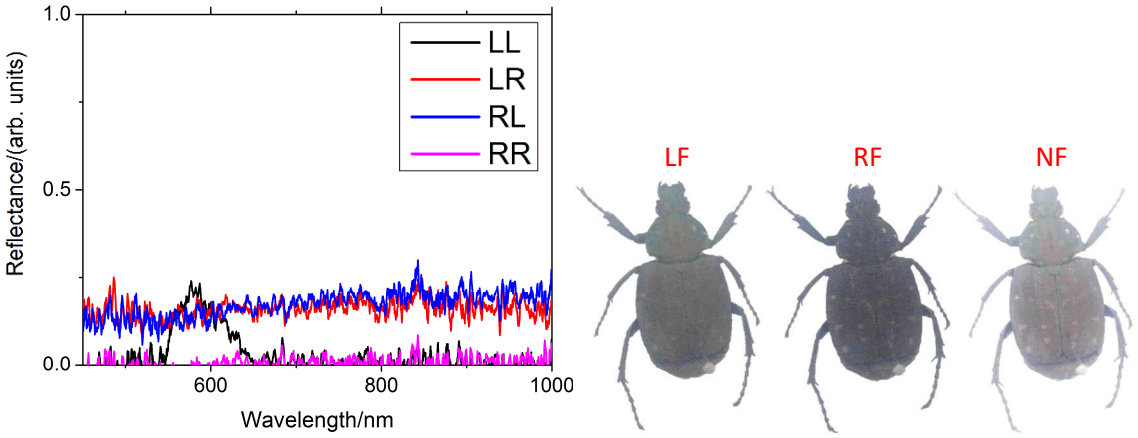


Figure A 114 – CP reflection spectra from the elytron of a *Gnorimus subopacus* beetle. This specimen was collected from Kalinovka, Pirmorskiy Kray, Russia in 2016. Taken with an integration time of 500ms. The specimen measures 22mm.

A3.5 - Melolonthinae

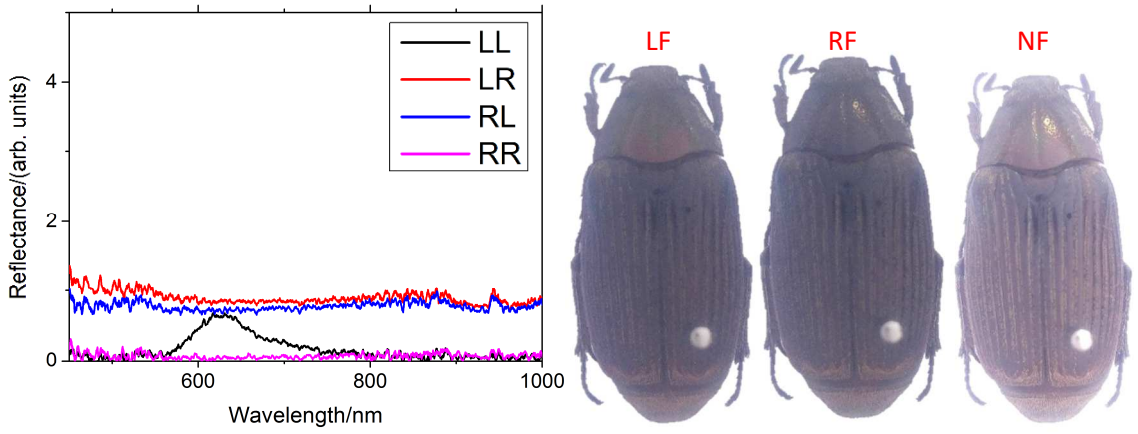


Figure A 115 – CP reflection spectra from the pronotum of a *Schoenherria hastata* beetle. This specimen was collected from Fraser Hill, Pahang, Malaysia in 2011. Taken with an integration time of 500ms. The specimen measures 29mm.

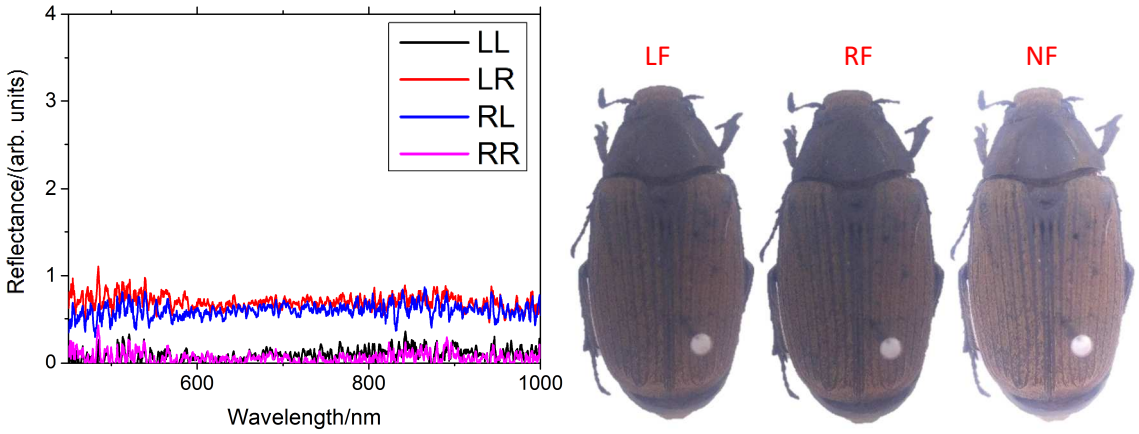


Figure A 116 – CP reflection spectra from the pronotum of a *Schoenherria hastata* beetle. This specimen was collected from Fraser Hill, Pahang, Malaysia in 2011. Taken with an integration time of 500ms.

A3.6 - Euchirinae

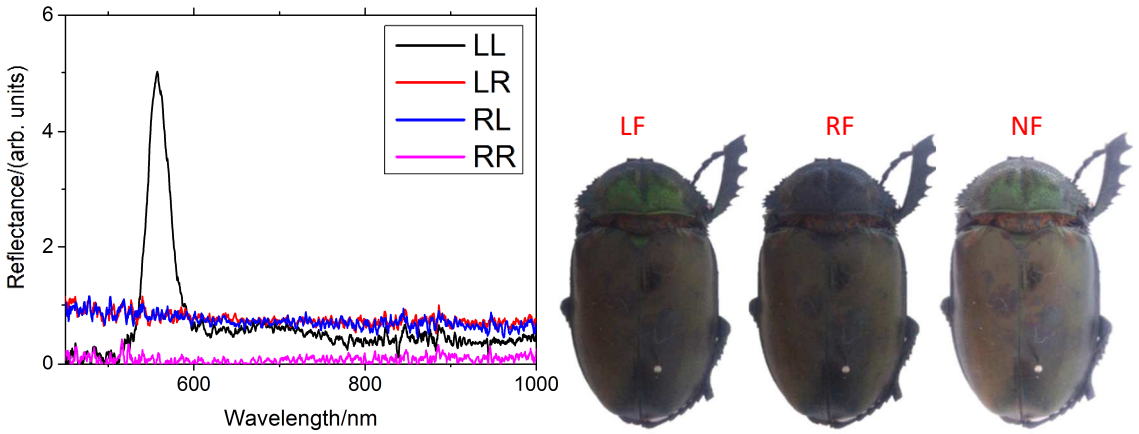


Figure A 117 – CP reflection spectra from the pronotum of a *Cheirotonus jasoni* beetle. This specimen was collected from Ba Na Mountain, Da Nang, Vietnam in 2015. The specimen measures 56mm.

A3.7 -Dynastinae

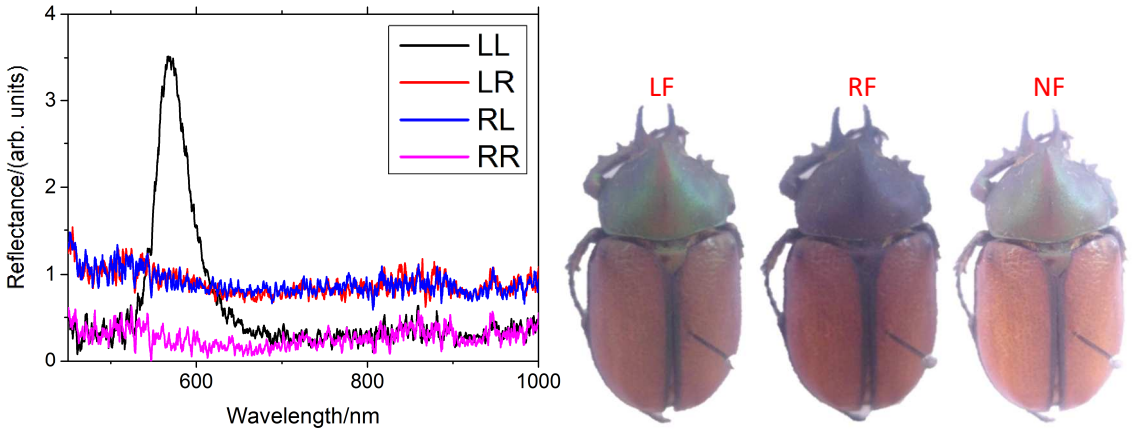


Figure A 118 – CP reflection spectra from the pronotum of an *Agaocephala urus* beetle. This specimen was collected from Águas Vermelhas, Minas Geraisin, Brasil in 2010. The specimen measures 29mm.

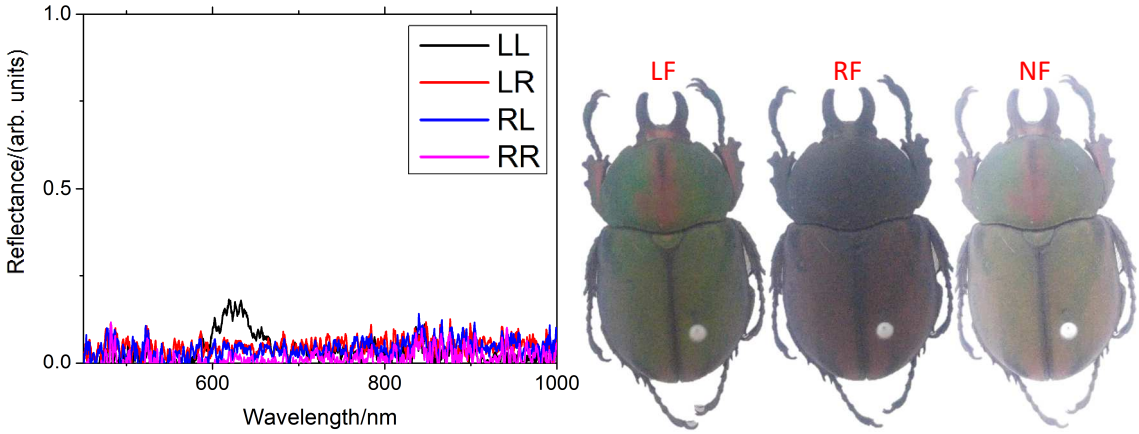


Figure A 119 – CP reflection spectra from the pronotum of an *Agaocephala bicuspis* beetle. This specimen was collected from Luepa, Gran Sabana, Venuzuela in 2015. Taken with an integration time of 500ms. The specimen measures 33mm.

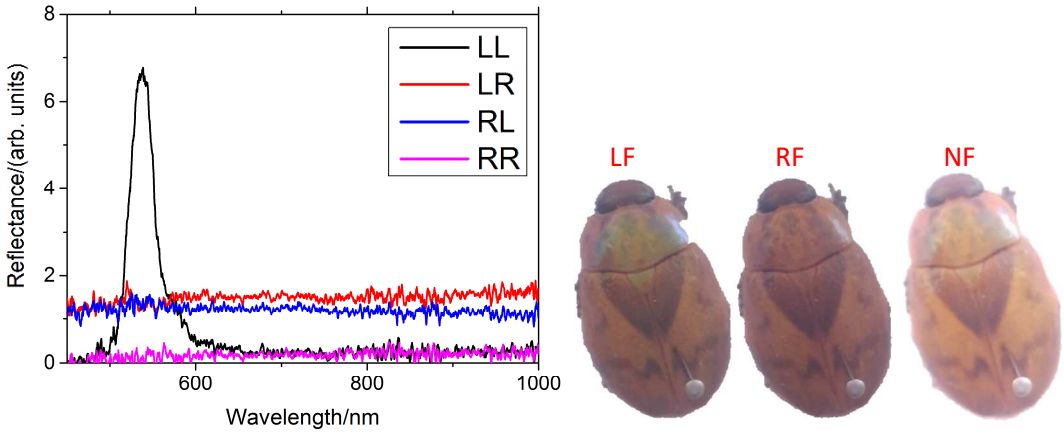


Figure A 120 – CP reflection spectra from the pornotum of an *Augoderia nitidula* beetle. This specimen was collected from Nova Fiburgo, Rio de Janiero, Brasil in 2012. The specimen measures 18mm.

A3.8 - Phaenomeridinae

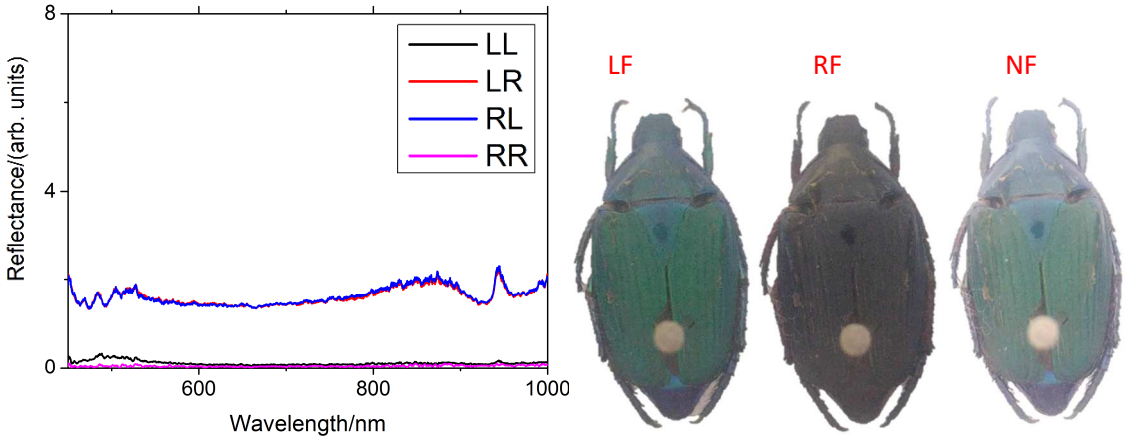


Figure A 121 – CP reflection spectra from the scutellum of a turquoise *Phaenomeris besckei* beetle. This specimen was collected from Tanzania. Taken with an integration time of 2000ms. The specimen measures 22mm.

A3.9 - Ceratocanthinae

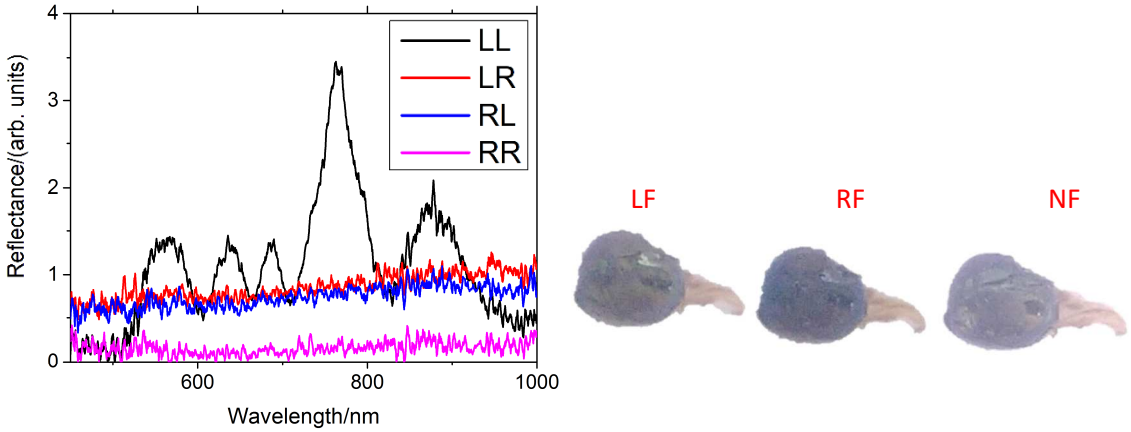


Figure A 122 – CP reflection spectra from the elytron of a *Ceratocanthus sp1.* beetle. This specimen was collected from Belizon, French Guiana in 2015. The specimen measures 5mm.

A3.10 – Underside Photographs

Further to Section 4.5.1 more underside variations were observed through CP filters.

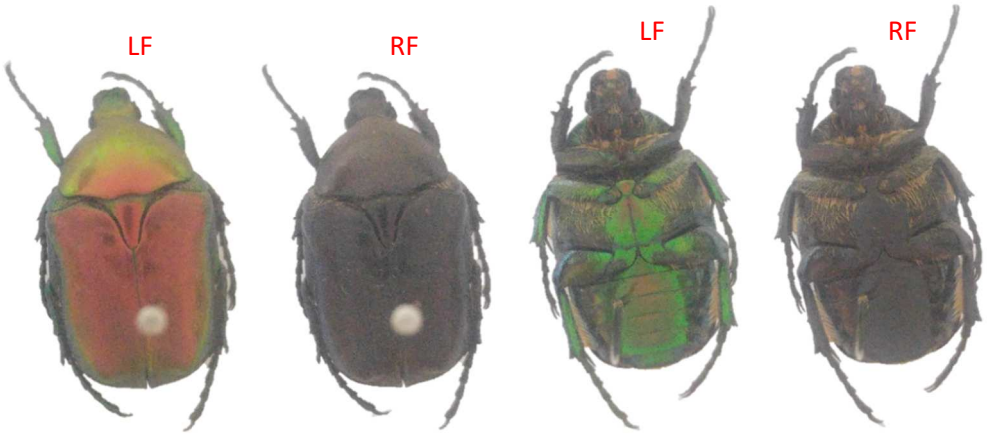


Figure A 123 – Photographs with CP filters of the upper side and underside of a *Protaetia angustata* pyrodea beetle.

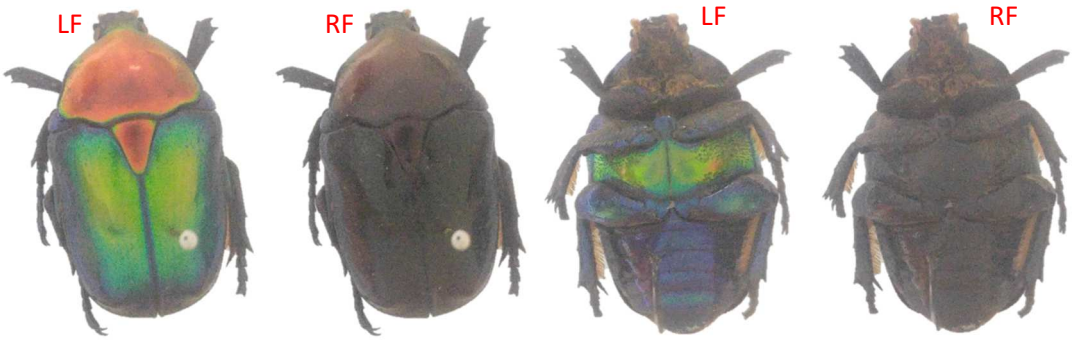


Figure A 124 – Photographs with CP filters of the upper side and underside of a *Protaetia speciosa jousselini* beetle.



Figure A 125 – Photographs with CP filters of the upper side and underside of a *Diabroctis mimas* beetle.

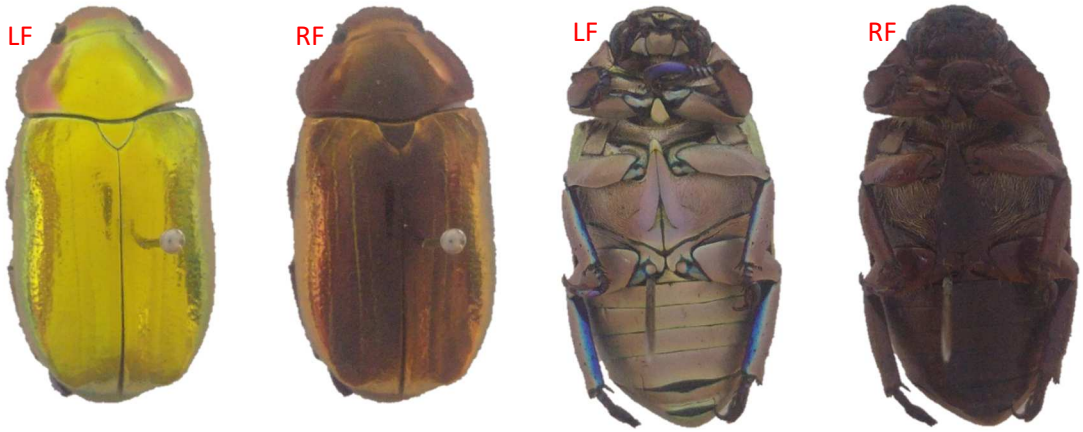


Figure A 126 – Photographs with CP filters of the upper side and underside of a *Chrysina aurigans* beetle.

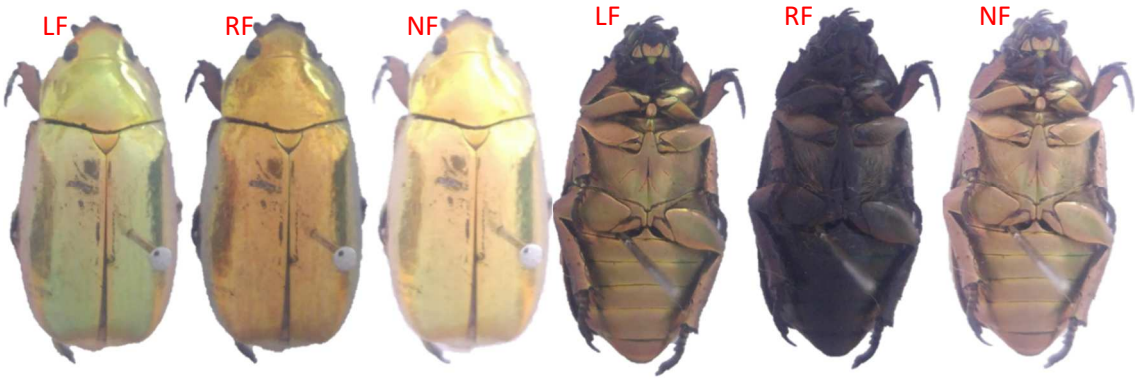


Figure A 127 – Photographs with and without CP filters of the upper side and underside of a *Chrysina resplendens* beetle.

A3.11 – Angular Variation

Further to Section 4.5.2 more angular variations were observed through CP filters.

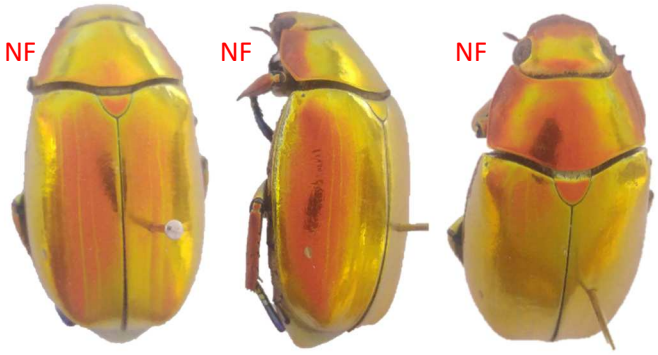


Figure A 128 – Photographs without of filter of a gold *Chrysina chrysargyrea* specimen at different angles.



Figure A 129– Photographs without of filter of a *Protaetia aeruginosa* specimen at different angles.

A4 - Modelling

Several basic modelling parameters are demonstrated in this section, the refractive index of the two orientations within a chitin layer was set to n_1=1.40 and n_2=1.45. The number of half pitches was set to 15 and the number of sublayers was set to 750. These three variables were varied in turn to demonstrate the effects upon model (in terms of bandwidth and reflectance intensity), the first of which is variation in birefringence (Figure A 130). The birefringent variation does not appear to greatly alter the peak width, but as the birefringence increases so does the reflectance.

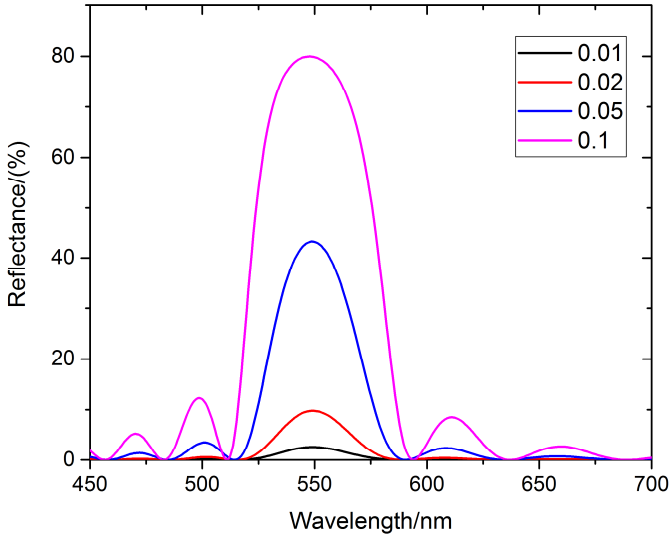


Figure A 130 – Birefringence variation in the model, from 0.01 to 1, keeping the lower refractive index n_1=1.40.

The variation in the number of half layers can be seen in Figure A 131. It can be seen that as the number of pitches decreases, then the reflectance decreases and also widens.

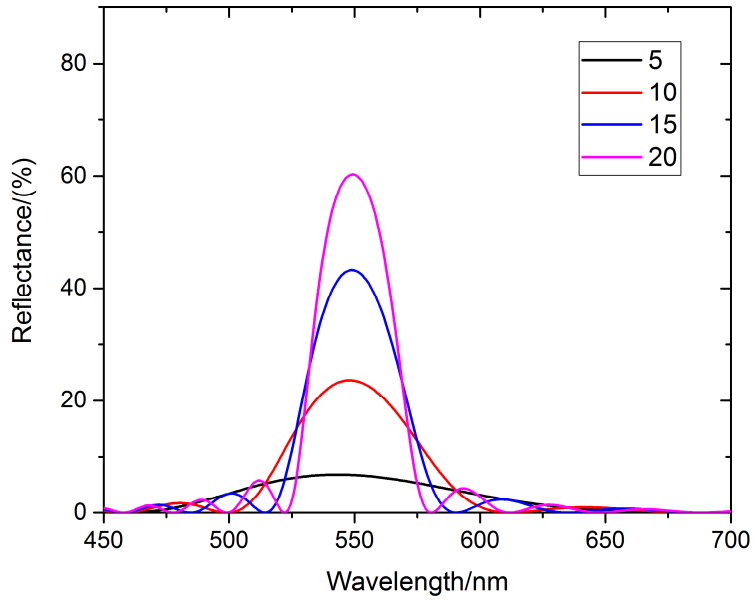


Figure A 131 – Variation in number of half pitches in the model.

The number of sublayers (or individual chitin layers) were also varied in the model, in Figure A 132. The number of sublayers seems to have little influence in responses for the values used.

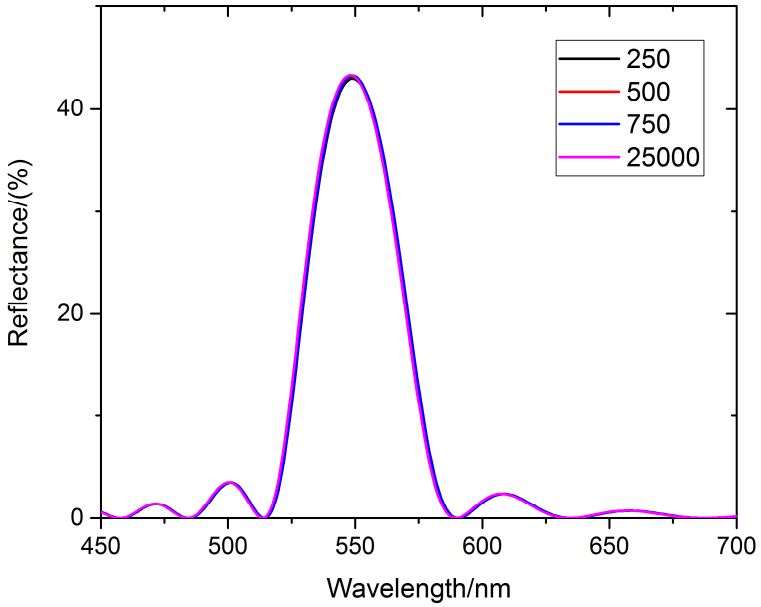


Figure A 132 – Variation in number sublayers in the model.

A4.1 - Modelling Parameters

The modelling parameter for the Figures in the modelling Chapter (5) are listed in Tables A 1-3.

	n1	n2	δn	k	Number of pitch values	Total pitches	Phase shifts/numbers
a)	1.48	1.5	0.02	0.01	1	10	0
b)	1.475	1.52	0.045	0.025	2	11	1
c)	1.487	1.52	0.033	0.0085	1	13.5	2
d)	1.48	1.52	0.04	0.009	1	14	3
e)	1.49	1.52	0.03	0.018	5	31.5	0
f)	1.5	1.58	0.08	0.0007	3	15	0
Average	1.49	1.53	0.041	0.012	2.2	15.8	

Table A 1 – Modelling parameters corresponding to Figure 5.14.

	n1	n2	δn	k	Number of Pitch Values	Total Pitches	Phase Shifts/numbers
a)	1.507	1.52	0.013	0.0028	7	16.5	0
b)	1.505	1.52	0.015	0.004	4	15	3
c)	1.451	1.52	0.069	0.023	1	8	1
d)	1.485	1.5	0.015	0.004	1	6.5	0
e)	1.48	1.5	0.02	0.008	1	6.5	0
f)	1.485	1.5	0.015	0.008	1	3.5	0
g)	1.48	1.5	0.02	0.004	1	7.5	0
h)	1.485	1.5	0.015	0.008	1	3.5	0
i)	1.48	1.52	0.04	0.017	7	3.1	0
Average	1.48	1.51	0.025	0.009	2.7	7.8	

Table A 2 – Modelling parameters corresponding to Figure 5.15. Involving refractive index n_1, n_2, birefringence **δn**, **k** (absorption) value, number of pitch values, the total pitches and number of phase shifts.

	n1	n2	δn	k	Number of pitch values	Total pitches	Shortest wavelength/nm
Silver	1.5	1.58	0.08	0.0007	43	83.9	446.6
Gold	1.5	1.58	0.08	0.0007	36	65.6	505.2
Red	1.5	1.58	0.08	0.0007	22	35.1	1.91
Average	1.5	1.58	0.08	0.0007	33.7	61.5	

Table A 3 – Modelling parameters corresponding to Figure 5.16.

A5 – Mueller Matrix Ellipsometer Alternative Methods

The ellipsometer was initial tried in various different setup arrangements and a different method to that described in Chapter 6. The first method discussed here used 16 different individual polarisation measurements as in Table A 4 [63], where the first letter denotes the incoming polarisation and the second letter denotes the measured or outgoing polarisation, the MM was calculated. The possible polarisations are horizontal (H), vertical (V), +45° (P) and right circularly polarised (R). It should be noted that only one LCVR was available and as such the measurements RR could not be taken and hence M_{33} could not be calculated in Section A5.2.

M_{00}=HH+HV+VH+VV	M_{01}=HH+HV-VH-VV	M_{02}=2PH+2PV-M_{00}	M_{03}=2RH-2RV-M_{00}
M_{10}=HH-HV+VH-VV	M_{11}=HH-HV-VH+VV	M_{12}=2PH-2PV-M_{10}	M_{13}=2RH-2RV-M_{10}
M_{20}=2HP+2VP-M_{00}	M_{21}=2HP-2VP-M_{01}	M_{22}=4PP-2PH-2PV-M_{20}	M_{23}=4RP-2RH-2RV-M_{20}
M_{30}=2HR+2VR-M_{00}	M_{31}=2HR-2VR-M_{01}	M_{32}=4PR-2PH-2PV-M_{30}	M_{33}=4RR-2RH-2RV-M_{30}

Table A 4 – MM and how to calculate using 16 different polarisation arrangements.

A5.1 - Fresnel rhombs

The experimental setup based upon using Fresnel rhombs and polarising cubes in transmission was used (Figure A 133). This setup was used with different polarisation inputs and outputs for transmission in air to calculate the Muller matrix elements in Table A 4. These were plotted over a broadband range (Figure A 134). The elements in Figure A 134a, ideally should be 1, however the elements deviate from 1 (especially m33). In Figure A 134b the elements should ideally be to zero, however a large error can be seen. This error is largely thought to be due to having to move the position of the Fresnel rhomb and linear polarising cubes, which unlike sheet polarisers change the light path.

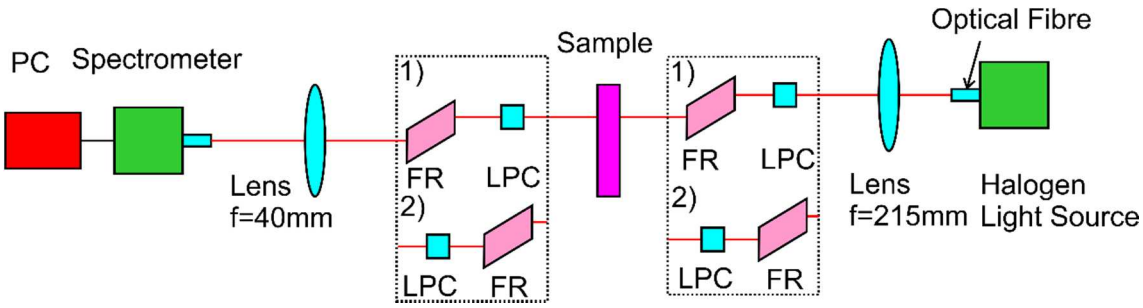


Figure A 133 – Transmission ellipsometer setup, with two independent positions for each arm of 1 and 2, with Fresnel rhombs (FR) and linear polarising cubes (LPC).

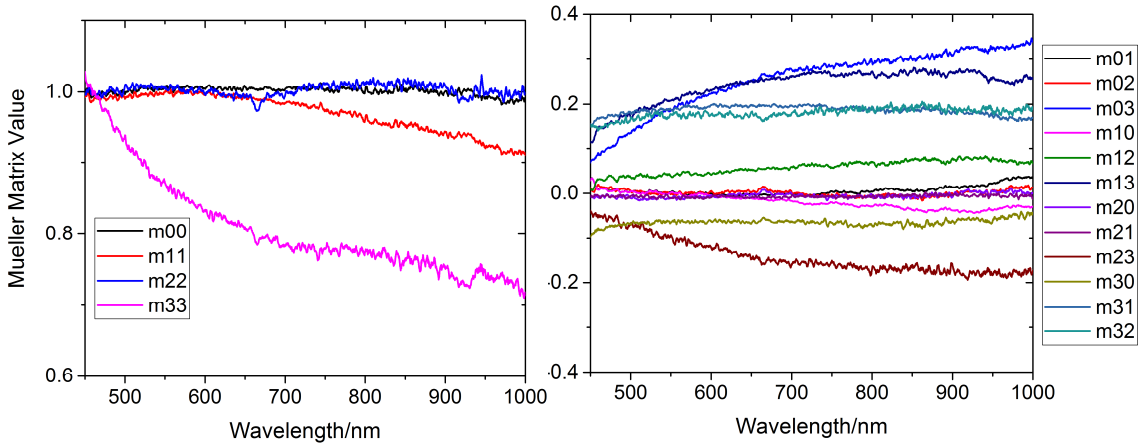


Figure A 134 – MM of purely Fresnel rhomb setups in transmission with air as a sample.

A5.2 - LCVR in one side-air

In this setup a LCVR was used as a one quarter (and a three quarter) waveplate for broadband measurements. The retardance values for each of these values were found using the method to find the retardance of a LCVR (Section 6.4.1). The setup had two independent positions (for the LCVR and linear polarising cube) for each arm in order to calculate the MM elements as in Table A 4.

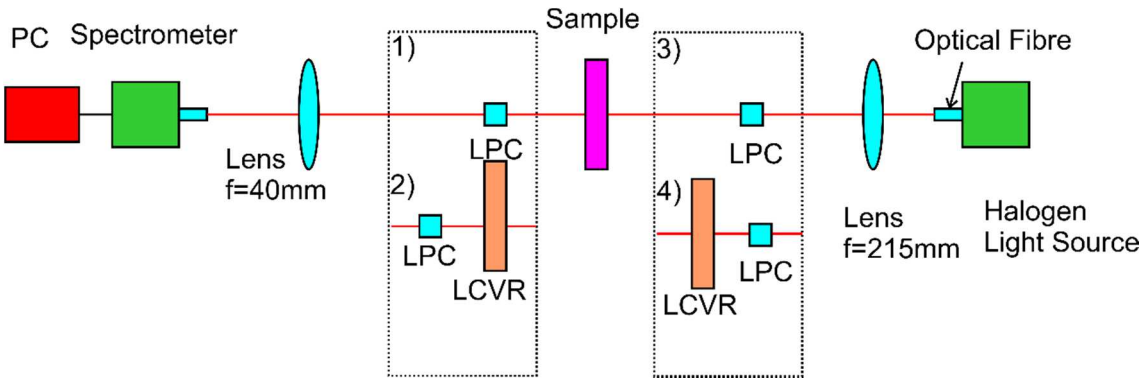


Figure A 135 – Transmission ellipsometer setup, with two independent positions for each arm of 1 and 2 (in the first arm) and of 3 and 4 (in the second arm), with a liquid crystal variable retarder (LCVR) and linear polarising cubes (LPC).

450nm			
1.00	0.03	0.01	0.04
0.03	0.99	0.01	0.04
-0.01	-0.01	1.00	0.05
0.06	-0.04	-0.05	N/A
650nm			
1.00	0.00	0.00	0.03
-0.01	0.99	0.05	0.06
0.00	-0.01	0.98	0.03
0.07	-0.05	-0.06	N/A
850nm			
1.00	0.00	-0.01	0.00
-0.04	0.95	0.08	0.07
-0.01	0.00	1.01	0.03
0.04	-0.06	-0.02	N/A

Table A 5 – MM for transmission through air at three different wavelengths; 450nm, 650nm and 850nm. Noting that element M_{33} is absent as only 1 LCVR was available. Theoretically this should be a diagonal matrix where $M_{00}=M_{11}=M_{22}=M_{33}=1$.

The MM transmission through air was calculated using this method for each of the three wavelengths (Table A 5).

Further to finding the MM of air, the MM of a quarter wave plate (of working wavelength 560nm) was obtained in Table A 6, again without matrix element M_{33}. The largest error in this MM is in the element M_{13} of 11.2%.

1.000	0.070	-0.020	0.075
0.055	0.953	-0.093	-0.071
0.032	-0.056	-0.027	-1.025
0.015	-0.112	0.995	N/A

Table A 6 – MM obtained experimentally for a quarter waveplate which operating wavelength is 560nm, where the fast axis is vertical. The theoretical values would be zero for all elements except M_{00}, M_{11}, M_{20} which should be 1 and $M_{32}=-1$.

A5.3 - Rotating only waveplates

The same calibration method as described in Chapter 6 was used in this setup. This setup had an advantage over the LCVR setup in that it is relative cheap in the components (using small

squares of linear polaroid sheet (LP) and a sheet quarter waveplate (QP)) (Figure A 136). The recorded transmission matrix for an 86° linear polariser was made (Figure A 137) this compared to Figure 6.18 in the LCVR calibration setup. It can be seen that this rotating waveplate setup is comparable in accuracy to the LCVR setup.

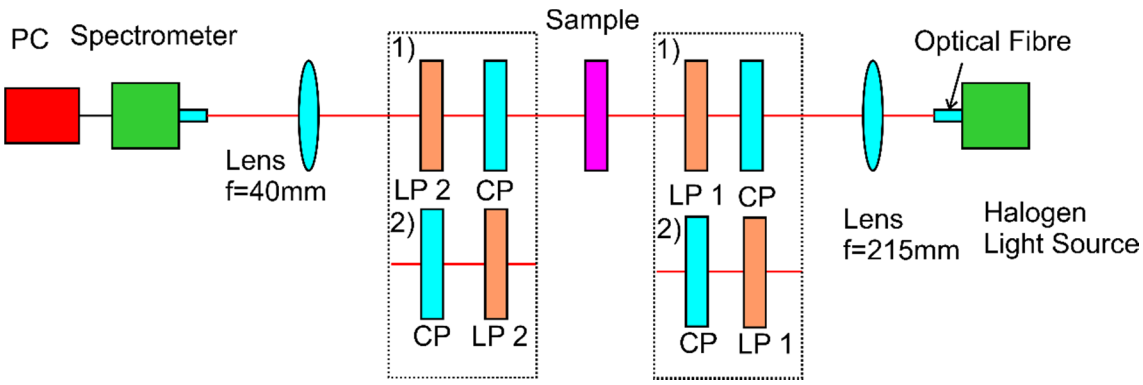


Figure A 136 – Transmission ellipsometer setup, with two independent positions for each arm of 1 and 2, with sheet linear polaroid (LP) and quarter waveplates (CP).

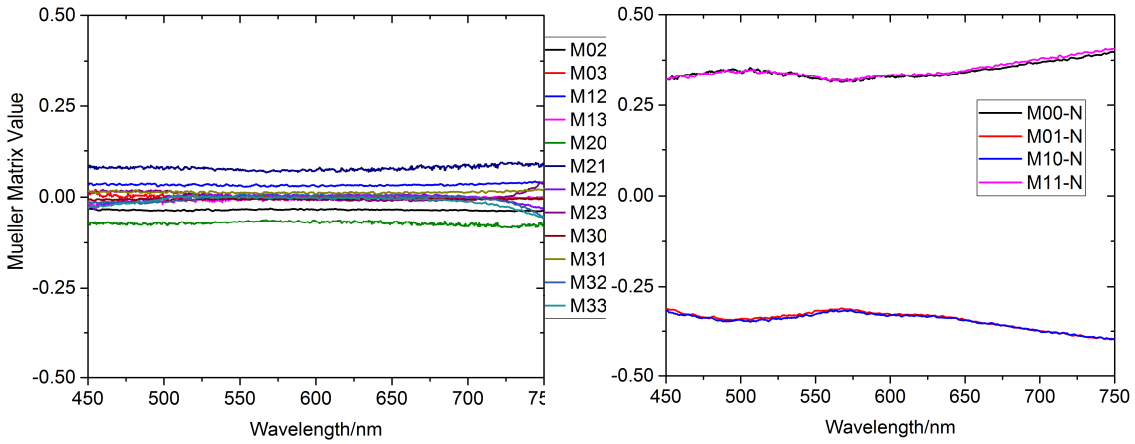


Figure A 137 – MM of purely rotatable system (with sheet linear polarisers and quarter waveplates) for a linear polariser in transmission at 86°.

A5.4 - Stability of LCVR

The stability of the LVCRs was given by the manufacturer in terms of temperature (Figure A 138) and also time (Figure A 139).

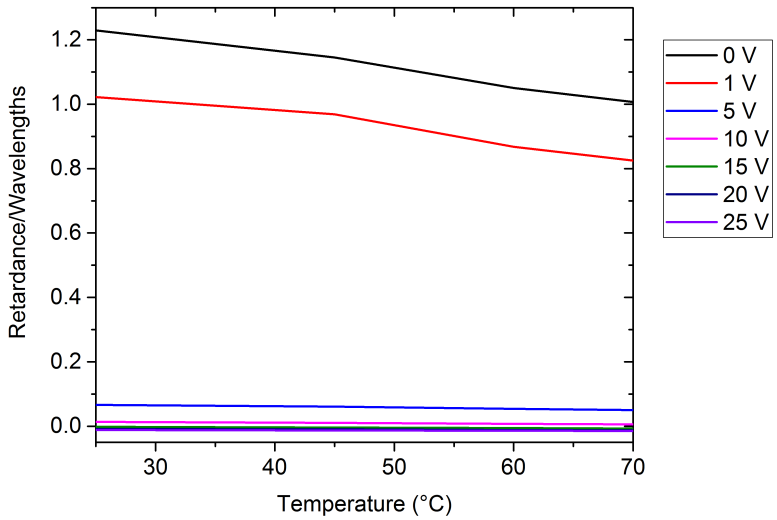


Figure A 138 – Temperature stability with driving voltage for a similar LCVR using data from the manufacturer [64].

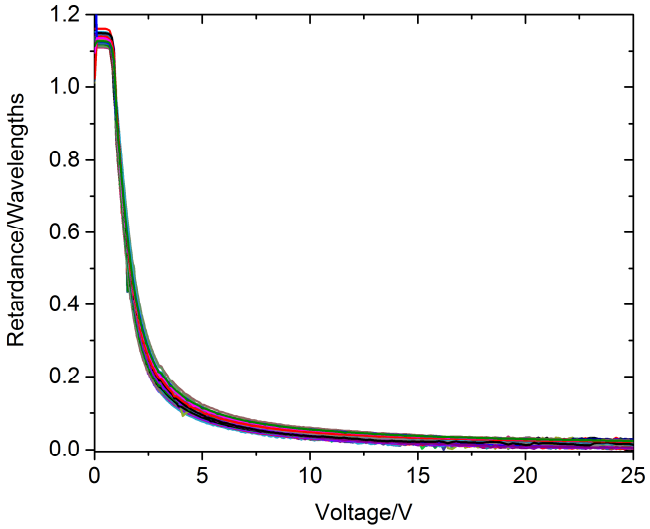


Figure A 139 – Long term stability over 154 weeks for a similar LCVR using data from the manufacturer [64].

A5.5 - LCVR MM Setup Delta Function

For the LCVR ellipsometer setup (Figure 6.1), different voltage combinations were investigated. The voltage combinations varied between four, five and six combinations. In this section the best and worst four (Figure A 141 and Figure A 140) and five (Figure A 142 and Figure A 143) combinations of voltage are presented.

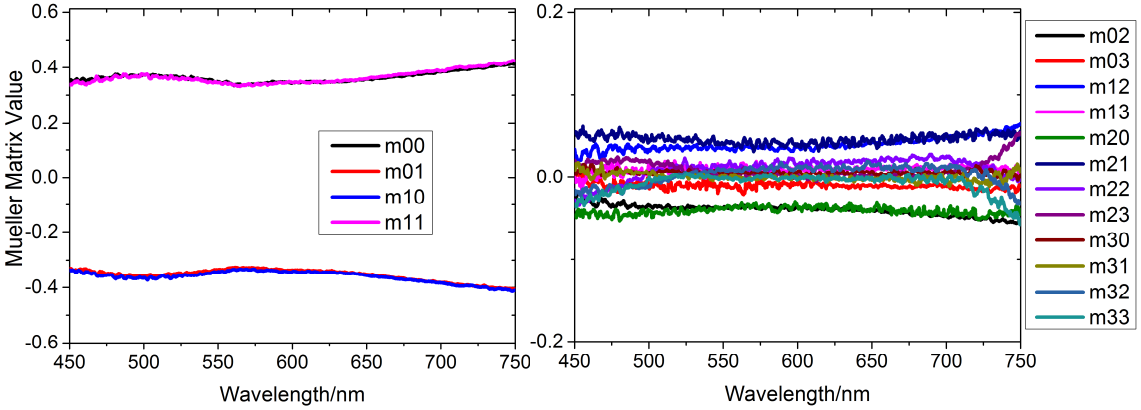


Figure A 140 – The best MM spectral results with four voltages combinations of the two LCVRs of (2.277V, 6.6V), (2.277V, 25.0V), (3.777V, 6.6V) and (3.777V, 25.0V), using a linear polariser at 86° as the test sample in transmission.

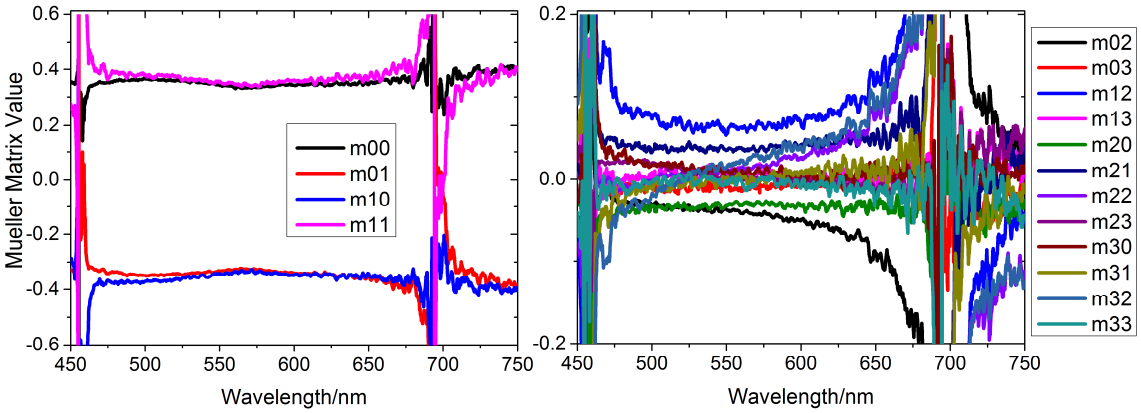


Figure A 141 – The worst MM spectral results with four voltage combinations of the two LCVRs of (2.277V, 25.0V), (6.494V, 25.0V), (3.777V, 6.6V) and (3.777V, 25.0V), using a linear polariser at 86° as the test sample in transmission.

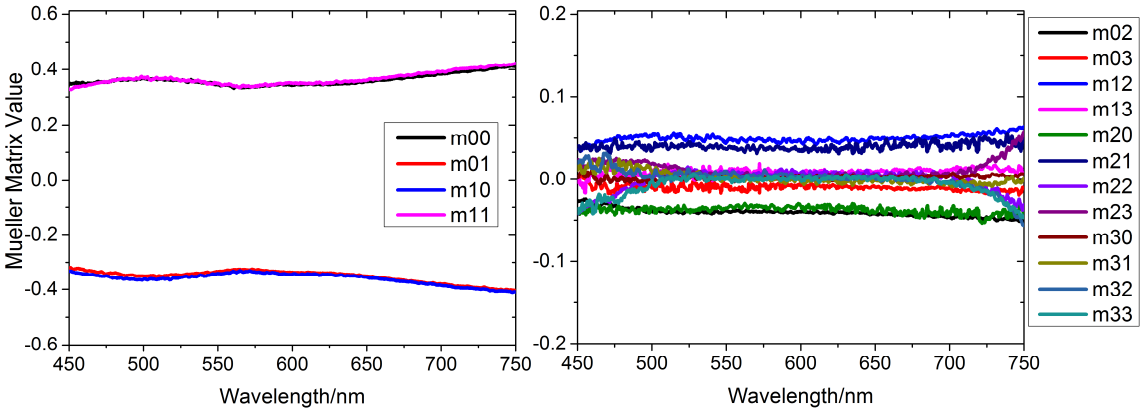


Figure A 142 – The best MM spectral results with five voltages combinations of the two LCVRs of (2.277V, 25.0V), (6.494V, 6.6V), (6.494V, 25.0V), (3.777V, 6.6V) and (3.777V, 25.0V), using a linear polariser at 86° as the test sample in transmission.

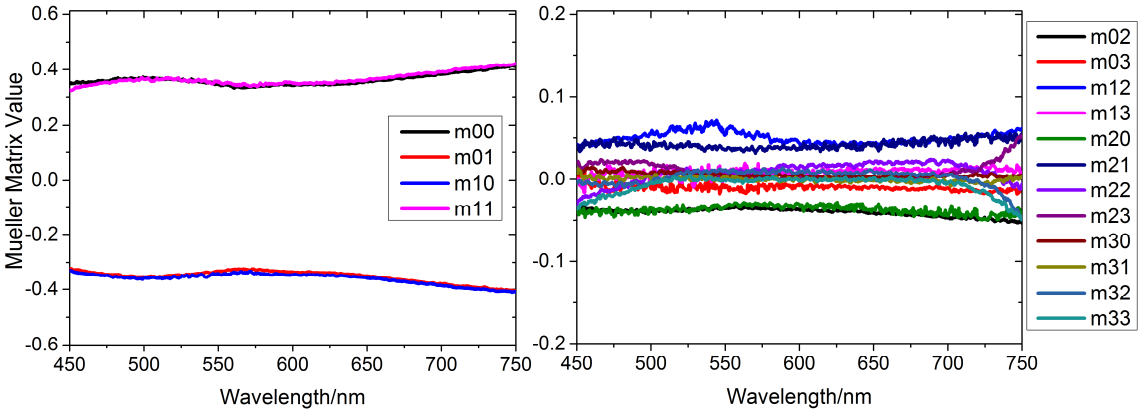


Figure A 143 – The worst MM spectral results with five voltages combinations of the two LCVRs of (2.277V, 6.6V), (2.277V, 25.0V), (6.494V, 6.6V), (6.494V, 25.0V), (3.777V, 6.6V) and (3.777V, 25.0V), using a linear polariser at 86° as the test sample in transmission.

A5.6 – Beetle MM

A5.6.1 - Typical species from each subfamily

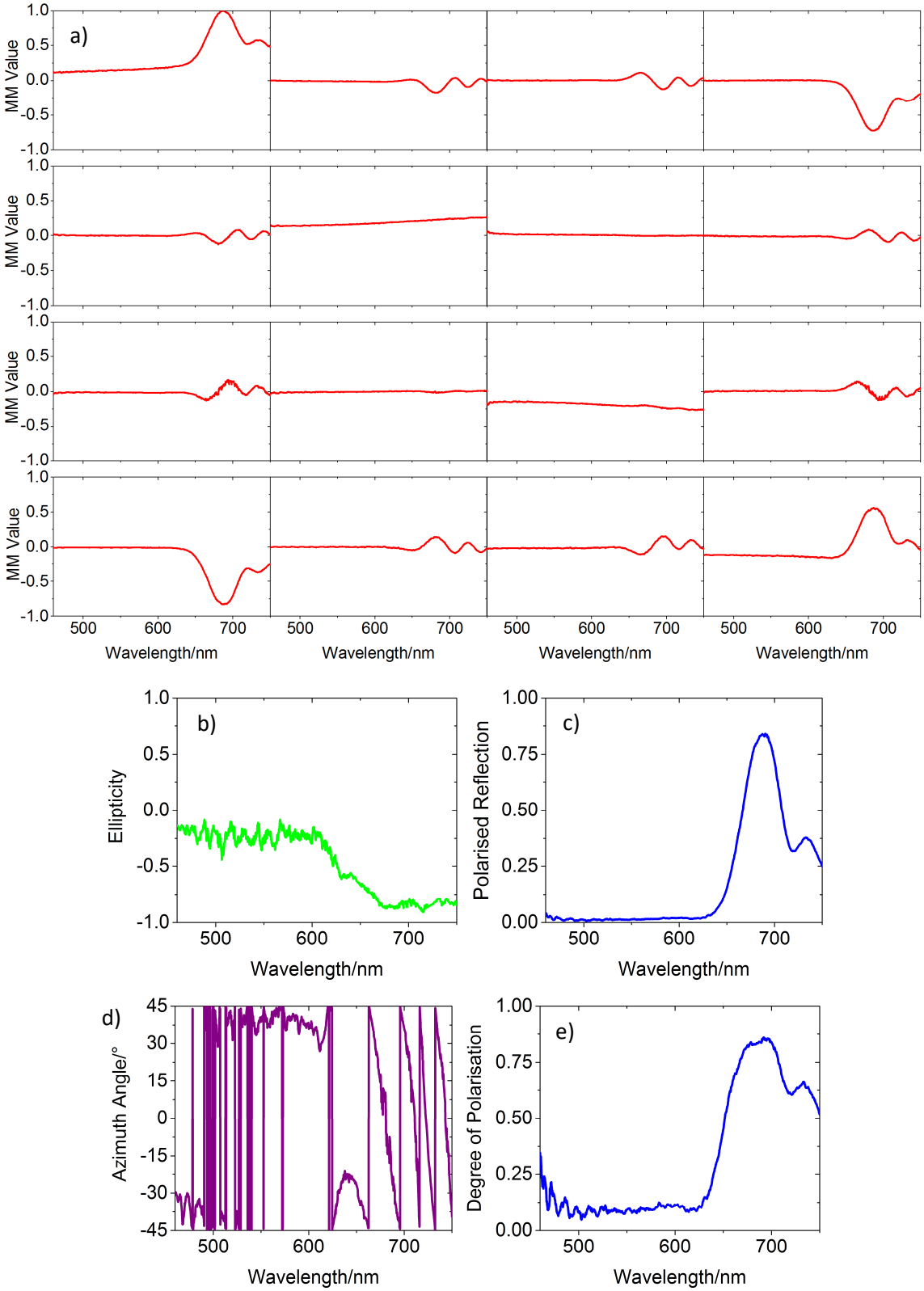


Figure A 144 – a) Normalised MM of reflection from the elytra of a *Ceratocanthopsis fulgida* beetle. b) The ellipticity, c) the polarised reflection, d) the azimuth angle and e) the degree of polarisation.

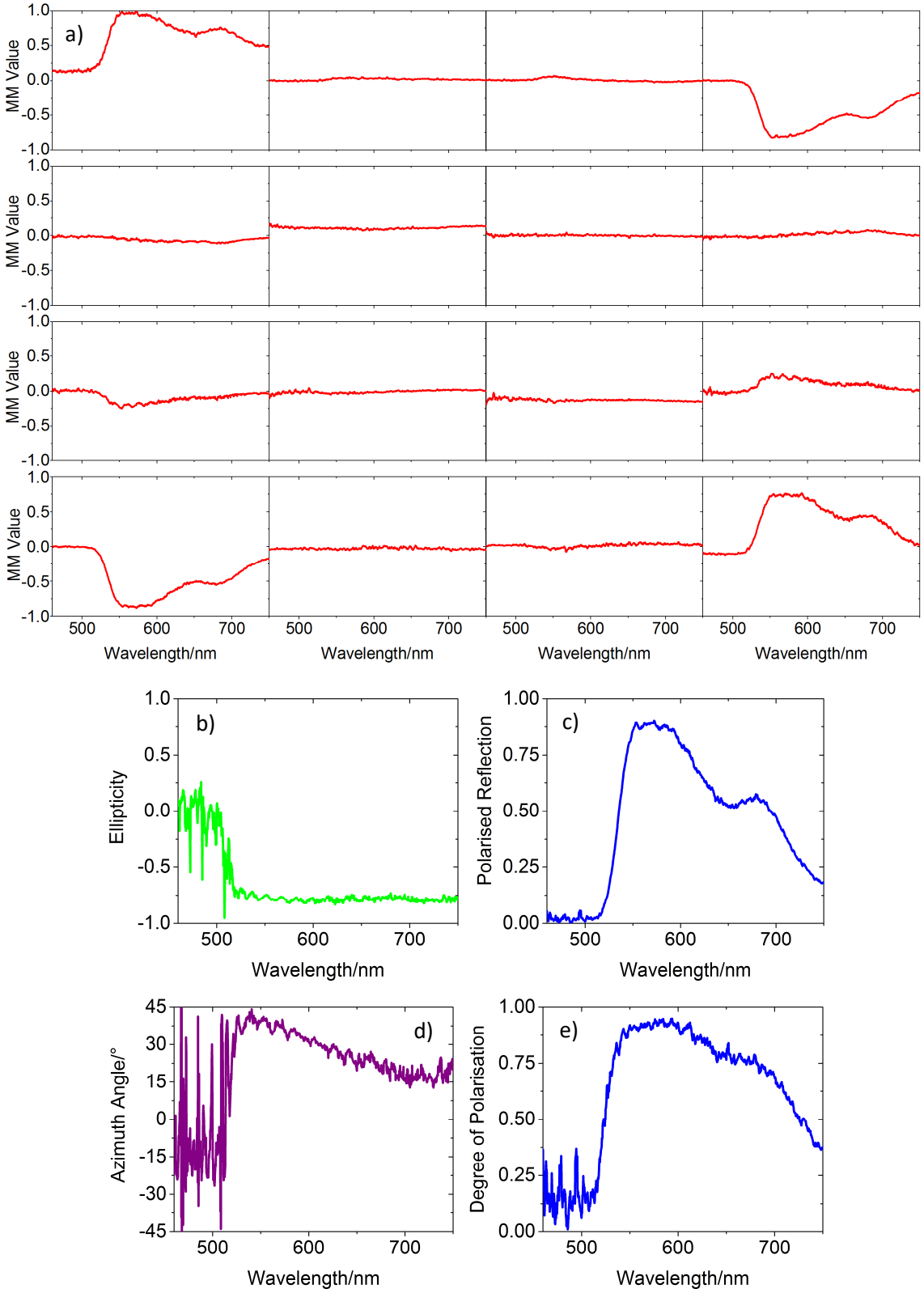


Figure A 145 – a) Normalised MM of reflection from the pronotum of a *Diabroctis mimas* beetle. b) The ellipticity, c) the polarised reflection, d) the azimuth angle and e) the degree of polarisation.

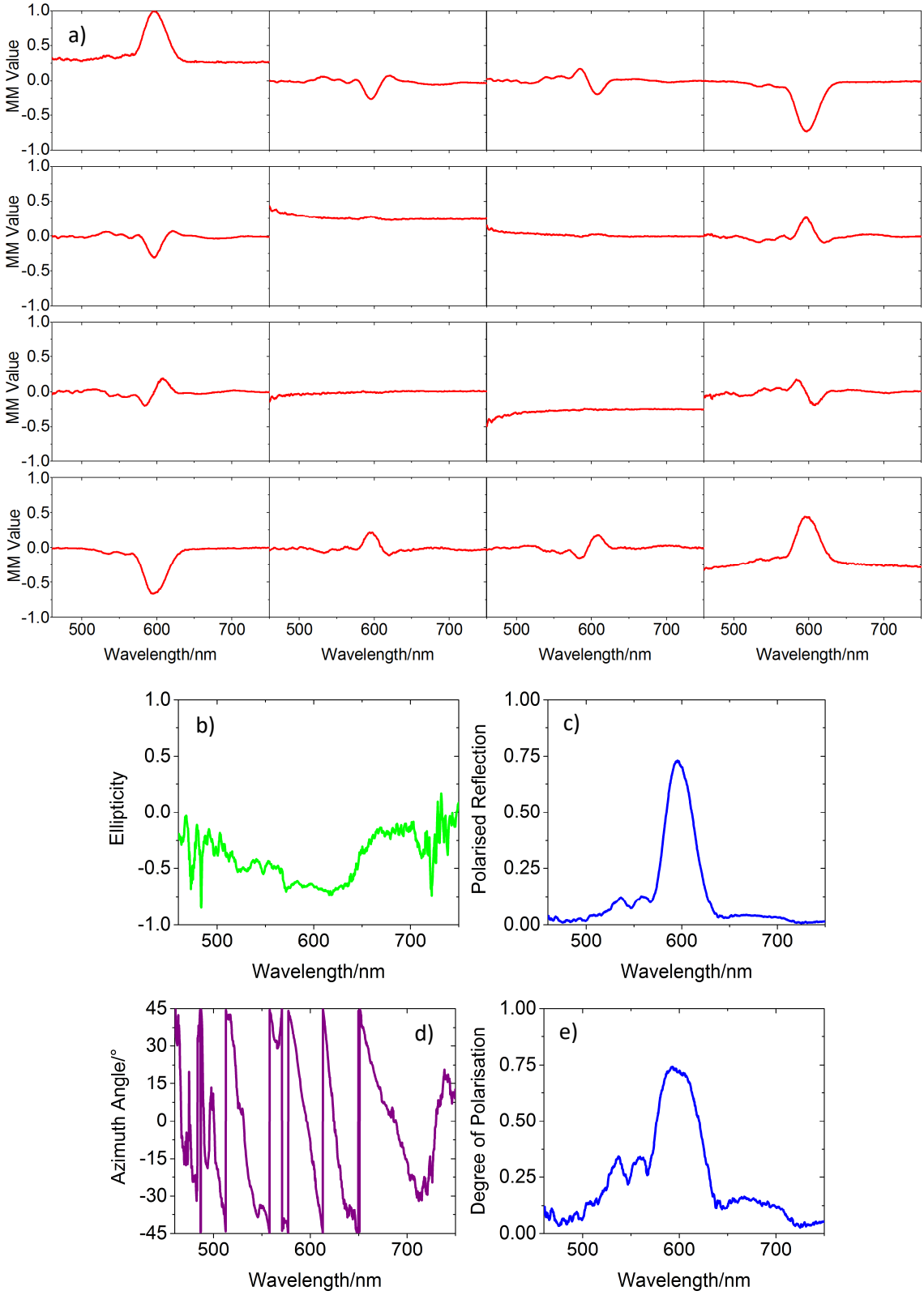


Figure A 146 – a) Normalised MM of reflection from the elytra of a *Gnorimus nobilis* beetle. b) The ellipticity, c) the polarised reflection, d) the azimuth angle and e) the degree of polarisation.

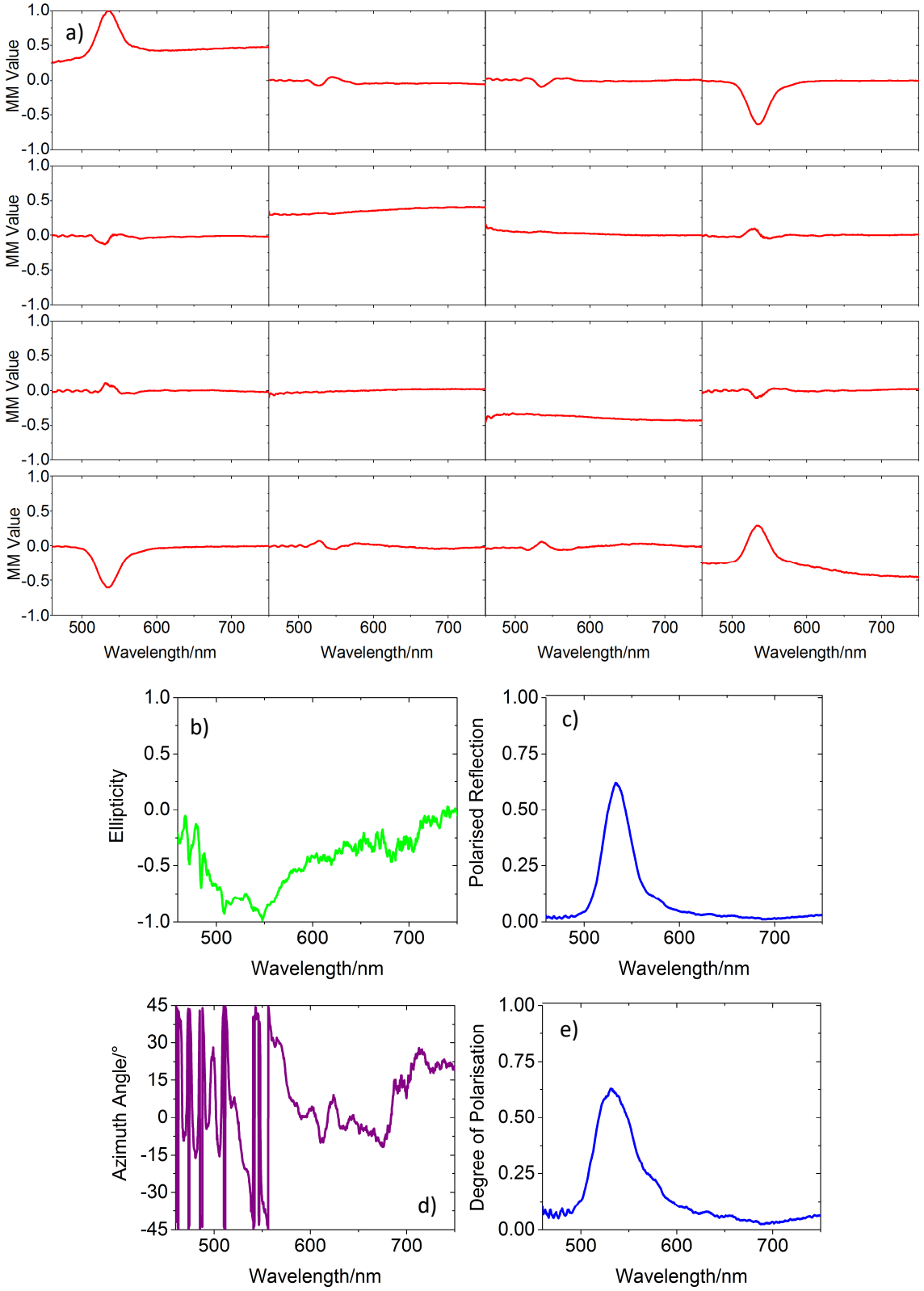


Figure A 147 – a) Normalised MM of reflection from the pronotum of an *Augoderia nitidula* beetle. b) The ellipticity, c) the polarised reflection, d) the azimuth angle and e) the degree of polarisation.

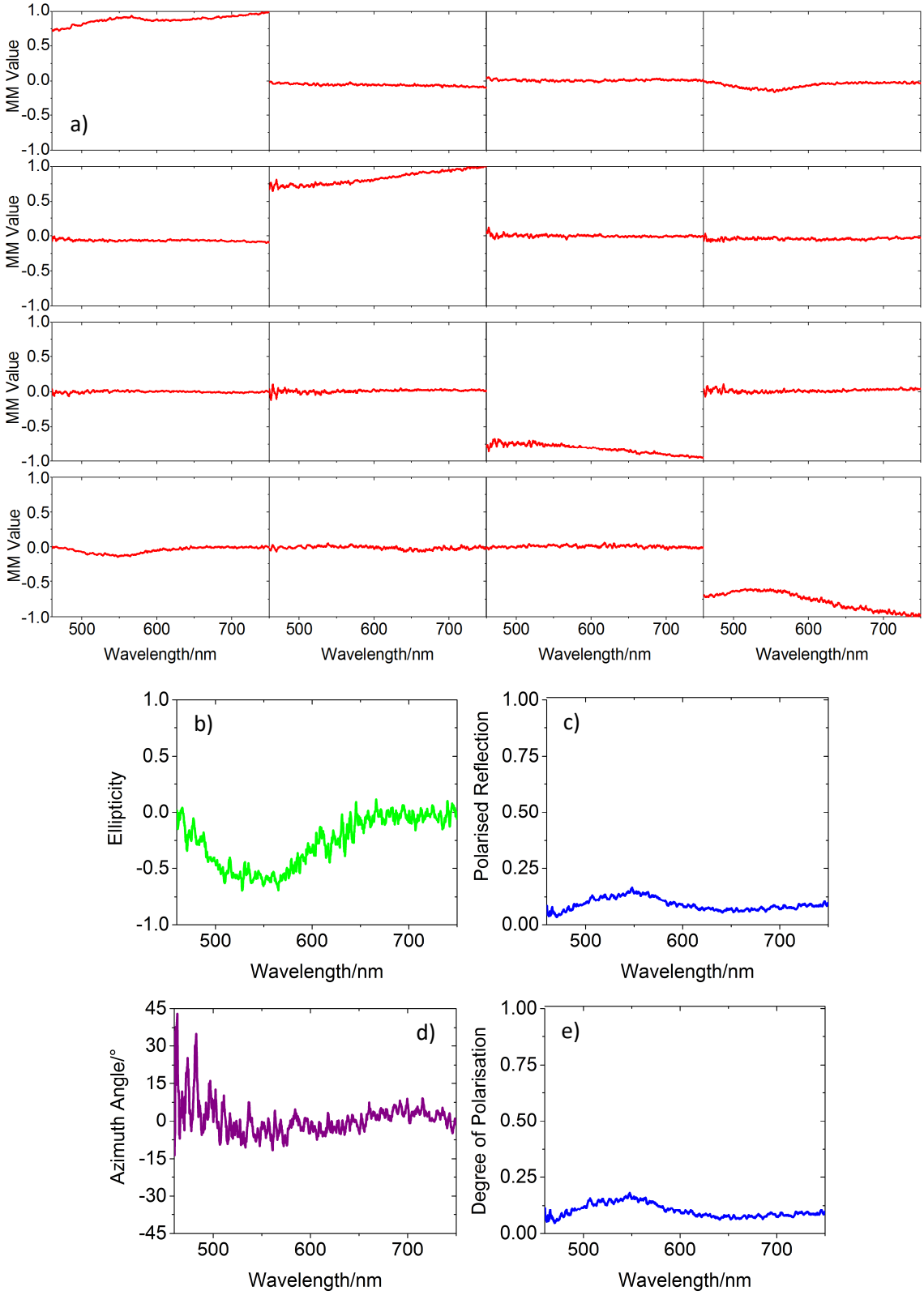


Figure A 148 – a) Normalised MM of reflection from the pronotum of a *Phaenomeris besckei* (green) beetle. b) The ellipticity, c) the polarised reflection, d) the azimuth angle and e) the degree of polarisation.

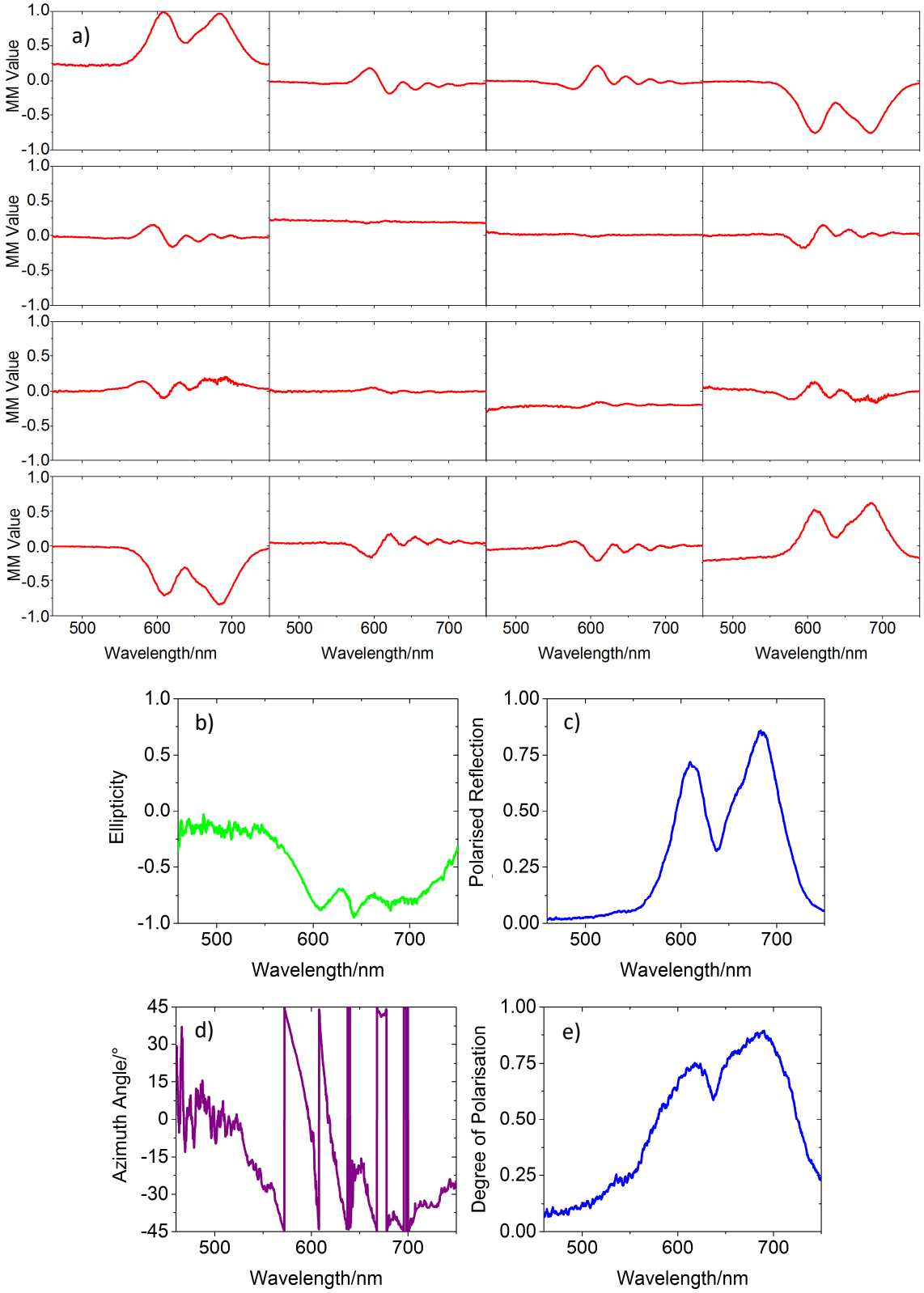


Figure A 149 – a) Normalised MM of reflection from the elytra of a *Protaetia angustata pyrodea* beetle. b) The ellipticity, c) the polarised reflection, d) the azimuth angle and e) the degree of polarisation.

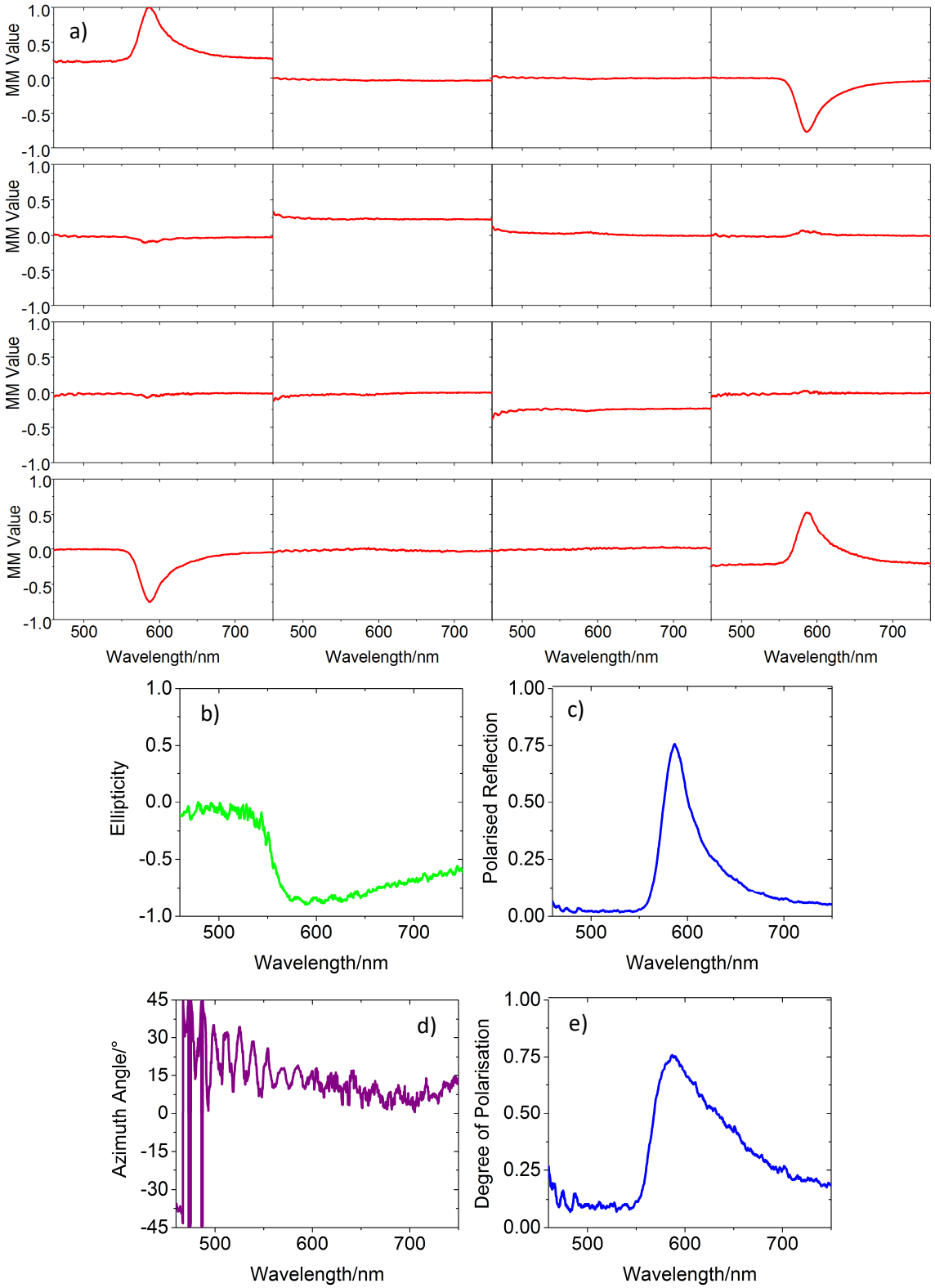


Figure A 150 – a) Normalised MM of reflection from the pronotum of a *Cheirotonus battareli* beetle. b) The ellipticity, c) the polarised reflection, d) the azimuth angle and e) the degree of polarisation.

A5.6.2 - Cetonia aurata aurata

The reflection MM from a *Cetonia aurata* of CP spectral shape (Figure 4.58) was done in this section.

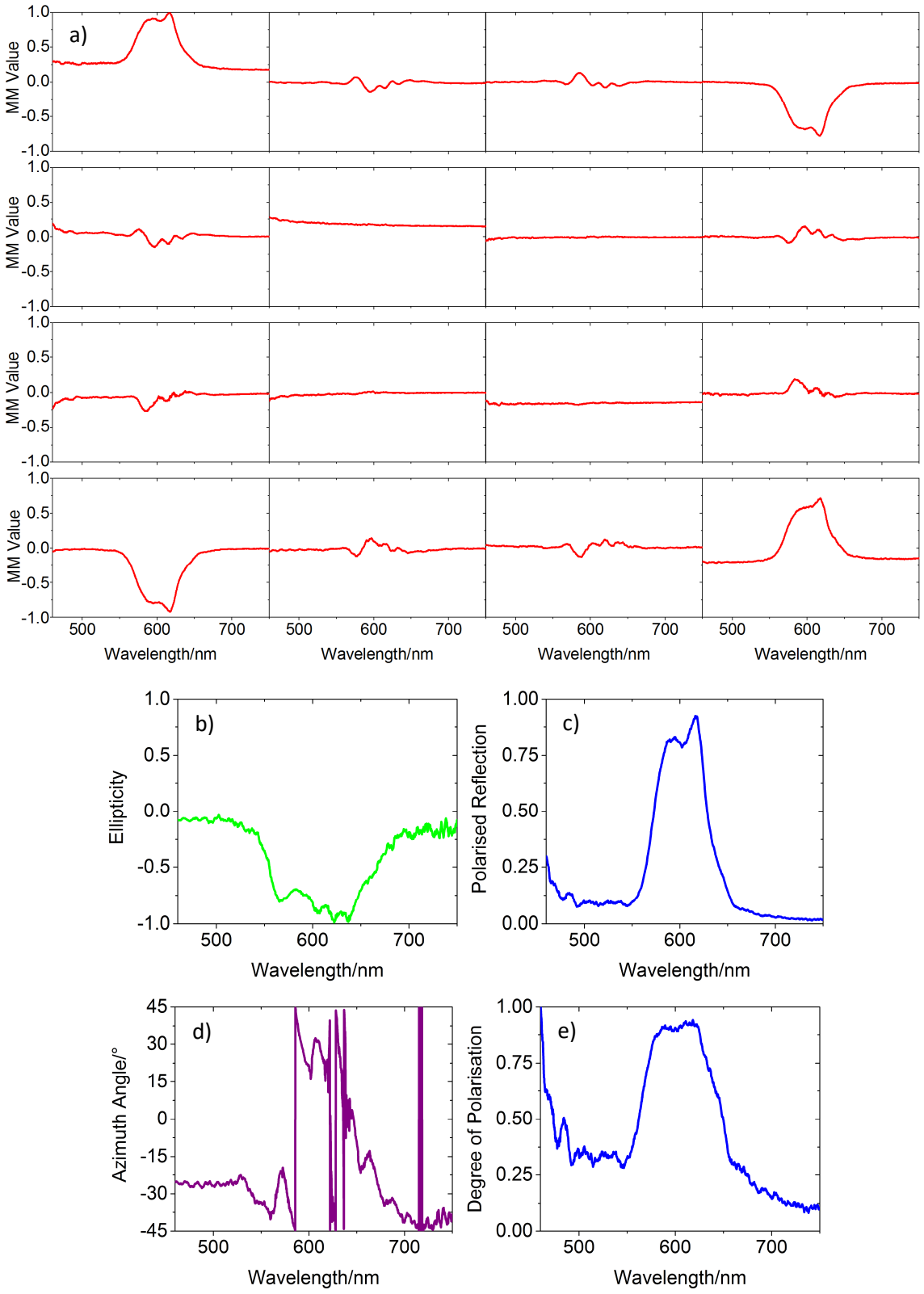


Figure A 151 – a) Normalised MM of reflection from the elytra of a *Cetonia aurata* (double close classification) beetle. b) The ellipticity, c) the polarised reflection, d) the azimuth angle and e) the degree of polarisation.

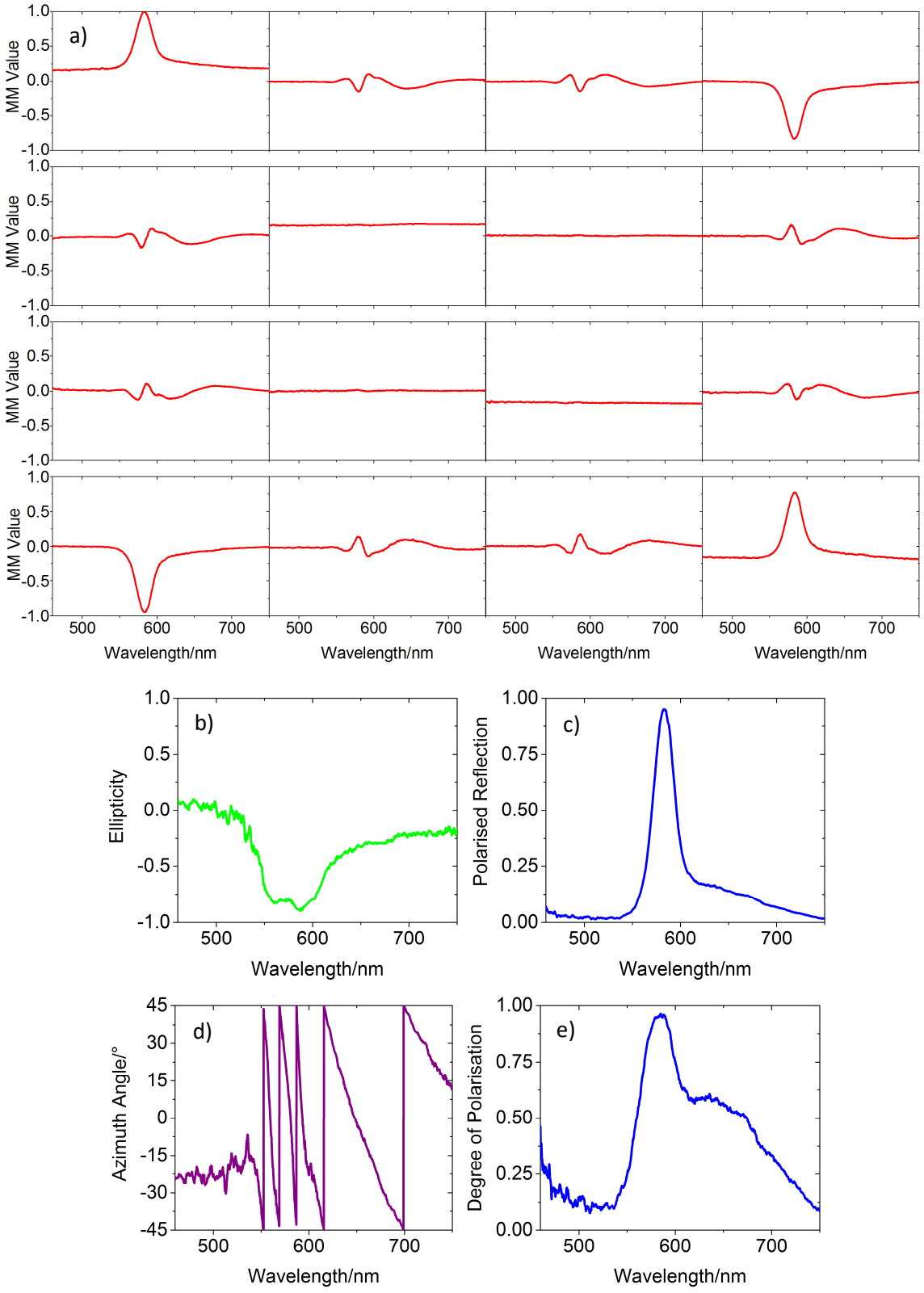


Figure A 152 – a) Normalised MM of reflection from the elytra of a *Cetonia aurata* (single peak classification) beetle. b) The ellipticity, c) the polarised reflection, d) the azimuth angle and e) the degree of polarisation.

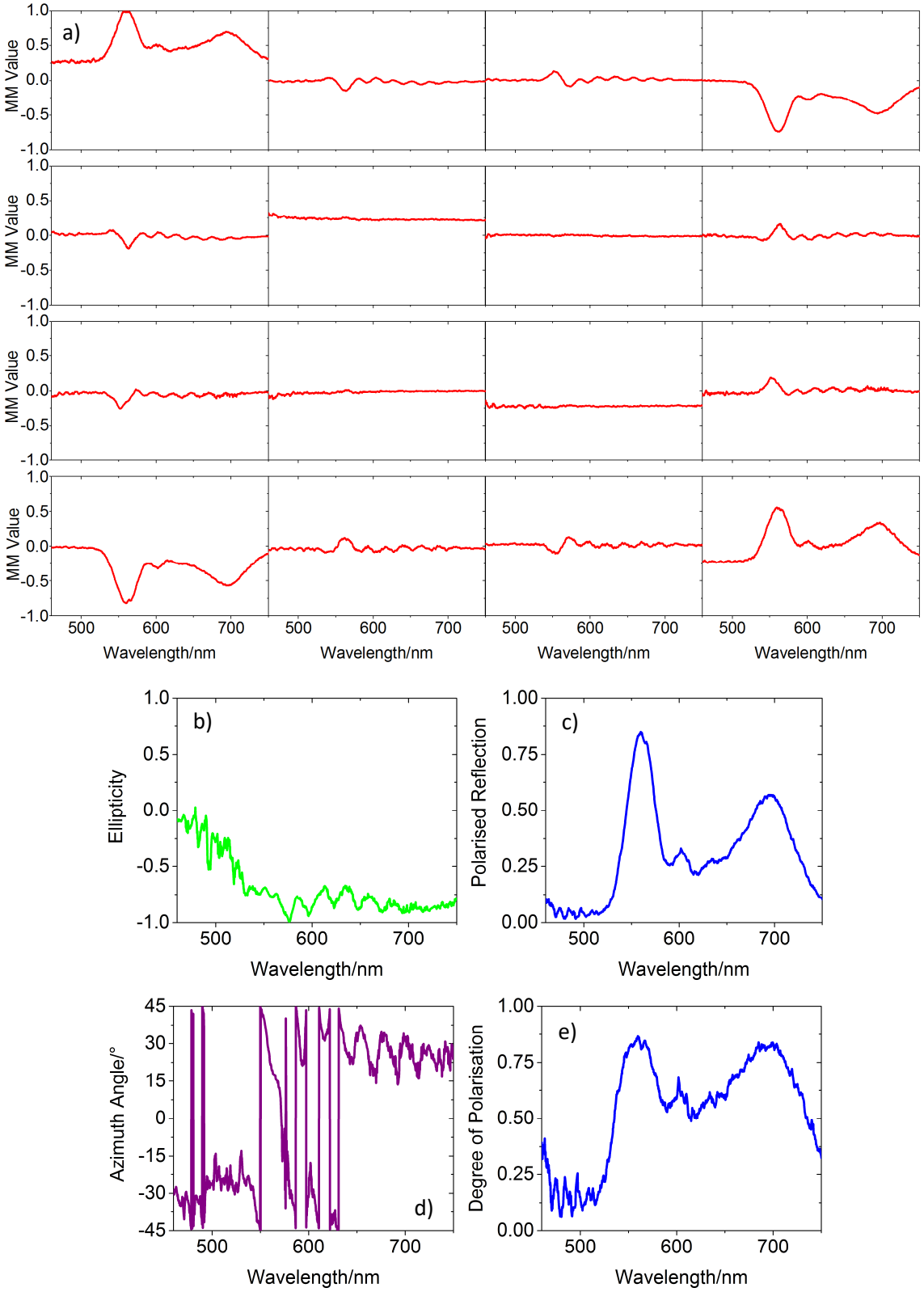


Figure A 153 – a) Normalised MM of reflection from the elytra of a *Cetonia aurata* (oscillations in between classification) beetle. b) The ellipticity, c) the polarised reflection, d) the azimuth angle and e) the degree of polarisation.

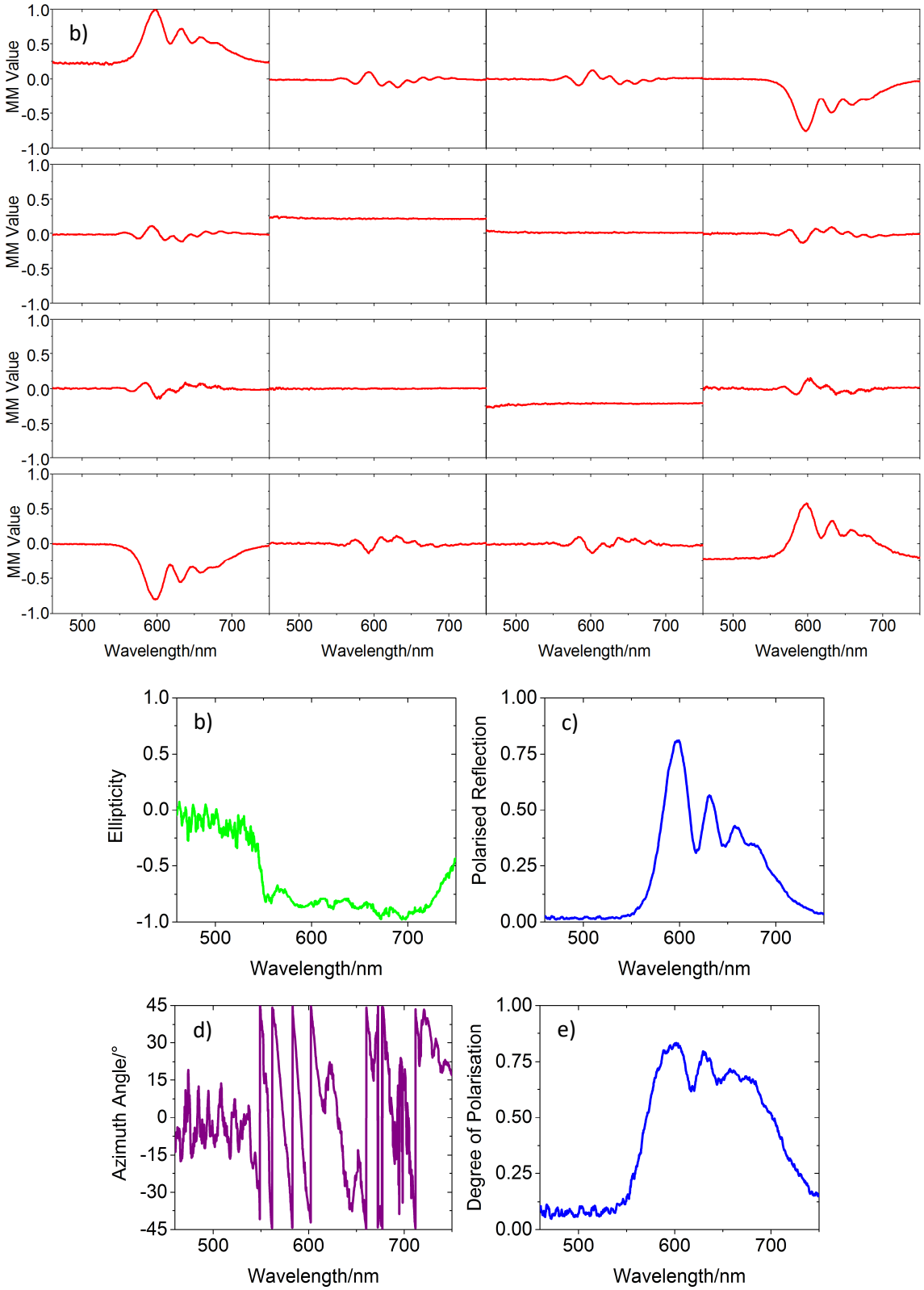


Figure A 154 – a) Normalised MM of reflection from the elytra of a *Cetonia aurata* (oscillation after classification) beetle. b) The ellipticity, c) the polarised reflection, d) the azimuth angle and e) the degree of polarisation.

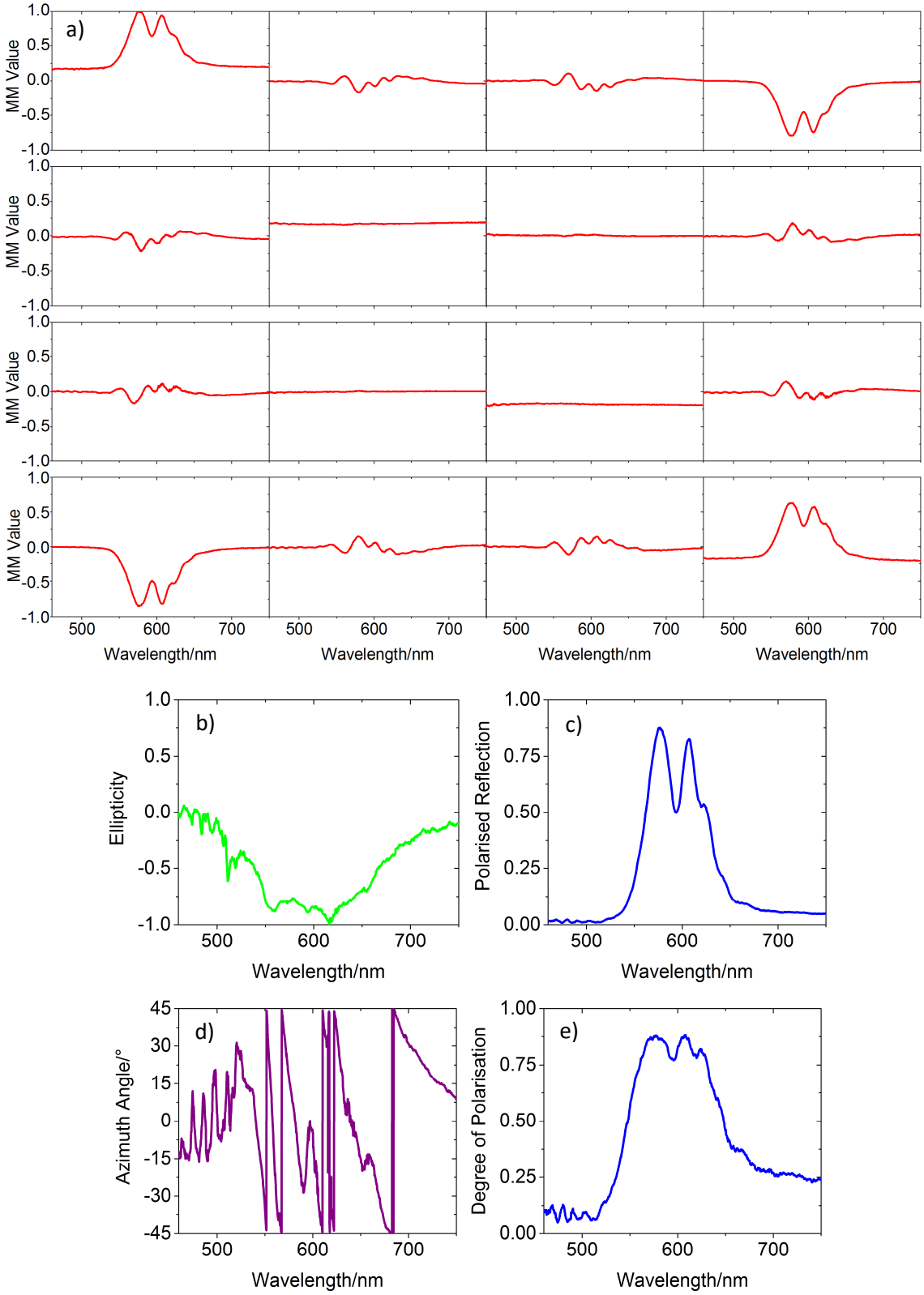


Figure A 155 – a) Normalised MM of reflection from the elytra of a *Cetonia aurata* (triple classification) beetle. b) The ellipticity, c) the polarised reflection, d) the azimuth angle and e) the degree of polarisation.

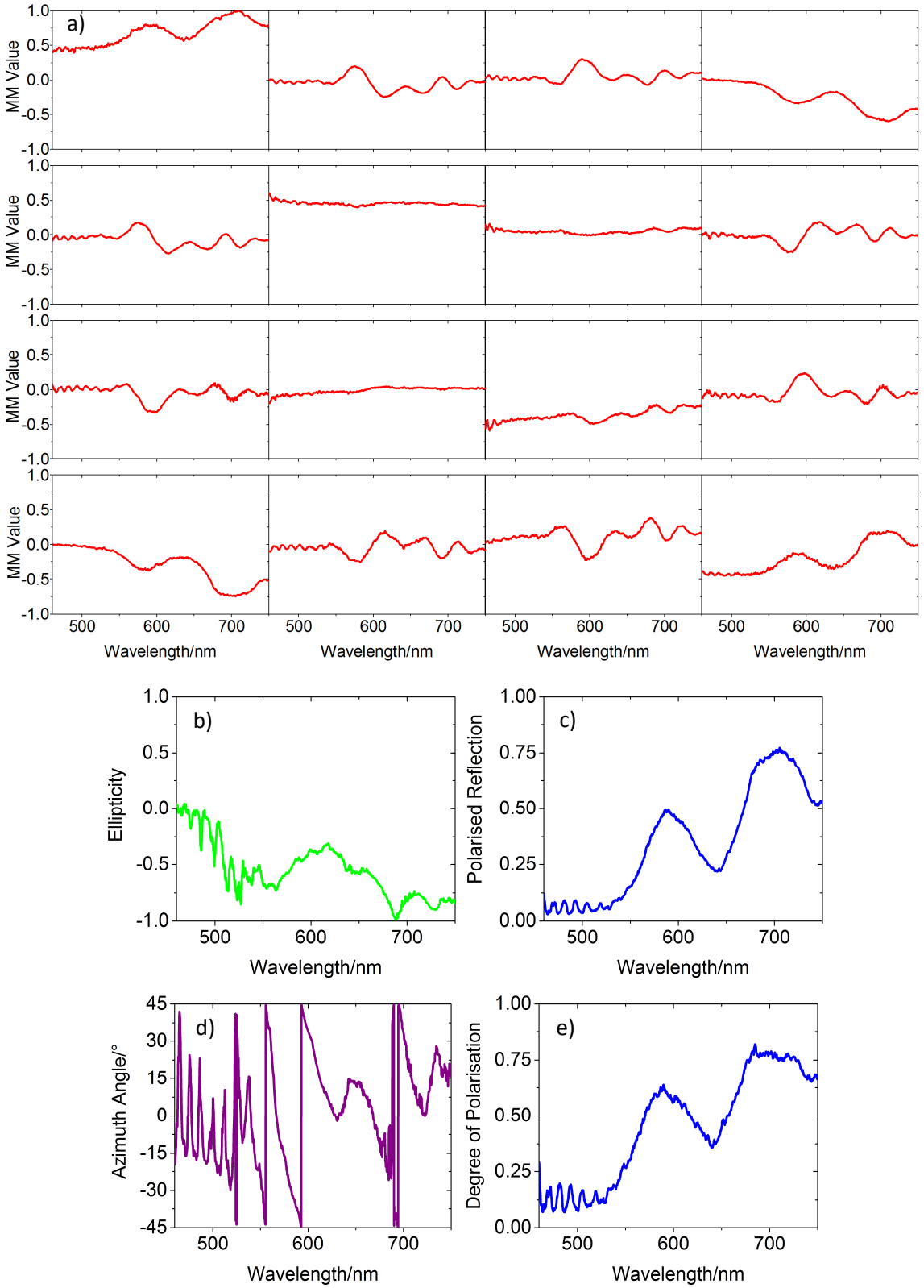


Figure A 156 – a) Normalised MM of reflection from the elytra of a *Cetonia aurata* (unclassified) beetle. b) The ellipticity, c) the polarised reflection, d) the azimuth angle and e) the degree of polarisation.

A5.6.3 - Chrysina

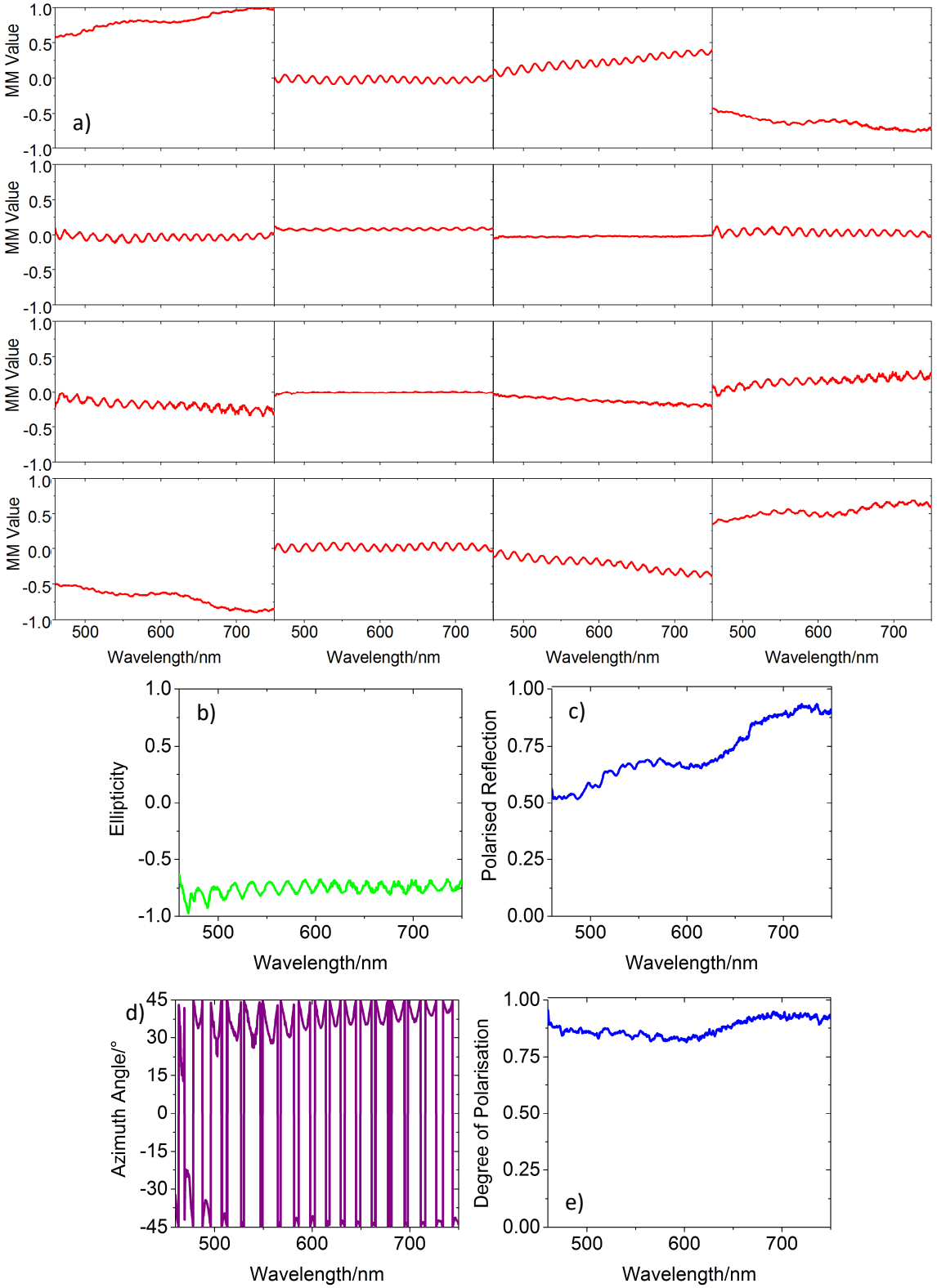


Figure A 157 – a) Normalised MM of reflection from the elytra of a *Chrysina limbata* beetle. b) The ellipticity, c) the polarised reflection, d) the azimuth angle and e) the degree of polarisation.

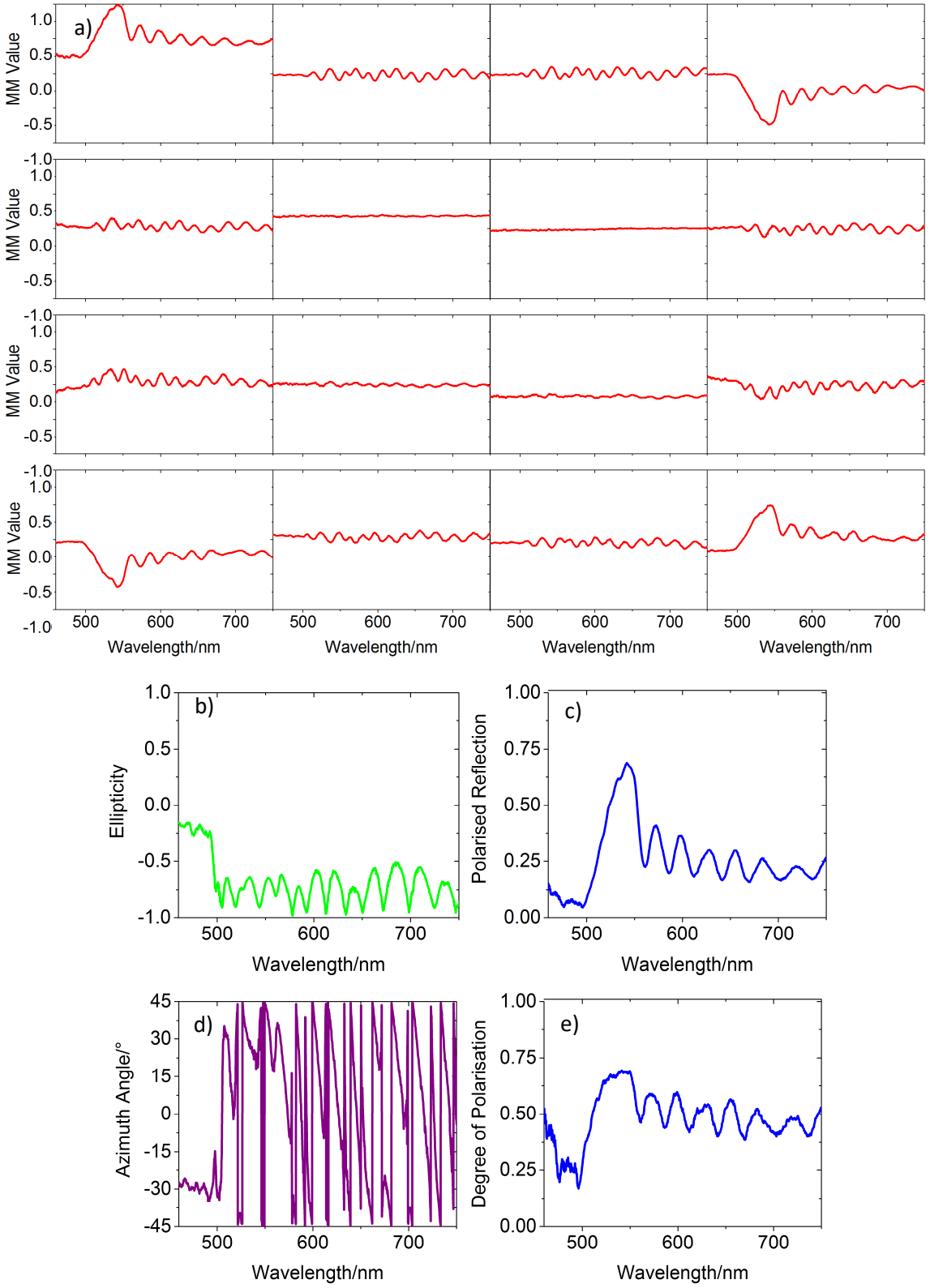


Figure A 158 – a) Normalised MM of reflection from the elytra of a *Chrysina chalcothea* beetle. b) The ellipticity, c) the polarised reflection, d) the azimuth angle and e) the degree of polarisation.

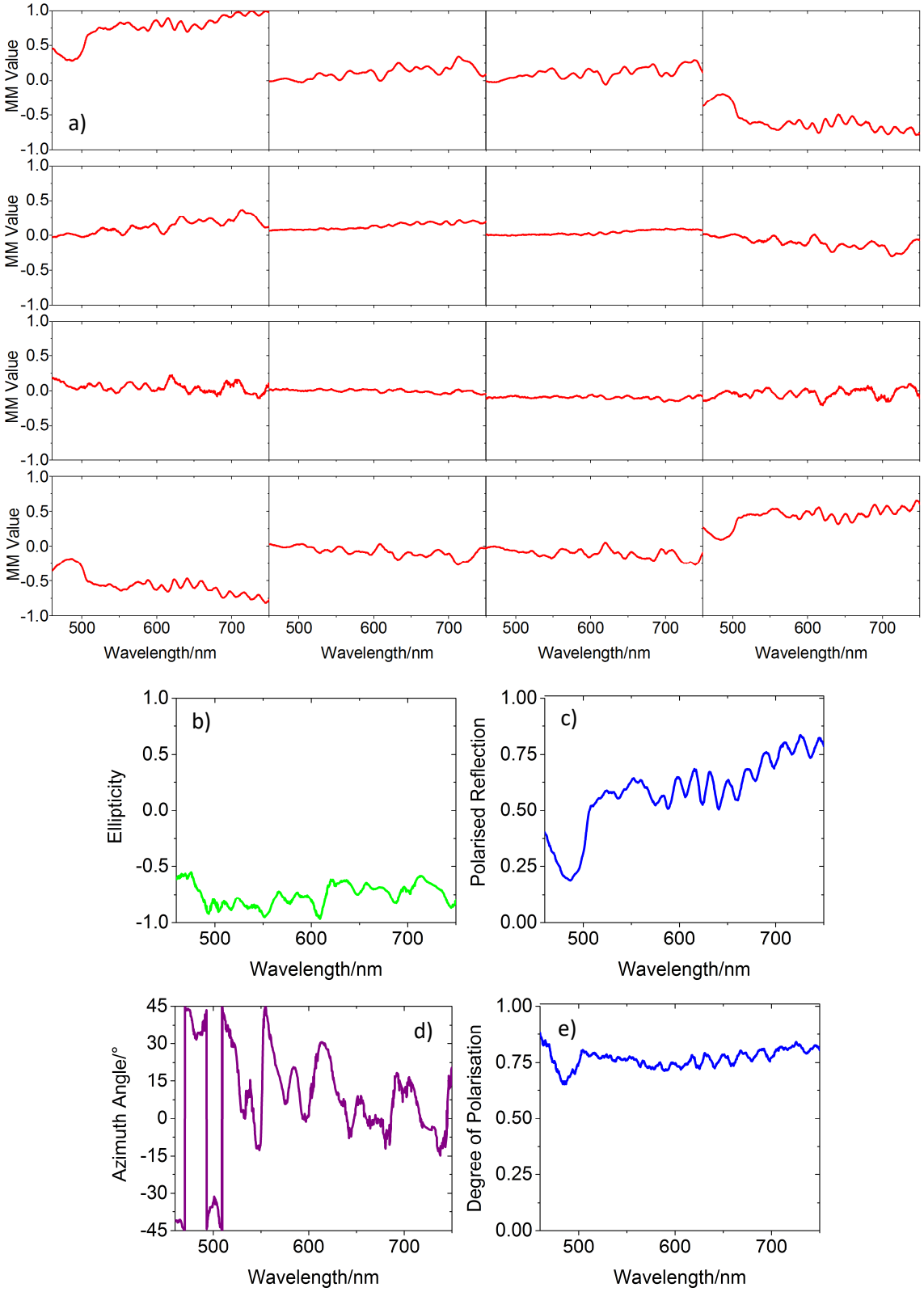


Figure A 159 – a) Normalised MM of reflection from the elytra of a *Chrysina argentola* beetle. b) The ellipticity, c) the polarised reflection, d) the azimuth angle and e) the degree of polarisation.

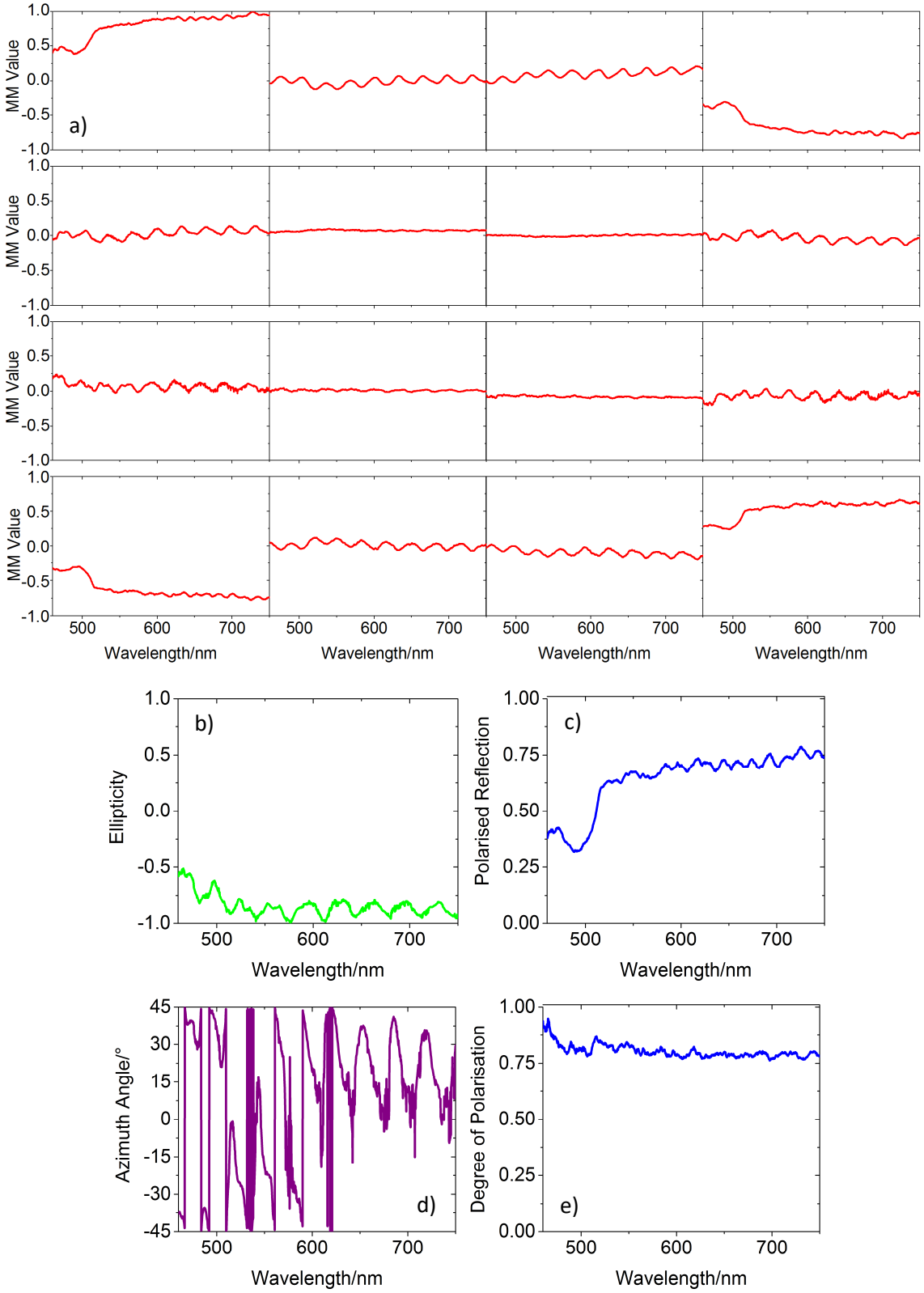


Figure A 160 – a) Normalised MM of reflection from the elytra of a *Chrysina pastori* beetle. b) The ellipticity, c) the polarised reflection, d) the azimuth angle and e) the degree of polarisation.

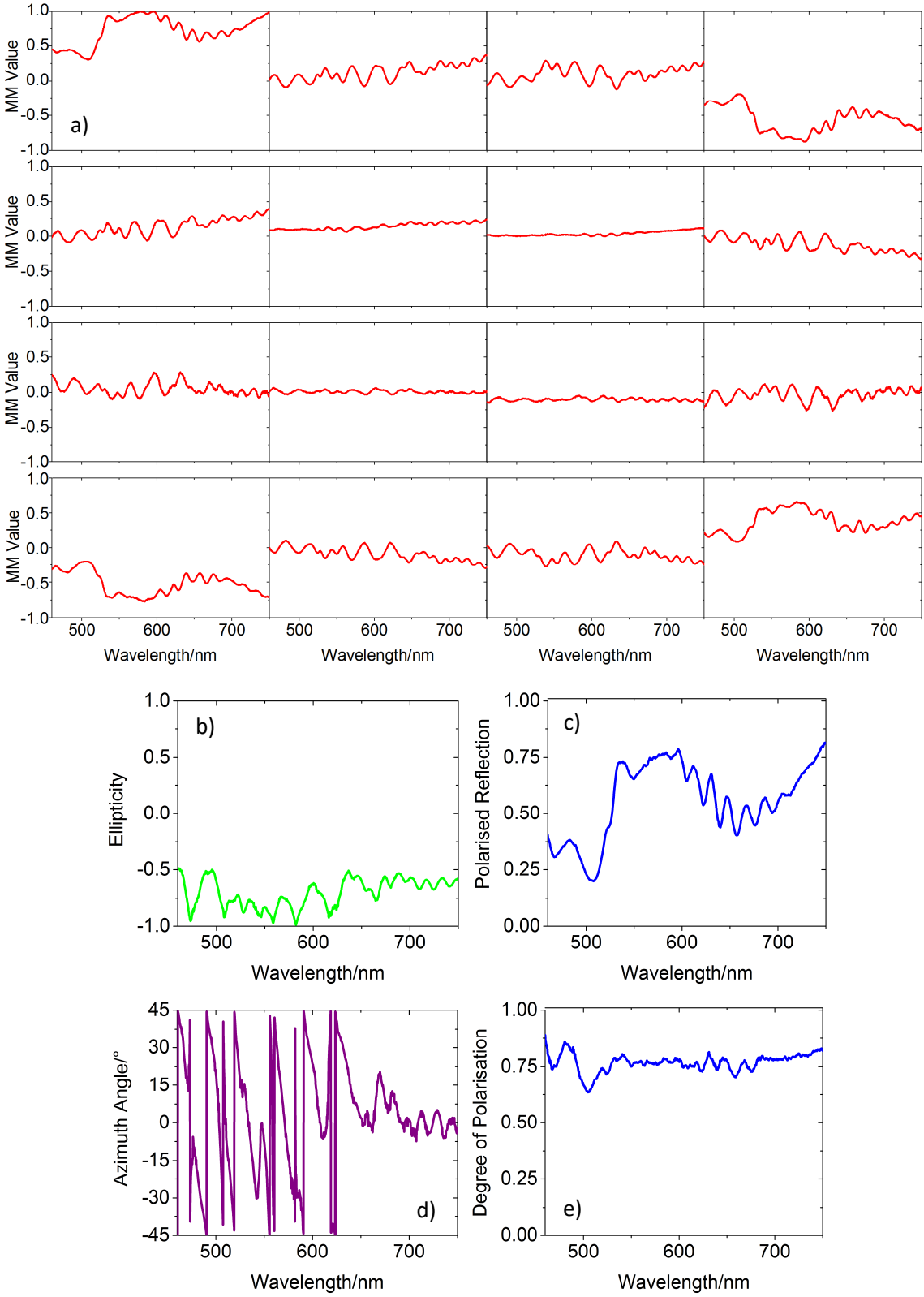


Figure A 161 – a) Normalised MM of reflection from the elytra of a *Chrysina batesi* beetle. b) The ellipticity, c) the polarised reflection, d) the azimuth angle and e) the degree of polarisation.

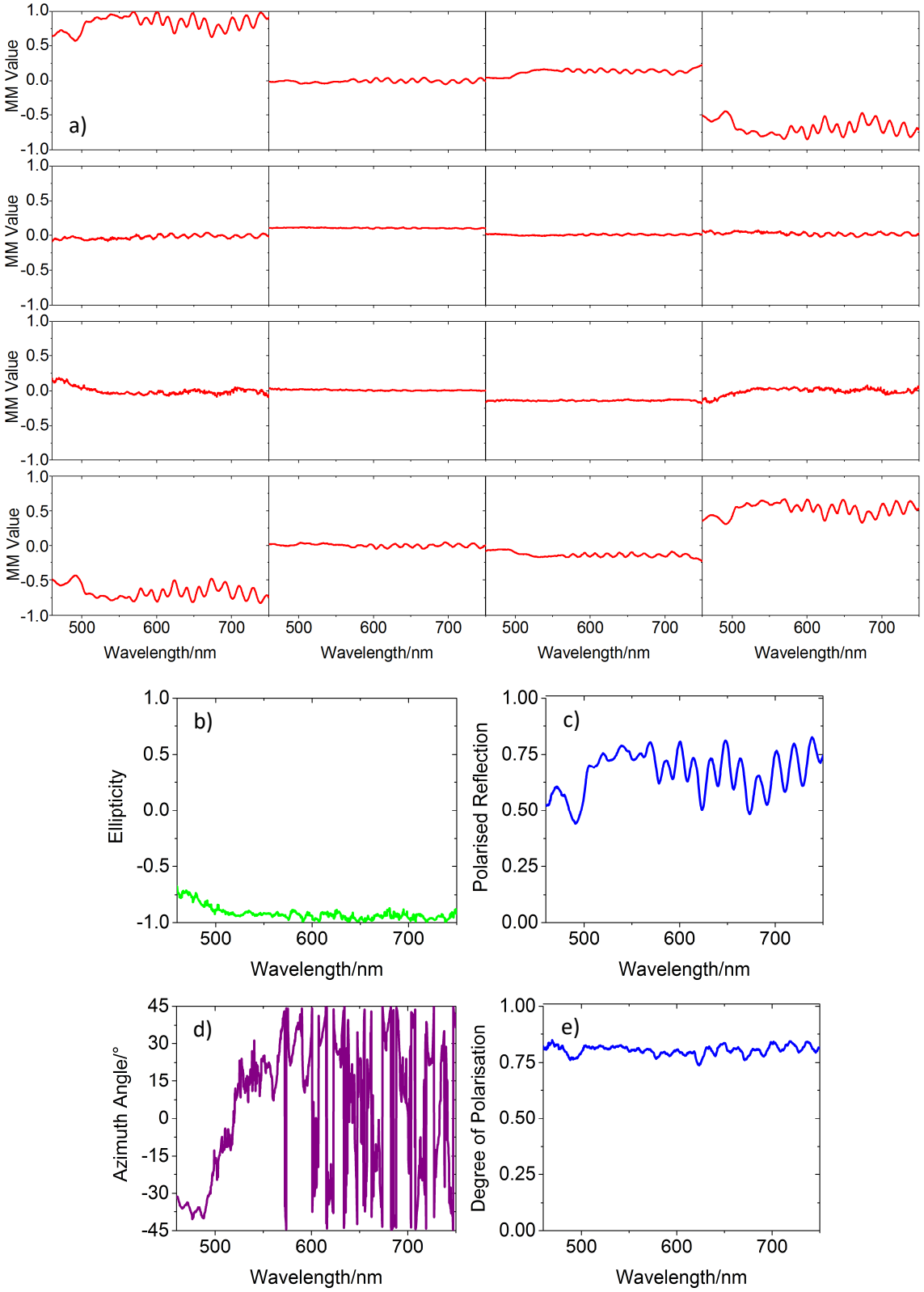


Figure A 162 – a) Normalised MM of reflection from the elytra of a *Chrysina strasseni* beetle. b) The ellipticity, c) the polarised reflection, d) the azimuth angle and e) the degree of polarisation.

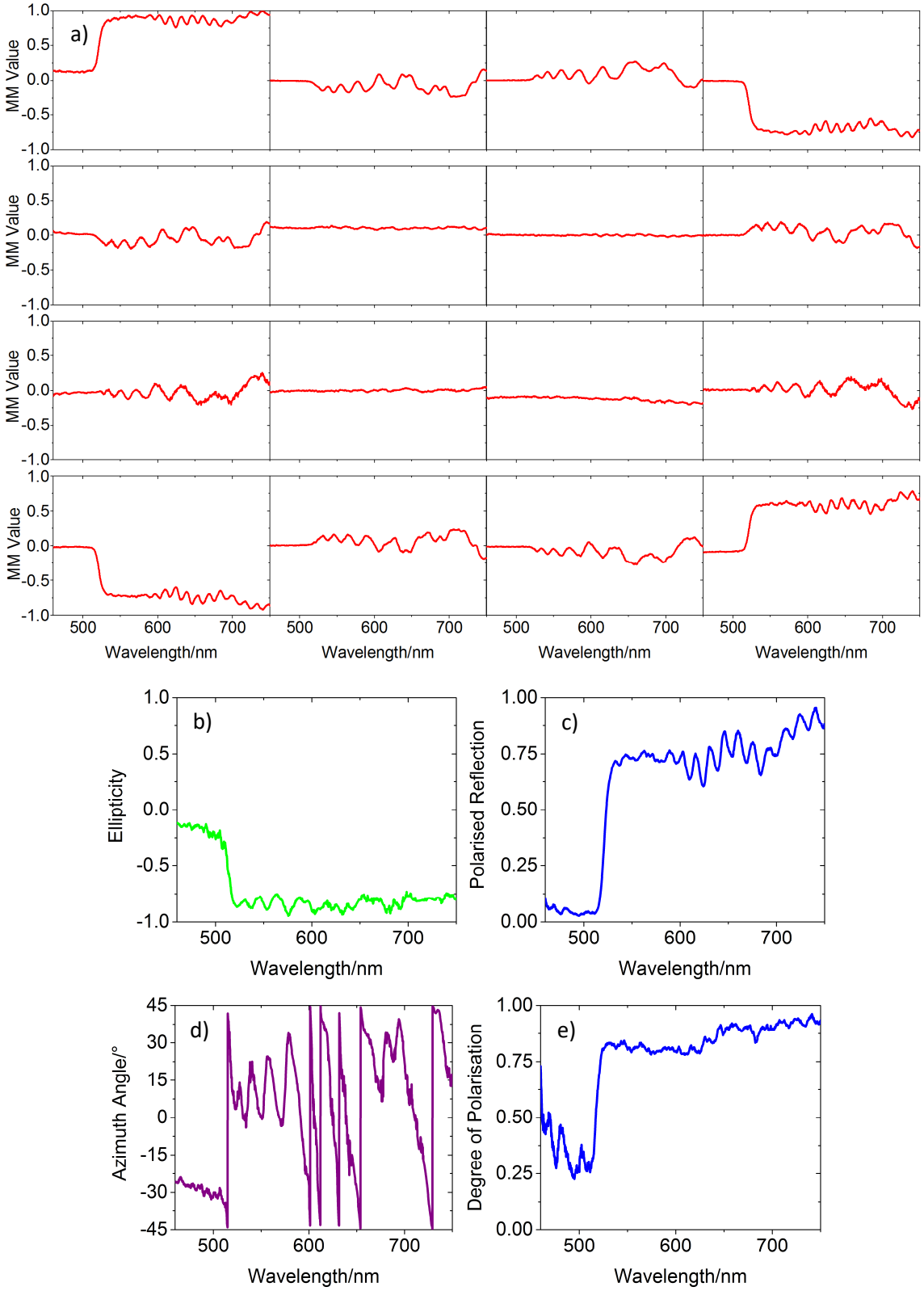


Figure A 163 – a) Normalised MM of reflection from the elytra of a *Chrysina aurigans* (gold) beetle. b) The ellipticity, c) the polarised reflection, d) the azimuth angle and e) the degree of polarisation.

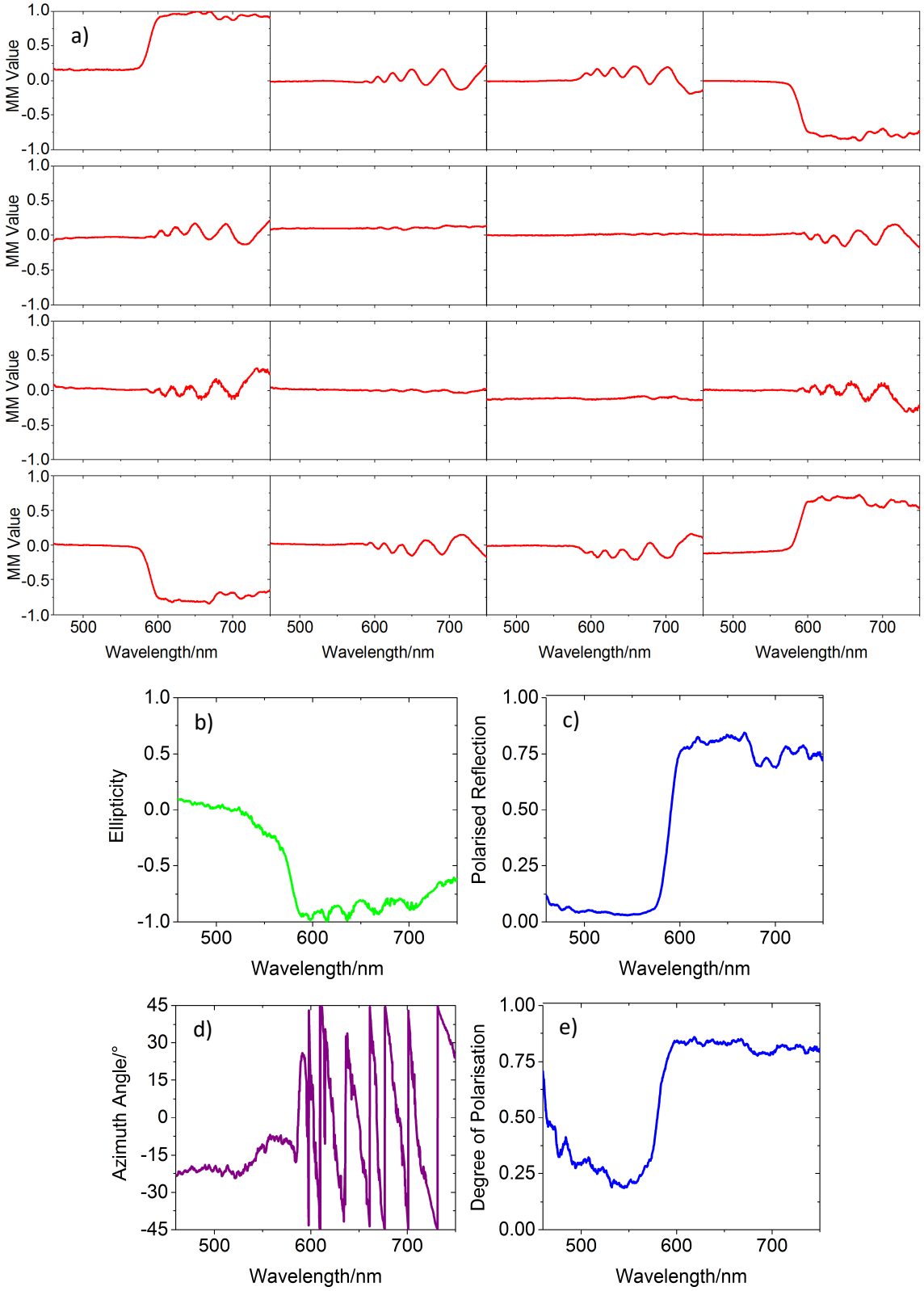


Figure A 164 – a) Normalised MM of reflection from the elytra of a *Chrysina aurigans* (light red) beetle. b) The ellipticity, c) the polarised reflection, d) the azimuth angle and e) the degree of polarisation.

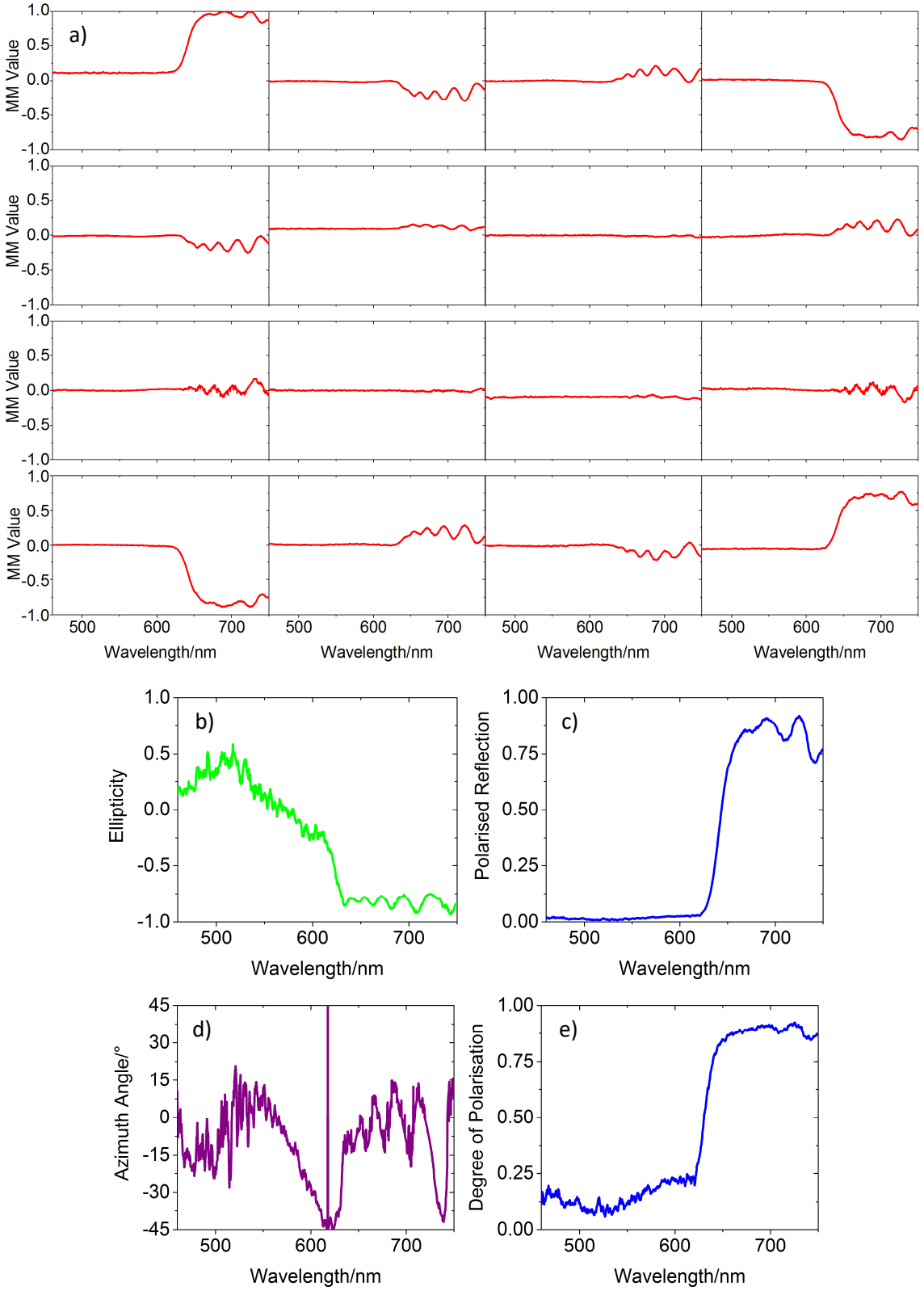


Figure A 165 – a) Normalised MM of reflection from the elytra of a *Chrysina aurigans* (dark red) beetle. b) The ellipticity, c) the polarised reflection, d) the azimuth angle and e) the degree of polarisation.

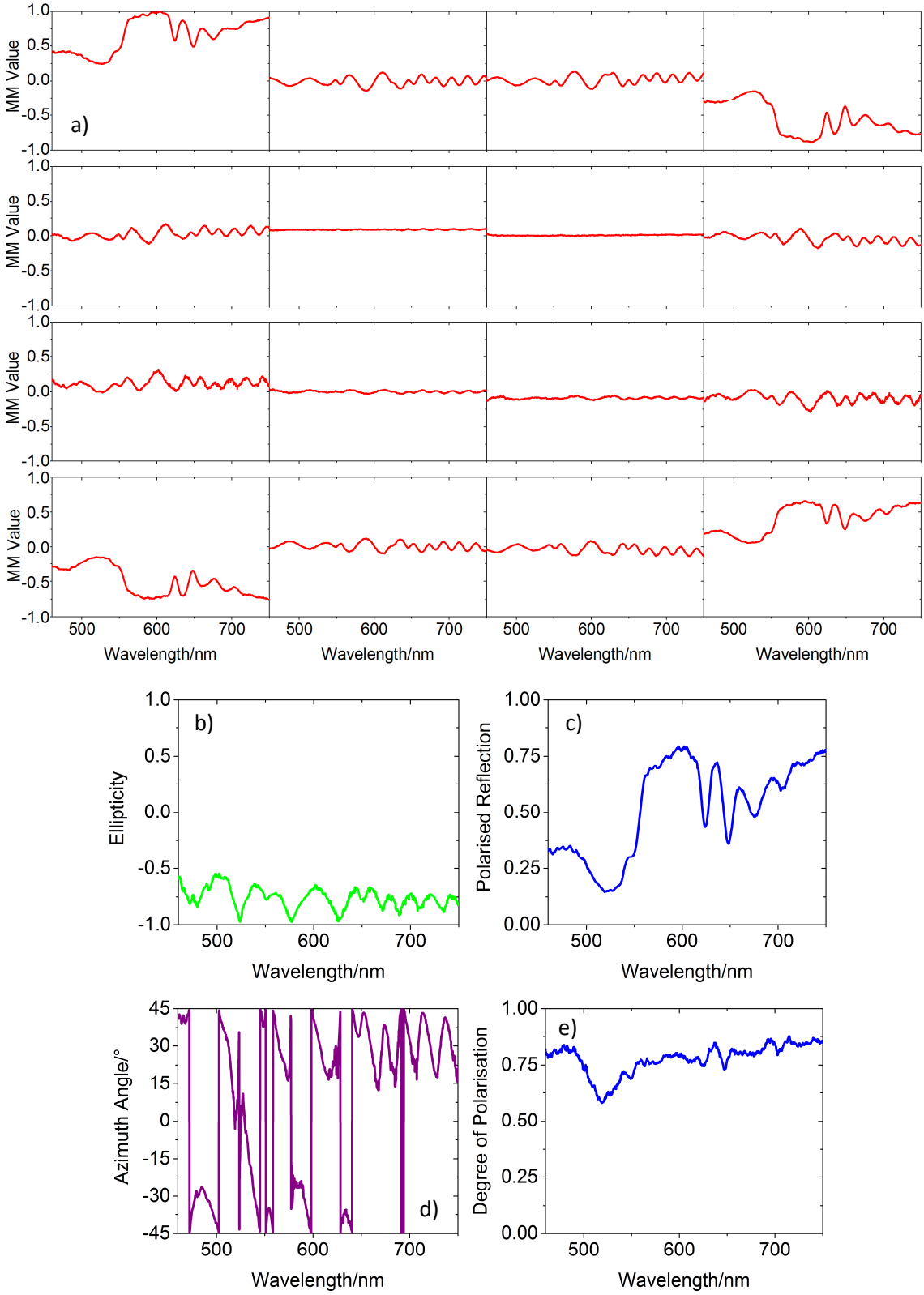


Figure A 166 – a) Normalised MM of reflection from the elytra of a *Chrysina cureoi* beetle. b) The ellipticity, c) the polarised reflection, d) the azimuth angle and e) the degree of polarisation.

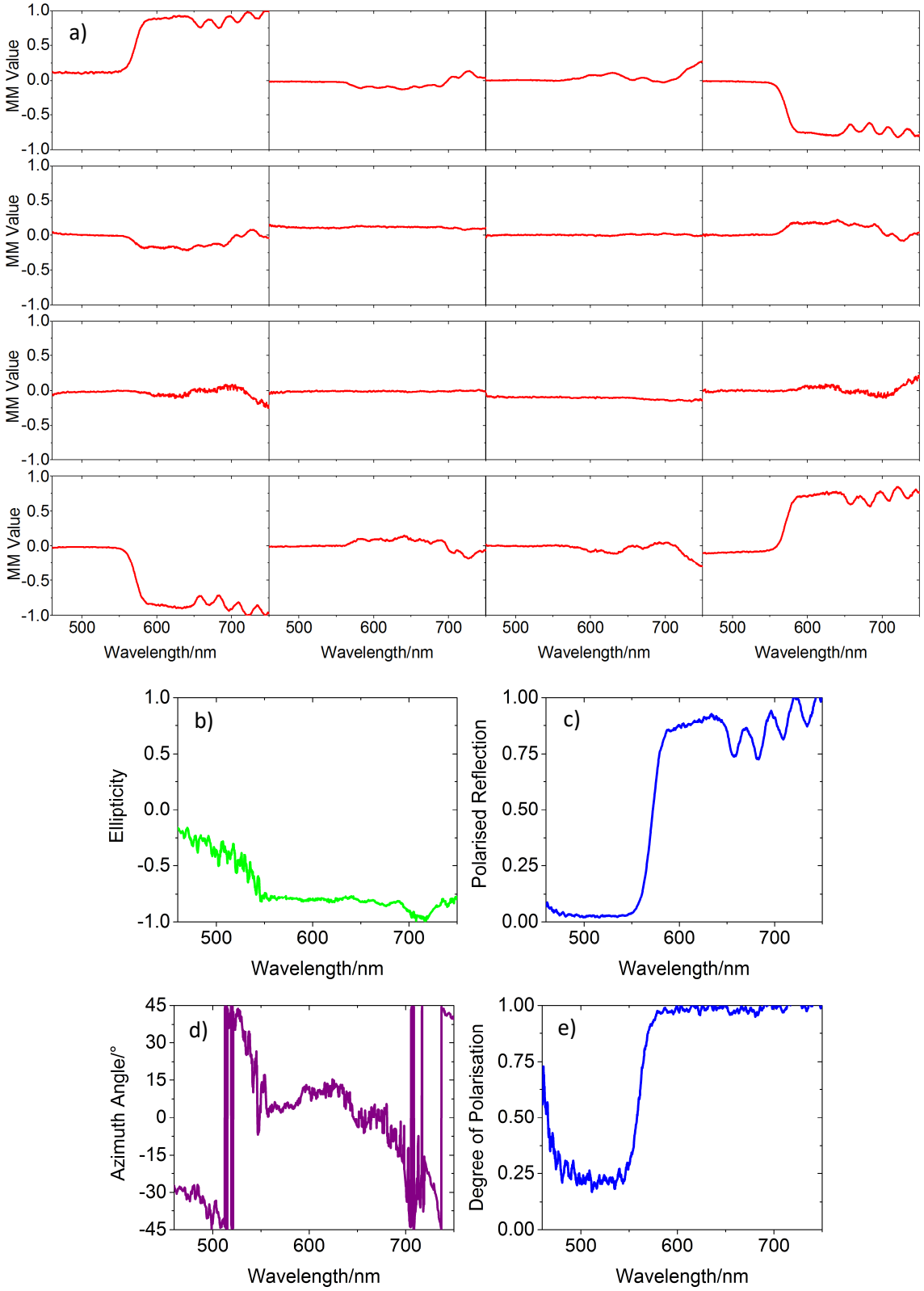


Figure A 167 – a) Normalised MM of reflection from the elytra of a *Chrysina chrysargea* (gold) beetle. b) The ellipticity, c) the polarised reflection, d) the azimuth angle and e) the degree of polarisation.

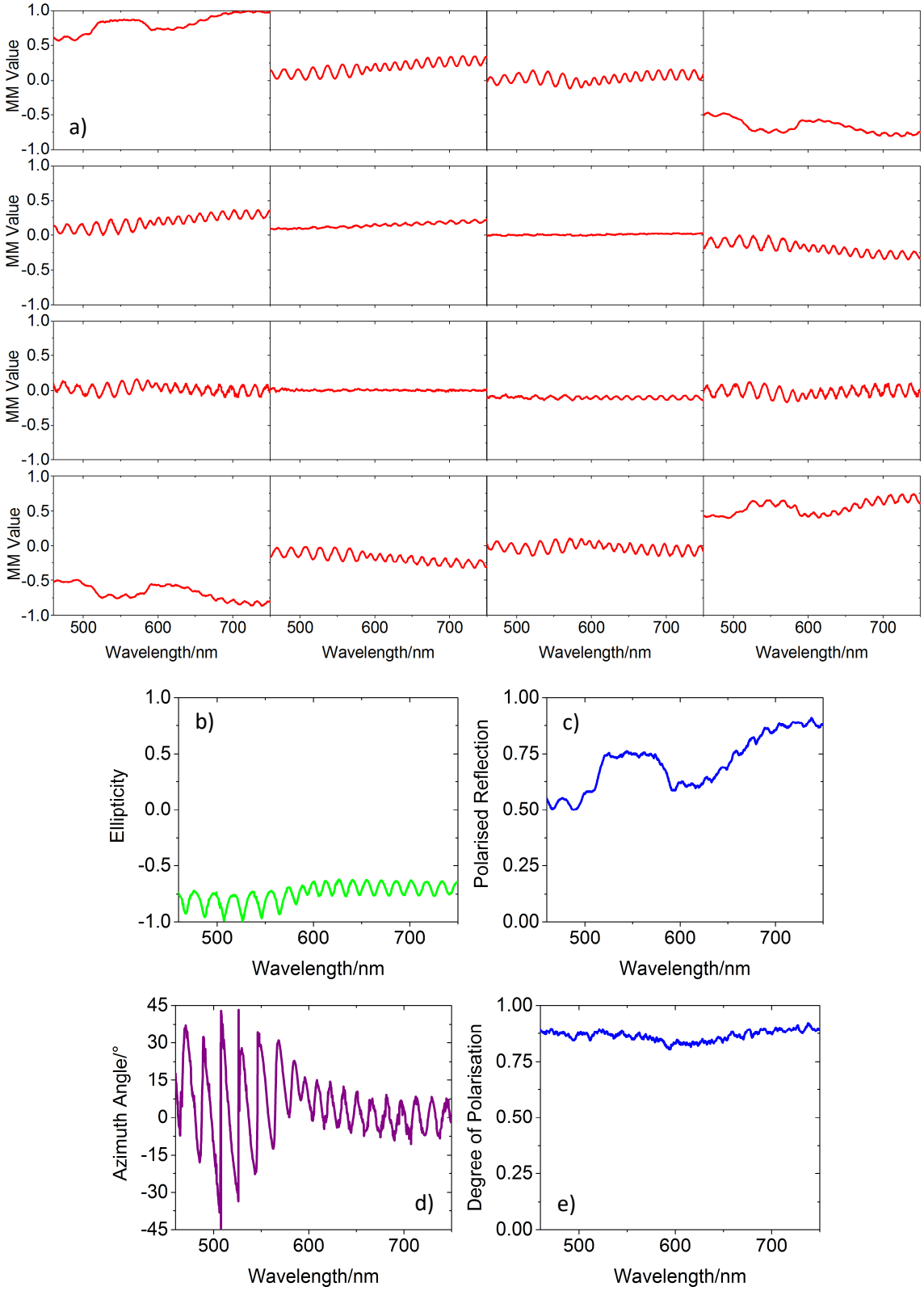


Figure A 168 – a) Normalised MM of reflection from the elytra of a *Chrysina chrysargea* (silver) beetle. b) The ellipticity, c) the polarised reflection, d) the azimuth angle and e) the degree of polarisation.

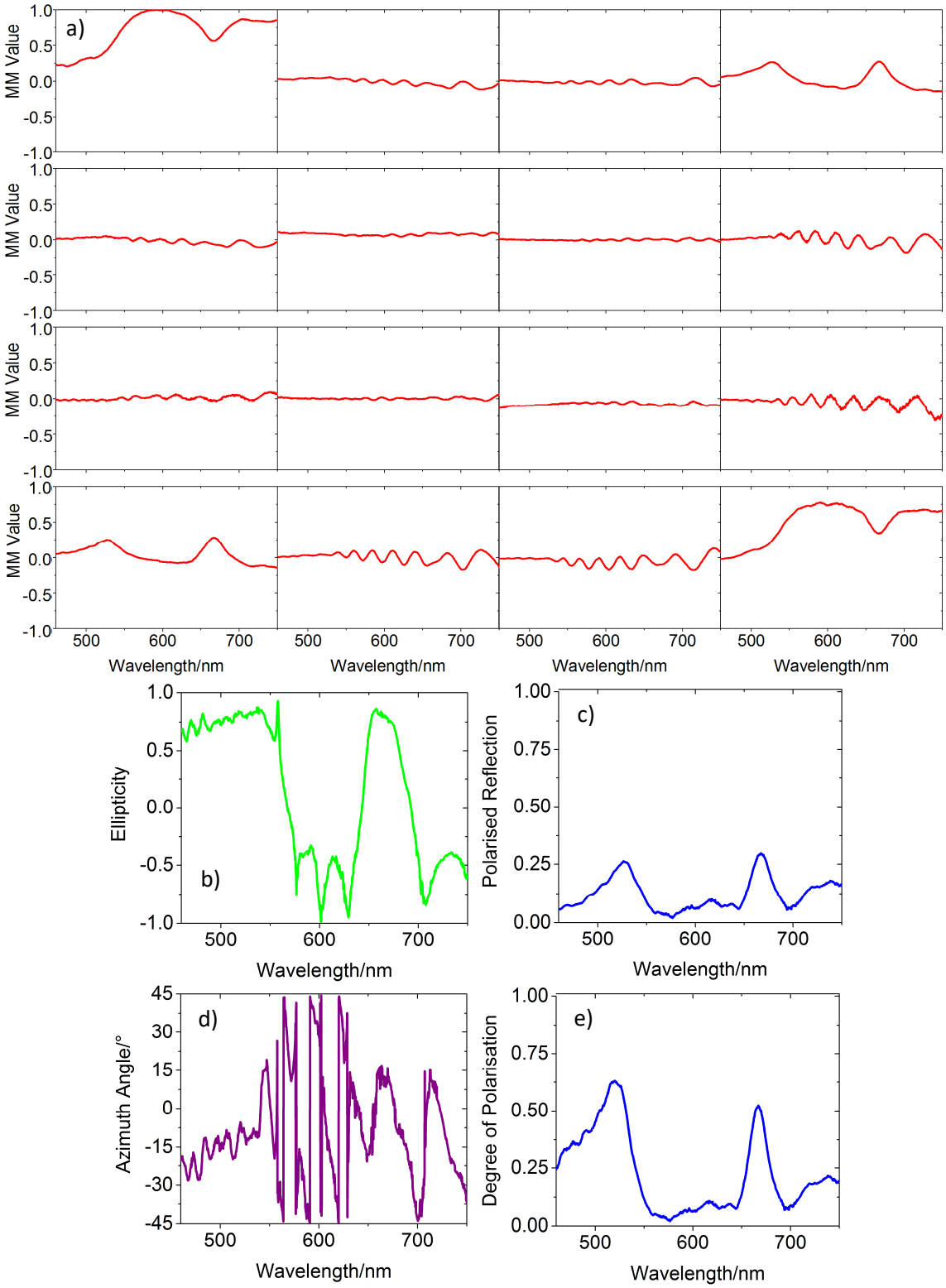


Figure A 169 – a) Normalised MM of reflection from the elytra of a *Chrysina resplendens* beetle. b) The ellipticity, c) the polarised reflection, d) the azimuth angle and e) the degree of polarisation.

A5.6.4 - Other Cetoniidae

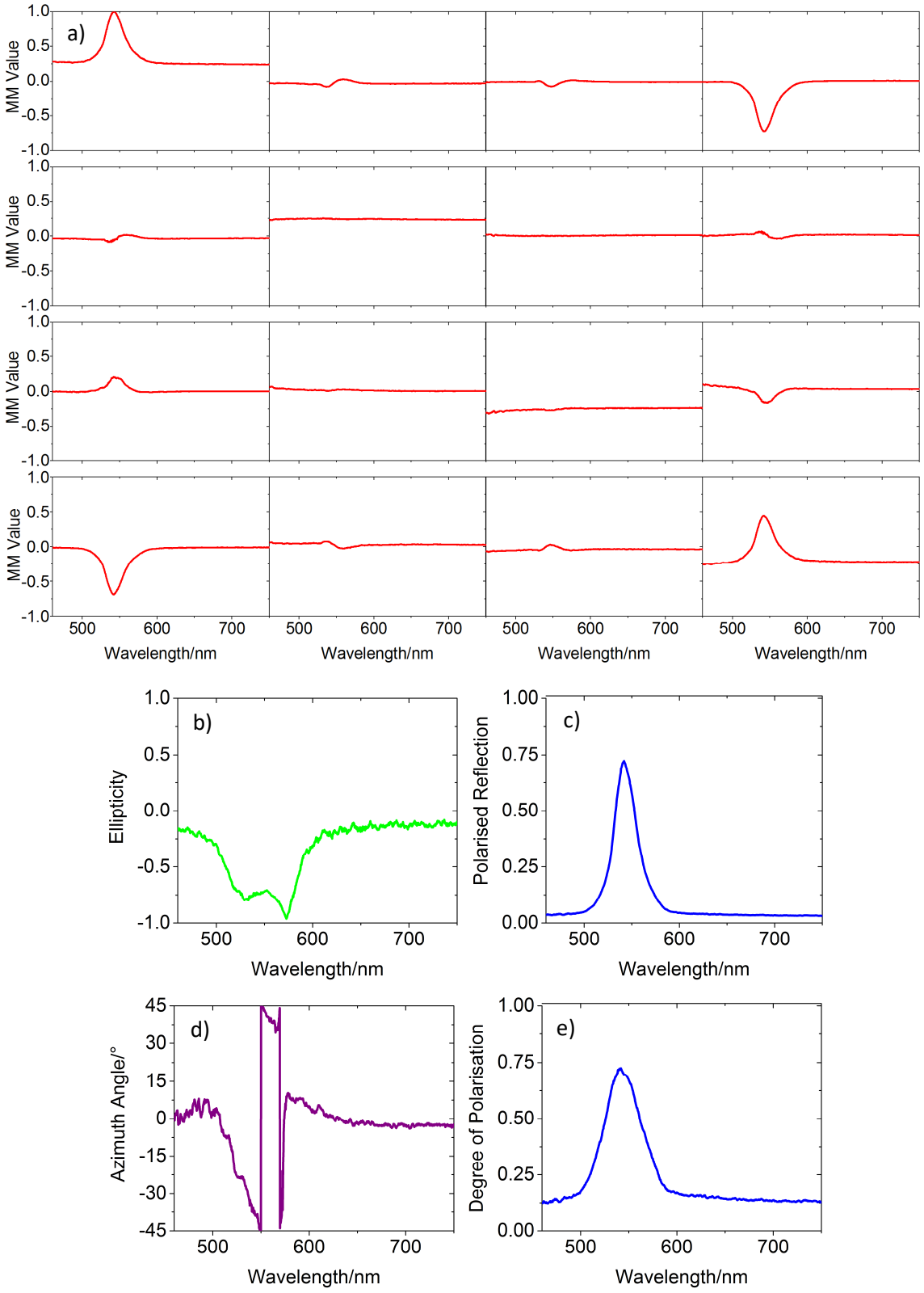


Figure A 170 – a) Normalised MM of reflection from the elytra of an *Agestrata orichalca* beetle. b) The ellipticity, c) the polarised reflection, d) the azimuth angle and e) the degree of polarisation.

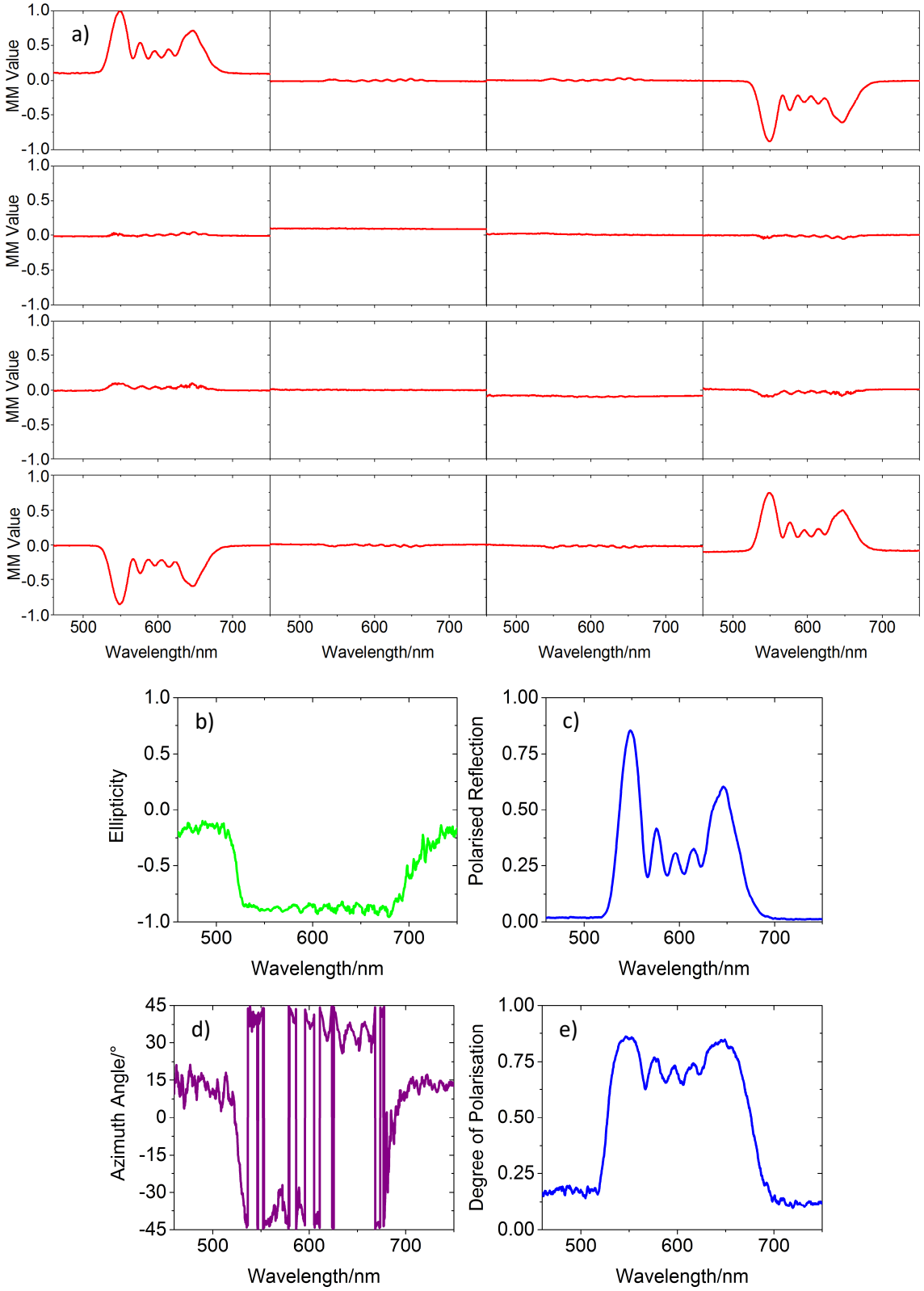


Figure A 171 – a) Normalised MM of reflection from the elytra of a *Protaetia brevitarsis* beetle. b) The ellipticity, c) the polarised reflection, d) the azimuth angle and e) the degree of polarisation.

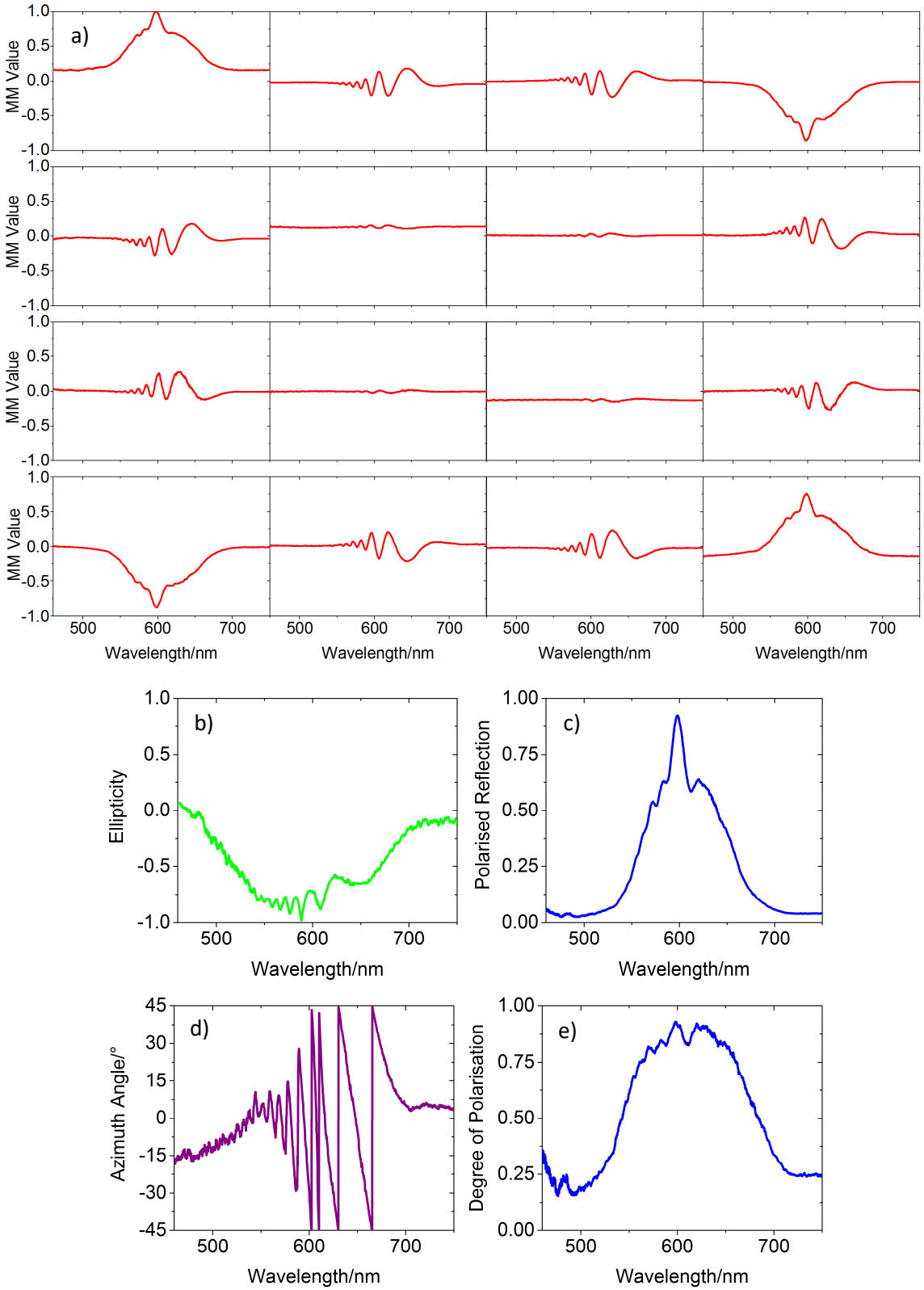


Figure A 172 – a) Normalised MM of reflection from the elytra of an *Agestrata luzonica* beetle. b) The ellipticity, c) the polarised reflection, d) the azimuth angle and e) the degree of polarisation.

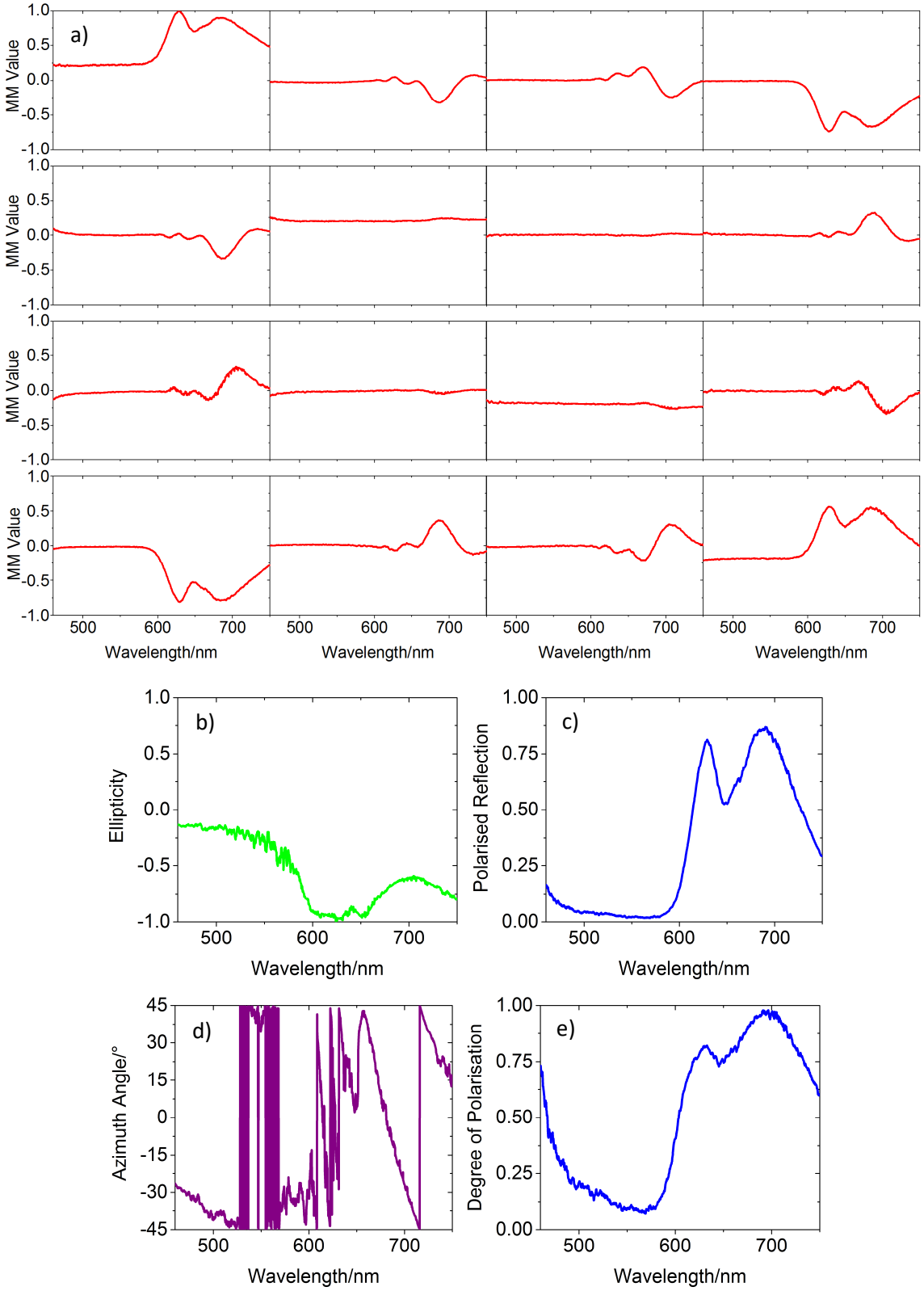


Figure A 173 – a) Normalised MM of reflection from the elytra of a *Protaetia aeruginosa* (red) beetle. b) The ellipticity, c) the polarised reflection, d) the azimuth angle and e) the degree of polarisation.

A5.6.5 - Other Rutelidae

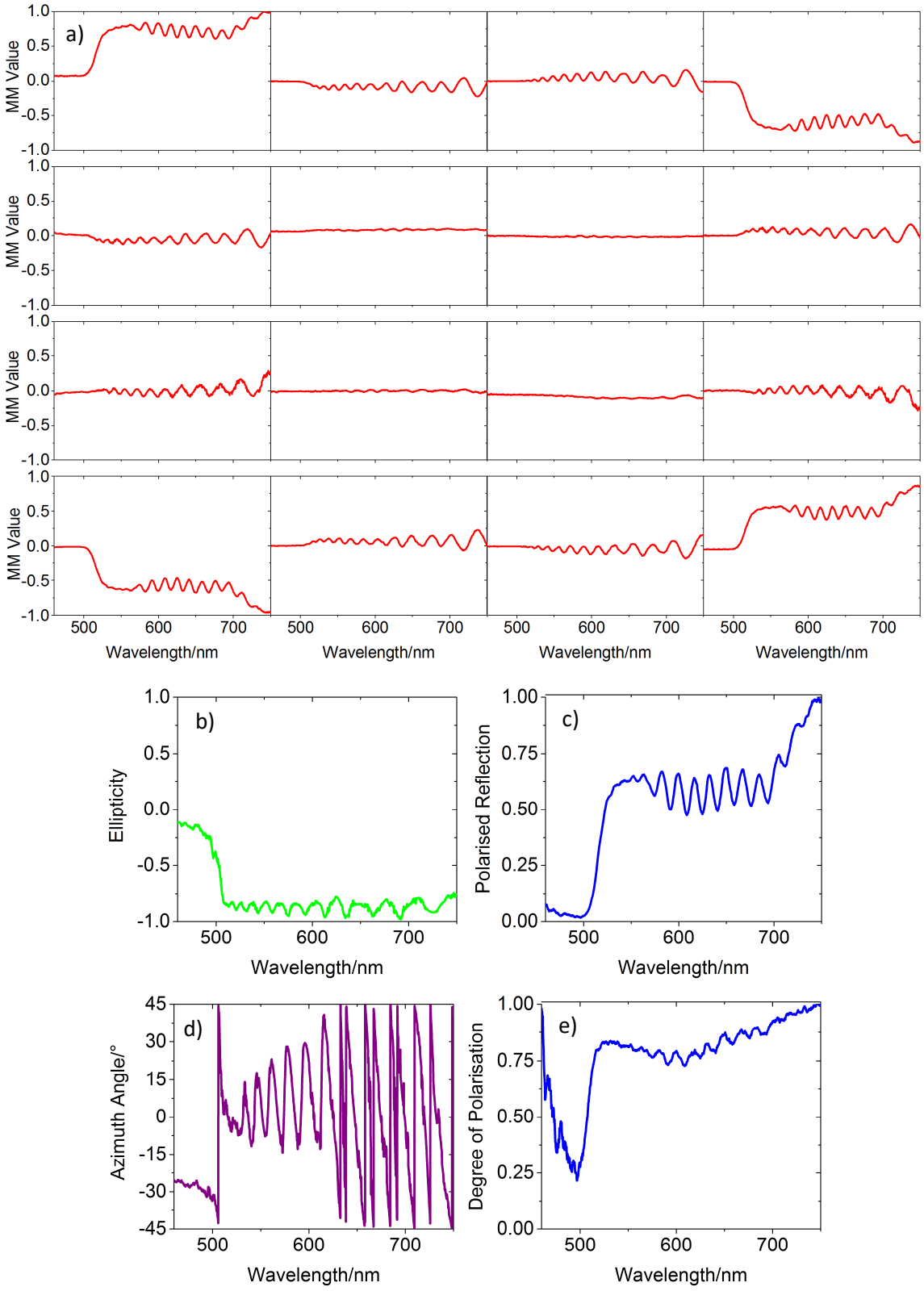


Figure A 174 – a) Normalised MM of reflection from the elytra of an *Anoplognathus aureus* beetle. b) The ellipticity, c) the polarised reflection, d) the azimuth angle and e) the degree of polarisation.

A5.6.6 - Other Phaenomeridae

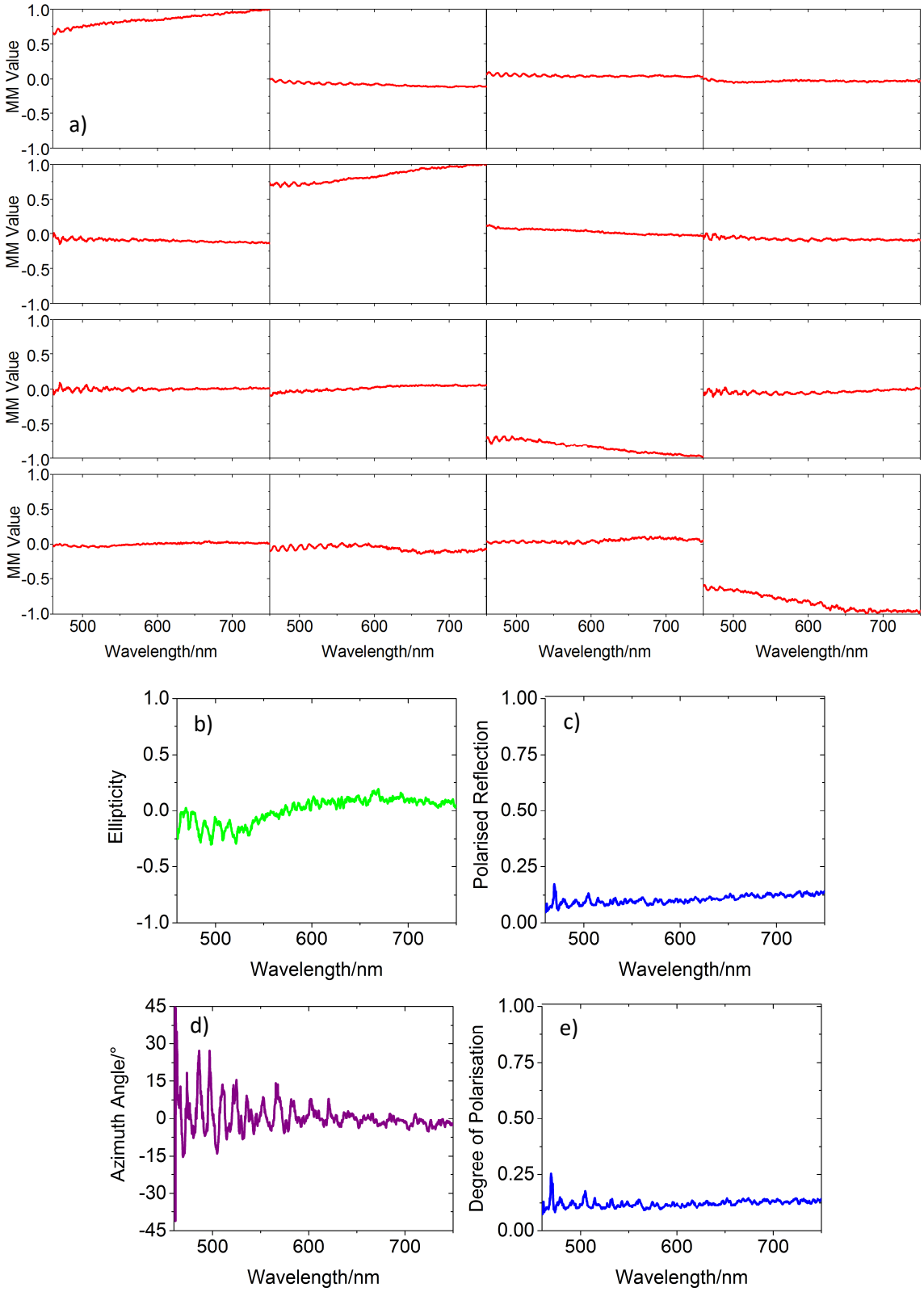


Figure A 175 – a) Normalised MM of reflection from the elytra of a *Phaenomeris besckei* (turquoise beetle). b) The ellipticity, c) the polarised reflection, d) the azimuth angle and e) the degree of polarisation.

References

[1] H. Tamura-Wicks, “Final Report : Polarised Light in Nature An Experimental Assessment of Beetles - MSci Thesis,” Imperial College, London.

[2] J. Mathieu and N. Faraggi, “Étude de la lumière polarisée circulairement réfléchie far certains coléoptères,” *Comptes Rendus*, vol. 205, pp. 1378–80, 1937.

[3] A. C. Neville and S. Caveney, “Scarabaeid beetle exocuticle as an optical analogue of cholesteric liquid crystals,” *Biol. Rev. Camb. Philos. Soc.*, vol. 44, pp. 531–562, 1969.

[4] O. Arteaga, “Natural optical activity vs circular Bragg reflection studied by Mueller matrix ellipsometry,” *Thin Solid Films*, vol. 617, pp. 14–19, 2016.

[5] M. Blahó, A. Egri, R. Hegedüs, J. Jósvai, M. Tóth, K. Kertész, L. P. Biró, G. Kriska, and G. Horváth, “No evidence for behavioral responses to circularly polarized light in four scarab beetle species with circularly polarizing exocuticle,” *Physiol. Behav.*, vol. 105, no. 4, pp. 1067–75, Feb. 2012.

[6] H. Arwin, R. Magnusson, J. Landin, and K. Järrendahl, “Chirality-induced polarization effects in the cuticle of scarab beetles: 100 years after Michelson,” *Philos. Mag.*, vol. 92, no. 12, pp. 1583–1599, Apr. 2012.

[7] H. Arwin, “Application of ellipsometry techniques to biological materials,” *Thin Solid Films*, vol. 519, no. 9, pp. 2589–2592, Feb. 2011.

[8] H. Arwin, L. Fernández del Río, and K. Järrendahl, “Comparison and analysis of Mueller-matrix spectra from exoskeletons of blue, green and red Cetonia aurata,” *Thin Solid Films*, vol. 571, pp. 739–743, Nov. 2014.

[9] H. Arwin, T. Berlind, B. Johs, and K. Järrendahl, “Cuticle structure of the scarab beetle Cetonia aurata analyzed by regression analysis of Mueller-matrix ellipsometric data,” *Opt. Express*, vol. 21, no. 19, pp. 22645–22656, 2013.

[10] C. Fallet, “Angle resolved Mueller polarimetry , applications to periodic structures) - PhD Thesis,” École polytechnique, 2011.

[11] J. Gustafson, “Optical Studies and Micro-Structure Modeling of the Circular-Polarizing Scarab Beetles Cetonia aurata, Potosia cuprea, Liocola marmorata,” Linköpings University, 2010.

[12] I. Daly, “Polarised Light in Nature An Experimental Assessment of Beetles - MSci Thesis,” Imperial College, London, 2012.

[13] R. Shamim, “Optical Studies of Nano-Structures in the Beetle Cetonia Aurata - MSc Thesis,” Linköpings University, 2009.

[14] L. Fernández del Río, “An Investigation of the Polarizing Properties and Structural Characteristics in the Cuticles of the Scarab Beetles Chrysina gloriosa and Cetonia aurata - MSc Thesis,” Linköpings University, 2012.

[15] X. Wu, *Structure-property-relations of Cuticular Photonic Crystals Evolved by Different Beetle Groups (Insecta, Coleoptera) - ISBN:9783844294965*. Berlin: epubli GmbH, 2014.

[16] R. Magnusson, J. Birch, C.-L. Hsiao, P. Sandström, H. Arwin, and K. Järrendahl, “In x Al 1-x N chiral nanorods mimicking the polarization features of scarab beetles,” vol. 9429, p. 94290A–1–8, Mar. 2015.

[17] H. Arwin, R. Magnusson, L. Fernández del Río, J. Landin, A. Mendoza-Galván, and K. Järrendahl, “Exploring polarization features in light reflection from beetles with structural colors,” *Proc. SPIE*, vol. 9429, no. 942909, pp. 1–13, Mar. 2015.

[18] H. Arwin, R. Magnusson, C. Fallet, K. Järrendahl, M. Foldyna, A. De Martino, and R. Ossikovski, “Sum decomposition of Mueller-matrix images and spectra of beetle cuticles,” *Opt. Express*, vol. 23, no. 3, pp. 4558–4567, 2015.

[19] L. T. Mcdonald, T. A. Starkey, and P. Vukusic, “Photonic architectures in beetles: twists and iridescence,” *Int. J. Des. Nat. Ecodynamics*, vol. 9, no. 4, pp. 266–275, Dec. 2014.

[20] R. Magnusson, H. Arwin, E. Garcia-Caurel, K. Jarrendahl, and R. Ossikovski, “Sum regression decomposition of spectral and angle-resolved Mueller matrices from biological reflectors,” *Appl. Opt.*, vol. 55, no. 15, pp. 4060–4065, 2016.

[21] R. Yang, A. Zaheri, W. Gao, C. Hayashi, and H. D. Espinosa, “AFM Identification of Beetle Exocuticle: Bouligand Structure and Nanofiber Anisotropic Elastic Properties,” *Adv. Funct. Mater.*, vol. 1603993, pp. 1–8, 2016.

[22] E. Muñoz-Pineda, K. Järrendahl, H. Arwin, and A. Mendoza-Galván, “Symmetries and relationships between elements of the Mueller matrix spectra of the cuticle of the beetle Cotinis mutabilis,” *Thin Solid Films*, vol. 571, pp. 660–665, Nov. 2014.

[23] A. Mendoza-Galván, E. Muñoz-Pineda, K. Järrendahl, and H. Arwin, “Evidence for a dispersion relation of optical modes in the cuticle of the scarab beetle Cotinis mutabilis,” *Opt. Mater. Express*, vol. 4, no. 12, p. 2484, Nov. 2014.

[24] A. C. Neville, “Metallic gold and silver colours in some insect cuticles,” *J. Insect Physiol.*, vol. 23, no. 10, pp. 1267–74, 1977.

[25] S. Lowrey, L. Silva, I. Hodgkinson, and J. Leader, “Observation and modeling of polarized light from scarab beetles,” *JOSA A*, vol. 24, no. 8, pp. 2418–2425, 2007.

[26] M. Xu, A. E. Seago, T. D. Sutherland, and S. Weisman, “Dual structural color mechanisms in a scarab beetle,” *J. Morphol.*, vol. 271, no. 11, pp. 1300–5, Nov. 2010.

[27] S. Caveney, “Cuticle Reflectivity and Optical Activity in Scarab Beetles: The Role of Uric Acid,” *Proc. R. Soc. B Biol. Sci.*, vol. 178, no. 1051, pp. 205–225, Jun. 1971.

[28] R. Hegedüs, G. Szél, and G. Horváth, “Imaging polarimetry of the circularly polarizing cuticle of scarab beetles (Coleoptera: Rutelidae, Cetoniidae),” *Vision Res.*, vol. 46, pp. 2786–2797, 2006.

[29] S. Y. Ching, G. Li, H. L. Tam, D. T. P. Goh, J. K. L. Goh, and K. W. Cheah, “Chirality in Rhomborhina Gigantea beetle,” *Opt. Mater. Express*, vol. 4, no. 11, pp. 2340–5, Oct. 2014.

[30] D. J. Brink, N. G. Van Der Berg, L. C. Prinsloo, and I. J. Hodgkinson, “Unusual coloration in scarabaeid beetles,” *J. Phys. D. Appl. Phys.*, vol. 40, no. 7, pp. 2189–2196, Apr. 2007.

[31] D. J. Brink, N. G. van der Berg, and L. C. Prinsloo, “The role of interface effects on the reflection of circularly polarised light from the thin-film structure of scarabus beetles,” *Surf. Interface Anal.*, vol. 40, no. 3–4, pp. 769–771, Mar. 2008.

[32] A. L. V. Davis, “Functional implications of temperature-correlated colour polymorphism in an iridescent, scarabaeine,” *Ecol. Entomol.*, vol. 33, pp. 771–779, 2008.

[33] G. W. Kattawar, “A Search for Circular Polarization,” *Opt. Photonics News*, no. September, pp. 42–43, 1994.

[34] D. J. Brink, N. van der Berg, and L. Prinsloo, “Multi-color reflection from chiral thin-film stacks,” *Proc. SPIE*, vol. 8094, no. 80940G, pp. 1–8, Sep. 2011.

[35] P. Gaubert, “Sur la polarisation circulaire de la lumiere reflechie pas les insectes,” *Comptes Rendus*, vol. 179, pp. 1148–1150, 1924.

[36] M. Akamine, K. Ishikawa, K. Maekawa, and M. Kon, “The physical mechanism of cuticular color in Phelotrupes auratus (Coleoptera, Geotrupidae),” *Entomol. Sci.*, vol. 14, no. 3, pp. 291–296, Jul. 2011.

[37] B. D. Wilts, H. M. Whitney, B. J. Glover, U. Steiner, and S. Vignolini, “Natural helicoidal structures: morphology, self-assembly and optical properties,” *Mater. Today Proc.*, vol. 1S, pp. 177–185, 2014.

[38] A. Parker, D. McKenzie, and M. Large, “Multilayer reflectors in animals using green and gold beetles as contrasting examples,” *J. Exp. Biol.*, vol. 1313, no. 1998, pp. 1307–1313, 1998.

[39] I. Hodgkinson, S. Lowrey, L. Bourke, A. Parker, and M. W. McCall, “Mueller-matrix characterization of beetle cuticle: polarized and unpolarized reflections from representative architectures,” *Appl. Opt.*, vol. 49, no. 24, pp. 4558–67, Aug. 2010.

[40] D. B. Thomas, A. Seago, D. C. Robacker, and A. Poe, “Reflections On Golden Scarabs,” *Am. Entomol.*, vol. Winter, pp. 224–230, 2007.

[41] D. H. Goldstein, “Polarization properties of Scarabaeidae,” *Appl. Opt.*, vol. 45, pp. 7944–7950, 2006.

[42] L. Fernández del Río, H. Arwin, and K. Järrendahl, "Polarizing properties and structure of the cuticle of scarab beetles from the Chrysina genus," *Phys. Rev. E*, vol. 12409, pp. 1–9, 2016.

[43] S. A. Jewell, P. Vukusic, and N. W. Roberts, "Circularly polarized colour reflection from helicoidal structures in the beetle Plusiotis boucardi," *New J. Phys.*, vol. 9, no. 99, pp. 1–10, Apr. 2007.

[44] L. Fernández del Río, "An Investigation of the Polarization States of Light Reflected from Scarab Beetles of the Chrysina Genus - BSc Thesis," Linköpings University, 2011.

[45] W. E. Vargas, M. Hernández-Jiménez, E. Libby, D. E. Azofeifa, Á. Solis, and C. Barboza-Aguilar, "Broadening of effective photonic band gaps in biological chiral structures: From intrinsic narrow band gaps to broad band reflection spectra," *EPL (Europhysics Lett.*, vol. 111, no. 64001, pp. 1–6, 2015.

[46] W. E. Vargas, M. Hernández-Jiménez, E. Libby, D. E. Azofeifa, C. Barboza, and Á. Solis, "Light Reflection by Cuticles of Chrysina Jewel Scarabs: Optical Measurements, Morphology Characterization, and Theoretical Modeling," *Opt. Photonics J.*, vol. 6, no. 7, pp. 146–163, 2016.

[47] C. Campos-Fernández, D. E. Azofeifa, M. Hernández-Jiménez, A. Ruiz-Ruiz, and W. E. Vargas, "Visible light reflection spectra from cuticle layered materials," *Opt. Mater. Express*, vol. 1, no. 1, pp. 85–100, Apr. 2011.

[48] E. Libby, D. E. Azofeifa, M. Hernández-Jiménez, C. Barboza-Aguilar, A. Solís, I. García-Aguilar, L. Arce-Marenco, A. Hernández, and W. E. Vargas, "Light reflection by the cuticle of C. aurigans scarabs: a biological broadband reflector of left handed circularly polarized light," *J. Opt.*, vol. 16, no. 82001, pp. 1–7, Aug. 2014.

[49] M. Hernández-Jiménez, D. E. Azofeifa, E. Libby, C. Barboza-Aguilar, Á. Solís, L. Arce-Marenco, I. García-Aguilar, A. Hernández, and W. E. Vargas, "Qualitative correlation between structural chirality through the cuticle of Chrysina aurigans scarabs and left-handed circular polarization of the reflected light," *Opt. Mater. Express*, vol. 4, no. 12, pp. 2632–45, Nov. 2014.

[50] D. E. Azofeifa, M. Hernández-Jiménez, E. Libby, A. Solís, C. Barboza-Aguilar, and W. E. Vargas, "A quantitative assessment approach of feasible optical mechanisms contributing to structural color of golden-like Chrysina aurigans scarab beetles," *J. Quant. Spectrosc. Radiat. Transf.*, vol. 160, pp. 63–74, Jul. 2015.

[51] V. Sharma, M. Crne, J. O. Park, and M. Srinivasarao, "Structural origin of circularly polarized iridescence in jeweled beetles," *Science*, vol. 325, no. 5939, pp. 449–51, Jul. 2009.

[52] P. Brady and M. Cummings, "Differential response to circularly polarized light by the jewel scarab beetle Chrysina gloriosa," *Am. Nat.*, vol. 175, no. 5, pp. 614–20, May 2010.

[53] L. Fernández del Río, H. Arwin, and K. Järrendahl, "Polarizing properties and structural characteristics of the cuticle of the scarab Beetle Chrysina gloriosa," *Thin Solid Films*, vol. 571, pp. 410–415, Nov. 2014.

[54] V. Sharma, M. Crne, J. O. Park, and M. Srinivasarao, "Bouligand Structures Underlie Circularly Polarized Iridescence of Scarab Beetles: A Closer View," *Mater. Today Proc.*, vol. 1, pp. 161–171, 2014.

[55] G. Agez, C. Bayon, and M. Mitov, "Multiwavelength micromirrors in the cuticle of scarab beetle Chrysina gloriosa," *Acta Biomater.*, vol. 48, pp. 357–367, Jan. 2017.

[56] A. Pace, "Cholesteric Liquid Crystal-Like Structure of the Cuticle of Plusiotis gloriosa," *Science (80-.).*, vol. 176, no. 4035, pp. 678–80, May 1972.

[57] L. McDonald, E. Finlayson, and P. Vukusic, "Untwisting the polarization properties of light reflected by scarab beetles," *SPIE BiOS*, vol. 9341, pp. 1–7, 2015.

[58] A. Michelson, "On metallic colouring in birds and insects," *Philos. Mag.*, vol. 21, pp. 618–623, 1911.

[59] E. D. Finlayson, L. T. McDonald, and P. Vukusic, “Optically ambidextrous circularly polarized reflection from the chiral cuticle of the scarab beetle Chrysina resplendens,” *J. R. Soc. Interface*, vol. 14, no. 131, 2017.

[60] S. Lowrey, C. Fraser, J. Leader, and I. Hodgkinson, “Colour and polarization signatures of Southland chafer beetles,” *ento.org.nz*, vol. 27, pp. 23–27, 2010.

[61] I. J. Hodgkinson, L. De Silva, P. Murray, Q. H. Wu, M. Arnold, and J. P. Leader, “Modeling optical reflectance from chiral micromirrors embedded in manuka beetles,” in *Proceedings of SPIE*, 2004, vol. 5509, pp. 15–23.

[62] L. De Silva, I. Hodgkinson, P. Murray, Q. H. Wu, M. Arnold, J. Leader, and A. Mcnaughton, “Natural and Nanoengineered Chiral Reflectors: Structural Color of Manuka Beetles and Titania Coatings,” *Electromagnetics*, vol. 25, no. 5, pp. 391–408, Jul. 2005.

[63] G. Yao and L. V Wang, “Two-dimensional depth-resolved Mueller matrix characterization of biological tissue by optical coherence tomography,” *Opt. Lett.*, vol. 24, pp. 537–539, 1999.

[64] Thorlabs, “Full-Wave Liquid Crystal Variable Retarders.” [Online]. Available: https://www.thorlabs.com/newgrouppage9.cfm?objectgroup_id=6339. [Accessed: 04-Dec-2015].